Transactions of the ASME®

Technical Editor
ARTHUR J. WENNERSTROM
Senior Associate Technical Editor
G. K. SEROVY
Associate Technical Editors
Advanced Energy Systems
M. J. MORAN
Environmental Control
H. E. HESKETH
Fuels and Combustion Technologies
R. E. BARRETT
Gas Turbine
T. H. OKIISHI
Internal Combustion Engine
J. A. CATON
Nuclear Engineering
S. M. CHO
Power
R. W. PORTER

BOARD ON COMMUNICATIONS
Chairman and Vice-President
R. NICKELL

Members-at-Large
J. LLOYD
R. REDER
F. SCHMIDT
M. FRANKE
M. KUTZ
T. MIN
F. LANDIS
R. ROCKE
W. WINER
R. GENTILE
R. MATES

President, E. L. DAMAN
Executive Director,
D. L. BELDEN
Treasurer, ROBERT A. BENNETT

PUBLISHING STAFF
Mng. Dir., Publ., JOS. SANSONE
Managing Editor,
CORNELIA MONAHAN
Sr. Production Editor,
VALERIE WINTERS
Editorial Prod. Asst.
MARISOL ANDINO

Transactions of the ASME, Journal of Engineering for Gas Turbines and Power (ISSN 0022-0825) is published quarterly (Jan., Apr., July, Oct.,) for $95 per year by The American Society of Mechanical Engineers, 345 East 47th Street, New York, NY 10017. Second class postage paid at New York, NY and additional mailing offices. POSTMASTER: Send address change to The Journal of Engineering for Gas Turbines and Power, c/o The AMERICAN SOCIETY OF MECHANICAL ENGINEERS, 22 Law Drive, Box 2300, Fairfield, NJ 07007-2300.
CHANGES OF ADDRESS must be received at Society headquarters seven weeks before they are to be effective. Please send old label and new address.
PRICES: To members, $27.00, annually; to nonmembers, $95.00.
Add $12.00 for postage to countries outside the United States and Canada.
STATEMENT from By-Laws. The Society shall not be responsible for statements or opinions advanced in papers or ... printed in its publications (B 7.1, para. 3).
COPYRIGHT © 1988 by the American Society of Mechanical Engineers. Reprints from this publication may be made on condition that full credit be given the TRANSACTIONS OF THE ASME—JOURNAL OF ENGINEERING FOR GAS TURBINES AND POWER, and the author, and date of publication be stated.
INDEXED by Applied Mechanics Reviews and Engineering Information, Inc.

Journal of Engineering for Gas Turbines and Power

Published Quarterly by The American Society of Mechanical Engineers
VOLUME 110 • NUMBER 3 • JULY 1988

TECHNICAL PAPERS

313 A Nonlinear Controller Design Method for Fuel-Injected Automotive Engines (87-ICE-43)
D. Cho and J. K. Hedrick

321 Optimizing Engine Operation by Monitoring the Working Gas Pulsations (87-ICE-45)
S. D. Haddad and C. Cempel

325 Advanced Real-Time Powertrain Systems Analysis (87-ICE-46)
B. K. Powell, G. P. Lawson, and G. Hogh

334 A Natural Gas Engine Combustion Rig With High-Speed Photography
W. E. Snyder, M. R. Wright, and S. G. Dexter

343 Improvement of Emissions From Diesel Engines
T. Morimatsu, T. Okazaki, T. Furuya, and H. Furukawa

349 Pielstick Experience With Dual-Fuel Engines and Cogeneration
G. Grosshans and M. Litzler

356 A Rankine Bottoming Cycle System for Heavy-Duty Applications
R. A. Cemenska

361 Experimental Investigation of Electrostatic Dispersion and Combustion of Diesel Fuel Jets
C. P. Bankston, L. H. Back, E. Y. Kwack, and A. J. Kelly

369 Simulation of the Gas Exchange Process of a Two-Stroke Cycle Gasoline Engine
K. Sato and M. Nakano

377 Studies on Combustion, Vibration, and Noise in High-Speed Diesel Engines Through Newly Developed Measuring Instruments (88-ICE-1)
S. Izumi, M. Takemi, M. Ishida, H. Suetsugu, T. Maeda, and Y. Yoshimura

385 Efficient and Low-Smoke Combustion of Various Low-Grade Fuels in High-Speed Small Diesel Engines (88-ICE-2)
T. Murayama, N. Miyamoto, T. Chikahisa, and S. Tosaka

393 Behavior of Band Spectra in Diesel Combustion Flames: a Study on Chemical Reactions in Diesel Combustion (88-ICE-3)
K. Nagase and K. Funatsu

399 Self-Ignition of Diesel Sprays and Its Dependence on Fuel Properties and Injection Parameters (88-ICE-14)
F. Pischinger, U. Reuter, and E. Scheid

405 A Dynamic Model of a Locomotive Diesel Engine and Electrohydraulic Governor (88-ICE-26)
C. I. Rackmil, P. N. Blumberg, D. A. Becker, R. R. Schuller, and D. C. Garvey

415 Progress on the Investigation of Coal-Water Slurry Fuel Combustion in a Medium Speed Diesel Engine: Part 1—Ignition Studies (88-ICE-4)
B. D. Hsu

423 Progress on the Investigation of Coal-Water Slurry Fuel Combustion in a Medium Speed Diesel Engine: Part 2—Preliminary Full Load Test (88-ICE-5)
B. D. Hsu

431 Operating Results of the Cooper-Bessemer JS-1 Engine on Coal-Water Slurry
A. K. Rao, C. H. Melcher, R. P. Wilson, Jr., E. N. Balles, F. S. Schaub, and J. A. Kimberley

437 Coal-Water Slurry Operation in an EMD Diesel Engine (88-ICE-28)
C. M. Urban, H. E. Mecredy, T. W. Ryan, III, M. N. Ingalls, and B. T. Jett

444 Experiments With Coal Fuels in a High-Temperature Diesel Engine (88-ICE-29)
W. E. Likos and T. W. Ryan, III

453 Effects of Fuel Overpenetration and Overmixing During Ignition-Delay Period on Hydrocarbon Emissions From a Small Open-Chamber Diesel Engine
T.-W. Kuo, K.-J. Wu, and S. Henningsen

462 The Application of Availability and Energy Balances to a Diesel Engine
A. C. Alkidas

470 A Study of Cylinder-to-Cylinder Distribution of Charge in a Six Cylinder Spark Ignition Engine
W. A. Woods and O. K. Sag

475 Promises and Challenges of the Low-Heat-Rejection Diesel
C. A. Amann

482 Heat Transfer With Insulated Combustion Chamber Walls and Its Influence on the Performance of Diesel Engines
G. Woschni and W. Spindler

(Contents continued on page 562)

Downloaded 03 Jun 2010 to 171.66.16.159. Redistribution subject to ASME license or copyright; see http://www.asme.org/terms/Terms_Use.cfm

(Contents Continued)

503 A Steady-State Air Motion Study in a V-6 Uniflow Scavenged Two-Stroke Diesel Engine
T. D. Doan, E. F. Crawford, and S. J. Hinkle

509 The Effect of Inlet Velocity Distribution and Magnitude on In-Cylinder Turbulence Intensity and Burn Rate—Model Versus Experiment
G. C. Davis and R. J. Tabaczynski

515 Study of the Steady-State Flow Pattern in a Multipulse Converter by LDA
P. Flamang and R. Sierens

523 The Effects of Engine Speed on the Scavenging Characteristics of a Two-Cycle Engine
T. Uzkan

531 A Three-Zone Scavenging Model for Two-Stroke Uniflow Engines
N. P. Kyrtatos and I. Koumbarelis

538 Mathematical Modeling of the Scavenging Process in a Two-Stroke Diesel Engine
A. Carapanayotis and M. Salcudean

547 The Matching of Diesel Engine to Exhaust Turbocharger—Improved Calculation Model at T-Junction
T. Morimune and N. Hirayama

556 Flow Field Surveys at the Rotor Inlet of a Radial Inflow Turbine
E. C. Miller, M. R. L'Ecuyer, E. F. Benisek

ANNOUNCEMENTS

324 Change of address form for subscribers

562 Errata on a previously published paper by
D. E. Brandt

Inside back cover Information for authors

Downloaded 03 Jun 2010 to 171.66.16.159. Redistribution subject to ASME license or copyright; see http://www.asme.org/terms/Terms_Use.cfm

A Nonlinear Controller Design Method for Fuel-Injected Automotive Engines

D. Cho
Assistant Professor,
Department of Mechanical and Aerospace Engineering,
Princeton University,
Princeton, NJ 08544

J. K. Hedrick
Professor,
Department of Mechanical Engineering,
University of California,
Berkeley, CA 94720

A nonlinear, "sliding mode" fuel-injection controller is designed based on a physically motivated, mathematical engine model. The designed controller can achieve a commanded air-to-fuel ratio with excellent transient properties, which offers the potential for improving fuel economy, torque transients, and emission levels. The controller is robust to model errors as well as to rapidly changing maneuvers of throttle and spark advance. The sliding mode control method offers a great potential for future engine control problems, since: it results in a relatively simple control structure that requires little on-line computing and no table lookups; it is robust to model errors and disturbances; and it can be easily adapted to a family of engines.

1 Introduction

An engine needs to operate smoothly, from an idle speed of several hundred rpm to its maximum speed of thousands of rpm, under varying inertial loads and disturbance forces as well as constantly varying throttle commands by the driver. In addition to the wide operating range, the inherent nonlinearities of the induction process and the cyclic nature of the torque production process make the design of a closed-loop fuel-injection controller a nontrivial task. However, stringent emission, fuel economy, and performance requirements make it a must.

Current fuel-injection controllers rely heavily on open-loop lookup tables stored in the on-board microprocessor, along with a PI control using oxygen sensor output from the exhaust manifold [1]. However, the lengthy, delicate calibration procedures required to create the lookup tables and to "tune" the controller make this method undesirable.

Other well-known linear control techniques such as LQR, pole placement, and LQG/LTR [2] can be applied to obtain a "robust" fuel-injection controller. However, the limited validity of linearized perturbation equations requires many local linearizations (including those at nonequilibrium), and leads to elaborate "gain scheduling." Since the "schedule" must be carefully established for different engines and operating conditions, this technique has little advantage over the current method.

In order to overcome the limitations of linear control methods, the "sliding mode" control method [3, 4] is proposed in this paper as a means of designing a closed-loop fuel-injection system. The subsequent sections discuss: the engine model used in the control design, the control objective, the motivation for using the sliding mode control method, and the closed-loop design for a fuel-injection system. The basics of the sliding mode control are also included in the Appendix.

Contributed by the Internal Combustion Engine Division and presented at the Energy-Sources Technology Conference and Exhibition, Dallas, Texas, February 15-20, 1987. Manuscript received by the Internal Combustion Engine Division November 1986. Paper No. 87-ICE-43.

2 Two-State Engine Model

For the purpose of developing and evaluating a fuel-injection controller, a two-state, continuous-time-domain engine model was developed, based on a more comprehensive, discrete-time-domain model by Dobner [5]. The inherent nonlinearities of the induction and the torque production processes were preserved in this simple, two-state model. Also, the cyclic nature of the SI engine is represented via time delays. Figure 1 depicts the schematic of the two-state model.

The first state is the mass of air in the intake manifold, $m_a(t)$, which is obtained by considering the conservation of mass as [5]

$$\dot{m}_a(t) = \dot{m}_{ai}(t) - \dot{m}_{ao}(t) \tag{1}$$

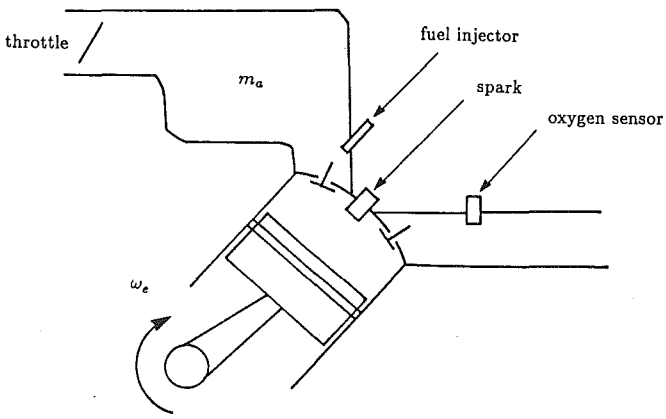


Fig. 1 Schematic of two-state engine model

Copyright © 1988 by ASME
Downloaded 01 Jun 2010 to 171.66.16.87. Redistribution subject to ASME license or copyright; see http://www.asme.org/terms/Terms_Use.cfm

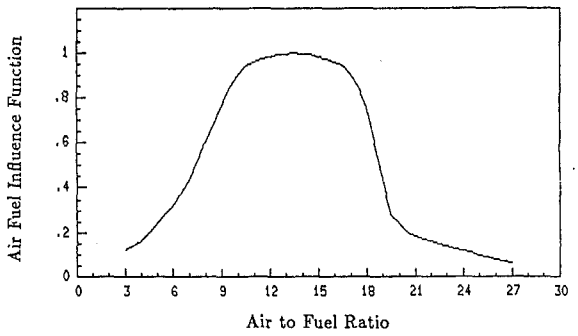


Fig. 2 Air fuel influence function (adapted from [5])

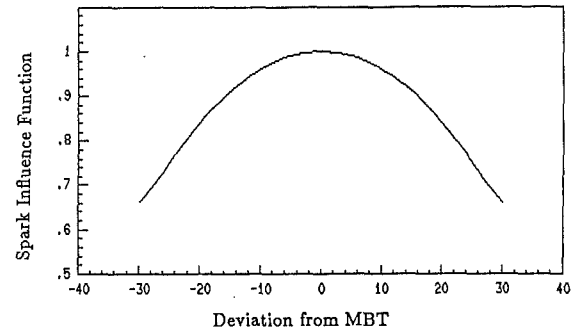


Fig. 3 Spark influence function (adapted from [5])

The mass flow rate of air entering the intake manifold $\dot{m}_{ai}(t)$ is

$$\dot{m}_{ai}(t) = k_1 \cdot TC(t) \cdot PRI(t) \tag{2}$$

where the normalized throttle characteristics $TC(t)$ are modeled as

$$TC(t) = 1 - \cos(k_2 \cdot \alpha(t) - k_3), \quad \alpha(t) = \text{throttle angle in deg} \tag{3}$$

and the choked flow characteristics through the throttle body $PRI(t)$ are modeled as

$$PRI(t) = 1 - \exp^{(2808 \cdot m_a(t) - 9)} \tag{4}$$

The mass flow rate of air leaving the manifold $\dot{m}_{ao}(t)$ is

$$\dot{m}_{ao}(t) = k_4 \cdot \eta_{\text{vol}}(t) \cdot m_a(t) \cdot \omega_e(t) \tag{5}$$

where the volumetric efficiency $\eta_{\text{vol}}(t)$ is modeled as

$$\eta_{\text{vol}}(t) = m_a^2(t)[k_5\omega_e(t) + k_6] + m_a(t)[k_7\omega_e(t) + k_8] + [k_9\omega_e(t) + k_{10}] \tag{6}$$

The second state is the engine speed $\omega_e(t)$, which models the rotational dynamics as [5]

$$I_{\text{eff}} \cdot \dot{\omega}_e(t) = T_{\text{ind}}(t) - T_{\text{fric}}(t) - T_{\text{aero}}(t) - T_{\text{roll}}(t) - T_{\text{dist}}(t) \tag{7}$$

where the indicated torque $T_{\text{ind}}(t)$ is

$$T_{\text{ind}}(t) = k_{11} \cdot \frac{\dot{m}_{ao}(t - \Delta t_{it})}{\omega_e(t - \Delta t_{it})} \cdot AFI(t - \Delta t_{it}) \cdot SI(t - \Delta t_{st}) \tag{8}$$

The engine friction torque $T_{\text{fric}}(t)$ is

$$T_{\text{fric}}(t) = k_{12} + k_{13} \cdot \omega_e(t) \tag{9}$$

The aerodynamic drag term lumped to the rotational dynamics, $T_{\text{aero}}(t)$, is

$$T_{\text{aero}}(t) = k_{14} \cdot \omega_e^2(t) \tag{10}$$

The rolling friction term lumped to the rotational dynamics, $T_{\text{roll}}(t)$, is

$$T_{\text{roll}}(t) = k_{15} \tag{11}$$

and I_{eff} is the effective rotational inertia, which includes the vehicle mass reflected through the tires and transmission. In equation (8), $AFI(t)$ is a normalized air fuel influence function through which the air-to-fuel ratio at the intake runners affects the torque production, and $SI(t)$ is a normalized spark influence function through which the spark retard (or advance) at the time of combustion affect the torque production. Figure 2 shows a typical air fuel influence function as a function of air-to-fuel ratio, and Fig. 3 shows a typical spark influence function as a function of the deviation in spark angle from *MBT* (i.e., minimum spark advance for best torque) in deg. Note that the torque production at time (t) is determined by the engine speed and the mass of air in the intake manifold at time ($t - \Delta t_{it}$) as well as the air-to-fuel ratio at time ($t - \Delta t_{it}$) and the spark advance at time ($t - \Delta t_{st}$). The intake to torque production time delay, Δt_{it}, and the spark-to-torque production time delay, Δt_{st}, are modeled as

$$\Delta t_{it} \approx \frac{5.5}{\omega_e} \text{ and } \Delta t_{st} \approx \frac{1.3}{\omega_e}$$

Table 1 Powertrain parameters

Symbol	Numerical value
k_1	0.1843 kg•s^{-1}
k_2	1.1980
k_3	1.720 deg
k_4	0.1030
k_5	24.5 kg^{-2}•s
k_6	-3.10×10^4kg^{-2}
k_7	-0.167 kg^{-1}•s
k_8	222.0 kg^{-1}
k_9	8.10×10^{-4} s
k_{10}	0.3524
k_{11}	1.0451×10^6 N•m•kg^{-1}
k_{12}	15.0 N•m
k_{13}	0.107 N•m•s
k_{14}	6.339×10^{-4} N•m•s^2
k_{15}	6.129 N•m
I_{eff}	2.675 kg•m^2

The constants k_1 through k_{15} and I_{eff} in equations (1) through (11) need to be determined empirically for different engines. Table 1 lists the parameters used in this study, which are typical of a midsized vehicle in first gear.

Although many states (such as exhaust pressure, EGR, transmission states, driveline states, etc.) are not included, the simple, two-state model predicts the inherent dynamic behavior (such as response to throttle, hesitation, peak torque, etc.) quite well, when compared to more complete models [5]. Some parts of the model have been experimentally validated [6], and an extensive experimental program is currently underway for the complete engine model validation.

Due to the continuous approximation of the combustion model, $\dot{m}_{ao}(t)/\dot{m}_{fi}(t)$ is used instead of the integrated rates, which is the actual air-to-fuel ratio in the combustion chamber. The integration of $\dot{m}_{ao}(t)/\dot{m}_{fi}(t)$ is not a trivial task due to valve overlap and backflow phenomenon at the intake port. However, since the cylinder contents are exhausted at the end of each cycle and a new cycle begins with a fresh charge, we feel that $\dot{m}_{ao}(t)/\dot{m}_{fi}(t)$ is an adequate model for the air-to-fuel ratio, and throughout this paper, $\dot{m}_{ao}(t)/\dot{m}_{fi}(t)$ is referred to as the air-to-fuel ratio.

The output, air-to-fuel ratio, is measured at the *exhaust* using an oxygen sensor. Thus, the output measurement is delayed by at least two revolutions as well as by the amount of sensor delay. A typical oxygen sensor, which responds to the variations in the exhaust gas composition, outputs a high voltage for richer than stoichiometric mixtures, and a low voltage for leaner than stoichiometric mixtures. During the transition from high to low voltage, the output voltage exhibits a linear range (for more detailed discussions, see [7, 8]).

Downloaded 01 Jun 2010 to 171.66.16.87. Redistribution subject to ASME license or copyright; see http://www.asme.org/terms/Terms_Use.cfm

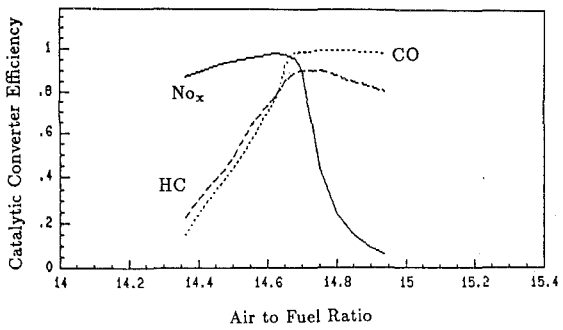


Fig. 4 A typical catalytic converter efficiency (adapted from [7])

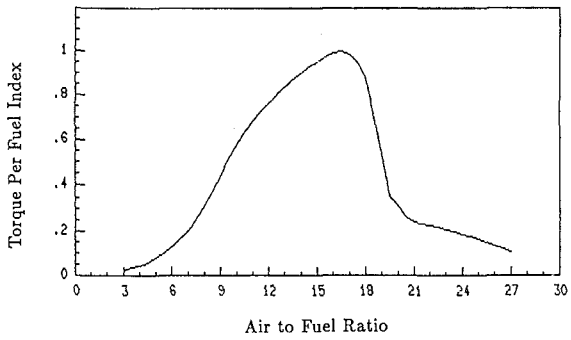


Fig. 5 Torque per fuel index

However, the linear band is very narrow and the operation can be affected by the temperature, age, and cleanliness of the sensor. Thus, for this study, the oxygen sensor is modeled to have a binary output voltage.

3 Control Objective

A fuel-injection controller needs to monitor the air-to-fuel ratio tightly in order to achieve:

- good emission characteristics
- smooth torque production
- maximum fuel economy

Figure 4 shows a typical catalytic converter efficiency as a function of the air-to-fuel ratio. It is seen that carbon monoxide and hydrocarbons are converted better at leaner mixtures, whereas the NO_x compounds are converted better at richer mixtures. The best tradeoff for overall efficiency is at the air-to-fuel ratio of 14.7 (i.e., stoichiometric ratio), and any deviation from that causes a substantial degradation of the conversion efficiency of one or more pollutants.

It is evident from the air fuel influence function depicted in Fig. 2 that the best engine torque can be attained at the air-to-fuel ratio of 13.5, which is approximately 8.2 percent richer than the stoichiometric mixture. However, for deviations of up to ± 2.0 from 13.5 in the air-to-fuel ratio, the air fuel influence function is maintained to within ± 3 percent of its maximum. For deviations greater than ± 2.0 from 13.5, the torque production efficiency starts to deteriorate substantially, falling below the 50 percent level for ± 5.0 deviation. Thus, the air-to-fuel ratio needs to be maintained between 11.5 and 15.5 for smooth torque production and hence, good drivability.

Figure 5 shows the index of torque produced per fuel consumed. This index is a measure of fuel economy, which was devised for this study and was computed from the air fuel influence function depicted in Fig. 2. That is, consider an amount of air, $\delta m_{ac}(t)$, and an amount of fuel, $\delta m_{fc}(t)$, in a cylinder at the time of torque production (t). The air-to-fuel ratio may be written as

$$\frac{A}{F}(t) = \frac{\delta m_{ac}(t)}{\delta m_{fc}(t)} = \phi(t) \tag{12}$$

For the spark advance fixed at *MBT*, the torque produced may be written as

$$T_{\text{ind}}(t) = k_{11} \cdot \delta m_{ac}(t) \cdot AFI(t) \mid_{\phi(t)} \tag{13}$$

Therefore, from equations (12) and (13), the torque produced per fuel consumed is

$$\frac{T_{\text{ind}}(t)}{\delta m_{fc}(t)} = k_{11} \cdot \phi(t) \cdot AFI(t) \mid_{\phi(t)} \tag{14}$$

For the air fuel influence function depicted in Fig. 2, the torque produced per fuel consumed is computed to be at its maximum when the air-to-fuel ratio is 16.7. Thus, define the torque per fuel index by normalizing equation (14) as

$$\eta_f = \frac{\phi(t) \cdot AFI(t) \mid_{\phi(t)}}{16.7 \cdot AFI(t) \mid_{16.7}} \tag{15}$$

Interestingly, this torque per fuel index deteriorates much faster for a *leaner* deviation from 16.7 than a *richer* deviation. This is illustrated in Fig. 5. Note that the air-to-fuel ratio of 16.7, which gives the maximum torque per fuel index of 1, is approximately 13.6 percent leaner than the stoichiometric mixture.

Clearly, the above criteria for determining the best air-to-fuel ratio represent a conflict. However, an air-to-fuel ratio of 14.7 ± 0.2 represents an excellent tradeoff. That is, at stoichiometry, the overall catalytic converter efficiency is at its maximum, the air fuel influence function is better than 98 percent of its maximum, and the torque per fuel index is better than 97 percent of its maximum. In addition, this coincides with the operating characteristics of current state-of-the-art oxygen sensors. Thus, the objective of a closed-loop fuel-injection controller, discussed in the following sections, is to maintain the air-to-fuel ratio within ± 0.2 or ± 1.4 percent of stoichiometric.

4 "Sliding Mode" Control

When designing a closed-loop controller, one most often evaluates the possibility of using a linear control method. In order to apply linear control techniques, the plant must be reasonably linear. The engine model, which is described in the continuous-time domain in equations (1)-(11), is extremely nonlinear. The resulting linearized perturbation equations are valid only for a very limited range of operating conditions, which leads to very elaborate gain scheduling. Since this must be done for different engines, the method does not lead to the development of a "generic" engine control methodology.

The sliding mode control method [3, 4] has recently been developed as an alternative to linear control methods in a number of application areas such as robotics and power plant control. It is a nonlinear controller design method that is directly applicable to a set of nonlinear dynamic equations and directly considers the robustness to model errors and disturbance uncertainties in the design process. These features make this method highly desirable for designing a closed-loop fuel-injection controller. The essentials of sliding mode control theory are included in the Appendix.

In this section, the sliding mode controller is designed for the two-state model discussed in Section 2. The control is formulated to be robust to possible model errors and disturbance uncertainties. The controller design and performance evaluations are divided into two parts. First in Section 4.1, the control is formulated assuming the air-to-fuel ratio can be measured without a time delay; however, the binary nature of the air-to-fuel ratio measurement is assumed. Then, in Section 4.2, the use of a current state-of-the-art oxygen sensor is considered. Also, the stability robustness issues of the sliding

Downloaded 01 Jun 2010 to 171.66.16.87. Redistribution subject to ASME license or copyright; see http://www.asme.org/terms/Terms_Use.cfm

mode controller associated with the time delayed feedback are also discussed in Section 4.2.

4.1 Oxygen Sensor Measurement Without Time Delay. As defined in Section 3, the objective of the control design is to keep the air-to-fuel ratio at 14.7 with a very arduous transient specification of maintaining the ratio between 14.5 and 14.9 at all times. That is

$$\frac{\dot{m}_{ao}(t)}{\dot{m}_{fi}(t)} = 14.7 \pm 0.2 \text{ for } t \geq 0 \tag{16}$$

where $\dot{m}_{ao}(t)$ is the mass flow rate of air leaving the intake manifold or entering the cylinders, and $\dot{m}_{fi}(t)$ is the mass flow rate of fuel entering the cylinders. The dynamics of the fuel-injection mechanism is modeled as

$$\tau_f \cdot \ddot{m}_{fi}(t) + \dot{m}_{fi}(t) = \dot{m}_{fc}(t) \tag{17}$$

where $\dot{m}_{fc}(t)$ is the fuel commanded at the injector, and τ_f is the time constant of injection mechanism.

It is possible to design an open loop control by solving equations (16) and (17) for the control $\dot{m}_{fc}(t)$. However, the model for $\dot{m}_{ao}(t)$ in equation (5) can contain errors such that

$$\dot{m}_{ao}(t)\,|_{\text{ACTUAL}} = (1+\gamma(t)) \cdot \dot{m}_{ao}(t)\,|_{\text{MODEL}} \tag{18}$$

In addition, the model for the fuel-injection mechanism can have errors such that

$$\tau_f\,|_{\text{ACTUAL}} = (1+\delta(t)) \cdot \tau_f\,|_{\text{MODEL}} \tag{19}$$

With these errors, the open-loop control cannot maintain the air-to-fuel ratio at the desired level of 14.7 ± 0.2.

The sliding mode control method can take these factors directly into consideration in the design. Since the design objective is to keep the air-to-fuel ratio at 14.7, let the surface $S(t)$ be defined as

$$S(t) \equiv \dot{m}_{ao}(t)\,|_{\text{ACTUAL}} - \beta \cdot \dot{m}_{fi}(t)\,|_{\text{ACTUAL}} \tag{20}$$

where $\beta = 14.7$, and the control objective is $S(t) \to 0$. The surface defined by $S(t) = 0$ can be guaranteed to be stable and "attractive" if the condition

$$S(t) \cdot \frac{dS(t)}{dt} < 0 \tag{21}$$

can be satisfied. If the control is formulated to satisfy equation (21), the magnitude of $S(t)$ will decrease and go to zero. We satisfy equation (21) by defining

$$\frac{dS(t)}{dt} \equiv -\eta \cdot \text{sgn}(S(t)), \qquad \eta > 0 \tag{22}$$

Equation (22) assures that the system will reach the surface $S(t) = 0$ in finite time. The time to reach the sliding surface, t_r, can be computed by integrating $dS(t)/dt$ and solving for $S(t_r) = 0$ as

$$\int_0^{t_r} -\eta \cdot \text{sgn}(S(t)) \cdot d\tau = -S(0) \Rightarrow t_r = \frac{|S(0)|}{\eta}$$

Once the system "reaches" $S(t) = 0$, the closed-loop dynamics will "slide" or "chatter" along $S(t) = 0$, for $t > t_r$.

Differentiating equation (20) and substituting into equation (22), we obtain

$$\ddot{m}_{ao}(t)\,|_{\text{ACTUAL}} - \beta \cdot \ddot{m}_{fi}(t)\,|_{\text{ACTUAL}} = -\eta \cdot \text{sgn}(S(t)) \tag{23}$$

Then, differentiating equation (18) and substituting the result with equations (17) and (19) into equation (23), we obtain the following control law

$$\dot{m}_{fc}(t) = \dot{m}_{fi}(t) + \frac{\tau_f\,|_{\text{MODEL}}}{\beta} \cdot \ddot{m}_{ao}(t)\,|_{\text{MODEL}} + \frac{\tau_f\,|_{\text{MODEL}}}{\beta} \cdot \Big[\Big(\gamma(t) + \delta(t) + \gamma(t) \cdot \delta(t) \Big) \cdot \ddot{m}_{ao}(t)\,|_{\text{MODEL}} + (1+\delta(t)) \cdot \dot{\gamma}(t) \cdot \dot{m}_{ao}(t)\,|_{\text{MODEL}} + \eta \cdot \text{sgn}(S(t)) \Big] \tag{24}$$

where

$$\ddot{m}_{ao}(t)\,|_{\text{MODEL}} = \frac{\partial \dot{m}_{ao}(t)\,|_{\text{MODEL}}}{\partial m_a} \cdot \dot{m}_a + \frac{\partial \dot{m}_{ao}(t)\,|_{\text{MODEL}}}{\partial \omega_e} \cdot \dot{\omega}_e \tag{25}$$

Equation (24) does not represent the final control law as yet, since the errors, $\gamma(t)$, $\delta(t)$, and $\dot{\gamma}(t)$, are not known exactly. However, careful modeling can give an upper bound for the imprecisions as

$$|\gamma(t)| < \gamma_{\max} \qquad |\delta(t)| < \delta_{\max} \quad \text{and} \quad |\dot{\gamma}(t)| < \dot{\gamma}_{\max} \tag{26}$$

Then, assuming the worst possible scenario of error combinations, the following control law may be obtained:

$$\dot{m}_{fc}(t) = \dot{m}_{fi}(t) + \frac{\tau_f\,|_{\text{MODEL}}}{\beta} \cdot [\ddot{m}_{ao}(t) + \kappa \cdot \text{sgn}(S(t))] \tag{27}$$

where

$$\kappa \geq (\gamma_{\max} + \delta_{\max} + \gamma_{\max} \cdot \delta_{\max}) \cdot (\ddot{m}_{ao}(t)\,|_{\text{MODEL}})_{\max} + (1+\delta_{\max}) \cdot \dot{\gamma}_{\max} \cdot (\dot{m}_{ao}(t)\,|_{\text{MODEL}})_{\max} \tag{28}$$

which is *robust* to the model errors, provided an upper bound can be found for the errors as specified in equation (26).

This control law leads to a "chattering" solution around $S(t) = 0$. The chatter magnitude is proportional to the robustness parameter κ; however, for a small κ, the transients become slow. The tradeoff problem between the chatter magnitude and the transient characteristics can be improved by the use of a *boundary layer* [4]; however, this method requires the knowledge of both the magnitude and the sign of $S(t)$. The oxygen sensor output can be used to obtain the sign of $S(t)$, since $S(t) > 0$ represents a lean air-to-fuel ratio and $S(t) < 0$ represents a rich air-to-fuel ratio, but the magnitude of $S(t)$ is unavailable. Thus, we take full advantage of the fact that the magnitude of $\ddot{m}_{ao}(t)$ becomes very large during transients and diminishes to zero in steady state, to improve the tradeoff problem as follows:

$$\kappa(t) = (\gamma_{\max} + \delta_{\max} + \gamma_{\max} \cdot \delta_{\max}) \cdot \left| \ddot{m}_{ao}(t)\,|_{\text{MODEL}} \right| + (1+\delta_{\max}) \cdot \dot{\gamma}_{\max} \cdot \dot{m}_{ao}(t)\,|_{\text{MODEL}} \tag{29}$$

Equation (27), with the robustness parameter $\kappa(t)$ as defined by equation (29), constitutes the sliding mode fuel-injection control, which is guaranteed to be robust to modeling errors, provided an upper bound can be found for the imprecisions. In addition, the designed control is robust to disturbances, such as varying throttle, spark influence, and load torque, since these terms do not appear in the control formulation.

In the control formulation so far, it was assumed that the sign of $S(t)$ can be obtained from the oxygen sensor output. In reality, the oxygen sensor output is delayed by at least 2 revolutions. However, let us first examine the performance of the sliding mode controller, assuming that the sign of $S(t)$ is available without a time delay.

For the performance evaluation of the designed sliding mode controller, the throttle was changed as shown in Fig. 6 to simulate a stop-and-go situation typical of an "EPA city cycle" test, the spark was retarded as shown in Fig. 7 to simulate a possible "torque droop" during shifts, and the disturbance torque was introduced as shown in Fig. 8 to include possible accessory torques.

The model errors in $\dot{m}_{ao}(t)$ and τ_f were also introduced in the performance evaluation. Since we do not know these errors exactly, errors of the following form were used to show the robustness characteristics of the controller to severe errors:

$$\gamma(t) \equiv -0.3 \sin(2\pi t) \text{ and } \delta(t) \equiv 0.3 \sin(2\pi t) \tag{30}$$

Equation (30) represents ± 30 percent errors with relatively fast frequencies in both the intake process model and the in-

Downloaded 01 Jun 2010 to 171.66.16.87. Redistribution subject to ASME license or copyright; see http://www.asme.org/terms/Terms_Use.cfm

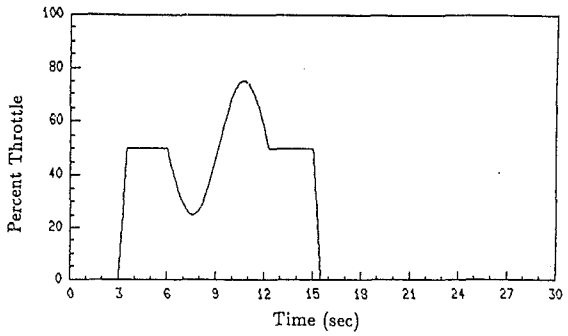


Fig. 6 Percent throttle changes

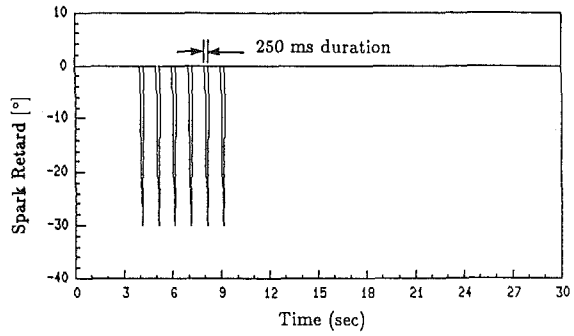


Fig. 7 Spark retard changes

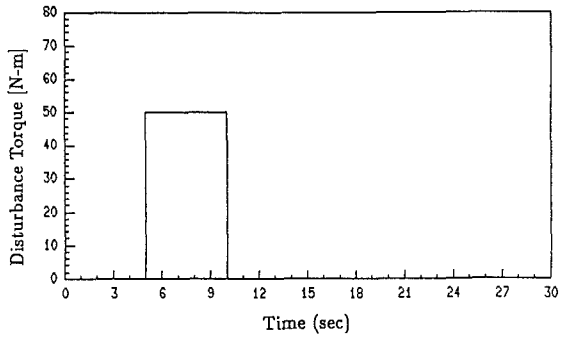


Fig. 8 Disturbance torque

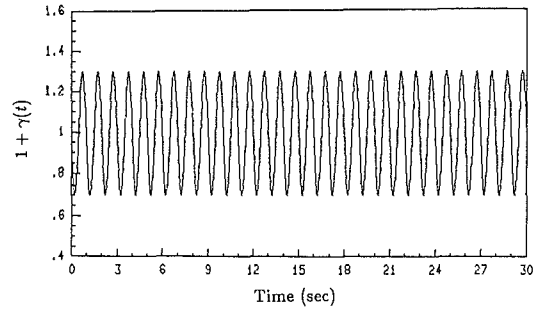


Fig. 9 Model error in induction process for Section 4.1

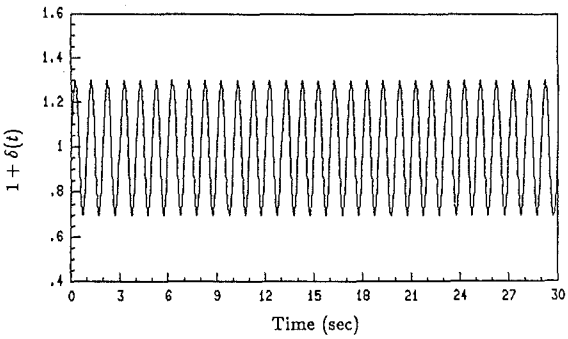


Fig. 10 Model error in injection mechanism for Section 4.1

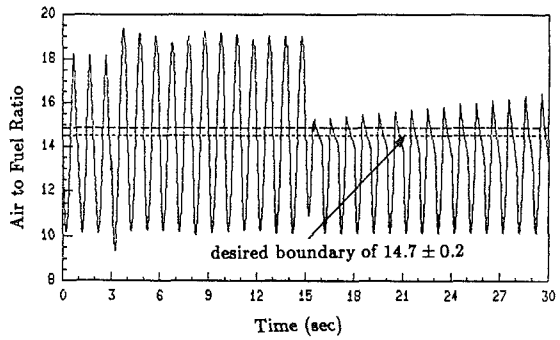


Fig. 11 Open-loop air-to-fuel ratio for Section 4.1

jection model. The corresponding $(1+\gamma(t))$ and $(1+\delta(t))$ are depicted in Figs. 9 and 10, respectively.

Under such severe model errors, the open-loop controller cannot achieve the desired levels of air-to-fuel ratio. The simulation results of an open-loop control strategy obtained from solving equations (16) and (17) are depicted in Fig. 11. Most of the current production fuel-injection controllers incorporate a PI feedback control using the oxygen sensor outputs to improve performance [1, 7]. However, an oxygen sensor only provides binary outputs with a very narrow linear band near the stoichiometric level (e.g., within ± 0.1 of the stoichiometry). Therefore, the closed-loop proportional and integral gains cannot be computed analytically and are calibrated largely based on the experience of the design engineer who often uses other parameters such as engine speed, vacuum level, and throttle rates as well the oxygen sensor's narrow linear band to design a closed-loop controller. This method of tuning is very dependent on the skills of the design engineer and is beyond the scope of this paper. The performance evaluation of the sliding mode controller is presented next.

To be robust to the errors defined by equation (30), the robustness parameter $\kappa(t)$ needs to be

$$\kappa(t) \geq 0.690 \cdot \left| \ddot{m}_{ao}(t) \mid_{\text{MODEL}} \right| + 8.168 \cdot \dot{m}_{ao}(t) \mid_{\text{MODEL}} \qquad (31)$$

The results of the closed-loop simulations using the control law defined by equation (27) and the robustness parameter by equation (31) are shown in Figs. 12, 13, and 14. As depicted in Fig. 12, the sliding mode controller is very successful in maintaining the air-to-fuel ratio within the prescribed boundary of 14.7 ± 0.2. Note that due to the switching nature of the sliding mode control, the air-to-fuel ratio constantly chatters about 14.7. This chatter magnitude is proportional to the robustness parameter. Although the magnitude of $\ddot{m}_{ao}(t)$ in the robustness parameter, given in equation (31), approaches zero in steady state, $\dot{m}_{ao}(t)$ always assumes a finite positive value, resulting in the chattering solution. However, unlike mechanical structures where high-frequency chatter can excite structural resonances, a chattering fuel rate command will not jeopardize the overall performance. That is, the air fuel influence function hardly changes for small deviations in the air-to-fuel ratio near stoichiometry (see Fig. 2); therefore, the effects on the torque production process are minimal. Also, the catalytic converter does not react infinitely fast to the changes in the air-to-fuel ratio, and fast oscillations in the air-to-fuel

Downloaded 01 Jun 2010 to 171.66.16.87. Redistribution subject to ASME license or copyright; see http://www.asme.org/terms/Terms_Use.cfm

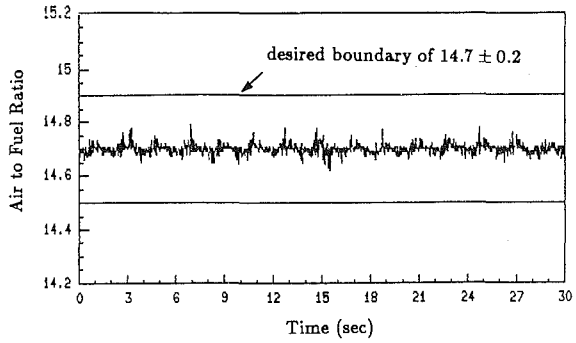


Fig. 12 Closed-loop air-to-fuel ratio for Section 4.1

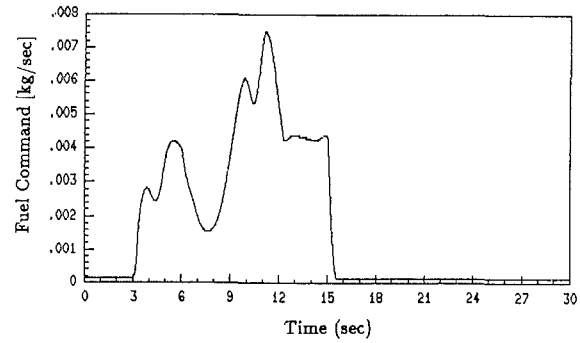


Fig. 13 Fuel command at the injector for Section 4.1

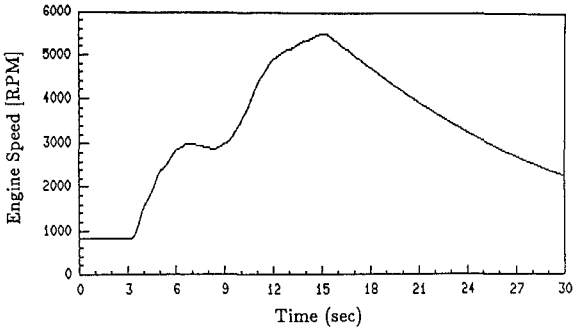


Fig. 14 Engine speed for Section 4.1

ratio of amplitude less than ± 0.3 can be actually beneficial to the converter efficiency due to an "averaging effect" (see [7]). The required closed-loop fuel control is shown in Fig. 13. Although the air-to-fuel ratio chatters as a result of chattering fuel control, the chatter magnitude in the fuel commands is less than 1 percent of the nominal value. Note that the large oscillation in the fuel control is due to the sinusoidal errors introduced in the model as well as to the changes in the throttle and spark. The corresponding engine speed, which is shown in Fig. 14, practically covers the entire operating range.

4.2 Time-Delayed Oxygen Sensor Measurement. In this section, we consider the full time-delayed measurement of $S(t)$, typical in current oxygen sensors. That is, the control law is modified to

$$\dot{m}_{fc}(t) = \dot{m}_{fi}(t) + \frac{\tau_f|_{\text{MODEL}}}{\beta} \cdot \left[\ddot{m}_{ao}(t)|_{\text{MODEL}} + \kappa(t)\cdot\text{sgn}(S(t-\Delta t_e))\right] \quad (32)$$

where the robustness parameter $\kappa(t)$ was defined in equation (29) and Δt_e represents the delay in the measurement of $S(t)$.

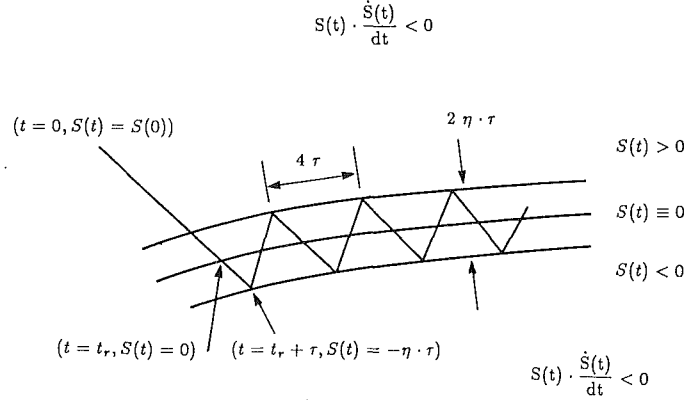


Fig. 15 Sliding surface with time-delayed feedback

Questions arise as to how does the use of time-delayed $S(t)$ influence the closed-loop system dynamics, especially concerning the stability robustness issues? We answer these questions by a piecewise linear analysis.

We make the problem completely general by considering the stability robustness issues of a system whose control law is formulated from $\dot{S}(t) = -\eta\cdot\text{sgn}(S(t-\tau))$. Consider initial conditions such that, $S(t)>0$ and $S(t-\tau)>0$ for $t\le 0^-$, as illustrated in Fig. 15. Then, for $0<t<t_r$, $S(t-\tau)>0$, and $\dot{S}(t) = -\eta$. Therefore, $S(t)$ approaches the surface defined by $S(t)=0$ with a slope of $-\eta$. For $t_r<t<t_r+\tau$, $S(t)<0$, but $S(t-\tau)>0$, and hence, both $S(t)$ and $S(t-\tau)$ keep moving with a slope of $-\eta$. This results in $S(t)$ moving past the surface defined by $S(t)=0$ and assuming a value $-\eta\cdot\tau$ at $t=(t_r+\tau)^+$, when the sign of $S(t-\tau)$ changes. For $t_r+\tau<t<t_r+3\tau$, $S(t-\tau)<0$, and $\dot{S}(t) = +\eta$. Therefore, $S(t)$ reverses direction and moves toward the surface defined by $S(t)=0$ with a slope of $+\eta$, until $t=(t_r+3\tau)^+$, when another switching occurs. This process continues with the switching occurring at $t=t_r+\tau\cdot(2k-1)$ where $k=1,2,\ldots,n$. The same results may be obtained for initial conditions such that $S(t)<0$ and $S(t-\tau)<0$ for $t\le 0^-$. The results of this analysis are:

- switching occurs at every 2τ resulting in the chatter frequency of $1/4\cdot\tau$
- chatter magnitude is $2\,\eta\cdot\tau$
- the attractiveness of the surface defined by $S(t)=0$ cannot be guaranteed, but the attractiveness of the boundary layer defined by $S(t)=\pm\eta\cdot\tau$ is guaranteed. That is, $S(t)\cdot\dot{S}(t)<0$ can be guaranteed only for $|S(t)|>\eta\cdot\tau$.

We summarize the effects of using the time-delayed air-to-fuel ratio measurement in the fuel-injection control problem as: (1) the increase in the chatter magnitude of the air-to-fuel ratio, (2) the decrease in the chatter frequency of air-to-fuel ratio, and (3) the decrease in the "attractiveness" of air-of-fuel ratio toward stoichiometry, by the amounts proportional to the amount of time delay.

The time delay associated with the oxygen sensor measurement is the transport time for an amount of air to enter the cylinders, go through combustion, and then travel down the exhaust system to reach the oxygen sensor. Typically, this is slightly smaller for an inline four-cylinder engine than a V-6 or V-8 engine, due to the amount of exhaust plumbing. In this paper, $(20\text{ ms} + 4\pi/\omega_e(t))$ was chosen for simulation. The same throttle, spark, and load torque changes as those used in Section 4.1 were used for the simulations. However, since the chatter magnitude increases proportionally to $\kappa(t)\cdot\Delta t_e$, in order to meet the design objective of maintaining the air-to-fuel ratio within desired boundary of 14.7 ± 0.2, the errors were reduced as follows:

Downloaded 01 Jun 2010 to 171.66.16.87. Redistribution subject to ASME license or copyright; see http://www.asme.org/terms/Terms_Use.cfm

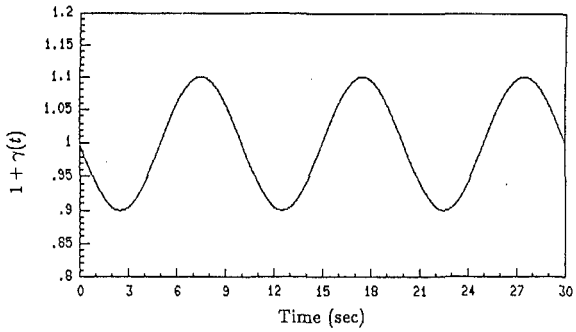


Fig. 16 Model error in induction process for Section 4.2

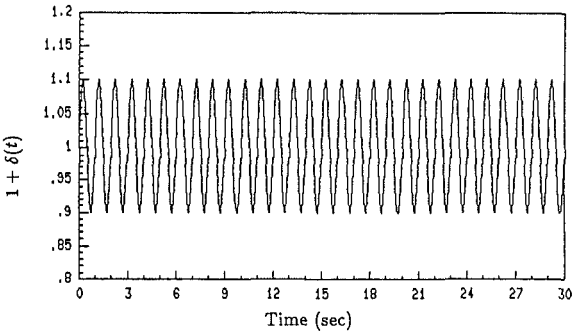


Fig. 17 Model error in injection mechanism for Section 4.2

$$\gamma(t) \equiv -0.1\sin(0.2\pi t) \text{ and } \delta(t) \equiv 0.1\sin(2\pi t) \qquad (33)$$

which represent ± 10 percent errors in both the intake process model and the injection model. The corresponding $(1+\gamma(t))$ and $(1+\delta(t))$ are shown in Figs. 16 and 17, respectively. Typically, the model errors on $\dot{m}_{ao}(t)$ are low frequency errors. Thus, the upper bounds defined by equation (33), i.e., $\gamma_{\max}=0.1$, $\dot{\gamma}_{\max}=0.1$ Hz, and $\delta_{\max}=0.1$, are within the achievable target range of modeling and measurement errors.

To be robust to the errors defined by equation (33), $\kappa(t)$ needs to be

$$\kappa(t) \geq 0.210 \cdot \left|\ddot{m}_{ao}(t)\,|_{\text{MODEL}}\right| + 0.691 \cdot \dot{m}_{ao}(t)\,|_{\text{MODEL}} \qquad (34)$$

The results of the closed-loop simulations using the control law defined by equation (32) and the robustness parameter by equation (34) are shown in Figs. 18 and 19 along the open-loop simulation results in Fig. 20. The air-to-fuel ratio, depicted in Fig. 18, has larger chatter magnitudes and longer oscillation periods when compared to Fig. 12 in Section 4.1. The chatter magnitudes become particularly large during fast throttle maneuvers at low engine speeds. This is because the magnitudes of both $\ddot{m}_{ao}(t)$ and Δt_e become large, resulting in a large robustness parameter $\kappa(t)$, and hence, the large chatter magnitude. However, due to the large value of $\kappa(t)$ during transients, the transients last only for short durations, and the overall performance remains acceptable. That is, the air-to-fuel ratio was contained within the desired boundary of 14.7 ± 0.2 for better than 92 percent of the simulated period. In addition, the duration for which the air-to-fuel ratio escapes the design boundary is so small that it probably does not affect the catalytic converter efficiency in any significant manner. Similarly, the effects on the air fuel influence function and the torque per fuel index are minimal. Although the air-to-fuel ratio chatters about the stoichiometric point, the required fuel command $\dot{m}_{fc}(t)$, depicted in Fig. 19, does not seem to exhibit any significant chatter. This is because the chatter magnitude is less than 1.5 percent of the nominal value.

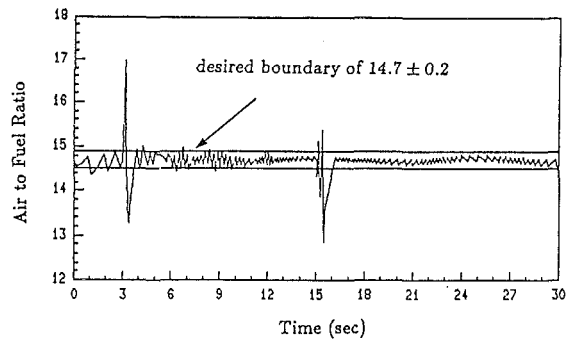


Fig. 18 Closed-loop air-to-fuel ratio for Section 4.2

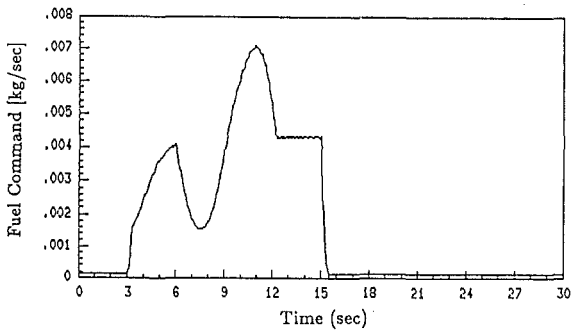


Fig. 19 Fuel command at the injector for Section 4.2

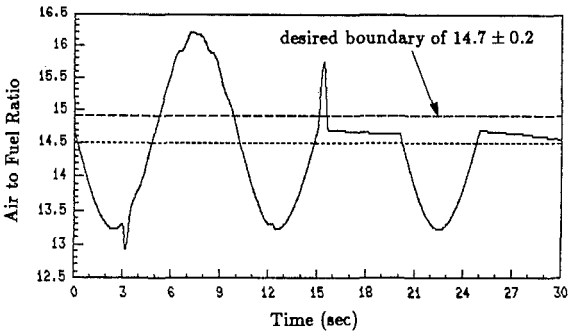


Fig. 20 Open-loop air-to-fuel ratio for Section 4.2

5 Discussion and Conclusions

The sliding mode control method is very useful for designing closed-loop engine control because of its applicability to nonlinear equations and its capability to consider model robustness issues directly. In this paper, it was shown that even with a time delay in the output measurement, the sliding mode method can guarantee the attractiveness of a closed-loop system outside the boundary layer defined by $S(t) = \pm\eta \cdot \tau$.

For the fuel-injection controller problem, given reasonable model and disturbance uncertainties, the sliding mode controller maintained the air-to-fuel ratio within the prescribed boundary of 14.7 ± 0.2 with good transient characteristics, even with the time-delayed oxygen sensor measurements. This is a strong result when one considers the fact that the designed controller maintained the air-to-fuel ratio within ± 1.4 percent of the desired value with uncertainties of ± 10 percent on both the intake process model and the fuel-injection model, as well as rapid, severe disturbances as shown in Section 4. However, the most attractive features of the sliding mode fuel-injection controller are:

Downloaded 01 Jun 2010 to 171.66.16.87. Redistribution subject to ASME license or copyright; see http://www.asme.org/terms/Terms_Use.cfm

- it does not rely on the narrow linear band of the oxygen sensor output for closed loop control
- it requires very little computing power
- the only part of the model that the control algorithm uses is $\dot{m}_{ao}(m_a, \omega_e)$ and the injector model (modeled as a first-order lag in this paper); thus, the robustness issues are only related to how these are modeled
- once the control is designed, it can be easily adapted to a number of engines

It is possible to obtain better performance, if either the upper bounds on the uncertainties can be relaxed or the time delay in the oxygen sensor can be reduced. Since the chatter magnitude increases proportional to $\kappa(t)\ \Delta t_e$, the chatter magnitude will decrease if either $\kappa(t)$ or Δt_e decreases. Also, if a "linear" oxygen sensor is available, the performance can be further improved, by the use of a *boundary layer in* $S(t)$. In addition, the robustness parameter $\kappa(t)$ can be adjusted according to the magnitude of $S(t)$, thereby providing more means to "tune" the tradeoff problem between the transient characteristics and steady-state chatter. The use of a linear oxygen sensor will also enable prescribing an arbitrarily time-varying desired air-to-fuel ratio (e.g., rich during acceleration, lean during deceleration, etc.). However, before implementation, the validity of the model needs to be evaluated along with the sensor requirements concerning measurement of the states.

6 Acknowledgments

This research was supported by a contract from GMR, Power Systems Research Department. The authors would like to acknowledge Mr. J. Moskwa of M.I.T. for the development of the two state engine model and Mr. R. Weeks, also of M.I.T., for valuable technical discussions.

7 References

1 Canale, R., et al., "General Motors Phase II Catalyst System," SAE Paper No. 780205, 1978.

2 Doyle, J. C., and Stein, G., "Multivariable Feedback Design: Concepts for a Classical/Modern Synthesis," *IEEE Transaction on Automatic Control*, Vol. AC-26, No. 1, Feb. 1981.

3 Utkin, V. I. (trans. by A. Parnakh), *Sliding Modes and Their Application in Variable Structure System*, MIR Publishers, Moskow, 1978.

4 Slotine, J. J. E., and Sastry, S. S., "Tracking Control of Non-linear Systems Using Sliding Surfaces, With Application to Robot Manipulators," *International Journal of Control*, Vol. 38, No. 2, 1983.

5 Dobner, D. J., "Dynamic Engine Models for Control Development. Part 1: Nonlinear and Linear Model Formulation," *International Journal of Vehicle Design*, 1982.

6 Tugcu, A. K., Hebbale, K. B., Alexandridis, A. A., and Karmel, A. M., "Modelling and Simulation of the Powertrain Dynamics of Vehicle Equipped With Automatic Transmission," GMR-5439, G. M. Research Labs., 1986; presented at the 1986 ASME Winter Annual Meeting, Anaheim, CA.

7 Falk, C. D., and Mooney, J. J., "Three-Way Conversion Catalysts: Effect of Closed-Loop Feed-Back Control and Other Parameters on Catalyst Efficiency," SAE Paper No. 800462, 1980.

8 Eddy, D. S., "Physical Principles of the Zirconia Gas Sensor," presented at the IEEE Vehicular Technology Conference, Cleveland, OH, Dec. 1973.

APPENDIX

Sliding Mode Control Theory [3, 4]

Consider a single input nonlinear system in the controllable canonical form

$$\begin{aligned} \dot{x}_1 &= x_2 \\ &\vdots \\ \dot{x}_m &= f(x, t) + b(x, t) \cdot u + d(t) \end{aligned} \tag{A1}$$

The controller to be designed should provide acceptable tracking error dynamics in the presence of model and disturbance uncertainties. Let the tracking error ϵ be defined as

$$\epsilon \equiv x_1 - x_{1d}(t) \tag{A2}$$

we can also define the *desired* tracking error dynamics by a surface $S(t) = 0$, defined as

$$S(t) \equiv c_1 \cdot \epsilon + c_2 \cdot \dot{\epsilon} + \cdots + c_n \cdot \frac{d^{n-1}\epsilon}{dt^{n-1}} \tag{A3}$$

where $c_1, \ldots, c_n$ are chosen so that $S(t) = 0$ yields acceptable error transients. If we can choose $u(t)$ so that $S\dot{S} < 0$, then we are guaranteed that $S(t) \to 0$. More strongly if we can choose $u(t)$ such that

$$S\dot{S} \leq -\eta \cdot |S|, \quad \eta > 0 \tag{A4}$$

then $S(t)$ will cross zero in finite time. It is straightforward to show that

$$\dot{S} = -\eta \cdot \mathrm{sgn}(S) \tag{A5}$$

will satisfy (A4), (A5), and (A3) (*with* $c_n = 1$), yielding

$$\dot{S} = c_1 \cdot \dot{\epsilon} + \cdots + c_{n-1} \cdot \frac{d^{n-1}\epsilon}{dt^{n-1}} + f + b \cdot u + d - \frac{d^n x_{id}}{dt^n} = -\eta \cdot \mathrm{sgn}(S) \tag{A6}$$

To consider the effect of modeling errors and unknown disturbances, let

$$f = f_{\text{model}} + \Delta f \text{ and } d = d_{\text{model}} + \Delta d \tag{A7}$$

where $|\Delta f| < \alpha$, $|\Delta d| < \beta$, $|d^n x_{id}/dt^n| < \gamma$, and for simplicity assume that we know $b(x, t)$ perfectly. Clearly the worst possible case (from the point of view of guaranteeing (A4)) is $\Delta f = \alpha \cdot \mathrm{sgn}(S)$, $\Delta d = \beta \cdot \mathrm{sgn}(S)$, $d^n x_{1d}/dt^n = -\gamma \cdot \mathrm{sgn}(S)$. Substituting these expressions into (A6) yields

$$u = -\frac{1}{b(x, t)}\left[c_1 \cdot \dot{\epsilon} + \cdots + c_{n-1} \cdot \frac{d^{n-1}\epsilon}{dt^{n-1}} + f_{\text{model}} + d_{\text{model}} + (\eta + \alpha + \beta + \gamma) \cdot \mathrm{sgn}S\right] \tag{A8}$$

The choice of (A8) guarantees (A4); thus $S(t)$ will go to 0 in finite time and then slide or chatter until $\epsilon = 0$.

Downloaded 01 Jun 2010 to 171.66.16.87. Redistribution subject to ASME license or copyright; see http://www.asme.org/terms/Terms_Use.cfm

S. D. Haddad
Professor,
Assistant Dept. Chairman,
Director of Graduate Programs
at UMC & UMKC,
Department of Mechanical and
Aerospace Engineering,
University of Missouri—Columbia,
Columbia, MO 65211

C. Cempel
Head of Diagnostic Research Group,
Polish Academy of Sciences,
Poznan, Poland

Optimizing Engine Operation by Monitoring the Working Gas Pulsations

Introduction

There are two main reasons why engine noise tends to increase during long periods of running. Firstly, engine tuning can change, and secondly, deterioration and wear can occur in the working parts of the engine. This causes higher impacts between mechanical parts, inefficient combustion, and rough operation, which means higher noise and vibration levels. In order to retain the original acceptable operational characteristics it is important to detect the onset of faults and to correct abnormal conditions before excessive deterioration occurs.

A number of researchers have tackled this problem in the context of pure engine diagnostics [1–3]. This paper describes a technique developed for the detection and diagnosis of faults in piston engines by monitoring the working gas pulsations during an acceleration-deceleration test, whereby it is possible to measure pulsation signal discriminants or algorithms [4] to detect engine faults. Some of these discriminants are discussed and some new ones are introduced.

Background Investigation

A piston engine produces useful work on the basis of efficient transfer of its working fluid of air and fuel passing through the various stages of an engine cycle: that is, the inlet system, combustion chamber, exhaust system, and partly into the crankcase space.

From basic engine thermodynamics it is evident that this working fluid or gas is intimately related to the quality of engine operation responding to changing operating conditions. In particular, changes in the pressure pulsations of this working gas are sensitive to changing engine operation, whether normal or abnormal.

In fact, it has been observed that a great deal of information can be extracted from inlet, exhaust, crankcase, and cylinder pressure pulsation processes. This is summarized as follows [4, 5]:

1 Working gas pulsations are a series of pulses with distinctive frequency and shape.

2 There is a repetition of events every two rotations of the crankshaft for a four-stroke engine.

3 There is an a-c and d-c component of each pulsation process, each carrying information about the condition of the engine.

In addition, it is important to realize that certain engine performance checking techniques can supplement and enhance the information obtained from the working gas pulsations. Cempel and Haddad [5] have developed the theory of both techniques outlined in the following sections.

Engine Performance Checking at Acceleration/Deceleration. In this approach engine rpm is observed during rapid acceleration of the engine with no load and deceleration with fuel cutoff. The engine speed change with time will have the shape shown in Fig. 1.

If we assume as a first approximation the linear dependence of engine friction with speed w, then the equation of motion for rotating engine parts will be (see Figs. 1 and 2)

$$I\dot{w} = M_i - fw$$

where $w = w_0$ for $t = 0$ in acceleration and $I\dot{w} = -fw$; $w = w_m$ for $t = 0$ in deceleration; I = moment of inertia of rotating parts; f = coefficient of friction of engine.

Figure 2 shows a simplified model of the engine used for the above analysis.

Solution of the above equation would give the following results:

$$M_i = \frac{\dot{w}_a I}{w_m - w_0} = \dot{w}_a I\left(\frac{w_m/w_0}{w_m/w_0 - 1}\right)$$

and

$$f = \frac{\dot{w}_d}{w_m} I = \frac{\dot{w}_a}{w_0} I\left(\frac{1}{w_m/w_0 - 1}\right)$$

where $\dot{w}_a$ = acceleration of engine, $\dot{w}_a \geq 0$; $\dot{w}_d$ = deceleration of engine, $\dot{w}_d \leq 0$; w_m = maximum engine speed; w_0 = idle engine speed.

Contributed by the Internal Combustion Engine Division and presented at the Energy-Sources Technology Conference and Exhibition, Dallas, Texas, February 15–20, 1987. Manuscript received by the Internal Combustion Engine Division November 1986. Paper No. 87-ICE-45.

Copyright © 1988 by ASME
Downloaded 01 Jun 2010 to 171.66.16.87. Redistribution subject to ASME license or copyright; see http://www.asme.org/terms/Terms_Use.cfm

It is seen that w_m/w_0, $\dot{w}_a$, and $\dot{w}_d$ can be obtained from the *A/D* test shown in Fig. 1. Since engine moment of inertia (I) is known, it would be easy to evaluate M_i and f, which constitute the basic factors for determining an engine's mechanical health.

Pulsation Discriminants and Their Use. Figure 3 shows three ideal *A/D* test results for engine torque, fuel delivered, and crankcase pressure. On the other hand Fig. 4 shows some measured and computed crankcase pressure for a certain engine in good condition. It can be seen that the signals of Fig. 4 deviate from the ideal case of Fig. 3 and these deviations can be quantified by using certain discriminants or algorithms, which characterize the mechanical health of the engine.

There are two general types of discriminant: dimensional discriminants, which give an absolute reading of level or amplitude, and dimensionless discriminants giving relative readings. The latter are somewhat better due to their insensitivity to changes with speed and load [4].

The following dimensional discriminants have been found to be the most useful for each pulsation process (see [5] for derivations):

- Average value of d-c pressure component

$$\bar{p} = E_t[p(t)] = \frac{1}{T}\int_0^T p(t)dt, \quad T = \text{observation time}, \quad E_t = \text{averaging operator}$$

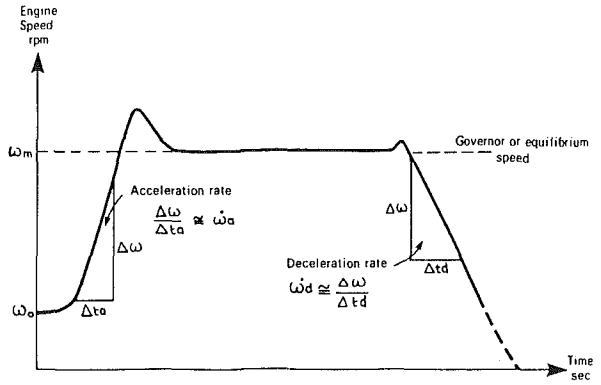


Fig. 1 The principle of acceleration-deceleration test

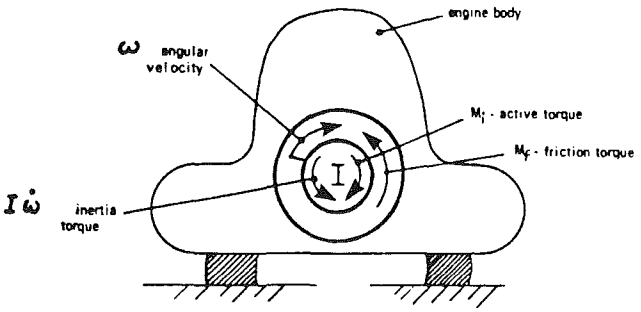


Fig. 2 The model of engine motion for A/D Test purposes

- Average peak value of a-c pressure component

$$\hat{p} = E_t\{\max_t[p(t) - \bar{p}]\}$$

- Average absolute value of a-c pressure component

$$|\tilde{p}| = E_t[|p(t) - \bar{p}|] = \frac{1}{T}\int_0^T |p(t) - \bar{p}|dt$$

- Average zero crossing or *Rice frequency* (f_0) of the a-c pressure component.
- Average frequency of positive crossing of a given level p as a percentage of $\hat{p}$, i.e., f_p.

Subsequently dimensionless discriminants can be calculated [5].

- Quality index $Q \equiv \bar{p}/\hat{p}$.
- Impulse index $J \equiv \hat{p}/|\tilde{p}|$.
- Band index $B \equiv f_0/f_p$.

The interpretation of each discriminant is different for each working gas pulsation process. A summary of the application of each process is shown in Table 1 and more thoroughly in [5].

Analysis of Table 1 together with defined discriminants properties give the following indications.

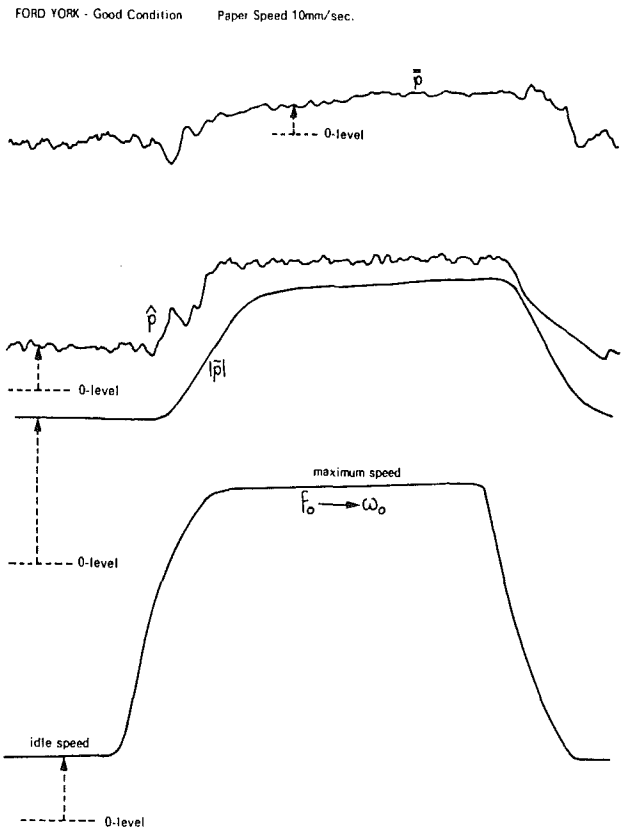


Fig. 4 Acceleration-deceleration test chart of four measured quantities: $\bar{p}$, $\hat{p}$, $|\tilde{p}|$, f_0, for crankcase pulsation $p_c(t)$

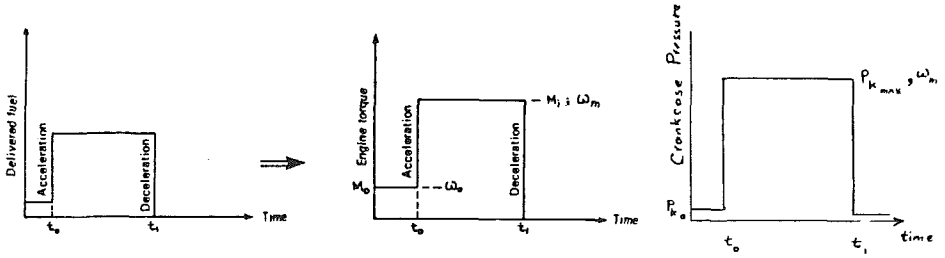


Fig. 3 Ideal acceleration-deceleration tests

Downloaded 01 Jun 2010 to 171.66.16.87. Redistribution subject to ASME license or copyright; see http://www.asme.org/terms/Terms_Use.cfm

Table 1 Areas of pressure pulsation application

Crankcase pressure $P_K(t)$	Engine performance, blowby intensity, cylinder-to-cylinder balance, engine tuning
Intake pressure $P_i(t)$	Inlet tract faults, engine tuning
Cylinder pressure $P_c(t)$	Performance tests, combustion quality investigations, engine tuning
Exhaust pressure $P_e(t)$	Under further investigation

Q_k (for crankcase) as a measure of cylinder blowby severity, as well as Q_c (for cylinder pressure) or Q_e (for exhaust pressure), can be a measure of combustion quality, and B_c can be a measure of combustion randomness, etc.

In most applications it has been found appropriate to use $\bar{p}$, Q, and f_0 as discriminants of condition and/or tuning of whole engine while B and J as discriminants of intercylinder balance [5].

Experiments and Results

Inlet, exhaust, crankcase, and cylinder pressure were measured for a Ford York diesel engine during an A/D test. These measurements were observed on a VDU and then tape recorded using the setup shown in Fig. 5. Subsequently these tape-recorded signals were processed as shown in Fig. 6 to obtain dimensional pulsation discriminants, as shown in Fig. 4 for crankcase pressure pulsations.

Four faults were simulated and the four pulsation processes were recorded during an acceleration-deceleration test. The discriminants were calculated. Table 2 gives a summary of test results for the crankcase pressure pulsation process. The rate of angular acceleration $\dot{w}$ is a measure of the indicated torque of the engine and this is shown in column 2. The results in columns 3, 4, and 5 show that for an engine in good condition $\bar{p}$ (overall blowby) and $\hat{p}$, $|\tilde{p}|$ (cylinder-to-cylinder blowby) are minimal. The last two columns contain the dimensionless factors of crankcase pulsation J_K, Q_K. Q_K can be termed the blowby intensity factor, which is at a minimum for a good engine or a restricted inlet, while the results for J_K confirm that it is suitable for use in engine diagnostic work. The highest readings of J_K occur when the timing is advanced, in which case the combustion rate is rapid and the blowby intensity severe.

Therefore crankcase pressure can be used as a method of:

- performance assessment (torque, power)
- blowby intensity measurement and cylinder-to-cylinder blowby
- engine optimum tuning at Q_K = min, J_K = min

In the same way the other three pressure pulsation processes were analyzed to produce dimensional and dimensionless discriminants, using a signal processing setup such as shown in Fig. 7; the results obtained for the various simulated faults are documented in [5].

The same procedure was repeated on a Perkins in-line 4.236 diesel engine and Ford V4 gasoline engine, showing that this method of pulsation monitoring at A/D test gives sensitive indication of engine operating conditions, which can be quantified for subsequent correction. This correction can be done either by the operator or by automatic control where possible (e.g., engine tuning).

In other words this diagnostic system can serve to retain normal engine operating conditions and consequently maintaining acceptable operating characteristics.

This aspect of engine noise control can be critical in areas where a specified overall noise level must be maintained at all times. That is, any engine abnormal operation that increases noise levels cannot be tolerated and so such a diagnostic package becomes most essential to prevent any deviation from normality. It is worth mentioning here that this same

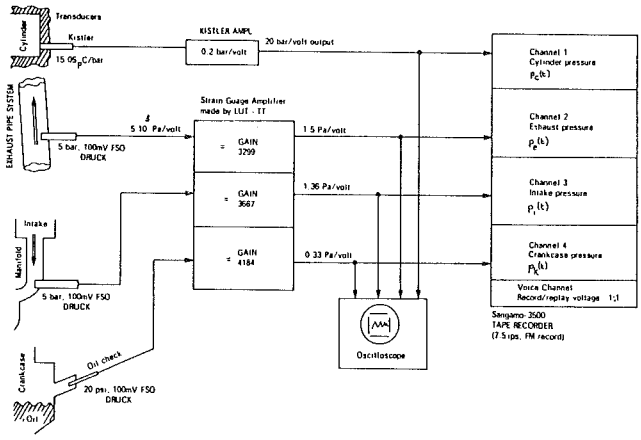


Fig. 5 Measuring setup diagram for pulsation recordings

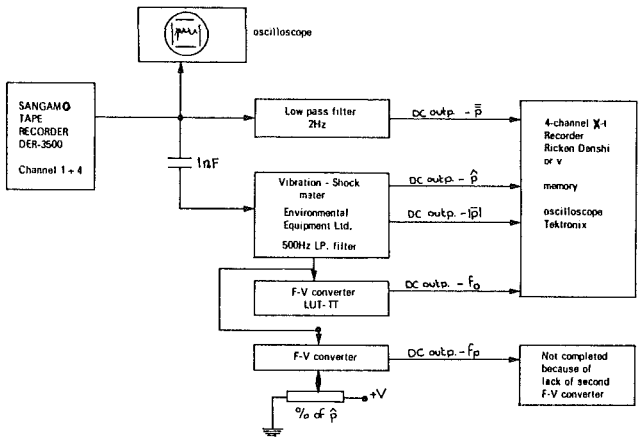


Fig. 6 Measurement setup for pressure pulsation signal processing

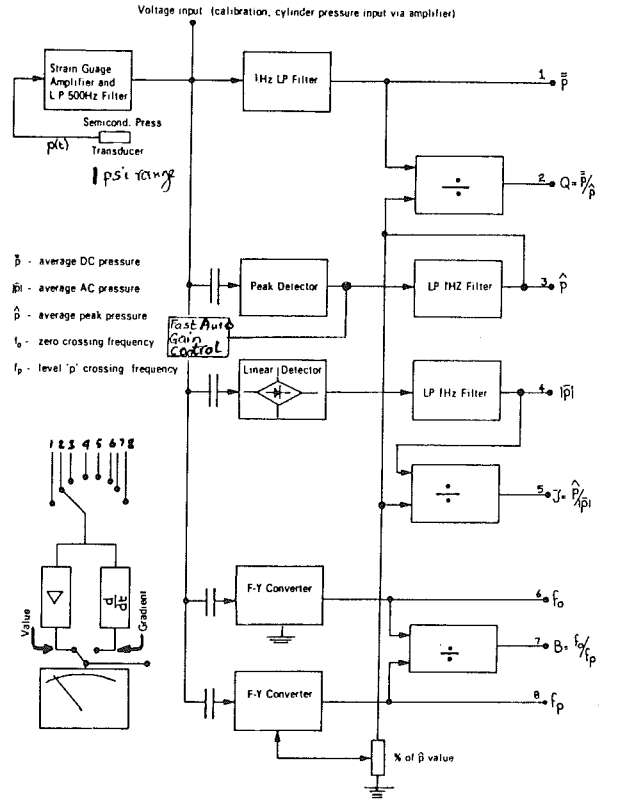


Fig. 7 Diagram of the instrumentation for pressure pulsation investigations

Downloaded 01 Jun 2010 to 171.66.16.87. Redistribution subject to ASME license or copyright; see http://www.asme.org/terms/Terms_Use.cfm

Table 2 Crankcase pressure $P_K(t)$ (arbitrary units) for Ford York engine

Discriminant	$f_0$min / $f_0$max	$\dot{w}_a$ / $\dot{w}_d$	$\bar{\tilde{p}}_{\min}$ / $\bar{\tilde{p}}_{\max}$	$\hat{p}_{\min}$ / $\hat{p}_{\max}$	$\lvert\bar{p}\rvert_{\min}$ / $\lvert\bar{p}\rvert_{\max}$	$Q_K$min / $Q_K$max	$J_K$min / $J_K$max
Good condition	6 40	21 14	1 7	5 14	18 31	2 5	2.8 4.5
Restricted inlet	8 41	21 14	1 9	5 18	17 41	2 5	2.9 4.4
Advanced timing (+8 deg)	8 40–45	21 13	1 10	5 15–20	17 30	2 5–6.6	2.9 5–6.6
Delayed timing (−8 deg)	9–10 38	20 12	3 8	5 14	16 34	6 5.7	3.1 4.1
Compression decrease	8 48	20 13	5 13–22	5 16	17 35	10 8.1–13.7	2.9 4.6

diagnostic package can be programmed to detect possible decreases in noise levels due to certain abnormal operations as well (e.g., a loose timing chain on the engine or a broken belt on the vehicle).

In such a case the overall system becomes more sophisticated and therefore would require justification in terms of cost effectiveness, safety considerations, level of required availability, reliability, legal requirements, etc.

Of course it must be remembered that there are other methods that have been developed to diagnose engine and machinery mal-operation to point out the required corrections. That of vibration measurement and analysis is considered the most well-developed technique, and it is outlined in [6–8].

For greater reliability, vibration measurements and analysis techniques can be incorporated alongside the pressure pulsation technique to an engine diagnostic package to enable subsequent correction for maintaining originally acceptable noise levels and operational characteristics of engines.

Conclusions

The theory and experiments described in this paper reveal that the working gas pulsations carry much information to detect changes in engine conditions. By means of dimensional and dimensionless pulsation process discriminants, coupled with the acceleration/deceleration test, the engine can be kept in good condition, thereby allowing originally healthy engine operation to be maintained at all times.

References

1 Sarna, D. S., and Steyaert, J. W., "Diagnostic Equipment for Military Vehicle Applications," SAE-780029, 1978.

2 Hadden, S. C., Hulls, L. R., and Sutphin, E. M., "Remote Diagnosis of Internal Combustion Engines," *Instrumentation Technology*, July 1976, pp. 43–48.

3 Kremidas, J. R., and Rothfusz, R. W., "Automatic Vehicle Diagnostic Systems," SAE-730205, 1973.

4 Cempel, C., "Diagnostically Oriented Measures of Vibroacoustical Processes," *Journal of Sound and Vibration*, Vol. 73, No. 4, 1980.

5 Haddad, S. D, and Cempel, C., "Engine Fault Diagnosis by Monitoring the Working Gas Pulsation," Loughborough University of Technology, Department of Transport Technology, Report No. TT81R01, Jan. 1981.

6 Cempel, C., *Fundamentals of Vibroacoustical Diagnostics* [in Polish], WNT-Press, Warsaw, 1982.

7 Haddad, S. D., "Noise and Vibration Applied to Engine Diagnostics," *Internoise 80*, Dec. 8–10, 1980.

8 Haddad, S. D., "The Optimal Maintenance Approach Using Condition Monitoring and Fault Diagnosis," Keynote Paper KII, The 1986 Maintenance Convention, Johannesburg, Oct. 30–31, 1986.

Downloaded 01 Jun 2010 to 171.66.16.87. Redistribution subject to ASME license or copyright; see http://www.asme.org/terms/Terms_Use.cfm

B. K. Powell

G. P. Lawson

G. Hogh

Control Systems Department,
Scientific Research Laboratory,
Ford Motor Company,
Dearborn, MI 48121

Advanced Real-Time Powertrain Systems Analysis

This paper describes a combined analytical and experimental hardware-in-the-loop powertrain systems analysis methodology. Central to the implementation of this methodology is a real-time dynamic system simulation computer such as the high-speed Applied Dynamics Model AD10. For automotive engine control system studies, wide bandwidth in-cylinder combustion pressure sensor signals are input to the AD10 computer. Control commands are calculated and communicated at high data rates to throttle valve, spark ignition, and fuel injector actuators. Both simulation and experimental results are presented. Using this approach, the functional improvements associated with various control philosophies can be determined.

Introduction

For many powertrain optimization and control problems neither testing nor computer simulation provides satisfactory solutions. Testing is reliable but is handicapped as a design tool because of the difficulty in performing design parameter variation studies. With computer simulation, design parameter studies are readily performed, but results may be unreliable due to inaccurate mathematical models of complex systems. A combination of real-time process simulation and hardware-in-the-loop testing may be the most effective approach to many powertrain analysis and vehicle control problems [1]. The ultimate simulation of on-board computer control functions linked to either powertrain hardware or a powertrain model would allow real-time analysis of potential control, sensor, actuator, and on-board computer requirements [2].

With the advent of on-board microcomputer controllers, a simulation of computer control functions, initially linked to a simulation of the process to be controlled, allows debugging of the real-time controller functions in a synchronous and, if desired, nonrandom environment where experimental replication is possible. This is a significant aid to powertrain control analysis and controller synthesis [3]. To be an effective tool, the process model must contain the key or dominant dynamic cause-and-effect relationships germane to real-time information processing and control system synthesis [4–6]. In the work presented here, the research deals with the concept of in-cylinder combustion pressure sensor based dynamic control [7, 8]. Consequently, in order to study a controller simulation that uses cylinder pressure information, it is necessary to develop a dynamic thermodynamic engine model that reflects the cause-and-effect relationships appropriate for in-cylinder pressure analysis.

Generally, models of the thermodynamic portion of the engine dynamic process are quasi-static, often single-cylinder representations, and have execution times much slower than real time, making such models impractical as a hardware-in-the-loop analysis and design tool [9, 10]. On the other hand, many earlier engine dynamic models [11–17], though suitable for real-time simulation, did not reflect the high-frequency thermodynamic characteristics necessary to simulate cylinder combustion pressure behavior. The high-speed, test hardware linkable Applied Dynamics Model AD10 computer [6] provides the necessary execution speed for advanced real-time powertrain simulation and control. In conjunction with a hybrid laboratory, a real-time nonlinear dynamic model of the powerplant process was developed. It is a four-cylinder thermodynamic model with manifold dynamics, port-injected fuel, and mass concentration dynamics, as well as sensor and actuator models. Model calibration and validation are conducted on-site. With a real-time process model, the on-board microcomputer controller representation can either control the real powerplant or the thermodynamic model, the concept of which is depicted in Fig. 1.

Sensors and actuators are an integral part of a control system, with the ultimate goal of the definition of sensor and actuator requirements commensurate with overall system cost and performance objectives. Developing a totally analytical methodology to define optimal sensor and actuator requirements is not a trivial task. It requires predictive models to quantify sensor, actuator, and system dynamic performance as well as procedures to assess sensor and actuator costs at a continuum of levels of their performance. Such models and procedures are not generally available even for many existing sensor, actuator, and powertrain components. In situations where sensors or actuators being contemplated do not yet exist, a totally analytical assessment methodology would be tenuous and credibility would become an overriding issue.

Real-time hardware-in-the-loop sensor and actuator assessment methodology may be the most fruitful approach to this complex problem. The concept is fairly straightforward, as depicted in Fig. 2. The idea is to simulate in hardware those components of the system that are difficult to model, while simulating in a real-time control computer (e.g., an AD10 computer system) those portions that are readily modeled.

Contributed by the Internal Combustion Engine Division and presented at the Energy-Sources Technology Conference and Exhibition, Dallas, Texas, February 15–20, 1987. Manuscript received by the Internal Combustion Engine Division November 1986. Paper No. 87-ICE-46.

Copyright © 1988 by ASME
Downloaded 01 Jun 2010 to 171.66.16.87. Redistribution subject to ASME license or copyright; see http://www.asme.org/terms/Terms_Use.cfm

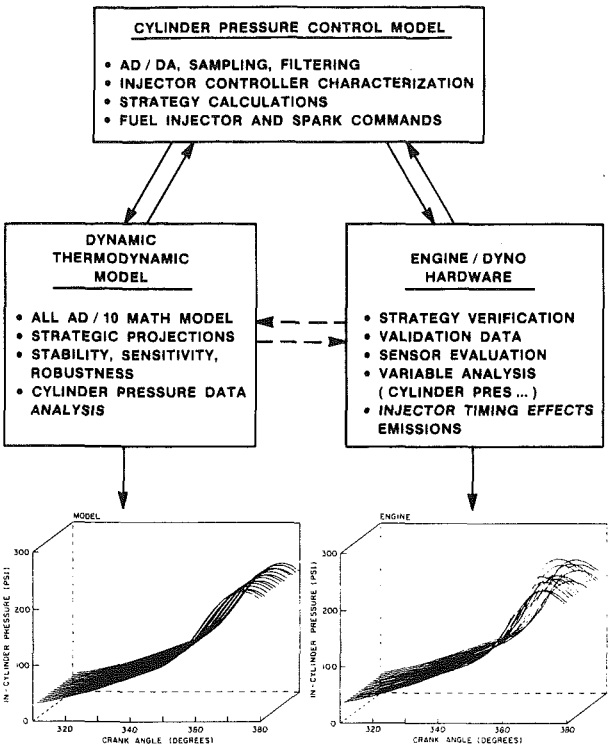


Fig. 1 Real-time engine control and analysis

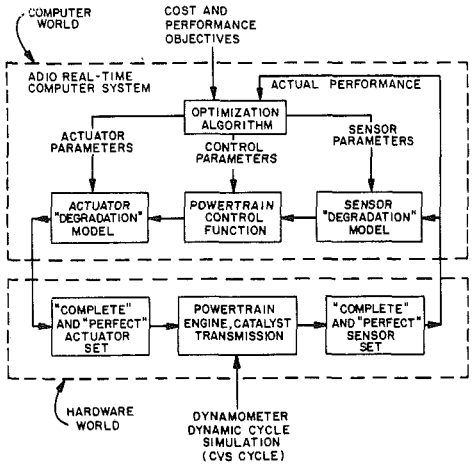


Fig. 2 "Hardware-in-the-loop" sensor and actuator assessment methodology

Beginning with a "complete" and "perfect" sensor and actuator set (e.g., extensive high-performance laboratory quality sensors and actuators), the dynamic effects of a degraded sensor and actuator set (degraded both in numbers and performance) can be simulated over any given dynamic powertrain cycle (e.g., CVS test). Conceptually, an optimization algorithm can search for the "optimum" sensor and actuator parameters (while maintaining optimum control parameter calibrations at each step) subject to specified system cost and performance objectives (i.e., a system "objective function" to be minimized or maximized).

Current research results with this advanced facility indicate that the concept of in-cylinder combustion pressure based engine control offers promise for a substantial improvement in the ability to control offers promise for a substantial improvement in the ability to control engine systems. Attendant to this improved control capability might also be the opportunity to realize truly robust systems that are highly tolerant of manufacturing variability, aging, and environmental disturbances. In-cylinder combustion pressure transducer technology, and associated integrated circuit digital signal processing technology, are both mature enough that they may possibly be ripe for low-cost on-board production engine application. Engine system that are taken to the outer limits of their operational envelopes, such as lean air dilution limit (for NO_x control without EGR or TWC), very high EGR dilution (for stoichiometric 0.4 NO_x systems), and high-performance operation (for maximum power with knock and preignition detection and control [7]), are the most likely first candidates for this advanced engine control technology.

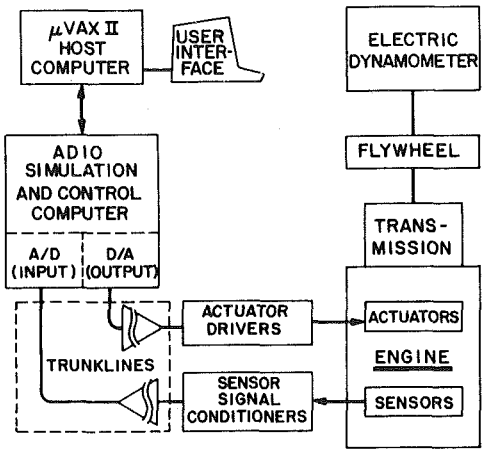


Fig. 3 Real-time control systems laboratory

This paper describes an analytical and experimental facility that contains a high-speed computer, an Applied Dynamics AD10, that is useful for hardware-in-the-loop control system analysis and high-speed dynamic simulation.

Laboratory quality in-cylinder combustion pressure sensor outputs are input directly into the AD10, and commands to throttle, spark, and fuel actuators are communicated at a high data rate for engine control. Both simulation and experimental results are presented. Using this approach the functional improvements associated with various control philosophies can be determined.

Real-Time Control Systems Laboratory Facility

For the purpose of assessing powertrain control system alternatives, a real-time control systems laboratory was configured as shown in Fig. 3. An engine is mechanically coupled to an electric dynamometer either directly through a propeller shaft or alternatively through its own transmission and compliant axle shaft. An optional flywheel may be utilized to simulate vehicle inertial effects closely in cases where the dynamic response bandwidths of the electric dynamometer and its associated controller are inadequate.

Extensive laboratory quality engine mounted sensors, including in-cylinder combustion pressure transducers, are interfaced to an Applied Dynamics Model AD10 high-speed computer through signal conditioners, low noise trunklines, and 12-bit analog-to-digital (A/D) converter inputs. Engine-mounted actuators, including throttle valve (stepper motor), spark ignition, and fuel injectors (port injection) are similarly interfaced to the AD10 digital-to-analog (D/A) converter outputs. Although only one is shown, the AD10 is actually interfaced to two dynamometer test cells to facilitate concurrent engine only, transmission only, or combined engine with transmission experiments.

While implementing the laboratory plan shown in Fig. 3, considerable care was exercised in instrumentation practices,

Downloaded 01 Jun 2010 to 171.66.16.87. Redistribution subject to ASME license or copyright; see http://www.asme.org/terms/Terms_Use.cfm

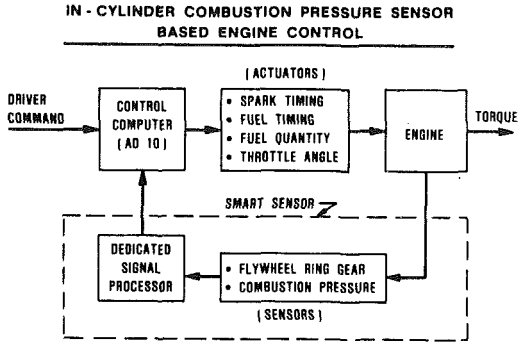


Fig. 4 In-cylinder combustion pressure sensor based control

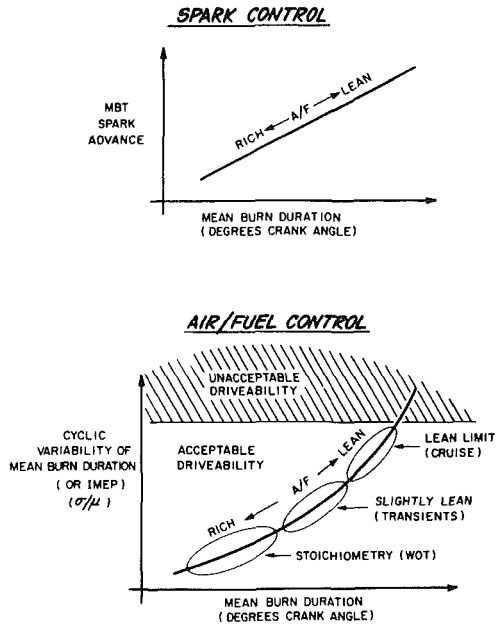


Fig. 5 Steady-state lean limit engine control strategy (spark and fuel control)

particularly grounding, shielding, and power conditioning. The critical trunklines that interface test cell sensor and actuator hardware with the AD10 computer (24 inputs, 24 outputs) utilize low-noise triaxial cable and include wide bandwidth (100 kHz maximum) isolation amplifiers (flux coupled to avoid potential ground loops) with adjustable gain and bandwidth control. Power conditioners are provided on all computer and instrumentation systems to minimize the effects of undesirable AC power line regulation and noise (SCR controlled electric dynamometers).

The Applied Dynamics International Model AD10 digital computer is a crucial component of this hardware-in-the-loop simulation facility. Generally, the primary AD10 application is in aerospace hardware simulation, development, and testing, being used for tasks in which analog or classical hybrid computers have previously been employed. Its advantage over these lies in the precision and repeatability of its numerical results, a characteristic that is due to its digital processors.

An AD10 operating under an MPS10 (Modular Programming System 10) software system and a Digital Equipment Corp. uVAX II under uVMS represent the computer environment in which the simulation runs are performed and the simulation embedded or stand-alone controllers are tested. The AD10 is a specialized, high-speed, multiple processor digital machine with analog (± 10 V) input/output channels designed for interfacing with test hardware. It achieves high computational throughput with separate parallel pipelined processors for arithmetic operations, numerical integration, table lookup, decision making, and input/output.

Program development for the AD10 is done on the VAX host and information structures consisting of object cost modules and data tables are downloaded prior to program execution. Control over execution of an AD10 program is also retained under the operator's interactive supervision via a VAX host resident "relate" program written in FORTRAN. At the end of or during a run, resulting data may be shipped back to the host for monitoring by the operator, either directly or via postprocessing graphic report generating data reduction programs. During AD10 operation, instructions are executed at a 20 to 30 MIPs rate on 16 bit fixed-point operands (48 bit operands within the Numerical Integration Processor) permitting significant size programs (500 to 1000 lines of code) to be executed at frame-times of 100 μs, for the 10 kHz update rates.

The engine data of primary interest are combustion pressures inside the cylinder, especially during the latter stages of charge compression and the early phase of the power stroke. The sensor employed to measure this property is a flush-mounted Kistler pressure transducer based on the piezoelectric effect of quartz. The sensor output is processed by a charge amplifier giving the computer a signal that has both a high S/N ratio and wide bandwidth. This signal is a voltage (± 10 V) analog of pressure and in turn is converted to the digital domain in the high-speed (100 kHz), dedicated (non-multiplexed) 12 bit A/D converters that are a part of the AD10's I/O peripheral.

The intended purpose of the laboratory facility is the exploration of the complete spectrum of possible powertrain control alternatives without regard to the limitations imposed by current automotive sensors, actuators, control strategies, or microprocessors.

Controller Requirements and Structure

Combustion Quality Feedback Control. Current automotive microprocessor based engine controllers implement primarily scheduled (open loop) and feedforward control strategies, with very little feedback and adaptive control. Next-generation engine controllers may have available (through new sensors) more and higher quality information about the combustion process in each cylinder, enabling improved feedback and adaptive control, as well as facilitating on-board functional diagnostics.

In particular, the concept of in-cylinder combustion pressure sensor based engine control (Fig. 4) offers promise for a substantial improvement in the ability to control engine systems. The idea (Fig. 4) is that a dedicated signal processor combines in-cylinder combustion pressure sensor signals with crankshaft position information to produce combustion process parameters, such as 0–90 percent mass fraction burn duration, work done per cycle, or "indicated" torque. These combustion parameters are then sent to an engine control computer (an AD10 in this figure) at a rate of once per engine cycle. The engine control computer then implements feedforward, feedback, and adaptive control. The actuators in this system are conventional electronic spark and sequential EFI, along with a stepper motor driven throttle actuator. A key requirement is a high-resolution crankshaft position sensor with probably 2 or 3 crankangle degree resolution, shown in Fig. 4 as a flywheel ring gear position sensor.

As an example of one of the more unusual control strategies possible with a combustion pressure sensor, Fig. 5 portrays a concept for determining steady-state lean limit air dilution and spark advance commands based upon burn duration control of the combustion process. For example, cylinder-by-cylinder 0–90 percent mass fraction burn duration can be calculated in

Downloaded 01 Jun 2010 to 171.66.16.87. Redistribution subject to ASME license or copyright; see http://www.asme.org/terms/Terms_Use.cfm

real time from combustion pressure and crank angle sensor information. For simplicity, this quantity is called "burn duration" in Fig. 5. For any given mean burn duration, MBT spark advance is very simply determined. As the air/fuel ratio increases, both the mean burn duration and its cyclic variability increase, as shown. The engine could be held at steady-state MBT spark advance and the lean limit by simply increasing cylinder-by-cylinder air/fuel ratio until an unacceptable level of cyclic variability is experienced in the burn duration (or, alternatively, the work done per cycle).

Controller Sampling, Calculation, and Control. The controller's main window on the combustion process is derived from cylinder pressure and cylinder volume information. With a data update rate of approximately 10 kHz and signals that are virtually noise-free, the program can resolve the duration of combustion to 1.5 crank angle degrees at 2500 rpm. Cylinder volume is calculated from crankshaft position information using a simple/straightforward kinematic model involving crank arm and connecting rod geometry.

Burn duration dynamic information is extracted from the combustion pressure trajectory using the methodology outlined by Rassweiler and Withrow [18]. This involves partitioning the change in pressure observed since the previous data were obtained into a component due to the isentropic pressure change caused by piston motion and attributing the remainder of the positive change to combustion of the air/fuel charge within the cylinder. Start of combustion for burn duration timing purposes is set at the same time as spark plug firing. Spark timing is thus both an output from the controller and an input to its combustion timing computations.

End of combustion is detected by monitoring the pressure change from the time point after spark plug firing to the time when there is no additional positive pressure change above that induced by piston motion. In fact, the small but significant heat loss to the cylinder walls during the latter stages of combustion therefore ensures that the transition from positive to negative pressure change over and above that due to piston motion is steep and so readily detectable.

Controller Mechanics

Program Architecture. The controller algorithms designed [19] to perform the abovementioned functions are implemented in the AD10 control computer largely within one of its processors, the ARP or arithmetic processor. The primary program design criterion was short execution time during the portion of the program loop that samples in-cylinder pressure, and from that computes burn characteristics. Once end of burn has been reached in a given cylinder and before the next cylinder is scheduled to fire, the short execution loop time requirement is relaxed.

The program was therefore structured on a three-level basis. On the first and most basic level are the input/output transactions and the high priority code modules that must be executed during every pass or cycle of the program (frametime). Scheduled on the basis of the cylinder's position in the 720 deg engine cycle to execute during a window of ± 48 deg centered on TDC of the compression to power-stroke phase is a second level of code modules that perform cylinder specific and burn event computation. The end of burn detection logic is maintained at this level, as are spark signal detection and the collection of pressure and volume information for mass charge computation. Lastly, end-of-burn logic is managed at the second level to reset and trigger a flag on which basis the cylinder specific, once-per-engine cycle calculations are performed. On the third and lowest level are end-of-burn modules, one for each cylinder and effectively synchronized with each cylinder. Engine cycle related data collection (especially for graphic presentation) is performed by some modules at this place in the program structure.

Controller Functions. The function of the engine controller is to regulate fuel and air flow into the combustion chamber and to ignite this charge via an appropriately timed firing of the spark plug. All this is done to meet the changing speed and torque demands of the vehicle's operator. The experimental setup employed for testing controller operation consists of procedures to run the engine/dynamometer at a fixed rpm over a series of regulated torque level changes. For example, starting from a low level (20 ft-lb) the A/F charge and spark setting are modified to rapidly transit to a higher load level (e.g., 70 ft-lb), which is maintained for a number of seconds before applying fuel flow, air flow, and spark advance changes to bring the engine back to its former load setting.

The primary control variable that is directly altered in response to load changes is throttle angle setting to control air flow. For precise and rapid throttle plate motion control a stepper motor driver unit is cog belt geared at a 5:1 ratio to the throttle plate shaft. The AD10 control program issues direction and step signals, the latter at up to a 2000 Hz rate. As A/F ratio alteration induces changes in charge burn duration, the secondary control variables of fuel quantity and spark setting come into action. The controller operates the fuel injector pulse width setting to maintain charge burn duration at a predetermined value. This target burn duration value may be selected by the operator to be either fixed or a function of engine speed and load. The overall effect is considerable latitude in A/F ratio control.

A Real-Time Thermodynamic Model

Model Structure. The structure of the dynamic thermodynamic model was synthesized primarily from two physically oriented substructures or models. The first substructure defines a mechanically linked four-cylinder pump with a pressure and two-zone temperature and time-dependent characterization for each cylinder as well as breathing into finite intake and exhaust plenums. The basic cycle analysis is modeled after that of Blumberg and Kummer [20]; Blumberg et al. [21]; and Tobler [22]. The second substructure or model consists of a throttle body with a dual plenum four-cylinder pocket manifold, fuel injectors and condensation dynamics, common exhaust plenum, and load and rotational dynamics. This primarily lumped parameter characterization is based on the models of Powell [14], Morris and Powell [2], and Dobner [16].

Thermodynamic Process. The model used for the present studies is not currently a comprehensive thermodynamic representation. In particular, several simplifying assumptions are made with respect to heat transfer, mass fraction burn behavior, and thermodynamic properties of burned and unburned gases, which are all at the heart of a rigorous thermodynamic representation. There are two primary reasons for this: (*i*) The necessity for developing a real-time cylinder pressure based control design model implies functional dependence on control variables such as in-cylinder air charge, fuel charge, and spark advance, and on estimates of residual faction, burn duration, mean effective pressure, and so on, and (*ii*) the lack of an emission requirement for the initial investigation, the modeling of which would also be dependent on accurate estimates of cylinder composition and temperature, perhaps in several temperature zones.

The main governing equation for the open system for each cylinder consists of the first law of thermodynamics

$$E = \Sigma_i h_i m_i + Q - W + \Sigma_e h_e m_e$$

where E is the internal energy rate change, Q is the rate of heat added, W is the work transfer rate by the changing volume, m_i is the mass flow rate into the system from the intake manifold, and m_e is from the exhaust manifold. The quantity h is the en-

Downloaded 01 Jun 2010 to 171.66.16.87. Redistribution subject to ASME license or copyright; see http://www.asme.org/terms/Terms_Use.cfm

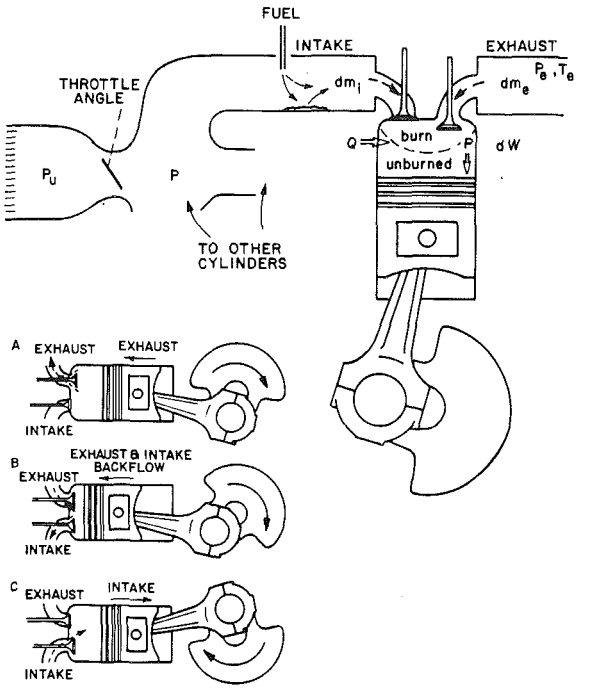


Fig. 6 Intake and exhaust flow events

thalpy per unit mass. In addition, the formulation employs the ideal gas law with uniform cylinder pressure. The charge is assumed to be a homogeneous mixture of air, vapor fuel, and residual gas during intake and before combustion. During combustion there exists a burned and unburned zone, with uniform composition and temperature, separated in volume by a burn propagation or mass fraction burn combustion rate relation. This is represented pictorially in Fig. 6.

For burned and unburned gases the differential internal energy is

$$dE = dE_u + dE_b, \qquad u = \text{unburned}, \quad b = \text{burned}$$
$$= C_v^u d(m_u T_u) + C_v^b d(m_b T_b)$$

where C_v is a constant volume specific heat, m is burned or unburned mass, and T is burned or unburned temperature. It is assumed that temperature and mass changes per unit time are larger than constant volume or constant pressure specific heats per unit time. Input and output enthalpy differentials are assumed to be

$$dH_i = c_p^i d(m_i T_i), \qquad i = \text{intake}$$
$$dH_e = c_p^e d(m_e T_e), \qquad e = \text{exhaust}$$

Substitution into the first law, and defining differential work as PdV, yields

$$dQ = C_v^b d(m_b T_b) + C_v^u d(m_u T_u) + PdV - c_p^i d(m_i T_i) - c_p^e d(m_e T_e)$$

If the burned and unburned gases are ideal and the cylinder pressure is assumed uniform, then

$$d(PV) = R_u d(m_u T_u) + R_b d(m_b T_b)$$

where $R = Cp - Cv$. Finally, defining the mass fraction burned as

$$x = m_b/(m_u + m_b)$$

yields one complete equation as

$$dP = \frac{C_v^u(\gamma_b - \gamma_u) m T_u dx + (\gamma_b - 1) dQ - \gamma_b p dv}{V + C_v^u(\gamma_b - \gamma_u)(1-x) m \left(\frac{\gamma_{u-1}}{\gamma_u}\right)\frac{T_u}{p}}$$
$$+ \frac{\frac{R_b}{C_v^b} C_p^i d(m_i T_i) + \frac{R_b}{C_v^b} C_p^e d(m_e T_e)}{V + C_v^u(\gamma_b - \gamma_u)(1-x) m \left(\frac{\gamma_{u-1}}{\gamma_u}\right)\frac{T_u}{p}}$$

where $\gamma = C_p/C_v$, with specific heats as functions of intake and exhaust concentrations as well as temperature.

The mass fraction burned rate is represented by a unimodal two-parameter beta function, the parameters of which are determined in situ, with dependence determined by fitting pressure curves to pressure changes during combustion for a range of engine operating conditions. The beginning of burning follows an ignition delay representation of Hires et al. [23]. Heat transfer is represented by a cylinder wall convection relation of Sherman and Blumberg [24], with assumed constant wall temperature and variable cylinder gas temperature.

The mass flow rate terms in the pressure rate equation are developed by assuming one-dimensional, steady, compressible flow of an ideal gas. Initial pressure and temperature losses before the opening are accounted for by assuming isentropic flow. The mass flow rates across the valve openings are given by the general quasi-steady equation [9, 25]

$$\dot{m} = A_e p_0 [\gamma/(RT_0)]^{0.5} \phi$$

where

$$\phi = \begin{cases} \left(\frac{2}{\gamma-1}\right)^{1/2} \sqrt{[(P_b/P_0)^{2/\gamma} - (P_b/P_0)^{(\gamma+1)/\gamma}]}; \\ \qquad (P_b/P_0) > \left(\frac{2}{\gamma+1}\right)^{\gamma/(\gamma-1)} \\ \left(\frac{2}{\gamma+1}\right)^{(\gamma+1)/[2(\gamma-1)]} \\ \qquad (P_b/P_0) \le \left(\frac{2}{\gamma+1}\right)^{\gamma/(\gamma-1)} \end{cases}$$

R is the specific gas constant, p_0 and T_0 are the upstream pressure and temperature, and P_b represents the downstream pressure. The effective area A_e is defined in terms of the flow area A, multiplied by a discharge coefficient C_D

$$A_e = C_D A$$

where C_D generally depends on several flow and geometric parameters. In general, flow reversal can occur any time the pressure ratio exceeds unity, in which case the upstream and downstream variables are reversed in the flow rate equation. The changing flow area A is a function of the valve lift profile, which is specified in terms of cylinder crankangle. The coefficient of discharge C_D is specified as a function of valve lift to seat diameter ratio [9, 23].

Inaccurate representation of mass flow rates ultimately causes significant deviation in the pressure rate equation, and component mass charge calculations. Thus, an accurate estimate of the combined effects of discharge coefficient and valve lift profiles is especially important during the valve overlap portion of the breathing process. Calibration of the parameters used in the simulation model was by comparison of cylinder pressure profiles during an engine pumping and

Downloaded 01 Jun 2010 to 171.66.16.87. Redistribution subject to ASME license or copyright; see http://www.asme.org/terms/Terms_Use.cfm

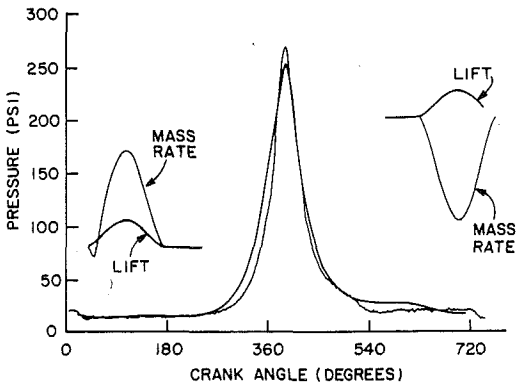


Fig. 7 An initial engine model in-cylinder pressure profile comparison with measured engine pressure data

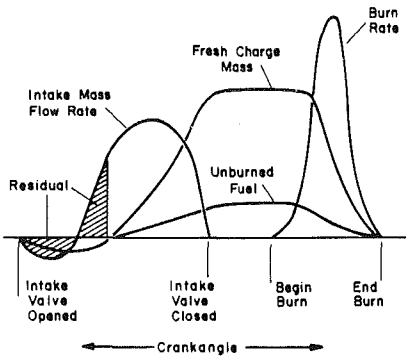


Fig. 9 General intake flow rate and constituent behavior during combustion

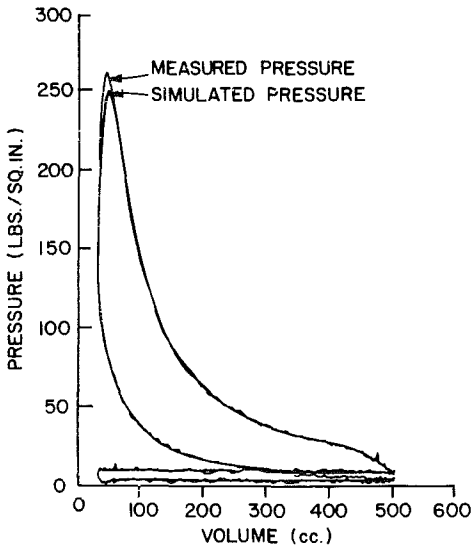


Fig. 8 Pressure indicator comparison after exhaust valve adjustment

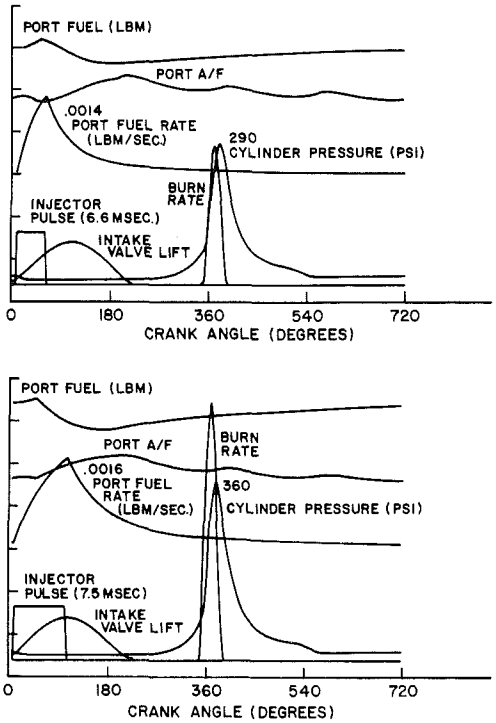


Fig. 10 Examples of parameter variation on engine model operation

light load mode at several different speeds and manifold pressure conditions. Such a comparison is shown in Fig. 7.

Shown also are lift profiles and typical mass flow rates. Adjustments to the exhaust valve flow rate geometric parameters would yield a more favorable comparison. Model and experimental comparison is shown in Fig. 8, after exhaust valve parameter adjustment, and is typical of results obtained at several speed and manifold pressure settings.

Intake Process. During the valve overlap period, mass backflow in both exhaust and intake systems for each cylinder is assumed to be a plug type flow. Only burned (residual) gas crosses the exhaust valves, whereas the charge entering the intake manifold during intake valve opening is the first to return during positive valve flow.

After complete induction of residual gas, the fresh charge induction begins. Induction of any component (vapor fuel, air, or EGR) is estimated by integration of the product of intake mass flow rate and component concentration, outside of the intake valve, during intake valve opening. The region immediately outside of each intake valve is referred to as the intake port (runner termination in an actual manifold) and the mass concentrations in each port are calculated by first assuming conservation of mass for each constituent in the port.

Thus

$$\frac{dm}{dt} = \dot{m}_{in} - \dot{m}_{out}$$

where m_{in} is air and fuel flow rate into the port volume and m_{out} is the ingested mass flw rate for that constituent. For example, for fuel

$$\dot{m}_{fout} = c_f \dot{m}$$

where c_f is the changing ratio of the mass of fuel in the port divided by the total mass in the port and m is the total changing ingested mass flow rate for a particular cylinder. The integration to obtain the constituent masses is a continuous process independent of crankangle. It is assumed that all fuel is burned during the combustion process and all fresh charge becomes residual. A pictorial representation of the process for one cylinder is shown in Fig. 9. It is assumed that there is some fuel condensation near each cylinder port and the fuel condensation model employed for the warm engine simulation is that of Aquino [26]. A simulation result for two different injector pulse widths (the same for all cylinders) is shown in Fig. 10. The injection timing is shown as injection into an open valve, which is not the general operating mode for the control study results presented herein. The figure shows the general behavior of the port ingestion fuel rate (characteristic of first-

Downloaded 01 Jun 2010 to 171.66.16.87. Redistribution subject to ASME license or copyright; see http://www.asme.org/terms/Terms_Use.cfm

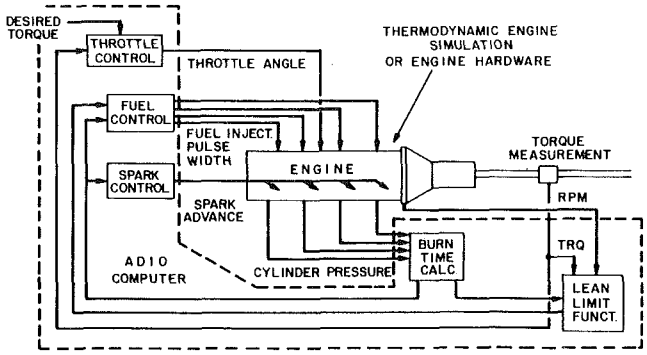


Fig. 11 Burn duration based engine control

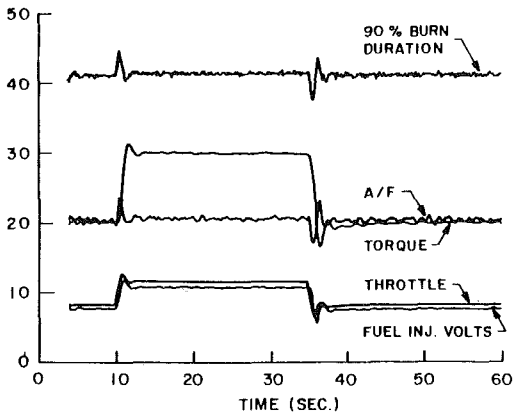


Fig. 12 Combined thermodynamic and cylinder pressure based control model

order fuel evaporation rate model), the port vapor fuel (which continually increases after injector firing is stopped due to local evaporation), and the varying local port A/F changing during the breathing of each cylinder.

Induction Process. The induction process consists of a throttle body embedded between an upstream single-channel plenum with air filter (or air measuring restriction) and a downstream intake plenum with a local port region near each intake valve. Manifold pressure is assumed uniform (no acoustic propagation) and the total air mass in the manifold, calculated from the ideal gas law, is prorated by runner volume. For the upstream plenum, the mass conservation equation is

$$\frac{dm_u}{dt} = \dot{m}_u - \dot{m}_a$$

where $\dot{m}_u$ is the mass flow rate through the upstream air measuring device (or filter) defined by a quasi-steady flow equation dependent on a ratio of atmospheric pressure and upstream manifold pressure, and m_a is the throttle body air flow rate given as a nonlinear separable function of upstream-manifold pressure ratio and the elliptic function of the discharge coefficient and throttle throat geometry (throttle angle).

Mass conservation applies to the intake manifold as

$$\frac{dm_i}{dt} = \dot{m}_{j\,in} - \dot{m}_{j\,out}$$

where $\dot{m}_j$ denotes air, vapor fuel, residual gas, or manifold leakage. The rate of change of manifold pressure, for constant intake temperature, is proportional to the difference in manifold ingress and manifold egress rates as

$$\dot{P} = K_p\left(\dot{m}_a + \sum_j \dot{m}_{fj} + \dot{m}_1 - \dot{M}\right)$$

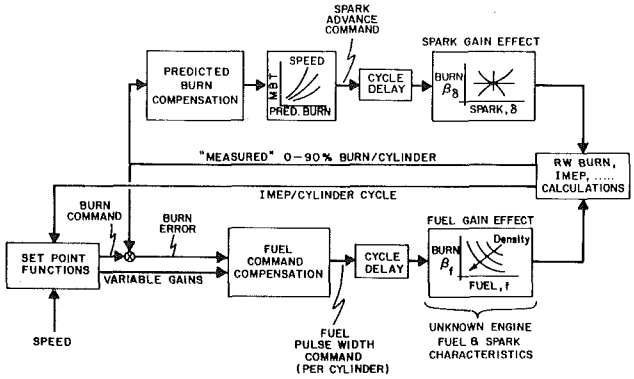


Fig. 13 Information flow of 0–90 percent mass fraction burn duration feedback control for each cylinder

where m_{fj} denotes the vapor fuel in the jth port, m_1 denotes leakage, and M denotes the mass rate pumped by any cylinder at any time. The proportionality constant K_p is a function of the gas constant, gas molecular weight, specific heat parameters, manifold temperature, and manifold volume.

For the assumed constant intake manifold temperature, separate energy conservation equations were not employed to develop a temperature profile as in Servati [26], and Servati and Aquino [27].

A lumped parameter approximation in the form of a differential in air concentration C_a was used as

$$\frac{dC_a}{dt} = \frac{1}{\tau_m}\left(\frac{m_a}{m} - C_a\right)$$

where τ_m is an approximation of manifold mass residence time, which is manifold and engine displacement dependent and is on the order of 30/rpm s.

Controller/Model Simulation. Linking the AD10 engine controller directly to the dynamic model is useful for the development of control logic, data sampling, and filtering. It is equally useful for static and dynamic, open loop and closed loop, strategy analysis and synthesis. Samples taken directly from each simulated cylinder time history are used to calculate burn duration (per cylinder), work (IMEP), etc., followed by control command generation and transmission to the engine simulation in a manner analogous to the actual hardware-in-the-loop process.

This is depicted in Fig. 11. Because of the desired computational sampling resolution (1 to 2 crankangle degrees) the combination of the controller and engine dynamic model requires a simulation slowdown with respect to real time. A simulation of the combination at 1800 rpm, for a "driver" throttle kick employing the burn duration control law presented in the next section, is shown in Fig. 12.

Combustion Pressure Based Control

The existence of in-cylinder combustion pressure sensors could radically alter thinking about engine control strategies. As suggested in the discussion on combustion quality feedback control, these sensors could effect feedback and adaptive trim of both charge dilution and spark advance in existing speed density or mass air flow systems. Figure 13 portrays, in some detail, the control concept mentioned earlier (Fig. 5). That is a concept for determining lean limit air dilution and spark advance commands based upon burn duration control of the combustion process. In particular, cylinder-by-cylinder 0–90 percent mass fraction burn duration is calculated in real time from combustion pressure and crank angle sensor information. For a given mean burn duration, MBT spark advance command is calculated from a priori experimentally obtained

Downloaded 01 Jun 2010 to 171.66.16.87. Redistribution subject to ASME license or copyright; see http://www.asme.org/terms/Terms_Use.cfm

relations. As the air/fuel ratio increases, both the mean burn duration and cyclic variability of IMEP increases. The engine is held at steady state MBT spark advance and a lean limit air/fuel ratio by simply increasing the cylinder-by-cylinder air/fuel ratio until an unacceptable level of cyclic variability in the work done per cycle is experienced. The main drawback of this control scheme is its relatively slow response to rapidly induced speed and/or load changes.

There are some additional considerations in dynamic spark and fuel control. For the spark advance control it is desirable to determine predicted burn to obviate knock and misfire, and to provide levels of ability to control for some operating modes (i.e., spark margin). This will generally provide a weak control loop (weak spark–fuel interaction at MBT) and liberal compensation gains can be chosen to affect a stability versus response tradeoff. An additional consideration is that the controller actually uses an "average" spark over four cylinders as there is one continually changing spark advance rather than a different advance for each cylinder. For fuel control, the burn duration command is based on engine speed, implicit emissions considerations from experimentally determined set point functions of engine speed and IMEP, and compensation for IMEP variability as well as inequities in work per cylinder.

The fuel command compensation shown in Fig. 13 is fundamentally a proportional and integral (PI) control. The inner loop control gains (variable gains) are maximized for nonoscillatory dynamic performance, which is dependent on burn rate sensitivity to air charge and fuel. The integral error function of the fuel loop is necessary in order to command and achieve 5 percent error resolution in burn.

Controller/Model Developments. While initial developments of the thermodynamic engine model and the combustion pressure based engine controller passed through several stages independently of each other, more recent work on both has been done in concert and with information and experience derived from controller–engine hardware experiments. The model–controller combination has proved very useful in implementing and testing modifications to the controller by providing a safe environment for exercising new code modulus destined to control engine–dynamometer hardware in operating regions where a "simple bug" might have catastrophic consequences. At the same time, the relative costs, in time, personnel, and facilities, of operating the model versus engine–dynamometer hardware encourage use of the former as long as it closely mirrors the performance of the latter.

Conversely, the development of the model has benefited from repeated comparisons with the "real hardware." The controller that they have in common has here been employed to examine functional differences. Thus when the end-of-burn detection procedure that successfully observed this event in the engine was unable to do so in the model, the comparison pointed to an incomplete accounting for pressure changes in the latter. By including an additional term for thermal loss to the cylinder walls in the model, the end of burn could be detected using the identical controller logic.

Results. While both engine model and controller development is continuing at the facility, there are a series of results that indicate the utility and support the validity of the methodology here described. For example, closed-loop control was applied to the actual engine hardware and this (and the model) was exercised over a series of ramped load trajectories as shown in Fig. 14 for the model and Fig. 15 for the engine.

There are differences in the high torque regions that may be ascribed to nonlinearities in this area of the model. The dynamics of the transition from one load level to another are also an area of difference, but one that points to more basic

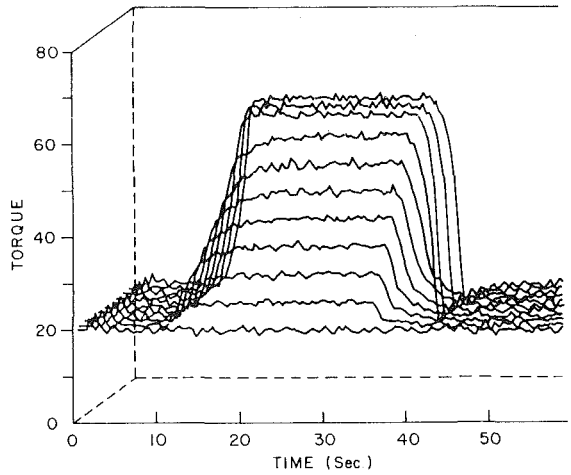


Fig. 14 Thermodynamic engine model multirun torque output; composite of eleven 60 s test runs of torque ramps from 20 to 70 ft-lb

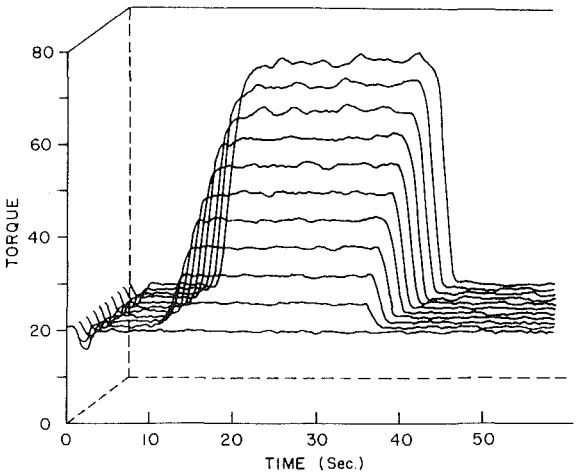


Fig. 15 Engine hardware multirun torque output; composite of eleven 60 s test runs of torque ramps from 20 to 70 ft-lb

disagreements between the model and engine that yet remain to be resolved. Despite these and other, less apparent differences, the overall similarity in engine hardware and engine model behavior is sufficiently high that basic controller functions pertaining to mass air and fuel flow and spark timing may be exercised on either plant with good dynamic fidelity.

Conclusions

The development of a real-time and dynamic thermodynamic engine simulation model and hardware-in-the-loop computer capability form an advanced analytical and experimental automotive powertrain control synthesis tool. In particular, investigation of high data rate information, such as in-cylinder pressure, as a potential feedback control variable, is feasible with such a facility.

Acknowledgments

The authors would like to acknowledge the contributions of data and data analysis by R. Stein and Z. Menzik; the technical consulting of R. Tabaczynski, R. Belaire, and W. Tobler; the dynamometer instrumentation of M. Smokowivtz; and the engine build and hardware-human-in-the-loop system running support of P. Roth. Finally C. Bock should be acknowledged for typing the manuscript.

Downloaded 01 Jun 2010 to 171.66.16.87. Redistribution subject to ASME license or copyright; see http://www.asme.org/terms/Terms_Use.cfm

References

1 Penn, G. R., "An Analog Model of a Powerplant Coupled to a Real Car for Structural Dynamic Development," SAE Paper No. 680147, Jan. 1968.

2 Morris, R. L., and Powell, B. K., "Modern Control Applications in Idle Speed Control," *Proceedings of the 1983 American Control Conference*, Vol. 1, June 22, 1983, pp. 79–85.

3 Auslander, D. M., and Tham, C. H., "Real Time Software for Control," published course notes, Mechanical Engineering, University of California, Berkeley, CA, 1985.

4 Athans, M., "The Role of Modern Control Theory for Automative Engine Control," SAE Paper No. 780852, Oct. 1978.

5 Howe, R. M., "Special Considerations in Real-Time Digital Simulation," *Poceedings 1983 Summer Computer Simulation Conference*, La Jolla, CA, pp. 64–71.

6 Howe, R. M., "Techniques for Optimizing Computer Performance in Real-Time Flight Simulation," *Proceedings of the Conference on Aerospace Simulation*, Jan. 23–25, 1986, La Jolla, CA.

7 Mosey, R. J., and Powell, J. D., "Closed Loop, Knock Adaptive Spark Timing Control Based on Cylinder Pressure," ASME *Journal of Dynamic Systems, Measurement, and Control*, Vol. 101, Mar. 1979.

8 Hubbard, M., Dobson, P. D., and Powell, J. D., "Closed Loop Control of Spark Advance Using a Cylinder Pressure Sensor," ASME *Journal of Dynamic Systems, Measurement, and Control*, Vol. 98, Dec. 1976.

9 Novak, J. M., "Simulation of the Breathing Processes and Air–Fuel Distribution Characteristics of Three-Valve, Stratified Charge Engines," SAE Paper No. 770881, Sept. 26, 1977.

10 Bedron, E. C., and Beretta, G. P., "General Thermodynamic Analysis for Engine Combustion Modeling," SAE Paper No. 850205, Feb. 25, 1985.

11 Delosh, R. G., et al., "Dynamic Computer Simulation of a Vehicle With Electronic Engine Control," SAE Paper No. 810447, 1981.

12 Garofalo, F. J., "Performance Capabilities of Various Air Measurement Techniques for Air/Fuel Ratio Feedforward Control Strategies on Electronic Fuel Metered Engines," The University of Michigan, June 30, 1975.

13 Prabhakar, R., Citron, S. J., and Goodson, R. E., "Optimization of Automotive Engine Fuel Economy and Emissions," ASME Paper No. 75-WA/Aut-19, Dec. 1975.

14 Powell, B. K., "A Simulation Model of an Internal Combustion Engine–Dynamometer System," *Proceedings of the Summer Computer Simulation Conference*, Newport Beach, CA, July 24, 1978.

15 Powell, B. K., "A Dynamic Model for Automotive Engine Control Analysis," *Proceedings of the 18th IEEE Conference on Decision and Control*, 1979, pp. 120–126.

16 Dobner, D. J., "A Mathematical Model for Development of Dynamic Engine Control," SAE Paper No. 800054, Feb. 1980.

17 Dobner, D. J., "Dynamic Engine Models for Control Development—Part 1: Nonlinear and Linear Model Formulation," *Application of Control Theory in the Automotive Industry*, Interscience Publication.

18 Rassweiler, G. M., and Withrow, L., "Motion Pictures of Engine Flames Correlated With Pressure Cards," SAE Paper No. 800131, Jan. 14, 1938 and Feb. 1980.

19 Hogh, G., "Event Driven Scheduling for Processing Automotive Combustion Data," Applied Dynamics International User's Society, Ann Arbor, MI, June 23, 1986.

20 Blumberg, P. N., and Kummer, J. T., "Prediction of NO Formation in Spark-Ignited Engines," *Combustion Science and Technology*, Vol. 4, 1971, pp. 73–95.

21 Blumberg, P. N., Lavoie, G. A., and Tabaczynski, R. J., "Phenomenological Models for Reciprocating Internal Combustion Engines," *Proceedings on Energy Combustion Science*, Vol. 5, 1971, pp. 123–167.

22 Tobler, W. E., "Thermodynamic Simulation—Modeling and Analysis," Progress Report on R35L6, Ford Motor Company, June 1980.

23 Hires, S. D., Tabaczynski, R. J., and Novak, J. M., "The Prediction of Ignition Delay and Combustion Intervals for a Homogeneous Charge, Spark Ignition Engine," SAE Paper No. 780232, Feb. 1978.

24 Sherman, R. H., and Blumberg, P. N., "The Influence of Induction and Exhaust Procession Emissions and Fuel Consumption in the Spark Ignited Engine," SAE Paper No. 770880, Sept. 1977.

25 Hamburg, D. R., and Hyland, J. E., "A Vaporized Gasoline Metering System for Internal Combustion Engines," SAE Paper No. 760288, Feb. 1976.

26 Aquino, C. F., "Transient A/F Control Characteristics of the 5 Liter Central Fuel Injection Engine," SAE Paper No. 810494, Feb. 1981.

27 Servati, H. B., "Investigation of the Behavior of Fuel in the Intake Manifold and its Relation to S. I. Engines," Ph.D. Thesis, University of California, Santa Barbara, CA, Mar. 1984.

28 Servati, H. B., and Aquino, C. F., "A Physically Based Wall Wetting Model to Predict Induction System Dynamics for Gasoline Engines," *Symposium on Simulation and Control of Ground Vehicles and Transportation Systems*, ASME Winter Annual Meeting, Anaheim, CA, Dec. 1986.

29 Wu, H., Aquino, C. F., and Chou, G. L., "A 1.6 Liter Engine and Intake Manifold Dynamic Model," ASME Paper No. 83-WA/DSL-39, 1983.

Downloaded 01 Jun 2010 to 171.66.16.87. Redistribution subject to ASME license or copyright; see http://www.asme.org/terms/Terms_Use.cfm

A Natural Gas Engine Combustion Rig With High-Speed Photography

W. E. Snyder
Professor,
Milwaukee School of Engineering,
Milwaukee, WI;
Vice President (Retired),
Waukesha Engine Division,
Dresser Industries, Inc.,
Milwaukee, WI

M. R. Wright
Development Engineer.

S. G. Dexter
Manager.

Large Engines Department,
Ricardo Consulting Engineers,
Shoreham-by-Sea, West Sussex,
United Kingdom

Engines today must satisfy stringent emission requirements but must at the same time have low fuel consumption. One method of approaching both of these goals in spark-ignited natural gas engines is with lean combustion. The use of as much as 80 percent excess air significantly reduces the peak combustion temperature and, as compared to a stoichiometric engine, reduces the NO_x emissions by up to 90 percent and the fuel consumption by up to 15 percent. One limitation on lean combustion, however, is the high energy needed for ignition. In larger engines, a small prechamber containing an easily ignitable near-stoichiometric mixture has proved to be both successful and popular as one method of producing the necessary high ignition energy. Although this form of stratified charge combustion has been known for many years, its development has largely been the result of "cut and try" procedures. Lack of access for suitable instrumentation, combined with the difficulty of isolating the individual variables which affect performance, has limited the fundamental understanding of the mechanism of prechamber combustion. This paper summarizes results from a research program where a constant-volume combustion rig is used to simulate engine operation. Emphasis is placed on high-speed photography of the prechamber combustion. A second program on a single-cylinder prechamber spark-ignited gas engine and a third on a multiple-cylinder engine will be reported in subsequent papers.

Constant-Volume-Combustion (CVC) Rig

The prechamber in a lean combustion natural gas engine serves two main purposes. These are (1) to provide an easily ignited near-stoichiometric mixture in the prechamber and (2) to create a high degree of turbulence near the spark plug. To simulate engine prechamber combustion adequately in a static rig, both of these conditions must be carefully reproduced.

During the compression stroke in an engine, some of the lean mixture originally in the main chamber flows into the prechamber with high velocity. This lean mixture combines with the gas already in the prechamber to produce the near-stoichiometric mixture required for easy ignition. The entering high-velocity gas also produces high turbulence, which in turn promotes rapid burning in the prechamber and subsequent stable burning in the main chamber.

To simulate these engine events, the CVC rig was designed with a valve, which is closed to separate the main chamber from the prechamber during the charging procedure and then opened to allow a prechamber gas inflow similar to that which occurs in an engine during the engine compression stroke.

The CVC rig is a full-size three-dimensional copy of the combustion chamber of the Ricardo 8.5 in. (216 mm) bore test engine at its top dead center position. It is designed for easy modification of the prechamber. Both chambers are fitted with windows for high-speed movies.

Figure 1 shows a simplified section of the rig. With the valve in the closed position, the main chamber is charged with a lean mixture of methane at a high pressure, and the prechamber is charged with pure methane at a lower pressure. To start the firing sequence, the valve is quickly withdrawn to allow some of the lean mixture from the main chamber to flow rapidly into the prechamber. The valve and the valve opening mechanism required to produce realistic conditions in a static device were major considerations in the early development of the CVC rig; the valve must be withdrawn at a rapid but carefully controlled rate in order to duplicate the engine flow

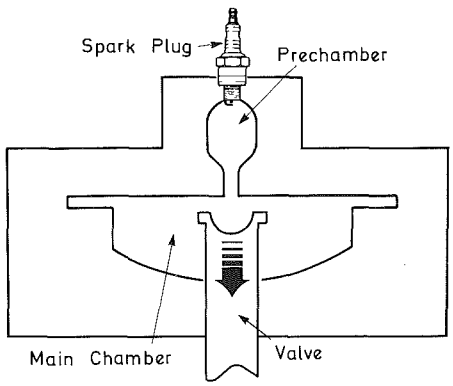


Fig. 1 Simplified section of CVC rig

Contributed by the Internal Combustion Engine Division and presented at the Internal Combustion Engine Division Technical Conference, Kansas City, Missouri, October 4-7, 1987. Manuscript received by the Internal Combustion Engine Division June 1987.

Copyright © 1988 by ASME
Downloaded 01 Jun 2010 to 171.66.16.87. Redistribution subject to ASME license or copyright; see http://www.asme.org/terms/Terms_Use.cfm

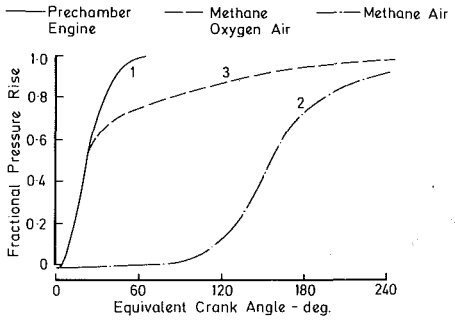


Fig. 2 Comparison of combustion rates

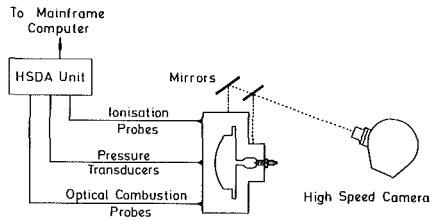


Fig. 3 Diagram of instrumentation

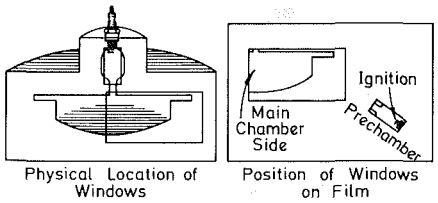


Fig. 4 Position of windows

conditions. At the appropriate time after valve opening, the spark plug in the prechamber is fired to initiate combustion.

The gases are all initially at ambient temperatures and the rig is not heated; therefore, combustion of a normal air–methane mixture in the rig prechamber would be slower than for the same mixture in an engine where the temperature at the end of compression is much higher than ambient. The heat release rate can be restored to that of the engine, however, by adding extra oxygen to the air, thereby reducing the diluent effect of the nitrogen, which slows combustion; a reduced proportion of nitrogen can compensate for the lower temperature. For this purpose, the rig is charged with a combination of air, methane, and oxygen to produce a mixture that has a combustion rate in the rig equal to that observed in an engine. Figure 2 compares the combustion rates of (1) an engine operating at 1200 rpm, (2) the CVC rig charged with normal air and methane, and (3) the CVC rig charged with oxygen-enriched air and methane. To obtain the proper rate, the oxygen-enriched air had an oxygen concentration of 42 percent.

The primary objective in developing the CVC rig was to obtain high-speed movies of the combustion processes in both the prechamber and the main chamber and to correlate these movies with other data. As shown diagrammatically in Fig. 3, the instrumentation includes the following:

- A high-speed camera operating at 14,000 frames/second.
- Pressure transducers in both the pre- and main chamber.
- Ionization probes, one in the prechamber throat and one in the main chamber.
- Optical combustion sensors, one in each chamber.
- A High-Speed Data Acquisition unit with the capability of recording eight channels with 12 bit resolution at a sampling frequency of 150 kHz.

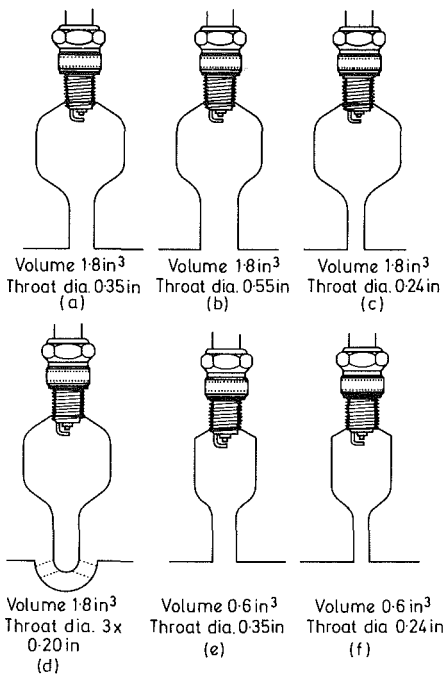


Fig. 5 Prechamber throat geometries

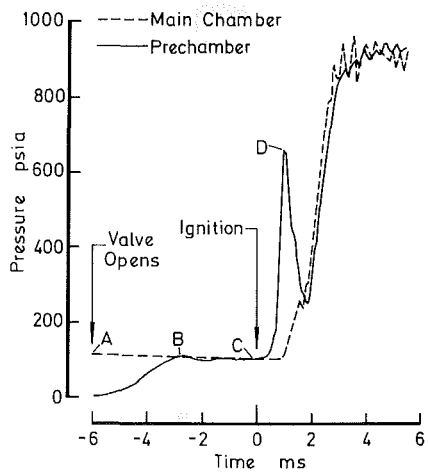


Fig. 6 Pressure diagram; throat diagram 0.35 in. (9 mm)

Figure 4 shows the position of the two windows used in the CVC rig and their orientation on the movie film. Note that because of the optics required for simultaneous photography of both windows, the prechamber is not in its true position in the films; rather, it is displaced to the right-hand portion of the film and appears at an angle. In the films, therefore, the prechamber flame progresses upward from the spark plug at the lower right toward the throat at the upper left.

Test Program

A number of different prechambers were tested with dimensions as shown in Fig. 5. Figure 5(*a*) with a throat diameter of 0.35 in. (9 mm) and a volume of 1.8 in.^{3} (30 cm^3) was considered "standard"; this volume is approximately 3 percent of the main-chamber volume at top dead center.

For all of the simulation runs, the prechamber was charged to an absolute pressure of 9 psia (0.6 bar) with pure methane, and the main chamber to an absolute pressure of 130 psia (9.0 bar) with a lean mixture of methane and oxygen-enriched air as described earlier. At ignition, the prechamber mixture was

Downloaded 01 Jun 2010 to 171.66.16.87. Redistribution subject to ASME license or copyright; see http://www.asme.org/terms/Terms_Use.cfm

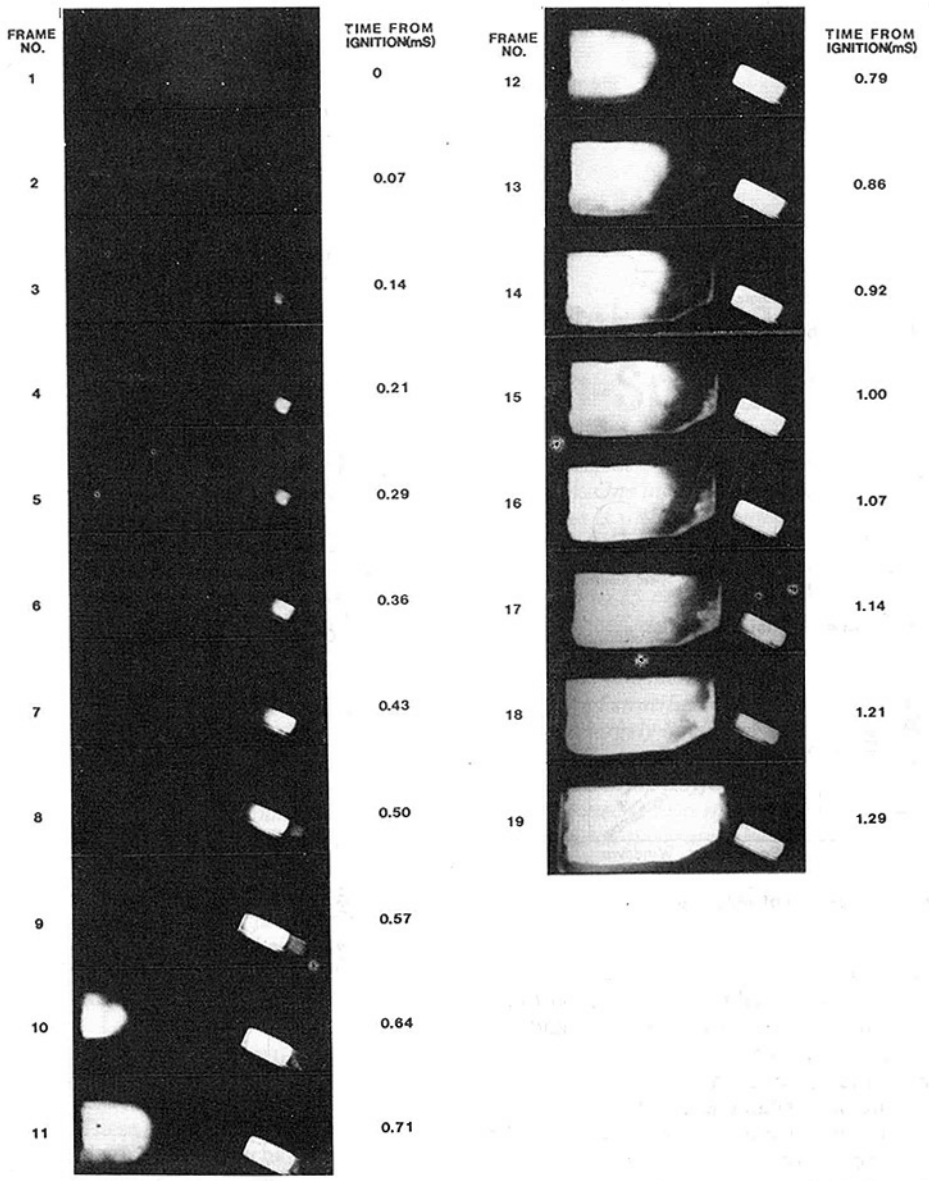


Fig. 7 Movie stills; throat diagram 0.35 in. (9 mm)

near-stoichiometric and the charge approximated full-load engine conditions near the end of the compression stroke.

Figure 6 shows data and Fig. 7 shows selected prints from the movie sequence for a typical test run with the standard prechamber. The sequence of events was as follows:

Prechamber Filling. As the valve opened, lean mixture from the main chamber flowed rapidly into the prechamber and mixed with the methane already there. The pressure in the prechamber rose in the interval from A to B as noted in Fig. 6. This event is equivalent to the compression stroke in an engine.

Ignition. After a controlled time interval, the ignition system was triggered to produce a spark at point C. Note that the time scale was set to zero at ignition.

Prechamber Combustion. Immediately after the spark occurred, the first visible flame could be seen as shown in Frame 1 in Fig. 7. The flame started as a small, slowly growing area around the electrode gap, where it seemed to linger for a short while before beginning to develop more rapidly.

The spread of the flame through the prechamber was generally seen to follow an orderly and expected course, almost as if it were a flame front passing through a quiescent charge. From the movies it could be seen that the flame speed accelerated to about 300 ft/sec (90 m/s). (For comparison, the flame speed in a quiescent chamber would be about 30 ft/sec (9 m/s) [1].) The flame speed in the prechamber is, of course, the sum of the speed of the flame with respect to the gas plus the speed of the gas itself due to the high rate of flow out of the prechamber throat; this latter effect becomes particularly significant as the flame approaches the throat.

The pressure in the prechamber started to rise as the prechamber burned—slowly at first, then more rapidly so that it formed a "spike" in the pressure trace at Point D where the maximum pressure is 650 psia (45 bar). As the pressure in the prechamber increased, the flow out of the prechamber rapidly increased and over much of the period was choked at the throat.

Main-Chamber Combustion. The jet from the prechamber entered the main chamber, moving downward from the top left-hand corner of the photograph as seen at Frame 9 in Fig. 7. From there it progressed across the main

Downloaded 01 Jun 2010 to 171.66.16.87. Redistribution subject to ASME license or copyright; see http://www.asme.org/terms/Terms_Use.cfm

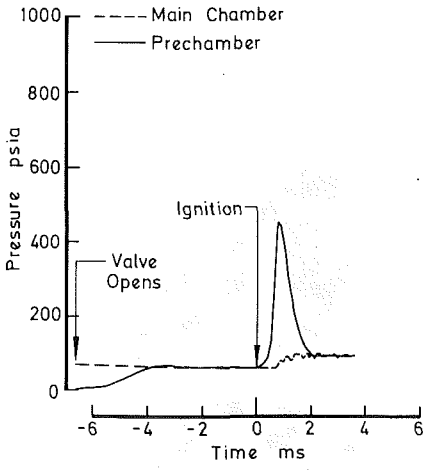


Fig. 8 Pressure diagram; throat diagram 0.35 in. (9 mm)

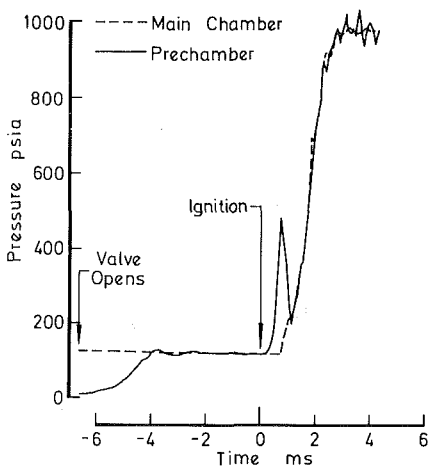


Fig. 10 Pressure diagram; throat diagram 0.55 in. (14 mm); lean main chamber

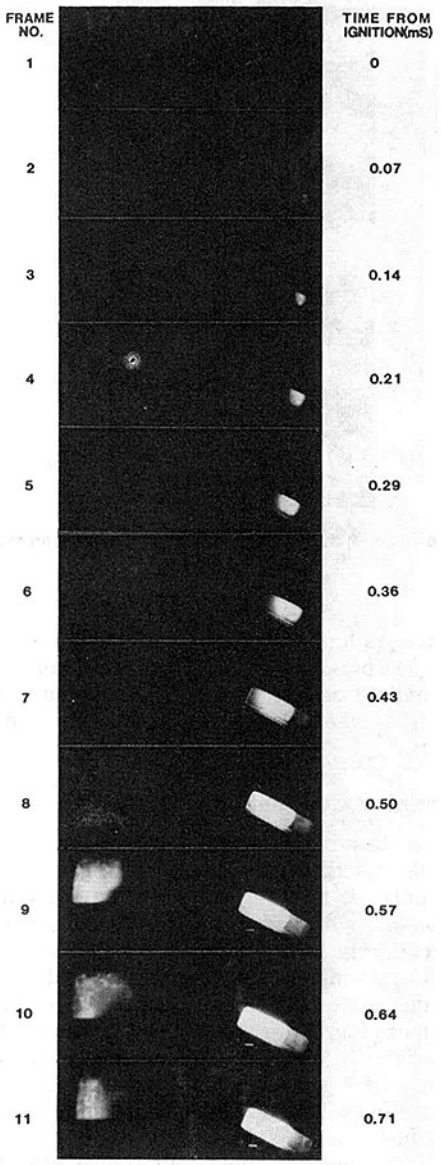


Fig. 9 Movie stills; throat diagram 0.35 in. (9 mm); air in main chamber

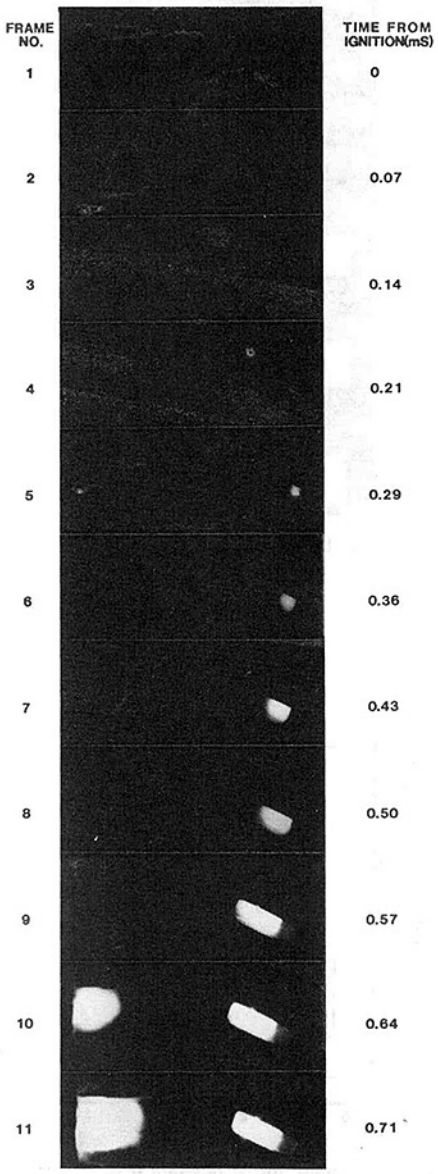


Fig. 11 Movie stills; throat diagram 0.55 in. (14 mm); lean main chamber

Downloaded 01 Jun 2010 to 171.66.16.87. Redistribution subject to ASME license or copyright; see http://www.asme.org/terms/Terms_Use.cfm

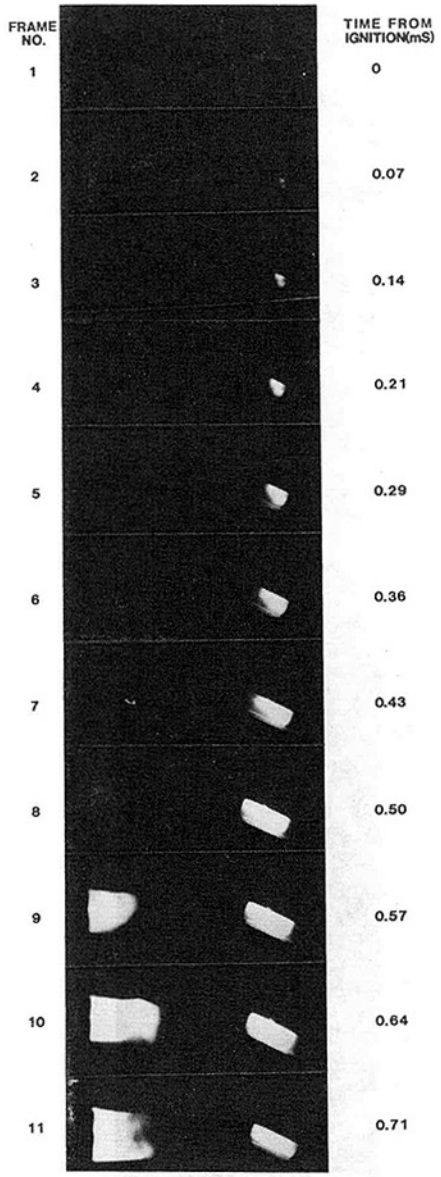


Fig. 12 Movie stills; throat diagram 0.55 in. (14 mm); air in main chamber

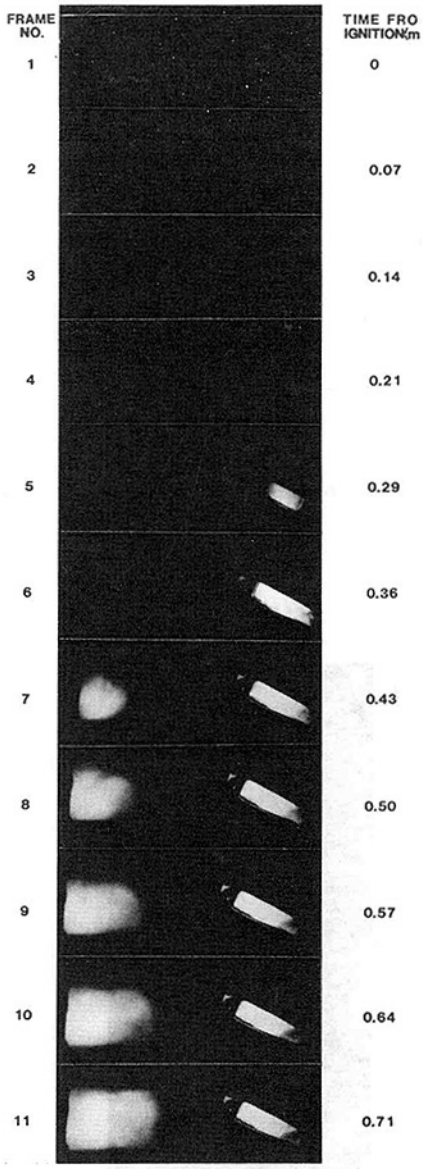


Fig. 14 Movie stills; throat diagram 0.24 in. (6 mm); lean main chamber

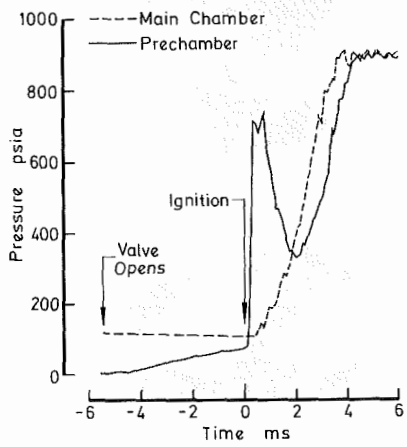


Fig. 13 Pressure diagram; throat diagram 0.24 in. (6 mm); lean main chamber

chamber at a gradually reducing velocity and in a fairly orderly fashion. The pressure in the main chamber continued to rise until the combustion was complete. The prechamber pressure also rose throughout this period as mixture re-entered the prechamber.

Main Chamber Containing Air Only

With a combustible mixture in the main chamber, as in the sequence just described, the flame due to gas emerging from the prechamber is indistinguishable from the flame due to combustion of the main chamber gas. To separate the two effects, several runs were made with only air in the main chamber; one example is shown in Figs. 8 and 9. Since there was no combustible gas in the main chamber, all of the flame that appears in Fig. 9 in Frames 7 and later must have come from gas originally in the prechamber. A comparison with the results from Fig. 7 (where the main chamber did contain combustible gas) indicates that the main-chamber gas is ignited very early in the process. In Fig. 9, the burning jet of gas reaches a maximum size about four frames after it first appears in the main chamber. In contrast, at a comparable frame

Downloaded 01 Jun 2010 to 171.66.16.87. Redistribution subject to ASME license or copyright; see http://www.asme.org/terms/Terms_Use.cfm

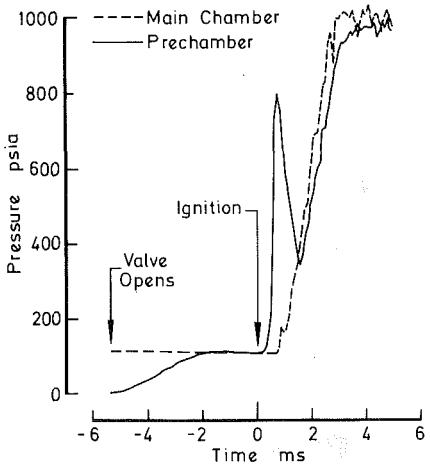


Fig. 15 Pressure diagram; throat diagram 3 × 0.20 in. (5 mm); lean main chamber

in Fig. 7, the flame has extended radially well into the main chamber. It thus appears that main-chamber combustion is initiated when the flame first enters the main chamber and that it proceeds rapidly, probably aided by the further expansion of the jet.

Reduced Throat Restriction

In the prechamber shown in Fig. 5(*b*), the nozzle flow restriction was reduced by increasing the throat diameter from 0.35 in. (9 mm) to 0.55 in. (14 mm). Figures 10 and 11 show the pressure diagrams and the movie stills with this larger diameter. The prechamber pressure spike decreased from 650 psia (45 bar) to 460 psia (32 bar). The photographs, however, show that the progress of the flame in both the prechamber and the main chamber remained essentially unchanged. Also, the combustion rate closely matched that of the standard prechamber. This observation lends support to the conclusion that the main-chamber combustion starts immediately when

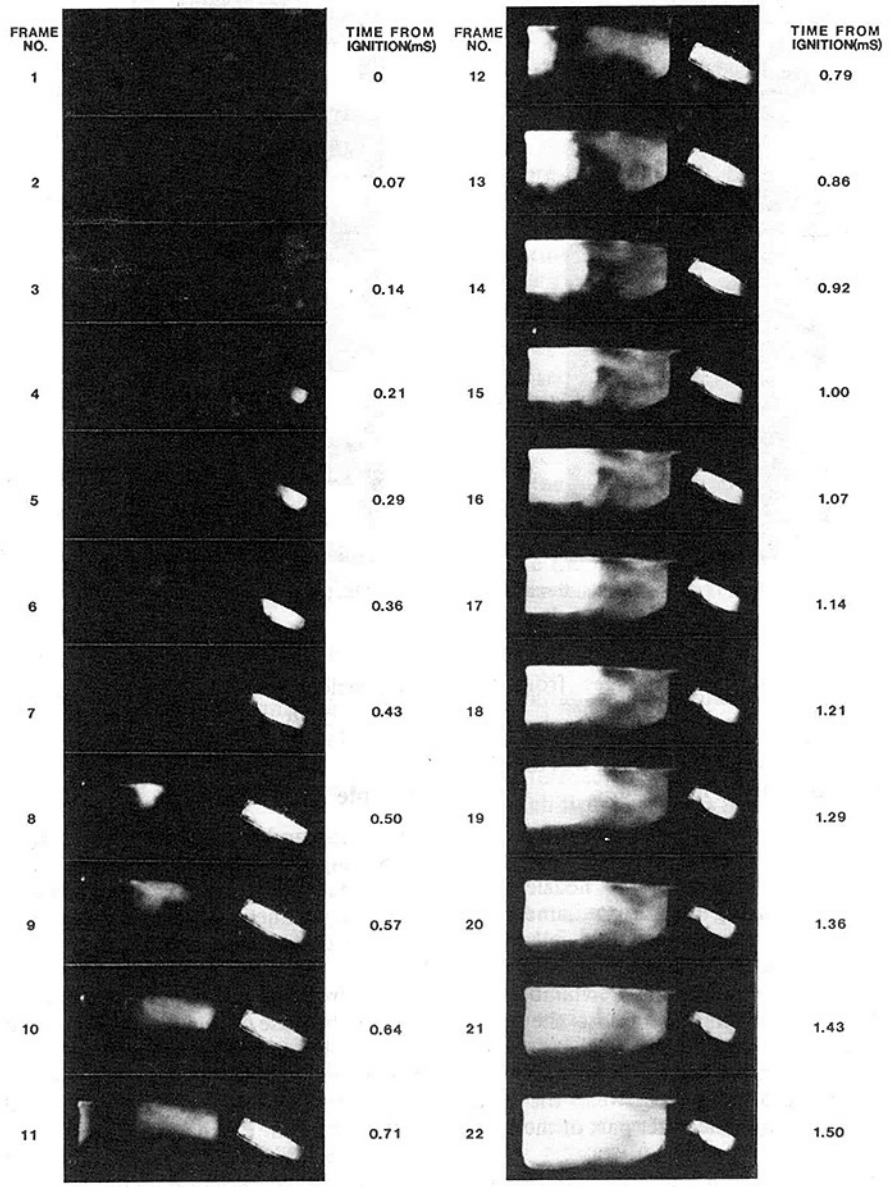


Fig. 16 Movie stills; throat diagram 3 × 0.20 in. (20 mm); lean main chamber

Downloaded 01 Jun 2010 to 171.66.16.87. Redistribution subject to ASME license or copyright; see http://www.asme.org/terms/Terms_Use.cfm

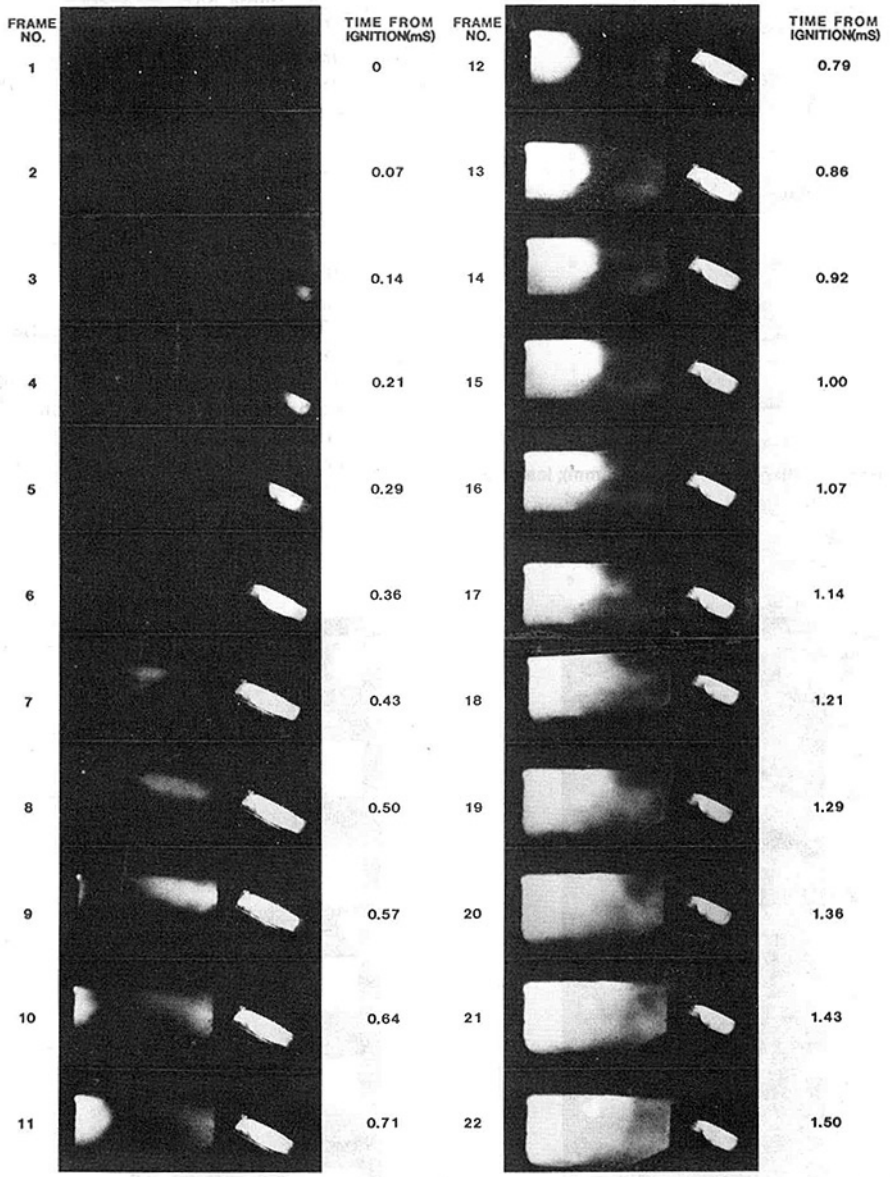


Fig. 17 Movie stills; throat diagram 3 × 0.20 in. (20 mm); partial misfire

the first portion of the burning gas emerges from the prechamber.

In Fig. 12, with only air in the main chamber, the jet from the prechamber is seen to be less well defined than was the case with the standard prechamber shown in Fig. 8.

Increased Throat Restriction

In the prechamber shown in Fig. 5(*c*), the nozzle flow restriction was increased by reducing the throat diameter to 0.24 in. (6 mm). As expected, the prechamber spike was sharper and higher, reaching a peak of 750 psia (52 bar), Fig. 13. As shown in Fig. 14, the flame crossed the prechamber at a much faster rate and penetrated entirely across the main chamber, striking the bottom of the piston bowl before igniting the main charge. The increased restriction of the throat is also shown by the pressure difference between the main chamber and the prechamber during the latter part of the combustion process.

In summary, tests with different throat diameters showed that a reduction in throat diameter increased the size and sharpness of the prechamber spike and increased the degree of torch penetration into the main chamber, but appeared to have only a relatively small effect on main-chamber combustion.

Multiple Hole Design

The prechamber of Fig. 5(*d*) had three holes, each of 0.20 in. (5 mm) diameter. This design is often called the "pepperpot" and is frequently used in gas engines. Three holes of 0.20 in. (5 mm) diameter gave a total exit area equal to that of the standard design with a 0.35 in. (9 mm) single-hole throat. Although the total areas were the same, the restriction to outflow from the pepperpot was considerably greater than the standard because of the more complicated exit flow geometry. For best photography, one of the holes was arranged to point parallel to the main-chamber window.

Figures 15 and 16 show the movie stills and pressure data for a typical run. Prechamber combustion proceeded as with a standard prechamber but with a higher peak pressure spike of 850 psia (59 bar) because of the higher restriction. Once the flame entered the main chamber, however, it moved across the chamber and ignited the main charge at the piston bowl wall.

Downloaded 01 Jun 2010 to 171.66.16.87. Redistribution subject to ASME license or copyright; see http://www.asme.org/terms/Terms_Use.cfm

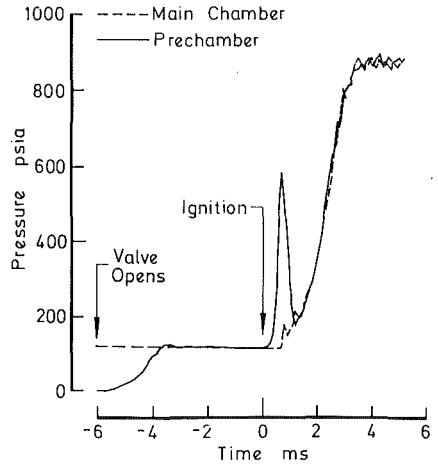


Fig. 18 Pressure diagram; throat diagram 0.35 in. (9 mm); low-volume prechamber

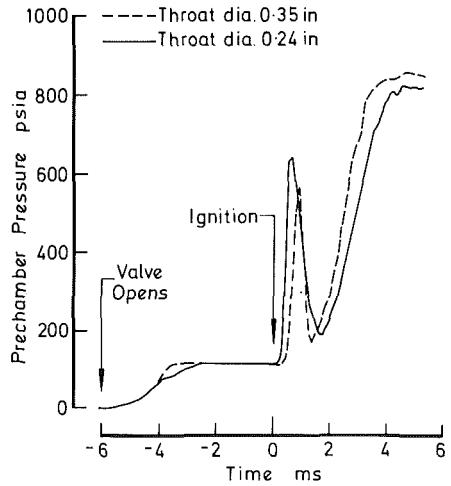


Fig. 19 Prechamber pressures; low-volume prechamber

The combustion from the two other jets could not be seen until their flames spread tangentially (shown as the spreading combustion area from the left edge of the viewing window).

A misfire can occur in an engine if the burning prechamber charge fails to ignite the lean main-chamber charge. Figure 17 shows movie stills where one of the three pepperpot jets "misfired" in the CVC rig and failed to ignite the main-chamber charge. The flame in direct view died out, but combustion was started by the other jets. Thus, for this run, only two out of the three pepperpot jets were successful in igniting the main-chamber charge.

Comparison with results from a single-hole throat with the same total hole area showed that the pepperpot prechamber increased the height of the prechamber pressure spike, increased the torch penetration, and appeared to increase the rate of main-chamber combustion.

Reduced Prechamber Volume

Tests with the prechamber volume reduced to one-third of the original, Figs. 5(*e*) and 5(*f*), showed only small changes in combustion. Figure 18 shows pressure data with the smaller volume prechamber, using a 0.35 in. (9 mm) diameter single-hole throat. The prechamber spike was less than that of the comparable run shown in Fig. 6 because of the smaller mass of prechamber charge, but the main-chamber combustion was very similar.

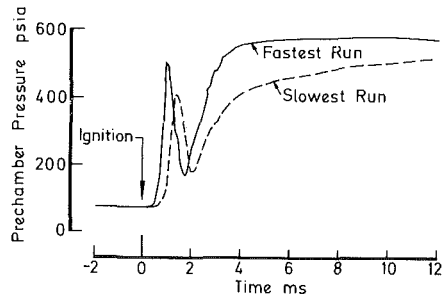


Fig. 20 Extent of pressure variations

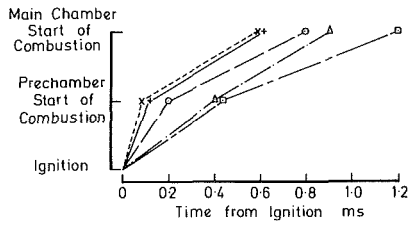


Fig. 21 Variation in timing of combustion events

Figure 19 shows a comparison of the prechamber pressure diagrams obtained with two different diameter throats. As expected, the height of the prechamber spike is increased with the more restrictive smaller throat, but the main-chamber combustion is not significantly altered.

Cycle-to-Cycle Variation

While testing the various prechamber builds, large variations in combustion from cycle to cycle were noticed. Figure 20 shows the fastest and the slowest combustion recorded from a series of tests with a 0.35 in. (9 mm) diameter single-hole prechamber throat, all with identical charging conditions. The difference is quite pronounced and in fact, the variation from cycle to cycle with a given geometry was in some cases larger than the average difference from one prechamber design to another. It was therefore decided to study cycle-to-cycle variation in more detail.

While the cycle-to-cycle portion of this study is not complete, some preliminary results should be mentioned here because this type of variation has been recognized as an important limitation to engine performance. Young [2] has published a detailed review of various studies of the cycle-to-cycle variations in engines. He concluded that variation in combustion is the fundamental cause of variations in both cylinder pressure and engine output. His study suggested that the differences originate in the early stages of combustion. Although firm proof was not available at that time, the variations appeared to be caused by fluctuations in velocity (i.e., turbulence) at the spark plug gap at the time of ignition.

Other studies have been concerned with cycle-to-cycle variations in engines using gasoline fuel. Patterson [3] and Hansel [4] showed that skip-firing a cylinder to reduce the presence of exhaust residuals and/or using a gaseous fuel to avoid the problem of fuel evaporation could reduce the amount of combustion variation. However, experiments on operating engines are always limited by the inability to control the large number of variables crucial to combustion. For this reason, the CVC rig combustion described here, with controlled but reasonably realistic engine conditions, offers an opportunity to study further the reasons for cycle-to-cycle variation.

Figure 21 shows results from five tests on the CVC rig made under identical charge conditions. For each test, the diagram shows the start of combustion for the prechamber and for the

Downloaded 01 Jun 2010 to 171.66.16.87. Redistribution subject to ASME license or copyright; see http://www.asme.org/terms/Terms_Use.cfm

main chamber. The delay between ignition and the start of prechamber combustion varied from 0.1 msec (equivalent to 0.7 crankshaft deg) to 0.5 msec (equivalent to 3.5 crankshaft deg).

There is also a variation in the length of time between the start of prechamber combustion and the start of main-chamber combustion. However, the major deviation seems to occur in the period between the time when the spark occurs and the time when a significant amount of flame has started in the prechamber. This variation can also be readily seen in the photographs.

Conclusions

These findings support the conclusion reached in previous studies that the details of events during the first stage of combustion are the major cause of cycle-to-cycle variations in combustion. However, because large variations occur in the CVC rig, which does not have many of the other variables that occur in an engine, it may well be that turbulence per se is not the most significant variable. The early results of this study suggest that mixing on a very small volume scale may be a much more significant factor. Turbulence, of course, influences the mixing process in an engine and the two effects are closely interrelated. Additional work with the CVC rig is being directed toward separating these two factors.

Acknowledgments

This work has been sponsored by the Gas Research Institute. We appreciate their support, particularly that of Allen D. Wells, Senior Project Manager, Engine Driven Systems. We would also like to acknowledge those individuals who have participated in the project, especially Chris Brooks of Ricardo Consulting Engineers.

References

1 Rose, J. W., and Cooper, J. R., *Technical Data on Fuel*, 7th ed., published by the British National Committee, 1977.

2 Young, M. B., "Cyclic Dispersion in the Homogeneous-Charge Spark-Ignition Engine—A Literature Survey," SAE Paper No. 810020, 1981.

3 Patterson, D. J., "Pressure Variations, a Fundamental Combustion Problem," SAE Paper No. 660129, 1966.

4 Hansel, J. G., "Lean Automotive Engine Operation—Hydrocarbon Exhaust Emissions and Combustion Characteristics," *SAE Transactions*, Vol. 71, 1971.

Downloaded 01 Jun 2010 to 171.66.16.87. Redistribution subject to ASME license or copyright; see http://www.asme.org/terms/Terms_Use.cfm

T. Morimatsu

T. Okazaki

T. Furuya

H. Furukawa

Engine Technical Center,
Oyama Plant, Komatsu Ltd.,
Japan

Improvement of Emissions From Diesel Engines

It is important to reduce emissions from diesel engines, which are used in the cogeneration systems. The mass transfer to the fuel spray plays various roles in fuel consumption rate and in trace species emission. High injection pressure and a re-entrant combustion chamber were used to make the mass transfer larger. The need for high injection pressure and controlled injection timing for NO_x led the authors to use the new Komatsu fuel injection pump. This pump, which has a re-entrant combustion chamber, resulted in clean engine emissions and confirmed the importance of air entrainment to the spray.

Introduction

There are many attractive features in cogeneration systems where engines supply power for electricity and give out heat for other utilizations. The users of cogeneration systems welcome high efficiency in the energy usage of fuel. Other features will be well described in the papers given in this conference.

The cogeneration systems have diesel or gas engines or gas turbines for power. Diesel engines have a better fuel consumption rate and emit less NO_x and rather more particulates and smoke in the exhaust gas than gas engines and gas turbines. This paper deals with diesel engines, which give out more power for electricity and emit less pollutants in the exhaust gas. Clean emissions would attract many users who worry about environmental pollution in cities.

The needs for a better fuel consumption rate for energy transformation since the oil crisis drive one to use direct injection diesel engines. The mass transfer to the injected fuel spray plays many roles in combustion and in the fuel consumption rate. This paper deals with the fuel consumption rate and emission in regard to the mass transfer. It also introduces a new injection pump, which delivers high injection pressure and has electronic variable injection timing for good fuel consumption and clean emissions.

Mass Transfer Index

It is important to improve the fuel consumption rate of diesel engines in order for the cogeneration system to have good efficiency in energy transformation for electricity. It is also important to reduce exhaust emissions, such as particulate, NO_x, etc. The fuel consumption rate is related to how much NO_x the exhaust gas has. An example is shown in Fig. 1. The engine tested was the Komatsu S6D170. The NO_x concentration is also related to the particulate emissions.

It has been indicated by one of the authors that mass transfer to the fuel spray of a direct injection diesel is a key to improving the fuel consumption rate [1]. The injected fuel spray entrains air in the cylinder of a diesel engine through momentum exchange. The spray is depicted in Fig. 2.

For the sake of clarity, consider the spray whose represent-

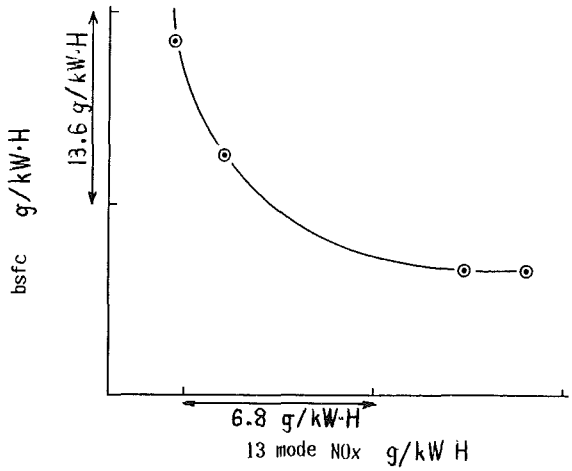


Fig. 1 Brake specific fuel consumption versus NO_x

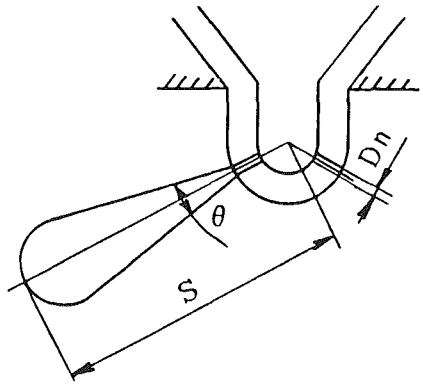


Fig. 2 Schematic view of the spray

Contributed by the Internal Combustion Engine Division and presented at the Internal Combustion Engine Division Technical Conference, Kansas City, Missouri, October 4-7, 1987. Manuscript received by the Internal Combustion Engine Division June 1987.

Copyright © 1988 by ASME
Downloaded 01 Jun 2010 to 171.66.16.87. Redistribution subject to ASME license or copyright; see http://www.asme.org/terms/Terms_Use.cfm

ative diameter is D. Its velocity is V relative to the surrounding air, which has density ρ_a. Air mass transfer to the spray (flame) is assumed similar to the heat transfer from air to cylinder. The mass flux is proportional to the MTi (Mass Transfer index):

$$\mathrm{MTi} = \rho_a V^{0.6}/D^{0.4} \tag{1}$$

By increasing the MTi value, one can improve the fuel consumption rate because the spray flame entrains much air to reduce the period of combustion duration. Past experiments confirm that the larger the MTi, the less the fuel consumption rate is, as shown in Fig. 3.

The representative velocity V and diameter D can be defined as follows:

The spray penetration in standing air at time t after the beginning of injection is

$$S = \left(\frac{D_n t}{\tan(\theta/2)}\right)^{1/2} \left(\frac{2c\Delta P_n}{\rho_a}\right)^{1/4} \tag{2}$$

where S = spray penetration; D_n = diameter of the injection nozzle; θ = cone angle of spray; c = flow coefficient of nozzle; $\Delta P_n = P_n - P_a$; P_n = injection pressure; P_a = pressure of surrounding air. The cone angle of the spray is

$$\theta = \frac{2\mathrm{Re}^{0.46}(L/D_n)\beta}{7.4\left[1-\exp\left(-\frac{1}{43.6}\frac{\rho_1}{\rho_a}\right)\right]} \tag{3}$$

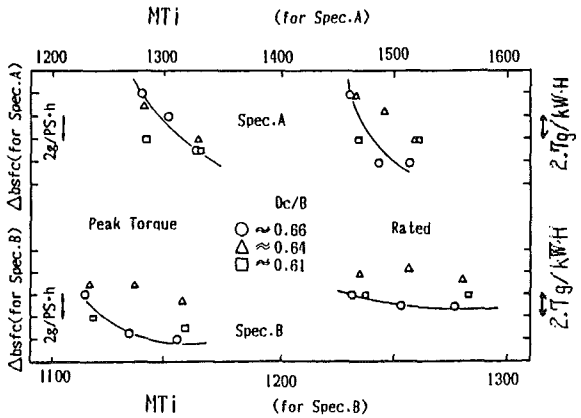


Fig. 3 Effect of Mass Transfer index on bsfc

where $\mathrm{Re} = D_n U_0/\nu$; $U_0 = \sqrt{2\Delta P_n/\rho_1}$; ν = kinematic viscosity of fuel; ρ_1 = density of fuel; $\beta = -0.0284\,(\rho_1/\rho_a)^{0.39}$. The intact length of the spray is

$$I = 4.21(L/D_n)^{-\beta}\sqrt{\frac{\rho_1}{\rho_a}}\,D_n \tag{4}$$

where L = length of nozzle.

The spray in swirl has its penetration and cone angle

$$S_p = \frac{S}{1+\frac{\pi r_s NS}{30U_0}} \tag{5}$$

$$\theta_p = \theta\left[2\left(1+\frac{\pi r_s NS}{30U}\right)^2 - 1\right] \tag{6}$$

where r_s = swirl ratio in the combustion chamber; N = engine speed. S_p and θ_p are shown n Fig. 4.

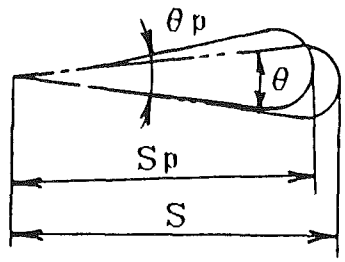


Fig. 4 Schematic view of the spray in swirl

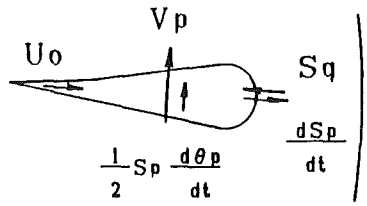


Fig. 5 Schematic of effective velocity on the injected spray

Nomenclature

bsfc = brake specific fuel consumption, g/kW•h
c = flow coefficient of nozzle
D = representative diameter of fuel spray, m
D_n = diameter of nozzle, m
I = intact length of spray, m
L = length of nozzle
MTi = mass transfer index defined in the body of paper, $\mathrm{kg/m^{2.8}\ s^{0.6}}$
N = engine speed, rpm
P_a = pressure of surrounding air, Pa
P_{me} = mean effective pressure of engine, MPa
P_n = injection pressure of fuel, Pa
Re = Reynolds number of injection
r_s = swirl ratio (swirl turn/engine speed)
S = spray penetration in standing air, m
S_p = spray penetration in swirl, m
Sq = squish velocity, m/s
t = time after the beginning of injection, s
U_0 = velocity of injection, m/s
V = representative velocity of spray, m/s
V_1 = representative velocity in direction of swirl, m/s
V_2 = representative velocity in direction of injection, m/s
V_p = swirl velocity, m/s
β = power defined in body of paper
ΔP_n = nozzle pressure difference, Pa
θ = cone angle of spray in standing air, deg
θ_p = cone angle of spray in swirl, deg
ν = kinematic viscosity of fuel, $\mathrm{m^2/s}$
ρ_a = density of air, $\mathrm{kg/m^3}$
ρ_1 = density of fuel, $\mathrm{kg/m^3}$

Downloaded 01 Jun 2010 to 171.66.16.87. Redistribution subject to ASME license or copyright; see http://www.asme.org/terms/Terms_Use.cfm

Table 1 Single-cylinder engine

Bore x Stroke	125 x 150 mm
Cylinder	1
Pme (brake mean effective pressure)	1.15 MPa
Speed	2100 rpm
injection system	KOMPICS [2]

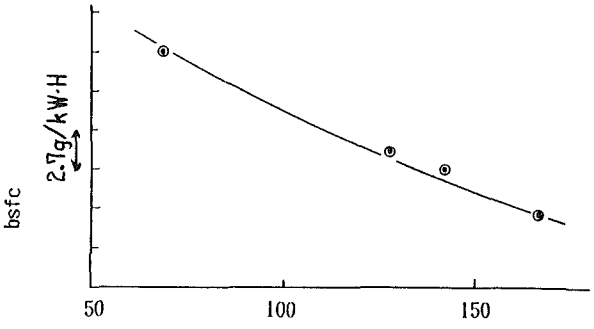


Fig. 6 Effect of injection pressure on bsfc

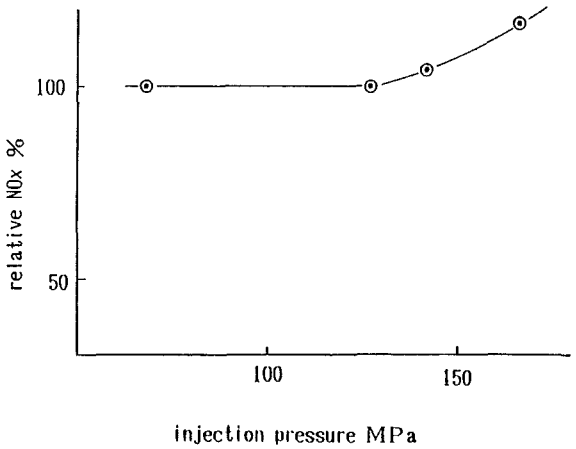


Fig. 7 Effect of injection pressure on NO_x

The representative diameter of the spray is defined as

$$D=\frac{S_p^2\sin^2(\theta_p/2)-I^2\tan^2(\theta/2)}{S_p-I}$$

$$\times\sqrt{1+\left(\frac{S_p\cos(\theta_p/2)-I}{S_p\sin(\theta_p/2)-I\tan(\theta/2)}\right)^2} \quad (7)$$

The area $\pi D(S_p-I)$ is equal to the peripheral area of the fuel spray cone.

The effective velocity of the spray in the swirl direction is given as (see Fig. 5)

$$V_1=V_p-2\,\frac{\pi r_s NS}{30U_0}\,\frac{dS}{dt}\,\frac{\pi}{180}$$

where V_p = swirl velocity; in the direction of injection

$$V_2=\frac{1}{2}\left(U_0+\frac{dS_p}{dt}\right)+Sq \quad (8)$$

where Sq = squish velocity. Thus the representative velocity of the spray is

$$V=\sqrt{V_1^2+V_2^2}$$

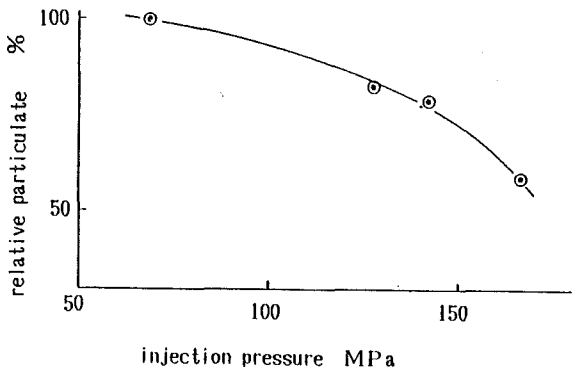


Fig. 8 Effect on injection pressure on particulate

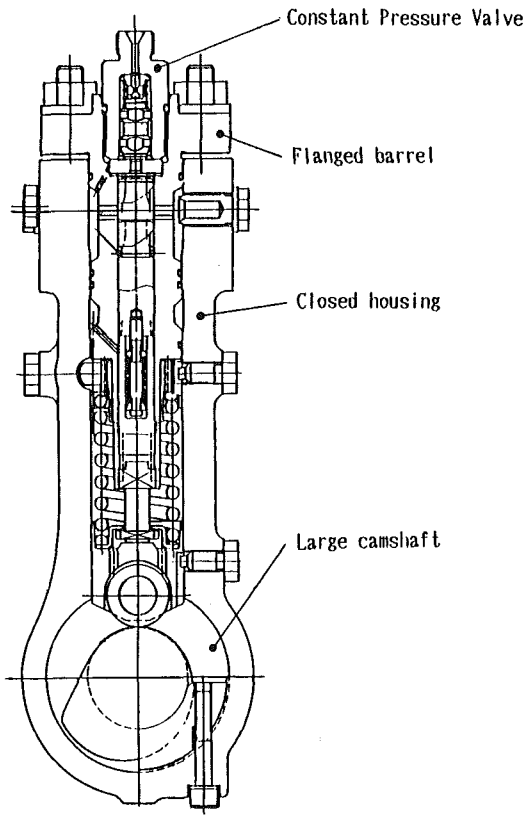


Fig. 9 Cross section of injection pump

One can deduce the followings from the above equations. High injection pressure and large squish velocity produce large MTi, the result being good combustion and reduced fuel consumption rate.

Preliminary Test

Increasing the MTi shortens combustion duration and reduces fuel consumption rate. On the other hand, it increases NO_x formation due to the high temperature of combustion. It decreases particulate emission because combustion is good.

A preliminary test was carried out in order to investigate the effect of injection pressure. A mini-dilution tunnel was used to measure the particulate emission. The specification of the engine tested are summarized in Table 1.

The brake fuel consumption rate, NO_x emission, and particulate emission are shown in Figs. 6, 7, and 8, respectively. These figures confirm that high injection pressure (i.e., large MTi) gives low fuel consumption rate (Fig. 6), low particulate emission, and rather high NO_x.

Downloaded 01 Jun 2010 to 171.66.16.87. Redistribution subject to ASME license or copyright; see http://www.asme.org/terms/Terms_Use.cfm

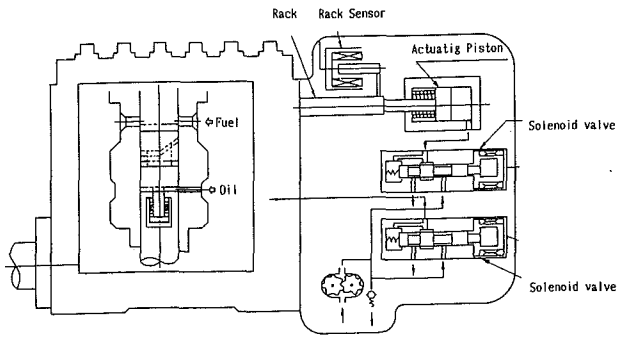


Fig. 10 Schematic of injection pump control

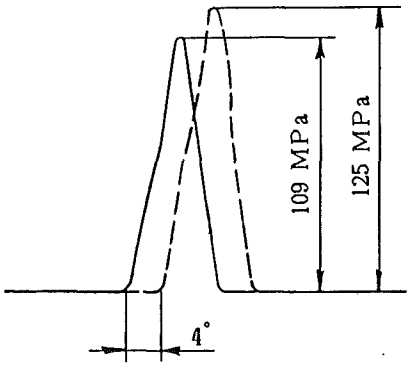


Fig. 11 Injection pressure by the divided plungers

New Injection Pump

The thermal NO forms the main part of NO_x in the cylinder of the engine. Therefore it is useful to delay the injection timing so as to reduce the time during which the combustion gas is exposed to high temperature. For this purpose it is attractive to control the timing freely (without mechanical restraint).

Air entrainment to the spray can improve the fuel consumption rate as shown above. High injection pressure is used to entrain much air.

The two items above led the authors to use a new fuel injection pump, which was under development by the authors' company. The new Komatsu fuel injection pump delivers high injection pressure and has a capability to control the timing electronically for the optimization of the NO_x-fuel consumption tradeoff. The main features of the pump are described below and shown in Fig. 9.

The pump camshaft has a large diameter base circle and flanged barrel elements to accommodate high injection pressure. The pump uses a constant pressure delivery valve in order to eliminate the cavitation erosion problem.

The solenoid with the spool valve and the rack with its eddy current type position sensor make a closed loop to control the rack position for fuel delivery using the oil pressure supplied by the gear pump. The second solenoid and the spool valve control the oil pressure, which is led to the spring chamber between the divided plungers as depicted in Fig. 10. Prestroke of the plunger (stroke to close the fuel port) is controlled under the equilibrium between the oil pressure force and the spring force.

Typical injection pressure and its timing variation are shown in Fig. 11. The controlled timing difference is 4 deg in the cam angle with an oil pressure difference of about 1 MPa.

Electronic control of the mechanism above enables the user of the pump to adjust the timing and the fuel delivery according to the engine speed, the engine load, etc.

Table 2 Experimental engine

Aspiration	Turbocharged and Intercooled
Injection	4 cycle direct injection
Bore x Stroke	95mm x 115mm
Cylinder	6 in line
Valves	2 over head valves per cylinder

Table 3 Combustion chambers

	troidal	reentrant
Schematic view of chamber		
Port Swirl Ratio tested	2.6	2.2

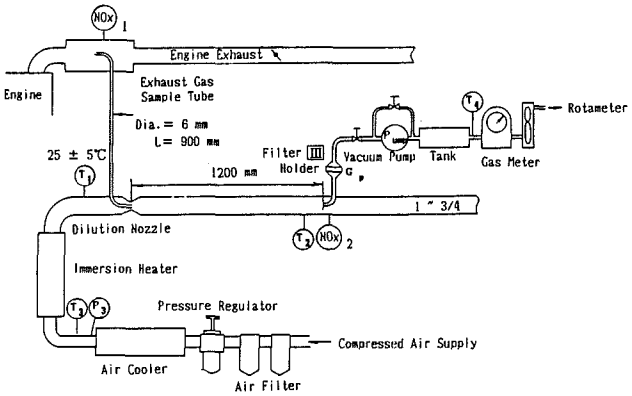


Fig. 12 Schematic of experimental setup

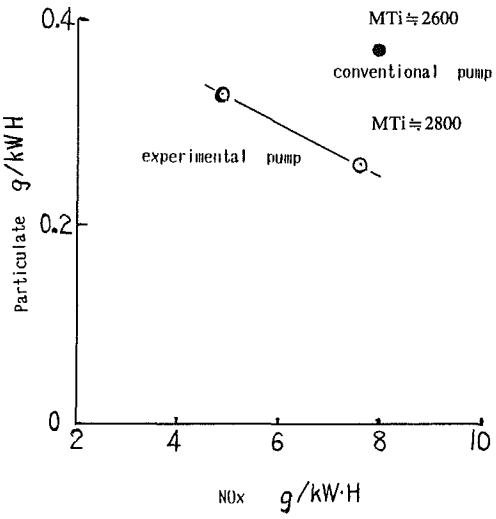


Fig. 13 Effect of the injection pump

Experiments on the pump described above indicate that it can improve both particulate emission and fuel consumption rate with high injection pressure, and that it can lessen NO_x emission with controlled injection timing.

Experimental Apparatus

The main features of the engine tested are shown in Table 2. This experimental engine is the Komatsu S6D95, which has good fuel economy and durability and is used on construction

Downloaded 01 Jun 2010 to 171.66.16.87. Redistribution subject to ASME license or copyright; see http://www.asme.org/terms/Terms_Use.cfm

machines. Various combustion chambers and the fuel injection system were used during the test.

The experimental apparatus with the engine is shown schematically in Fig. 12. There are two chemiluminescent detectors for NO_x emission. A sampling tube is inserted in the exhaust pipe on the engine and connected to a mini-dilution tunnel. The tube is 6 mm in i.d. and 900 mm in length. Compressed air is supplied into the tunnel through a filter, a pressure regulator, a cooler, and a heater. Air temperature is maintained at 298 ± 5 K. Exhaust gas merges with the air at the nozzle. Particulates in the diluted gas are sampled in a fiber filter by a vacuum pump 1200 mm downstream at the nozzle. Diluted gas flow rate is measured by a gas meter.

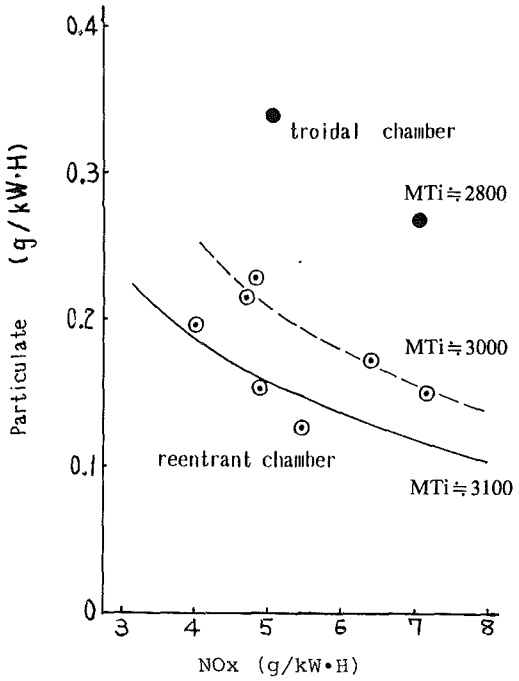


Fig. 14 Effect of the re-entrant chamber

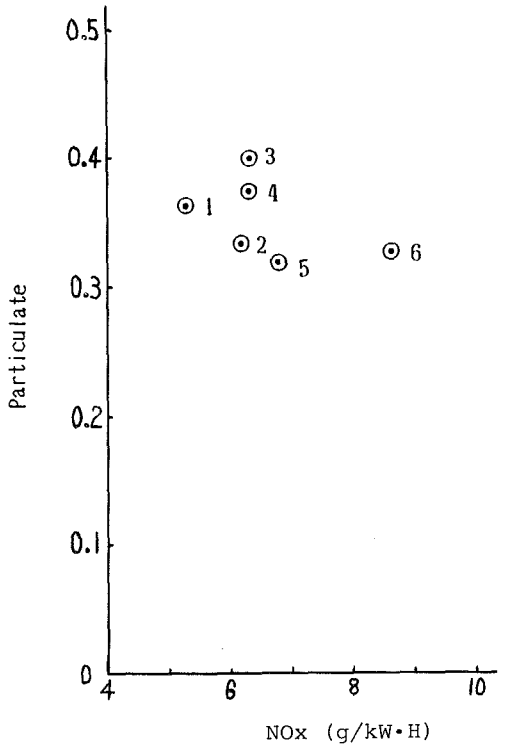


Fig. 15 Effect of controlled timing

NO_x concentration in the diluted gas is compared with that of the exhaust gas to calculate the dilution ratio. An orifice is used to measure the air flow rate of the engine. Fuel flow rate is measured by a rotameter.

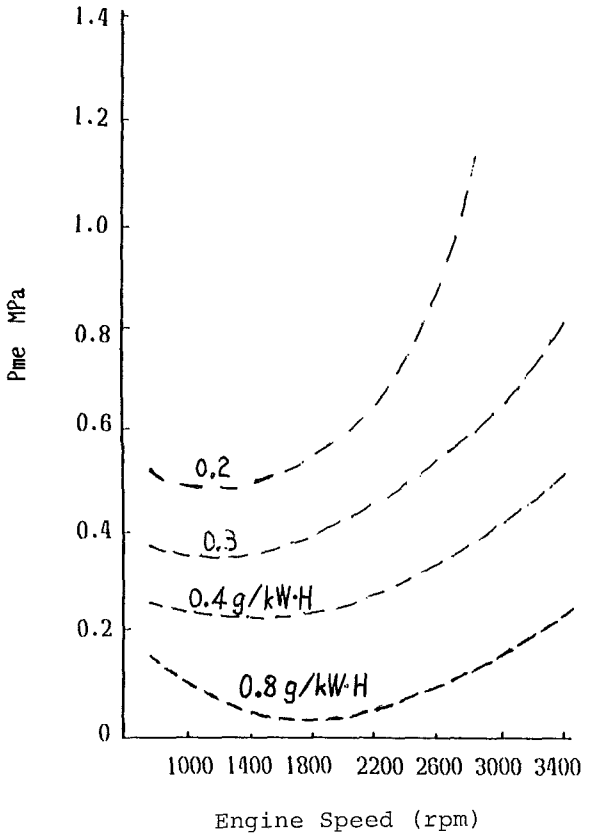


Fig. 16 Particulate result

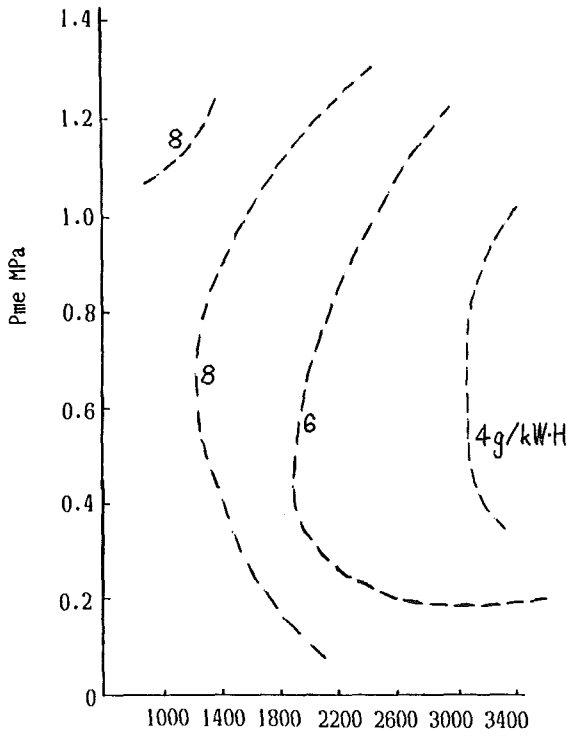


Fig. 17 NO_x results

Downloaded 01 Jun 2010 to 171.66.16.87. Redistribution subject to ASME license or copyright; see http://www.asme.org/terms/Terms_Use.cfm

Experimental Results

Air motion in the combustion chamber has much influence on the combustion in view of the MTi theory. A conventional toroidal combustion chamber and re-entrant chamber were tested to confirm their effect on the relation between NO_x and particulate emission. Their features are shown in Table 3.

The conventional toroidal chamber produced 0.37 g/kW•h of particulates with a conventional injection pump and gives 0.25 g/kW•h with the new Komatsu pump (Fig. 13). The plunger diameter of the former pump is 10.5 mm. The latter is 11 mm. Therefore the injection pressure of the experimental system is higher than that of the conventional one. High injection pressure of fuel, that is a large MTi, results in low particulate emission with the same NO_x level.

Figure 14 shows the result with the re-entrant combustion chamber. The result of the toroidal chamber is also plotted for comparison. The injection pump is the experimental one. The re-entrant chamber has some effects on the particulate emission. The solid and dotted lines in Fig. 14 represent constant injection pressure lines. The solid one is 120 MPa, and the dotted one is 110 MPa. We confirm here again the high injection pressure produces low particulates.

An electronically controlled experimental injection pump gives a good performance in the mode test (Fig. 15). The numbers in Fig. 15 correspond to the sets of the injection timings, which are controlled according to the load and to the speed of the engine. Electronically controlled timing can make the exhaust gas clean.

The high pressure injection system and the electronically controlled injection timings give a good performance in emission from the diesel engine. Figures 16 and 17 show particulate and NO_x emissions versus engine speed and load (mean effective pressure). Particulates are denser in low load than in high load. The sampled particulate filters are heated in argon to estimate what proportion of the particulate matter is organic and what proportion is dry soot. The result is that the organic fraction is higher in low load than in high load.

Conclusion

High pressure injection and electronically controlled injection timing with new divided plungers show good performance with respect to emission level.

It is also noted that the re-entrant combustion chamber has some effects in the exhaust emission of the diesel engine.

These two factors support the MTi theory that air entrainment into the spray flame influences the quantity of chemical pollutants.

Acknowledgments

It is a pleasure to acknowledge that support for this research was partially provided by the Petroleum Energy Center. The authors wish to thank Komatsu Ltd. for allowing publication of this paper.

References

1 Komiyama, K., Tokunaga, K., and Morimatsu, T., "Study on Combustion and Mixture Forming Processes in Diesel Engines," *Komatsu Technical Review*, Vol. 27, No. 1, 1981, pp. 1-7 [in Japanese].

2 Hiraki, H, Satomi, H., Sato, F., and Kizawa, H., "Development of KOMPICS-II," Conference on Mechanical and Electronical Control of Engine, the Marine Engineering Society in Japan, 1986 [in Japanese].

Downloaded 01 Jun 2010 to 171.66.16.87. Redistribution subject to ASME license or copyright; see http://www.asme.org/terms/Terms_Use.cfm

Pielstick Experience With Dual-Fuel Engines and Cogeneration

G. Grosshans
Manager,
Department for Engine Concepts and Thermodynamics,
ALSTHOM CEMT,
St-Denis, France

M. Litzler
Test Department Engineer,
ALSTHOM CEMT,
St-Denis, France

SEMT PIELSTICK has developed since 1971 a range of medium-speed dual-fuel engines with relatively high air–fuel ratios, which enable ratings similar to diesel engines. The PC 2.3 DF.C of 1971 was developed up to 535 hp/cyl. and was followed by the PC 2.5 DF.C of 600 hp/cyl. This later engine was applied in the West German cogeneration plan of a textile factory, giving more than 82 percent use of primary energy. This engine may also be used as a pollution-abating machine, because it traps toxic solvent vapors, which are burned in the engine, reducing furthermore the apparent (paid) energy consumption. Thanks to the lean air–gas mixture, the very severe West German limits on pollution could be fulfilled without any extra depolluting device. The newest development is the PA 5 DF engine of the same philosophy, which will cover the 1000 to 3600 kW range.

Introduction

Dual-fuel reciprocating engines are an interesting alternative for cogeneration plants. Their good thermal efficiency is sometimes their major advantage and their multifuel ability (natural gas or heavy fuel) gives the customer the possibility to modify its primary energy sources according to (unpredictable) economic variations.

Nevertheless, this solution is not widespread, with some exceptions, like the Federal Republic of Germany, where about 300 cogeneration plants with reciprocating gas engines are in service. The main reason for this moderate success is the high price of dual-fuel engines compared to other prime movers with the same power.

This was explained in the following manner: The power of such engines burning natural gas is limited by knocking to a brake mean effective pressure of about 12 bar running on natural gas. Because the market is small, it is not worth developing a specific engine type and most manufacturers, at least in Europe, offer modified Diesel engines. These engines are built to withstand the stresses of modern highly supercharged industrial engines rated at around 20 bar b.m.e.p. and are limited to 60 percent of this power. This gives expensive engines and reduces furthermore the market. A way to escape this unpleasant state of affairs was to attempt to develop dual-fuel engines developing mean effective pressure similar to their Diesel counterparts.

This development started by PIELSTICK around 1971 at the request of Fairbanks Morse (Colt Industries) in the United States on the PC 2 medium-speed engine of 400 mm bore and 460 mm stroke. It was made possible by careful analysis of the detonation process.

Contributed by the Internal Combustion Engine Division and presented at the Internal Combustion Engine Division Technical Conference, Kansas City, Missouri, October 4–7, 1987. Manuscript received by the Internal Combustion Engine Division June 1987.

Detonation Process

Knocking normally starts at the periphery of the combustion chamber during combustion in a zone where the mixture is not already burning. A sudden compression occurs, caused by the rapid expansion of the burning zone, and the self-ignition limits may be overstepped. In this case of mass ignition, a local discontinuity of pressure occurs, generating a system of waves reflected on the cylinder walls, weakly damped by the gas viscosity and the combustion chamber expansion. Local pressure measurements (Fig. 1) show a high-frequency oscillation, suddenly occurring during combustion, generally about the time when the maximum combustion pressure would have been reached in normal combustion. This phenomenon is not always related to pre-ignition.

The maximum pressure relevant to the stresses exerted on the engine parts is an instantaneous mean value, which may be approximated by filtering the high frequencies and seeking the maximum of the filtered signal. Even this maximum pressure

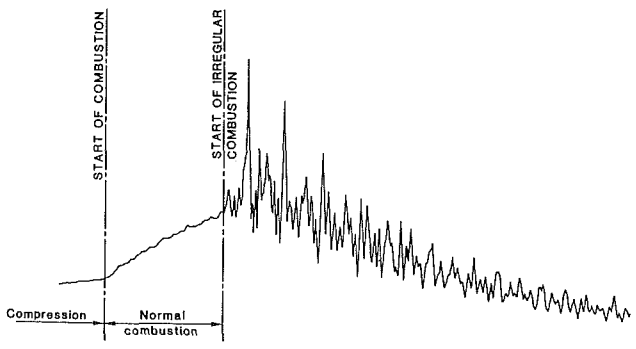


Fig. 1 Pressure registration on a PC 2.5 DF-C engine during one detonation cycle

Copyright © 1988 by ASME
Downloaded 01 Jun 2010 to 171.66.16.87. Redistribution subject to ASME license or copyright; see http://www.asme.org/terms/Terms_Use.cfm

is generally higher in the case of detonations because of the higher combustion speed.

The consequence is, in addition to an unpleasant noise of the engine, the destruction of the boundary layers in the combustion chamber by the pressure waves. The heat exchange is strongly activated and the temperature of the walls increases. This thermal overstress can be very dangerous (low cycle fatigue of cylinder heads, thermal expansion of piston head, seizure, etc.).

The parameters influencing detonation have been described in [1]. They are:

1 Fuel Octane Index. This cannot be easily modified.

2 Temperature Conditions at End of Compression Stroke. General temperature must be high enough to assure self-ignition of pilot injection but well below self-ignition of the gas mixture. It depends on air manifold temperature and compression ratio.

Local temperature can be altered by "hot spots." An advantage of the PC engine was that it was developed mainly as a marine engine with heavy fuel ability, and the hot spots were eliminated for vanadium corrosion. Inadequate oil additives can also create hot spots on the piston head.

3 Firing Timing and Pilot Fuel Quantity. The timing is of well-known influence (see for instance control of automotive engines). The pilot fuel quantity controls the energy level and surface of initial igniting. One must not forget that this energy input is at least ten times greater than for a spark-ignited engine. For practical reasons (geometry), the pilot fuel quantity cannot be decreased under 5 percent of the full load energy ouput if full load is to remain feasible in the Diesel mode.

4 Air-Fuel Ratio. This is a parameter one can adjust with the most freedom: It is easy to measure, as it is correlated with the gas temperature at the end of the cycle and the easily measurable exhaust gas temperature (Fig. 2).

Generally, the gases to be burned allow an air-gas ratio up to more than twice stochiometric mixture before misfiring occurs. This provides for a large area where parameters can be adjusted.

A leaner mixture allows high b.m.e.p. and reduces NO_x emissions, but CO emission increases and the misfiring limit is nearer.

A richer mixture increases thermal efficiency but is nearer to the knock limit, increases NO_x and decreases CO emissions as consequences of higher combustion temperatures.

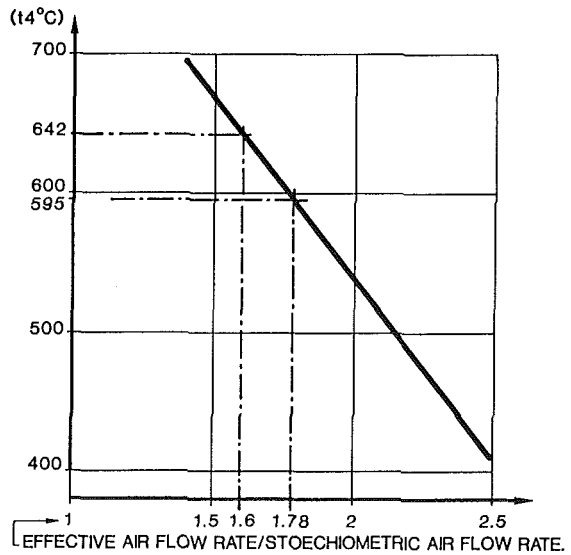


Fig. 2 Temperature at turbine inlet versus air-fuel ratio

PC 2.3 DF

This engine, which was developed in the early 1970s, could run with a b.m.e.p. of 15 bar giving 500 hp/cyl. Later on, the power was increased to b.m.e.p. 16 bar and 535 hp/cyl.

One of the particularities of this engine, of which 30 have been delivered (among them 18 in the United States), from the 6 in line to the 18 cylinders in a Vee, is its gas admission system (Fig. 3). Natural gas is directly introduced in the cylinder at the beginning of the compression stroke through a valve actuated by a small injection pump.

The advantages of this system are:

1 Safety (no explosive air gas mixture outside the cylinder).

2 Easy control of the engine, which reacts to the governor nearly like Diesel engines, thanks to the small injection pump, which meters the gas quantity introduced in the cylinder by the opening duration of the valve.

Two difficulties to master were:

1 To get a quasi-constant gas pressure at cylinder head entry. This obliged us to design a gas inlet system "breaking" the stationary pressure waves that may occur.

2 To assure a homogeneous air-gas mixture preventing local variations of air-fuel ratio leading to knock. This proved to be satisfactorily done by giving a certain amount of swirl to the intake air, with the help of spoon-shaped "scoops" machined on the cylinder head, which forms the ceiling of the combustion chamber.

Another important feature of this engine type is the air-fuel ratio control (Fig. 4). Basically, a certain amount of compressed air from the turbocharger is recirculated at its inlet through a bypass. Its quantity is limited by a butterfly valve actuated by a regulator keeping a constant exhaust gas temperature.

The system includes a correction from the governor lever position closing the flap in case of quick load increase. This avoids detonations during load "steps."

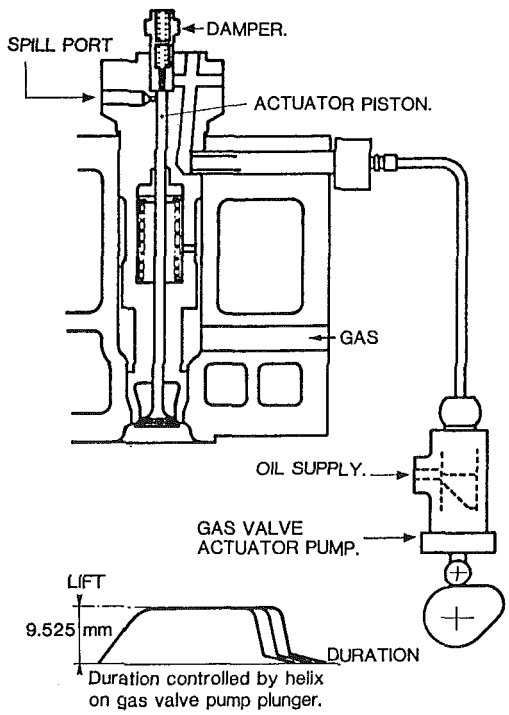


Fig. 3 Gas admission system of PC 2.3 engines

Downloaded 01 Jun 2010 to 171.66.16.87. Redistribution subject to ASME license or copyright; see http://www.asme.org/terms/Terms_Use.cfm

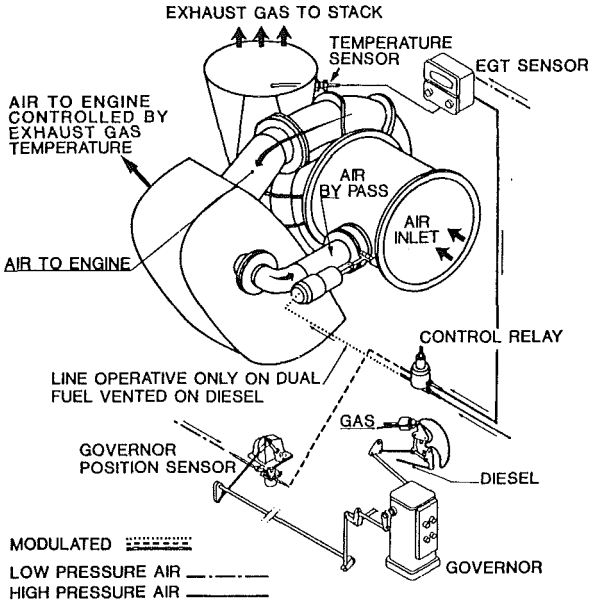


Fig. 4 Air-fuel ratio control system of PC 2.3 DF-S engines

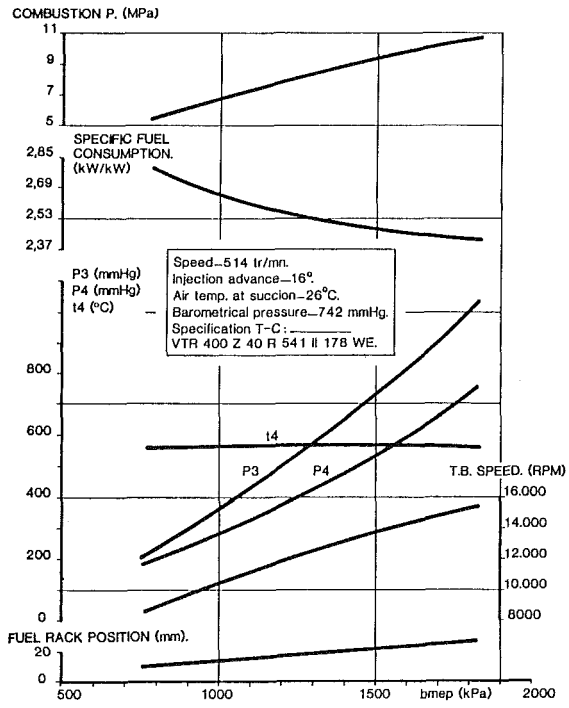


Fig. 5 12 PC 2.3 V 400 DF-S in gas mode

Figure 5 gives recorded performances of a 12 PC 2.3 DF.C engine.

PC 2.5 DF.C Engine

Around 1980, increased interest arose to run this type of engine on gasifier's gas.

The first problem to solve was to introduce into the cylinder a gas whose low calorific value was up to ten times lower than natural gas. The specific stochiometric mixture of hydrocarbons being nearly constant (0.25 MJ/(n) m^3), the gas volume is around 1/3 of the total volume introduced into the cylinder. It was decided to use a carburetor. This allowed us also to

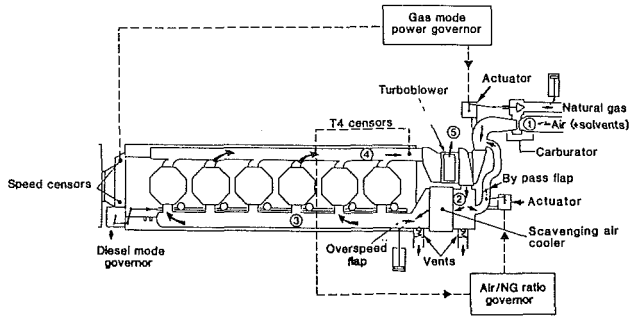


Fig. 6 Gas feeding and governing systems of the 6 PC 2.5 DF-C engine

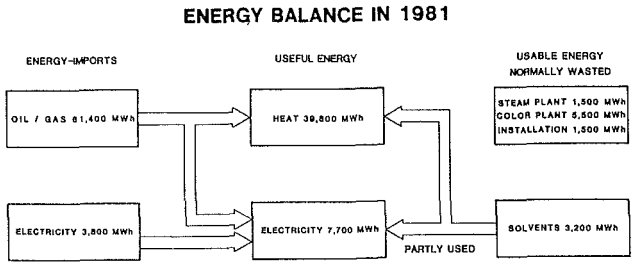


Fig. 7 Energy balance of HEIDENHEIM plant in 1981

make use of unpressurized gas if the mixer was built before the blower.

A first six-cylinder engine was built and tested in 1981 by WAERTSILAE in Finland as a variant of the newer PC 2.5 engine with the same bore and stroke.

Thanks to the increase of firing pressure limitation (130 instead of 110), the natural gas rating was increased up to 18.3 bar b.m.e.p., corresponding to 600 hp to be compared to 650 hp for liquid fuel only.

Figure 6 shows a diagram of the engine gas feeding system. A specially designed carburetor is fitted before the turboblower. The air-gas mixture is therefore perfectly homogeneous, avoiding any load balance problem between cylinders.

Apart from the air-gas feeding system, other important differences in comparison with the PC 2.3 DF.C engine are:

- Reduced cam overlap to avoid direct flow of gas into the exhaust manifold.
- Inlet valve closure near bottom dead center, which artificially reduces the compression ratio at nominal speed and increases it at starting speed to improve the detonation limit without affecting the starting ability of the engine in diesel mode.
- Special piston head to bring the compression ratio down to 10.5.
- Electronic governor with separate actuators for the diesel fuel rack and for the gas metering valve of the carburetor.
- An additional electronic governing system is added to control the air-gas ratio as shown in Fig. 6.

The first engine ran on wood gasifier gas in Finland. An 18-cylinder engine has been ordered to ALSTHOM by French Electricity Board with a rated power of 7 MW. It is installed in French Guyana and will be fed by a Canadian BIODEV gasifier in May 1987 [2]. The main difference with the Finnish prototype is that the carburetor air is fitted after the turbochargers, which enables one to get rid of fouling of the scavenge air coolers by the tar coming with the low calorific value gas. This solution has also become standard on PC 2.5 engines running on natural gas (for better control of the engine).

Downloaded 01 Jun 2010 to 171.66.16.87. Redistribution subject to ASME license or copyright; see http://www.asme.org/terms/Terms_Use.cfm

This type of engine, built in Germany by BLOHM & VOSS, was chosen for the HEIDENHEIM cogeneration plant.

Concept of the Heidenheim Plant

C. F. PLOUCQUET is a textile factory in West Germany, which has to destroy toxic solvent vapors emanating from the dyeing and waterproofing workshops.

An examination of the energy flow for the factory, which was carried out in 1981 (Fig. 7), showed that:

1 The heat requirement was 100 percent fulfilled by the existing power station with a steam turbine producing 40 percent of the electricity used.

2 The rejected heat from machine ventilation and dyeing water was not used.

3 Due to a change in the process, only about 1/3 of the air–solvent mixture coming from the factory could be burned in the boilers of the steam plant.

The company management decided therefore to re-examine the entire energy concept of the factory with the following requirements:

- Reduction in energy needs and costs.
- Use of neglected heat rejections.
- Treatment of solvent-containing air in order to comply with pollution requirements and take advantage of the energy content.

This last point proved to be the major difficulty. These solvents are mixtures with variable proportions of organic products such as:

- Methyl ethyl cetane $CH_3\text{-}CO\text{-}C_2H_5$
- Dimethyl formamide $HCO\text{-}N\text{-}(CH_3)_2$
- Toluene $C_6H_5\text{-}CH_3$
- Isopropanol $CH_3\text{-}CHOH\text{-}CH_3$
- Ethylacetate $CH_3\text{-}COOC_2H_5$

Typical concentration can be about 1–2 percent of the mass of the air flow.

It was not industrially possible to separate these products from the air; chemical absorption and catalytic burning were uneconomical. The only remaining solution was therefore to burn them in addition to a main fuel.

As explained in more detail in [3], four main variant solutions were considered for the plant and the selection was made according to the following ratio:

$$S = \frac{\text{mechanical power}}{\text{heat rejection}}$$

- Thermal afterburning $S = 0$
- Steam turbine $S = 0.2$ to 0.25
- Gas turbine $S = 0.3$ to 0.5
- Reciprocating engine $S = 0.65$ to 1.

In this case, the reciprocating (gas) engine was the most attractive choice due to its higher mechanical efficiency. The coverage of the heat demand led to an engine with sufficient mechanical power to produce all the electricity for the plant. The other extreme solution, thermal afterburning, would have meant a reduction in the electricity produced of about 50 percent, too much heat from the boilers, and therefore no possibility for using low-temperature heat.

A forecast of the future energy balance of the factory is shown in Fig. 9, which can be compared with Fig. 7.

The main differences are an important reduction in fuel imports (oil and gas), the practical disappearance of electricity imports, and export to the local electricity company (about 25 percent of the power generated).

The dual fuel engine cogeneration plant was installed at the end of 1984 and during 1985 intensive tests were carried out. The 1985 energy balance is different from that predicted as the heat regeneration installation is not completely installed. Because of the missing heat coming from the steam and color plant, the engine was operated at higher outputs. Furthermore, the engine was not continuously trapping solvents. Therefore, the fuel imports and electricity exports are higher (71,000 MW/h and 4000 MW/h, respectively).

An important parameter in making the final engine choice was its multifuel ability. Natural gas had been foreseen as the main fuel but, as the burning of solvent vapors in a gas engine was unknown, another economical alternative had to be available in case of failure. The ability to operate on heavy fuel oil was a strong point in favor of the 6 PC 2.5 DF.C engine, which was finally selected.

Solvents

After engine installation, complete performance tests were carried out on site without trapping solvents. The heat balance measured in the gas mode is given in Table 2.

Figure 10 shows the engine parameters in terms of load in diesel and dual-fuel modes. In the dual-fuel mode, the pilot fuel injection is constant and corresponds to 5 percent of full load injection.

The effect of the air–gas ratio governing system can be observed: The exhaust temperature $T4$ is constant (635°C in this case) down to about 45 percent of nominal power. Below this value, the bypass flap is fully open and can no longer control the air–fuel ratio.

The scavenge air pressure drops sharply at partial load

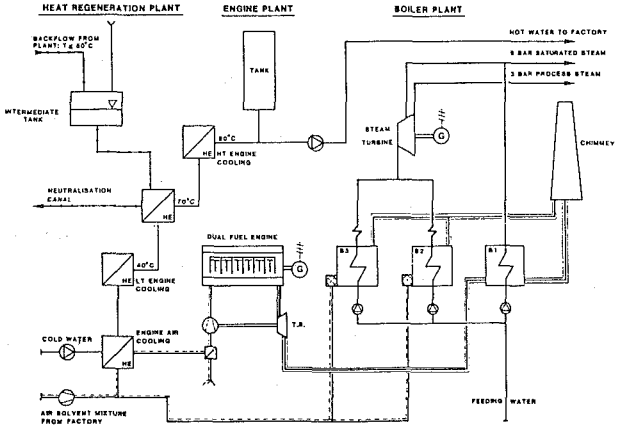


Fig. 8 General layout of HEIDENHEIM cogeneration plant

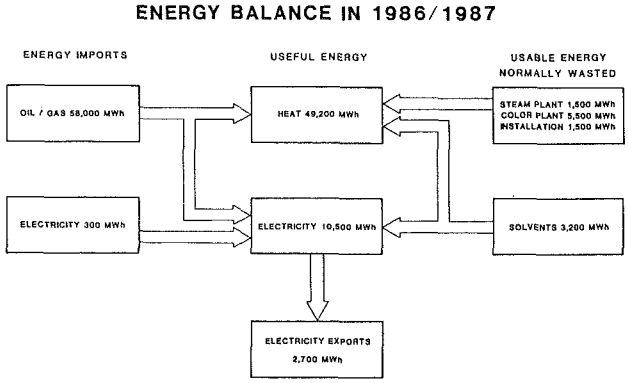


Fig. 9 Estimation of HEIDENHEIM plant's energy balance in 1986/1987

Downloaded 01 Jun 2010 to 171.66.16.87. Redistribution subject to ASME license or copyright; see http://www.asme.org/terms/Terms_Use.cfm

Table 1 Results of performance tests

Power charge factor	100 %	75 %
Electrical power (kW)	2 650	1 920
Steam power (kW) saturated steam at 6 bar ...	1 085	903
Hot water 1 (20°C - 65°C) Heating power (kW)	1 252	941
Hot water 2 (18°C - 26°C) Heating power (kW)	366	300
Total heating power (kW)	2 703	2 144
Mechanical efficiency	43.5 %	41.8 %
Electrical efficiency	41.8 %	40.1 %
Heat used	44.4 %	45.3 %
Total use of primary energy .	86.2 %	85.4 %
Air flow (kg/sec)	3.72	

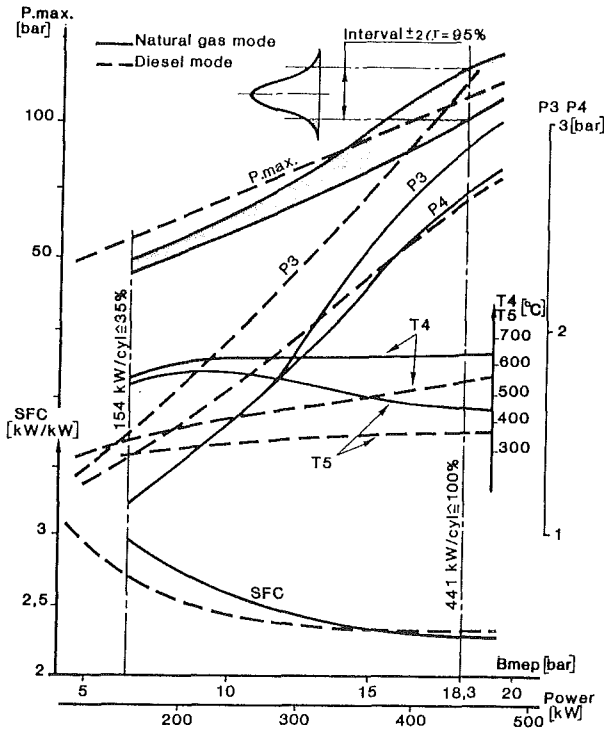


Fig. 10 Performances of 6 PC 2.5 DF-C engine in gas and diesel mode

because of the bypassed air flow in the gas mode. This explains the shape of the maximum combustion pressure curves.

The maximum pressure fluctuation at 100 percent load is ±10 bar around the mean value, which is considered as normal for such engines.

Table 2 Exhaust emission at full load in dual-fuel mode

Test n°	1	2	3	legal limit
Air excess (-) ...	1.84	1.90	1.99	
NOx emission mg/m^3	2370	1875	1350	2000
Co emission mg/m^3	470	550	660	650
Emission values related to 5 % O_2 as stipulated by the law				

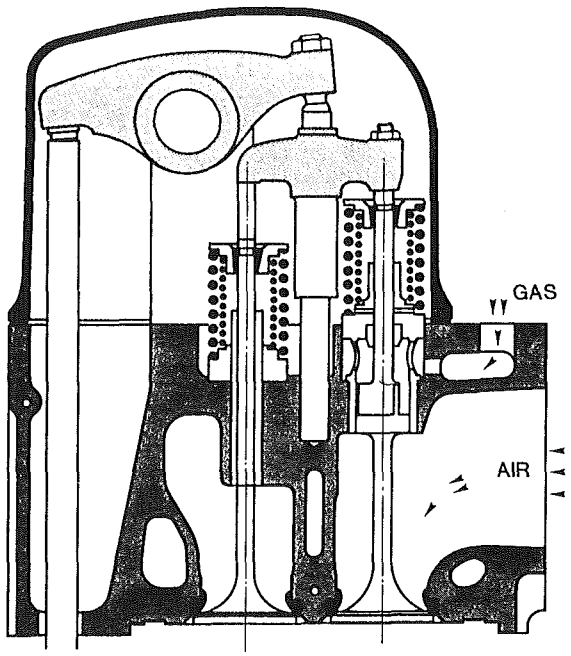


Fig. 11

These tests were followed by others in the gas mode. Depending on the solvent composition and concentration, detonation was eventually encountered with the initial engine settings.

It was tried to reduce the output and increase the air-gas ratio so as to operate the engine on the worst solvents the factory could produce. This appeared to be practically impossible: It was necessary to operate at about 60 percent maximum power with the exhaust temperature reduced to 600°C instead of 635°C. Under these conditions, the engine was running very irregularly because it was approaching the misfire limit.

A solution seemed to be to monitor the engine continuously, modifying the parameters when detonation occurs and switching to diesel operation in the worst cases. It was therefore decided to design and fit an automatic engine control system based on detonation detection.

The development and fitting of this device was done during 1985 as described in [4]. Two independent detonation detectors are fitted on this engine.

One is based on thermocouples directly fitted in the combustion chamber. Their temperature increases in a drastic way if the cylinder is knocking. They are watched by an automatic device normally used for exhaust gas temperatures, which shifts automatically back to diesel mode in case of hard knocking. The other one is based on accelerometers fitted on

Downloaded 01 Jun 2010 to 171.66.16.87. Redistribution subject to ASME license or copyright; see http://www.asme.org/terms/Terms_Use.cfm

each cylinder. Almost like the systems fitted on recent cars' engines when a certain frequency is detected, it means that the corresponding cylinder (or one of its neighbors) is knocking and that air–fuel ratio has to be increased. If this turns out to be insufficient, a diesel mode switching will be ordered.

The engine has accumulated nearly 13,000 running hours as of Mar. 1987. In the following, first operating results are being discussed. Further results will be given when presenting this paper at the conference.

Pollution and Service Experience

The government of the Federal Republic of Germany has enforced a new law limiting the emissions of power plants in early 1986. Therefore, official exhaust emissions measurements have been carried out on the abovedescribed engine in Mar. 1986.

Critical values of dual-fuel engines are NO_x and CO. Normally, measures to reduce the NO_x emission, e.g., increase of air excess, would increase the CO emission and vice versa. With the original adjustment giving an air excess of 1.84 at full load in the dual-fuel mode, the legal limit for NO_x was exceeded. When decreasing the air excess the values developed as given by Table 3. The adjustment used during test No. 2 was adopted for further operation.

Unfortunately, the emission values measured in the diesel mode were less favorable. At full load, an NO_x emission of 2420 mg/m^3 (related to 5 percent O_2) was measured, whereas the CO emission with 120 mg/m^3 was as low as expected.

When feeding solvent polluted air to the engine, there was only little change in diesel mode. However, a slight increase of exhaust emissions was noted.

The increase of hydrocarbon emissions indicated that about 1.5 percent only of the solvents left the engine unburned. In dual-fuel mode about 1.8 percent of the natural gas plus solvent mixture fed to the engine was found in the exhaust as unburned hydrocarbons. However, the measuring devices did not allow us to separate the unburned gas from unburned solvents. Contrary to the observations in diesel mode, in dual-fuel mode only the CO emissions increased when feeding solvents, whereas the NO_x emissions were considerably reduced. In fact, it is possible and necessary to use the original adjustment of air excess without exceeding the legal limits.

After only 635 running hours, before fitting the anti-knocking devices, a heavy accident happened due to uncontrolled knocking in gas mode and with high solvent content in the air. Three seized piston/liner assemblies had to be removed, which, fortunately, could be done within a few days. Thereupon it was decided to burn solvents again only after fitting suitable safety devices. In the meantime, the engine has operated for 3630 hours in the gas + solvent mode without any further problems. The inspection of a piston/liner assembly carried out after 9120 running hours (including 2835 with solvents) has not shown any anomaly, the wear rates being still within the tolerances of the new parts.

These good results were confirmed by the scheduled 12,000 hour inspection.

Minor problems were met in the fuel injection system:

- The nozzle cooling water temperature had to be increased to avoid corrosion at the nozzle tip and body.
- A lubrication system had to be added to the diesel fuel racks to avoid corrosion and sticking caused by too low fuel leaks of the injection pumps in gas mode.

Within one year (7/1/85 to 6/30/86) the engine ran for 5350 hours (95 percent in gas mode) giving a mean output of 1810 kW (electrical) and 2005 kW (thermal). This represents a 71 percent load factor.

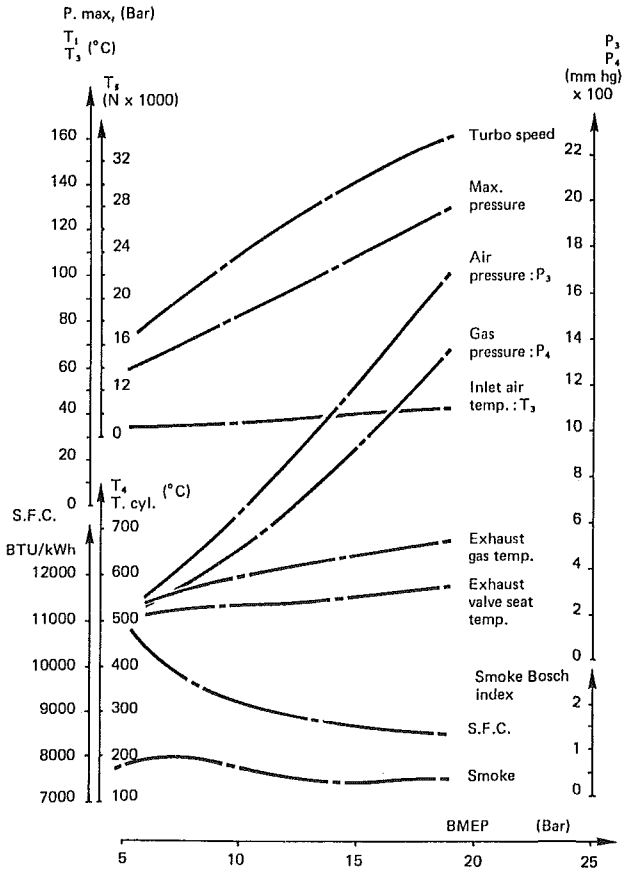


Fig. 12 4 PA5 V dual fuel in diesel mode

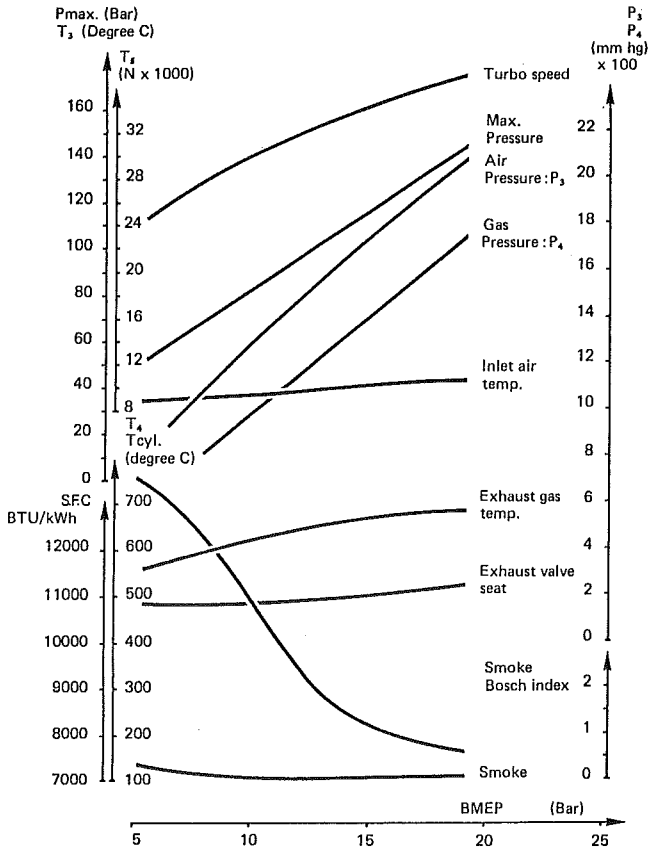


Fig. 13 4 PA5 V dual fuel in gas mode

Downloaded 01 Jun 2010 to 171.66.16.87. Redistribution subject to ASME license or copyright; see http://www.asme.org/terms/Terms_Use.cfm

New Developments

The same philosophy has been applied to a smaller engine, the PA 5 DF. The PA 5 is a 255 mm × 270 mm engine rated at 220 kW/cyl. in Diesel mode (19.15 bar b.m.e.p.). In the dual-fuel version, gas is introduced in the scavenge air duct of each cylinder through a valve with a collar. The power of the engine is then controlled by gas pressure (Fig. 11).

The first engine was delivered by NIIGATA with reduced power in 1985. At the beginning of 1987, a four-cylinder development engine ran in St. Denis, France up to 220 kW/cyl. (300 hp/cyl.), which equals the nominal power of the PA 5 on diesel mode.

The results of this development work can be appreciated in Figs. 12 and 13, which give the various operating parameters at a constant speed of 1000 ppm.

The following remarkable results are worth noticing:

- Total efficiency at full load 45 percent
- Emission of NO_x at full load 1.7 g/kW•h
- Low temperature of components exhaust valve seat. 520°C on

Research on knocking limits has also been performed, without reaching this limit, even with the following evolution of engine conditions at full load:

- Temperature of the charged air 45 to 70°C
- Reduction of air excess
- Pilot fuel quantity 5 to 40 percent
- Injection advance 19 to 24°CA

It is generally assumed that a long duration of combustion and a high level of temperature are necessary to have NO_x emission.

As the PA 5 duration of combustion is very short (about 45°CA), this explains our very good results for NO_x combustion.

The high level of total air excess is responsible for the absence of knocking.

This will allow us to project a new range of dual-fuel engines for the 1000 to 3500 kW range.

References

1 Daugas, C., and Grosshans, G., "Gas Fed Engines Progress," D5 conference CIMAC, Oslo, 1985.

2 Boillot, M., and Migeot, Jl., "La Centrale à bois de DEGRAD DES CANNES," *Entropie*, Special CIMAC issue, 1987.

3 Stadler, F. H., Taubert, G., and Weireter, K., "Ein Grossmotor verwendet Loesungsmitteldaempfe umweltschonend," *Energie Spektrum*, Apr. 1986, pp. 40–43.

4 Grabbe, D., Weireter, K., and Grosshans, G., "A Highly Supercharged Dual Fuel Engine Reduces Emission in Burning Solvents," CIMAC, Warsaw, 1987.

Downloaded 01 Jun 2010 to 171.66.16.87. Redistribution subject to ASME license or copyright; see http://www.asme.org/terms/Terms_Use.cfm

A Rankine Bottoming Cycle System for Heavy-Duty Applications

R. A. Cemenska
Research Department,
Caterpillar, Inc.,
Peoria, IL 61629

Fuel costs represent a major portion of the total operating expense of a heavy-duty engine in continuous service. Many new technologies are being developed to lower engine fuel consumption, but a 10–15 percent reduction in fuel costs is now achievable using Rankine Bottoming Cycle (RBC) technology. System economics require integration of state-of-the-art technology in the turbine, heat exchangers, and automatic controls. This paper describes the design and initial test results of a project to demonstrate a diesel engine–RBC power plant. The system was constructed for a Caterpillar 3500 series 16-cylinder (3516) engine with a combined output of 1415 kW. Initial test results have demonstrated a 10.4 percent fuel savings at a thermal efficiency of 44.5 percent. The RBC module is a steam-based, stand-alone unit featuring unattended operation through the use of on-board water treatment, a once-through boiler, automatic control system, and a unique design three-stage–dual pressure steam turbine. The modular concept allows the system to be adapted to other engines and alternative heat sources.

Introduction

The oil embargo of 1973 made the world acutely aware that fuel supplies were limited. Manufacturers of heavy-duty diesel engines have responded by developing new technologies for reduced fuel consumption. Lower fuel consumption is particularly important in large, heavy-duty, high load factor applications where fuel costs can represent 70–80 percent of the total annual operating cost.

Caterpillar is developing technology to reduce engine fuel consumption including electronic controls, improved combustion, turbocompounding, and insulated combustion chambers [1, 2]. Further reductions in fuel consumption are possible by recovering the "waste heat" and converting it to shaft power using a "Bottoming Cycle" [3].

A program was started in 1981 to evaluate the fuel saving potential of Rankine Bottoming Cycle (RBC) technology. In its simplest form, the RBC system consists of a boiler to recover the energy, an expander to convert the energy to shaft work, and a condenser and feedpump to close the loop (Fig. 1). RBC technology has the potential to reduce the Brake Specific Fuel Consumption (BSFC) of current diesel engines by 10–15 percent.

The goals of the Caterpillar program are:

1 12 percent reduction in brake specific fuel consumption
2 14 percent increase in power
3 Customer payback period of one year (based on fuel costs of $1.25 per gal).

The fuel consumption and power goals were based on cycle simulation studies. The performance results were combined with a simplified cost model to estimate the customer payback period. A one-year payback period was judged to be acceptable to potential users.

This paper describes the design and initial test results of a Rankine Bottoming Cycle system for a Caterpillar 3500 series 16-cylinder (3516) heavy-duty, diesel engine rated at 1270 kW. The combined system output is 1415 kW.

System Design

It was evident from the beginning that the RBC performance depended on five key design factors:

1 fluid selection
2 thermodynamic cycle selection
3 turbine efficiency
4 boiler efficiency
5 control strategy

Extensive computer simulations were used to size the individual components and predict system performance. The performance and cost models were combined to compare tradeoffs in fluid selection, thermodynamic cycle, and the designs of the turbine, boiler, and control system. These topics will be discussed in the order listed, but in fact the alternatives are interrelated and were considered jointly in many cases.

Fluid Selection

The properties of the working fluid have a major impact on the performance and commercial acceptability of an RBC system. In particular, the fluid characteristics:

Contributed by the Internal Combustion Engine Division and presented at the Internal Combustion Engine Division Technical Conference, Kansas City, Missouri, October 4–7, 1987. Manuscript received by the Internal Combustion Engine Division June 1987.

Copyright © 1988 by ASME
Downloaded 01 Jun 2010 to 171.66.16.87. Redistribution subject to ASME license or copyright; see http://www.asme.org/terms/Terms_Use.cfm

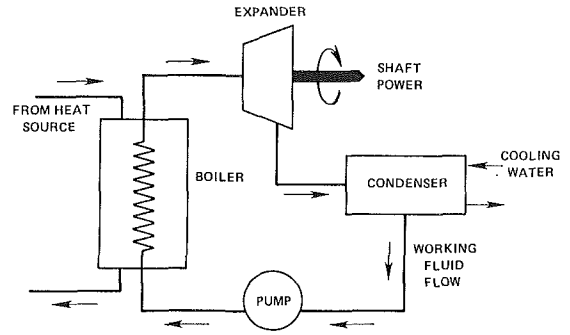


Fig. 1 Simplified Rankine Bottoming Cycle (RBC) schematic

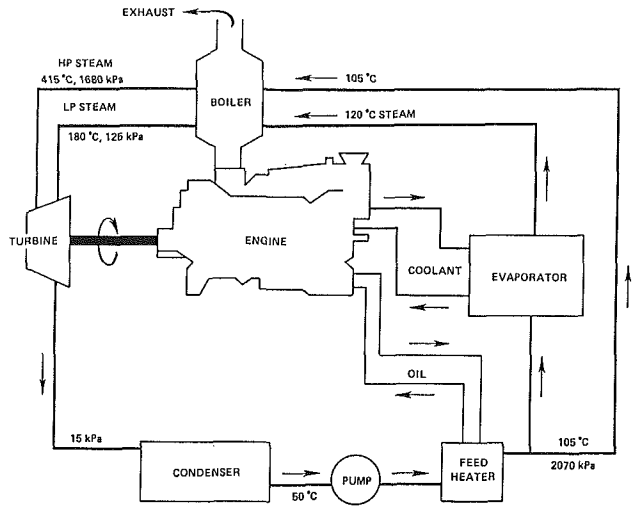


Fig. 2 RBC system schematic

1 define the temperature and pressure limits of the thermodynamic cycle and thus limit the theoretical efficiency;

2 define the toxicity hazard;

3 define the cost envelope by setting the material requirements and heat exchanger sizes.

Initially, more than 50 fluid alternatives were screened by weighing such factors as cost, material compatibility, temperature stability, and safety hazard.

Six fluids were selected for more detailed evaluation:

1 Water

2 RC1 (60 percent pentafluorobenzene/40 percent hexafluorobenzene—Monsanto Corp.)

3 35 percent 2-methyl pyridine/65 percent water

4 F85 (85 percent trifluorethanol/15 percent water)

5 Ammonia

6 Toluene

The final evaluation considered the fluid hazard, heat exchanger volume, and performance. The rating criteria for the fluid safety hazard and the composite results are summarized in Table 1. The results of the fluid evaluation, heat exchanger analysis, and the net system power are summarized in Table 2. F-85 was used as the base (1.0) for the comparisons.

Steam was selected as the working fluid because of its low fluid hazard and excellent cost/power ratio. Initial estimates indicated that the steam system could meet the one-year customer payback period in production quantities.

Thermodynamic Cycle

The thermodynamic cycle defines the theoretical efficiency limits of the RBC system. High efficiency requires high cycle temperatures and pressures and high heat exchanger effectiveness. Single pressure steam cycles deviate considerably

Table 1 RBC fluid alternatives

FLUID	WEIGHTED RISK IN RBC SYS.
WATER	0
RC-1 PENTAFLUOROBENZENE HEXAFLUOROBENZENE/ (60%/40% MOLAR)	.2
2 - METHYLPYRIDINE/ WATER (35%/65% MOLAR)	.8
F85 TRIFLUOROETHANOL/ WATER (85%/15% MOLAR)	1.0*
AMMONIA	1.1
TOLUENE	1.3

*F85 WAS USED AS THE BASE (1.0) FOR COMPARISON.

FACTORS CONSIDERED:
- FLAMMABILITY
- EYE CONTACT
- INHALATION
- INGESTION

Table 2 Relative ratings of RBC system alternatives

SYSTEM (NOTE 1)	FLUID HAZARD	HEAT EXHANGER VOLUME	POWER	MFG. COST	MFG. COST / POWER
STEAM-DUAL PRESSURE	0	.95	1.00	.95	.95
RC-1	.20	1.15	0.85	1.50	1.75
2 METHYLPYRIDINE - 35% WATER - 65%	.80	1.00	1.00	1.00	1.00
F85 (NOTE 2)	1.00	1.00	1.00	1.00	1.00
AMMONIA	1.10	0.85	.80	1.05	1.30
TOLUENE	1.30	1.10	1.05	1.05	1.00

NOTE 1 - RBC SYSTEM DESIGNS WERE IDENTIFIED FOR EACH FLUID

NOTE 2 - F85 WAS USED AS THE BASE (1.0) FOR THE COMPARISONS.

Table 3 Steam cycle comparison

	SINGLE PRESSURE	DUAL PRESSURE
HIGH PRESSURE (kPaA)	1720	1720
LOW PRESSURE (kPaA)	—	140
EXHAUST HEAT RECOVERY	YES	YES
JACKET WATER HEAT RECOVERY	NO	YES
RELATIVE POWER RECOVERY	1.0	1.60
RELATIVE MFG. COST	1.0	1.18
RELATIVE MFG. COST/ POWER	1.0	.74

Downloaded 01 Jun 2010 to 171.66.16.87. Redistribution subject to ASME license or copyright; see http://www.asme.org/terms/Terms_Use.cfm

Table 4 Steam turbine comparison

	CATERPILLAR	COMMERCIAL MULTIPLE STAGE	COMMERCIAL CURTIS STAGE
EFFICIENCY	80%	70%	50%
BLADE ROWS	6	12 - 14	4
SIZE: LENGTH X DIAMETER (MM)	510 x 410	860 x 600	600 x 600
RELATIVE MFG. COST	1.0	4.0	3.0

Table 5 Turbine performance results

PERFORMANCE AT RATED SPEED (TOTAL-TO-TOTAL)		
	MEASURED	PREDICTED
OVERALL TURBINE		
EFFICIENCY	82.6	80.3
POWER (kW)	195.8	196.7
FLOW (% RATED)	97	100
PRESSURE RATIO	103.4	103.4
H.P. STAGE		
EFFICIENCY	75.6	73.6
PRESSURE RATIO	11.8	10.4
L.P. STAGE		
EFFICIENCY	88.6	85.7
PRESSURE RATIO	8.4	9.0

from the optimum Rankine cycle because of the high heat of vaporization of water. The efficiency of practical steam cycles can be increased by using multiple pressure levels in a given cycle. The performance potential of multiple pressure cycles was evaluated using computer simulations and component cost models. Table 3 shows the results of a comparison between a single and dual-pressure steam RBC system.

The dual-pressure system was selected because it has more power than a single-pressure system with only a small increase in estimated cost.

The complete RBC schematic is shown in Fig. 2. The fluid state points listed are for the full load design point. As shown on the schematic, energy recovery in the exhaust boiler is supplemented by the collection of energy from the jacket water and engine oil. The energy distributions for the base engine and the engine plus RBC system are shown in Fig. 3.

Components

Steam Turbine. The power output of the RBC system is strongly related to the efficiency of the steam turbine expander. Turbine efficiency also affects the condensing conditions and hence condenser size. A number of turbine options were evaluated before the final design was selected. The results of a comparison between three alternatives in the 200 kW size range are summarized in Table 4.

The Caterpillar design was selected because it had the best performance/cost relationship and the design was readily adaptable to the dual-pressure cycle.

The Caterpillar turbine design (Fig. 4) consists of a single high-pressure (HP) stage followed by two low-pressure (LP) stages. The first stage is a partial admission supersonic impulse design while the low-pressure stages are conventional reaction stages. The required mixing volume between the HP diffuser and LP inlet is minimized by designing the HP exit conditions to be the same as the LP steam inlet conditions. The turbine is sealed with carbon face seals and is supported by rolling element bearings. The steam is expanded 3 to 4 percent beyond saturation to extract the maximum amount of

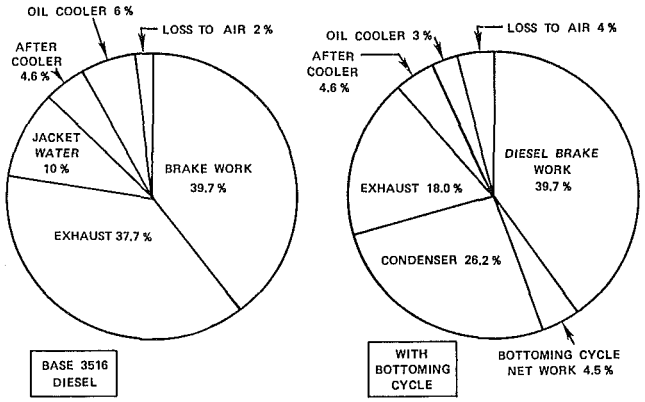
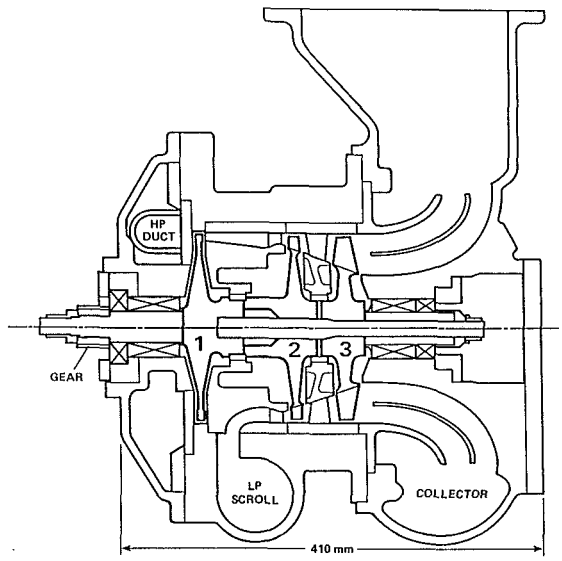


Fig. 3 Energy distribution



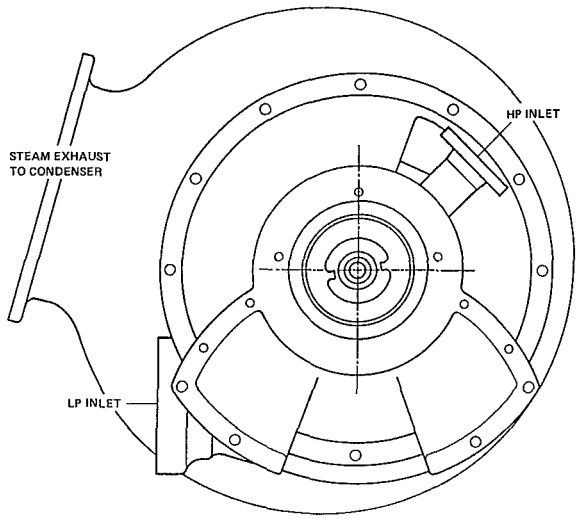


Fig. 4 RBC turbine

work while avoiding moisture in the blade rows. The output shaft is coupled to the engine crankshaft using a two-stage reduction gearbox and a fluid coupling to isolate torsional vibrations.

The turbine was judged to be a high performance risk component of the RBC system and hence extensive component tests were conducted to verify performance expectations. As summarized in Table 5, turbine performance was quite

Downloaded 01 Jun 2010 to 171.66.16.87. Redistribution subject to ASME license or copyright; see http://www.asme.org/terms/Terms_Use.cfm

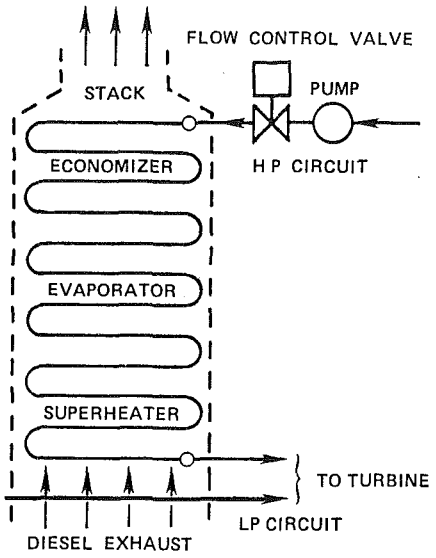


Fig. 5 Once-through boiler concept

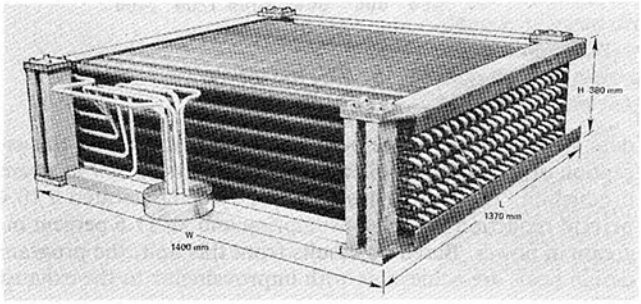


Fig. 6 RBC boiler core

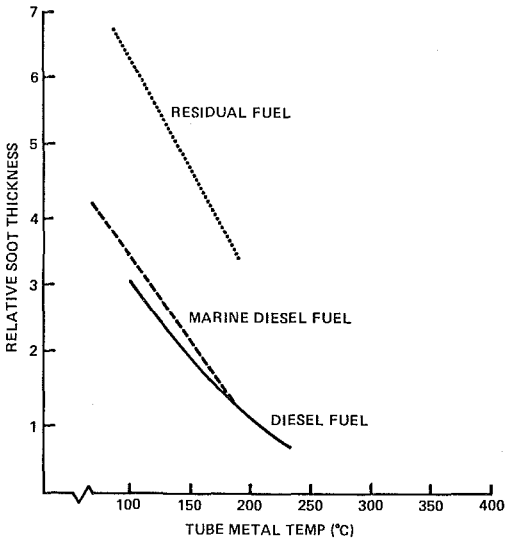


Fig. 7 Steady state soot thickness versus tube temp

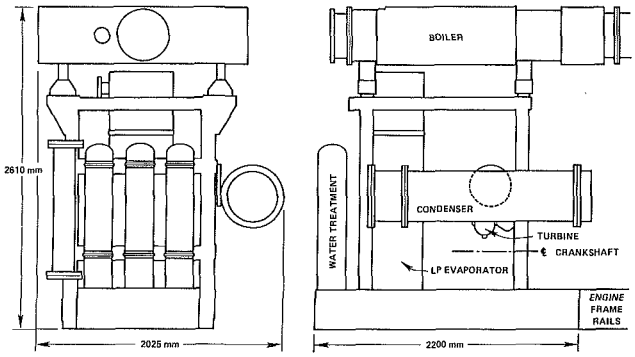


Fig. 8 RBC package dimensions

satisfactory compared to the level predicted for the design. The turbine efficiency of 82.6 percent exceeded the 80.3 percent prediction at the design point and fell within 3 percent of the prediction over the operating map.

Exhaust Boiler. The exhaust boiler is the largest component in the RBC system and accounts for approximately 1/3 of the total cost. The design is based on the once-through concept developed for our Solar combined cycle turbine engine program [4, 5]. In this concept the economizer, evaporator, and superheater sections are connected together directly without intermediate steam drums (Fig. 5). The once-through concept has several advantages over conventional designs:

1 The steam drums, blowdown, and chemical additions for boiler water chemistry control are eliminated, thus reducing volume and cost.

2 Soot blowers are eliminated because gas side soot can be removed by operating the unit "dry" with the tubes and fins heated to exhaust temperature. The soot then rapidly "cooks off" similar to the process in a self-cleaning oven.

3 The design is inherently safe because of the small steam volume.

4 The once-through concept has a short time constant for quick control response. This feature allows a floating pressure control mode without requiring a steam valve at the outlet.

The boiler "core" is shown in Fig. 6. It consists of both a LP and HP circuit. The LP circuit superheats the saturated steam coming from the evaporator while the HP circuit preheats, evaporates and superheats the HP flow in the economizer, evaporator, and superheater zones. Finned tubes are used throughout to provide a compact package. The fin spacing was varied with local temperature to account for soot loading. The LP and HP flows leaving the boiler are routed directly to the turbine.

Soot fouling in the boiler was one of the major durability concerns. Tests were run on boiler tube sections in the exhaust of a diesel engine to simulate various conditions expected in operation. The soot thickness was found to reach a constant value (steady state) after 200–300 hours of operation. Typical steady-state results are presented in Fig. 7. The soot thickness was found to be a strong function of local metal temperature and time and is also related to the quality of the fuel being used. These data were used to design the boiler fin spacing for operation in the fully fouled (steady-state soot thickness) condition. Long-term test data on a full-size boiler will be required to validate the design criteria.

Packaging. Several packaging concepts were evaluated during the design process. The concept selected for final design consisted of a self-contained RBC module mounted in front of the engine. The front-mounted module option (Fig. 8) was selected because:

1 The RBC Module can be shipped fully assembled and factory tested.

2 Engine accessibility for normal maintenance operations is not affected.

3 Driving directly into the crankshaft eliminated the need to upgrade the engine's front geartrain for the additional power and is readily adaptable to 8, 12, and 16 cylinder engines.

In addition, the front mount option was judged to be the most likely alternative for application to competitive engines.

Downloaded 01 Jun 2010 to 171.66.16.87. Redistribution subject to ASME license or copyright; see http://www.asme.org/terms/Terms_Use.cfm

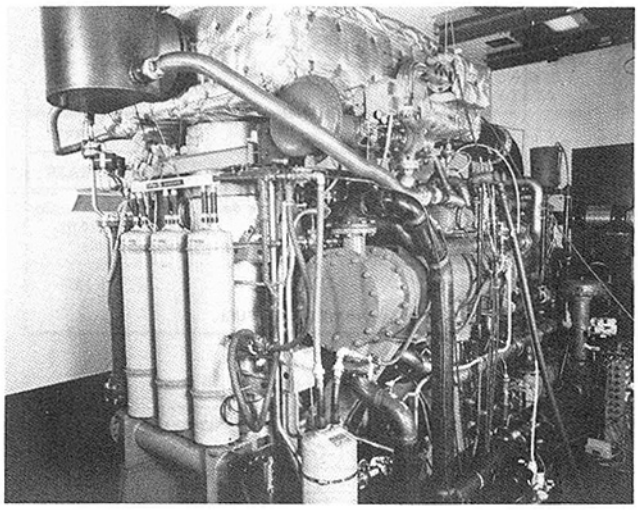


Fig. 9 RBC system

A photograph of the RBC system installed in the test cell is shown in Fig. 9.

Automatic Control. The control is a digital based acquisition and control system designed to operate the RBC module as an unattended system. The control provides both a normal operating mode and a development mode.

During normal mode conditions the control requires only a "start" command from the operator. It is programmed to cycle through all conditions (startup, run, boiler cleaning, and shut down) without operator intervention. Automatic boiler cleaning can be disabled if desired. In this case, the control signals the operator with a light when cleaning is required, and the operator initiates the cleaning cycle with a button. Appropriate software has been provided to detect out-of-range conditions. The control is programmed to take various actions (up to and including a safety shutdown) depending on the severity of the situation. Data leading up to an unexpected shutdown are recorded for later analysis. The control algorithm provides maximum power from the system by running the turbine against the wetness limit as monitored by the condenser conditions.

A development mode has been provided as an aid to laboratory and field development. Manual and semi-automatic modes have been provided for use by a test engineer. The system can be interrogated to determine system temperatures, pressures, and turbine speed.

Performance Test Results

The RBC system has currently accumulated 120 hours of performance testing. The performance results with the manual control are summarized in Fig. 10 at 1800 rpm (rated speed) and 1500 rpm (approximate peak torque). As shown, the RBC system results in a 8.0–13.0 percent reduction in fuel consumption over a wide range of speed and load. Performance with the automatic control is within 2 percent of the optimum performance identified during the manual control tests.

Summary

Caterpillar has designed a waste heat recovery system, based on a Rankine Bottoming Cycle, which offers a potential fuel savings of 12 percent and a 14 percent increase in power. To

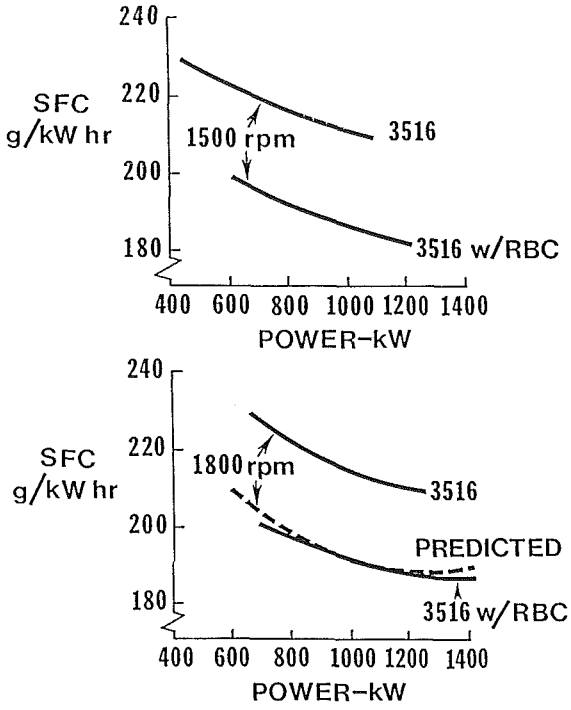


Fig. 10 RBC test results

date all components have performed as expected with the exception of the exhaust boiler, which is somewhat low in steam production. The system has consistently demonstrated a 10.4 percent reduction in fuel consumption and an 11.6 percent increase in power. Based on results from this unit, the program design goals are achievable with improvements to the exhaust boiler.

The RBC module is currently undergoing testing at the Caterpillar Technical Center to further develop the automatic control and boiler cleaning strategy and to demonstrate initial durability acceptable for a field installation. Plans are currently underway to commence long-term durability tests to provide additional insight into:

1 Component durability
2 Material compatibility
3 Water side fouling in the heat exchangers
4 Service and operating procedures

In addition, further effort is planned to:

1 Reduce the component count.
2 Identify lower cost materials. (Stainless steel was used in the initial design to avoid the effects of corrosion during the performance development process.)
3 Develop a scaling procedure for other diesel and spark ignition engines.

References

1 Moncelle, M. E., and Fortune, C. G., "Caterpillar 3406 PEEC (Programmable Electronic Engine Control," SAE Paper No. 850173, 1985.
2 Wilson, D. E., "The Design of a Low Specific Fuel Consumption Turbocompound Engine," SAE Paper No. 860072, 1986.
3 Barrett, J. R., et al., "Heat Recovery System Including a Dual Pressure Turbine," US Patent No. 4,586,338, May 6, 1986.
4 Duffy, T. E., Archibald, J. P., and Campbell, A. H., "Steam Generators and Combined Cycle Power Plants Employing the Same," US Patent No. 4,627,387, Dec. 9, 1986.
5 Truman, P., "Commercial Operation of the RACER Combined-Cycle System," ASME Paper No. 85-GT-152, 1985.

Downloaded 01 Jun 2010 to 171.66.16.87. Redistribution subject to ASME license or copyright; see http://www.asme.org/terms/Terms_Use.cfm

C. P. Bankston
Assoc. Mem. ASME

L. H. Back
Fellow ASME

E. Y. Kwack
Assoc. Mem. ASME

Jet Propulsion Laboratory,
California Institute of Technology,
Pasadena, CA 91109

A. J. Kelly
School of Engineering and Applied Sciences,
Princeton University,
Princeton, NJ 08544

Experimental Investigation of Electrostatic Dispersion and Combustion of Diesel Fuel Jets

An experimental study of electrostatically atomized and dispersed diesel fuel jets has been conducted. A new electrostatic injection technique has been utilized to generate continuous, stable fuel sprays at charge densities of 1.5–2.0 C/m^3 of fluid. Model calculations show that such charge densities may enhance spray dispersion under diesel engine conditions. Fuel jets were injected into room temperature air at one atmosphere at flow rates of 0.25–1.0 cm^3/s and delivery pressures of 100-400 kPa. Measured mean drop diameters were near 150 μm with 30 percent of the droplets being less than 100 μm in diameter at typical operating conditions. The electrical power required to generate these sprays was less than 10^{-6} times the chemical energy available from the fuel. The spray characteristics of an actual diesel engine injector were also studied. The results show considerable differences in spray characteristics between the diesel injector and electrostatic injection. Finally, ignition and stable combustion of electrostatically dispersed diesel fuel jets was achieved. The results show that electrostatic fuel injection can be achieved at practical flow rates, and that the characteristics of the jet breakup and dispersion have potential application to combustion systems.

Introduction

Combustion in diesel engines is significantly affected by fuel spray injection and flow characteristics (Heinein, 1976). Many methods for improved mixing and dispersion of the spray to reduce local fuel rich regions have been investigated for improved combustion and reduced soot formation. In general, the breakup of fuel jets in diesel engines is accomplished by high-pressure injection in the range 20 MPa (for indirect injection) up to about 140 MPa (for direct injection). Furthermore, swirl is imparted to the flow field in the chamber to assist the fuel–air mixing process further, and soot formation is strongly dependent upon swirl characteristics. However, fuel-rich regions apparently still persist in current engines, and methods for improved mixing and reduced soot formation continue to be of interest.

Techniques for improving in-cylinder combustion characteristics include mechanical, chemical, and electrical methods. Mechanical methods include the adjustment of injection timing and changes in injection geometries (Pischinger and Cartellieri, 1972; Khan et al., 1972). Chemical concepts usually rely upon fuel additives or the application of catalysts on cylinder surfaces (Gaffney et al., 1980). Electrical concepts have been based on observed electrical phenomena in the combustion process. Electric fields have been applied to the combustion chamber (Ahmad et al., 1980) or plasma devices have been proposed to enhance the combustion process. Recently, studies of microexplosions in fuel–water and fuel–alcohol mixtures have led to the possibility that such a breakup process could be utilized to enhance dispersion of the injected fuel (Wang and Law, 1985).

The concept being studied here involves the injection of a fuel jet that is electrostatically broken up and dispersion enhanced by the repulsion of like-charged droplets. Previously, this concept has not proven practical due to the inability to produce sprays at practical flow rates with liquid charge densities capable of significantly dispersing fuels (Newgard and Noon, 1964; Luther, 1962). This paper describes an experimental study of electrostatically dispersed diesel fuel jets utilizing a new electrostatic device, the Spray Triode, and ignition and combustion of these jets.

Background

Model calculations were carried out by Bellan (1983)[1] that show the effect of charged droplets on the dispersion of a fuel spray under diesel engine conditions. That model predicts the expansion of an initially spherical droplet spray cloud of radius R_0, due to the repulsion of uniformly charged and distributed droplets. The model assumes a given fuel mass and total charge, and calculates drop cloud radius versus time for expansion into a quiescent environment without drag. The function $F(n_0/n)$ in Bellan (1983) to which the radius factor (R/R_0) is related by $(R/R_0)=(n_0/n)^{1/3}$ is given by

Contributed by the Internal Combustion Engine Division for publication in the JOURNAL OF ENGINEERING FOR GAS TURBINES AND POWER. Manuscript received by the Internal Combustion Engine Division July 28, 1987.

[1] In Bellan (1983), the Table I values $n^0 \times 10^4$ should be $n^0 \times 10^{-4}$.

Copyright © 1988 by ASME
Downloaded 01 Jun 2010 to 171.66.16.87. Redistribution subject to ASME license or copyright; see http://www.asme.org/terms/Terms_Use.cfm

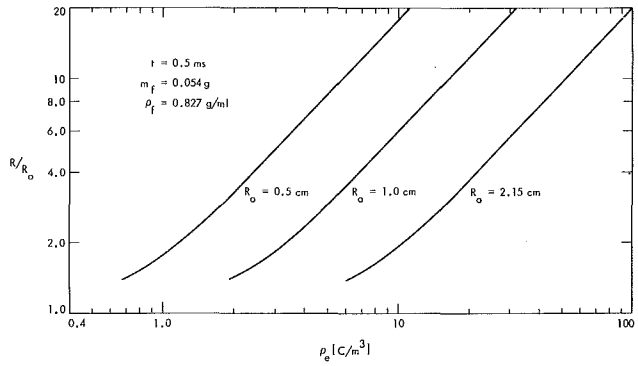


Fig. 1 Charged spray droplet cloud expansion ratio versus charge density

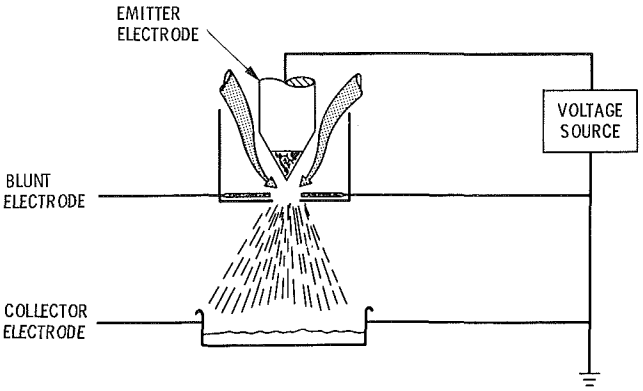


Fig. 2 Charge injection electrostatic Spray Triode

$$F\left(\frac{n_0}{n}\right) = \kappa \Delta t \left(\frac{\rho_e}{\rho_f}\right)\left(\frac{2m_f}{R_0^3}\right)^{1/2} \quad (1)$$

with κ a conversion constant. Using this relationship, we have calculated spray cloud dispersion versus charge density in 0.5 ms, and the results are plotted in Fig. 1. For example, Fig. 1 shows that a spherical spray volume 1 cm in radius and containing 54 mg of diesel fuel will expand by a radius factor of 1.4 in 0.5 ms at a charge density of 2 C/m^3. At 5 C/m^3, the same spray will expand by a radius factor of three.

The very high resistivities of liquid hydrocarbon fuels (10^{10}–10^{12} ohm-m) (Luther, 1962; Kelly, 1981, 1982), however, have presented practical difficulties in producing electrostatically charged sprays at flow rates above 0.1 cm^3/s (Newgard et al., 1964; Luther, 1962). Most previous efforts have attempted to utilize a two-electrode configuration whereby the liquid was fed through a tube with a sharp orifice tip set at a high voltage potential. However, it was found that such an arrangement was very inefficient at imparting charge to nonconducting liquids. More recently, Miller et al. (1987) have observed electrostatic effects when a high-voltage probe was placed near the outlet of a conventional fuel injector/atomizer. However, no drop charge densities were measured and the observed effects were a 7 percent reduction in drop mean diameter and a modest increase in combustion efficiency in combustor experiments. The electrostatic spray device conceived and demonstrated by Kelly (1981, 1982) has overcome many of these previous limitations.

The spray device diagrammed in Fig. 2 is a charge injection Spray Triode characterized by an emitter electrode immersed in the fluid flow and a second, immersed "blunt" electrode, containing an orifice through which the liquid is injected. The electrode pair forms a submerged field emission electron gun,

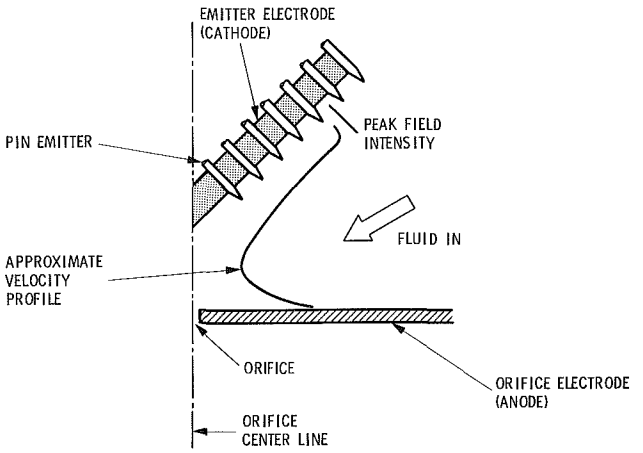


Fig. 3 Electrostatic charge injection schematic

with the collector (such as a cylinder wall) forming the third electrode of the Triode. The emitter tip is composed of a metal oxide eutectic material containing tungsten metal fibers (Chapman et al., 1972). The metal fibers cover the surface of the tip as indicated diagrammatically in Fig. 3 and act as points of concentration of electric field strength. These materials can be formulated with a surface fiber count of 10^6/cm^2 (Kelly, 1982). For a given set of flow conditions, emitter tip location, and voltage, electrons are emitted into the fluid stream and are transported through the orifice in the blunt electrode. Electrical field strengths in the emission gap are greater than 10^7 V/m.

Nomenclature

d = spray drop diameter, m
d_{10} = arithmetic mean diameter, m
d_{32} = volume-surface mean diameter, m

$$F\left(\frac{n_0}{n}\right) = \left[\left(\frac{n_0}{n}\right)^{1/3}\left[\left(\frac{n_0}{n}\right)^{1/3} - 1\right]\right]^{1/2} + 1/2 \ln\left[\left(\left[1 - \left(\frac{n}{n_0}\right)^{1/3}\right]^{1/2} + 1\right)\Big/ \left(1 - \left(1 - \left(\frac{n}{n_0}\right)^{1/3}\right)^{1/2}\right)\right]$$

m_f = fuel mass, g
n = spray cloud drop density, cm^{-3}
n_0 = initial spray cloud drop density, cm^{-3}
R = spray cloud radius, cm
R_0 = initial spray cloud radius, cm
q = electronic charge = 1.602×10^{-19}C
T = aerodynamic liquid jet breakup parameter, equation (4)
Δt = time increment, s
u = liquid jet velocity, m/s
γ = liquid surface tension, N/m
ϵ_0 = permittivity of free space = 8.85×10^{-12}C/V-m
κ = $3.50 \times 10^9 g^{1/2}$cm$^{3/2}$/C-s
μ_f = liquid viscosity, kg/m-s
ρ_e = charge density per unit volume of liquid, C/m^3
ρ_f = fuel density, g/cm^3
ρ_g = gas density, g/cm^3

Downloaded 01 Jun 2010 to 171.66.16.87. Redistribution subject to ASME license or copyright; see http://www.asme.org/terms/Terms_Use.cfm

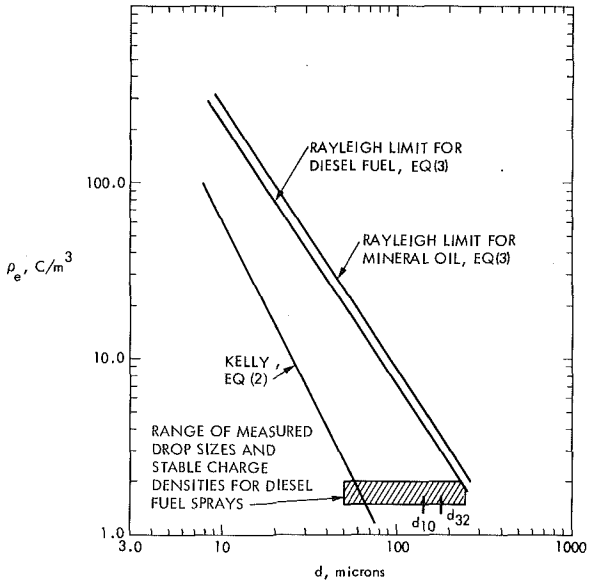


Fig. 4 Droplet size versus charge density

Charge densities of up to 1.8 C/m^3 have previously been reported for Marcol-87 (viscosity = 25 cp) (Kelly, 1982) using a Spray Triode. Mean drop diameters in the 50-μm range have been measured for Turbojet A at 2.6 C/m^3 (Kelly, 1982). Also, Kelly has utilized a statistical equilibrium end-state model to predict the characteristics of charged liquid sprays (Kelly, 1978, 1982). The results are illustrated in Fig. 4. The model predicts that the charge density-drop size relationship is independent of fluid properties and is given by the relationship

$$\rho_e = (1.06 \times 10^{-17}\ \text{J}) \frac{12\epsilon_0}{qd^2} \tag{2}$$

The Rayleigh limit[2] is also plotted on Fig. 4 and is given by the relation

$$\rho_e = 12(2\epsilon_0\gamma)^{1/2} d^{-1.5} \tag{3}$$

The data obtained in this study are shown on Fig. 4, and will be discussed later. Note that the theory predicts that sprays in the 20-100-μm diameter range can be charged at levels that were estimated to be necessary for effective dispersion under diesel engine conditions.

Experimental

An electrostatic spray device of the type depicted in Fig. 2 has been utilized to produce sprays of a highly refined hydrocarbon (mineral) oil of approximately 25 cp viscosity under noncombusting conditions and of No. 2 diesel fuel (approximately 6 cp) under combusting and noncombusting conditions. Experiments were conducted at one atmosphere pressure and room temperature conditions. In the present work we have tested a Spray Triode wth two orifice sizes, 422 and 173 μm, at steady flow rates of 0.25-1.0 cm^3/s, and liquid supply pressures of 100-400 kPa. The experimental setups for noncombusting and combusting experiments are illustrated in Fig. 5.

For noncombusting experiments (Fig. 5*a*), the Spray Triode is positioned to inject vertically downward into a metal can, which acts as the collector electrode. The Spray Triode is 0.82 cm in diameter and 11.3 cm long (Fig. 6). The injected stream

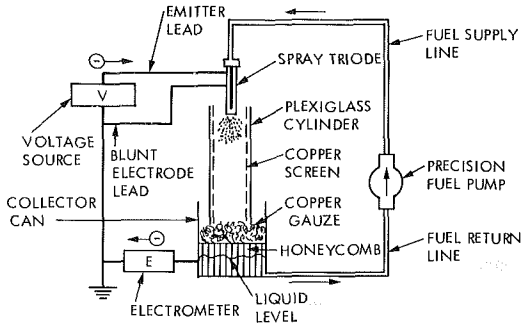


Fig. 5(*a*) Cold spray setup

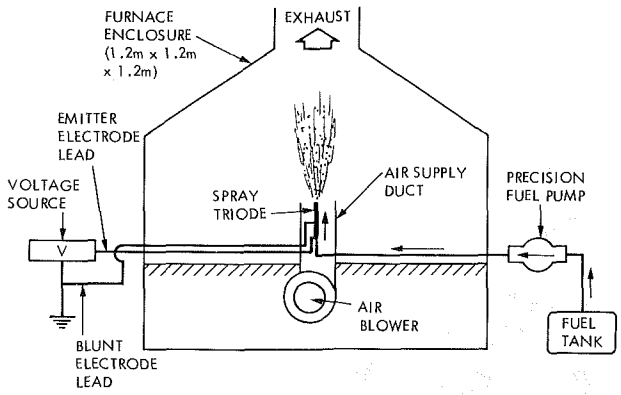


Fig. 5(*b*) Combustion setup

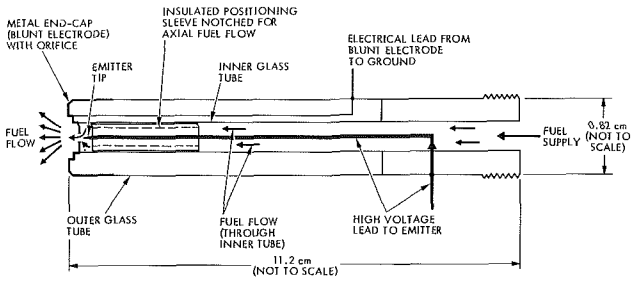


Fig. 6 Detailed diagram of Spray Triode

is directed into a 11.4-cm-dia plexiglass tube, which sits in the metal can. The plexiglass tube allows spray development to be observed while all of the liquid and charge can be collected for measurements. Approximately 1/2 of the can volume is occupied by aluminum honeycomb and copper gauze in order to insure that the accumulated charge on the liquid is effectively grounded. The plexiglass tube is also lined with copper wire screen, which in turn is in contact with the metal can grounding material in order to collect the charge deposited on the tube walls by the dispersed spray.

Spray charge densities are determined by measuring the current carried by the fluid with an electrometer in series between collector electrode and ground (Fig. 5*a*). Charge density is then calculated by dividing the electric current by liquid volume flow rate. Fuel flow is controlled by a positive displacement precision metering pump, which was calibrated for the liquid under study.

Characterization of the spray was carried out by flash illumination and visual photography. Sprays were typically photographed using a 65-mm micro Nikkor lens and an EG&G 0.5 microsecond synchronized, spark-gap flash. An object distance of 54 mm, and image distance of 492 mm gave a magnification of 7.5×. Analysis of the negatives was carried

[2]The Rayleigh limit is the charge density at which the electrostatic repulsion force associated with the drop surface charge is sufficient to overcome surface-tension forces for a given drop size. At the Rayleigh limit, no further accumulation of charge is possible without drop disruption or breakup.

Downloaded 01 Jun 2010 to 171.66.16.87. Redistribution subject to ASME license or copyright; see http://www.asme.org/terms/Terms_Use.cfm

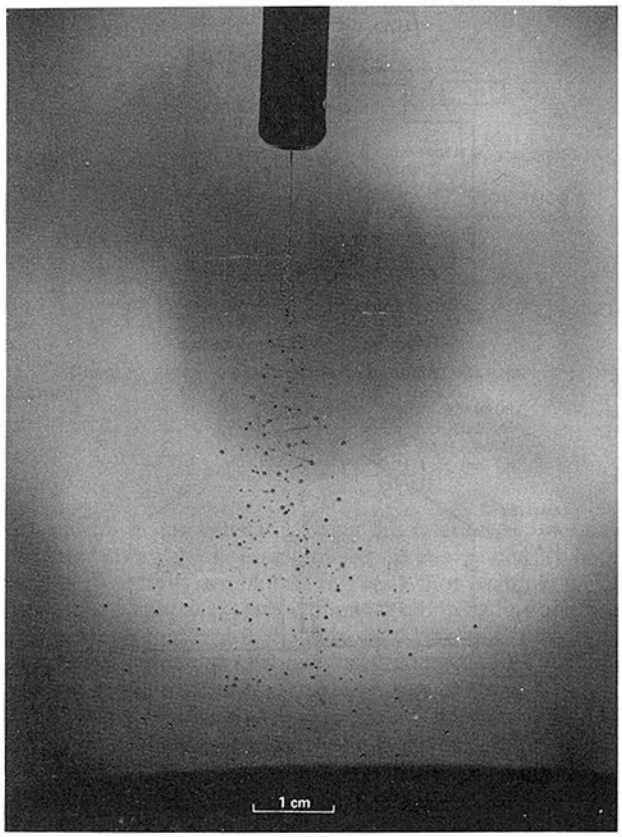


Fig. 7 Mineral oil spray pattern from 422-μm orifice Spray Triode at 0.33 cm^3/s and 1.5 C/m^3

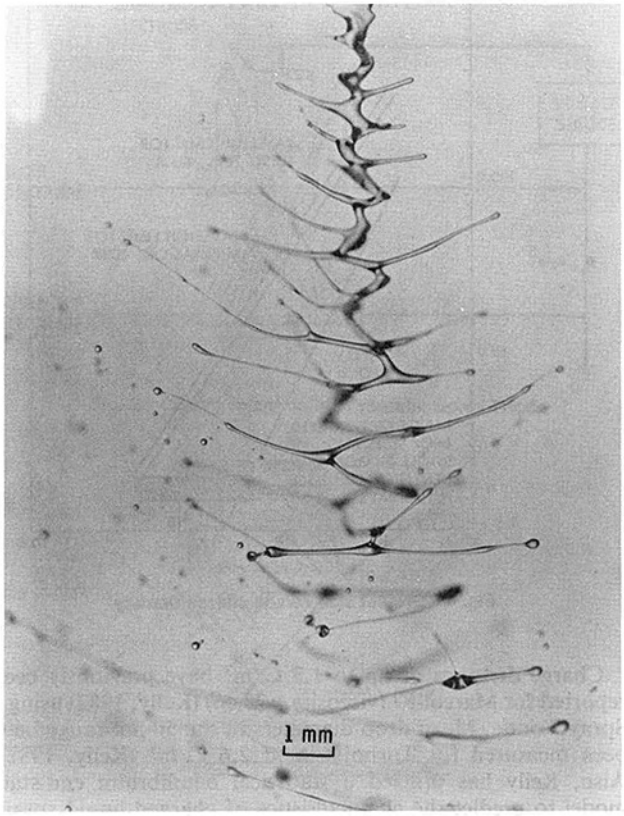


Fig. 8 Magnified view of electrostatic spray breakup process for mineral oil at 0.8 cm^3/s from 422-μm orifice

out using a De-Anza ID-5400 image processing system. The negative is placed on a light table in view of a video camera. The analog signal from the video camera is digitized and fed directly to an array processor, which controls the data flow and writes the data into memory at a rate of 30 frames/s in a 512×512 pixel matrix. Images are stored on a mass storage device for processing using a PDP 11/34 minicomputer. Available software operations include image enhancement, filtering, drop contour detection and shape analysis, and classification by size distribution. Each droplet is sized individually. The system has been previously applied to the analysis of fuel sprays (Fleeter et al., 1982).

For combustion experiments, the Spray Triode was mounted to inject fuel vertically upward in a ventilated furnace/hood enclosure as shown in Fig. 5(b). The device was located at the outlet of a 10-cm co-annular tube through which metered air was introduced. A propane pilot flame was used to ignite the spray as discussed later. Voltage and flow rate conditions replicated cold flow experiments for which detailed characteristics had been obtained.

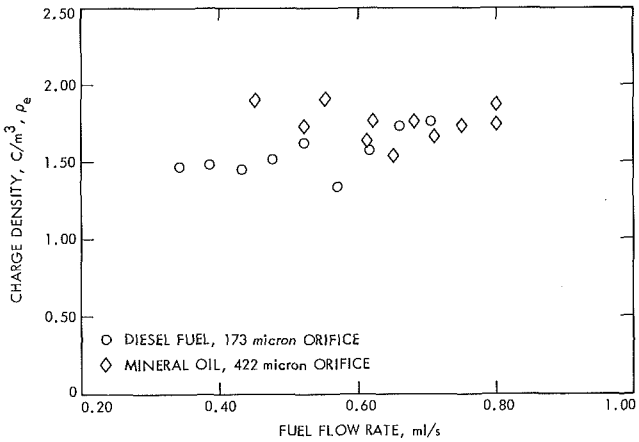


Fig. 9 Liquid flow rate versus charge density

Results

Figure 7 shows the spray breakup pattern for mineral oil at 0.33 cm^3/s and a charge density of 1.5 C/m^3. The outlet jet velocity is 2.4 m/s with the 422 micron orifice. The location of jet breakup can be adjusted to begin at any location relative to the orifice by adjusting the applied voltage and flow conditions. In Fig. 7 the voltage is -10 kV and the power required to charge and disperse the stream is 2.5 mW. For comparison, the chemical energy available from this spray, if ignited, would be 10-12 kW. The spray cone angle for these conditions is approximately 50 deg and can be increased to essentially 360 deg at higher charge densities or lower flow rates. Note that the jet is injected into a quiescent environment and no co- or counterflowing air jet is present. Also, no fluid breakup is observed at zero applied voltage (not shown), i.e., the narrow fuel jet observed at the orifice exit in Fig. 7 spans the entire field of view from top to bottom (at least 10 cm) if the voltage is set to zero.

In Fig. 8, a magnified view of an 0.8 cm^3/s mineral oil jet is characterized by the stretching and distortion of the fluid and a whipping motion leading to eventual breakup. The spray divergence angle under these conditions was 15-20 deg. Charge densities of up to 4 C/m^3 have been achieved with both mineral oil and No. 2 diesel fuel under transient conditions. For the spray device presently under study, stable/steady operation could be sustained at charge densities between 1.5

Downloaded 01 Jun 2010 to 171.66.16.87. Redistribution subject to ASME license or copyright; see http://www.asme.org/terms/Terms_Use.cfm

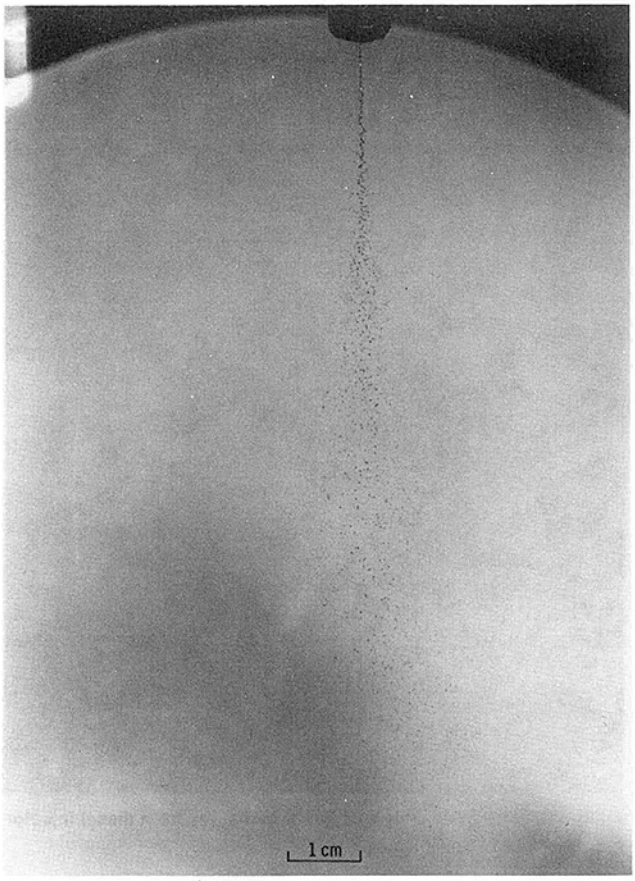


Fig. 10(*a*) Diesel fuel spray pattern from 173-μm orifice Spray Triode at 0.5 cm^3/s and 1.5 C/m^3



Fig. 10(*b*) Magnified region of electrostatically dispersed diesel fuel spray taken 4 cm downstream of orifice (Fig. 10a)

and 2.0 C/m^3. Typically for a given set of operating conditions, measured charge densities are relatively constant over a range of flow rates (Fig. 9). This is consistent with the previous results of Kelly (1982).

Drop sizes have been analyzed both by hand and by image processing techniques utilizing negatives of spray photos. Figure 10(*a*) shows a diesel spray generated at 0.5 cm^3/s and approximately 1.5 C/m^3 with the 173-μm orifice. Figure 10(*b*) is typical of magnified images used for drop sizing taken approximately 4 cm downstream of the orifice on the centerline. The results show arithmetic mean drop diameters (d_{10}) to be near 140-150 μm. Approximately 85 percent of the drops are below 200 μm in diameter and about 30 percent are less than 100 μm. No drops larger than 300 μm were observed. The volume-surface mean diameter was 180 μm. These data are shown in Fig. 4, where the total sample size was typically 150-200 drops. Similar measurements for mineral oil using the 422-μm orifice operating at 0.33 cm^3/s with a charge density of 1.5 C/m^3 resulted in mean drop diameters (d_{10}) near 200 μm. The numbers of drops in the samples for size calculations are too few to ensure statistical accuracy. However, these drop sizes do fairly represent our observations of approximately 50 spray photographs at several locations in the sprays under different spray conditions.

The size data are seen to fall below the Rayleigh limit and above the level predicted by Kelly (Fig. 4). These (173-μm orifice) data represent the most stable and steady operation of the Spray Triode for our test conditions. Deviation from the statistical equilibrium theory may be due to charge distribution effects in the fluid stream at the orifice injector. At Princeton, Kelly has calculated that a nonuniform charge distribution in the orifice exists, which will lead to deviations from a simple application of the equilibrium theory. A greater number of larger drops would be the result. Also larger orifice diameters lead to larger drops as indicated by the size data for the 422-μm orifice. In any case, the data confirm that charge densities of at least 2 C/m^3 are definitely achievable in practical situations and that higher charge densities may be possible with optimized designs. The highest charge density yet reported for early Spray Triode designs was 2.6 C/m^3 (Kelly, 1982).

For reference purposes, photographs of the spray from an actual diesel engine injector have been obtained by injecting into one atmosphere air. The injector is from a 50 hp Volkswagen diesel engine and the instantaneous injection rate is of the order of 10 cm^3/s. It operates by a spring-loaded pintle valve and has an orifice diameter of 1 mm. The valve opens when fuel line pressure reaches approximately 20 MPa. Upon opening, the orifice delivers an annular fuel jet at a velocity of approximately 20 m/s. Once the pressure drops the valve closes, having delivered the fuel pulse in less than 10 ms. In these experiments, fuel pressure was set at 20.7 MPa by a hand-operated, single-pulse-injection test pump; and fuel was released by solenoid valve to deliver a single 68-mg mass of fuel. Figure 11(*a*) shows the overall spray characteristics for the Bosch diesel injector. Note the extent of the dense central core of the jet, which extends for several centimeters beyond the injection orifice. A large number of small droplets is observed 6-7 cm downstream of the orifice and 1-2 mm off the jet centerline in the magnification of Fig. 11(*b*). These drops have a measured d_{32} of approximately 60 μm; however, this is not representative of the entire spray since many larger irregular droplets, which have characteristic sizes of 500 μm or greater, are observed to persist in the central core.

Downloaded 01 Jun 2010 to 171.66.16.87. Redistribution subject to ASME license or copyright; see http://www.asme.org/terms/Terms_Use.cfm

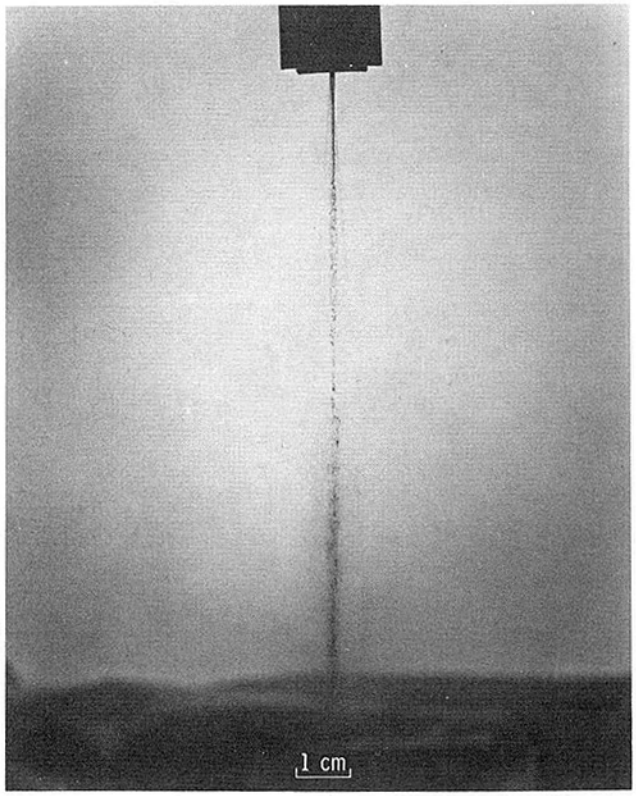


Fig. 11(*a*) Diesel fuel spray pattern from diesel engine injector



Fig. 11(*b*) Magnified view of diesel fuel spray from diesel injector

While instantaneous flow rates are greater for the diesel injector than for the Spray Triodes studied to date, and the flow is pulsed, the differences in breakup characteristics are considerable. In particular, the ability to disperse even the largest droplets from the central core is evident in the Spray Triode photographs. To date, our Spray Triode flow rates have been limited to just above 1 cm^3/s due to pressure limitations on the present devices. A new high-pressure, high-temperature design has recently been fabricated and follow-on studies of injection into high-pressure air are presently under way.

Also, since these comparisons are at ambient temperature and pressure, they are not a direct indication of how such jets will behave under high-pressure diesel conditions. For example, the experiments by Reitz and Bracco (1982) found a dependence of the conical spray divergence angle for injected water, glycerol, and water/glycerol mixtures on gas pressure up to 20 atm. While their experimental conditions were not generally the same as described herein, some overlap in the aerodynamic breakup parameter

$$T=\frac{\rho_f}{\rho_g}\left(\frac{\gamma}{\mu_f u}\right)^2 \tag{4}$$

does exist ($T \geq 0.1$). Their general conclusion was that the spray angle increased with increasing gas density, where no divergence angle greater than 21 deg was measured. In our Spray Triode experiments, spray divergence angles of 15-25 deg were measured at 0.8 cm^3/s, and greater divergence angles were possible under different flow conditions at one atmosphere gas pressure. Thus, electrostatic spray injection into one atmosphere results in a spray plume comparable to aerodynamic breakup at higher pressures, and it is plausible that dispersion will increase with gas density, based on the trends observed by Reitz and Bracco (1982). Preliminary results from our high-pressure studies confirm this.

Electrostatically dispersed diesel fuel jets have been ignited using a propane pilot flame placed in the spray 4-5 cm downstream of the point of jet breakup (Fig. 12*a*). Co-flowing air was supplied through the co-annular tube (Fig. 5*b*) at 60 cm/s. Fuel flow rate was varied from 0.5-0.7 cm^3/s and the Spray Triode was operated in the 1.5-2.0 C/m^3 range. Thus, mean drop diameters would be expected to be in the 150-μm range. Also, mean drop densities at the point of ignition were estimated to be 200-1000/cm^3. Using the 173-μm orifice, fuel jet outlet velocities were approximately 20 m/s.

A luminous flame region of 20-30 cm in length was sustained in the spray cone (Fig. 12*b*). The spray cone subtended a total angle of approximately 25 deg. Combustion appears to occur throughout the volume of the spray and the luminous region oscillated somewhat. This is evident in Fig. 12(*c*), where streaks of burning single droplets are observed as they emerge from a luminous region. All droplets were not combusted in this configuration as some were observed to penetrate the flame region and disperse in all directions for the flow conditions considered. This occurred despite the fact that overall fuel/air ratios were lean ($f/a=0.59$). Clearly, new flame-holding techniques will be required in order to optimize an electrostatically dispersed spray in a continuous burner. Attempts to ignite the fuel jet at zero applied voltage (no breakup) resulted in a very small (2-3 cm) flame along the part of the fuel jet that was directly in the pilot flame.

Summary

A new electrostatic technique has been investigated for injection, dispersion, and combustion of diesel fuel jets. The experimental results to date, in one atmosphere air at continuous flow rates, show that fuel sprays can be generated with charge densities at a level that may enhance fuel dispersion under diesel engine conditions. The spray characteristics are observed to differ considerably from an actual diesel fuel injector, where rapid breakup can be achieved without very large droplets remaining in the core of the jet. The electrostatically

Downloaded 01 Jun 2010 to 171.66.16.87. Redistribution subject to ASME license or copyright; see http://www.asme.org/terms/Terms_Use.cfm

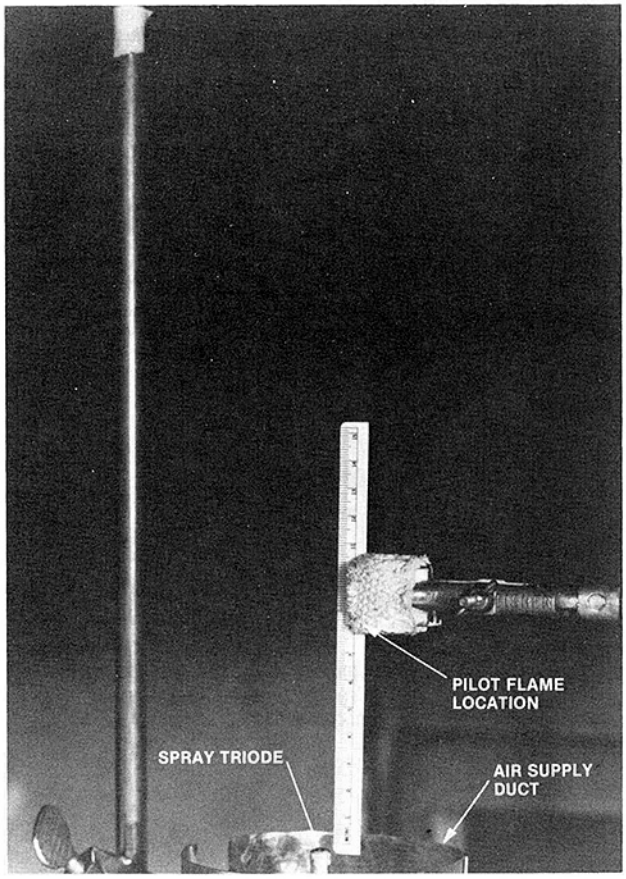


Fig. 12(a) Electrostatic spray combustion injection geometry

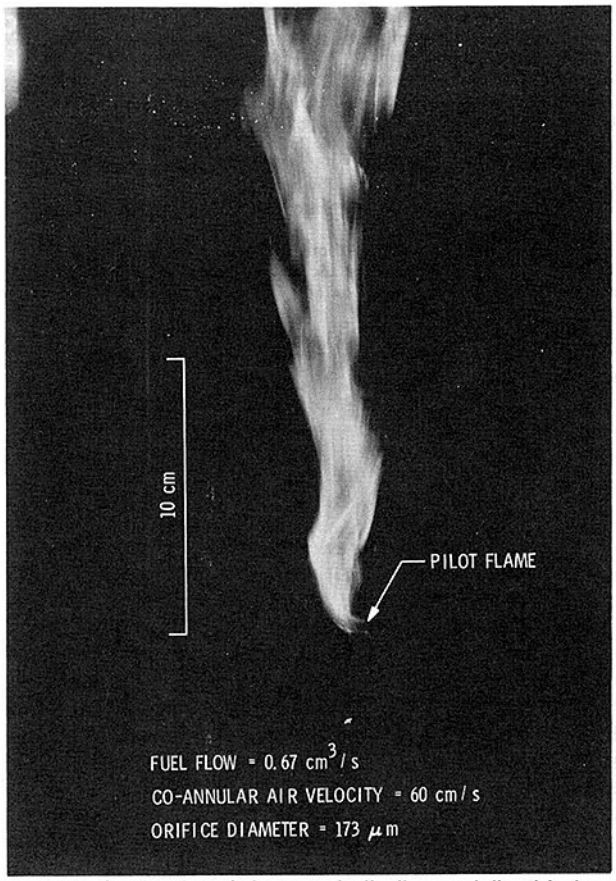


Fig. 12(b) Combustion of electrostatically dispersed diesel fuel spray

generated sprays have been successfully ignited and combustion sustained.

For engine injection, these sprays have the potential for rapid dispersion at lower pressure differences than presently used in conventional injectors. Also, rapid droplet evaporation in flames may lead to further disruptive breakup of individual drops if the Rayleigh limit is reached (Roth and Kelly, 1980). Demonstration of this technique under realistic engine conditions is now in order, and injection of electrostatically dispersed sprays under high-pressure conditions will be investigated in a subsequent phase of this study.

Acknowledgments

This paper describes the results of research carried out by the Jet Propulsion Laboratory, California Institute of Technology and was supported by the US Army Research Office through an agreement with the National Aeronautics and Space Administration. The authors also thank Messrs. D. C. Schneider and J. J. Godley for their contributions in fabrication and assembly of the test setup, and in the conduct of the experiments. The Spray Triode is used by permission of Mr. Harold Simmons of the Parker Hannifin Corporation.

References

Ahmad, T., Speck, C. E., and Sing, D. C., 1980, "Effect of Electric Fields Applied within the Prechamber on Particulate Emissions From a Diesel Engine," presented at the Fall Technical Meeting, Western States Section, Combustion Institute, General Motors Research Report No. GMR-3326.

Bellan, J., 1983, "A New Approach to Soot Control in Diesel Engines by Fuel Drop Charging," *Combustion and Flame*, Vol. 1, pp. 117–119.

Chapman, A. T., Gerdes, R. J., Wilson, J. C., and Clark, G. W., 1972, "Unidirectional Solidification Behavior in Refractory Oxide–Metal Systems," *Journal of Crystal Growth*, Vol. 13/14, pp. 765–771.

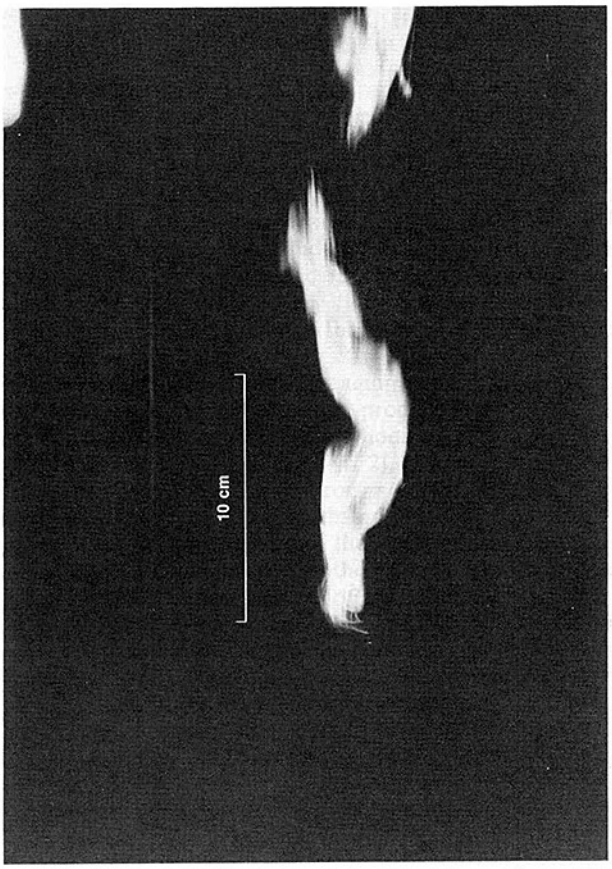


Fig. 12(c) Electrostatically dispersed diesel fuel flame showing intermittent behavior

Downloaded 01 Jun 2010 to 171.66.16.87. Redistribution subject to ASME license or copyright; see http://www.asme.org/terms/Terms_Use.cfm

Fleeter, R., Toaz, R., and Sarohia, V., 1982, "Application of Digital Analysis Techniques to Antimisting Fuel Spray Characterization," presented at the ASME Winter Annual Meeting, Paper No. 82-WA/HT-23.

Gaffney, J., Sapieza, R., Butcher, T., Krishna, C., Marlow, W., and O'Hare, T., 1980, "Soot Reduction in Diesel Engines: a Chemical Approach," *Combustion Science and Technology*, Vol. 24, pp. 89–92.

Heinein, N. A., 1976, "Analysis of Pollutant Formation and Control and Fuel Economy in Diesel Engines," *Prog. Energy Combust. Sci.*, Vol. 1, pp. 165–207.

Kelly, A. J., 1978, "Electrostatic Spray Theory," *J. Applied Physics*, Vol. 49, pp. 2621–2628.

Kelly, A. J., 1981, Electrostatic Atomizing Device, US Patent No. 4,255,777.

Kelly, A. J., 1982, "The Electrostatic Atomization of Hydrocarbons," *Proceedings of the Second Int. Conf. on Liquid Atomization and Spray Systems*, June 1982.

Khan, I. M., Wang, C. H. T., and Langridge, B. E., 1972, "Effect of Air Swirl on Smoke and Gaseous Emissions From Direct-Injection Diesel Engines," SAE Paper No. 720102.

Luther, F. E., 1962, "Electrostatic Atomization of No. 2 Heating Oil," *Proc. Second API Research Conference on Distillate Fuel Combustion*, API Publication No. 1701.

Miller, J. A., Biblarz, O., Zajdman, A., Manning, W. W., II, and Mavroudis, J. A., 1987, "Electrostatic Spray Modification in Gas Turbulent Combustion," *J. Propulsion and Power*, Vol. 3, No. 2, pp. 187–192.

Newgard, P. M., and Noon, A. W., 1964, "Electrostatic Atomizer and Burner Research," Distillate Fuel Combustion Conference, API Publication No. 1725.

Pischinger, R., and Cartellieri, W., 1972, "Combustion System Parameters and Their Effect Upon Engine Exhaust Emissions," SAE Paper No. 720756.

Reitz, R. D., and Bracco, F. V., 1982, "Mechanism of Atomization of a Liquid Jet," *Physics of Fluids*, Vol. 25, No. 10, pp. 1730–1742.

Roth, D. G., and Kelly, A. J., 1980, "Analysis of the Disruption of Evaporating Charged Droplets," IEEE No. CH1575-0/80/0000, pp. 998–1004.

Wang, C. H., and Law, C. K., 1985, "Microexplosion of Fuel Droplets Under High Pressure," *Combustion and Flame*, Vol. 59, pp. 53–62.

Downloaded 01 Jun 2010 to 171.66.16.87. Redistribution subject to ASME license or copyright; see http://www.asme.org/terms/Terms_Use.cfm

Simulation of the Gas Exchange Process of a Two-Stroke Cycle Gasoline Engine

K. Sato
Professor.

M. Nakano
Lecturer.

Department of Mechanical Engineering,
Shibaura Institute of Technology,
Omiyashi, Saitama, Japan

This report deals with a study concerning the scavenging performance of a two-stroke cycle gasoline engine under the following conditions: the throttle of the carburetor is set at variable levels, the delivery ratio is set at a predetermined level, the engine speed is varied, and the scavenging and exhaust ports are set at different heights. If the properly selected factors stipulated for a scavenging model are used, the calculated results can be made as consistent as the measured results of the carburetor set at full throttle, as discussed in the previous reports [1, 2]. The mass diffusion, mixing, and short-circuit factors make up the essential coefficients. The factors represent major characteristics: blow-back, return-blow, and the loss of fresh gases. These phenomena are more clearly illustrated by three-dimensional representations of the gas components in the scavenging passage and exhaust pipe. The analyses of these functions may provide an effective means of improving the scavenging performance, i.e., the delivery ratio, trapping efficiency, and charging efficiency.

Introduction

Most of the studies [3–5] concerned with simulating the gas exchange process of a two-stroke cycle gasoline engine that have been conducted so far have assumed that, regardless of whether the scavenging passage is considered a part of the crankcase, gases in the scavenging passage have the same composition as those in the crankcase. This is the case even when the scavenging passage is considered a separate pipe. In these studies, it is generally assumed that residual and fresh gases are perfectly mixed in the cylinders when scavenging passages and exhaust pipes are attached to them. However, an examination of real engines reveals that their scavenging performance is seldom identical with perfectly mixed scavenging when the cylinder type or engine speed changes. In the case of a real engine, it is further to be noted that due to blow-back and return-blow from the cylinder to the scavenging side, a substantial amount of burned gases remains in the scavenging passage and crankcase.

In our previous reports [1, 2], an attempt was made to work out a simulation that could identify a variety of scavenging performances other than perfectly mixed scavenging while giving careful consideration to gas flows and burned gases remaining in the scavenging passage.

A set of treatments could be utilized to achieve this goal. It required the preparation of a scavenging model, the stipulation of a mass diffusion factor, a mixing factor, and a short-circuit factor for such models, the use of the Fluid in Cell Method (FLIC Method) [6], and the Step Method [7].

Since the previous report put particular emphasis on the development of a simulation, the carburetor was set at full throttle and the major elements of efficiency for determining the scavenging performance – the delivery ratio and the trapping efficiency – changed simultaneously depending on the cylinder types and the engine speeds. This prevented us from identifying the relationship between these two elements of efficiency, the changes in the cylinder type, and the engine speed.

In this report, however, the carburetor was throttled to different levels, while the delivery ratio was set at a predetermined level. The scavenging performance was then examined exhaustively according to the variations of engine speed and at the different heights of the scavenging and exhaust ports. A study was also conducted on how to produce better engine performance. This study used two methods:

1 As in the previous reports [1, 2], the pressure and efficiency during the gas exchange process were determined by using the above factors which are based on such characteristics as blow-back, return-blow, and the loss of fresh gases. The results of these calculations were then compared with the data obtained from the measurement of real engines.

2 The characteristics thus ascertained were presented more clearly by a three-dimensional representation of the gas components in the scavenging passage and exhaust pipe. The method of simulation is given in the Appendix.

Experimental Equipment and Procedure

The test engine is a general-purpose air-cooled 160 cm^3 two-stroke cycle schnürle type gasoline engine. The heights of its scavenging and exhaust ports vary over seven degrees, i.e., Types A, F, G, H, I, J, K. Specifications for this engine are given in Table 1.

Contributed by the Internal Combustion Engine Division for publication in the JOURNAL OF ENGINEERING FOR GAS TURBINES AND POWER. Manuscript received by the Internal Combustion Engine Division November 20, 1985.

Copyright © 1988 by ASME
Downloaded 01 Jun 2010 to 171.66.16.87. Redistribution subject to ASME license or copyright; see http://www.asme.org/terms/Terms_Use.cfm

Table 1 Appropriative dimensions of engine

Cylinder type		A	F	G	H	I	J	K
Open and shut angle of port	α_a (±BDC)	61	70	76	82	70	70	70
	α_e (±BDC)	56	56	56	56	66	49	37
	α_I (±TDC)	61	61	61	61	61	61	61
Height of port	σ_a	.211	.272	.325	.360	.272	.272	.272
	σ_e	.176	.176	.176	.176	.246	.140	.088
	σ_I	.316	.316	.316	.316	.316	.316	.316

Diameter×Stroke D×S = 60×57
Appearant comp.ratio $\varepsilon' = 6.96$
Crankcase volume ratio $\varepsilon_k = V_k / V_h = 2.63$
Height of port $\sigma = h/S$(h:Height)
Width of port $\beta = b/\pi D$
$\beta_a = 0.159$ $\beta_e = 0.271$ $\beta_I = 0.239$
Subscript a = Exhaust, e = Scavenging, I = Inlet

Experimental methods are as follows: The quantity of air supplied is measured by a laminar flow meter. Fuel consumption is determined by means of a volumetric meter. Direct-reading gas analyzers are used to measure the CO_2, CO, and O_2 components of the exhaust gas. A strain pressure indicator is provided to measure the pressure, including the mean effective pressure through an engine analyzer. On the other hand, a semiconductor pressure indicator is provided to measure the pressure in the exhaust pipe, the inlet pipe, the scavenging passage, and the crankcase. An alternating current dynamometer is provided to absorb the load on the engine, and both the excess air ratio and the delivery ratio are adjusted by means of the carburetor's throttle and needle valve to stay at a desired level. The inlet and exhaust pipes are 211 and 131 mm in length, respectively. The scavenging passage is 70 mm in length.

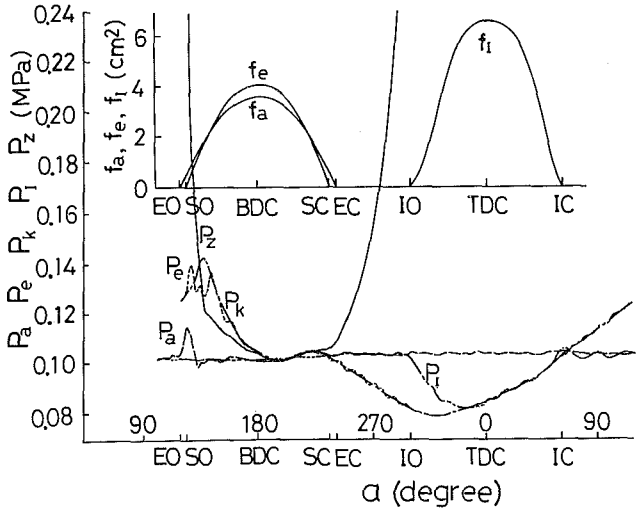


Fig. 1 Pressure diagrams by experimental investigation (Type A, 2000 rpm)

Results of the Experiment

Pressure. Figure 1 shows the measured results of pressures P_z, P_k, P_a, P_e, and P_I in the cylinder, crankcase, exhaust pipe, scavenging passage, and inlet pipe. The pressures P_z, P_k, P_a, P_e, and P_I are measured at the cylinder head, at the center position of the crankcase, and at the distances of 54 mm, 32 mm, and 32 mm from the cylinder wall, respectively. The Type-A cylinder is used in the diagram. The engine speed n and excess air ratio λ are 2000 rpm and 0.86. The values of the

Nomenclature

C_{pi} = specific heat of component i at constant pressure, J/(kg•K)
e = internal energy, J/kg
EC = crank angle at close of exhaust port, deg
EO = crank angle at opening of exhaust port, deg
G_a = mass of gases discharged from cylinder, kg
G_e = mass of fresh gas supplied in cylinder, kg
G_h = mass of fresh gas occupying stroke volume under atmospheric conditions (P_0, T_0), kg
G_I = mass of fresh gas supplied in crankcase, kg
G_n = mass of fresh gas retained in the cylinder, kg
H = enthalpy, J
$(\Delta H_{f298})_i$ = chemical enthalpy of component i, J
I_i = mass flux of component i, kg/(s•m²)
IC = crank angle at close of inlet port, deg
IO = crank angle at opening of inlet port, deg
K = total enthalpy, J/kg
M_i = molecular weight of component i, kg/mol
n = engine speed, rpm
n_i = number of moles of component i, mol
P = pressure, Pa
P_{mi} = indicated mean effective pressure, Pa
Q = amount of heat transferred, J
q_x = heat flux, J/(s•m²)
r = mixing factor in pipe and volume parts
SC = crank angle at close of scavenging port, deg
SO = crank angle at opening of scavenging port, deg
T = temperature, K
t = time, s
u = velocity of flow, m/s
V = volume, m³
α = crank angle, deg
ϵ_m = mass diffusion factor, m²/s
ϵ_q = thermal diffusion factor, m²/s
$\epsilon\tau$ = momentum diffusion factor, m²/s
ρ = density, kg/m³
τ_{xx} = momentum flux, Pa
ϕ_d = short-circuit factor
ϕ_m = cylinder mixing factor

Definitions

blow-back = the phenomenon in which combustion gas is blown into scavenging passage from the cylinder after the opening of the scavenging port
loss of fresh gas = the phenomenon in which fresh gas is discharged into the exhaust pipe from the cylinder during the gas exchange process
return-blow = the phenomenon in which mixed gas or fresh gas is returned into the scavenging passage from the cylinder before the closure of the scavenging port

charging efficiency, $\eta_c = G_n/G_h$
delivery ratio, $L = G_e/G_h$ $(L_k = G_I/G_h)$
relative charge, $C_{rel} = G_z/G_h$
scavenging efficiency, $\eta_s = G_n/G_z$
trapping efficiency, $\eta_{tr} = G_n/G_e$ (where $\eta_c = L \cdot \eta_{tr} = C_{rel} \cdot \eta_s$)

Downloaded 01 Jun 2010 to 171.66.16.87. Redistribution subject to ASME license or copyright; see http://www.asme.org/terms/Terms_Use.cfm

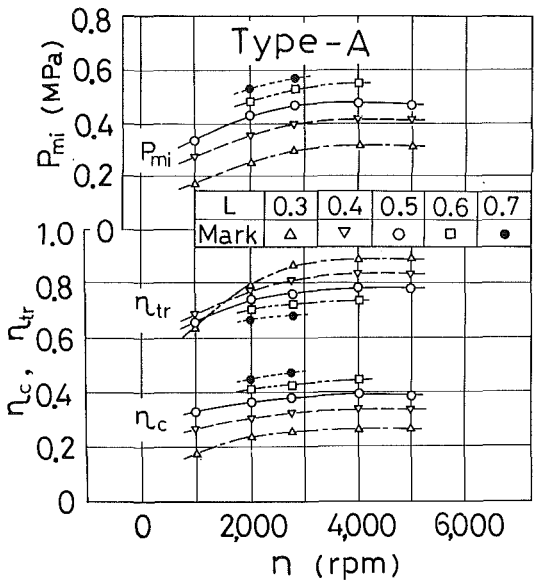


Fig. 2 η_{tr}, η_c, and P_{mi} for constant L and n

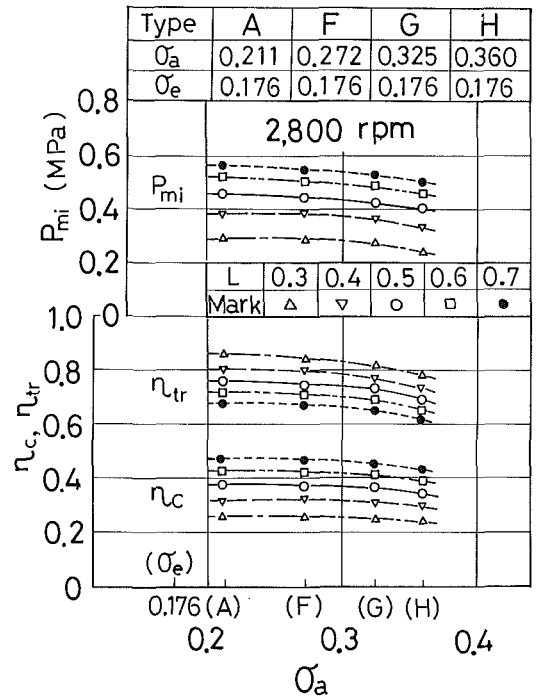


Fig. 3 η_{tr}, η_c, and P_{mi} for constant L, unchanging height σ_e of scavenging port, and changing height σ_a of exhaust port divided by stroke

delivery ratio L, the trapping efficiency η_{tr}, and the charging efficiency η_c are 0.5, 0.74, and 0.37, respectively. The pressure of each is shown at the average level of 100 cycles.

The major characteristics of this type are depicted in Fig. 1. A rapid increase in pressures P_k and P_e on the scavenging side immediately ensues upon the opening of the scavenging port. The pressures P_z and P_e in the cylinder then balance out; this phenomenon is due to the blow-back of burned gases. Soon after the piston passes the bottom dead center, P_e falls below P_z, due to the return-blow of fresh gases to the scavenging side after once flowing into the cylinder. After the pressures P_k and P_e on the scavenging side balanced out with the cylinder pressure P_z, P_z remains higher than P_a until P_z balances out with P_a past the bottom dead center. This means that there is a loss of fresh gases, which flow to the exhaust side. In regard to other characteristics, P_e vibrates at two to three cycles after the opening time (SO) of the scavenging port. Pressures P_z, P_k, P_a, and P_e keep vibrating at approximately the same cycle soon after the piston passes the bottom dead center. The diagram also shows the area of the scavenging port f_e, that of the exhaust port f_a, and that of the inlet port f_I.

Efficiency and Performance

Engine Speed Variation. Figure 2 gives the trapping efficiency η_{tr}, the charging efficiency η_c, and the indicated mean effective pressure P_{mi} of a Type-A cylinder when the engine speed n is increased from 1000 rpm to 5000 rpm within a parameter of ratio L. In this diagram, the delivery ratio L was determined by measuring the fresh gas quantity, while trapping efficiency was obtained by Tomizuka's equation [8] $\eta_{tr} = 1 - O_2/22$ based on an oxygen concentration of O_2 percent as determined by an exhaust gas analysis. η_c is represented as the product of L and η_{tr}; it is found that this value is virtually proportional to P_{mi}. As is apparent from this diagram, the trapping and charging efficiencies tend to increase as the engine runs faster if the delivery ratio is kept constant. In other words, if fresh gases flow in at a constant rate, the loss of fresh gases decreases while the amount of charged fresh gases increases as the engine runs faster. This means higher engine performance, and it is also found in different types of cylinders. It should be noted here that η_{tr} decreases sharply at a low speed and low delivery ratio, for instance, at 1000 rpm and at $L = 0.3$. The decrement of η_{tr} arises from the fact that unburned gas is discharged into the exhaust gas by incomplete combustion or miss fire [9]; therefore, η_c and P_{mi} will also probably decrease appreciably.

Variation of Variant Delivery Ratios. As shown in Fig. 2, if the delivery ratio L becomes higher when the engine speed is kept constant and no incomplete combustion occurs, then the trapping efficiency η_{tr} decreases whereas the charging efficiency η_c and the indicated mean effective pressure P_{mi} increase. In other words, fresh gases flow in at a higher rate, and at the same time, the loss of fresh gases increases if the carburetor throttle is opened wider at a constant engine speed. Since the amount of charged fresh gases increases, however, higher engine performance can be achieved.

Constant Height of the Scavenging Port and Variation of the Height of the Exhaust Port. Figure 3 shows η_{tr}, η_c, and P_{mi} of cylinder Types A, F, G, and H, in that order, when the exhaust port is set at different heights and the scavenging port is installed at a fixed level. The test was conducted at an engine speed of 2800 rpm within the parameter of the delivery ratio. As is apparent from the diagram, η_{tr}, η_c, and P_{mi} decrease as the position of the exhaust port becomes higher. In other words, the installation of the exhaust port at a higher position brings about a greater loss of fresh gases and a smaller amount of charged fresh gases, resulting in reduced engine performance. Cylinder Type H is a typical example of this phenomenon.

Constant Height of Exhaust Port and Variation of the Height of the Scavenging Port. Figure 4 presents η_{tr}, η_c, and P_{mi} of cylinder Types K, J, F, and I, in that order, when the scavenging port is set at different levels and the exhaust port is installed at a fixed height. These efficiency and pressure levels were recorded at an engine speed of 2800 rpm within the parameter of the delivery ratio. The diagram indicates that η_{tr}, η_c, and P_{mi} worsen if the scavenging port is installed too high or too low; all of them reach this optimum when the opening is set midway between these positions. Among the cylinder types examined, the Type-F cylinder version has scavenging ports installed at such optimum positions. This cylinder can achieve high performance, yielding a smaller loss of fresh gases and a larger amount of charged fresh gases.

Downloaded 01 Jun 2010 to 171.66.16.87. Redistribution subject to ASME license or copyright; see http://www.asme.org/terms/Terms_Use.cfm

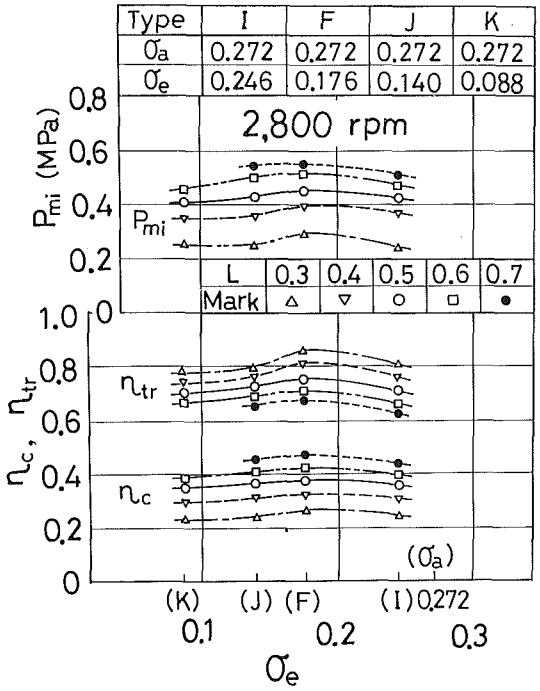


Fig. 4 η_{tr}, η_c, and P_{mi} for constant L, unchanging height σ_a of exhaust port, and changing height σ_e of scavenging port divided by stroke

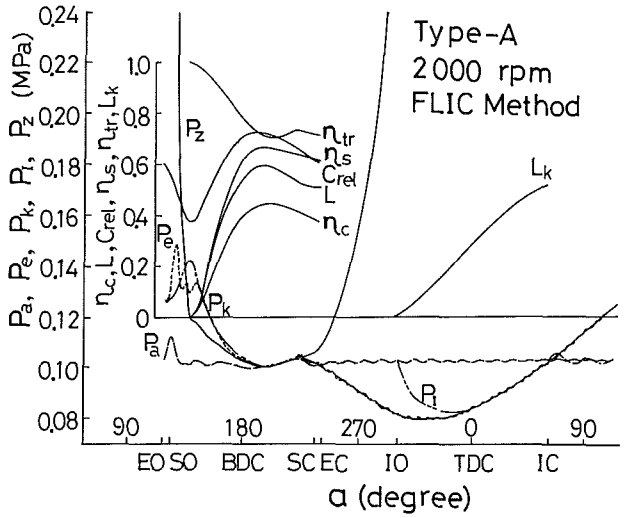


Fig. 5 Pressure diagrams and efficiencies by theoretical investigation

Results of Calculation

Figure 5 gives the results of the simulation of cylinder of Type A at an engine speed of 2000 rpm, a delivery ratio of $L = 0.5$, and an excess air ratio of $\lambda = 0.86$ (an air–fuel ratio of 13). The diagram shows a number of pressure and efficiency curves relative to crank angle α during the gas exchange process. Table 2 shows such initial values as the pressure P_{za}, the temperature T_{za}, and the crankcase pressure P_{ka} (this is equal to the initial value of the scavenging port) at the opening time (*EO*) of the exhaust port. The table also breaks down the different elements of efficiency at the end of the gas exchange process, i.e., the closing time (*EC*) of the exhaust port and the closing time (*IC*) of the inlet port.

This study took into account a number of factors based on the previous reports [1, 2]. The table gives the cylinder wall

Table 2 Data for simulation of Fig. 5

Specifications for calculation	Efficiencies of calculated result
Cylinder = Type-A	C_{rel} = 0.613 (at 119 degree)
n = 2000 rpm	= 0.602 (at 241 degree)
λ = 0.86	η_s = 0.606 (at 241 degree)
P_{za} = 0.275 MPa	η_{tr} = 0.724 (at 241 degree)
T_{za} = 1080 K	η_c = 0.365 (at 241 degree)
P_{ka} = 0.123 MPa	L = 0.505 (at 236 degree)
ϵ_m = 0.02 m²/s	L_k = 0.515 (at 61 degree)
ϵ_d = 0	
ϵ_τ = 0	
r = 0.12(for blow-back)	
r = 0.001(for return-blow)	
ϕ_m = 0.82	
ϕ_d = 0	
T_w = 373 K	
A/A_{max} = 0.18	

temperature T_w and the values of factors ϵ_m, ϵ_q, ϵ_τ, r, ϕ_m, and ϕ_d, respectively. Of these the following factors are particularly important for this report: the mixing factor r for the scavenging passage and the crankcase due to blow-back and return-blow, the cylinder mixing factor ϕ_m and the short-circuit factor ϕ_d, which are closely related to the loss of fresh gases from the exhaust, and the mass diffusion factor ϵ_m for the transfer of the gas component in the scavenging passage and exhaust pipe.

To set the delivery ratio at a specified level, the throttle on the inlet side was adjusted to the properly selected throttle area of the carburetor. The throttle ratio is given as the ratio of A to A_{max}; the denominator represents the inlet pipe's cross-sectional area A_{max} and the numerator represents the throttle area A. This is also part of the data on the table.

Just as in the previous simulation of the carburetor set at full throttle, this diagram and table show that even if the carburetor throttle is varied, the use of properly selected ϕ_m, ϕ_d, r, and other factors can achieve pressure diagrams and efficiencies during the gas exchange process that are very consistent with the measured results (Fig. 1).

Discussion

Variation of Engine Speed. Figure 6 shows the relationship between efficiencies η_{tr} and η_c and factors ϕ_m, ϕ_d, and r at varying engine speeds ranging from 1000 to 5000 rpm. These data include trapping efficiency η_{tr}, charging efficiency η_c, mixing factors ϕ_m and r, and short-circuit factor ϕ_d, which have been derived from a study based on the constant delivery ratio ($L = 0.5$) in Fig. 2 as well as on the development of pressure diagrams in Fig. 5. As indicated in Fig. 6, the trapping and charging efficiencies improve as the engine speed increases while the delivery ratio is kept constant. Use of properly selected factors makes the results of such calculation very consistent with the findings of experiments on a real engine. To keep the delivery ratio constant, the diagram suggests, r must be set at a markedly high level, both in high and low-speed ranges, because substantial return-blow occurs in a low-speed range as shown by the second curve from the bottom of the diagram, while much blow-back appears in a high-speed range as indicated by the bottom curve. Large ϕ_m and ϕ_d have to be chosen for a low-speed range where a substantial loss of fresh gases occurs toward the exhaust side. For a high-speed range, on the other hand, these factors should be set at a low level because the loss of fresh gases becomes insignificant in this speed range.

The phenomena, including blow-back, return-blow, and fresh gas loss, are also observable from the similar pressure diagrams in Figs. 1 and 5. The initial values and factors for the

Downloaded 01 Jun 2010 to 171.66.16.87. Redistribution subject to ASME license or copyright; see http://www.asme.org/terms/Terms_Use.cfm

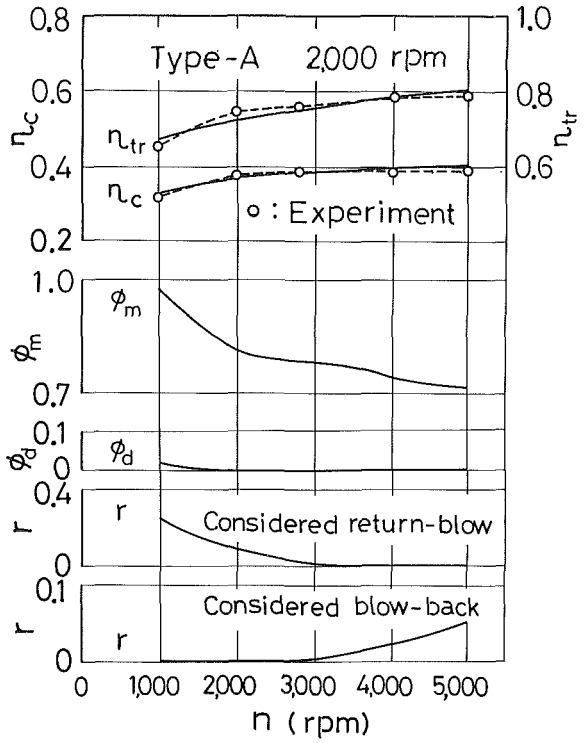


Fig. 6 η_{tr}, η_c, ϕ_m, r, and ϕ_d for constant L and n

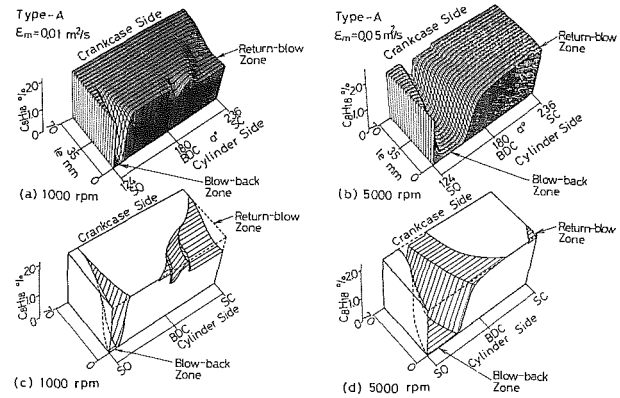


Fig. 7 Three-dimensional indication of gas component (C_8H_{18}) at scavenging passage for changing engine speeds

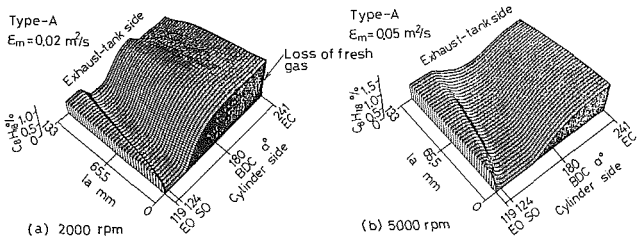


Fig. 8 Three-dimensional indication of gas component (C_8H_{18}) at exhaust pipe for changing engine speeds

development of pressure diagrams and calculation of efficiency in the speed range of 1000 rpm to 5000 rpm noted above are given on Table 3.

Such phenomenon as blow-back, return-blow, and fresh gas loss can be shown more clearly by three-dimensional representation, a few instances of which are given in Figs. 7 and 8.

Figure 7 concerns the gas component C_8H_{18} in the scavenging passage. It was found that a marked large return-blow zone appears in a low-speed range (1000 rpm as in diagrams (*a*) and (*c*)), while in a high-speed range (5000 rpm as in (*b*) and (*d*)), a marked large blow-back zone is seen.

Table 3 Data for simulation of Fig. 6

P_{za} =	0.224~0.314 MPa (not in any special order)
T_{za} =	945~1200 K (not in any special order)
P_{ka} =	0.120~0.123 MPa (not in any special order)
ε_m =	0.01 ~0.05 m²/s
T_w =	373 K (constant)
r =	0~0.055 (for blow-back)
r =	0.255~0.002 (for return-blow)
ϕ_m =	0.98 ~0.72
ϕ_d =	0.02 ~0

Figure 8 gives three-dimensional representations of the gas component C_8H_{18} in the exhaust pipe. As shown in the two diagrams, a substantial amount of fresh gases is lost in the low-speed range (2000 rpm as in (*a*)) where little blow-back takes place, resulting in a smaller starting angle of fresh gas inflow and a longer period of fresh gas loss. Some back flow appears in the latter half of the scavenging stroke, but it is negligible. In the high-speed range (5000 rpm in (*b*)), on the contrary, little loss of fresh gases occurs because of a wider starting angle of fresh gas inflow and a shorter period of fresh gas loss due to increased blow-back.

Constant Height of the Scavenging Port and Variation of the Height of the Exhaust Port. Figure 9 shows the relationship between the efficiencies η_{tr} and η_c and the factors ϕ_m, ϕ_d, and r in the same manner as discussed in the above section when the exhaust port is set at four different heights in cylinder Types A, F, G, and H. This study is based on the appropriate data obtained from Fig. 3, given a constant delivery ratio of $L = 0.5$. When the delivery ratio is kept constant and the exhaust port is set at a higher position, according to Fig. 9, efficiency – specifically the trapping and charging efficiencies – is unfavorably affected. As noted above, use of properly selected factors provides calculations that are very consistent with the measured results. For instance, as Fig. 9 suggests, care should be taken to use greater ϕ_m and ϕ_d if the exhaust port is installed at a higher position, since the loss of fresh gases increases on the exhaust side. When the exhaust port is lowered, on the other hand, the loss of fresh gases decreases appreciably, and therefore, smaller ϕ_m and ϕ_d are preferable.

A phenomenon such as fresh gas loss is more clearly illustrated by the three-dimensional representation.

Figure 10 gives three-dimensional representations of the gas component C_8H_{18} in the exhaust pipe. In these diagrams, the loss of fresh gases decreases appreciably when the exhaust port is set at a lower position (as Type A in (*a*)) because blow-back increases, resulting in delayed inflow of fresh gases and a shorter period of fresh gas loss. When the exhaust port is raised (as Type H in (*b*)), on the other hand, no blow-back appears any longer, resulting in an earlier inflow of fresh gases and a longer period of fresh gas loss. In other words, installation of the exhaust port at a higher position increases the loss of fresh gases.

Constant Height of the Exhaust Port and Variation of the Height of the Scavenging Port. Figure 11 presents the relationship between the efficiencies η_{tr} and η_c and the factors ϕ_m, ϕ_d, and r in the same way as noted above when the scavenging

Downloaded 01 Jun 2010 to 171.66.16.87. Redistribution subject to ASME license or copyright; see http://www.asme.org/terms/Terms_Use.cfm

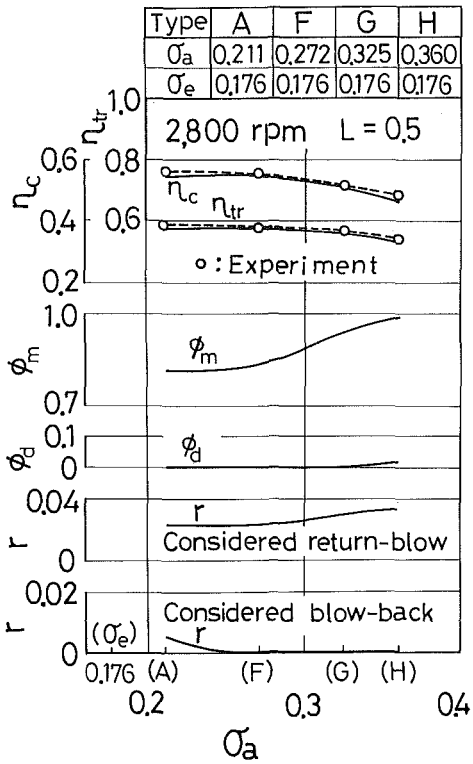


Fig. 9 η_{tr}, η_c, ϕ_m, r, and ϕ_d for constant L, unchanging height σ_e of scavenging port, and changing height σ_a of exhaust port divided by stroke

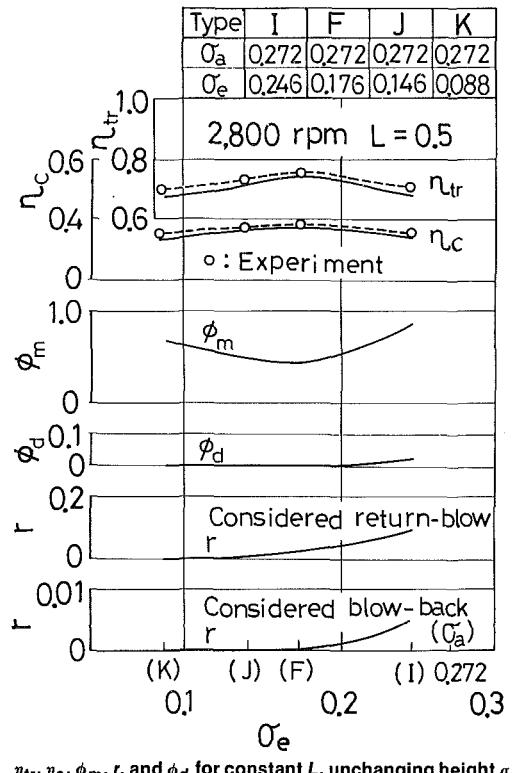


Fig. 11 η_{tr}, η_c, ϕ_m, r, and ϕ_d for constant L, unchanging height σ_a of exhaust port, and changing height σ_e of scavenging port divided by stroke

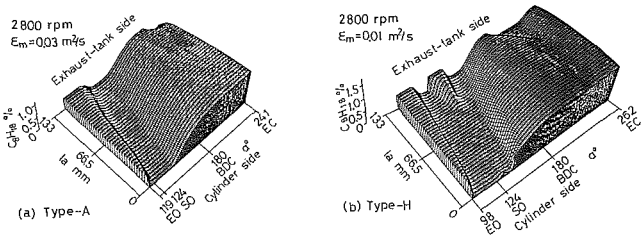


Fig. 10 Three-dimensional indication of gas component (C_8H_{18}) at exhaust pipe for changing height of exhaust port

port is installed at four different heights as in cylinder Types K, J, F, and I, respectively. This work is based on the appropriate data from Fig. 4, given a constant delivery ratio of $L = 0.5$. The curves in Fig. 11 indicate that when the delivery ratio is kept constant and the position of the scavenging port is varied, the trapping and charging efficiencies worsen appreciably regardless of whether this opening is set at a higher or lower position. These efficiencies reach their maximum when the scavenging port is set at a medium height. The use of properly chosen factors yields calculations that are very consistent with the measured results. The relationship between the efficiencies η_{tr} and η_c and the factors ϕ_m, ϕ_d, and r as in the preceding sections is not discussed here.

Constant Engine Speed and Variation of Delivery Ratios. An example of calculated efficiencies at 2000 rpm is given below:

$L = 0.505,\ 0.707\ (L_k = 0.515,\ 0.715)$
$\eta_{tr} = 0.724,\ 0.669$
$\eta_c = 0.365,\ 0.473$

The variations in η_c, η_{tr}, and L as given in Fig. 2 suggest that improvement of efficiency can be achieved better by increasing the quantity of delivery rather than by reducing the discharged fresh gases, because increased delivery increases the amount of charged fresh gases at a higher rate.

Conclusions

This study may be summarized as follows:

1 If properly selected factors are used, calculated results in an experiment with varying levels of carburetor throttle can be made to be consistent wtih those made from the measured results of a test with the carburetor set at full throttle as discussed in the previous reports [1, 2]. Among these essential coefficients are the mixing and short-circuit factors, which represent major characteristics, including blow-back and return-blow toward the scavenging side and the loss of fresh gases on the exhaust side. The values of the selected factors ϕ_m, ϕ_d, r, and ϵ_m for each cylinder type and engine speed are brought within the range of: $0.72 \le \phi_m \le 0.99$; $0 \le \phi_d \le 0.04$; $0 \le r \le 0.255$ (for return-blow) or $0 \le r \le 0.055$ (for blow-back); and $0 \le \epsilon_m \le 0.06$.

2 Such phenomena as blow-back, return-blow, and fresh gas loss can be shown more clearly by the three-dimensional representations of the gas components in the scavenging passages and the exhaust pipe.

3 The following suggestions may provide an effective means of improving the engine performance, i.e., the charging efficiency:

(*a*) Better results may be achieved at a high speed in a test by varying the engine speed and keeping the delivery ratio constant.

(*b*) When improvement efforts are made without changing the exhaust lead (difference between the vertical positions of the exhaust and scavenging ports), more favorable results may be obtained by installing the scavenging port at a proper height for extending the effective stroke than by setting this opening too high and making the effective stroke shorter.

(*c*) If the carburetor throttle is made larger without changing the cylinder type and the engine speed, better results can probably be obtained by using a higher delivery ratio than by improving the trapping efficiency.

Downloaded 01 Jun 2010 to 171.66.16.87. Redistribution subject to ASME license or copyright; see http://www.asme.org/terms/Terms_Use.cfm

Acknowledgments

In carrying out this study, a number of experts offered the writers valuable information and assistance. We wish to thank: Dr. Hideo Fujita, an engineering advisor for Mistubishi Heavy Industries; Mr. Kazuo Kido, an engineering advisor at Mitsubishi Motors; staff members of Sasamura Foundation, Inc.; and a group of postgraduate and undergraduate students. Most of the calculations in this study were performed by a computer at Tokyo University.

References

1 Sato, K., and Kido, K., "Simulation of the Gas Exchange Process in a Small Two-Stroke Cycle Engine (1)," *Bulletin of JSME*, Vol. 26, No. 217, 1983, pp. 1178–1187.

2 Sato, K., and Nakano, M., "Simulation of the Gas Exchange Process in a Small Two-Stroke Cycle Engine (2)," *Bulletin of JSME*, Vol. 26, No. 217, 1983, pp. 1188–1197.

3 List, H., and Rely, G., "Die Einschaltung von Behältern in des Einström- und Ausströmsystem," *Der Ladungswechsel der Verbrennungskraftmaschine*, Vol. 4, No. 1, Springer-Verlag, Vienna, 1949, pp. 65–74: List, H., "Spül- und Auspuffsystem mit Kleinen Behältern," *Der Ladungswechsel der Verbrennungskraftmaschine*, Vol. 4, No. 2, Springer-Verlag, Vienna, 1950, pp. 196–228.

4 Kaji, A., and Hatsuta, K., "A Cycle Simulation of Two-Stroke Cycle Gasoline Engine," preprint of Japan Society of Mechanical Engineers, No. 720, Apr. 1972, pp. 153–156.

5 Blair, G. P., and Caboon, W. L., "A More Complete Analysis of Unsteady Gas Flow Through a High-Specific-Output Two-Cycle Engine," SAE Paper No. 720156, 1972.

6 Gentry, R. A., Martin, R. E, and Daly, B. J., "An Eulerian Differencing Method for Unsteady Compressible Flow Problems," *Journal of Computational Physics*, No. 1, 1966, pp. 87–118.

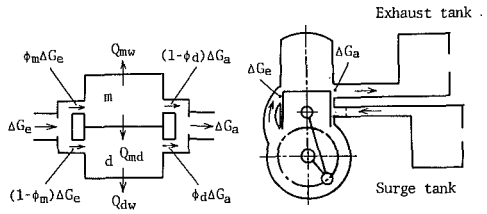
7 Patterson, D. J., "A Comprehensive Cycle Analysis and Digital Computer Simulation for Spark-Ignited Engine," Ph.D. Thesis, Dept. of Mechanical Engineering, University of Michigan, Ann Arbor, MI, 1962, pp. 85–103.

8 Tomizuka, K., and Shibata, H., "On Methods of Measuring the Charging Efficiency of Two-Stroke Engine," Research Report of Aeronautics Research Institute, Tokyo University, No. 61, Sept. 1929, pp. 455–479.

9 Miyabe, H., and Shimomura, T., "The Influences of the Inlet and Exhaust Pipe Length on the Scavenging Performance of a Crankcase-Compressed Two Stroke Gasoline Engine," *Transactions of JSME*, Vol. 31, No. 222, 1965, pp. 308–316.

Table 4 Dimensions of volume and pipe system

surge tank	0.125 m^3
crankcase	420 cm^3
cylinder	160 cm^3
exhaust tank	0.318 m^3
inlet pipe	cross section $=4.66\times10^{-4}$ m^2 length $=0.211$ m
scavenging passage	cross section $=6.68\times10^{-4}$ m^2 length $=0.07$ m
exhaust pipe	cross section $=8.11\times10^{-4}$ m^2 length $=0.131$ m



(a) Internal state of cylinder (b) Entire picture of system

Fig. 12 Model for simulation of gas exchange process

APPENDIX

Treatment for Simulation of the Gas Exchange Process

Figure 12 shows a model introduced to simulate the gas exchange process in a two-stroke cycle gasoline engine. Figure 12(*a*) describes the internal state of a cylinder, while Fig. 12(*b*) gives a comprehensive picture of the system comprising both pipe and volume. Table 4 gives the size of each part for the system on Fig. 12(*b*).

The gas exchange process is simulated under the following assumptions:

1 The working fluid is a mixture of air containing combustion gases and a fuel of C_XH_Y type.

2 There exists a one-dimensional unsteady flow of compressible fluid in the part made up by the pipe. Three diffusion phenomena (mass, momentum, and thermal diffusion) are particularly present in the scavenging passage and exhaust pipe; the data for these phenomena are given as the factors ϵ_m, ϵ_T, and ϵ_q. Furthermore, the supplement enthalpy is set to provide an energy balance against mass diffusion. The initial concentration is given by using the factor r to represent the mixture ratio of fresh gas to combustion gas.

3 In the part made up by the volume, the gas is considered to be stagnant and divided into two regions (mixing m and stratified d), as shown in Fig. 12(*a*). The factors ϕ_m and ϕ_d denote the intensities of the inflow and outflow. The factor r is used in the same above-mentioned way to denote the initial concentration. Finally, the quantity of state is calculated as incrementally small change ranging from one to five steps (Step Method) [7].

Basic Equation for the Flow

Given the momentum flux τ_{xx}, heat flux q_x, and mass flux I_i on the above assumption (2), the one-dimensional unsteady flow's continuity equation, the momentum equation, the energy equation, and the component i's continuity equation, can all be related in terms of a vector as follows:

$$\frac{\partial \mathbf{W}}{\partial t}+\frac{\partial \mathbf{W}u}{\partial x}=-\mathbf{D}-\mathbf{E} \tag{1}$$

$$\mathbf{W}\equiv\begin{pmatrix}\rho\\ \rho u\\ \rho K\\ \rho_1\\ \rho_2\\ \vdots\\ \rho_m\end{pmatrix},\quad \mathbf{D}\equiv\begin{pmatrix}0\\ \dfrac{\partial P}{\partial x}\\ \dfrac{\partial (Pu)}{\partial x}\\ 0\\ 0\\ \vdots\\ 0\end{pmatrix},$$

Downloaded 01 Jun 2010 to 171.66.16.87. Redistribution subject to ASME license or copyright; see http://www.asme.org/terms/Terms_Use.cfm

$$\mathbf{E} \equiv \begin{bmatrix} 0 \\ \dfrac{\partial \tau_{xx}}{\partial x} \\ \dfrac{\partial q_x}{\partial x} + \dfrac{\partial}{\partial x}(\tau_{xx} u) \\ \dfrac{\partial I_1}{\partial x} \\ \dfrac{\partial I_2}{\partial x} \\ \vdots \\ \dfrac{\partial I_m}{\partial x} \end{bmatrix}$$

$$\tau_{xx} = -\frac{4}{3}\rho\epsilon_r \frac{\partial u}{\partial x}, \quad q_x = -C_{pf}\rho\epsilon_q \frac{\partial T}{\partial x},$$

$$I_i = -\rho\epsilon_m \frac{\partial y_i}{\partial x}, \quad y_i = \frac{\rho_i}{\rho}, \quad K = e + \frac{1}{2}u^2$$

In the FLIC method [6], the value F^{n+1} (ρ, e, y_i) of $(n+1)\Delta t$ is obtained from the quantity of state F^n (ρ, e, y_i) of each cell at the time $n\Delta t$ by means of two-step forward differences over time.

Gas Exchange Process

Initial Quantity of State in the Volume and Pipe System. Given λ as the excess air ratio, the reaction equation for determining the composition of a combustion gas using assumption (1) is expressed as follows:

$$C_xH_y + \lambda\left(x+\frac{y}{4}\right)O_2 + \frac{79.01}{20.99}\lambda\left(x+\frac{y}{4}\right)N_2 = n_{O_2}O_2 + n_{N_2}N_2 + n_{CO_2}CO_2 + n_{CO}CO + n_{H_2O}H_2O + n_{H_2}H_2 \quad (2)$$

This assumes that C_8H_{18} is used as fuel. Let the number of moles in a fresh and a combustion gas be denoted by n_{fi}, n_{ei}, $i = 1, 2, \ldots, m$, and supposing that the mass ratio of a fresh gas to a combustion gas is $(1-r):r$, then the mixed gas composition n_{Bi} and the mass fraction y_{Bi} are obtained as follows:

$$n_{Bi} = (1-r)n_{fi} + rn_{ei} \quad (3)$$

$$y_{Bi} = \frac{n_{Bi}M_i}{\sum_{j=1}^{m} n_{Bj}M_j} \quad (4)$$

The gas composition in the pipe and a volume part can be obtained from the above mass fraction.

For example, the gas composition takes an appropriate assumed value r if blow-back or return-blow for the scavenging passage and the crankcase is taken into account; otherwise, $r=0$.

Since mass transfer and combustion are treated in a manner similar to a pipe, the supplement enthalpy $(\Delta H_{m298})_{C_xH_y}$ is established in addition to the chemical enthalpy of a fuel, so that the enthalpy H_f of fresh gas can be made equal to the enthalpy H_e of combustion gas to maintain the energy balance [1]. The enthalpy is expressed as follows:

$$H = \sum_{i=1}^{m} n_i(\Delta H^0_{f298})_i + n_{C_xH_y}(\Delta H^0_{m298})_{C_xH_y} + \sum_{i=1}^{m} n_i \int_{298}^{T} C_{pi}\,dT \quad (5)$$

Under these conditions, the enthalpy H_B of the mixed gas becomes: $H_B = H_f = H_e$. This is under the stipulation that the chemical enthalpy $(\Delta H_{f298})_i$ is one as prescribed in the literature [7]. Therefore, the concept of isenthalpic constant pressure combustion can also be applied to mass transfer.

Calculation in the Gas Exchange Process

When the initial conditions for the pipe and volume system are established, the state of each step is calculated as a series of incrementally small changes composed of five steps based on assumption (3). The subscript 0 stands for the initial state and the subscripts $1 \sim 5$ correspond to the states in steps 1 to 5.

Step 1. Inflow and Outflow at Constant Pressure. In the stratified region, the numbers of moles, enthalpy, and mass are expressed as follows:

$$\left.\begin{aligned} n_{d1i} &= n_{d0i} + \Delta n_{dei} - \Delta n_{dai} \\ H_{d1} &= H_{d0} + \Delta H_{de} - \Delta H_{da} \\ \sum_{i=1}^{m} n_{d1i}M_i &= \sum_{i=1}^{m} n_{d0i}M_i + (1-\varphi_m)\Delta G_e - \varphi_d \Delta G_a \end{aligned}\right\} \quad (6)$$

The above equations also apply to the mixing region. Taking a look at the whole picture (subscript t), therefore,

$$\left.\begin{aligned} n_{t1i} &= n_{d1i} + n_{m1i} \\ H_{t1} &= H_{d1} + H_{m1} \\ \sum_{i=1}^{m} n_{t1i}M_i &= \sum_{i=1}^{m} n_{d1i}M_i + \sum_{i=1}^{m} n_{m1i}M_i \end{aligned}\right\} \quad (7)$$

The masses ΔG_e and ΔG_a, which flow in and out within a very short period of time, can be determined on the basis of boundary conditions at the end of a pipe [1] by using the regression curve for flow coefficients along with the pressure ratio and the port area ratio.

Step 2. Mixing at Constant Pressure. The gas flowing in Step 1 gets mixed separately with the gases that already exist in each region under constant pressure and settles to a uniform state, so that the volume of the system undergoes a change.

Step 3. Recompression to the Original Volume. The volume of the system changed in Step 2 is isentropically recompressed to the original volume V_{to}.

Step 4. Change of Volume Due to Motion of Piston. In the same way as in Step 3, the volume of the system changes isentropically from V_{to} to V_{t4} due to the motion of the piston.

Step 5. Constant Volume Heat Transfer. The internal energy on the whole undergoes a change due to heat transfer between the inside and the outside of the system. Entropy changes in the stratified region as a result of heat transmission from the mixing region as well as from heat transmission to the wall. In Fig. 12(*a*) the heats Q_{mw}, Q_{dw}, and Q_{md} are transferred between the mixing region and the wall, the stratified region and the wall, and the stratified and the mixing regions, respectively [1].

The quantities of states P, T, and V are determined from the above relations given in steps 1 to 5, and the efficiencies C_{rel}, η_c, L, η_{tr}, and η_s are calculated according to these definitions.

Downloaded 01 Jun 2010 to 171.66.16.87. Redistribution subject to ASME license or copyright; see http://www.asme.org/terms/Terms_Use.cfm

S. Izumi
Advisor,
Engine Division,
Mitsubishi Heavy Industries,
Tokyo 100, Japan

M. Takemi
Chief Engineer,
Engine Design Division,
Mitsubishi Heavy Industries,
Sagamihara 229, Japan

M. Ishida
Professor,
Faculty of Engineering,
Nagasaki University,
Nagasaki 852, Japan

H. Suetsugu
Associate Professor,
Faculty of Engineering,
Nagasaki Institute of Applied Science,
Nagasaki 851-01, Japan

T. Maeda
Manager,
Product Engineering Dept.,
Ono Sokki Co., Ltd.,
Tokyo 146, Japan

Y. Yoshimura
Research Associate,
Faculty of Engineering,
Nagasaki University,
Nagasaki 852, Japan

Studies on Combustion, Vibration, and Noise in High-Speed Diesel Engines Through Newly Developed Measuring Instruments

The authors have been conducting studies on the reduction of exhaust emissions using a high-speed diesel engine. By applying composite countermeasures consisting of five items: (1) timing retard, (2) optimization of fuel injection system, (3) water-in-oil type emulsified fuel, (4) application of ignition improver, and (5) an increase in air flow quantity, an exhaust NO_x level less than half of the original was attained while retaining the original low levels of fuel consumption, smoke density, and engine noise. The authors developed new measuring instruments in order to grasp the true nature of combustion, especially to clarify the delicate change in combustion. By using these instruments, the combustion phenomena were analyzed accurately, speedily, and synthetically on various aspects such as combustion mode, vibration, noise, thermal loading, heat balance, etc. The complicated combustion behavior in the cylinder has been clarified in part by simultaneous measurement of cylinder pressure at several points.

1 Introduction

The demand for marine diesel engines has decreased substantially due to excessive production of ships during the past ten years. Utilization of a diesel engine for electric power generation has been promoted to attain the merits of high power rate, low fuel consumption, and durability.

The authors have conducted studies on the reduction of exhaust emissions and noise while maintaining good engine performance using a small-sized high-speed diesel engine with a cylinder bore of 110 mm and a maximum speed of 2500 rpm. This paper deals with measures to counter environmental conditions by optimization of the fuel injection system including timing retard, utilization of water-emulsified fuel and ignition improver, and an increase in air flow quantity by improvement of the supercharging system.

Marine diesel oil A40 and heavy fuel C1500 having a viscosity of 2.8 and 180 cSt @50°C, respectively, and a mixed gas oil blended with light cycle gas oil AD040 having cetane index 40 are used for the combustion tests.

2 Development of New Measuring Instruments

2.1 Multichannel Combustion Analyzer

Combustion Analyzer CB-466. Four different kinds of phenomena, such as cylinder pressure at two points, fuel injection pressure at the inlet of the fuel injection nozzle, and needle valve lifting, were simultaneously measured at every 0.25 deg of crank angle for 1000 continuous cycles, and the second

Contributed by the Internal Combustion Engine Division and presented at the Eleventh Annual Energy-Sources Technology Conference and Exhibition, New Orleans, Louisiana, January 10–13, 1988. Manuscript received by the Internal Combustion Engine Division September 25, 1987. Paper No. 88-ICE-1.

Copyright © 1988 by ASME
Downloaded 01 Jun 2010 to 171.66.16.87. Redistribution subject to ASME license or copyright; see http://www.asme.org/terms/Terms_Use.cfm

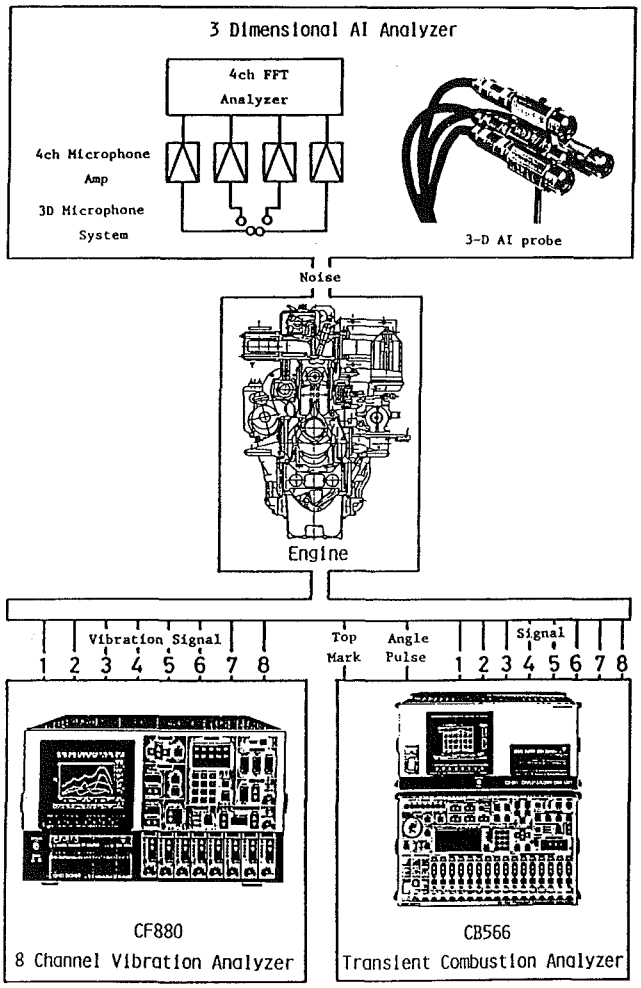


Fig. 1 Newly developed measuring system

derivatives such as average cycle, pressure rise rate, heat release rate, and injection rate were computed on-line and real-time.

Transient Combustion Analyzer CB-566. The authors have developed the eight-channel combustion analyzer CB-566 with a storage capacity of 10^6 words/channel to measure the transient behavior of combustion, in which the data of 350 continuous cycles at every ¼ deg of crank angle can be stored. This combustion analyzer was capable of measuring a delicate

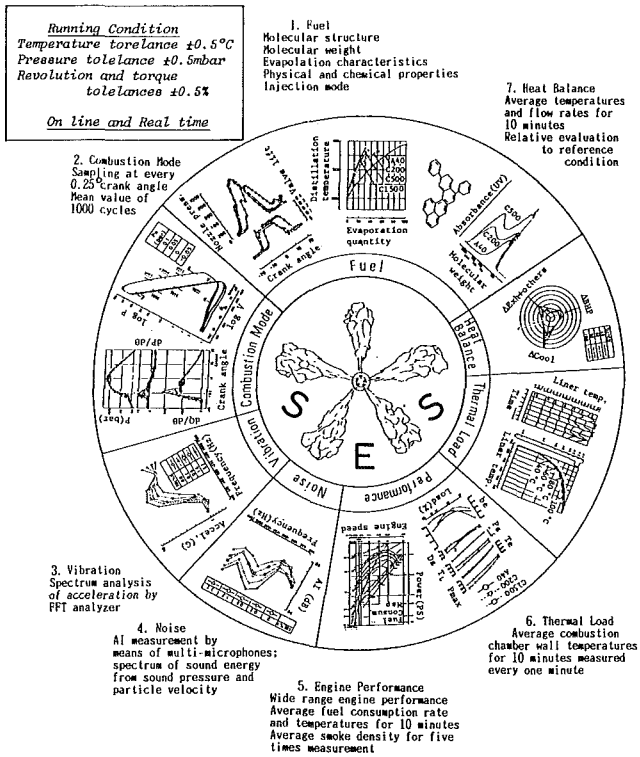


Fig. 2 Synergistic-evaluation system on combustion

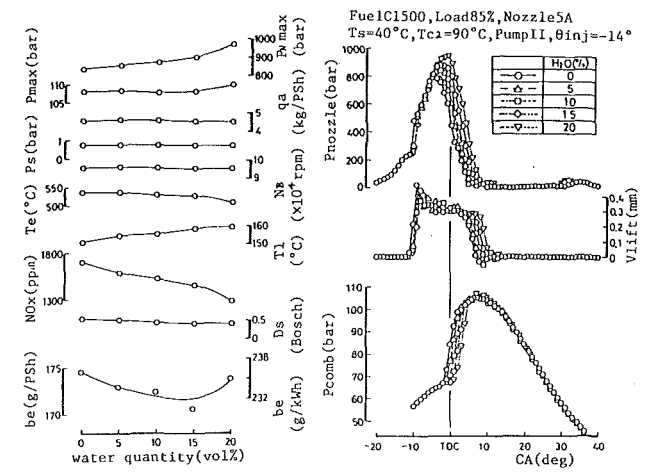
change in cylinder pressure at every cycle accurately, speedily, and continuously, and also at several points in the cylinder simultaneously. The authors have tried to clarify the combustion behavior in the whole combustion chamber.

2.2 Multichannel Vibration Analyzer. The authors have developed eight-channel vibration analyzer CF-880 to measure accelerations simultaneously at eight optional points on engine component parts and also to analyze quantitatively the vibration spectrum at individual points and vibration mode on-line and real-time. There are many factors that cause engine vibrations and it is very difficult to ascertain separately and correctly the vibration behavior due to the individual vibration source. However, studies were made on the relationship between vibration and combustion by ascertaining a change in vibration behavior due to only a change in combustion mode under the strictly regulated engine operating condition.

Nomenclature

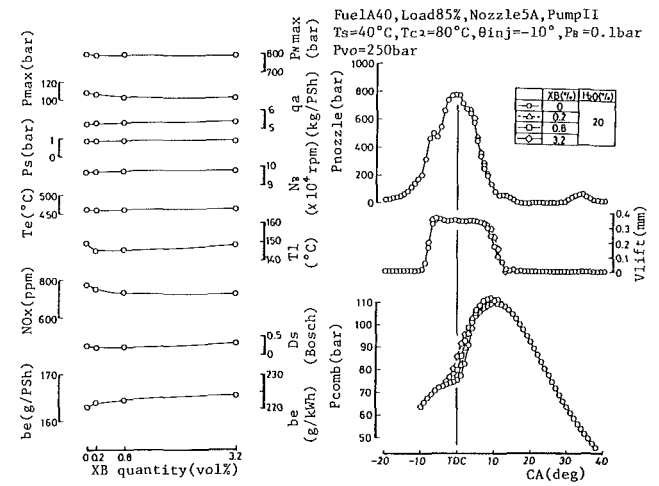
AI = acoustic intensity, dB
$AI\ o.a.$ = overall value of acoustic intensity, dB
be = specific fuel consumption rate, g/kWh, g/PSh
CA, θ = crank angle, deg
Ds = smoke density, Bosch
$dP/d\theta$ = rate of pressure rise, bar/deg
$dQ/d\theta$ = rate of heat release, J/deg
H_2O = water quantity, percent
NB = speed of turbocharger, rpm
NO_x = concentration of nitric oxide, ppm
Pcomb = combustion pressure, bar
Pmax = maximum combustion pressure, bar
PNmax = maximum fuel injection pressure, bar
Pnozzle = fuel pressure at nozzle inlet, bar
PB = boosting pressure at blower inlet, bar
Ps = suction air pressure at engine inlet, bar
qa = specific air consumption rate, kg/PSh
$Tc2$ = cooling water temperature at engine outlet, °C
Te = exhaust gas temperature at turbine inlet, °C
Tf = fuel temperature at injection pump inlet, °C
Tl = liner temperature at top ring position, °C
Ts = suction air temperature at engine inlet, °C
Vlift = needle valve lift, mm
XB = ignition improver quantity, percent
ΔBHP = increment of net thermal efficiency, percent
ΔCool = increment of cooling loss and others, percent
ΔExh = increment of exhaust loss, percent

Downloaded 01 Jun 2010 to 171.66.16.87. Redistribution subject to ASME license or copyright; see http://www.asme.org/terms/Terms_Use.cfm



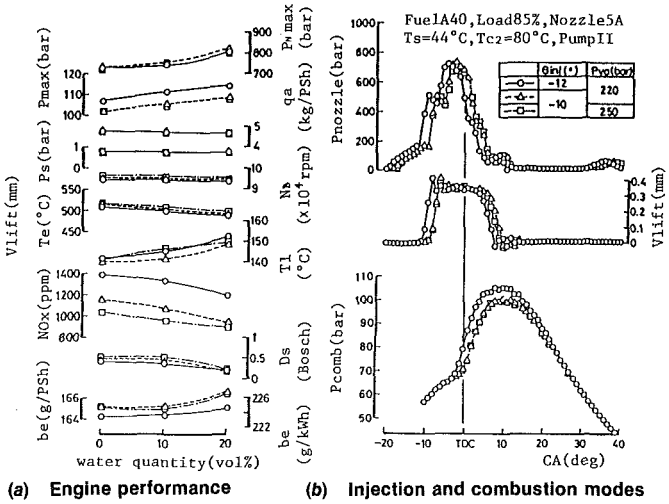
(a) Engine performance (b) Injection and combustion modes

Fig. 3 Water quantity variation (fuel C1500)



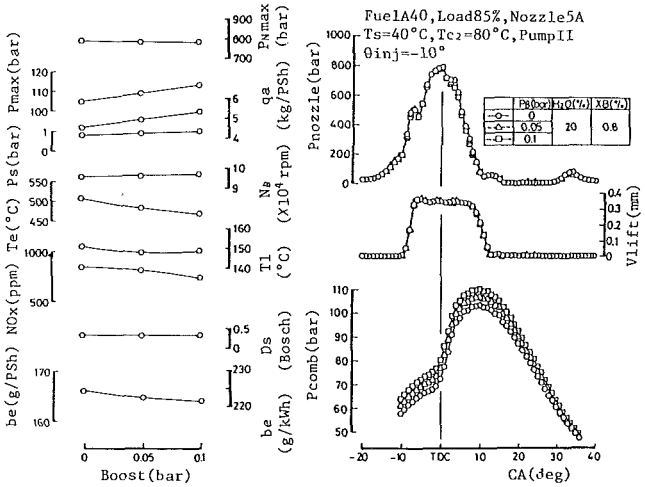
(a) Engine performance (b) Injection and combustion modes

Fig. 4 Ignition improver quantity variation (fuel A40)



(a) Engine performance (b) Injection and combustion modes

Fig. 5 Fuel injection system variation (fuel A40)



(a) Engine performance (b) Injection and combustion modes

Fig. 6 Air flow quantity variation (fuel A40)

θinj (deg)	Nozzle type	Pvo (bar)	Water (%) 0	10	20	PB (bar) 0	.05	.1	XB (%)
-14	5B	220	◎ (ref)			0			0
-12	5A		○	◑	●				
-10			△	▲	▲				
		250	□	◨	■				
			20			◇	◈	◆	0.8

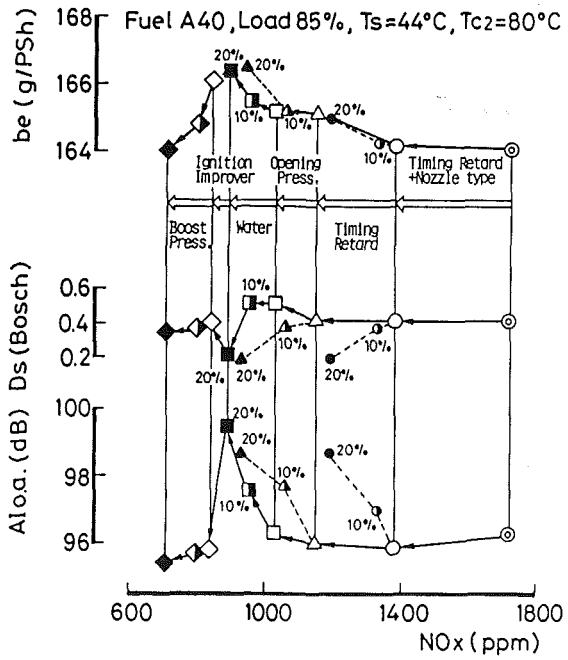


Fig. 7 Effects of countermeasures on air pollution

2.3 Three-Dimensional Acoustic Intensity Meter. The authors have measured on-line and real-time the noise as energy, not as sound pressure, through an acoustic intensity meter with the dual-microphone system and without an anechoic chamber [1]. Going one step further, the authors have developed a 3-D Acoustic Intensity Meter, which is capable of measuring three-dimensional AI vectors instantly through a combination AI probe consisting of four microphones and a four-channel FFT analyzer, without using an anechoic chamber.

Figure 1 shows the newly developed measuring system.

2.4 Synergistic-Evaluation System "SES." By utilizing the abovementioned three different types of measuring instrument, the combustion behavior was mainly evaluated from the viewpoints of (1) combustion mode, (2) vibration, and (3) noise. The actual condition of combustion was totally evaluated and ascertained from another four kinds of viewpoints: (4) fuel characteristics, (5) engine performance, (6) thermal load based on combustion chamber wall temperature distribution, and (7) heat balance. Figure 2 shows "Synergistic-Evaluation System" on combustion.

Downloaded 01 Jun 2010 to 171.66.16.87. Redistribution subject to ASME license or copyright; see http://www.asme.org/terms/Terms_Use.cfm

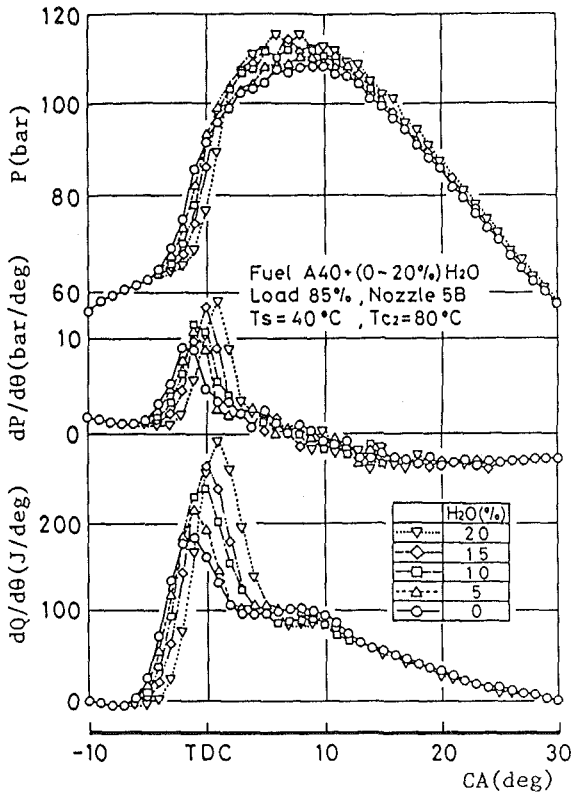


Fig. 8(a) Combustion mode

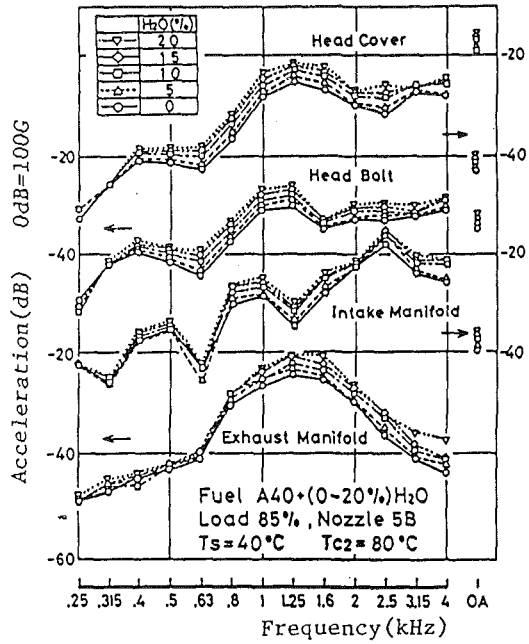


Fig. 8(b) Vibration spectrum

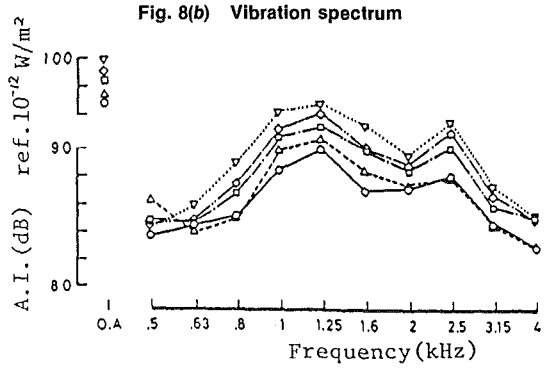


Fig. 8(c) Acoustic intensity spectrum

Fig. 8 Change in combustion due to emulsified fuel (fuel A40)

3 Combustion Test on Exhaust Emissions

3.1 Emulsified Fuel. The water-in-oil type emulsified fuel was made with a high-speed mixer, and in the case of fuel A40 the appropriate emulsifier was added up to 0.5–1.0 percent (vol.) of the fuel. In applying this method, the water droplets in fuel oil were made smaller than 5 μm in size and distributed uniformly.

3.2 Water Quantity Variation in Emulsified Fuel. Figure 3(*a*) shows a change in engine performance at the time of adding water of 0–20 percent to heavy fuel C1500 at 85 percent load on the propeller law characteristics. Due to 20 percent addition of water, NO_x was reduced by about 300 ppm; smoke density and fuel consumption were also reduced to some extent.

Figure 3(*b*) shows a change in injection and combustion modes due to the addition of water in the case of nozzle 5A. The injection duration increases and the injection pressure rises. The ignition lag becomes greater, and the maximum combustion pressure rises. The engine vibration and noise increase due to the increase in pressure rise rate. To reduce the vibration and noise, ignition improver was added as mentioned in the following section.

3.3 Ignition Improver Quantity Variation. Figure 4(*a*) shows an example of the effect of ignition improver in 20 percent water-emulsified fuel on engine performance. Figure 4(*b*) shows the injection mode, the needle valve lifting, and the combustion mode. The addition of ignition improver hastens ignition and recovers the ignition delay due to the addition of water, and then the maximum combustion pressure decreases. At this time, fuel consumption and smoke density hardly change, but NO_x decreases by 50 ppm by adding ignition improver in the amount of 0.8 percent.

3.4 Fuel Injection System Variation. In order to reduce NO_x, studies were made on the fuel injection timing retard, and on optimization of the fuel injection system such as the number of nozzle holes, nozzle hole area, valve opening pressure, etc. The number of nozzle holes was changed by using four holes (type 4B), five holes (type 5B), and six holes (type 6B) with the injection hole area kept constant. Type 6B showed the minimum value of NO_x, but was inferior in fuel consumption. On the other hand, an experiment was conducted changing the injection hole area ratio of 1.0 (type 5A), 0.88 (type 5B), and 0.76 (type 5C) without changing the number of injection holes. The three nozzles showed nearly the same fuel consumption, but the nozzle type 5A showed the lowest value of NO_x level.

Figure 5(*a*) shows the engine performance in the case that the injection timing θinj was delayed from 12° BTDC to 10° BTDC and that the valve opening pressure of the nozzle type 5A was raised from the standard of 220 bar to 250 bar. Figure 5(*b*) shows the injection and combustion modes in that case. In any water adding rate, the fuel consumption increases by approximately 1 g/PSh due to the timing retard of 2 degrees CA, but NO_x decreases by about 230 ppm. Moreover, 30 bar rise of the valve opening pressure resulted in the reduction of NO_x by 120, 106, and 50 ppm with the fuel consumption kept constant when the water adding rates were 0, 10, and 20 percent, respectively. Incidentally, the decrease of NO_x due to 20 percent addition of water at this time was 140 ppm, which was only about 50 percent of that shown in Fig. 3(*a*).

3.5 Air Flow Quantity Variation. Figure 6(*a*) shows the engine performance at the time when the suction air pressure was raised by means of a motor-driven blower, using fuel A40

Downloaded 01 Jun 2010 to 171.66.16.87. Redistribution subject to ASME license or copyright; see http://www.asme.org/terms/Terms_Use.cfm

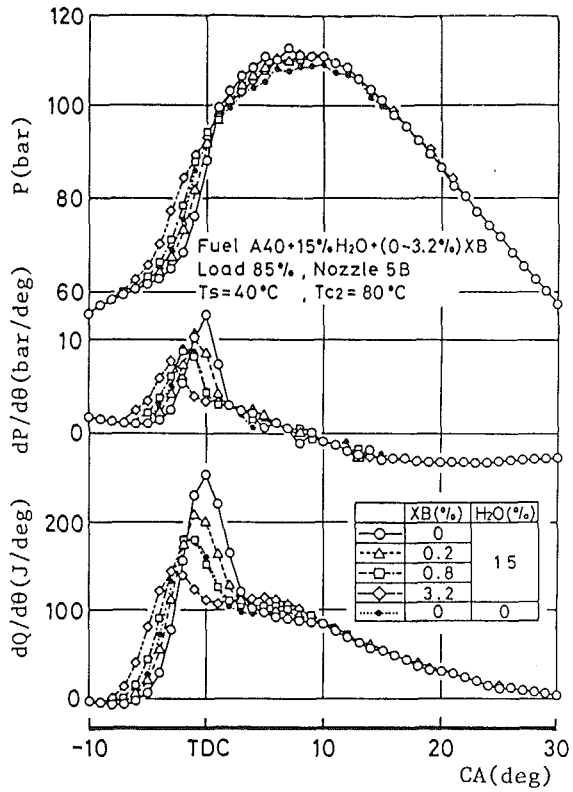


Fig. 9(*a*) Combustion mode

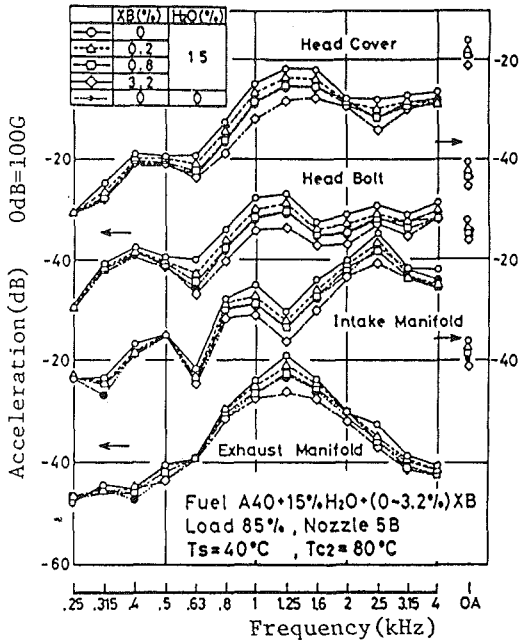


Fig. 9(*b*) Vibration spectrum

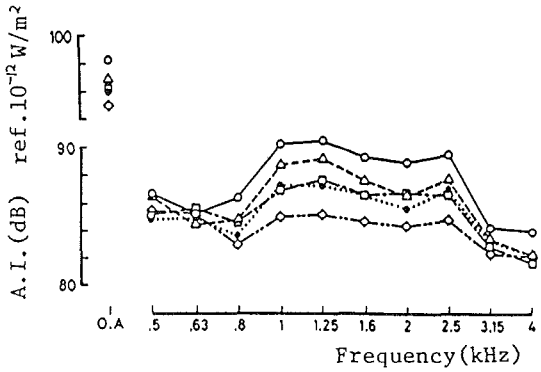


Fig. 9(*c*) Acoustic intensity spectrum

Fig. 9 Change in combustion due to ignition improver (fuel A40)

added with 20 percent water and 0.8 percent ignition improver; and Fig. 6(*b*) gives injection, needle valve lifting, and combustion modes. By increasing the suction air pressure by 0.1 bar, fuel consumption, NO_x, and smoke density were reduced by 2.2 g/PSh, 130 ppm, and 0.05 Bosch, respectively.

Moreover, improvement in exhaust emissions and engine performance is being carried on by improving the turbocharging system instead of increasing the suction air pressure by means of a motor-driven blower.

3.6 Composite Countermeasures for Exhaust Emissions. Figure 7 shows the results of composite countermeasures taken for the control of environmental condition in the case of marine diesel oil A40, and also shows fuel consumption, smoke density, and noise in their relation to NO_x. The countermeasures consist of the following five items, which show their representative values of NO_x reduction.

Countermeasures		NO_x reduction
A1. Timing retard I	14° → 12°BTDC	(ppm)
B1. Optimization of fuel injection system I	Nozzle type; 5B → 5A	340
A2. Timing retard II	12° → 10°BTDC	230
B2. Optimization of fuel injection system II	Valve opening pressure; 220 → 250 bar	120
C. Water-emulsified fuel	20 percent water	140
D. Ignition improver	0.8 percent XB	50
E. Increase in air flow quantity	Boost pressure; 0.1 bar	130
Total reduction of NO_x		1010 ppm

With the fuel consumption, smoke density, and acoustic intensity (AI) maintained on the level slightly lower than the original 164.1 g/PSh, 0.42 Bosch, and 96.3 dB, the NO_x value was reduced by about 60 percent from the initial 1720 ppm (shown by mark ◎) to 710 ppm (shown by mark ♦).

4 Synthetic Consideration on Combustion, Vibration, and Noise

4.1 Change in Combustion Due to Emulsified Fuel. Figure 8 shows the changes in (*a*) combustion mode, (*b*) vibration spectrum, and (*c*) AI spectrum at the time when an added amount of water was increased to marine diesel oil A40. With the water addition rate increased, ignition was delayed, and the maximum rate of pressure rise increased; as a result, the vibration and noise of various engine component parts noticeably increased within the frequency range of 500 to 4000 Hz. Moreover, it was ascertained that an increase in ignition delay takes place nearly in proportion to the added amount of water. It is concluded that an increase in the maximum rate of heat release and the reduction in combustion duration resulted from the improvement of combustion due to the addition of water. The vibration spectrum at various engine components is different depending upon the structural peculiarities of individual engine components, but the peak frequency was 1.25 kHz at various engine components, excepting 2.5 kHz at the intake manifold. Accordingly, the peak frequencies appeared at 1.25 kHz and 2.5 kHz in the AI spectrum integrated around the combustion chamber, as shown in Fig. 8(*c*).

4.2 Change in Combustion Due to Ignition Improver. Figure 9 shows the changes in (*a*) combustion mode, (*b*) vibration spectrum, and (*c*) AI spectrum at the time when an added amount of ignition improver XB was increased in 15 percent water-emulsified marine diesel oil A40. The solid circles in the figure show the value obtained at the time when

Downloaded 01 Jun 2010 to 171.66.16.87. Redistribution subject to ASME license or copyright; see http://www.asme.org/terms/Terms_Use.cfm

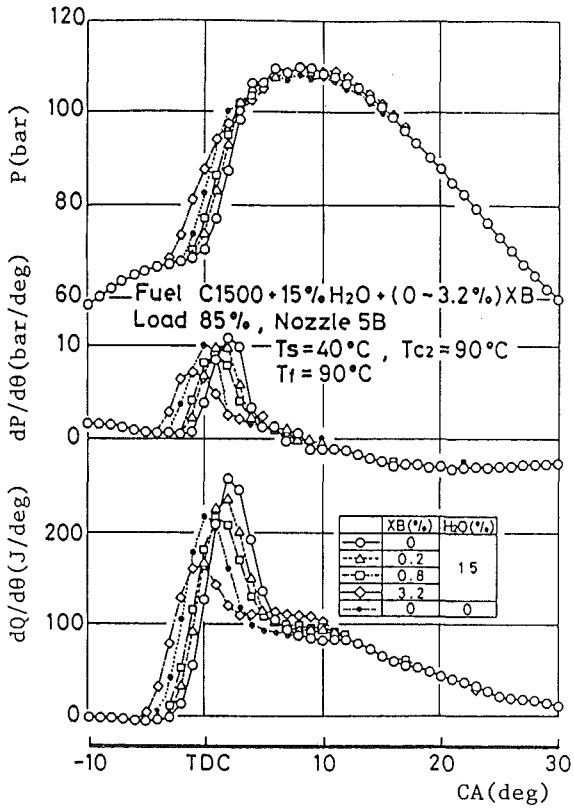


Fig. 10(*a*) Combustion mode

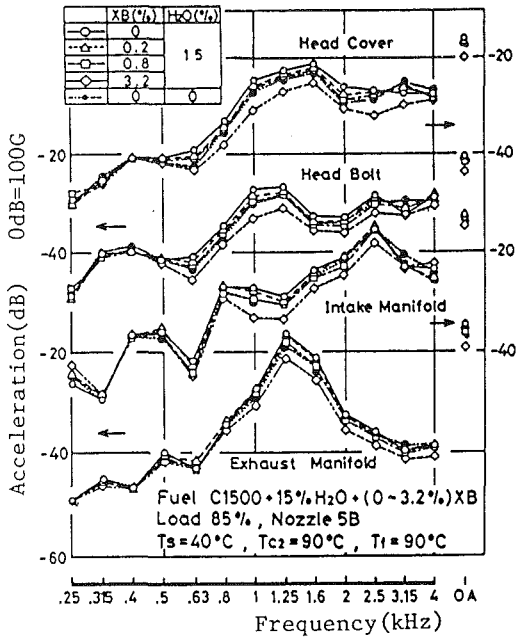


Fig. 10(*b*) Vibration spectrum

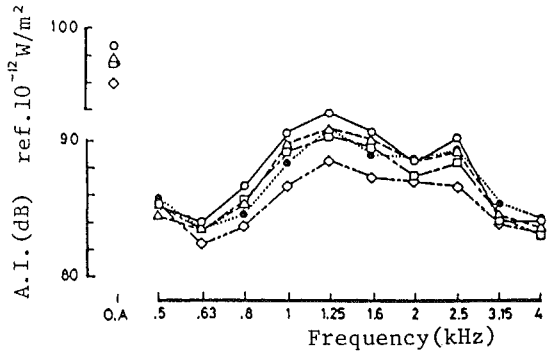


Fig. 10(*c*) Acoustic intensity spectrum

Fig. 10 Change in combustion due to ignition improver (fuel C1500)

the water and ignition improver were not added. As seen from the comparison between the solid circles and open circles, there occurs ignition delay, an increase in pressure rise rate, and an increase in vibration and noise when the water is added. On the other hand, by increasing the addition rate of the ignition improver, ignition starts earlier, and the pressure rise rate, vibration, and noise decrease together. The combustion mode, vibration, and noise were made to agree with the initial condition by adding ignition improver of 0.8 percent.

Figure 10 also shows the effect of the ignition improver addition rate on (*a*) combustion mode, (*b*) vibration spectrum, and (*c*) AI spectrum in 15 percent water-emulsified heavy fuel C1500. The tendency of the effect is nearly the same as in the case of Fig. 9.

4.3 Additional Evaluation of Combustion Based on SES. Figure 11 shows a mutual comparison between marine diesel oil A40 and heavy fuel C1500 in regard to the increment of ignition delay due to the addition of water and to the decrement due to the addition of ignition improver. When water is added by 15 percent to both fuels A40 and C1500, there arises the increment of ignition delay by about 1.2 deg of crank angle, but the ignition delay can be resumed by adding 0.4 percent of ignition improver to A40 and about 1 percent of ignition improver to C1500.

Figure 12 shows an example of the effect of water addition on (*a*) combustion chamber wall temperature distribution and (*b*) heat balance. Due to an increase in the added amount of water, the cylinder liner temperature rises and the cooling loss increases. However, the improvement in combustion and the reduction in combustion duration serve to reduce the exhaust gas temperature and exhaust loss, and so the net thermal efficiency has been improved slightly in this case. Furthermore, it is concluded that the cylinder liner temperature rise results from an increase in penetration due to the addition of water.

Through various special measuring instruments developed recently, various phenomena of combustion can be evaluated mutually and in various ways, and a synthetic evaluation method of combustion phenomena has been established.

5 Further Studies on Combustion Behavior

5.1 Simultaneous Measurement of Cylinder Pressure at Two Points. In order to grasp the whole combustion behavior in the combustion chamber, it is necessary to make a mutual comparison of the indicator diagrams obtained from a number of pressure sensors arranged at various points of the combustion chamber in regard not only to average cycle but also to individual cycles measured simultaneously. Piezo sensors were fitted at two points as shown in Fig. 13. The sensors Pc1 and 2 were fitted to one cylinder head, and Pc3 and 4 to another cylinder head. The center positions of the piezo sensors Pc1, 2, 3, and 4 are +6, −1, +12, and +1 mm distant from the inside surface of the cylinder liner in the direction of cylinder center, respectively.

5.2 Fluctuation of Cylinder Pressure. Figure 14 shows the comparison of cylinder pressure fluctuation measured by the piezo sensors Pc1 and Pc2 at the time when the engine speed was settled at 2368 and 1984 rpm with Pme kept at the constant value of 7.18 bar in the combustion test on degraded gas oil AD040. At both engine speeds, the piezo sensor Pc1 located near the piston cavity shows earlier starting of the sudden pressure rise, lower pressure rise rate, and smaller pressure fluctuation amplitude arising after the sudden pressure rise

Downloaded 01 Jun 2010 to 171.66.16.87. Redistribution subject to ASME license or copyright; see http://www.asme.org/terms/Terms_Use.cfm

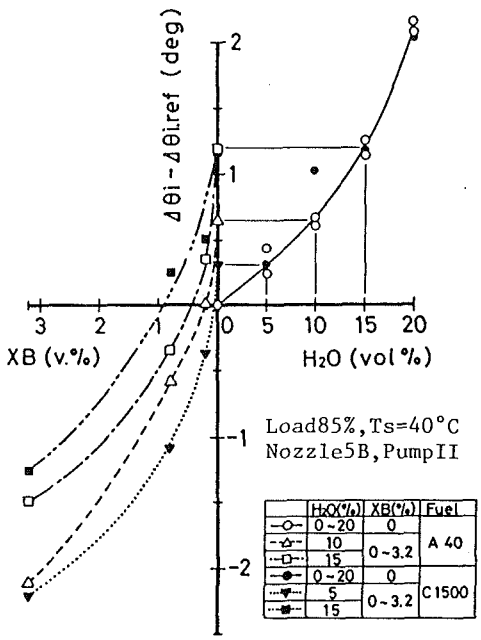


Fig. 11 Comparison of relative ignition delay

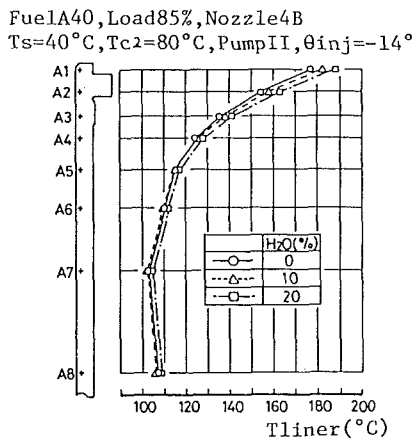


Fig. 12(*a*) Cylinder liner temperature

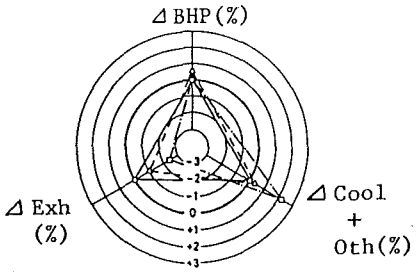


Fig. 12(*b*) Heat balance

Fig. 12 Additional combustion evaluation by SES

than the piezo sensor Pc2, located in the neighborhood of the inside surface of the cylinder liner. The difference in the starting of sudden pressure rise depends on the difference in the distance between the piston cavity and the location of the piezo sensor. The reason for the larger pressure fluctuation amplitude shown by the piezo sensor Pc2, it is considered, is that kinetic energy is converted into pressure when pressure wave arising in the cavity reflects on the inside surface of the cylinder liner. The pressure fluctuation after 10°ATDC corresponds approximately to the fluctuation whose one wave length is the same as the cylinder bore.

Figure 15(*a*) shows a comparison of cylinder pressure modes

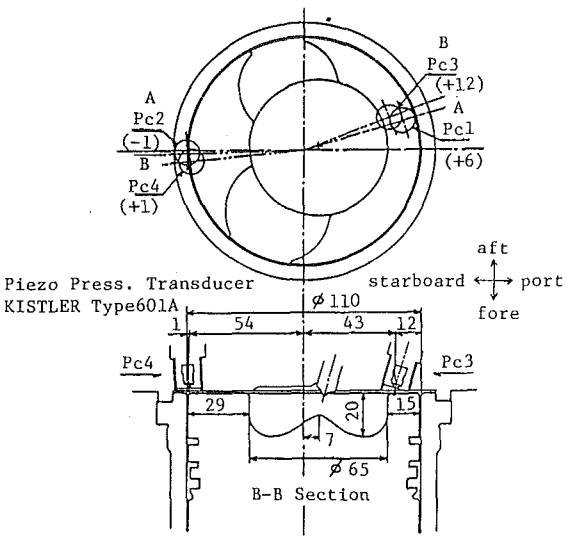


Fig. 13 Cylinder pressure measuring points

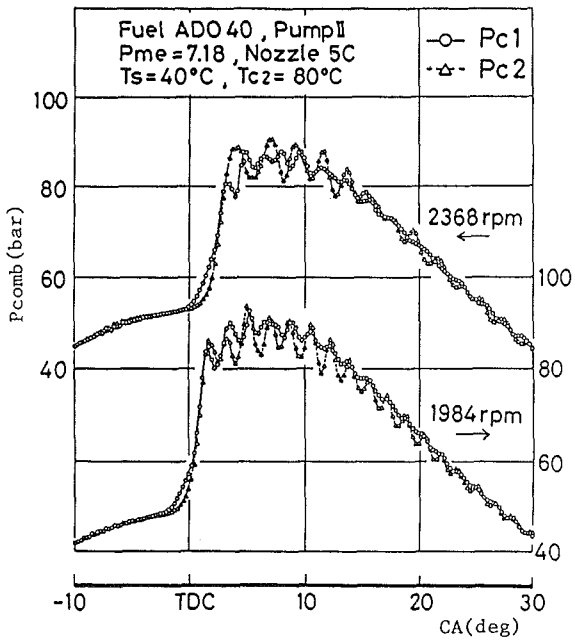


Fig. 14 Comparison of cylinder pressure fluctuation

at different measuring points in the combustion test of fuel C1500. The piezo sensors Pc3 (+12 mm), Pc1 (+6 mm), and Pc2 (−1 mm), which are located closer to the center of the combustion chamber in the order, show earlier starting of sudden pressure rise and smaller fluctuation amplitude in the order of their location. Despite the fact that the cylinder head in which the piezo sensor Pc3 was fitted was different from that in which the other two were fitted and measurement was made at different times of engine operation, the cylinder pressures measured by the three piezo sensors have mutual relationship clearly; this is a very noteworthy phenomenon.

Figure 15(*b*) shows a comparison of cylinder pressure mode between the average of 1000 cycles and some individual cycles. As shown before, the average of 1000 cycles has repeatability in spite of pressure fluctuations. But in the individual cycles, it is apparent that the cylinder pressure has changed appreciably at every cycle. This shows that the injection rate changes at every cycle due to rack vibration, etc.

As shown in Figs. 16(*a*) and 16(*b*), however, the cylinder pressures of the individual cycles measured simultaneously at the two points clearly show the relative difference between the

Downloaded 01 Jun 2010 to 171.66.16.87. Redistribution subject to ASME license or copyright; see http://www.asme.org/terms/Terms_Use.cfm

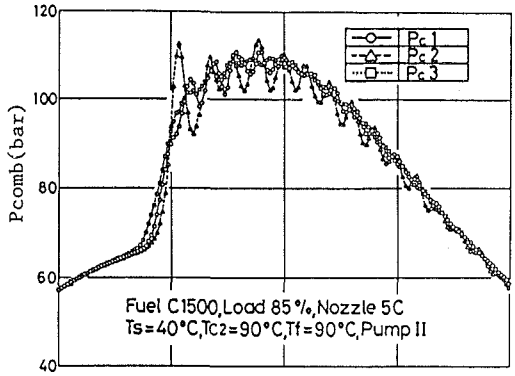


Fig. 15(*a*) Three measuring points (averaged cycle)

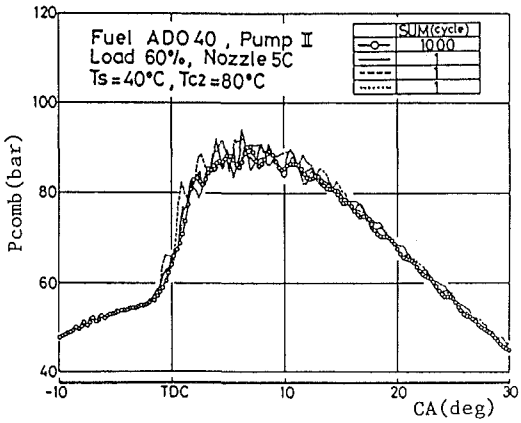


Fig. 15(*b*) Averaged cycle and individual cycles

Fig. 15 Comparison of cylinder pressure modes

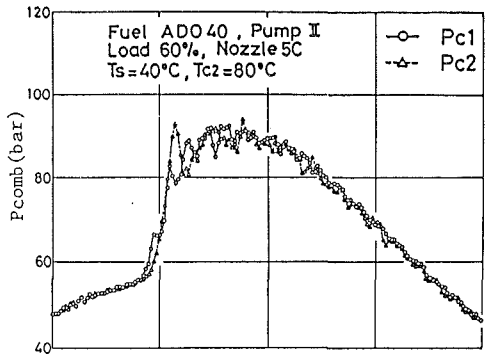


Fig. 16(*a*) A certain cycle

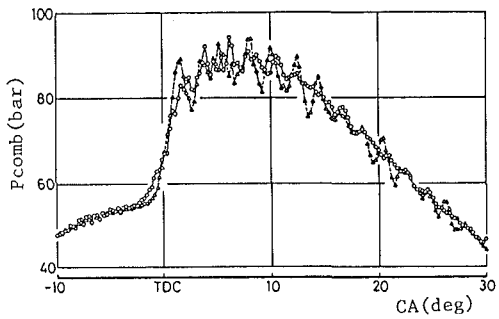


Fig. 16(*b*) Next cycle

Fig. 16 Comparison of individual cycle pressure mode between two points

two measuring points. The peculiarity of the cylinder pressure at the respective measuring points is quite obvious as shown in Fig. 15(*a*).

6 Conclusions

The multichannel combustion analyzer, multichannel vibration analyzer, and three-dimensional acoustic intensity meter were newly developed to clarify the delicate change in combustion and to analyze accurately and speedily the true nature of combustion. Combustion tests have been conducted for reducing exhaust emissions – mainly exhaust NO_x, smoke, etc. – using a small-sized high-speed diesel engine. The following conclusions were obtained by analyzing and evaluating combustion phenomena synthetically from various viewpoints of engine vibration, noise, and combustion mode.

1 In making up countermeasures for exhaust emissions, mainly NO_x, about 40 percent of the initial NO_x value was attained with fuel consumption, smoke density, and noise kept at the initial low level by applying composite countermeasures of optimization of the fuel injection system including timing retard, utilization of water-emulsified fuel and ignition improver, and an increase in air flow quantity.

2 Utilization of water-emulsified fuel for the reduction in NO_x causes increases in ignition delay, engine vibration, and noise, but vibration and noise can be reduced by adding a small amount of ignition improver without aggravating engine performance.

3 When the rate of water addition is within 20 percent, the cylinder liner temperature rises and the cooling loss increases; but as the exhaust gas temperature falls due to shortening of combustion duration, the exhaust loss decreases and there is little change in net thermal efficiency.

4 Through the newly developed combustion analyzer, it became possible to make simultaneous measurement of cylinder pressure at many points. Various phenomena in relation to combustion were evaluated independently and mutually, and the whole combustion phenomenon in the combustion chamber has been partly made clear.

Although the indicator diagram essential for combustion research has been studied thoroughly by many research people over a long period, it is still very difficult to grasp the real combustion status due to its delicate and fine destination. Through untiring research work being done in cooperation with experts from a major oil supplier and the measuring technique field, a part of the real combustion status is starting to be disclosed. Further, in concert with experts in related industries from parts of the world, the authors desire untiringly to challenge the mysterious play of combustion with the power of the younger generation, which has very pliable brains and should be able to realize the words of C. F. Kettering, "There is nothing permanent but change."

Acknowledgments

The authors wish to thank Mr. H. Imamura of Mobil Sekiyu K.K., H. Motoyama of Taiho Kogyo K.K., and their colleagues at Nagasaki University and Nagasaki Institute of Applied Science for their untiring efforts and cooperation.

References

1 Izumi, S., et al., "Degraded Fuel Combustion and Noise in High Speed Diesel Engines," D.79, 16th CIMA at Oslo, 1985–1986.

Downloaded 01 Jun 2010 to 171.66.16.87. Redistribution subject to ASME license or copyright; see http://www.asme.org/terms/Terms_Use.cfm

T. Murayama
Professor.

N. Miyamoto
Professor.

T. Chikahisa
Associate Professor.

Hokkaido University,
Sapporo, Japan

S. Tosaka
Full-Time Lecturer,
Hokkaido Institute of Technology,
Sapporo, Japan

Efficient and Low-Smoke Combustion of Various Low-Grade Fuels in High-Speed Small Diesel Engines

In low-speed large diesel engines, low-grade or heavy petroleum fuels have long been used as an economy measure. Efficient use of various low-grade fuels has recently become a topic of great concern also for high-speed small diesel engines. This paper describes and analyzes improvements of the thermal efficiency and smoke emissions by fuel heating and blending with low-viscosity fuels in high-speed diesel engines with a range of low-grade or high-viscosity fuels.

1 Introduction

With decreased availability of high-quality fuels, there is great interest in using low-grade fuels also in high-speed engines. However, these fuels usually cause poor combustion, increased exhaust gas emissions, and large deposit buildups. The objective of the investigation here is to achieve an efficient and clean combustion of high-viscosity fuels by fuel heating and by blending with low-viscosity fuels.

When fuel is heated to a sufficiently high temperature, there is a rapid formation of bubbles at the injector nozzle. The phenomenon is known as "flash-boiling," and many investigations have been conducted to apply it to improvements in spray atomization. Gerrish and Ayer [1] first applied fuel heating to internal combustion engines in 1933. More recently, the effects of fuel heating were investigated by Yamazaki et al. [2] and Kim et al. [3]. Yamazaki et al. reported improved engine performance and exhaust gas emissions in DI and IDI diesel engines, when diesel fuel and alcohol fuels were heated to 50–200°C. With flash-boiling injection of alcohol fuel, Kim et al. reported improvements in SI engine performance and dual-fueled CI engine emissions. These investigations, however, were for light fuels and for fuel temperatures up to only 200°C.

There have also been many investigations on fuel blending, particularly with alcohol fuels. Pischinger et al. [4] used emulsified fuels of methanol and gas oil blends, while Mori [5] used castor oil–ethanol–gas oil blends, both showing improved smoke and NO_x emissions. Fishinger et al. [6] investigated engine performance with soybean oil–diesel fuel blends, while Barsic et al. [7], Humke [8], and Ullman et al. [9] investigated particulate emission with vegetable oil–diesel fuel blends. They show somewhat different results, but generally, deposit and particulate emissions increase with increases in vegetable oil content.

The present investigation covers the heating range up to 450°C for B-heavy oil, solvent refined coal-2 (SRC-2), rapeseed oil, and coal oil mixtures (COM: in the experiments carbon black was used instead of coal slurry). The paper gives spray characteristics, engine performance, and exhaust gas emissions with these fuels.

2 Experimental Apparatus and Procedures

The investigation was conducted on two types of diesel engines as listed in Table 1. Engine A was used for the fuel heating experiments, and engine B was used for the fuel blending experiment.

Table 2 shows the properties of the fuels. The carbon in

Table 1 Engine specifications

Description	Engine A	Engine B
Engine name	KOMATSU 1D-105	YANMAR TR-15
Combustion chamber	Direct injection chamber	Pre-combustion chamber type
Bore × Stroke	105 × 125 mm	102 × 106 mm
Piston displacement	1082 cm³	866 cm³
Compresion ratio	17.5	19.5
Rated output	16 kW/2500 rpm	11 kW/2600 rpm
Injection pump	Bosch A-type	Bosch A-type
Plunger diameter	9.0 mm	10.0 mm
Injection nozzle	ND-DLL A152S32	NP-DN4SD24
Nozzle opening pres.	24.5 MPa(250 kg/cm²)	11.8 MPa(120 kg/cm²)

Table 2 Fuel specifications

	Diesel fuel	B-Heavy oil	SRC-2	Rapeseed oil	Carbon
Net calorific value kJ/kg	43126	41660	39750	36887	33440
Specific gravity (15°C)	0.82	0.91	0.98	0.92	—
Kinematic viscosity (30°C cSt)	4.8	51.6	7.2	51.7	—

Contributed by the Internal Combustion Engine Division and presented at the Eleventh Annual Energy-Sources Technology Conference and Exhibition, New Orleans, Louisiana, January 10-13, 1988. Manuscript received by the Internal Combustion Engine Division September 25, 1987. Paper No. 88-ICE-2.

Copyright © 1988 by ASME
Downloaded 01 Jun 2010 to 171.66.16.87. Redistribution subject to ASME license or copyright; see http://www.asme.org/terms/Terms_Use.cfm

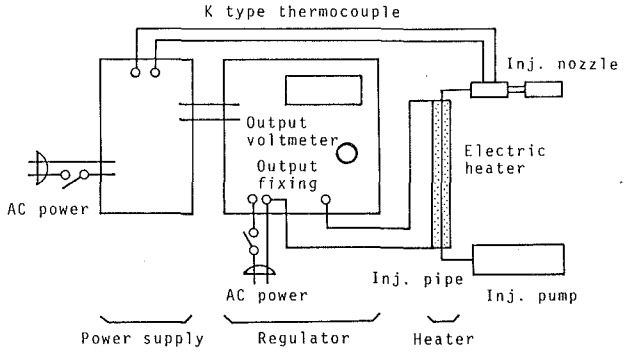


Fig. 1 Fuel heating system

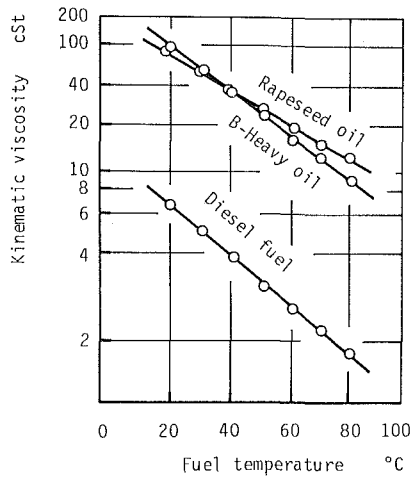


Fig. 2 Relationship between kinematic viscosity and fuel temperature for various fuels

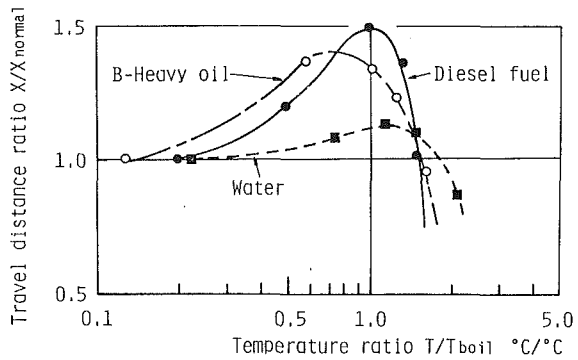


Fig. 3 Relation between fuel temperature and spray travel (at 3.0 ms after injection)

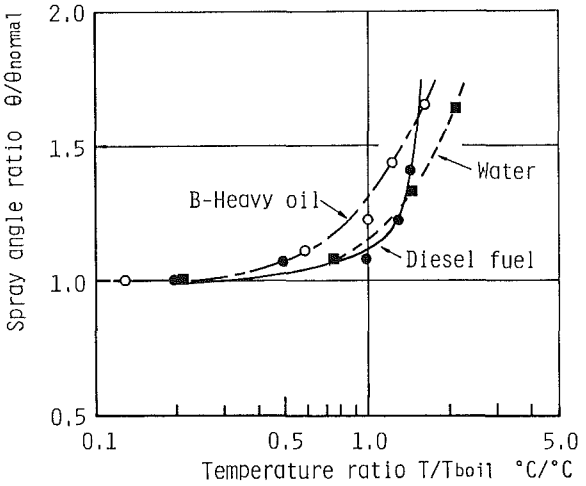


Fig. 4 Relation between fuel temperature and spray angle (at 3.0 ms *after injection*)

COM has a mean diameter of 700 nm, and it is blended in the diesel fuel with a surfactant, 1 wt. percent lecithin, to prevent precipitation of the carbon.

In the fuel heating experiment, the fuel temperature was varied from ambient to 450°C with electric heaters wound around the fuel injection pipe. An outline of the fuel heating system is shown in Fig. 1. The fuel temperature was measured with a K-type thermocouple installed at the end of the high-pressure injection pipe, and it was controlled automatically with a voltage regulator. To avoid uncontrolled injection with the heated fuel, the volume of the delivery valve in the injection pump, the springs in the injection line, and the injection nozzle were specially manufactured and adjusted.

The viscosity of the fuel was measured with a rotating cylinder viscosimeter. NO_x was measured with a CLD analyzer, and a Bosch smokemeter was used for the exhaust smoke. The HC concentration in the exhaust gas was measured with gas chromatography with an FID detector. The pressure in the main combustion chamber was A/D converted, and stored in a microcomputer. For the IDI engine, the rate of heat release was calculated from the main chamber pressure data, assuming a uniform pressure and the constituent concentration in the combustion chamber.

For the measurement of penetration distance and cone angle of the spray, photographs of the spray injected into the atmosphere were taken with a stroboscope. To measure spray droplet diameters, fuel was injected vertically down on a spray receiver filled with Peretex LT150, 880 mm below the injection nozzle. The droplets suspended in the receiver were then observed microscopically.

3 Experimental Results and Discussion

3.1 Combustion Improvements With Heated Fuels

3.1.1 Spray Characteristics With Increased Fuel Temperature. Prior to the main experiments, the viscosity of fuels, spray characteristics, and droplet size of the sprays were measured.

Figure 2 shows the temperature dependence of the viscosity for various fuels. The viscosity changes of B-heavy oil and rapeseed oil are similar, and at similar temperatures the viscosity is about ten times higher than for diesel fuel. The viscosity decreases with increasing fuel temperature.

Figure 3 shows how spray travel distance changes with temperature, and Fig. 4 shows changes in the spray angle. The abscissa is the fuel temperature ratio based on the boiling temperature, and the ordinate is the spray travel ratio and spray angle ratio relative to the values at a fuel temperature of 30°C. In the figure, 100°C is used as the boiling temperature for water, 150°C for diesel fuel, and 200°C for heavy oil.

The figures show that with fuel temperature increases the spray travel increases gradually below the boiling point and decreases dramatically above the boiling point. The spray angle also increases remarkably above the boiling point, $T/T_{boil} = 1$. The abruptly reduced spray travel and markedly expanded spray angle above the boiling point are considered to result from enhanced atomization of the fuels due to flash boiling phenomena.

Figure 5 is a microscopic comparison of spray droplets for heavy oil at fuel temperatures of 50°C and 300°C. It clearly

Downloaded 01 Jun 2010 to 171.66.16.87. Redistribution subject to ASME license or copyright; see http://www.asme.org/terms/Terms_Use.cfm

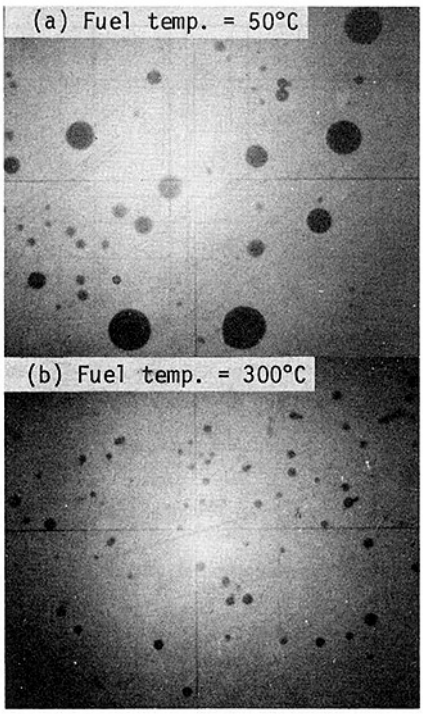


Fig. 5 Spray droplets at different fuel temperatures (B-heavy oil)

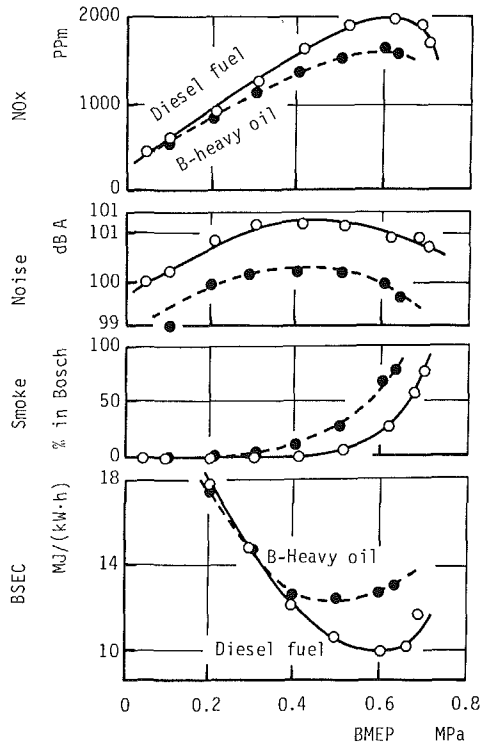


Fig. 6 A comparison of engine performance between B-heavy oil and diesel fuel without fuel heating

shows enhanced atomization of the spray with high fuel temperatures.

3.1.2 Improved Combustion of Low-Grade Fuels by Fuel Heating. The optimum fuel injection timing for brake specific energy consumption (BSEC) was almost constant, independent of fuel temperature, load, and kind of fuel. Therefore, the fuel injection timing was maintained at 13.5°CA BTDC in the following investigation for the fuel heating experiment.

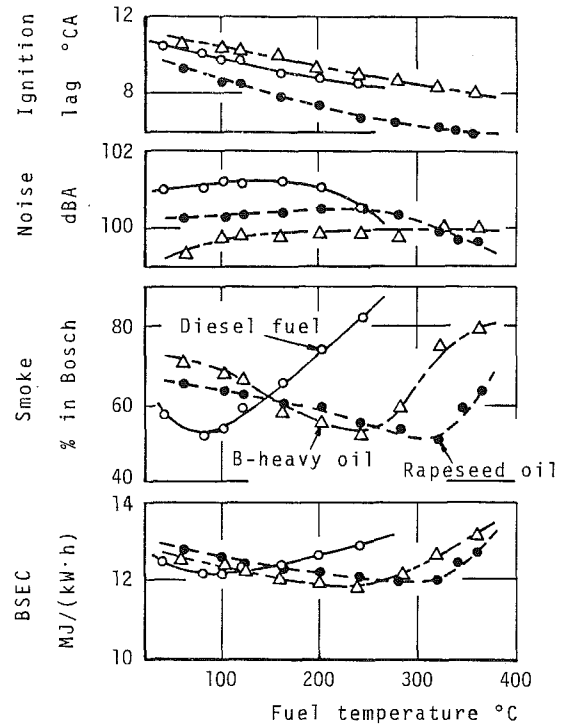


Fig. 7 Effects of fuel temperature on engine performance (diesel fuel, B-heavy oil, rapeseed oil)

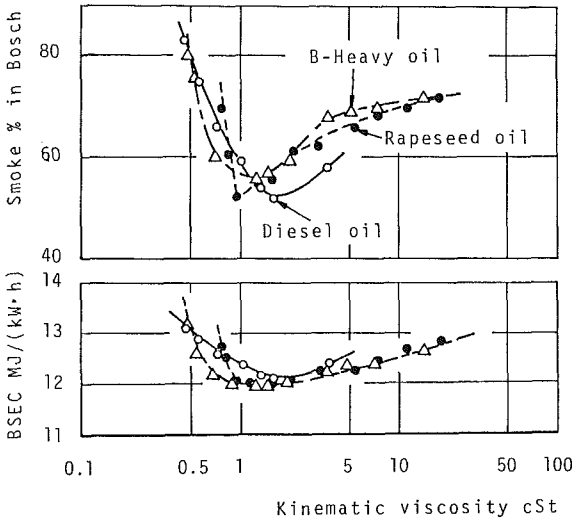


Fig. 8 BSEC and smoke emission plotted for the kinematic viscosity of heated fuels

Prior to the experiment on fuel heating, the basic engine performance with diesel fuel and B-heavy oil for the no-heating condition was compared. The result is shown in Fig. 6, which shows increased smoke and BSEC and decreased NO_x and engine noise with B-heavy oil. These differences in the two fuels become more significant in the high brake mean effective pressure range (BMEP). Thus, the object of the experiment is to remove the deterioration in BSEC and smoke by fuel heating.

Figure 7 shows the effect of the fuel temperature on engine performance at the fixed injection timing and load (BMEP). There is an optimum fuel temperature for a specific energy consumption and smoke emission for each fuel. This fuel temperature is about 90°C for diesel fuel, 240°C for B-heavy oil, and 300°C for rapeseed oil. The improvement in specific energy consumption and smoke emission is larger for heavy fuels than for diesel fuel. It was also shown that when fuel temperature increases, ignition lag and engine noise decrease,

Downloaded 01 Jun 2010 to 171.66.16.87. Redistribution subject to ASME license or copyright; see http://www.asme.org/terms/Terms_Use.cfm

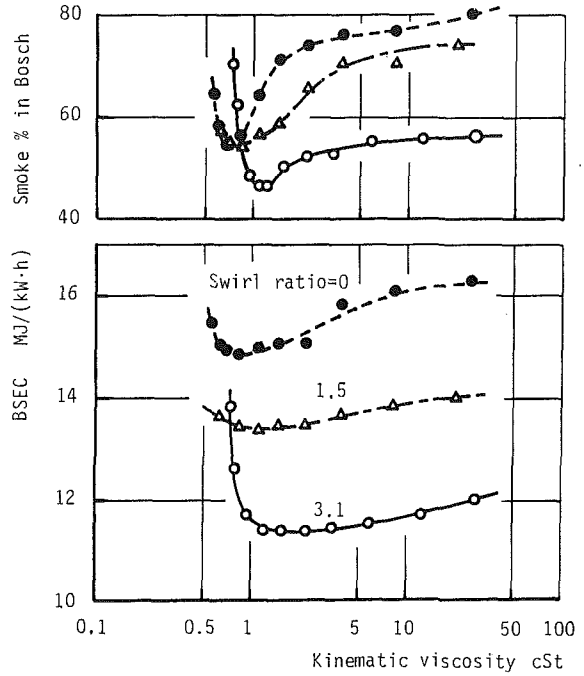


Fig. 9 Effects of swirl ratios on the changes in BSEC and smoke emissions for kinematic viscosity

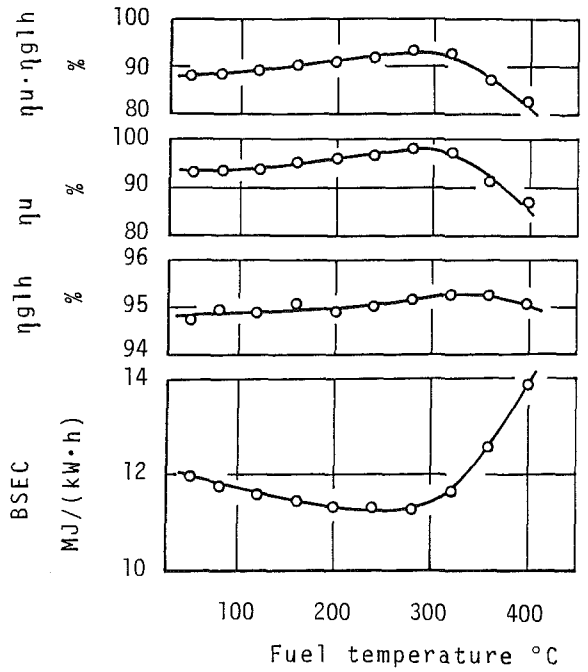


Fig. 10 Change in BSEC, degree of constant volume combustion ηglh, and combustion efficiency ηu, for different fuel temperatures (rapeseed oil)

while the NO_x concentration increases slightly with B-heavy oil and rapeseed oil.

Figure 8 is a rearrangement of the results of Fig. 7 to show the results with reference to the viscosity of the fuels, with the BSEC and smoke emissions plotted for the various fuels. The data for the three different fuels appear close together and there is an optimum value between 0.9–3 cSt. The spray characteristics are strongly affected by fuel viscosity, and this suggests that improvement in the spray characteristics is a major reason for the fuel heating effects.

To investigate the effects of viscosity in more detail, the relationship between the fuel viscosity and the engine performance was examined for various swirl ratios, as shown in Fig. 9. Fuel heating is effective also for different swirl ratios. The optimum viscosity increases slightly with increasing swirl ratio, i.e., at higher swirl ratios the fuel can be more viscous. This may be due to differences in fuel penetration.

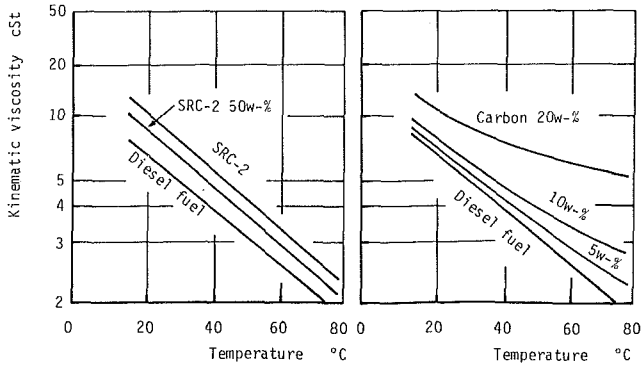


Fig. 11 Kinematic viscosity of SRC-2 and COM

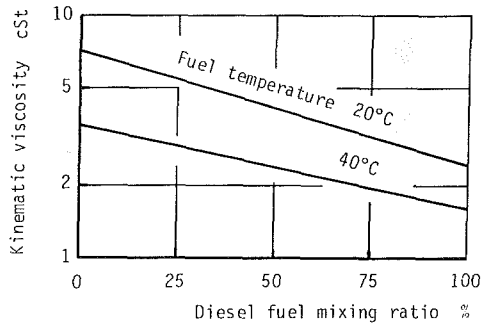


Fig. 12 Relationship between kinematic viscosity and diesel fuel-SRC-2 mixing ratio

To investigate the reasons for the improved BSEC with fuel heating, the change in degree of constant volume combustion and combustion efficiency were examined for different fuel temperatures, and the results are shown in Fig. 10. Here the combustion efficiency was calculated from the exhaust CO concentration. The combustion efficiency ηu increases with increases in the fuel temperature, while the degree of constant volume combustion ηglh also increases slightly, resulting in improved BSEC. The change in the product of ηu and ηglh corresponds to the change in BSEC. As a result the improvement in thermal efficiency with fuel heating can be considered to result mainly from improved combustion efficiency and partially from the degree of constant volume combustion.

Ordinarily, the degree of constant volume combustion decreases due to prolonged combuston when the ignition lag is short. However, with fuel heating, when the ignition lag decreases, the combustion terminates relatively fast and the degree of constant volume combustion still increases slightly, while the cooling loss and the mechanical loss appear to decrease due to the more moderate combustion. With overheated fuel, the thermal efficiency and the degree of constant volume combustion decrease significantly, possibly due to reduce spray penetration and extremely short ignition lag.

3.2 Combustion Improvements in Low-Grade Fuels by Blending With Low-Viscosity Fuels

3.2.1 Viscosity of Low-Grade Fuel - Diesel Fuel Blends. Figure 11 shows the kinematic viscosity of COM, SRC-2, and diesel fuel for different temperatures. The ordinate is in log-log, and the abscissa is in log scale. The kinematic viscosity increases, with increases in the blending ratio of SRC-2 and carbon in the fuel. For SRC-2 blended fuel, the viscosity has a linear relationship with temperature.

Downloaded 01 Jun 2010 to 171.66.16.87. Redistribution subject to ASME license or copyright; see http://www.asme.org/terms/Terms_Use.cfm

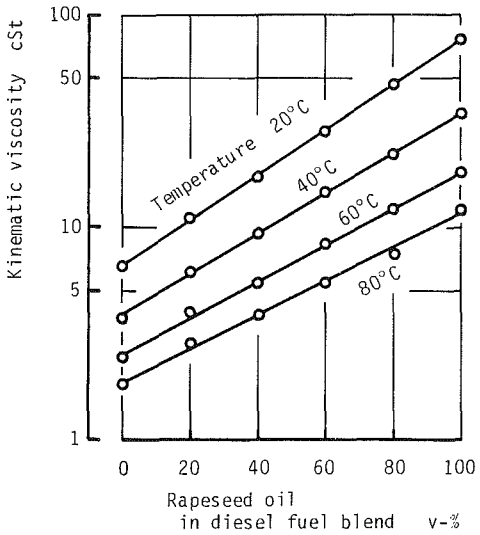


Fig. 13 Kinematic viscosity for different vegetable oil-diesel fuel blends

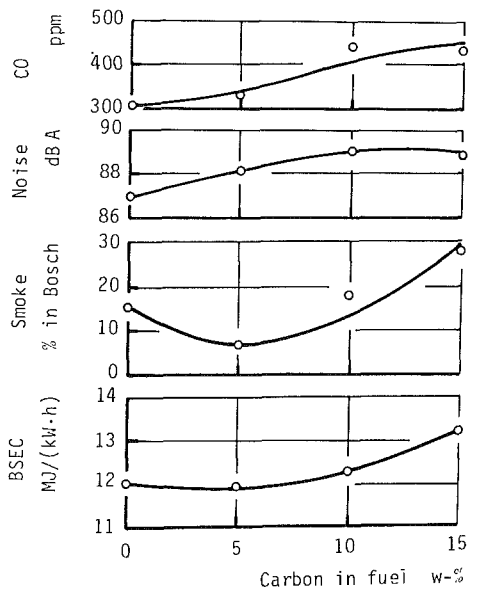


Fig. 14 Changes in engine performance and exhaust gas emissions with the blending ratios of COM (1200 rpm, BMEP = 0.5 MPa)

The kinematic viscosity of COM, on the other hand, does not show a linear relationship with temperature, as is often the case for mixtures of solids and liquids.

Figure 12 shows kinematic viscosity as a function of the diesel fuel mixing ratio at 20°C and 40°C: The ordinate is in log scale. There is a linear relationship between the viscosity and the mixing ratio at constant temperature, and the viscosity at any mixing ratio can be determined from the values of the base fuels with the following equation:

$$\log \nu = a\alpha + b$$

where ν = kinematic viscosity (cSt), α = mixing ratio (percent), and a and b = constants (for SRC-2 and diesel fuel mixture at 40°C, $a = -3.35 \times 10$ and $b = 0.545$).

Figure 13 shows the viscosities for rapeseed oil-diesel fuel blends. The ordinate is log scale, and it shows a linear relationship between the viscosity and the mixing ratio. When 20 percent diesel fuel is blended, i.e., 80 percent rapeseed oil in Fig. 13, the viscosity decreases to 1/2.

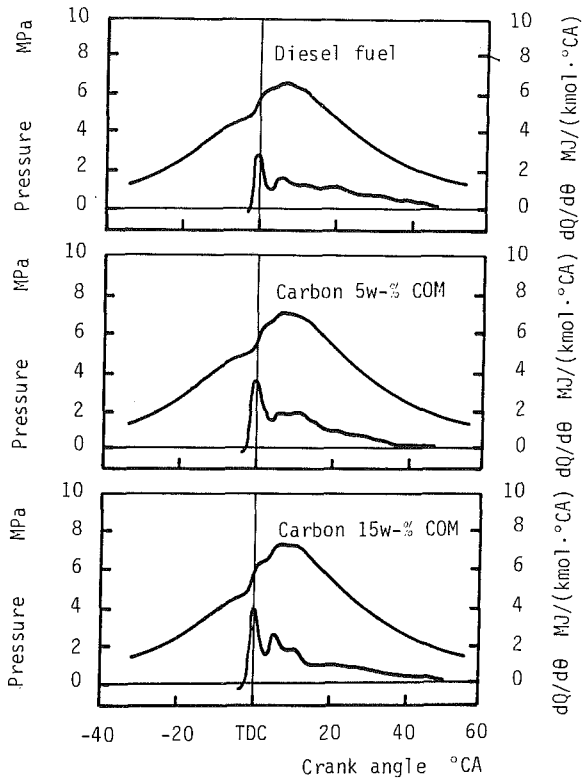


Fig. 15 Comparison of indicator diagrams and rates of heat release for different blending ratios of COM (1200 rpm, BMEP = 0.5 MPa)

3.2.2 Improved Combustion of Low-Grade Fuels by Blending With Diesel Fuel. The amount of carbon in the COM is limited by problems of wear and plugging of fuel lines. In this experiment the fuel line plugged when the carbon amount exceeded 20 wt. percent. However, there was little wear in the nozzle and the plunger of the injection pump after 50 h of operation.

Figure 14 shows the engine performance and emissions with COM as functions of the carbon ratio in the fuel. With increasing carbon content, engine noise and CO emissions increase, while the ignition lag stays constant. The smoke and BSEC show a minimum at a carbon ratio of 5 wt. percent. This corresponds to the changes in degree of constant volume combustion.

Figure 15 shows the indicator diagrams and rates of heat release for different blending ratios of COM. With increasing carbon content, the amount of premixed combustion increases, causing higher engine noise. The combustion duration is the shortest with the carbon ratio at 5 wt. percent, corresponding to the lowest smoke and BSEC. These changes appear to be caused by differences in spray atomization and penetration distance at different COM blending ratios resulting from different viscosities.

Figure 16 shows the effects of the blending ratio on engine performance and emissions when using SRC-2. With increasing SRC-2 ratio, engine noise, NO_x, CO, and CO emissions increase. The exhaust smoke decreases until a 25 vol. percent blending ratio, and for ratios above 25 vol. percent, the smoke emissions remain nearly unchanged. The brake specific energy consumption shows a minimum at 25–50 vol. percent.

The increase in engine noise and NO_x is due to longer ignition lag and larger premixed combustion of the SRC-2 blended fuel as shown in Fig. 17, which shows the indicator diagrams and rates of heat release for different SRC-2 blending ratios. The larger premixed combustion of SRC-2 is due to its lower cetane number and smaller spray droplets, compared to the

Downloaded 01 Jun 2010 to 171.66.16.87. Redistribution subject to ASME license or copyright; see http://www.asme.org/terms/Terms_Use.cfm

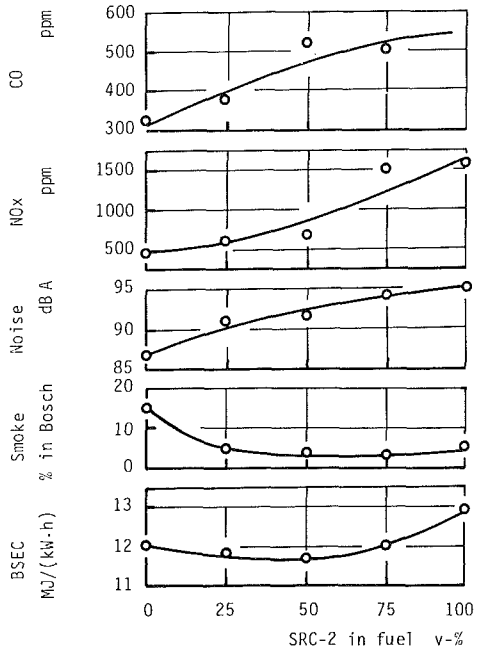


Fig. 16 Changes in engine performance and exhaust gas emissions with the blending ratios of SRC-2 in the fuel (1200 rpm, BMEP = 0.5 MPa)

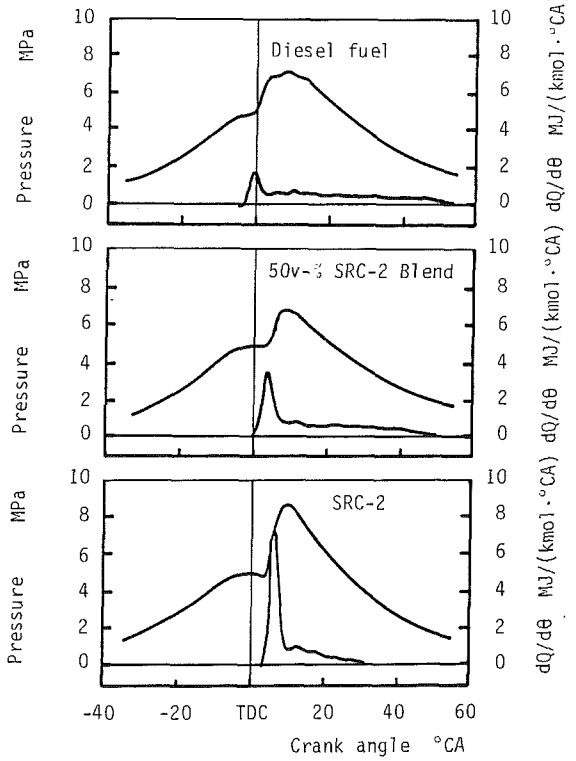


Fig. 18 Changes in engine performance for different vegetable oil-diesel fuel blends (2500 rpm, BMEP = 0.4 MPa)

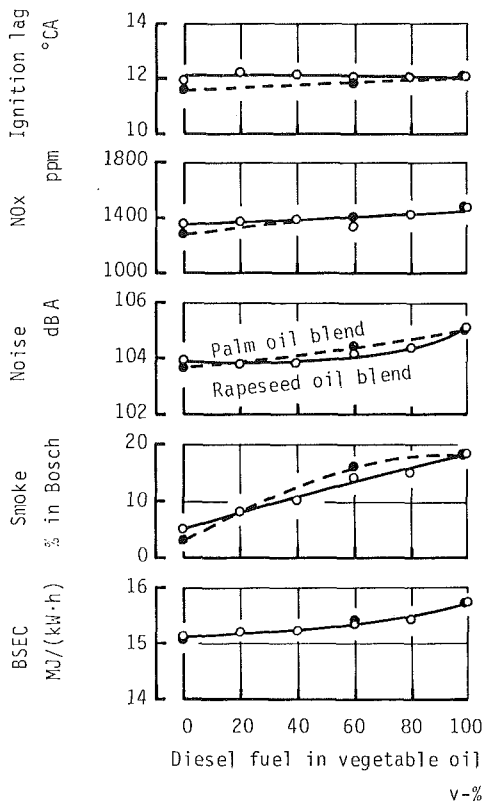


Fig. 17 Comparison of indicator diagrams and rates of heat release for different blending ratios of SRC-2 and diesel fuel (1200 rpm, BMEP = 0.5 MPa)

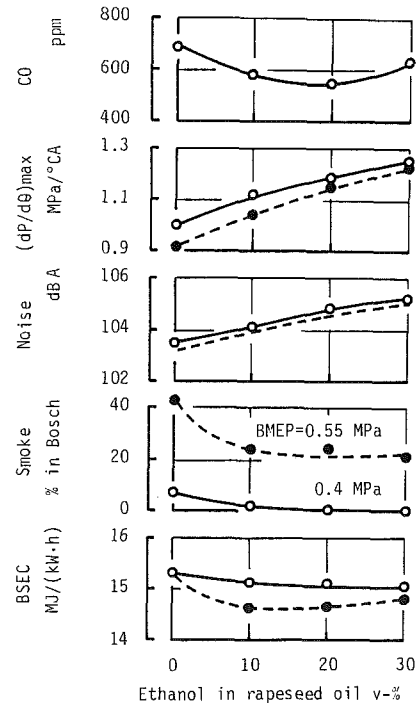


Fig. 19 Changes in engine performance for different rapeseed oil-ethanol blends (2500 rpm, BMEP-0.4 MPa, 0.55 MPa)

diesel fuel. Because of this larger premixed combustion, BSEC decreases with improvements in the degree of constant volume combustion. However, too large increases in the premixed combustion cause large mechanical and cooling losses, suggested by the large maximum pressure and rate of pressure rise, and this results in increased BSEC. The decrease in smoke emissions may be attributed to the greater premixed combustion and larger oxygen content in the SRC-2 blended fuel.

Engine performance and emissions were also investigated for rapeseed oil blended with diesel fuel. The result is shown in Fig. 18, where the fuel temperature is maintained at 56°C. As the diesel fuel content increases, BSEC, smoke density, engine noise, and NO_x concentration increase almost linearly, while the ignition lag stays constant. The reduction in smoke density with the decrease in diesel fuel content may be attributed to an

Downloaded 01 Jun 2010 to 171.66.16.87. Redistribution subject to ASME license or copyright; see http://www.asme.org/terms/Terms_Use.cfm

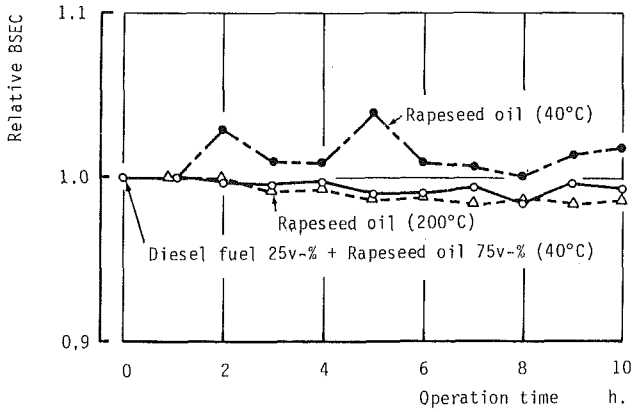


Fig. 20 Relative BSEC change in long-term operation (1400 rpm)

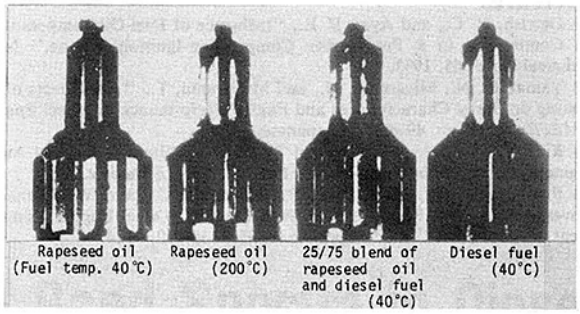


Fig. 21 Carbon deposit buildup on the nozzle tip after 10 h operation

increase in the oxygen content in the blended fuel. Although the figure shows that pure vegetable oil gives the best engine performance and emissions, a 75 percent vegetable oil–25 percent diesel fuel blend is recommended particularly because of the influence of carbon deposits, as will be explained later.

Figure 19 shows engine performance and emissions when rapeseed oil is blended with ethanol at BMEP 0.4 MPa and 0.55 MPa. As the ethanol content increases, BSEC and smoke density decrease, while the maximum rate of pressure rise and noise increase. When ethanol exceeds 30 percent, there is extraordinary combustion variation, and for efficient and clean combustion without significant increases in the engine noise the ethanol content is limited to about 10–20 percent.

When the engine was operated for extended periods with vegetable oils, there were severe carbon deposit buildup and sticking of the piston rings. The cause of these problems appears to be large droplet size, low volatility, and long penetration distance, as well as the chemical properties of vegetable oils. Heating of the fuel and blending with diesel fuel or alcohols tend to reduce the droplet size of the spray and improve evaporation, and this may reduce the carbon deposit buildup and the sticking of the piston rings.

Figure 20 shows the time history for the relative BSEC, BSEC divided by the initial value at "zero" time, when the engine has reached a steady temperature. The figure shows the results for pure rapeseed oil at 40°C and 200°C, and for the diesel fuel–rapeseed oil blend. As the preliminary experiment showed carbon deposit builds up faster at lower engine loads and speed, the engine was operated in 1 h cycles at 1400 rpm with a BMEP of 0.1 MPa for 45 min, then at 0.55 MPa for 15 min, when the measurement was conducted. The 0.55 MPa BMEP was selected for the measurements to give a more reliable BSEC than at the lower loads. Increases in the relative BSEC are considered to be caused by carbon deposits around the nozzle tip.

The figure shows that the relative BSEC for low-temperature rapeseed oil increases during long-term operation and it shows large fluctuations, suggesting extensive carbon deposit formation and frequent breaking up of the deposits. The relative BSEC for both the higher temperature rapeseed oil and diesel fuel–rapeseed oil blend show smaller fluctuations and stay almost constant, indicating that the heating of the fuels and the blending with diesel fuel are effective in reducing the carbon deposit buildups.

Figure 21 shows photographs of the carbon deposit at the nozzle tip after 10 h operation under four different conditions. The most extensive carbon deposit is with 40°C rapeseed oil, and the smallest with diesel fuel; the carbon deposits with the 200°C rapeseed oil and the diesel fuel–rapeseed oil blend fall between these two. When the engine was operated with rapeseed oil without heating, there was some sticking of the top piston ring. The heating of the fuel and the blending with diesel fuel appear to be effective in preventing the sticking of the piston ring. The recommendable blending ratio for low carbon deposits was 25 percent diesel fuel–75 percent rapeseed oil.

It was found that a higher diesel fuel content did not always result in smaller carbon deposits. This indicates that there is an optimum blending ratio for a fuel, and that a high content of low viscous fuel may cause more carbon deposits. It was also observed that there was significantly larger carbon deposit buildup on the cooler parts of the combustion chamber wall. Thus, to reduce carbon deposits it is important to maintain a sufficiently high wall temperature. More detailed specifications of the conditions under which carbon deposit buildup occurs will require further investigation.

4 Conclusion

The results obtained in this investigation may be summarized as follows:

1 At specific, higher fuel temperatures, significant reductions were obtained in the brake specific energy consumption (BSEC) and smoke emission. This results mainly from the improved combustion efficiency and degree of constant volume combustion due to enhanced atomization with the heated fuel.

2 The improvements with fuel heating are mainly a function of fuel viscosity, and are independent of the kind of fuel. In terms of BSEC and smoke emission, the optimum viscosity of the fuels was nearly identical, 0.9–3.0 cSt. The optimum viscosity increases slightly with increases in the swirl ratio in the combustion chamber.

3 Compared to the diesel fuel, Solvent Refined Coal-2 (SRC-2) blended fuel and coal oil mixture (COM) result in less BSEC and smoke, but also higher engine noise and NO_x emissions. The optimum blending ratio appears to be about 25 vol.-percent SRC-2 and 5 wt. percent carbon in the fuels. Blending 25 vol. percent diesel fuel with rapeseed oil suppressed carbon deposit buildup dramatically with a minimum increase in BSEC, smoke, and engine noise.

4 Carbon deposit buildup and piston ring sticking, primary problems especially in regular long-term operation with high-viscosity fuels, were improved significantly by fuel heating and blending with low-viscosity fuels.

Acknowledgments

The authors wish to express their appreciation to General Sekiyu of the R&D Encouragement & Assistance Foundation for his financial aid for this project. Appreciation is also extended to Dr. H. Ogawa and Dr. Y. Oh for their cooperation in this investigation.

Downloaded 01 Jun 2010 to 171.66.16.87. Redistribution subject to ASME license or copyright; see http://www.asme.org/terms/Terms_Use.cfm

References

1 Gerrish, H. C., and Ayer, B. E., "Influence of Fuel-Oil Temperature on the Combustion in a Prechamber Compression-Ignition Engine," NACA Technical Note 565, 1933.

2 Yamazaki, N., Miyamoto, N., and Murayama, T., "The Effects of Fuel Heating on Spray Characteristics and Engine Performance in Diesel Engine," *JSME(B)*, 1983, pp. 49–499 [in Japanese].

3 Kim, Y., Iwai, N., Suto, H., and Tsuruga, T., "Improvement of Alcohol Engine Performance by Flash-Boiling Ignition," *JSAE Review*, 1980.

4 Pischinger, F. F., Burghardt, P., Havenith, C., and Weidmann, K., "Investigations on a Passenger Car Swirl-Chamber Diesel Engine Using Different Alcohol Fuels," SAE Paper No. 830552, sp-542, 1984.

5 Mori, M., "Ethanol Blended Fuels for Diesel Engine," 4th Int. Symp. on Alcohol Fuel Tech., 1980.

6 Fishinger, M., Engelman, W., and Guenther, D., "Service Trail of Waste Vegetable Oil as a Diesel Fuel Supplement," SAE Paper No. 811215, 1981.

7 Barsic, N. J., and Humke, A. L., "Performance and Emissions Characteristics of a Naturally Aspirated Diesel Engine With Vegetable Oil Fuels," SAE Paper No. 810262, 1981.

8 Humke, A. L., and Barsic, N. J., "Performance and Emissions Characteristics of a Naturally Aspirated Diesel Engine With Vegetable Oil Fuels (Part 2)," SAE Paper No. 810955, 1981.

9 Ullman, T., Hare, C., and Baines, T., "Heavy-Duty Diesel Emissions as a Function of Alternate Fuels," SAE Paper No. 830377, 1983.

Downloaded 01 Jun 2010 to 171.66.16.87. Redistribution subject to ASME license or copyright; see http://www.asme.org/terms/Terms_Use.cfm

Behavior of Band Spectra in Diesel Combustion Flames: a Study on Chemical Reactions in Diesel Combustion

K. Nagase
Senior Researcher.

K. Funatsu
Researcher.

Car Laboratory,
Railway Technical Research Institute,
The Japan Railways Group (JR),
Tokyo, Japan

When a precombustion chamber type Diesel engine is operated under light loads and at low speeds, it is observed that the ignition flames in its main combustion chamber are generated in several stages under specific conditions of fuel injection. The authors, by observing the multistage ignition flames through an optical fiber probe inserted into the chamber, confirmed a number of band spectra emitted from some substances and CH radicals, existing in the flames, and have made clear some aspects of the chemical reactions taking place in Diesel combustion.

Introduction

The spectra of combustion flames contain a lot of information on their properties, state of combustion, intermediate products in the process of combustion, etc. In case of Diesel engines, therefore, spectral analysis has been regarded as an effective means to make clear the real state of combustion and, accordingly, investigations on the measurement of flame spectra in this analysis have been carried out and the results have been reported [1, 2].

However, all the wavelengths measured in those investigations have been limited to the intermediate infrared range. Further, as the influence of soot adhering to the observation window was not always sufficiently evaluated, the measured values could hardly be regarded as correct.

Most of the band spectra emitted from the flames (which are generated by the chemical reaction) in the combustion process of hydrocarbon are in the ultraviolet and visible ranges [3]. These flames are called "low-temperature flames," and their existence has long been confirmed with spark ignition engines [4]. In the case of Diesel engines, existence of the low-temperature flames has been inferred [5]. However, their measurement has been thought impracticable because of the adverse effects of soot and the like [2]. As previously reported, the authors inserted heat-resistant optical fibers sealed in special metallic holders into the combustion chambers of a Diesel engine, and after evaluating the effect of soot adhering to the window, proposed a measuring method for the flame spectra in the visible and near-infrared ranges [6]. Even by this method, however, measurement of the spectra in detail has been impossible so far.

The authors inserted an optical fiber into the main combustion chamber of a precombustion chamber type Diesel engine, and confirmed the band spectra of C_2, H_2O, and CH radicals existing when the flame spectra exit successively in several stages from the main chamber (referred to as "multistage ignition" hereafter), only when the engine is operated in the low-speed and light-load modes.

Experimental Apparatus

The experimental apparatus used in this study are described briefly in the following.

Test Engine and Fuel. The test engine is a single-cylinder precombustion chamber type built on the basis of a standard high-speed Diesel engine DMF15HS type for railway cars, specifications of which are shown in Table 1. It is directly coupled with a Ward-Leonard controlled d-c motor. Starting, loading, and speed control of the test engine are done through the motor. A supercharger is not used, and the air is supplied at the specified temperature and pressure by an independent blower system, corresponding to the operation mode of the engine. The fuel is JIS No. 2 gas oil.

Fuel Injection Control System. In addition to the conventional overflow type fuel injection pump originally built into the engine, another fuel injection and control system previously proposed by the authors [7, 8] was used, which freely controls the injection period and quantity by electronically con-

Table 1 Specification of JR type DMF15HS Diesel engine

Items	Type and dimensions
Combustion chamber	Pre-combustion chamber
Number of cylinders	6
Bore	140 mm
Stroke	160 mm
Rated speed	1600 rpm
Rated output	140kW

Contributed by the Internal Combustion Engine Division and presented at the Eleventh Annual Energy-Sources Technology Conference and Exhibition, New Orleans, Louisiana, January 10–13, 1988. Manuscript received by the Internal Combustion Engine Division August 10, 1987. Paper No. 88-ICE-3.

Copyright © 1988 by ASME
Downloaded 01 Jun 2010 to 171.66.16.87. Redistribution subject to ASME license or copyright; see http://www.asme.org/terms/Terms_Use.cfm

trolling the fuel injection pressure (referred to as "injection pressure control system" hereafter).

Spectrophotometric Device Using Optical Fibers. Figure 1 shows the layout for detection and spectroscopic analysis of the flame using the optical fibers. This layout and the method for evaluating the attenuation due to soot adhering to the light incidence end of the optical fiber (referred to as "loss by soot" hereafter) are the same as those in the previous report [6]. As shown in Fig. 1, the visual field of the fiber is about 20 deg at the light incidence end. It is too narrow to cover the whole volume of flame. As a countermeasure, use of a beam condensing lens or optical fiber of special plastic with a higher numerical aperture could be considered. However, the lens involves the risk of decreased transmission of some specific spectra due to aberration, while the plastic fiber requires a cooling device to cope with its inferior resistivity to heat. On the other hand, cooling might result in an increased difficulty due to the more soot adhering to the cooled window at lower temperature. Accordingly, with the understanding of the problem in the visual field, the present practice has been adopted, giving priority to its simplicity, convenience, and maintenance. The optical fibers are quartz fibers with excellent transmission characteristics for the spectra in visible and near-infrared ranges currently used for telecommunication. In some specific cases, quartz with superior transmission characteristics for ultraviolet spectrum range as shown in Fig. 2 is used.

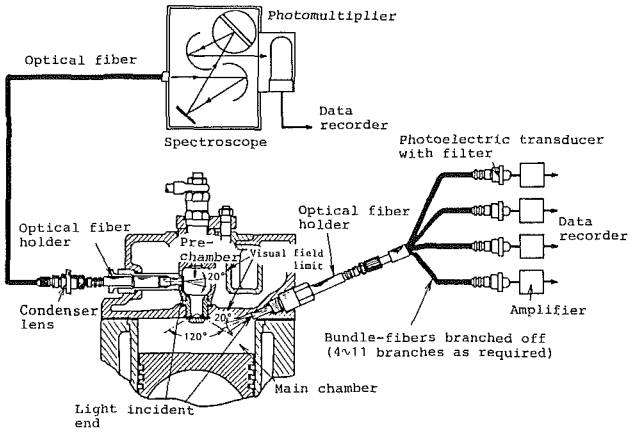


Fig. 1 Schematic diagram of flame detecting and measuring system

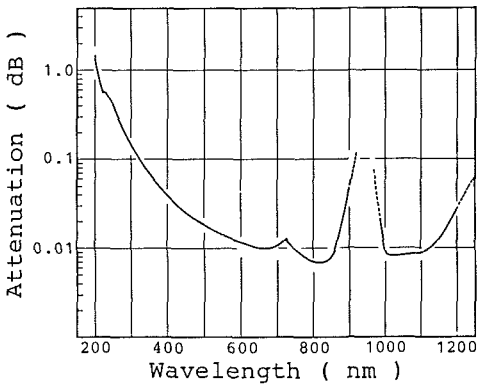


Fig. 2 Transmission characteristic of optical fiber

Under some specific operation modes in which loss by soot underwent no change while running the engine, in addition to the method previously described [6], another analysis was employed in the following way. The input flame image was transmitted through a fiber to the spectroscope with half width of 0.5 nm, as shown in the top of Fig. 1. After the image was divided into fine spectral widths successively (not simultaneously) by the spectroscope, it was converted into electric energy, amplified in the electronic photomultiplier, and stored in the data recorder. Effective sensitivity limit of the photomultiplier was 190 nm and almost all the spectra existing in the low-temperature flames could be detected. Also, a camera with normal spectral sensitivity film (ISO 3000) was set in place of the photomultiplier to take the flame spectrograms.

Multistage Ignition

Multistage Ignition Under Injection Pressure Control. When the test engine was run at its medium speed (1200 rpm), ignition flame could scarcely be observed in the main combustion chamber in the light-load range, when a high injection pressure was used [8]. Figure 3 shows an example of the change of combustion flame related to the change of injection pressure set at every 2.0 MPa from 11.8 MPa up to 21.6 MPa. The group of curves with identical index numbers (from 1 at the top down to 5 at the bottom) shows, respectively: (1) needle valve lift; (2) in-cylinder pressure (1.96 MPa/div); (3) prechamber flame; (4) main chamber flame; (5) crank angle. Each flame curve is a superposition of five exposures. Center wavelength of filter is 950 nm. Crank position is marked every 10 deg (5 deg for each 10 deg before and after TDC). Loss by soot was not compensated for.

In order to detect a faint flame as accurately as possible in the main chamber, the ratio of its amplification to that of prechamber was set at 4 times for the injection pressures 11.8~13.8 MPa, 25 times for 15.7 MPa, and 200 times for higher pressures. Even with such an increased amplification, the flame is hardly detected in the main chamber at high injection pressures. At 17.7 MPa, generation of very faint flames in two stages was observed. Multistage ignition phenomena of this kind were observed more clearly in the lower speed range.

Multistage Ignition in Case of Overflow Type Injection Pump. It was first thought that such multistage ignition as above could take place only in under specific conditions of control by means of injection pressure. Therefore, the authors tried the conventional overflow type injection pump on the same engine in various running conditions. Figure 4 is an example of the most distinguished multistage ignition, wherein the load was 50 percent, and the static injection timing was set constant at −37.5 deg CA, originally to be used in the speed range above 1200 rpm. Under the condition fixed as above,

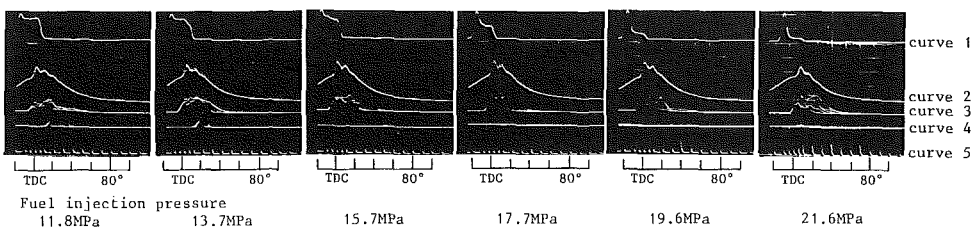


Fig. 3 Behavior of combustion flames under various injection pressures

Downloaded 01 Jun 2010 to 171.66.16.87. Redistribution subject to ASME license or copyright; see http://www.asme.org/terms/Terms_Use.cfm

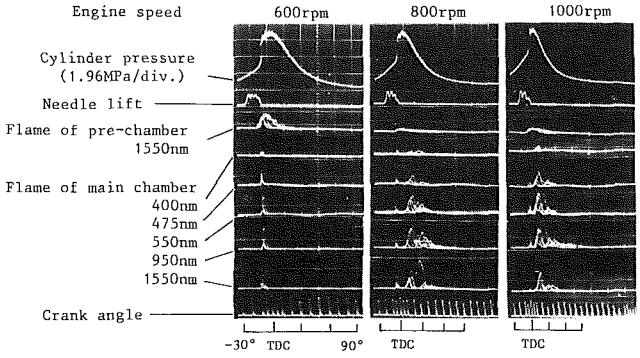


Fig. 4 Generation of multistage ignition at various speeds

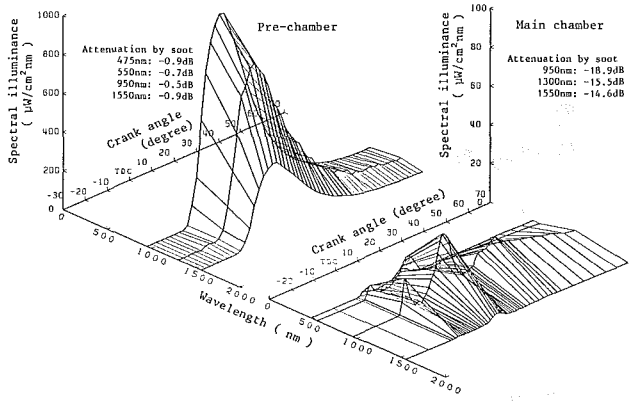


Fig. 5 Spectral emission from both chambers compared (multistage ignition in main chamber "M.S.I." hereafter)

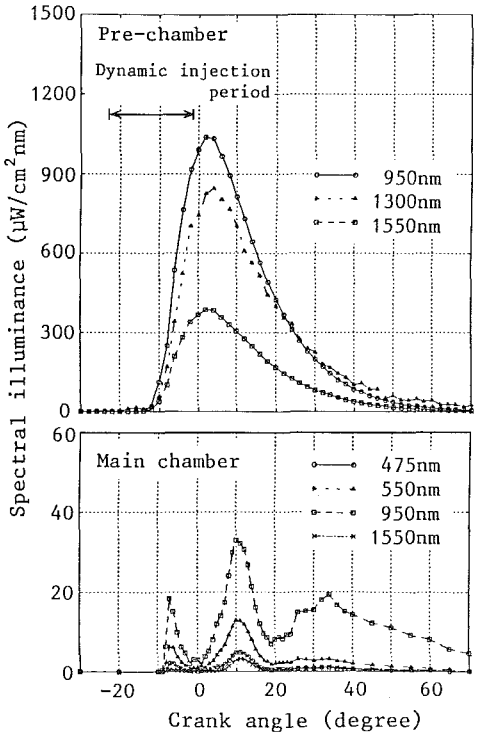


Fig. 6 Change of spectra in both chambers following the crank motion (M.S.I.)

the engine was run at various speeds. Figure 4 shows the flames in the prechamber and those of various wavelengths in main chamber. As shown in the figure, smooth combustion is observed in the prechamber throughout all the speed ranges, whereas generation of marked multistage ignition is seen in the

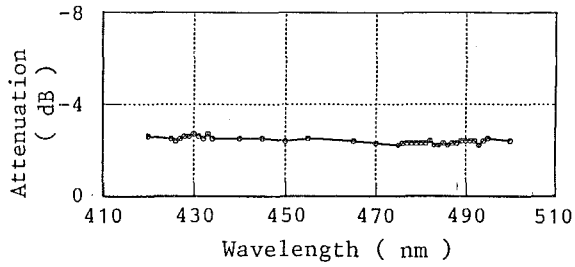


Fig. 7 Transmission decrement at the window of main chamber (M.S.I.)

main chamber at 800 rpm. Maximum value of the injection pressure in this case is about 17.7 MPa, identical with that in the experiments of Fig. 3. However, with these data only, it is impossible to make clear the behavior of flames in both combustion chambers.

Results of Experiments and Comments

Causes for Multistage Ignition. As shown in Figs. 3 and 4, no abnormality is detected in the behavior of the needle valve lift at the generation of multistage ignition. Consequently, the phenomena are not attributable to injection systems. Therefore, the authors examined the change of flame spectra in both chambers in the operation mode shown in Fig. 4.

The result is shown in Fig. 5, and cross sections of Fig. 5 at several wavelengths are given in Fig. 6. The number of wavelengths was limited to four for reasons of the instrumentation. All measured values in these figures are the mean values of 100 strokes with compensation for loss by soot given in Fig. 5 for each wavelength. Also, dynamic injection period is given in Fig. 6.

Spectral illuminance of the prechamber flame is high. It implies the generation of an intense flame. However, attenuation due to soot on the window is also large as given in Fig. 5, and illuminance measurement was impossible in the visible range (550 nm) where the attenuation was too large. Compared with the smooth combustion in the prechamber, ignition in the main chamber took place in about three stages. Although presumption of the causes for such phenomena is very difficult, the authors would like to analyze as follows:

1 When a small quantity of fuel is injected into the prechamber at high pressure, a heavy mist is formed there. Moreover, as the fuel injection is done rather earlier than TDC, it takes a long time before the fuel mist is ignited. This ignition time lag let the strong blowing up from the main chamber continue and diffuse farther the fuel mist. As a result, combustion is almost completely done in the prechamber, leaving little for the main chamber.

2 As the injection pressure is lowered, and together with it, the injected fuel quantity increases, and a part of flame and fuel gets into the main chamber, causing the combustion also to take place in the main chamber.

3 However, in addition to the blowing up from the main chamber to the prechamber around TDC, the cooling effect [9] on the mixture in the narrow space above the piston head is also strong. Therefore, even if a faint flame is generated in the main chamber under such circumstances, it becomes difficult to keep the flame burning, and the flame disappears halfway.

The phenomenon that all of the multistage ignition flames are once extinguished near TDC is presumably caused by the above-described process.

Band Spectra of Visible Wavelength Range. The result of a long run test under the condition of 880 rpm and 50 percent load resulting in the frequent generation of multistage ignition showed no change in loss by soot of flame spectra in the main chamber. Figure 7 shows loss by soot corresponding to the

Downloaded 01 Jun 2010 to 171.66.16.87. Redistribution subject to ASME license or copyright; see http://www.asme.org/terms/Terms_Use.cfm

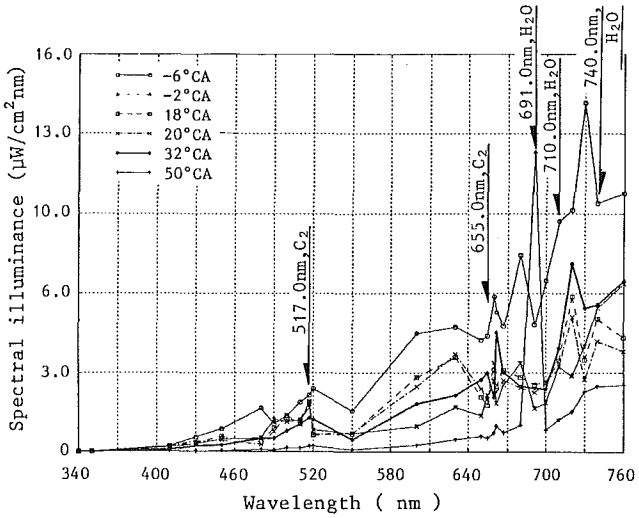


Fig. 8 Visible range spectra at principal crank angles (M.S.I.)

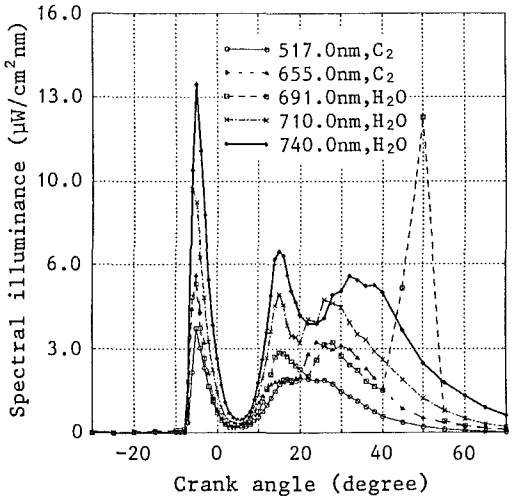


Fig. 9 Change of visible range spectra following the crank motion (M.S.I.)

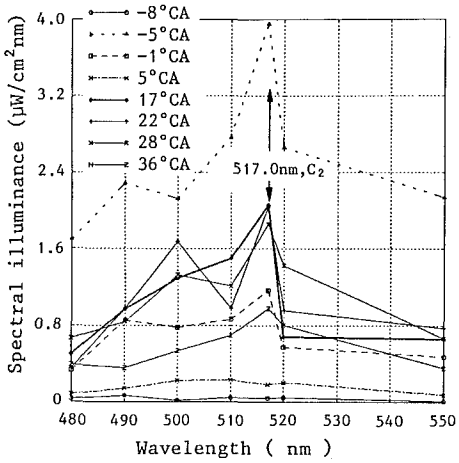


Fig. 10 Detail of the wavelength range around 517 nm (C_2 band spectrum) at principal crank angles

wavelength in the above test. Under such circumstances, correct results in analyzing the flame spectra were obtained by means of a sequential or successive process, combining a spectroscope and electronic photomultiplier as shown on the left side of Fig. 1. Thus, the authors measured the visual flame spectra of multistage ignition in the operation mode nearly the same as the above, using the overflow type pump. Figure 8 shows the flame spectra derived from the data obtained by the above method at the principal crank angles. The increment of the measured wavelength was about 5 nm, but it was adjusted finer or coarser according to the degree of steepness in the change of spectral illuminance. This diagram shows that the band spectra of C_2, H_2O, etc., exist in the flames of multistage ignition.

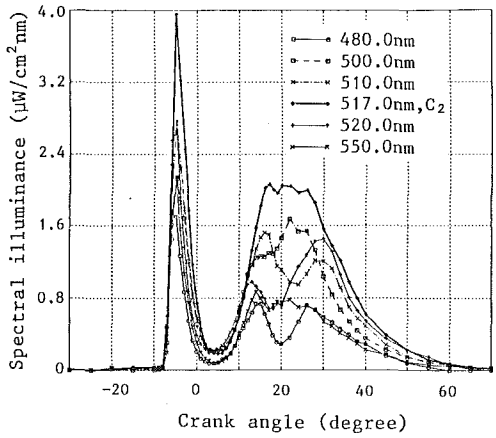


Fig. 11 Change of the spectra in Fig. 10 following the crank motion

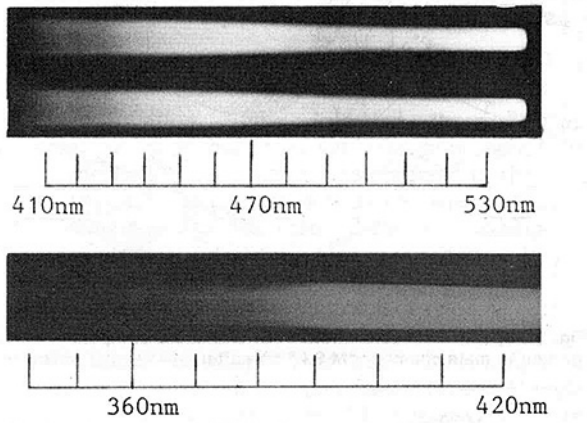


Fig. 12 Spectrogram of M.S.I. (center wavelength of the spectrograph = 470 nm, 380 nm)

In order to make it more clear and accurate, changes of the band spectra (of Fig. 8) following the piston or crank motion are shown in Fig. 9. Figure 10 shows a spectrogram in the range of 517 nm wavelength in detail where C_2 band spectrum is detected as in Fig. 8. Figure 11 shows the changes of spectra in this range following the piston stroke. As in shown by a change of the H_2O band spectrum at about 50 deg CA in Fig. 9 for example, distinguished generation of a specific band spectrum is observed at a specific position in the piston stroke. The process of carbon production in the flame is also surmised from Figs. 11 and 12. It is mentioned that minute errors resulted in wavelength because of the lost motion in the driving mechanism for diffraction grating in the spectroscope.

Band Spectrum of CH Radial. The details of spectral range including the band spectrum of CH are not clearly seen in Fig. 8. Therefore, the authors tried to take a photo of a spectrogram for the wavelength range covering the ultraviolet and visible rays using a special optical fiber with excellent ultraviolet transmission. As a result of the trial, existence of spectra was confirmed in the range of wavelengths down to about 350 nm. Examples are given in Fig. 12, which was taken by means of the spectrometer with its center wavelength set at 380 nm and 470 nm.

Downloaded 01 Jun 2010 to 171.66.16.87. Redistribution subject to ASME license or copyright; see http://www.asme.org/terms/Terms_Use.cfm

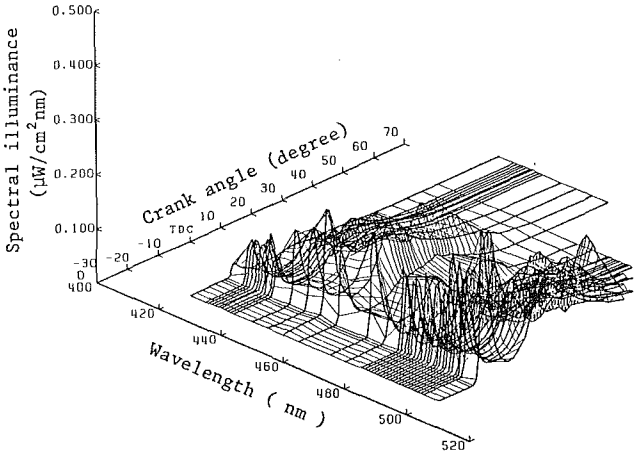


Fig. 13 State of spectra in the range of 420 nm ~ 500 nm wavelengths at various crank angles

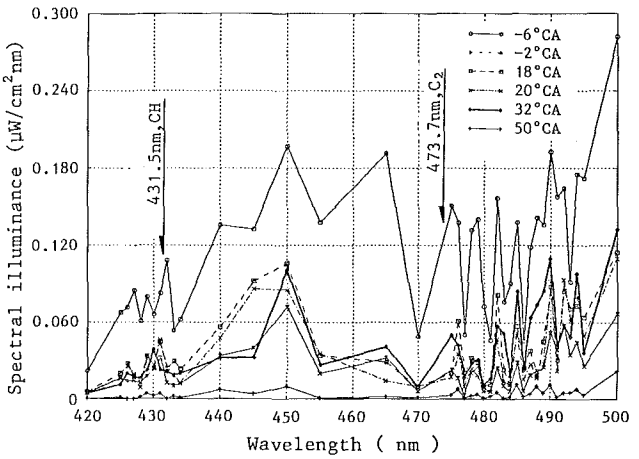


Fig. 14 420 nm ~ 500 nm spectra at principal crank angles

Next, the range of wavelengths from 420 nm to 500 nm was measured under conditions almost the same as in Fig. 8. Figure 13 is the result, and Fig. 14 shows the profiles of sections obtained by slicing Fig. 13 at specific stroke positions. The detail of spectra in the neighborhood of 430 nm is shown in Fig. 15, and Fig. 16 shows their change in Fig. 15, following the piston or crank motion. Figure 17 shows the equivalent for the spectra around 480 nm. As shown by the data in Fig. 14, the band spectrum of the radical CH (431.5 nm)—regarded as a low-temperature flame—exists in Diesel combustion flames, although the illuminance of these band spectram is low. This band spectrum is generated at high temperature and high pressure. The phenomenon of marked radiation of this spectrum prior to the generation of bright flame was not observed.

Again, the authors measured the range of wavelengths below 420 nm. However, the spectral illuminance in this range was so faint that the band spectra of CHO (387 nm) and OH (306 nm) radicals—both had been surmised to be in this range and detectable by the aforementioned apparatus—were not at all detected.

Chemical Reactions in Diesel Combustion. As shown in Figs. 13 and 14, a band spectrum is emitted from the CH radical under high pressure and temperature and together with many other spectra. The authors did not observe a phenomenon characteristic of spark ignition engines, in which band spectra of this kind were generated in advance of the bright flames [4]. As shown in Figs. 15 and 16, these band spectra exist not only in the early stage of combustion, but also hold considerably long in the burning flame. On the other hand, the existence of the C_2 band spectrum (517 nm) was

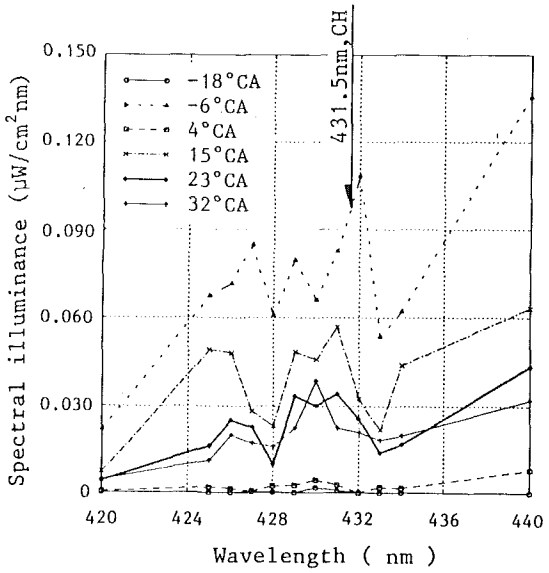


Fig. 15 Detail of the spectra around 430 nm at principal crank angles

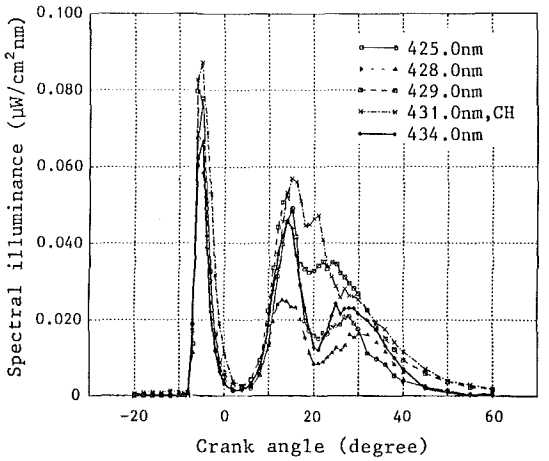


Fig. 16 Change of the spectra around 430 nm following the crank motion

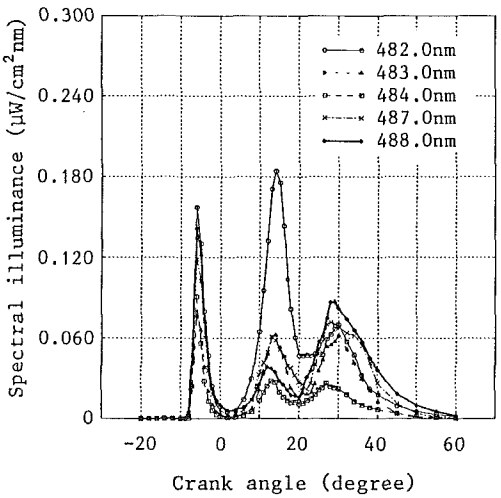


Fig. 17 Change of the spectra around 480 nm following the crank motion

already detected at the initial stage of combustion (−5 deg CA), as shown by Figs. 10 and 11. Accordingly, in the case of multistage ignition, it is likely that the thermal cracking of fuel (hydrocarbon) takes place not only at the beginning of com-

Downloaded 01 Jun 2010 to 171.66.16.87. Redistribution subject to ASME license or copyright; see http://www.asme.org/terms/Terms_Use.cfm

bustion, but continues over a long period, and that carbon exists in the flame already in the earliest stage of combustion.

As shown in Figs. 8, 14, and 17, in the range of wavelengths near 485 nm and 630 nm, a remarkable generation of band spectra is observed, names of the related emitting substances being unidentified, at some specific stroke positions. It is inferred from such phenomena that various complex intermediate products are yielded in the combustion process of the flames. Analysis of those intermediate products will be the subject of research in the future.

As described above, a variety of band spectra is contained in Diesel flames. It is presumed that those band spectra are generated by light-emitting chemical reactions inherent in the combustion of complex paraffin series hydrocarbons. It must also be mentioned that the range of wavelengths without any remarkable band spectrum is not so wide in the case of Diesel flames, as shown by Figs. 8 and 14. From this point of view, it is essential to be very cautious in selecting the suitable wavelength of the spectrum, in the case when its illuminance is to be measured by means of two-color method [10].

According to Lyn, the spectra of Diesel combustion flames in the intermediate infrared range are quite similar to those of the diffusion flames of acetylene [1]. On the other hand, when air is mixed into the acetylene diffusion flames, the spectral configuration changes completely and prominent band spectra are generated. Therefore, in the case of band spectra measurement for Diesel combustion flames, which has been difficult because of the adverse effect of soot, it may be suggested to employ some means of burning the flame in an excessive supply of air, for instance, such as the multistage ignition in the current experiments, in which a very small flame was blown out from the prechamber. The measurement would then be considerably facilitated.

Conclusions

The authors inserted optical fibers into the combustion chambers of a precombustion chamber type Diesel engine, and carried out a measurement of spectra emitted by the Diesel combustion flame and an analysis of burning flames in the low-speed range of the engine. As the result of the experiments, the following facts have been made clear:

1 When the engine is operated under light load and at low speed, the phenomena of "multistage ignition" are observed, in which the ignition flames are generated in the main combustion chamber in several stages under some specific conditions of fuel injection.

2 The multistage ignition flames are generated under certain circumstances, i.e., the air blown up from the main chamber promotes the diffusion of fuel mist in prechamber, and the faint flames blown out from the prechamber or generated in the main chamber are extinguished halfway due to the cooling effect by the narrow piston clearance near TDC.

3 Existence of the band spectra from C_2, H_2O, and CH radicals has been confirmed in the multistage ignition flames.

4 In the multistage ignition flames, a band spectrum, that of the CH radical at 431.5 nm, exists at high temperature and high pressure, and no distinguishable light is observed prior to the generation of bright flame.

5 Spectra of CHO and CH radicals, which are presumed to be in the range of wavelengths shorter than 400 nm, are not detected.

6 The Diesel combustion flame contains a number of band spectra emitted presumably from the intermediate products of the combustion process, which cannot be identified.

7 In the course of the above experiments, some aspects of the chemical reaction in Diesel combustion have been made clear.

Acknowledgments

Throughout the course of the investigation, Professor Emeritus Dr. G. T. Sato and Professor Dr. O. Kawaguchi of Keio University, Professor Dr. H. Fujimoto of Dohshisha University, and Assistant Professor Dr. A. Yoshida of Tokyo Denki University; encouraged the authors with valuable advice. In executing the experimental work, members of the Control Research Group for Diesel Cars, Car Control Laboratory, Railway Technical Research Institute, Japanese National Railways—The Japan Railways Group (JR) at present—gave the authors close cooperation. The authors would like to express sincere gratitude for their advice and cooperation.

References

1 Lyn, W. T., "Diesel Combustion Study by Infra-red Emission Spectroscopy," *Journal of the Institute of Petroleum*, Vol. 43, No. 398, 1957, pp. 25–46.

2 Heinrich, G., Prescher, K., and Finsterwalder, G., "Spektrometrisches Mess-verfahren zur Untersuchung der Verbrennung im Dieselmotor," *MTZ*, Vol. 39, No. 9, 1978, pp. 385–390.

3 Lewis, B., and Elbe, G., *Combustion, Flames and Explosions of Gases*, Academic Press, New York, 1951.

4 Ball, G. A., "Photographic Studies of Cool Flames and Knock in an Engine," *5th Symposium on Combustion*, 1955, pp. 366–372.

5 Kawaguchi, Y., Terada, K., Masuda, M., and Maki, T., "An Optical Study on Diesel Combustion in Dual Fuel Injection System," *Journal of JSME*, Vol. 45, No. 392, 1979, pp. 589–596 [in Japanese].

6 Nagase, K., Funatsu, K., Muramatsu, Y., and Kawakami, M., "An Investigation of Combustion in Internal Combustion Engine by Means of Optical Fibers," *Trans. SAE*, No. 851560, 1986, pp. 5817–5827.

7 Nagase, K., and Fukushima, Y., "A Fuel Injection System for Diesel Engine by Injection Pressure Control," *Bull. JSME*, Vol. 29, No. 252, 1986, pp. 1788–1794.

8 Nagase, K., Yamane, A., and Funatsu, K., "An Investigation Into the Behavior of Burning Flame in the Diesel Engine Combustion Chamber," The 17th CIMAC Conference, No. D-58, June 1987.

9 Nishida, K., Hiroyasu, H., Ariai, M., and Yoshikawa, S., "Characterization of Combustion Processes in the Pre-chamber and Main Chamber of an Indirect Injection Diesel Engine by High-Speed Photography," SAE Paper No. 861181, 1986.

10 Uyehara, O. A., Myers, P. S., Watson, K. M., and Wilson, K. M., "Flame-Temperature Measurement in Internal-Combustion Engines," *Trans. ASME*, Vol. 68, No. 1, 1946, pp. 16–30.

11 Robinson, J. W., *Handbook of Spectroscopy*, Vol. 1, CRC Press, FL, 1979.

Downloaded 01 Jun 2010 to 171.66.16.87. Redistribution subject to ASME license or copyright; see http://www.asme.org/terms/Terms_Use.cfm

Self-Ignition of Diesel Sprays and Its Dependence on Fuel Properties and Injection Parameters

F. Pischinger

U. Reuter

Aachen Technical University,
Aachen, Federal Republic of Germany

E. Scheid

FEV Motorentechnik,
Aachen, Federal Republic of Germany

The self-ignition process in diesel engines is influenced by many parameters, which are partially interrelated. In order to separate the influence of basic parameters, a special high-pressure, high-temperature vessel has been designed that allows injection in short intervals under defined and repeatable conditions. The evaluated parameters include: cetane number, viscosity and volatility, vaporization behavior, and ignition improving additives. In addition to other factors, the investigations showed that the cetane number itself is not sufficient to characterize the self-ignition properties especially of heavy fuels and fuels containing ignition improvers. Additionally, the influence of injection parameters was evaluated, including injection quantity, pressure level, and nozzle design.

Introduction

Due to changing needs for mineral oil products, the quality of diesel fuels is expected to be lowered in the future [1]. At the same time, alternative fuels like methanol are being discussed as substitutes for crude oil, or for use to reduce pollutant emissions [2]. As a result, additional knowledge concerning these future fuels is necessary, for example their ignition behavior.

As a rule, ignition quality is rated by using the ASTM D613 test procedure. Published investigations in the last five years [3–6] showed that, especially in the case of future fuels, the ignition quality did not always correlate with the cetane number.

The self-ignition process in diesel engines is very complex. Therefore, the influence of individual engine or fuel parameters on self-ignition usually cannot be investigated in an engine without considering secondary influences. In addition, the testing at low temperature conditions in engines proved to be difficult [7]. A better separation of basic parameter influences is possible with a combustion chamber, which allows injection in short intervals under constant and "diesellike" temperatures and pressures.

Test Configuration

The results, presented in this paper, refer to an experimental test configuration, of which the essential part consists of a high-pressure chamber. Air continuously flows through the chamber under pressures up to 60 bar and temperatures up to 600°C. These conditions are comparable to those of actual diesel engines as they occur during the period of ignition delay.

Figure 1 shows a longitudinal section of the chamber. The compressed and heated air is turned toward the vertical direction by straightening blades installed in the upper portion of the chamber. This geometry, in combination with the low volume flow rate, produces a block-shaped velocity profile, which has a mean value of 0.1 m/s. To minimize heat losses,

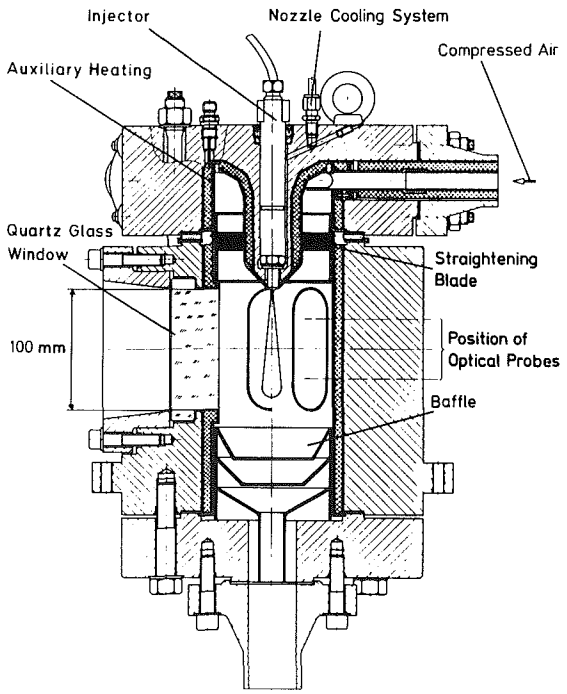


Fig. 1 Longitudinal section of the observation chamber

Contributed by the Internal Combustion Engine Division and presented at the Eleventh Annual Energy-Sources Technology Conference and Exhibition, New Orleans, Louisiana, January 10–13, 1988. Manuscript received by the Internal Combustion Engine Division August 24, 1987. Paper No. 88-ICE-14.

Copyright © 1988 by ASME
Downloaded 01 Jun 2010 to 171.66.16.87. Redistribution subject to ASME license or copyright; see http://www.asme.org/terms/Terms_Use.cfm

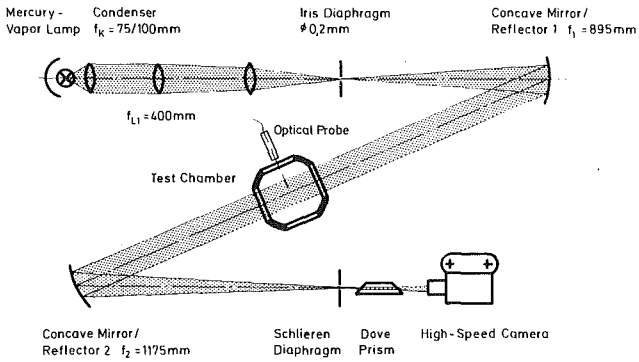


Fig. 2 Optical arrangement

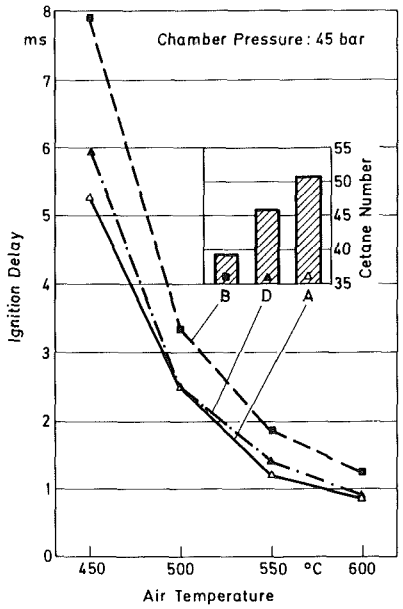


Fig. 3 Influence of cetane number on ignition delay

thereby generating an approximately isothermal temperature profile, all flow paths are equipped with ceramic insulation in addition to an auxiliary electrical liner heater. The observation section is produced by four quartz glass windows, 100 mm high and 40 mm wide. The distance between them is 90 mm, so that wall influences on the injection spray can be neglected.

Figure 2 shows the optical arrangement used to study the spray and ignition behavior with the help of high-speed Schlieren photography. The ignition was detected by a photomultiplier using three stacked optical probes each with a view angel of 20 deg, so that the entire spray could be observed. Figures 1 and 2 show the position of these probes. This optical system can detect light in the wavelength range from 250 nm to 650 nm. Ignition is indicated by a steep increase of the photomultiplier signal.

The spray was injected vertically through a water-cooled one-hole nozzle. In most of the experiments single injections

Table 1 Properties of investigated fuels

FUEL CODE		A	B	B*[1]	C	D	E	F[2]	G	H[3]
Cetane Number	–	50.6	39.1	50.6	50.0	45.6	45.4	56.3	>39	52[4]
Density at 15°C	kg/l	0.8468	0.8751	0.8751	0.8529	0.8441	0.8619	0.6838	0.931	0.8163
Distillation 5% Recovery at	°C	205.5	207	207	197.5	139	204	BP = 98.4	220	62.4
Distillation 90% Recovery at	°C	341	342	342	381	370	375.9		=450	190.1
Kinematic Viscosity at 20°C	mm^2/s	5.055	4.662	4.662	6.309	4.31	6.18	0.604	60.5	0.82
Calorific Value	MJ/kg	45.5	44.67	44.67	45.38	44.98	45.0	48.1	43.82	23.47

[1] $B^* = B$ + Ignition Improver
[2] n-Heptane
[3] Methanol + 12Vol-% 2-Ethyl-Hexylnitrate
[4] Ignition delay derived under practical operation of a DI-truck diesel engine

were obtained by using an electromagnetic valve to close a bypass line in the injection system during one pump revolution. On the other hand especially high-pressure injections were carried out with a quick-acting control rack displacement device. In both cases the injections proved to be exactly identical to injections of continuously running mode. In order to control the injection conditions, the pressure in the injection line as well as the needle lift signal of the injection nozzle were measured. Hence, the ignition delay could be calculated as the time difference between the start of the needle lift and the first light signal. Additional details can be found in [8]. The following results represent mean values of 32 single measurements per operating point analyzed by statistical methods.

Influence of Fuel Properties

The important physical and chemical properties of the investigated fuels are summarized in Table 1. The goal of selecting specifically these fuels was to separate as far as possible the influence of the fuel properties on the ignition delay. Investigated parameters are: cetane number, addition of ignition improver, volatility, and viscosity.

All experiments were conducted with a Bosch type one-hole injection nozzle with an orifice diameter of 0.3 mm and a Bosch injection pump type MW with a plunger diameter of 8 mm and a prestroke of 3.0 mm. The camshaft speed was 800 rpm. The injected calorific energy $m_B \times H_0$ was maintained constant at 832 J per injection, corresponding to a volume of 21.5 mm for fuel C. This is about the quantity of a single spray for a medium-speed truck engine operating at full load.

Cetane Number. Figure 3 shows the ignition delay for three different fuels A, B, and D. The chamber pressure was 45 bar and the chamber temperature was varied between 450°C and 600°C.

As expected, the low-cetane fuel B (CN = 39.1) has the longest ignition delay. It can be ascertained that the ignition delay for fuel A (CN = 50.6) is about 2/3 of the value measured for fuel B. This is also valid at chamber air pressures of 40 bar and 50 bar. This ratio is nearly independent of temperature. Fuel D with the medium cetane number (CN = 45.6) exhibits an ignition delay between the values of A and B but coming significantly closer to values of A. This is also valid at air pressures of 40 bar and 50 bar. In the example shown in Fig. 3, at 500°C and 600°C the ignition delay of fuel

Nomenclature

a, c_1 = fuel-dependent constant, ms × bar^n
b = estimated middle activation energy, K
c_2 = fuel-dependent constant, K
f = focal length, mm
H = calorific heat, MJ/kg
K = condenser
L = lens
m_B = fuel mass, kg
n = pressure-dependent constant
p = pressure, bar
Q = injection quantity, mm^3
t = time after start of injection, ms
Δtz = ignition delay, ms
T = temperature, K
T_0 = fuel-dependent reference temperature, K
ϕ = diameter, mm
ϕ_{JH} = orifice diameter of injection nozzle, mm

Downloaded 01 Jun 2010 to 171.66.16.87. Redistribution subject to ASME license or copyright; see http://www.asme.org/terms/Terms_Use.cfm

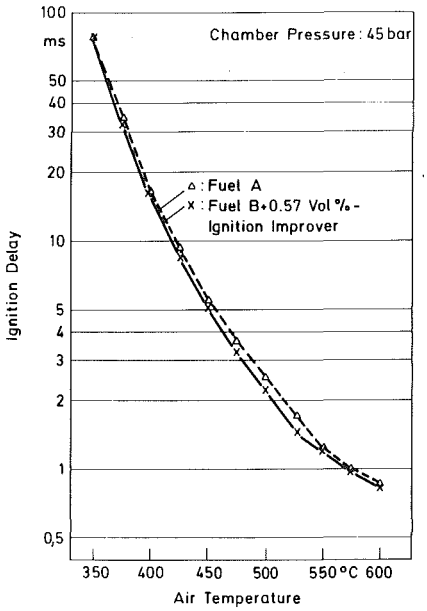


Fig. 4 Influence of ignition improver on ignition delay

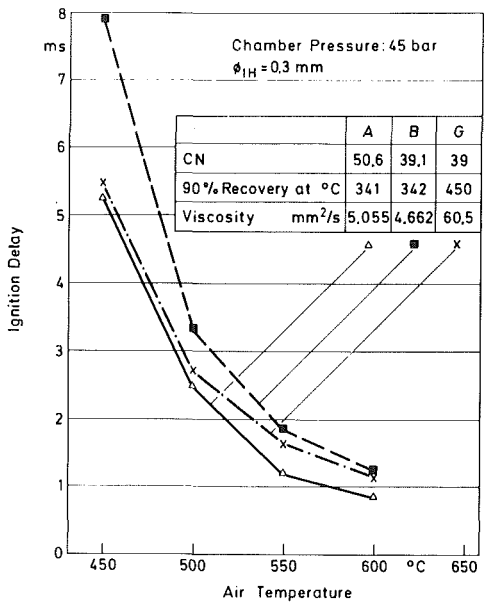


Fig. 6 Influence of fuel viscosity and volatility on ignition delay

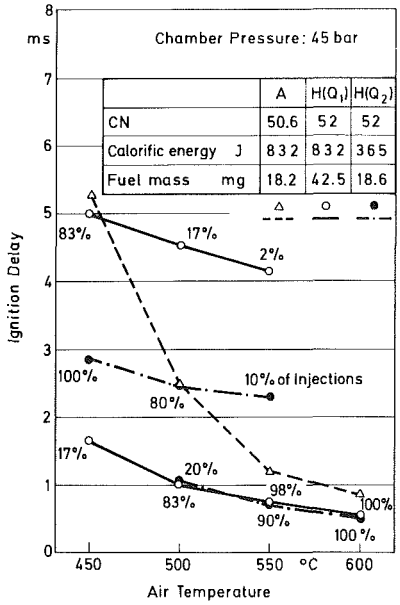


Fig. 5 Ignition delay of methanol with ignition improver

D is about the same as that of fuel A. This shows that the cetane number is not suited to characterize the self-ignition quality of fuels under all conditions.

To increase the cetane number of fuel B up to 50.6 (equal to the number of fuel A) an ignition improver was added. The added amount of a blend of different oktylnitrates (CF 26 DII, internal specification of Esso) was only 0.57 vol percent. Within the range of high temperatures, the ignition delay of the mixture, which is called B*, shows in Fig. 4 a good correspondence with the ignition delay values of fuel A, whereas in the temperature range between 425°C and 525°C the ignition performance of B* slightly predominates. In the low-temperature range below 425°C, the ignition delay curve again approaches the values of fuel A.

Engine investigations led to the result that ignition improvers do not have an influence on the ignition delay at very low temperatures, e.g., under cold start conditions. This may be attributed to wall effects, which are not present with the pressure chamber experiments.

A completely different behavior is shown by fuel H, which is methanol, containing 12 vol percent 2-ethylhexylnitrate as ignition improver. In Fig. 5 there is shown a comparison between the ignition delay curve of fuel A and two different injected amounts of fuel H. The injection quantities of H were 42.5 mg termed as Q_1 and 18.6 mg for Q_2. Q_1 led to the same injected energy as in the case of fuel A. Between 450°C and 600°C fuel H exhibits unsteady behavior between two levels of ignition delay. In Fig. 5 the frequency of the respective ignition delay is indicated by percentage of total injections. The ignition delay corresponding to the cases of high ignition performance is nearly independent of the injection quantity and indicates earlier ignition than for fuel A. The higher level of ignition delay for fuel H depends on the injection quantity and shows markedly longer ignition delays for Q_1 than in the case of Q_2.

Viscosity and Volatility. Figure 6 shows the ignition delay versus temperature for fuels with considerably different viscosity and volatility. The viscosity of fuels A and B is in the range of normal Diesel fuels, whereas fuel G is a heavy fuel with high viscosity. As indicated by the 90 percent recovery temperature, fuel G has a lower volatility than fuels A and B. The ignition delay of fuel G corresponds nearly with the low cetane rated fuel B at high temperatures while approaching fuel A at low temperatures. The cetane number of 39 for fuel G is therefore misleading for engines with low compression temperature, where a rating of higher than 45 would certainly by appropriate.

Even if the ignition delay is not very different, volatility and viscosity has a marked influence on spray development and combustion. Figure 7 shows Schlieren photographs for fuel A and G at 45 bar and 500°C. As indicated by the white-blue area on a green background, part of the fuel spray is already evaporated for fuel A at 1.25 ms after the start of injection, whereas fuel G shows no sign of vaporization until ignition at 2.85 ms. The arrows indicate the points of ignition. Fuel A burns with a bright yellow color after ignition of the completely evaporated spray, while fuel G shows a yellow-red flame indicating the formation of soot.

Considering the time history of the spray vaporization, it can be observed that, while boiling temperature, i.e.,

Downloaded 01 Jun 2010 to 171.66.16.87. Redistribution subject to ASME license or copyright; see http://www.asme.org/terms/Terms_Use.cfm

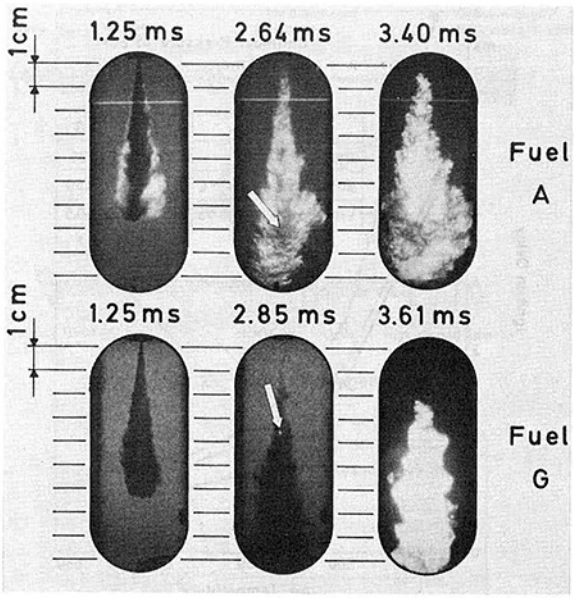


Fig. 7 Spray development and ignition for fuels of different viscosity and volatility; chamber pressure = 45 bar; chamber temperature = 500°C; fuel quantity = 21.5 mm^3

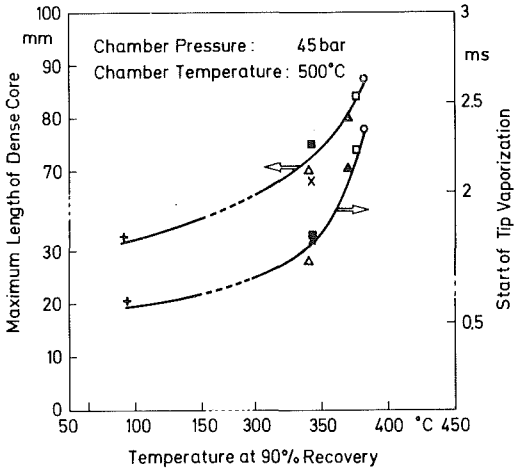


Fig. 8 Influence of fuel volatility on start of spray tip vaporization and maximum length of dense core; chamber pressure = 45 bar; chamber temperature = 500°C

temperature at 90 percent recovery is rising, the point of time at which the spray tip begins to evaporate is delayed. Therefore, the maximum length of the dense core of the spray increases. This relation is shown in Fig. 8 for the investigated fuels.

Calculation of Ignition Delay

As already observed in previous figures, the air temperature plays a dominant role. Early publications tried to describe self-ignition by a one-stage reaction mechanism resulting in exponential rise of reaction rate with temperature T. Furthermore, it can be deduced from reaction kinetics that the ignition delay is inversely proportional to the pressure p. Based on these fundamental considerations, a large number of authors [e.g. 9, 10] described the ignition delay Δtz, even of multicomponent fuels, with an exponential equation of the form

$$\Delta tz = \frac{a}{p^n} \cdot e^{b/T} \tag{1}$$

The coefficients a, b, and n must be determined empirically. For fuel C the values given in Fig. 9 were found for the best approximation by using the method of Gaussian least-squares errors considering measured data at chamber air temperatures of 450°C, 500°C, 550°C and 600°C and pressures of 40 bar, 45 bar, and 50 bar. For a pressure of 45 bar the ignition delay data curve corresponding to equation (1) is also shown in Fig. 9 in comparison to measured data.

In addition to the results obtained by using the observation chamber, ignition delay data of a real diesel engine for the same fuel are plotted. It can be seen that, in the lower temperature range between 450°C and 500°C a more deflected curve would be necessary for an optimum correspondence of measured and calculated data than of the above given equation. This behavior can be ascertained for all investigated fuels at chamber pressures of 40 bar, 45 bar, and 50 bar.

Therefore, a new equation was developed, which has the form

$$\Delta tz = \frac{c_1}{p^n} \cdot e^{c_2/(T-T_0)} \tag{2}$$

Within this equation the temperature T is substituted by the

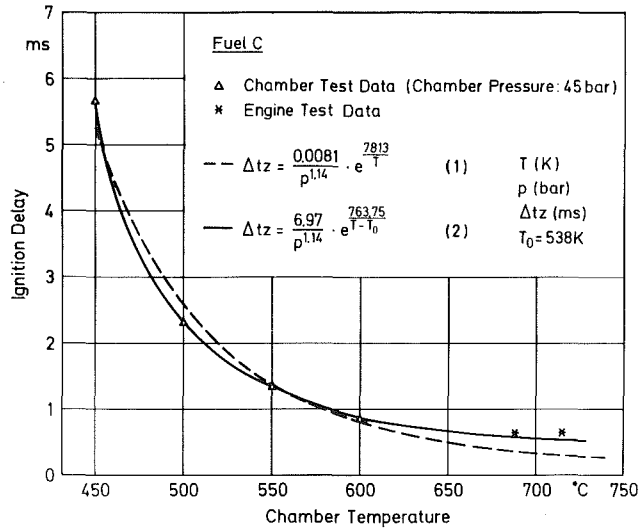


Fig. 9 Empirical equation for calculation of ignition delay

difference $T - T_0$. For fuel C the reference temperature T_0 is 538 K; at this temperature no ignition can be observed. The coefficients c_1 and c_2 are adjusted for best approximation to the test data (Fig. 9). As shown in Fig. 9 (solid line), the correspondence between measured and calculated data is significantly improved.

Influence of Injection Parameter

Nozzle Hole Diameter and Injection Pressure. To investigate the influence of nozzle hole diameter and injection pressure, the orifice diameter was varied between 0.2 mm and 0.3 mm; the amount of fuel injected was 14 mm^3/stroke. The camshaft speed of the injection pump and the nozzle opening pressure were adapted in an attempt to keep the injection duration as constant as possible. This method worked properly with nozzle orifice diameters of 0.2 mm and 0.25 mm; injection duration decreased with 0.27 mm and 0.3 mm diameters.

Figure 10 shows the ignition delay for the different nozzle hole diameters. The chamber temperature was adjusted to values of 450°C, 500°C, 550°C, and 600°C. The boxes around the mean value show the confidence interval of each measuring point regarding a statistical certainty of 95 percent.

Under the previously identified boundary conditions, it can be determined that the ignition delay for high-pressure injec-

Downloaded 01 Jun 2010 to 171.66.16.87. Redistribution subject to ASME license or copyright; see http://www.asme.org/terms/Terms_Use.cfm

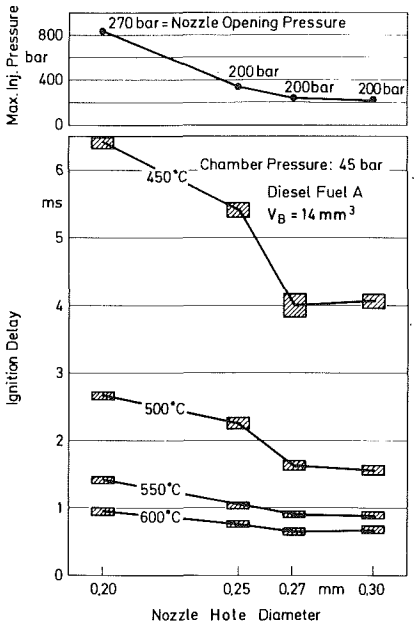


Fig. 10 Influence of nozzle hole diameter on ignition delay

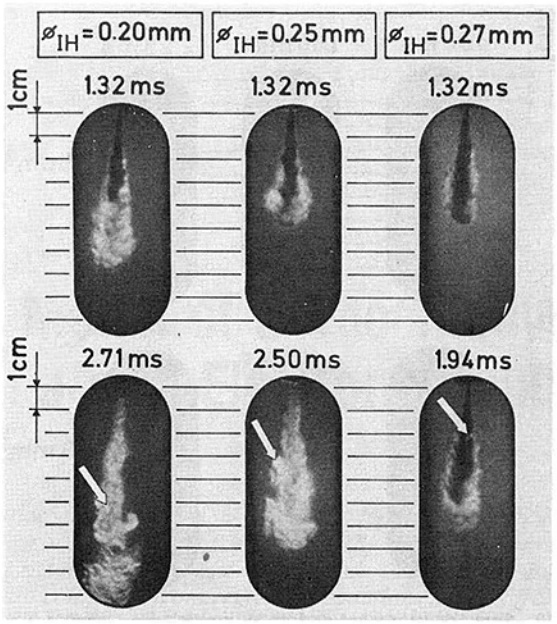


Fig. 11 Spray development and spray ignition for different nozzle orifice diameters; chamber pressure = 45 bar; chamber temperature = 500°C; fuel A; fuel quantity = 14 mm³; arrow indicates point of ignition

tions through a single hole of small diameter is longer than in the case of low-pressure injection through large nozzle hole diameters. This dependence is obviously valid in the diameter range between 0.2 mm and 0.27 mm. As the maximum injection pressure came close to the nozzle opening pressure of 200 bar in the case of the 0.27 mm as well as the 0.3 mm nozzle hole diameter, the needle only lifted to expand the fuel at nearly the same pressure level in both cases. This led to nearly the same ignition delay. Hence, it follows that the ignition delay increases with higher pressure injections. Another method to obtain higher injection pressures is to shorten the injection duration by increasing the camshaft speed. Investigations with higher camshaft speed confirmed these results. Also other publications [11, 12] show that an increased injection pressure may cause a longer ignition delay.

Concerning low-pressure injections, previous published investigations [16] show ignition delays of injections in the pressure range below 200 bar. In this range an increase of the ignition delay with decreasing pressure was observed.

In order to understand this relationship between injection pressure and ignition delay, it is useful to examine the Schlieren photographs as shown in Fig. 11. In the upper row the developed spray is shown at the same point of time after injection through an orifice diameter of 0.2 mm, 0.25 mm, and 0.27 mm. It can be ascertained that at higher injection pressure spray tip penetrations and vaporization are more pronounced. In the lower part of Fig. 11 Schlieren photographs of the same sprays are shown at the time of ignition. The left picture (high-pressure injection) shows a quite evaporated and even raveled spray. The spray of the 0.25 mm diameter orifice appears more coherent but is also completely evaporated. Contrary to this, the low-pressure spray of the 0.27 mm diameter orifice still exhibits a large liquid core when ignition takes place. The arrows indicate the point of ignition. It can be concluded that accelerated evaporation and mixture formation result in an increase of the ignition delay. This can be explained by the drop in temperature due to more complete evaporation. Investigations concerning this fact are still in progress.

The combustion process is significantly different for the different hole diameters. For the high-pressure injection, the flame is almost white and spreads with a relatively high velocity. This coincides with the engine experience that the high-

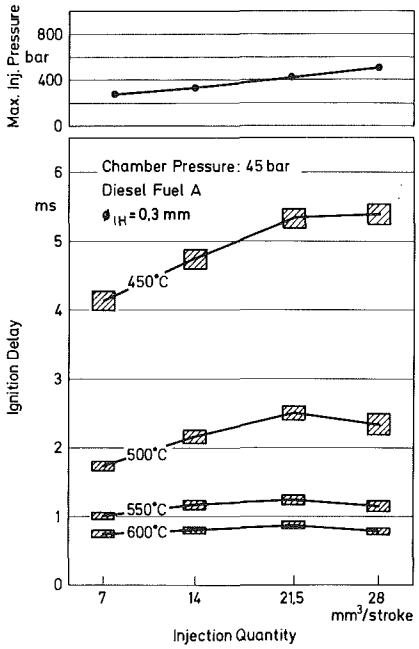


Fig. 12 Influence of injection quantity on ignition delay

pressure injection produces a quicker combustion combined with a lower tendency for soot emissions but a higher noise level. If the fuel is injected through a 0.27 mm nozzle a slower flame propagation can be observed. As a result of uncomplete vaporization the liquid fuel is partially decomposed into soot and the flame color turns into yellow.

Injection Quantity. Figure 12 shows the influence of the injection quantity on the ignition delay for different chamber temperatures. The camshaft speed of the injection pump was held constant at 800 rpm and a single-hole nozzle with an orifice diameter of 0.3 mm was used. The injection quantity was varied by shifting the control rack, so that the injection duration was extended with an increasing amount of injected

Downloaded 01 Jun 2010 to 171.66.16.87. Redistribution subject to ASME license or copyright; see http://www.asme.org/terms/Terms_Use.cfm

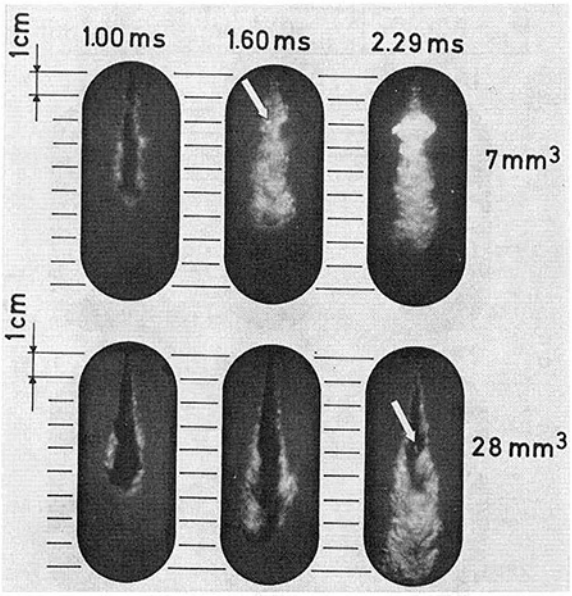


Fig. 13 Spray development and spray ignition for different injection quantities $Q = 7$ mm^3, 28 mm^3; chamber pressure = 45 bar; chamber temperature = 500°C; fuel A; arrow indicates point of ignition

fuel. At all chamber temperatures a continuously prolonged ignition delay had been measured with increasing injection quantity in the range between 7 mm^3 and 21.5 mm^3. At first, the results seem surprising compared to stationary engine investigations. The ignition delay shortens with increasing load [13]. However, under actual engine conditions the temperature level of the cylinder charge rises with increasing injection quantity, which in turn causes shorter ignition delay.

In contrast to engine conditions, the observation chamber used by the authors allows all boundary conditions to be kept constant. Therefore, the effect of injection quantity can be studied separately. Figure 13 presents Schlieren photographs for two different injection quantities at three times after the start of injection. These pictures may explain the prolonged ignition delay for the high-quantity spray. As shown in the lower row of the photographs the ignition may be delayed by an extinguishing effect caused by the continued injection of liquid fuel.

As a result of the longer ignition delay, the yellow flame spreads very quickly with higher fuel quantity. This behavior explains clearly the phenomenon of the acceleration noise during engine operation. Acoustic investigations on engines [14] show that the combustion noise of diesel engines at first increases rapidly when the injection quantity is changed from low load (respectively idle) to full load and then decreases to lower stationary values. In this case, the temperature of the cylinder charge remains on a lower level for a short time before increasing due to the increased load.

Conclusions

The high-temperature vessel that has been designed to study the development and ignition of fuel sprays under "diesellike" air temperatures and pressures proved to be a suitable instrument especially for the use of optical measurement techniques. This new equipment was used to determine the influence of diesel fuel parameters on the ignition behavior. The following conclusions are based on the test results.

Methanol containing ignition improver exhibits a considerable unstable ignition behavior between two levels of ignition delay indicating a different ignition mechanism than for mineral oil fuels. Therefore, the cetane number cannot be a good indicator for the ignition performance of such alternative fuels.

The vaporization of the spray tip of low boiling and low viscous fuels starts earlier than those of high volatility and viscosity.

A new equation to calculate ignition delay was developed that shows a significant improved correspondence between measured and calculated data.

The investigations proved that the ignition behavior is also influenced by the injection parameters.

The ignition delay of fuels being injected through a single hole nozzle into approximately quiescent air, without wall effect, increases with decreased nozzle orifice diameter respectively high injection pressure. The drop of local mixture temperature caused by more rapid vaporization seems to be an explanation.

An increased amount of injected fuel can cause a longer ignition delay under constant chamber temperatures. This seems to be the result of an extinguishing effect caused by the longer injection of liquid fuel. This also explains the acceleration noise of diesel engines under transient conditions.

Acknowledgments

The authors wish to thank the Deutsche Forschungsgemeinschaft for their financial contribution to these investigations and the Commission of the European Communities (CEC) for their support by providing special analyzed fuels.

References

1 Dabelstein, W. E., et al., "Der Fahrzeug-Dieselmotor u. seine Kraftstoff-Qualitäts- und Energiesaspekte," presented at "Technische Arbeitstagung," Stuttgart-Hohenheim, March 24, 1982.

2 Pischinger, F., Hilger, U., et al., "Suitability of the Hot-Surface Ignition Engine for Using Alcohol Fuels," *Symposium on Alcohol Fuels*, Paris, France, Oct. 1986, pp. 20–23.

3 Gülder, Ömer L., et al., "Ignition Quality Rating Methods for Diesel Fuels—A Critical Appraisal," SAE Paper No. 852080, 1985.

4 Murphy, M. J., "An Improved Cetane Number Predictor for Alternative Fuels," SAE Paper No. 831746, 1983.

5 Sieber, D. L., "Ignition Delay Characteristics of Alternative Diesel Fuels: Implications on Cetane Number," SAE Paper No. 852102, 1985.

6 Needham, J. R., "The Combustion and Ignition Quality of Alternative Fuels in Light Duty Diesels," SAE Paper No. 852101, 1985.

7 Henein, N. A., and Lee, Chiu-Shan, "Autoignition and Combustion of Fuels in Diesel Engines Under Low Ambient Temperatures," SAE Paper No. 861230, 1986.

8 Pischinger, F., Knoche, K. F., Reuter, U., Scheid, E., et al., "Spray Combustion Chamber With Optical Access, Ignition Zone Visualisation and First Raman Measurements of Local Air-Fuel Ratio," SAE Paper No. 861121, 1986.

9 Hiroyasu, H., "Diesel Engine Combustion and Its Modeling," *Comodia*, 1985, pp. 53–75.

10 Schmidt, F. A. F., *Verbrennungskraftmaschinen*, Vol. 4, Springer-Verlag, 1967.

11 Sitkei, G., "Über den dieselmotorischen Zündverzug," *MTZ*, Vol. 24, 1963, p. 6.

12 Sato, J., et al., "Aspect of Diesel Spray and Combustion in High Pressure and High Temperature Atmosphere," *CIMAC*, 1985, p. D76.

13 Tsao, et al., "Gas Temperatures During Compression in Motored and Fired Diesel Engines," *SAE Trans.*, Vol. 70, 1962.

14 Pischinger, F., and Schmillen, K., "A New Measuring Method for the Direct Determination of Diesel Engine Combustion Noise," SAE Paper No. 790267, 1979.

15 Pischinger, F., Reuter, U., and Scheid, E., "Influence of Fuel Quality and Injection Parameters on Self-Ignition of Diesel Sprays," *CIMAC*, 1987, p. D112.

16 Pedersen, P. S., and Ovale, B., "A Model for the Physical Part of the Ignition Delay in a Diesel Engine," SAE Paper No. 740716, 1974.

Downloaded 01 Jun 2010 to 171.66.16.87. Redistribution subject to ASME license or copyright; see http://www.asme.org/terms/Terms_Use.cfm

C. I. Rackmil

P. N. Blumberg

Integral Technologies Incorporated,
Westmont, IL

D. A. Becker

R. R. Schuller

Electromotive Division—GMC
LaGrange, IL

D. C. Garvey
Woodward Governor Company,
Fort Collins, CO

A Dynamic Model of a Locomotive Diesel Engine and Electrohydraulic Governor

As part of a comprehensive simulation of a prototype locomotive propulsion system, a detailed model has been developed that predicts the dynamic response of an experimental two-stroke, turbocharged and intercooled diesel engine. Engine fueling and brake torque are computed from regression equations derived from an extensive data base. Corrections are applied to the calculated steady-state torque to account for dynamic deviations of in-cylinder trapped air–fuel ratio from the steady-state value. The engine simulation accurately represents the operation of the turbocharger, which is gear-driven at low turbocharger speeds, and freewheels through an overrunning clutch when exhaust energy accelerates the turbocharger beyond its geared speed. Engine fueling level, i.e., rack, is determined from a dynamic simulation of an electrohydraulic governor, which responds to the difference between the desired and the actual engine speeds. The governor representation includes: (1) finite rate of change of engine set speed; (2) load regulator feedback for control of applied engine loads; and (3) fuel limiting under conditions of excessively high load demand. The fundamentals of the engine/governor model are given in the paper along with examples that emphasize the dynamic operation of these particular components.

Introduction

A diesel-electric locomotive is a complex propulsion system whose overall performance depends on the individual performance of its many subsystems and on the control of dynamic interactions between the subsystems. The major subsystems that comprise a typical locomotive propulsion system are as follows:

1 diesel engine, including basic two-stroke engine, rack-actuated unit injectors, and turbocharged/intercooled air delivery system [1];

2 electrohydraulic governor, including basic regulation of engine speed at a selected set point, and auxiliary functions of fuel limiting and load regulation under conditions of excessive engine loading;

3 electrical transmission system, comprised primarily of main generator, companion alternator for main generator excitation, axle-hung traction motors/generators, and a resistance dissipation grid for braking modes of operation;

4 electrical control system, a microcomputer-based system that monitors and controls the state of the main generator to provide the desired traction power (or braking effort) without placing undue load on the diesel engine [2].

Figure 1 shows a schematic of a typical propulsion system illustrating the components mentioned in the subsystem descriptions above.

In order to aid in component integration and control system development activities, a comprehensive dynamic simulation of a prototype locomotive propulsion system was undertaken. The utility and applicability of this type of simulation has been demonstrated in a recent publication [3]. The structure of the overall simulation is shown in Fig. 2, indicating the major subsystem models included in the simulation and their interactions. In the present paper, our attention will be restricted to the diesel engine and electrohydraulic governor simulation, which together represent a complex prime power subsystem whose proper operation and control is critical to the performance of the locomotive.

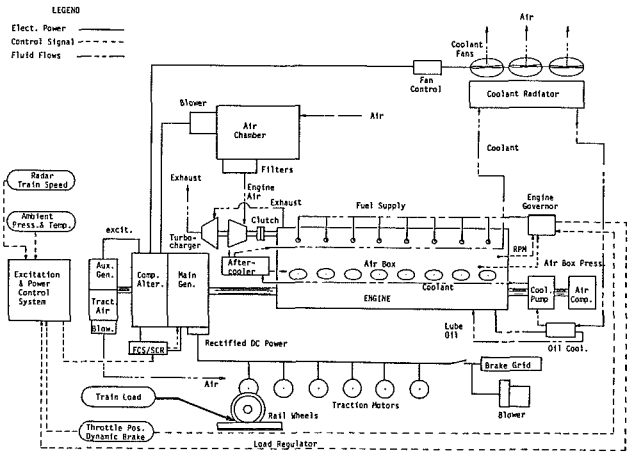


Fig. 1 Schematic of locomotive propulsion system

Contributed by the Internal Combustion Engine Division and presented at the Eleventh Annual Energy-Sources Technology Conference and Exhibition, New Orleans, Louisiana, January 10–13, 1988. Manuscript received by the Internal Combustion Engine Division September 1987. Paper No. 88-ICE-26.

Copyright © 1988 by ASME
Downloaded 01 Jun 2010 to 171.66.16.87. Redistribution subject to ASME license or copyright; see http://www.asme.org/terms/Terms_Use.cfm

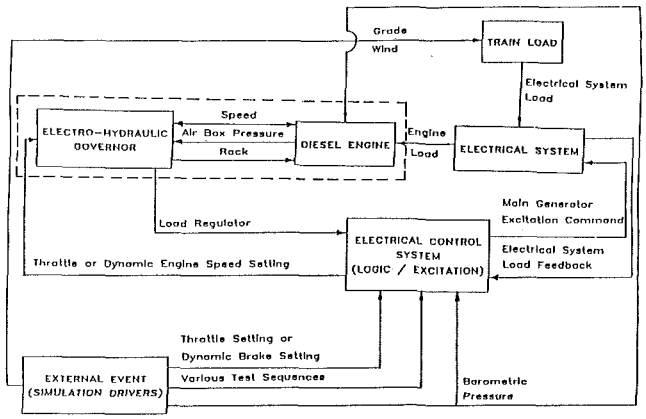


Fig. 2 Schematic of locomotive propulsion system simulation showing the major subsystems (dashed line indicates focus of current paper)

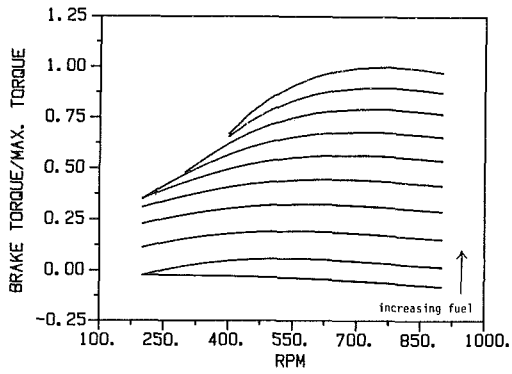


Fig. 3 Normalized brake torque versus rpm and rack for the experimental diesel engine

Typical Locomotive Propulsion System Operation

In the locomotive propulsion system, there are eight discrete engine speed settings in addition to an idle speed setting, which, together, span the engine operating range of 200 to approximately 900 rpm. The choice of speed setting is selected by the locomotive operator by means of a discretized throttle lever.

The electrical system, which constitutes the engine load, is separately controlled to a specific maximum power output level at each throttle setting, chosen so as not to exceed an efficient engine output capability at the given speed setting. In addition to regulating the electrical system load, which is placed on the engine at a steady-state throttle setting, the electrical system controller also "rate-limits" the power increase or decrease in traversing between throttle settings so as to match the engine's ability for simultaneous acceleration and production of shaft power (or deceleration and reduction in shaft power), including engine dynamic effects such as turbocharger inertia and engine thermal inertia.

It is the function of the engine governor both to maintain the selected engine speed at steady-state and to control the rate of change of engine speed when throttle position is changed. The governor also provides a feedback signal to the electrical system controller to reduce load when the required fueling to maintain engine speed is too high and directly limits the fuel in the event that engine load is not reduced quickly enough.

A major challenge of the overall control system design and integration is to ensure that the electrical system and engine function as a synchronized unit to prevent undesirable phenomena such as engine under-speeding or excessive smoke output, while still maintaining responsive propulsion system operation.

Objectives of the Engine and Governor Subsystem Model

In view of the overall objectives of the locomotive simulation, the requirements that were imposed on the engine and governor subsystem model were as follows:

1 dynamic, i.e., time-dependent calculation of engine output torque and trapped air–fuel ratio including the effects of (1) turbocharger and air system dynamics; (2) rack lash, if present; (3) delay in torque production with respect to rack position change; and (4) ambient pressure and temperature.

2 calculation of dynamic air box pressure in the engine for use by the governor in determining whether load regulation or fuel limiting is required;

3 dynamic calculation of rack position (i.e., fueling) as controlled by the governor, including all inputs affecting rack such as engine set-speed change, electrical system load torque variation, and fuel limiting, when required;

4 dynamic feedback from the governor to the electrical load control system for reduction in power setting in response to excessive fuel requirement at a given speed and airbox pressure (i.e., load regulation function);

5 acceptance of arbitrary and, in some cases, irregular electrical system load torque profiles as might be imposed by the main generator during (1) normal operation or (2) during discontinuous events such as generator winding transition (from parallel to series or vice versa) or control system performance testing characterized by deliberate, abrupt changes in engine load torque;

6 dynamic calculation of engine speed in response to the difference between engine output torque and engine load torque.

Diesel Engine Submodel

Engine Torque Output. Several alternative approaches can be taken in constructing an engine torque model for a dynamic system simulation. At the most fundamental level, a complete thermodynamic treatment of individual cylinders can be constructed, using standard "filling and emptying" modeling techniques for inlet and exhaust plenums [4–6]. The computed pressure history versus crank angle in each cylinder is used to calculate the instantaneous torque output of the engine. This approach can be computationally costly and introduces the uncertainty associated with representing the combustion process in the thermodynamic cycle calculation. For the purpose of the present analysis, a regression formulation based on engine dynamometer data for an experimental engine is used as a starting point for calculating engine brake torque output, averaged over all cylinders. The regression represents the steady-state engine brake torque as a function of engine speed and rack position. In the engine simulated there is no independent control over injection timing so that the load advance characteristics of the injectors are implicitly built into the regression. Figure 3 shows the normalized brake torque calculated from the regression over the full operating range of the engine, extending from 200 rpm to 900 rpm and from zero fueling to high levels of fueling. The regression extends into the motored, negative torque region for low fueling values. The lowest torque curve is, in fact, the hot, motoring friction torque as determined from engine dynamometer coast-down tests.

The calculation of engine torque takes place in two steps: Fuel per cycle to all cylinders is first calculated from rack and engine speed and then engine torque is calculated from engine speed and fuel per cycle. Thus, as a result of this calculation, the instantaneous fuel flow is also determined, allowing for

Downloaded 01 Jun 2010 to 171.66.16.87. Redistribution subject to ASME license or copyright; see http://www.asme.org/terms/Terms_Use.cfm

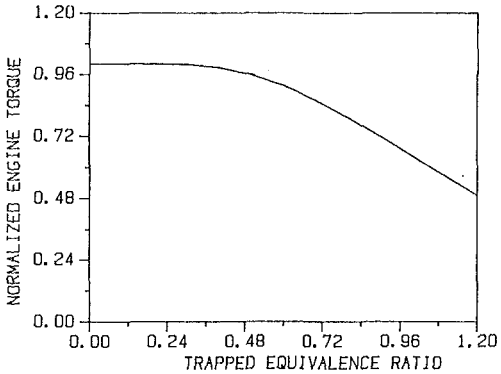


Fig. 4 Normalized engine torque versus trapped equivalence ratio as used in torque correction

calculation of trapped and overall air–fuel ratio, as described subsequently.

Values of engine torque computed from the regression equations correspond to steady-state air system and engine structure thermal conditions (temperatures, pressures, mass flow rates, and in-cylinder component temperatures). During a transient, instantaneous trapped equivalence ratios can differ substantially from the steady-state values implicit in the torque regression, resulting in torque levels that can differ significantly from the steady-state values. To account for this effect, a correction factor is applied to the torque regression values before they are used in the simulation at any point in time. The correction factor is calculated as the ratio between the torque at the instantaneous trapped equivalence ratio and the torque that would be obtained at the steady-state trapped equivalence ratio corresponding to the instantaneous engine speed and fuel rate. A single normalized torque versus trapped equivalence ratio curve, as shown in Fig. 4, is used to form the ratio of torques. The curve has been generated from a diesel engine cycle simulation code [8] and captures the dominant effect of air–fuel ratio on torque produced, i.e., a deteriorating combustion efficiency as the air–fuel ratio becomes richer. Instantaneous trapped equivalence ratio is computed by the dynamic air system simulation incorporated in the engine model.

A further feature of the engine torque model is the delay in torque produced in response to a change in fueling level. This delay is comprised of three parts: (1) time from rack position change until fuel is injected into any cylinder; (2) time for fuel to burn in a given cylinder and produce a torque moment at the crank throw; and (3) time for the new torque level to be produced in sufficient number of cylinders so as to be assignable to the engine as a whole. This total delay is in the neighborhood of 100 deg of crank rotation and is reflected in the calculated engine torque output with respect to changes in rack position.

Air System Representation. As mentioned above, the diesel engine model also simulates the dynamics of the air system. The model computes instantaneous values of all pressures, temperatures, and mass flow rates as well as turbocharger speed and trapped and overall equivalence ratios. The air system calculations provide values of air box pressure and trapped equivalence ratio for use by the governor and torque submodels of the simulation, respectively. Figure 5 presents a schematic of the air system as represented by the engine model. The turbocharger compressor provides all scavenging and must be gear driven at low speeds to perform this function. At higher speeds it "free wheels" through an overrunning clutch since sufficient power is available at the turbine to drive the compressor at a speed above the gear-driven speed.

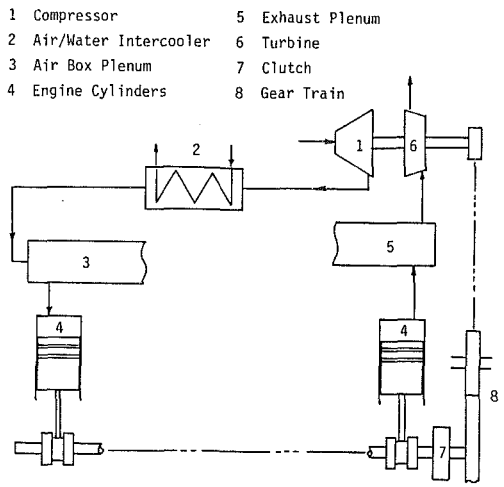


Fig. 5 Schematic of components in air system model for the diesel engine

The air system simulation is based on a combined quasi-steady component treatment and a filling and emptying analysis for the major plenums. A brief overview of the treatment of each component follows. A more detailed description of the modeling approaches, including a list of governing equations, exists in [3] and will not be repeated here.

Plenums. The plenums included in the engine system model are the air box and exhaust plenums. They are treated as control volumes of uniform gas pressure and temperature with heat transfer across their boundaries. A single plenum wall temperature is computed dynamically from an energy balance using a lumped thermal inertia for the wall to represent the plenum structure warmup/cooldown characteristics. Standard literature correlations are used to calculate the heat transfer coefficients for the inner and outer surfaces, which are assumed to transfer heat by forced convection only.

Compressor. The compressor is modeled in a quasi-steady way using a standard steady-state compressor map, which is assumed to apply at any instant of time. The map is accessed using the instantaneous, dynamic values of pressure ratio and turbocharger speed to obtain mass flow and efficiency. When calculating the pressure ratio, compressor inlet pressure is corrected for a pressure drop across the engine air filter and inlet ducting. The compressor data used in the simulation are stored in nondimensional form, which allows compressor data to be scaled with instantaneous compressor inlet conditions within the simulation, as well as with compressor size.

Turbine. The turbine is treated in a quasi-steady state manner similar to the compressor. Steady-state maps provide turbine mass flow and efficiency values from instantaneous values of turbine pressure ratio, inlet temperature and speed. As with the compressor data, the turbine data are stored in nondimensional form, which allows for scaling of the data with instantaneous turbine inlet conditions and component size.

Intercooler. The air–water intercooler is represented as a quasi-steady heat exchanger with a dynamically varying structure temperature. The air charge mass flow is calculated from the pressure drop across the intercooler using a friction factor versus average gas velocity curve. Coolant mass flow rate is computed as a function of engine speed. Charge and coolant exit temperatures are computed from a quasi-steady-state enthalpy balance between the two flows and the intercooler structure. The structure temperature is determined from integration of the energy equation governing its lumped thermal

Downloaded 01 Jun 2010 to 171.66.16.87. Redistribution subject to ASME license or copyright; see http://www.asme.org/terms/Terms_Use.cfm

inertia to account for warmup or cooldown. Forced convection heat transfer coefficients on the coolant and charge flow sides are determined from standard heat transfer correlations as a function of mass flow rate, but are calibrated using actual intercooler effectiveness factor data.

Engine Cylinder. As with the other air system components, a quasi-steady-state treatment of the engine cylinder is employed in the engine model for simulating its interaction with the remainder of the air system. Empirical correlations specific to the experimental diesel engine under consideration provide instantaneous values of engine mass flow rate and exhaust temperature during a simulation.

Total engine air mass flow supplied to the engine is computed from a correlation between steady-state mass flow data and a pressure parameter formed from the absolute air box pressure and the pressure drop across the engine, as outlined in [7] and demonstrated in [3].

For the purpose of calculating the exhaust temperature, the total air mass flow supplied to the engine is separated into two mass flows: (1) a trapped air mass flow, representing the portion of air mass flow supplied to the engine that is trapped in the cylinder at the end of the scavenge process; and (2) a short-circuited air mass flow, representing the portion of air mass flow supplied to the engine that passes through the cylinder during the scavenge process directly to the exhaust plenum. The short-circuited mass flow to the exhaust plenum is taken to be at the air box temperature. The separate air mass flows are determined from calculations of scavenge ratio and trapping efficiency. Scavenge ratio is computed directly from its definition as the ratio of the delivered air mass flow divided by the ideal mass flow that could be delivered based on air box conditions and cylinder volume. Trapping efficiency is computed as a function of scavenge ratio from an experimentally determined correlation.

The total exhaust gas flow exiting the cylinder is taken to be the sum of the short-circuited air mass flow and the total trapped gas mass flow. The temperature associated with the exhausted trapped gas flow is determined from an overall temperature rise across the engine. Steady-state temperature rise data, stored as a function of engine speed and trapped equivalence ratio, are used to compute an uncorrected temperature rise across the engine. The steady-state temperature rise value is corrected for engine structure temperature effects by adding a fraction of the difference between the instantaneous average in-cylinder wall temperature and the steady-state value corresponding to the instantaneous engine speed and trapped equivalence ratio, thereby introducing the effect of increased or reduced heat transfer, which occurs under thermally nonequilibrated conditions. The instantaneous in-cylinder surface temperature is computed from an approximate solution of the energy equation governing the thermal inertia associated with the engine structure, employing a time constant that reflects this inertia. Steady-state values of mean in-cylinder surface temperature are obtained from curves generated by ITI's cycle simulation code, IRIS [8].

Corrected temperature rise values are added to the air box temperature to obtain the final exhausted trapped gas flow temperature. This temperature is combined with the temperature of the bypass air flow in an enthalpy-weighted average to determine the final engine exhaust temperature.

Turbocharger Dynamics. Turbocharger speed is determined from the integration of the angular momentum equation governing the turbocharger inertia. Turbocharger inertia torque is given by the difference between the turbine work and the sum of the compressor and turbocharger friction works. Turbocharger friction work is computed as a fraction of the turbine work using a turbocharger mechanical efficiency, which is a function of corrected turbocharger speed. During the integration, dynamically integrated turbocharger speed is compared with the gear-driven turbocharger speed to determine whether the turbocharger is in a gear-driven or free-wheeling state. Whenever the integrated turbo speed falls below the gear-driven speed, the turbo is gear driven and turbo speed is held at the gear-driven speed.

Engine Model Predictions

Engine Model Validation at Steady State. Steady-state calculations of engine operating points were performed and comparisons made to actual engine data in order to validate the predictions of the engine model. Table 1 gives a relative comparison of several calculated and measured engine operating points covering a range of engine speeds and loads. The table shows percentage differences between the data and the simulation for air box pressure and temperature, exhaust pressure and temperature, engine air mass flow rate, turbocharger speed, and torque. The results indicate that the steady-state agreement is of sufficient accuracy for the level of detail incorporated in the model, generally within 2-3 percent.

Sample Transient Predictions of the Diesel Engine Model. Figures 6(*a*) and 6(*b*) show the engine system response to imposed ramps in both rack, i.e., fueling, and load torque. The ramp rates and absolute values have been chosen to be representative of a transient corresponding to a throttle 0 (idle) to throttle 8 increase in demanded power for the prototype locomotive. The engine set speed at idle is 200 rpm and at throttle 8 it is 904 rpm. Figure 6(*b*) shows, with respect to the imposed ramp in load torque, the computed engine torque that results from the increase in rack and dynamic variation of air–fuel ratio. Figure 6(*a*) shows, in addition to the imposed increase in fueling, integrated engine and turbocharger speed. Up to approximately 25 s in the simulation, the turbocharger is gear driven. At that point, the turbo acceleration exceeds that of the engine-driven turbocharger gearing resulting in the onset of the free-wheeling mode. This can be observed in Fig. 6(*a*) from the noticeable increase in turbocharger speed that occurs while the rate of change of engine speed is decreasing rapidly. Note that the final turbocharger speed is approximately 18,500 rpm in the freewheeling mode whereas the gear driven speed would have been approximately 15,200 rpm at the final engine speed.

Table 1 Relative comparison of steady-state engine simulation predictions with engine measurements

Speed Load Point		% Difference[1]						
RPM	% Max. Torque	$\dot{m}_a$	N_{TC}	P_{AB}	T_{AB}	P_{EXH}	T_{EXH}	BTORQ
901.1	100	-2.5	-1.9	-3.2	-1.0	-2.8	1.8	.1
731.0	67	-1.6	.58	-.4	.4	.9	1.9	3.0
570.5	66	-2.0	.7	.2	.7	.6	2.0	1.9
340.3	53	-12.1	.6	.2	2.2	.2	6.6	2.7

Nomenclature:
- $\dot{m}_f$ = fuel rate
- $\dot{m}_a$ = air mass flow rate
- N_{TC} = turbocharger speed
- P_{AB} = air box pressure
- T_{AB} = air box temperature
- P_{EXH} = exhaust pressure
- T_{EXH} = exhaust temperature
- BTORQ = engine brake torque

[1] % difference defined as (predicted-measured)/measured

Downloaded 01 Jun 2010 to 171.66.16.87. Redistribution subject to ASME license or copyright; see http://www.asme.org/terms/Terms_Use.cfm

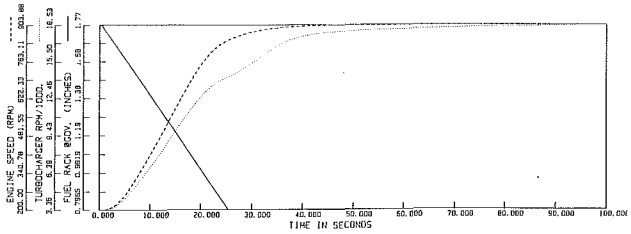


Fig. 6(a) Rack (fueling), turbocharger speed, and engine speed versus time

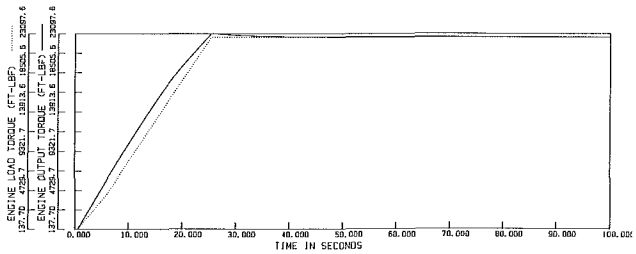


Fig. 6(b) Engine brake torque output and load torque versus time

Fig. 6 Transient diesel engine simulation in response to representative fueling and load torque ramps

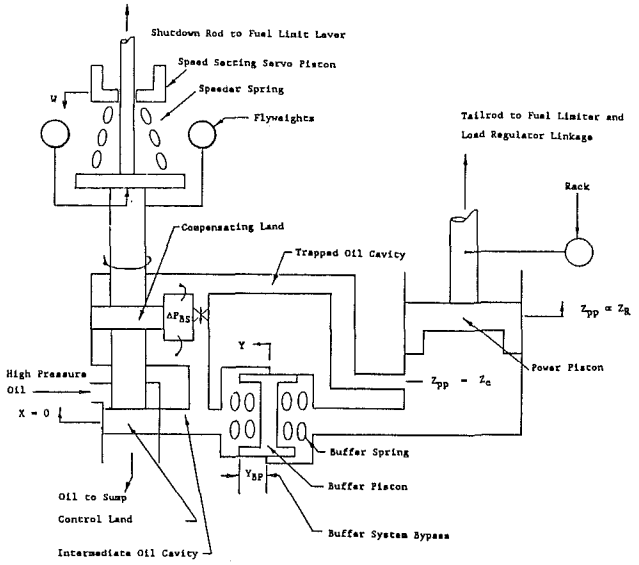


Fig. 7 Schematic of the buffer compensated electrohydraulic governor

Although the main turbocharger acceleration during both gear driven and free-wheeling modes matches the general time scale of the engine speed transient (i.e., approximately 35 s), the turbocharger transient extends over the entire 100 s time scale of the simulation. This results from the relatively slow warmup of the engine structure as the speed/load point is changed from idle to rated power. Although not shown in the plots presented, the mean engine structure temperature is continually increasing over the time of the simulation, resulting in more exhaust enthalpy flow and turbine work. This produces higher compressor outlet pressure and more air mass flow. Only at several hundred seconds is a complete steady-state condition reached in all variables, i.e., structure temperature, turbo speed, engine torque, trapped equivalence ratio, etc.

Transient validation of the engine model was performed in the context of the complete locomotive simulation. These results are described in a subsequent section, which presents integrated engine/governor simulations.

Electrohydraulic Governor Submodel

An integral part of the prototype locomotive control system is the electrohydraulic governor. The basic function of the governor is to control engine speed. It carries out this function by determining fueling (rack), consistent with current engine operating conditions and/or requested changes in desired engine speed. Auxiliary features of the governor, which have been incorporated into the governor submodel, are fuel limiting and load regulation. During fuel limiting and load regulation, dynamic control of rack and load, respectively, are introduced to prevent operating conditions that produce undesirable combinations of fueling and air box pressure (smoke) at given throttle settings.

A complete set of state-space differential equations and supporting relationships describing governor operation was developed for use in the governor simulation. The derivation was based, in part, on general analytical descriptions of electrohydraulic governors, which can be found in [9, 10].

Basic Governor Fuel Control. The buffer compensated governor is schematically shown in Fig. 7. The hydraulic governor utilizes a spring and centrifugal flyweight force balance on a pilot valve, which diverts fluid to and from a trapped oil cavity, in turn displacing the main fuel control (power) piston Z_{pp}. A buffer compensated governor, like the one considered, modulates rack response by introducing an additional pilot valve force, which is dependent on the rate of change of rack. As engine speed responds to varying conditions of load and output torque, rack is increased or decreased in a prescribed manner in order ultimately to maintain set-speed.

During steady-state operation of the governor, the main pilot valve plunger is balanced (at $X=0$) by a combination of centrifugal, spring, and pressure forces. The buffer system is in equilibruim with the buffer piston at $Y=0$ ($\Delta P_{BS}=0$), and the power piston is positioned to deliver a fuel rate necessary for the engine to maintain the speed specified by the speed setting piston position, W. Engine speed is maintained at its specified value, by delivering the required fueling at any of a range of steady-state load torques (isochronous speed control). The governor is gear driven by the engine, with its speed differing slightly from engine speed in accordance with the governor-to-engine gear ratio (ϕ_{GE}). Throttle settings uniquely determine a specific set of steady-state speed setting servo piston positions, which correspond to a set of requested engine or, equivalently, governor speeds. Fueling is determined by the power piston position, which is linearly linked to rack position.

Governor transients result from variations in engine speed or from changes in throttle settings. Throttle changes act to displace the speed setting pilot valve plunger from its seat. High-pressure hydraulic oil (internally supplied to the governor by a gear pump) enters a cavity above the speed setting piston at a rate determined by the number and size of the regulating ports in the pilot valve bushing. In the governor simulation, the rate of movement of the speed setting piston position is prescribed as a linear function of time.

A positive displacement (increasing set-speed) of the servo piston position causes compression of the speeder spring, and an imbalance of forces on the main pilot valve plunger. The pilot valve control land moves off its seat in the $-X$ direction. High-pressure hydraulic fluid enters the governor buffer system, simultaneously moving the buffer and power piston (Y and Z_R). As the pressure difference across the buffer system (ΔP_{BS}) builds, so does the upward force exerted on the pilot valve at the compensating land. The force on the compensating land continues to increase with increasing ΔP_{BS} until it balances the increased speeder spring force, reseating the

Downloaded 01 Jun 2010 to 171.66.16.87. Redistribution subject to ASME license or copyright; see http://www.asme.org/terms/Terms_Use.cfm

pilot valve control land. At this point the power piston has attained a new position corresponding to a higher fueling rate. The buffer system comes into equilibrium as fluid passes through the compensating needle valve from the intermediate to trapped oil pressure cavities of the buffer system [11]. At the same time the buffer system equilibrates, the engine is accelerating to a new set point in response to the higher fueling rate. The degree to which an ideal response is met (i.e., no overshoot or undershoot in engine speed) is dependent on the compensating needle valve setting and the dynamic rates of a number of inputs: in particular, speed setting piston position, load, and brake torques. During a decrease in set-speed, the governor operates in a similar manner with the control land moving in the $+X$ direction and hydraulic fluid in the buffer system emptying to the governor sump. Governor and buffer system responses to load induced variations in engine speed are similar to those described above, with the initial imbalance of main pilot valve forces resulting from changes in fly-weight speed.

Buffer System Bypass, Compensation Cutoff, and Rack Lash. Additional features of the governor, which have also been incorporated into the governor submodel, are buffer system bypass and compensation cutoff. In order to characterize any mechanical lash present between the governor's power piston and the spill port positions of the individual injectors, a lash model was built into the unit injector rack description. Effective rack position at the engine, hence, fueling at the injectors, is unchanged while in the lash region.

During buffer system bypass, the buffer piston moves beyond its bypass position, $Y = \pm Y_{BP}$, and normal operation of the buffer system is circumvented. Under these conditions, hydraulic fluid is allowed to pass directly between the trapped and intermediate oil cavities. A more immediate response for increases or decreases in fueling is, therefore, facilitated. This type of response is advantageous during rapid changes in reference speed (servo position) and load torque.

Under conditions of low fueling and fast decreases in load torque, normal governor response would temporarily decrease fueling below that required to maintain reference speed. Compensation cutoff occurs when the power piston dips below a specified value, preventing flow through the compensating needle valve ($Z_{pp} = Z_c$, Fig. 7). Normal equilibration of the buffer system does not occur, causing a momentarily sustained downward force on the compensating land. Under these conditions, compensation cutoff prevents underfueling, and possible underspeeding, by maintaining a temporarily higher reference speed, through the sustained downward force on the compensating land.

Load Regulation and Fuel Limiting. Integral with the hydraulically actuated fuel controller, described above, are the load regulator and fuel limiter, which control fueling and load during operating conditions, which would otherwise lead to undesirable engine operation.

The load regulator acts to maintain proper engine operation by providing a feedback signal to reduce engine load. Reduced load regulated fueling occurs as a result of a decreasing main generator electrical load, which in turn produces a value of rack consistent with a set of load regulated limits, which are dependent on air box pressure and throttle position (engine speed).

The load regulator is schematically shown in Fig. 8. During non-load regulated operation, the load control pilot valve (LCPV), S, is below its seat and positioned so that fluid is supplied to a servo motor driven rheostat in order to move it in the direction of increasing generator load. The rheostat is at its stopped position for maximum generator excitation. Under these conditions, the electrical control system microcomputer

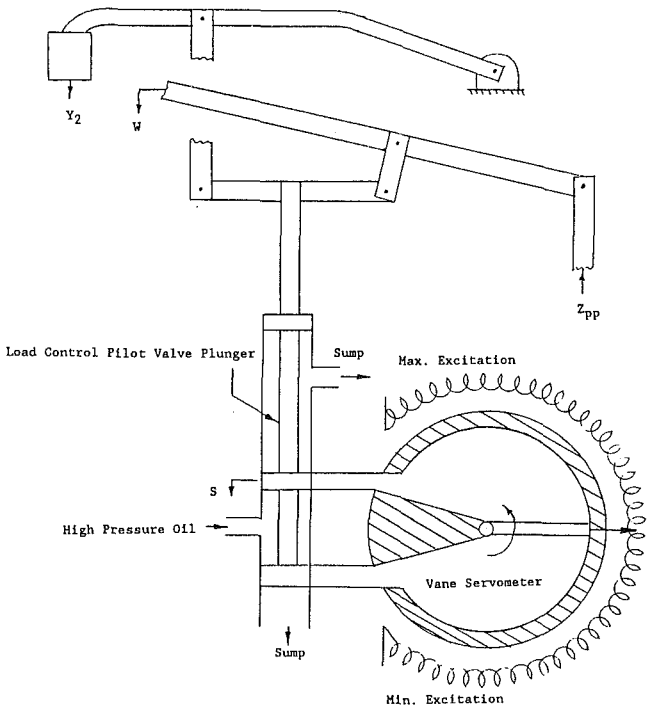


Fig. 8 Schematic of the governor load regulator and associated linkage

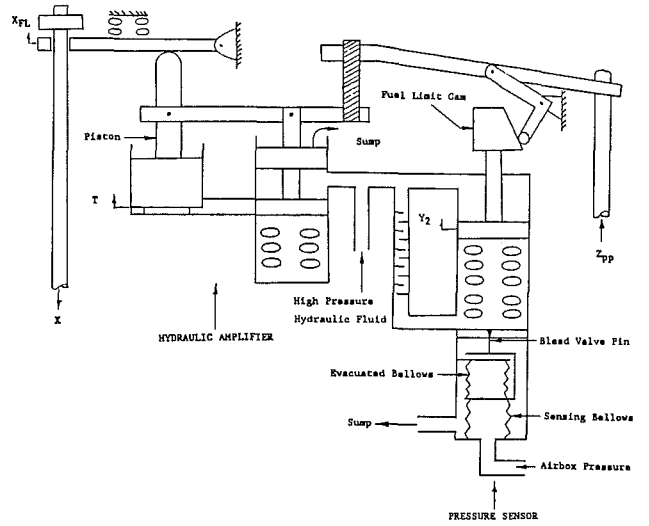


Fig. 9 Schematic of the governor fuel limiter and associated linkages

maintains the generator load at its limited value for the throttle setting. Pilot valve positions above the seated position produce servo motor rotation, which decreases generator load in proportion to the rheostat position through the electrical control system. The position of the LCPV is dictated by the simultaneous positions of the power piston, Z_{pp}, servo position, W, and air box sensor piston, Y_2, through the various linkages shown.

Under certain conditions of load and air box pressure, pilot valve position is no longer prescribed by the balance of flyweight, pressure, and spring forces, but is determined by the fuel limiter (Fig. 9). During fuel limiting, governor pilot valve position and therefore rack is dictated by the position of the fuel limit lever at the shutdown rod, which is physically connected to the governor's main pilot valve.

The fuel limit lever moves when the hydraulic amplifier (H.A.) pilot valve moves below its centered position. Integra-

Downloaded 01 Jun 2010 to 171.66.16.87. Redistribution subject to ASME license or copyright; see http://www.asme.org/terms/Terms_Use.cfm

tion of the H.A. begins when the H.A. pilot valve is below its centered position and continues until the fuel limit lever returns to its lowest (stop) position. At any time the integrated value of fuel limit lever position (X_{FL}) is greater than the force-balanced pilot valve position, fuel limiting is active and actual pilot valve position is prescribed by X_{FL}. The H.A. pilot valve position is given by the instantaneous positions of the power piston, Z_{pp}, air box sensor piston, Y_2, H.A. piston, T, gain of the fuel limit cam, bell crank and follower, and the lengths of the fuel limit linkages (shown in Fig. 9). Since load regulated fueling is lower than that prescribed by the fuel limiter, fuel limiting becomes possible during transient operation only, with steady-state engine output power control being accomplished by the load regulator or, preferably, the electrical control system limits on generator output power.

Initialization. The initialization of the governor submodel under non-load regulated conditions proceeds with all state variables set to their steady-state values and rack position implicitly determined from equating the initial load torque and the brake torque calculated from the torque regression. Initial, steady-state governor values are determined by setting the left-hand sides of the system differential equations to zero. Doing this indicates steady-state pilot valve position and buffer system pressure drop are equal to zero.

The initialization of the load regulator proceeds by first determining the load control pilot valve position. If the LCPV is below its seated position, the simulation is not load regulated at the initial steady-state condition and the governor initialization proceeds in normal fashion. If the LCPV is above its seated position, an iteration between load regulator (i.e., main generator load torque), rack position, and air box pressure takes place until the load regulator pilot valve is balanced (seated). Since steady-state load regulation precludes fuel limiting, initial H.A. piston position is simply set equal to its minimum value.

Electrohydraulic Governor Simulation. A transient governor subsystem simulation, which demonstrates basic governor and engine response to a change in load torque, is illustrated in this section. Simulations exhibiting load regulation and fuel limiting are discussed in a subsequent section demonstrating the combined engine/governor model in conjunction with engine load torques obtained from the integrated locomotive propulsion system code.

Figures 10(*a*), 10(*b*), and 10(*c*) predict governor and diesel engine response to a ramped change in load torque: 10 percent increase in one speed. Initial steady-state conditions of load torque and engine speed are maintained from 0 to 0.5 s. Initial differences in load and brake torque ($0.5 < t < 1.8$ s, Fig. 10*a*) produce a drop in engine speed (Fig. 10*b*). (Note here that the convention for rack is that lower numerical values imply larger values of fueling rate.) The (lower) centrifugal force of the governor fly weights against the speeder spring force causes an uncentering of the main pilot valve plunger (Fig. 10*c*). A pressure difference between trapped and intermediate cavities of the buffer system builds, producing a somewhat more sluggish response in power piston movement (rack). As expected, the power piston reaches a maximum when the main pilot valve passes its centered position ($X = 0$). Initial and final rack values produce engine brake torques that balance the steady-state load, at each condition, respectively. Initial and final values of main pilot valve position and buffer system pressure drop exhibit their equilibrium (null) values.

Integrated Engine/Governor Simulations in Locomotive Context

After integration of the full locomotive propulsion system code (electrical system and controls, diesel engine, and governor submodels), a large number of simulations were performed in order to: (1) compare results to existing data, and (2) identify key dynamic elements responsible for producing observed locomotive behavior. Certain specific engine/governor responses (i.e., rack response to dynamic engine speed; engine torque/air box pressure response to dynamic rack and engine speed; load regulation and fuel limiting in response to dynamic air box pressure and electrical control) could only be accurately simulated in the context of the load torques imposed by the full locomotive propulsion system. Thus, the full prototype locomotive simulation code was used to carry out these simulations. Two of these simulations are presented below. The discussion concentrates on the engine/governor response. Each simulation exercises the locomotive system code through specific logic and operating conditions necessary to obtain engine load torque, which then drives the engine/governor dynamic response. Quantitative comparisons are made to strip chart records of brush recorder data collected during field tests of a prototype locomotive, under identical operating conditions.

Throttle 0-8, Minimal Load. This simulation is conducted by dropping out the generator field contactor (GFC) during an initial steady-state idle throttle "0" condition. This insures that there is no main generator electrical load during the engine's acceleration to a higher set-speed. The throttle is then changed from 0 to 8. With no generator excitation current present, engine load torque is comprised only of accessory loads and generator losses, all of which are currently represented in the integrated locomotive system code. The major contribution to the system response from the diesel engine submodel is in the calculation of brake torque with corrections

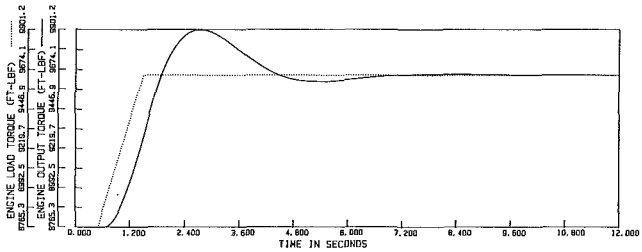


Fig. 10(*a*) Engine output torque and engine load torque

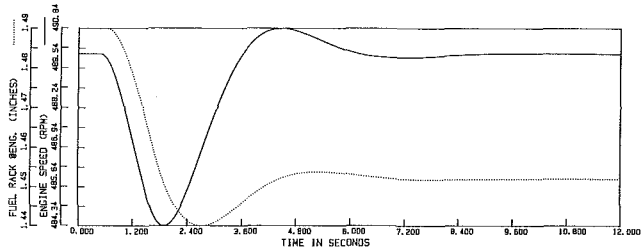


Fig. 10(*b*) Engine speed and rack position at the engine

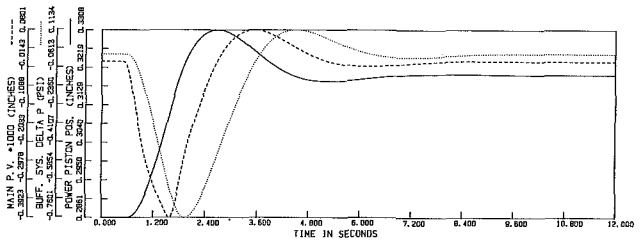


Fig. 10(*c*) Power piston position, ΔP_{BS}, and main pilot valve position

Fig. 10 Simulated response of the diesel engine and electrohydraulic governor to a ramped change in load torque

Downloaded 01 Jun 2010 to 171.66.16.87. Redistribution subject to ASME license or copyright; see http://www.asme.org/terms/Terms_Use.cfm

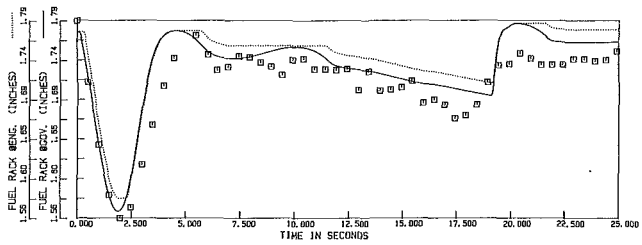


Fig. 11(*a*) Fuel rack at the governor, equivalent fuel rack at the engine, and measured fuel rack at the governor (data points)

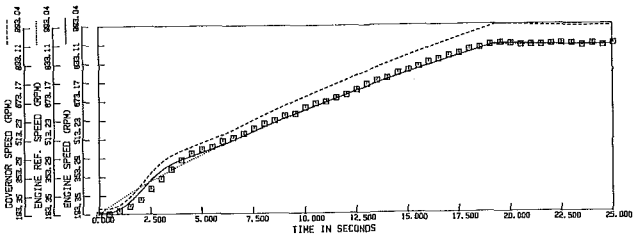


Fig. 11(*b*) Engine speed, reference engine speed, governor speed, and measured engine speed (data points)

Fig. 11 Simulated results of the minimal load, throttle 0 to 8 simulation with comparisons to strip chart data

as a function of dynamic air/fuel ratios (see earlier discussion of Diesel Engine Submodel).

Simulation results of the minimal load, 0 to 8 throttle increase are compared to digitized strip chart records in Figs. 11(*a*) and 11(*b*). In these two figures, solid lines are used to compare predicted responses to measured values. Dashed and dotted lines feature simulation variables of additional interest. The curve representing the desired engine reference speed (Fig. 11*b*) reflects the rate of governor speeder spring and speed setting servo movement as well as the speeder spring calibration. Characteristics of measured governor rack response (Fig. 11*a*) are an initial peak in fuel rack position (1.56 in. at 2 s) followed by a minimum of approximately 1.77 at 5 s and a slow rise to 1.68 at 17.5 s. Measured rack data show some deviations due to scatter. Simulated rack shows delays in equivalent fueling at the engine (Fuel Rack @ Engine) due to rack lash and torque delays previously discussed. Engine speed (Fig 11*b*) shows nearly a 1 s delay prior to any appreciable increase over idle speed, a knee from 1 to 6 s followed by a nearly constant rate of climb to a set-speed of 904 rpm at 19 s, with a slight overshoot at 20 s. Simulated responses of rack and engine speed are shown to produce excellent agreement with measured values.

Dead Load Pick Up. Simulation of the prototype locomotive during a dead load pick up (DLPU) test is shown in Figs. 12(*a–e*). The DLPU test is performed in self-load test mode, with the voltage and current output of the main generator being dissipated in an electrically resistive grid. Initial conditions correspond to steady-state throttle 8 operation: engine speed at 904 rpm, main generator output power equal to its maximum traction power rating, and all other electrical control references at their maximum limit values. The generator field contactor (GFC) is then dropped out, which causes excitation current to the main generator to decay according to the main generator field time constant. Generator output power, and therefore engine load, is reduced to near zero as the excitation current decays over the time the GFC is open. With control references remaining at their limits, picking up or closing the GFC results in a control response characterized by large, rapid increases in excitation current and generator output power. In this way, rapid transients in engine load may be achieved (Fig. 12*a*). This, in turn, invokes governor responses for fuel limiting and load regulation.

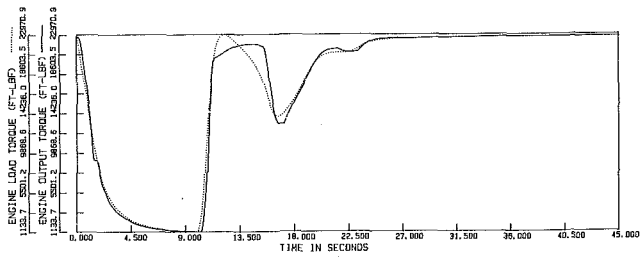


Fig. 12(*a*) Engine output torque and engine load torque

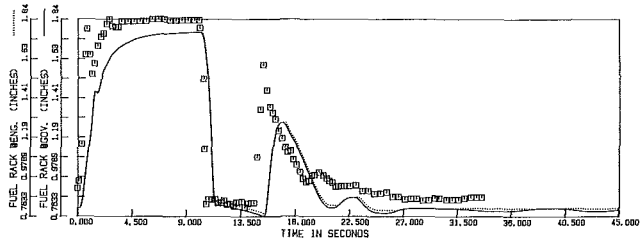


Fig. 12(*b*) Fuel rack at the governor, equivalent fuel rack at the engine, and measured fuel rack at the governor (data points)

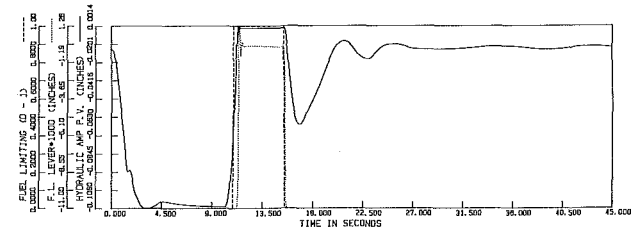


Fig. 12(*c*) Hydraulic amplifier pilot valve position, fuel limit lever position, and fuel limiting flag; a fuel limit flag of 1 corresponds to a fuel limiting condition

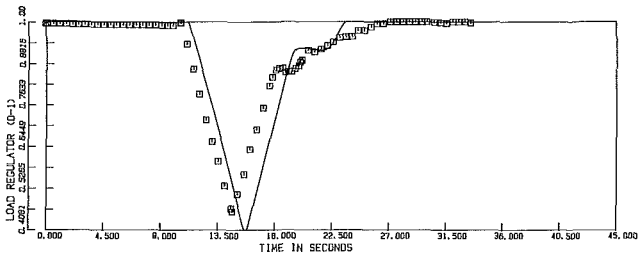


Fig. 12(*d*) Simulated and measured values of load regulator multiplier (data points)

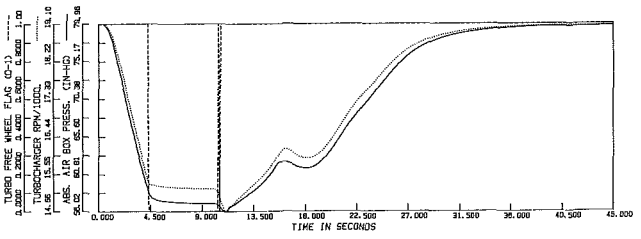


Fig. 12(*e*) Absolute air box pressure turbocharger speed and turbocharger free-wheel flag. A turbocharger free-wheel flag equal to 1 corresponds to a free-wheeling turbocharger and a free-wheel flag equal to 0 corresponds to a gear-driven turbocharger.

Fig. 12 Simulated results of the DLPU simulation with comparisons to strip chart data

Governor fuel rack response can be found in Fig. 12(*b*). Characteristics of the predicted rack response during GFC drop out are: an initial value of 0.81 in. and a steep rate of increase (decreased fueling) with an abrupt change in slope at about one second. Examination of strip chart records of rack show initial values of approximately 0.84 in. and a single ring at 0.5 to 1.0 s. Although the timing of the change in slope of

Downloaded 01 Jun 2010 to 171.66.16.87. Redistribution subject to ASME license or copyright; see http://www.asme.org/terms/Terms_Use.cfm

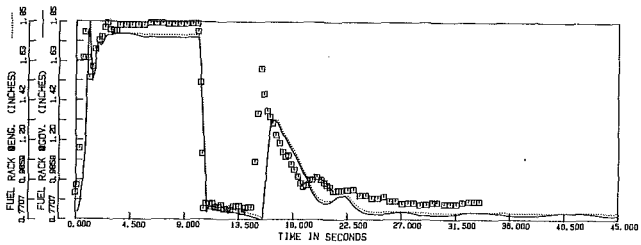


Fig. 13 Simulated results of the DLPU simulation with a fixed value of generator field time constant: fuel rack at the governor, equivalent fuel rack at the engine, and measured fuel rack at the governor (data points)

simulated rack ($t = 1.0$ s) is approximately the same as the data, the amplitude of the ring is not reproduced.

Examination of key buffer system variables indicates that the abrupt change in slope of simulated rack at $t = 1.0$ s is caused by buffer system bypass. With the buffer piston against its bypass position ($\Delta P_{BS} = 8.25$ psi), the rapid rate of decline in fueling prior to the change in slope is caused by the rapid exchange of governor hydraulic fluid (from trapped to intermediate oil cavities) through the bypass port, thus producing a temporary underfueling condition (see previous discussion of buffer system bypass).

Further investigations into the amplitude of this ring indicated that it is heavily influenced by the initial rate of change in load ($t < 1.0$ s). Examination of generator output power data during the DLPU test indicated that transient generator dynamics may be responsible for differences in rates of change of simulated as compared to actual loads. The rate of change in load is tied to the main generator description, which currently utilizes a quasi-steady representation for the calculation of ouput d-c rectified voltage given generator rpm, output rectified d-c current, and stator winding configuration and as such, includes no intrinsic dynamics.

In order to illustrate the effects of larger predicted rates of change in load on predicted rack response during the DLPU test, an additional simulation was performed in which the main generator field time constant was set to a selected fixed value (instead of utilizing empirical equations for its dynamic calculation). This produced a rate of decrease in load that more closely simulates generator output power, during the period 0.0 to 1.0 s in the DLPU test. Under this condition, the buffer system bypass port is open longer and simulated rack can be seen to decrease faster, and undershoot by a larger margin, which is a better representation of actual rack response. A simulation utilizing the fixed value of generator time constant can be seen in Fig. 13, where simulated rack is again compared to measured data for the DLPU test. (Note that since the actual field time constant is expected to change in a dynamic manner, fixing its value over the entire simulation cannot be justified. The above example does, however, demonstrate the ability to modify component descriptions in an overall system simulation, in order to resolve key elements of specific system responses.)

Other interesting features of rack response during the DLPU test occur after the GFC is picked up at 10.0 s. Referring again to the simulation that utilized dynamic calculations of generator field time constant and its effect on rack (Fig. 12*b*), characteristics of the predicted rack response during GFC pickup are: a rapid decrease (increase in fueling) to a value of 0.83 in., followed by a minor oscillation and slow descent for approximately 4 s to a value of 0.76 in. The equivalent strip chart data show a rapid decrease to 0.82 in., followed by slight oscillations and a slow descent for 4 s to 0.80 in. As can be seen from Fig. 12(*c*), the plateau in fueling is a fuel-limited event. The minor oscillations in rack are caused by oscillations in the fuel limit lever, which acts (through the dynamics of the hydraulic amplifier) on the main pilot valve plunger.

The load regulator multiplier (Fig. 12*d*) integrates to a value of 0.41 from 1.0 in approximately 4 s, which corresponds to its maximum rate (1.0 to 0.0 in 7 s). From 0.41 it integrates up to about 0.92 in 0.39 s with one slightly damped oscillation and then up to 1.0. Strip chart records show similar behavior with the exception of a generally longer period of load regulation. The minimum strip chart values is 0.42, followed by a gradual rise with one (or maybe two) damped oscillations from about 0.86 up to 1.0.

Simulated diesel engine responses of air box pressure and turbocharger speed to the transient load and rack of the DLPU test are shown in Fig. 12(*e*). Air box pressure declines during the rapid decreases of load and fueling associated with GFC drop out. Energy in the exhaust gases diminishes to the point where the free-wheel speed falls below the gear-driven turbocharger speed and the turbocharger compressor becomes gear driven ($t = 4.5$ s). During GFC pickup, the abrupt change in load causes engine speed to drop initially, resulting in a decrease in turbo speed and air box pressure at $t = 10$ s. Because of a rapid reduction in engine speed, the gear-driven clutch "drops out" under the free-wheeling turbo at $t > 10$ s. The turbocharger speed and absolute air box pressure again begin to rise ($t = 10$ to 15 s) in response to a higher level of fueling and exhaust gas energy. An overspeed condition at $t = 16$ to 18 s results in a rapid decrease in fueling, which ultimately causes turbo speed to decrease. The near-constant fueling rates that exist for $t > 20$ s cause a gradual increase and leveling off of turbo speed and air box pressure to their final steady-state values. (Note that since the simulation starts at full steady-state power and returns to this condition in a relatively short time period, the engine structural thermal inertia does not significantly influence the transient response of the diesel engine.) Comparisons of simulated results of air box pressure and turbocharger speed to brush recorder data produced excellent agreement in both the nature of the specific responses and magnitudes of the transients.

Conclusions

1 Comprehensive dynamic models of an experimental two-stroke engine and an electrohydraulic governor have been developed as part of an overall prototype locomotive propulsion system simulation.

2 The models exhibit the correct physical behavior and compare well with available data.

3 The integrated engine-governor code can be used to study specific governor-engine interactions as well as interactions between all the locomotive propulsion system subsystems.

4 Because of its detailed representation of the engine-governor system, this part of the simulation can be used as a basis for exploring electrical control issues impacting engine performance.

Acknowledgments

The work described in this paper was carried out by ITI under contract to EMD, which provided active technical input during its execution. Special mention should be made of the valuable assistance provided by S. Vargyai, K. Sinko, and P. Gottemoller of the EMD engine group.

References

1 Kotlin, J. J., Dunteman, N. R., Chen, J., and Heilenbach, J. W., "The General Motors EMD Model 710G Series Turbocharged Two-Stroke Cycle Diesel Engine," ASME Paper No. 85-DEP-24, 1985.

Downloaded 01 Jun 2010 to 171.66.16.87. Redistribution subject to ASME license or copyright; see http://www.asme.org/terms/Terms_Use.cfm

2 Becker, D. A., "An Application of Microprocessor Technology to Diesel-Electric Locomotives," SAE Paper No. 860754, 1986.
3 Jennings, M. J., Blumberg, P. N., and Amann, R. W., "Dynamic Simulation of Detroit Diesel Electronic Control System in Heavy Duty Truck Powertrains," SAE Paper No. 861959, 1986.
4 Watson, N., and Marzouk, M., "A Non-linear Digital Simulation of Turbocharged Diesel Engines Under Transient Conditions," SAE Paper No. 770123, 1977.
5 Winterbone, D. E., and Loo, W. Y., "A Dynamic Simulation of a Two-Stroke Turbocharged Diesel Engine," SAE Paper No. 810377, 1981.
6 Goyal, M. R., "Simulation of a Turbocharged Diesel Engine to Predict the Transient Response," ASME Paper No. 78-DGP-11, 1978.
7 Schmidt, W., and Hinkle, S., "Parametric Analysis of a Turbocharged Two-Stroke Cycle Diesel Engine Air System," ASME Paper No. 78-DGP-5, 1978.
8 Morel, T., Keribar, R., Blumberg, P. N., Fort, E. F., "Examination of Key Issues in Low Heat Rejection Engines," SAE Paper No. 860316, 1986.
9 Woodward Governor Company, "Analytic Representation of Mechanical-Hydraulic and Electro-Hydraulic Governors," Woodward Bulletin No. 25067, © Woodward Governor Company, 1978.
10 Garvey, D., "Slide Rule Analysis of Engine-Governor Performance," Woodward Governor Company PMCC 73-13.
11 Davies, M., "Governors and Governor Gear," *Diesel Engine Reference Book*, © Butterworth and Co. Ltd. 1984, Chap. 13, pp. 7–11.

Downloaded 01 Jun 2010 to 171.66.16.87. Redistribution subject to ASME license or copyright; see http://www.asme.org/terms/Terms_Use.cfm

Progress on the Investigation of Coal-Water Slurry Fuel Combustion in a Medium Speed Diesel Engine: Part 1—Ignition Studies

B. D. Hsu
Transportation Systems,
General Electric Company,
Erie, PA 16531

A micronized de-ashed coal-water slurry (CWS) fuel of approximately 50 percent coal loading has been successfully ignited and burned in one GE 7FDL engine cylinder at 1050 rpm. For this study, only about 1/3 of the full load fuel engery was supplied due to limitations of the fuel injection equipment used. Three types of ignition methods have been investigated: compression ignition with no ignition aid; separate diesel pilot fuel injection to ignite the CWS fuel; combined CWS and pilot diesel fuel injection (stratified pilot ignition). Conditions of ignition and the burning characteristics that immediately followed using the above three ignition methods are described.

Introduction

Under the sponsorship of the US Department of Energy (DOE), Morgantown Energy Technology Center (METC), the General Electric Company is conducting a program to study the technical and economical feasibility of using coal fuel to power a locomotive. Some results of this study on the economic assessments and CWS fuel combustion bomb tests have already been published in past years [1-3]. This paper is the first in a series to report on the full-scale single-cylinder engine test results.

The single-cylinder engine performance tests using CWS fuel are being conducted at GE-TS in three phases. Correspondingly, three different systems of fuel injection equipment (FIE) are used. They are briefly described as follows:

• **Phase I—Ignition Studies of the CWS in an Engine Cylinder.** System I FIE was used during this phase of the work. It was a modified standard size diesel fuel FIE with a CWS isolation pump placed between the high-pressure pump and the injector to prevent plunger sticking. Due to the low volumetric energy density of the CWS compared to diesel fuel, only 1/3 of the needed full load energy could be handled by this system. Ignition and the burning of the CWS fuel that immediately followed were the purposes of this study. Three types of ignition methods were investigated: direct compression ignition, separate pilot diesel fuel injection ignition, and combined CWS and pilot diesel fuel (hereinafter called "stratified pilot") ignition.

• **Phase II—Full Load Engine Tests.** System II FIE is used. This is an upscaled version of System I FIE capable of supplying the full load energy needed by the engine. Combustion of the CWS under full load condition is the main subject of study. Fuel injection quality is expected to be poor at engine part load [3]. Therefore very limited exploratory efforts are devoted to engine partial load conditions. Some engine emissions data and wear data of engine parts of standard materials are also expected to be gathered. The above-mentioned three types of ignition methods are further investigated.

• **Phase III—Full Range Engine Tests Using System III FIE.** The accumulator CWS FIE developed by GE Corporate Research and Development [3] will be used. This CWS FIE is expected to perform well over a wide range of engine load conditions. Engine tests are to determine the limit of such ranges. Optimization of engine combustion is to be sought. Emissions and wear will continue to be studied.

This paper summarizes the findings of Phase I—ignition studies of the CWS fuel in the single-cylinder engine test.

Ignition Methods

Three methods of igniting the CWS in the engine cylinder have been investigated. They are as follows:

• Compression ignition: CWS was ignited solely by the compression temperature generated inside the engine cylinder.

• Separate pilot diesel fuel injection: A separate pilot injector was used to supply a small amount of pure diesel fuel to ignite the CWS which was injected through the main injector. Two separate injectors were used in this case.

• Stratified pilot fuel injection: A small amount of diesel fuel was delivered to the cylinder through the main fuel injector. As the fuel was discharged from the injector, the first part

Contributed by the Internal Combustion Engine Division and presented at the Energy-Sources Technology Conference and Exhibition, New Orleans, Louisiana, January 10-14, 1988. Manuscript received by the Internal Combustion Engine Division July 21, 1987. Paper No. 88-ICE-4.

Copyright © 1988 by ASME
Downloaded 01 Jun 2010 to 171.66.16.87. Redistribution subject to ASME license or copyright; see http://www.asme.org/terms/Terms_Use.cfm

consisted essentially of diesel fuel, followed by mostly CWS. The first part of the fuel was easily ignited due to high concentration of diesel fuel and the heat thus generated assisted the burning of subsequently entered CWS. Only one injector is used.

Test Hardware

Tests were conducted using a 7FDL two-cylinder engine (Fig. 1). The combustion system is a quiescent type with direct fuel injection. The inlet manifold air pressure and temperature are externally controlled. The exhaust back pressure can also be manually adjusted. The bore and stroke of the engine are 229 mm and 267 mm, respectively. The maximum speed of the engine is 1050 rpm. For this test, only the left-side engine cylinder was set up to run on CWS. The right-side cylinder ran on regular diesel fuel. Before CWS was introduced into the left cylinder, the engine was warmed up and brought up to test speed by the right cylinder. After the inlet and exhaust manifold conditions (pressure, temperature, etc.) were adjusted to the prescribed test requirements, the rack control solenoid of the left-side CWS pump was activated and CWS was injected into the cylinder. The instrumentation installed in the left-side cylinder recorded the ignition and combustion of the CWS. Two injectors and a pressure transducer were installed in the coal-fired left cylinder as shown in Fig. 2. The centrally mounted main injector had ten holes of 0.40-mm diameter and 150-deg spray included angle. The main injector was used to inject CWS fuel. The pilot diesel fuel injector was mounted to the side in the cylinder. It is of the same dimension as the main injector, except only three of the ten holes on the injector tip are drilled. For the present investigation, a piston crown with compression ratio 12.7 was used. A diaphragm isolation pump was employed in the main CWS injection system. The system schematic is shown in Fig. 3.

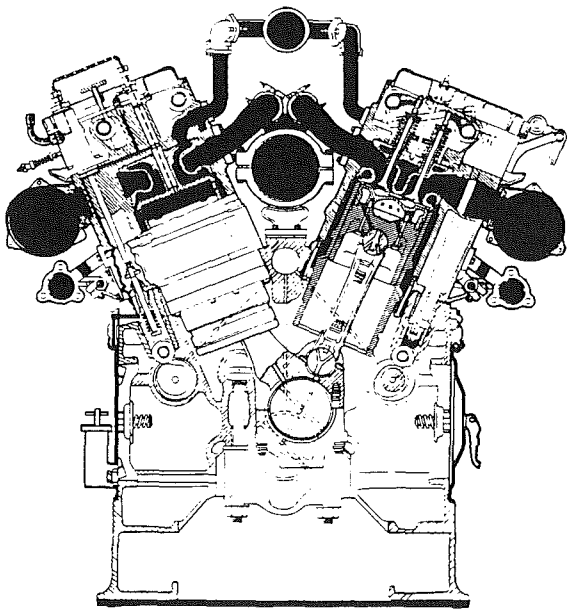


Fig. 1 7FDL two-cylinder research engine

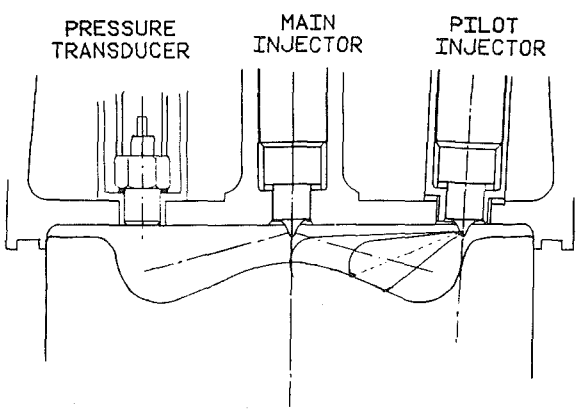


Fig. 2 CWS test cylinder layout

Instrumentation and Data Reduction

The general instrumentation layout is shown in Fig. 4. Cylinder pressure data were collected on a crank-angle basis. Fifty cycles were averaged in the digital oscilloscope for further processing. A continuous recording of 80 cycles was also stored in the memory to evaluate combustion consistency in repeated cycles. In addition to measuring the amount of CWS used, three parameters were collected for CWS fuel injection. They were: the injector needle lift; the injector pressure, which was measured very close to the injector tip; and the diesel fuel line pressure at the other side of the diaphragm pump. All these data were also collected on a 50-cycle average basis.

The power generated by the coal-fired cylinder was determined by the indicated power in kW calculated with the recorded cylinder pressure trace. Thermodynamic first law calculations were done using cylinder pressure versus volume data to obtain average cylinder temperature and heat release information. In the heat release calculation, heat losses to cylinder walls were estimated by Annand's method [4]. Gas face temperatures of the exposed surfaces were estimated with an empirical equation derived by French [5]. The air–fuel ratio in the Annand equation was modified to account for heating value difference of coal and diesel fuel. The "Relative Cycle Efficiency" method derived by the author [6] was used to evaluate the effect of the calculated heat release shape on cycle efficiency quantitatively.

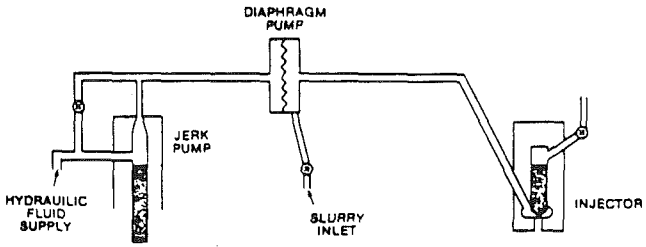


Fig. 3 Schematic diagram of the positive displacement fuel injection system

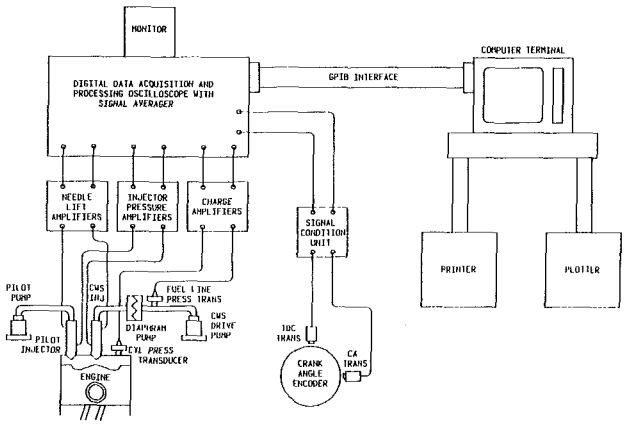


Fig. 4 CWS engine testing data aquisition and processing system

Downloaded 01 Jun 2010 to 171.66.16.87. Redistribution subject to ASME license or copyright; see http://www.asme.org/terms/Terms_Use.cfm

In this paper, ignition is arbitrarily defined at the starting point of significant, continuous net positive heat release. All pressures quoted are absolute.

Fuels and Additives

The CWS used was prepared by OTISCA Industries, Inc. The coal is cleaned to contain only 0.36 percent ash and micronized to a mean particle size of 2.88 microns. The nominal lot analysis of product coal is shown in Table 1. The percentage of solids in CWS prepared by OTISCA was about 55 percent. When it was used in the diaphragm pump as received, no injection occurred. The CWS was then diluted to various concentrations and successful injection was obtained. Subsequently it was found that when the coal loading in CWS exceeded 50 percent the fuel line pressure drop was very large, resulting in very low injector pressure.

A typical comparison of 53 and 48 percent CWS fuel line and injector pressure trace is shown in Fig. 5. The maximum fuel line pressure of the 53 percent CWS was recorded at 64.4 MPa and the injector maximum pressure was only 31.7 MPa. The pressure drop is 32.7 MPa. For the 48 percent CWS case, the pressure drop is seen to be only 19.1 MPa. As pointed out by Farmayan et al. [7], the CWS fuel atomization quality has a dominant effect on coal burnout. In the present investigation, high injector pressure was the main factor to improve atomization. Therefore the coal concentrations in all tests were maintained at 47 to 49 percent. The water soluble lubricant UCON 50-HB-5100 is generally used to prevent injector needle sticking. In the case where diesel fuel was used for stratified pilot ignition, anti-agglomerating additive TRITON X-114 was added to CWS at 2.5 percent coal weight.

Compression Ignition Results

Basic Characteristics. When CWS was injected into the cylinder under normal engine conditions and at standard diesel fuel static injection timing, no combustion was observed. In Fig. 6, the recorded cylinder pressure traces before and after CWS injection are compared. Almost no difference is seen between them, suggesting no combustion occurred after CWS fuel was introduced. On the same figure, the injector needle lift recording and the calculated average cylinder temperature traces are also plotted. At the start of CWS needle lift (16.5 deg BTDC), the average cylinder temperature was close to 890 K and it increased to 960 K at TDC. According to combustion bomb test results using similar FIE [2], temperatures of this order, given sufficient time, will result in CWS ignition. However, as indicated by the study of Walsh et al. [8], a finite time is needed to evaporate the water in CWS before ignition can occur. The approximate 4–5 ms ignition delay measured in combustion bomb study [2] probably is mostly used for water evaporation. At the tested engine speed of 1050 rpm, 5 ms corresponded to about 30 deg crank angle. In Fig. 6, it can be seen that 30 deg crank angle after injection start (at about 15 deg ATDC), due to the piston downward movement, the average cylinder temperature has dropped below 890 K. Therefore, inadequate temperature after evaporation led to ignition failure.

A case of successful CWS ignition is shown in Fig. 7. On the upper part, the comparison of cylinder pressure traces before and after CWS fuel injection is drawn. The needle lift of CWS injection is also shown. From the needle trace the injection timing is seen to be notably much advanced over that shown in Fig. 6.

The static injection timing was set at 65 deg BTDC, yielding 51.4 BTDC dynamic timing. In this run, the inlet air temperature was raised from 85°C to 100°C. The difference of the cylinder pressure traces before and after fuel injection clearly shows that combustion of CWS did occur. As a result 45.6 kW was developed. In Fig. 7(*B*), the calculated cylinder average temperatures and heat release rates are shown. Ignition is seen to have occurred at about 11 deg BTDC. The 40 deg crank-angle ignition delay corresponds to approximate 6 ms in time, which is close to that observed in the combustion bomb [2]. The difference in temperature histories during the ignition delay period for combustion bomb and engine test should be noted. While the temperature in this period is more or less constant for bomb test, it starts at a low level and keeps rising in an actual engine.

Comparing the temperature curves before and after CWS fuel injection in Fig. 7(*B*), it can be seen that the water in CWS has lowered the cylinder temperature considerably before combustion. However, at the time of ignition (about 11 deg BTDC), the temperature could still reach 890 K, which was needed for ignition.

Table 1 Coal nominal lot analysis

Proximate Analysis		Ultimate Analysis	
% Ash	0.36	% Carbon	86.15
% Volatile	33.67	% Hydrogen	5.15
% Fixed Carbon	65.97	% Nitrogen	1.26
		% Chlorine	0.11
Mean Particle Size		% Sulfur	0.59
Mass Mean Dia.		% Ash	0.36
(microns)	2.88	% Oxygen (diff)	6.39
Heating Value			
High Heating Value (kJ/kg)		35580	

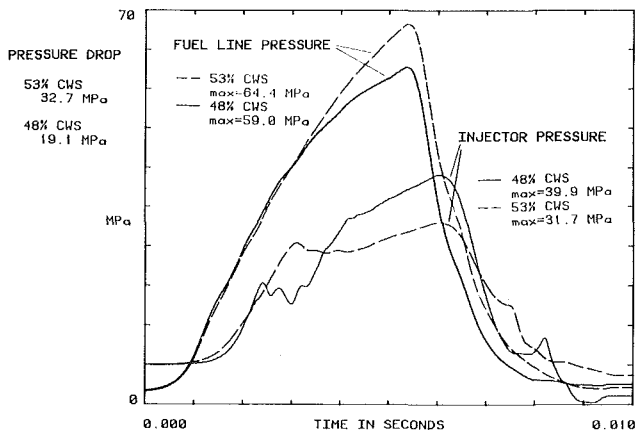


Fig. 5 Fuel line and injector pressure of 2 coal percent CWS at 1050 rpm

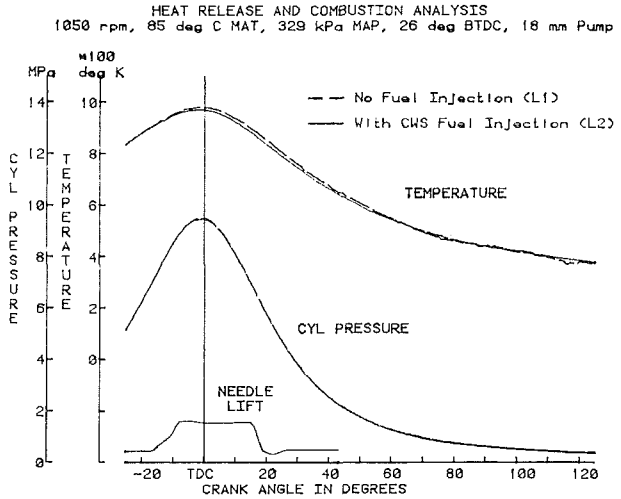
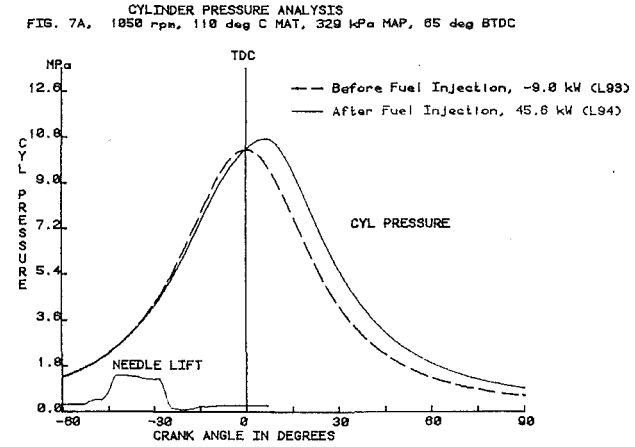


Fig. 6 Compression ignition, no combustion

Downloaded 01 Jun 2010 to 171.66.16.87. Redistribution subject to ASME license or copyright; see http://www.asme.org/terms/Terms_Use.cfm



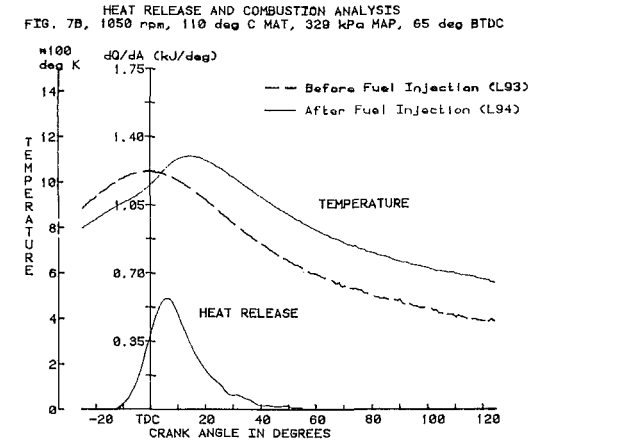


Fig. 7 Compression ignition, basic characteristics

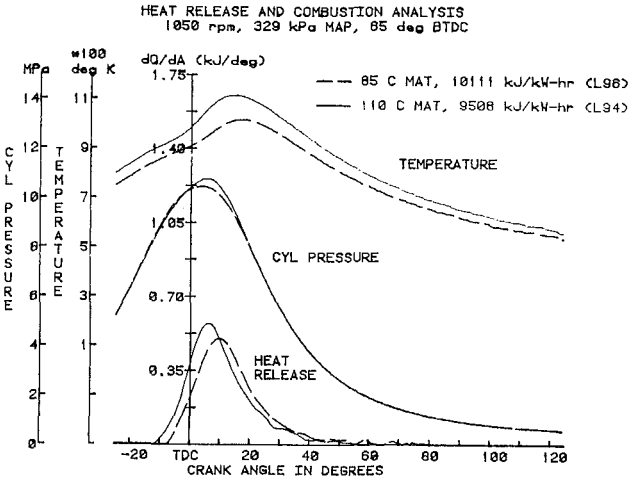


Fig. 8 Compression ignition, MAT effect

Inlet Manifold Air Temperature (MAT) Effect. 110°C and 85°C MAT were compared at 1050 rpm and 65 deg BTDC static injection timing. Results are shown in Fig. 8 and Table 2.

As was expected, lower MAT (L96) led to longer ignition delay, Table 2, column (5). From the cylinder temperature comparison in Fig. 8, it can be seen that temperature is lower for the lower MAT case all through the cycle. The heat release rate of the L96 run was lower and later in the cycle, which caused all the combustion indicators in Table 2, columns (8)-(11) to be inferior.

Table 2 Compression ignition, MAT effect (1050 rpm, 329 kPa MAT, 65 deg BTDC)

Ignition Indicators					
Run	MAT °C	Dyn. Inj. °BTDC	Ignition °BTDC	Ign. Del. °CA	Cyl Temp @ Ign °K
(1)	(2)	(3)	(4)	(5)	(6)
L94	110	51.4	11.4	40.0	900
L96	85	52.1	7.0	45.1	875

Combustion Indicators					
Run	Pmax MPa	Power kW	Fuel Burnt %	Rel. Eff. %	SFC kJ/kw-hr
(1)	(7)	(8)	(9)	(10)	(11)
L94	10.7	45.6	88.2	94.6	9508
L96	10.8	45.0	81.2	91.8	10111

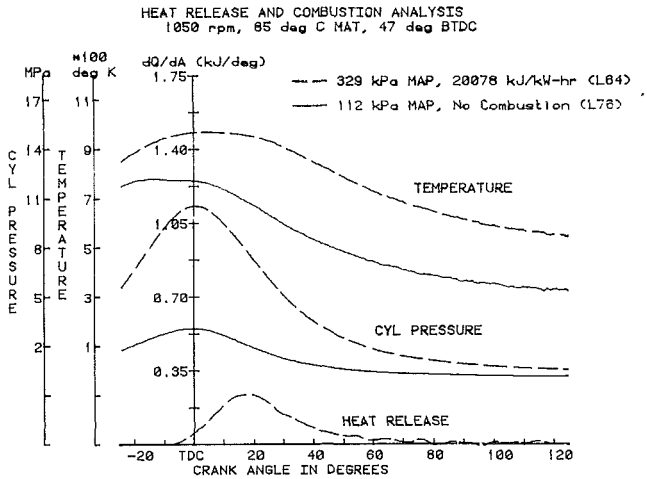


Fig. 9 Compression ignition, MAP effect

Inlet Manifold Air Pressure (MAP) Effect. Comparison runs of 329 kPa and 112 kPa MAP were performed at 1050 rpm, 47 deg BTDC static injection timing, and 85°C MAT. The results are shown in Fig. 9. From the temperature trace in Fig. 9, it is seen that no combustion occurred for the lower MAP case of 112 kPa (L76). Consequently, the heat release rate is zero. It should be noted that the mass of air trapped in the engine cylinder is less at lower MAP. Approximately the same amount of CWS was injected into the cylinder in both cases; therefore, about the same amount of heat was extracted from the trapped air charge to evaporate the water for the two cases. The temperature drop after water evaporation would be more for the lower MAP case. This is seen in the temperature comparison in Fig. 9. In fact, for the 112 kPa MAP run, the maximum temperature only reached 780 K, which was too low for ignition to happen. Another factor that might also have contributed to the ignition failure is the poor atomization quality as observed in the combustion bomb [2], when CWS was injected into lower density air. The environment of low gas temperature and low density together is certainly very unfavorable for ignition and combustion.

Summary—Compression Ignition. With limited number of tests run, successful ignition depended on the average cylinder temperature after water (in CWS) evaporation and the inlet air pressure. If the temperature was below 890 K, ignition of CWS by compression alone did not occur.

Downloaded 01 Jun 2010 to 171.66.16.87. Redistribution subject to ASME license or copyright; see http://www.asme.org/terms/Terms_Use.cfm

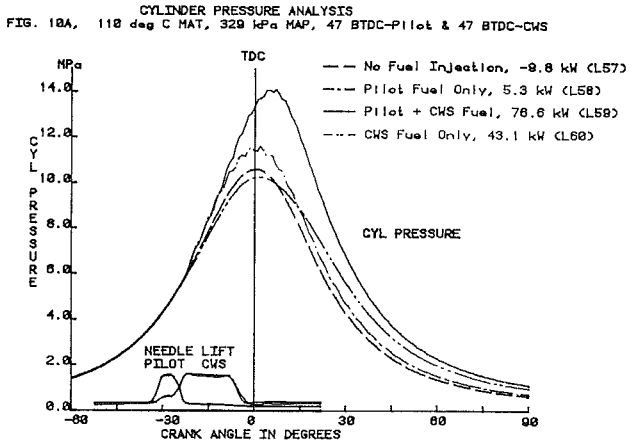
Separate Pilot Diesel Fuel Injection Ignition Results

Basic Characteristics. The minimum amount of pilot diesel fuel used in this study was 90 mm^3/stroke due to injection hardware limitations. This amounts to about 6–7 percent of full load energy. Since the FIE used in the present study can only provide about 30 percent of the heat input, the pilot fuel amount in actual tests is about 17–19 percent.

A typical combustion record of CWS in engine cylinder with separate pilot diesel fuel injection is shown in Fig. 10. In order to study the effect of pilot fuel, comparison curves of "No fuel injection," "Pilot fuel only," "Pilot + CWS fuel," and "CWS fuel only," are shown together. Table 3 lists the main results.

The following points can be noted:

- From Fig. 10(*A*) and Table 3 (column (7)), it is seen that with pilot fuel only (L58), the combustion brought the peak cylinder firing pressure to 11.6 MPa. Adding CWS injection (L59) increased it up to over 14 MPa. Without pilot fuel (CWS fuel only, L60) it was even lower than the peak pressure without fuel injection (L57), although combustion did take place. In the two cases involved with pilot injection (with and without CWS), strong pressure waves were recorded by the transducer and combustion knock in the test cell was heard. It was the typical diesel knock caused by early diesel fuel injection with a long ignition delay.
- In Fig. 10(*B*), the calculated average cylinder temperature and rate of heat release are shown. With pilot diesel fuel injection only (L58), the rate of heat release started at 24 deg BTDC. The shape of the heat release curve is of a typical early diesel fuel injection type. Almost all the fuel was burned in the premixed state immediately after ignition. When CWS fuel was injected together with pilot fuel (L59), the first part of the heat release shape did not change. This was because not much CWS had been injected into the cylinder up to the time of diesel fuel ignition. The start of CWS combustion is clearly characterized by the rising of the second hump of the heat release trace. It is interesting to note that without pilot fuel (L60), CWS started to burn at 7 deg BTDC, while with pilot fuel it advanced to 18 deg BTDC (Fig. 10*B* and Table 3, column (4b)). With pilot fuel, the maximum heat release rate of CWS was also much higher (Fig. 10*B*).
- As summarized in Table 3 (column (8)), the 76.6 kW obtained using pilot + CWS fuels (L59) is much higher than the sum of the individual cases using each type of fuel separately (L58 and L60). This is explained by the change in heat release shape (Fig. 10*B*). Using pilot + CWS fuels together (L59), the heat release is concentrated about TDC, whereas in the other two cases (L58 and L60), they are off TDC. Thus the indicators of "Relative Efficiency" (column (10)), are 96.8 percent for the former case and 93.4 and 87.4 percent for the latter two. Due to the late burning of L60, the calculated "% Fuel Burnt" (column (9)) is only 75.5 percent. The fuel consumption (column (11)) is lowest for the case of using pilot fuel and CWS together.
- Without pilot fuel, the CWS ignition delay is seen to be 25.4 deg crank angle (L60, column (5b)). With pilot fuel (L59), the ignition delay of the CWS part has been shortened to 14.4 deg crank angle. From the temperature curves, it is easily seen that before ignition, CWS had experienced much higher average cylinder temperature when pilot fuel was used. The local temperature close to the first ignited portion of CWS probably was even higher.



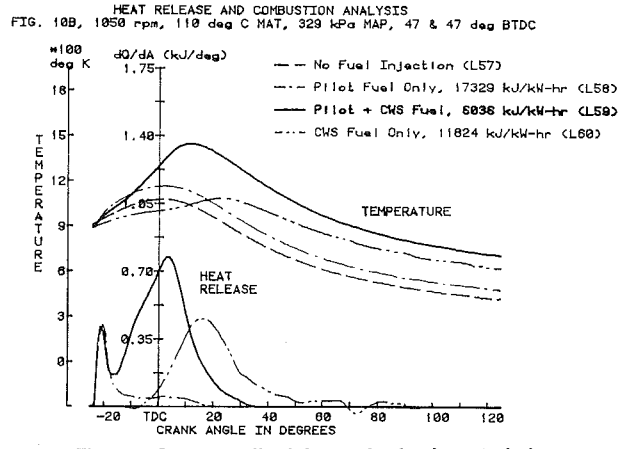


Fig. 10 Separate pilot injector, basic characteristics

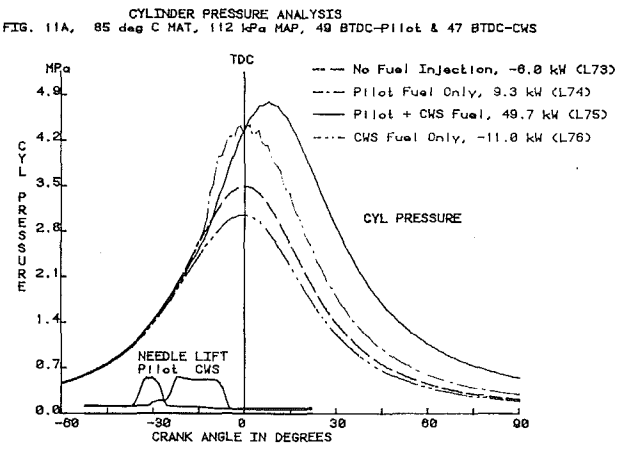
Low MAP Case. A run was made with only 112 kPa MAP at 1050 rpm and 85°C MAT. The static injection timings were 49 deg BTDC for pilot fuel and 47 deg BTDC for CWS fuel. For comparison, runs under the same conditions without fuel injection, with pilot fuel only, and CWS fuel only are shown together in Fig. 11 and Table 4.

Table 3 Pilot fuel injection (1050 rpm, 110°C MAT, 329 kPa MAP, 47 deg BTDC-Pilot and 47 deg BTDC-CWS)

Ignition Indicators								
Run	Fuel	Dyn. Inj. °BTDC		Ignition °BTDC		Ign. Del. °CA		Cyl Temp. @ CWS Ign. °K
		Pilot	CWS	Pilot	CWS	Pilot	CWS	
(1)	(2)	(3a)	(3b)	(4a)	(4b)	(5a)	(5b)	(6)
L57	No Fuel	-	-	-	-	-	-	-
L58	Pilot Only	33.8	-	24.0	-	9.8	-	-
L59	Pilot + CWS	33.8	32.4	24.0	18.0	9.8	14.4	1011
L60	CWS Only	-	32.4	-	7.0	-	25.4	983

Combustion Indicators					
Run	Pmax MPa	Power kW	Fuel Burnt %	Rel. Eff. %	SFC kJ/kW-hr
(1)	(7)	(8)	(9)	(10)	(11)
L57	10.6	-23.3	-	-	-
L58	11.6	5.3	100	93.4	17329
L59	14.1	76.6	98.7	96.8	8038
L60	10.3	43.1	75.5	87.4	12079

Downloaded 01 Jun 2010 to 171.66.16.87. Redistribution subject to ASME license or copyright; see http://www.asme.org/terms/Terms_Use.cfm



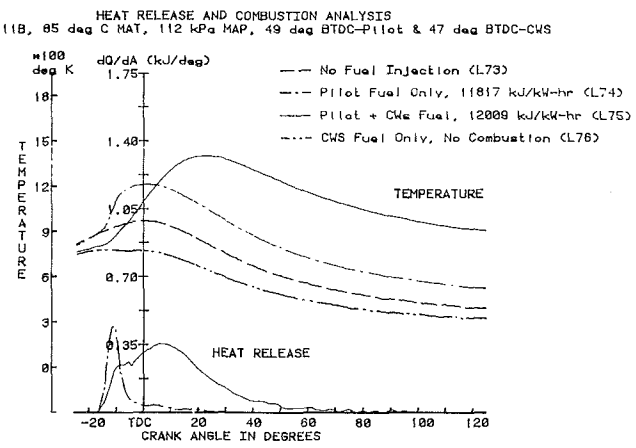


Fig. 11 Separate pilot injector, low MAP

Table 4 Pilot fuel injection, low MAP (1050 rpm, 85°C MAT, 112 kPa MAP, 49 deg BTDC-Pilot and 47 deg BTDC-CWS)

Ignition Indicators								
Run	Fuel	Dyn. Inj. °BTDC		Ignition °BTDC		Ign. Del. °CA		Cyl Temp. @ CWS Ign. °K
		Pilot	CWS	Pilot	CWS	Pilot	CWS	
(1)	(2)	(3a)	(3b)	(4a)	(4b)	(5a)	(5b)	(6)
L73	No Fuel	-	-	-	-	-	-	-
L74	Pilot Only	36.6	-	16.3	-	20.3	-	-
L75	Pilot + CWS	36.6	31.1	16.3	4.0	20.3	27.1	1000
L76	CWS Only	-	31.1	-	NC*	-	NC*	780**

Combustion Indicators					
Run	Pmax MPa	Power kW	Fuel Burnt %	Rel. Eff. %	SFC kJ/kW-hr
(1)	(7)	(8)	(9)	(10)	(11)
L73	3.5	-6.0	-	-	-
L74	4.4	9.3	100	96.9	12072
L75	4.8	49.7	72.3	90.2	12009
L76	3.1	-11.0	0	-	NC*

* - No Combustion
** - Maximum Cylinder Temperature

• In this case, CWS was ignited only because pilot diesel fuel was present. Without the latter, no combustion was observed (L76). However, injecting pilot fuel alone (L74), only 9.3 kW power was developed (Table 4, column (8)). Adding CWS (L75) brought the power up to 49.7 kW. Most of the power was generated by CWS combustion.

• In the present case, the diesel fuel ignition delay is very long (column (5a)). It did not start to burn until 16.3 deg BTDC (column (4a)), which is well after the CWS fuel injection start of 31.1 deg BTDC (column (3b)). Therefore, unlike the cases with high MAP, the pilot fuel heat release shapes are very different with (L75) and without (L76) CWS fuel (Fig. 11*B*). The water in CWS has evidently suppressed the initial high burning rate of pilot diesel fuel. However, the latter was still high enough to cause some knocking waves on the cylinder pressure trace (Fig. 11*A*, L75).

• The start of the CWS combustion can still be seen on the heat release trace (L75) to be at about 4 deg BTDC. The corresponding average cylinder temperature is 1000 K (column (6)).

Pilot Fuel Injection Timing Effect. While fixing the CWs fuel static injection timing at 47 deg BTDC, the pilot fuel static injection timing was varied from 41 deg to 49 deg BTDC. The test results are shown in Table 5 and Fig. 12. For comparison, the run without pilot fuel injection (L52) is included as a baseline.

• In Fig. 12(*A*) and Table 5 (column (7)), the peak cylinder firing pressure is seen to increase with pilot fuel injection timing advance. It is also seen that the pressure waves of diesel knock exist on all pressure traces using pilot fuel injection. In the needle lift part of Fig. 12(*A*), the 41 deg BTDC pilot timing case (L51) is seen to have pilot fuel started to inject into engine cylinder much later than CWS injection. Even so, diesel knock persisted. Only on the trace without pilot fuel (L52) were no diesel knock pressure waves seen.

• From the calculated heat release traces in Fig. 12(*B*), the overall start of combustion is seen to be dictated by the pilot fuel injection timing. Again, the start of CWS combustion in each case is very evident. It also advances with the pilot fuel

Table 5 Pilot fuel injection timing effect (1050 rpm, 110°C MAT, 329 kPa MAP, 49 deg BTDC-CWS)

Ignition Indicators								
Run	Pilot Fuel Tim. °BTDC	Dyn. Inj. °BTDC		Ignition °BTDC		Ign. Del. °CA		Cyl. Temp. @ CWS gn. °K
		Pilot	CWS	Pilot	CWS	Pilot	CWS	
(1)	(2)	(3a)	(3b)	(4a)	(4b)	(5a)	(5b)	(6)
L52	No Pilot	-	32.9	-	6.8	-	26.1	987
L51	41	25.2	32.3	19.3	13.3	5.9	19.0	994
L55	44	31.0	32.7	22.2	15.3	8.8	17.4	1017
L59	47	33.8	32.3	24.2	16.5	9.6	15.8	1022
L71	49	36.9	32.0	25.5	18.0	11.4	14.0	1006

Combustion Indicators					
Run	Pmax MPa	Power kW	Fuel Burnt %	Rel. Eff. %	SFC kJ/kw-hr
(1)	(7)	(8)	(9)	(10)	(11)
L52	10.2	37.5	71.3	87.8	13000
L51	12.3	67.8	91.8	95.6	8718
L55	13.5	74.2	97.5	96.6	7966
L59	14.1	76.6	98.7	96.8	8038
L71	14.5	70.8	97.9	96.7	8162

Downloaded 01 Jun 2010 to 171.66.16.87. Redistribution subject to ASME license or copyright; see http://www.asme.org/terms/Terms_Use.cfm

timing (column (4a)), although the injection timing of CWS remains unchanged.

- Therefore, the ignition delay of the CWS part becomes shorter as pilot fuel timing is advanced (column (5b)). It is interesting to note that the temperature at which CWS combustion started (column (6)) did not change very much.
- Since the heat release diagrams have changed their shapes and relative position to TDC, the efficiencies of the runs are expected to be different. Because extremely early and very late heat release are both detrimental to cycle efficiency, some optimum pilot fuel injection timing exists. From Table 5, columns (8)–(11), it is seen to be between runs L55 and L59.

Summary—Separate Pilot Fuel Ignition

- Combustion of pilot diesel fuel can ignite CWS fuel, which otherwise would not burn under similar engine conditions.
- In the cases where CWS could be ignited without pilot fuel, the introduction of the latter enhanced the CWS combustion both in the sense of shortening the ignition delay and increasing the heat release rate.
- The overall start of combustion in the engine cylinder was determined by the pilot diesel fuel injection timing. The start of combustion of the CWS part of the fuel was also dictated by the start of pilot fuel combustion.
- Under engine conditions when the pilot diesel fuel ignition delay was short, the heat release pattern of pilot diesel fuel part remained unchanged with or without subsequent CWS fuel injection. If the ignition delay of diesel fuel was long enough to extend well into subsequent CWS injection, then the high initial pilot fuel combustion rate was suppressed by the CWS presence in the cylinder.
- In all cases tested, combustion roughness, characterized by the knocking wave superimposed on cylinder pressure trace, was always present.

Stratified Pilot Ignition Results

The amount of diesel fuel that was stratified into CWS in this series of tests is about the same as that delivered by the separate pilot injector. The results of a stratified pilot run (L92) at 1050 rpm are shown in Fig. 13 and Table 6. The MAT was set at 110°C, MAP at 329 kPa, and the static injection timing at 52 deg BTDC. As before, baseline (L91) with no fuel injection was used for comparison.

- Compared to the no-pilot-fuel run L94 in Table 2, the ignition delay has been shortened from 40 deg to about 30 deg crank angle. This is believed to be caused by the mostly diesel fuel injected during the first part of the injection duration.
- On the cylinder pressure trace, the stratified pilot did not induce knocking wave. It is believed to be the effect of pilot fuel dilution by CWS.
- The diesel fuel that mixed with the later entering CWS fuel raised the heat release rate significantly. The result was a highly concentrated short duration heat release diagram (Fig. 13*B*) with 97.9 percent relative efficiency, column (10). If it is timed correctly, then the efficiency indicators would be good. Columns (8), (10), and (11) in Table 6 show the actual results.

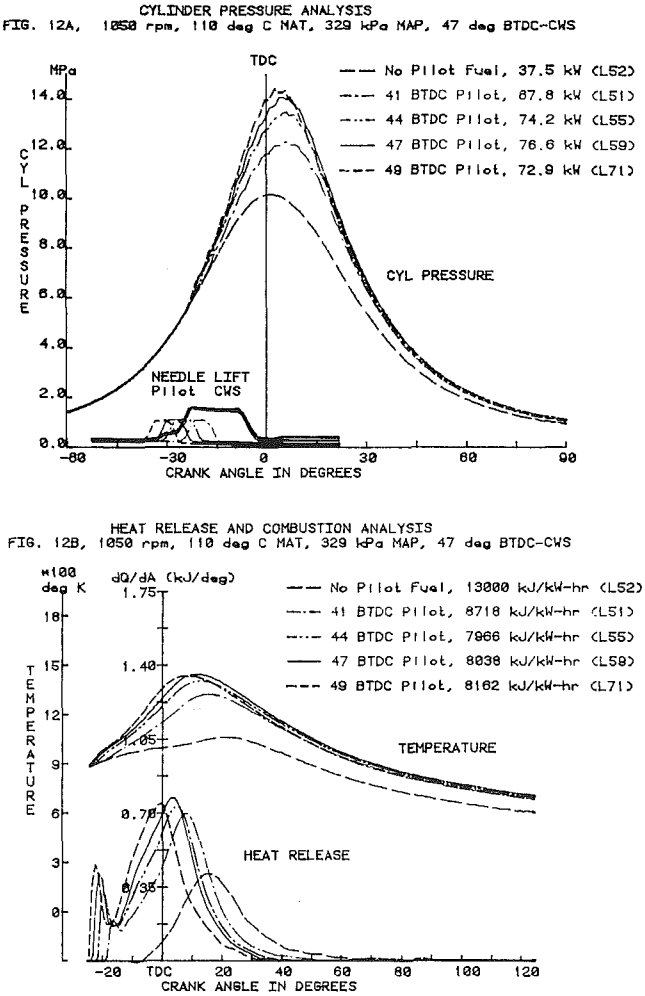


Fig. 12 Separate pilot injector, pilot timing effect

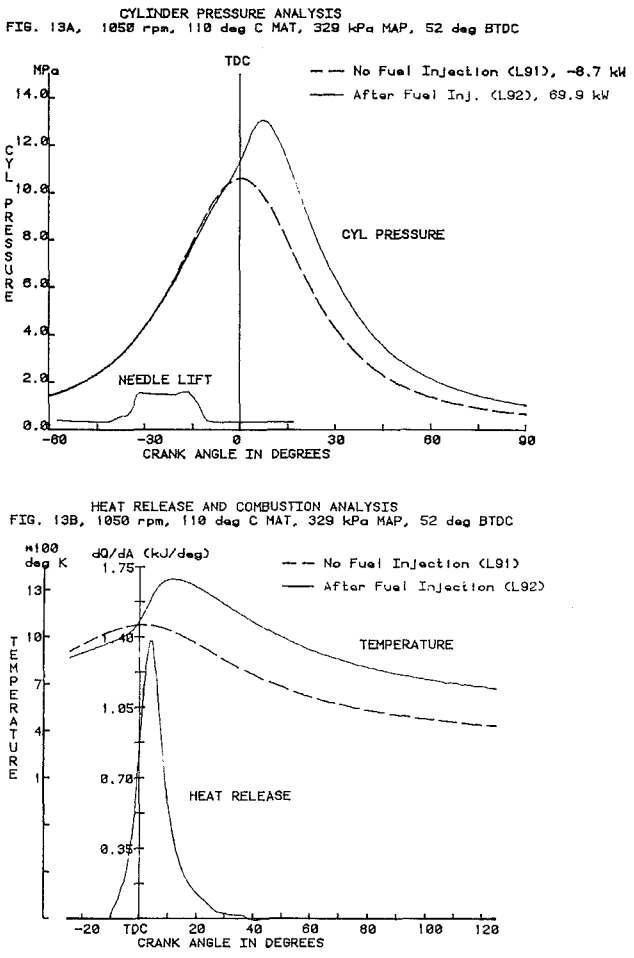


Fig. 13 Stratified pilot ignition

Downloaded 01 Jun 2010 to 171.66.16.87. Redistribution subject to ASME license or copyright; see http://www.asme.org/terms/Terms_Use.cfm

Table 6 Strafified pilot injection (1050 rpm, 110°C MAT, 329 kPa MAP, 52 deg BTDC)

Ignition Indicators					
Run	Fuel	Dyn. Inj. °BTDC	Ignition °BTDC	Ign. Del. °CA	Cyl Temp @ Ign °K
(1)	(2)	(3)	(4)	(5)	(6)
L91	No Fuel	-	-	-	-
L92	Sta. Pilot	40.4	10.0	30.4	972

Combustion Indicators					
Run	Pmax MPa	Power kW	Fuel Burnt %	Rel. Eff. %	SFC kJ/kW-hr
(1)	(7)	(8)	(9)	(10)	(11)
L91	10.6	-8.7	-	-	-
L92	13.1	69.9	94.0	97.9	8124

Table 7 Three types of ignition comparison (1050 rpm, 110°C MAT, 329 kPa MAP)

ITEM	COMPRESSION IGNITION	SEPARATE PILOT	STRATIFIED PILOT
Highest Heat Release Rate (kJ/°CA)	0.57	0.77	1.29
Calculated % of Fuel Burnt	88.2	98.7	94.0
Relative Efficiency (burnt part, %)	94.6	96.8	97.9
Specific Fuel Eff. (kJ/kW-hr)	9508	8038	8124
(at kW)	(45.6)	(76.6)	(69.9)

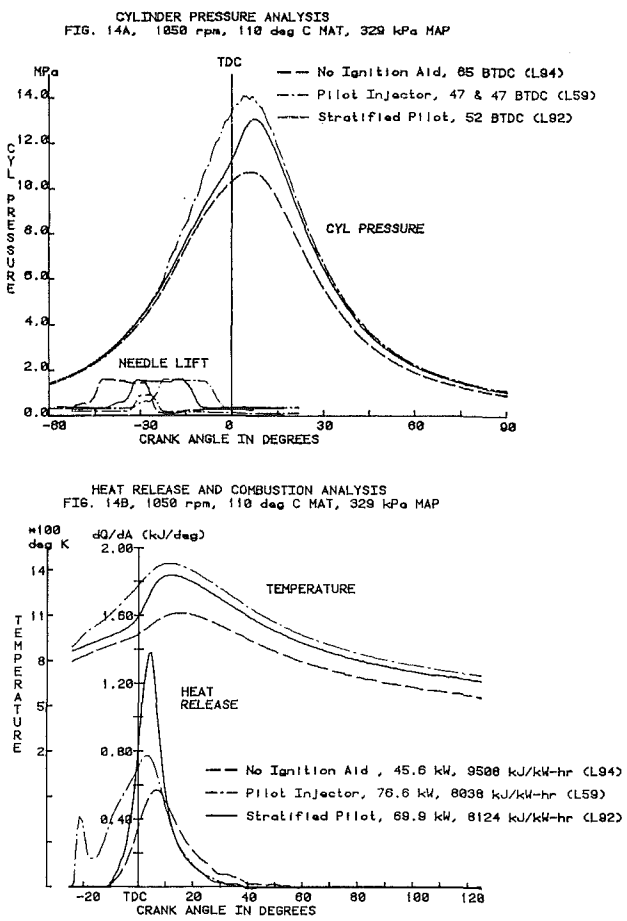


Fig. 14 Three types of ignition comparison

Conclusions

- Approximately 50 percent coal loading CWS has been successfully ignited in GE 7FDL engine cylinder at 1050 rpm without major changes in engine parameters.
- Before CWS could be ignited, a finite time was needed for the water in CWS droplet to heat up and evaporate. Ignition will succeed only if at the end of this period sufficient temperature was maintained. In all the successful CWS combustion runs, the average cylinder temperature at ignition was above 890 K.
- CWS combustion was obtained with all three types of ignition technique investigated. Limited by the amount of fuel energy that could be put into the engine cylinder (1/3 of full load) and the maximum injection pressure (40 MPa at injector), the optimum results of each type of ignition are compared in Table 7 and Fig. 14.

Acknowledgments

Support of this study, and permission to publish the results, from the General Electric Company and Morgantown Energy Technology Center, DOE (contract No. DEAC 21-85MC 22181) are gratefully acknowledged. The author would like to thank Mr. R. J. Johnson, Dr. G. L. Leonard, Dr. S. D. Savkar of GE-CR&D, Mr. J. R. Beal, Mr. E. G. Bricker, Dr. P. L. Flynn of GE-TS, and Mr. L. K. Carpenter of DOE METC, for their many valuable contributions to this project. Mr. D. J. Lecker's effort in acquiring test data is also greatly appreciated.

References

1 Hapeman, M. J., and Savkar, S. D., "Economic Assessment of Coal-Burning Diesel Locomotives," ASME Paper No. 86-ICE-14, 1986.

2 Leonard, G. L., and Fiske, G. H., "Combustion Characteristics of Coal/Water Mixtures in a Simulated Medium-Speed Diesel Engine Environment," ASME Paper No. 86-ICE-15, 1986.

3 Leonard, G. L., and Fiske, G. H., "A Comparison of a Positive Displacement Fuel Injection System With an Accumulator Based System for Coal-Fueled Diesel Engine Applications," ASME Paper No. 87-ICE-32, 1987.

4 Annand, W. J. D., "Heat Transfer in the Cylinder of Reciprocating Internal Combustion Engines," *Proc. Instn. Mech. Engrs.*, Vol. 177, No. 36, 1963.

5 French, C. C. J., "Taking Heat Off the Highly Boosted Diesel," S.A.E. Paper No. 690463, 1969.

6 Hsu, B. D., "Heat Release, Cycle Efficiency and Maximum Cylinder Pressure in Diesel Engine—The Use of an Extended Air Cycle Analysis," *S.A.E. Transactions*, 1984, p. 4.766.

7 Farmayan, W. F., et al., "NO_x and Carbon Emission Control in CWS Combustion," *Proceedings of the Sixth International Symposium on Coal Slurry Combustion and Technology*, Orlando, FL, 1984, p. 165.

8 Walsh, P. M., et al., "Ignition and Combustion of Coal–Water Slurry in a Confined Turbulent Diffusion Flame," presented at the 20th International Symposium on Combustion, Ann Arbor, MI, Aug. 1984.

Downloaded 01 Jun 2010 to 171.66.16.87. Redistribution subject to ASME license or copyright; see http://www.asme.org/terms/Terms_Use.cfm

Progress on the Investigation of Coal-Water Slurry Fuel Combustion in a Medium Speed Diesel Engine: Part 2—Preliminary Full Load Test

B. D. Hsu
Transportation Systems,
General Electric Company,
Erie, PA 16531

Full load (186 kW/cyl) operation using CWS fuel at 1050 rpm has been achieved on a single-cylinder GE-7FDL test engine. No major changes in engine parameters were made. With normal inlet air conditions, 3–5 percent pilot diesel fuel, separately injected or stratified into the main coal charge, was used. Inlet air temperature had to be raised about 40° C if no pilot diesel fuel was used. The coal burnout was about 95 percent and the cycle efficiency was comparable to using diesel fuel. The NO_x and CO emissions were about 1/2 of those obtained normally with diesel fuel. The maximum heat release rate was higher than diesel fuel operation which resulted in higher maximum cylinder firing pressure. The combustion characteristic and its dependence on some fuel characteristics and inlet air parameters are discussed. Increasing coal burnout while limiting maximum cylinder firing pressure is the main objective of near future studies.

Introduction

This is the second in a series of papers to report on the test of a GE-7FDL single-cylinder engine on coal-water slurry (CWS) fuel at GE-TS in Erie under the sponsorship of DOE-METC. As already outlined in the first paper [1], combustion at full load is the subject of this Phase II single cylinder engine study, and the system II fuel injection equipment (FIE) is used. The discussion in this paper only deals with the engine full load condition, which is approximately 186 kW/cyl (1.93 MPa MEP) at 1050 rpm.

At the time of this writing, the Phase II engine test is still in progress. It was found that much more work needs to be done on FIE parameters, combustion chamber layout, fuel compatibility and specification, etc. In the overall coal fuel engine program, there is a parallel effort to improve the wear properties of engine parts. At this stage, the parts used are made only from the standard materials used in a conventional diesel fuel engine. Although the parts did not break down during the tests, the engine performance deterioration due to wear (e.g., injector hole enlargement) was evident. This brought some difficulties to the study of combustion due to the continuous change of some parameters. Furthermore, a new accumulator-based FIE still under development [2] is expected to be tested soon and to perform better than the system II FIE used in this study. Therefore the results on full load test reported here are considered preliminary. Nevertheless, since a very limited amount of knowledge on the details of actual coal fuel diesel engine combustion has been published, the insights gained so far are worth summarizing.

In several test runs, using CWS fuel, over 190 indicated kW (2.0 MPa MEP) load at 1050 rpm has been achieved. The excess air ratio at this load could be down to about 1.6. Normally, using diesel fuel at full engine load, the excess air ratio is over 1.9. In a quiescent chamber direct injection diesel engine such as the GE-7FDL model, engine overall combustion indicators deteriorate very rapidly when excess air ratio drops below 1.9. Since engine combustion was not optimized during most of the runs, the engine test load was usually set at 90 to 95 percent full engine load.

If not otherwise noted, the fuel used in this study is a 49 percent loading Kentucky Blue Gem coal CWS prepared by Otisca Industries, Ltd. The detail specification is listed in the section on "Fuel Effect." The instrumentation and the data reduction procedures used are similar to those used in the first paper [1] of this series, and shall not be described again here.

Test Hardware

The test engine used in this Phase II test is the GE-7FDL two-cylinder engine with 229 mm bore and 267 mm stroke, as used in the Phase I test [1] and shown in Fig. 1. A new cell was built recently for the coal fuel engine test in which the exter-

Contributed by the Internal Combustion Engine Division and presented at the Energy-Sources Technology Conference and Exhibition, New Orleans, Louisiana, January 10–14, 1988. Manuscript received by the Internal Combustion Engine Division July 21, 1987. Paper No. 88-ICE-5.

Copyright © 1988 by ASME
Downloaded 01 Jun 2010 to 171.66.16.87. Redistribution subject to ASME license or copyright; see http://www.asme.org/terms/Terms_Use.cfm

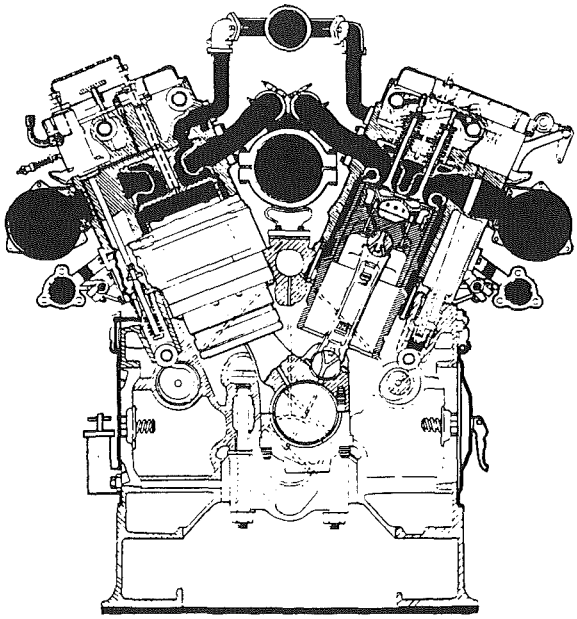


Fig. 1 7FDL two-cylinder research engine

nally controlled inlet air pressure can be raised to 722 kPa and inlet air temperature can be heated to 205°C. There are stainless steel tanks of 800 liters capacity available to hold CWS fuel for the prolonged period of engine testing.

As before, only one cylinder (left side) of the engine is equipped to burn coal fuel and the other cylinder (right side) has standard diesel fuel injection equipment. In the Phase I test, the pure diesel fuel burning right cylinder of the engine ran continuously during the test. During engine warmup, the dynamometer load was carried only by the right-side diesel-fueled cylinder. When a fixed amount of CWS was fed into the left-side coal-fueled cylinder, the dynamometer load was then carried by both cylinders. The engine governor only controlled the right cylinder diesel fuel pump and reduced the diesel fuel injection when the left side coal fuel cylinder fired up. In the current Phase II test, the governor can be selected to control both or either the diesel-fueled or the coal-fueled cylinder. After engine warmup, the diesel-fueled cylinder is actually turned off, and only the coal-fueled cylinder carries the dynamometer load.

The coal-fueled cylinder combustion chamber layout is similar to that in the Phase I test, except the compression ratio has been raised to 13.0 and the main coal fuel injector is much larger in diameter to handle the full load CWS quantity (up to 4 cm^3/stroke of fuel injection). The CWS injection drive pump made by Lucas Bryce uses a 24-mm-dia plunger instead of the 20-mm plunger used in the system I test. The layout of the system II FIE is shown in Fig. 2. There is a continuous low-pressure fuel supply system, which employs a progressive cavity pump with a pressure regulating device to feed the high-pressure injection diaphragm pump. Separate electronic scales are used to measure the CWS fuel, the pilot diesel fuel (if used), and the injector back fluid flow. Outputs of the scales are fed into a digital storage oscilloscope so that a regression of the acquired data can be performed at the end of each run to obtain more precise flow rates as well as the associated statistical parameters.

CWS fuel injector tips with eight different injector hole configurations (designated type A to G) are scheduled to be tested. They range from 10 to 24 holes with diameters of 0.4 to 0.63 mm. The pilot fuel injector tips are from two to four holes with diameters of 0.30 to 0.35 mm. They are all made by Bryce.

A sampling probe has been installed into the coal burning

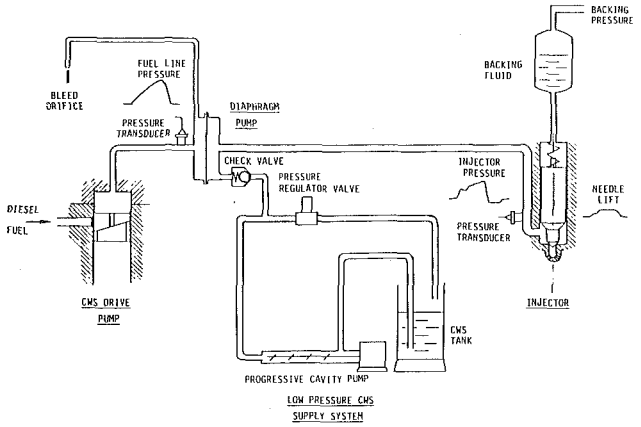


Fig. 2 Coal-water-slurry fueled diesel engine: system II fuel injection equipment

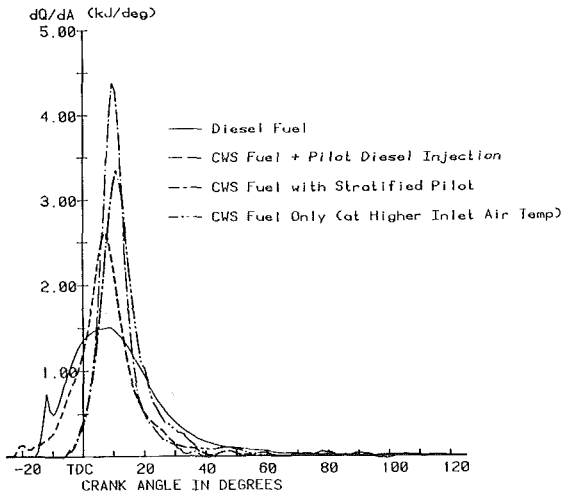


Fig. 3 Heat release and combustion analysis: diesel fuel and *coal-water slurry fuel comparison*

cylinder exhaust branch pipe. Particulate samples can be gathered employing a Mott sintered stainless steel 0.5 μm filter. The sampled gas can then be sent through heated tubes to exhaust emission analyzers.

Recent Performance Results

Successful full load runs were achieved with all three types of ignition methods described in the previous paper [1]. Table 1 lists the results.

It is seen that the specific fuel consumption (SFC) values of the coal fuel runs with or without pilot fuel were very comparable to the standard diesel fuel operation, which is very low for this size engine. Even the highest SFC of the coal fuel runs (compression ignition only) yielded an indicated thermal efficiency close to 40 percent. It should be pointed out that for the above coal fuel runs, the calculated burnout values showed that there was 6–10 percent fuel unburned. The main objective of near future work is to burn the last few percent of the coal fuel in engine cylinder. When that goal is achieved, the SFC of the coal fuel engine should be closer to or even better than normal diesel fuel operation. The reason that the SFC of the coal fuel runs is not excessive, albeit with the unburned fuel, lies in their high "Relative Cycle Efficiencies." Relative cycle efficiency as used in this study is a parameter derived some years ago by the author [3] to quantify the timely burning of fuel in a reciprocating internal combustion engine. It can be visualized graphically as the concentration of the area under the heat release curve about the engine TDC. A comparison of the heat release curves of the runs listed in Table 1 is shown in Fig. 3.

Downloaded 01 Jun 2010 to 171.66.16.87. Redistribution subject to ASME license or copyright; see http://www.asme.org/terms/Terms_Use.cfm

Table 1 Full load test results

Ignition Method	Pilot (%)	SFC (kJ/kW-hr)	Burn out (%)	Rel. Eff. (%)	Pmax (MPa)	Test (kW)	Run #
Separate Pilot Stratified	5	8721	90.3	96.20	17.5	182	21
Pilot Compression only	6	8400	93.8	96.21	16.5	181	15
Ref. Stnd. Diesel	0	9044	92.1	93.28	15.9	185	06
	100	8141	100*	94.47	15.4	197	10

*Assumed

Table 2 Burnout calculation comparison (percent)

Ignition Method	Heat Balance	Ash Balance	Run#
Pilot Ignition	91.2	96.6	03
Compression Only	92.1	94.9	06

Table 3 NO_x and CO emission comparison (ppm)

Emission	Diesel Fuel Ref. [8]	CWS Fuel Run 03 (w/pilot)	CWS Fuel Run 06 (w/o pilot)
NOx	1025	383	488
CO	582	242	386

The three coal fuel runs are seen to have much higher peak heat release rates than the normal diesel fuel run. Their shapes are also more concentrated, although not necessarily close to TDC. (The latter can be adjusted somewhat by changing the fuel injection timing.) The timely burning of the coal fuel runs evidently compensated somewhat for the loss in efficiency due to the unburned coal. It is also interesting to note that the usual kinetic and diffusive burning stages seen with diesel fuel combustion cannot be observed with these CWS fuel runs.

The peak firing pressure values of the coal fuel runs are seen to be all higher than the reference diesel fuel run. Again, this can be explained by the concentration of the heat release curve [3]. Although high heat release rates are seen with CWS combustion, not all fuel is burned before the exhaust valves begin to open. One of the reasons could be the impinging of CWS fuel on the combustion chamber walls, as seen with some combustion bomb tests [4]. The other reason probably is the agglomeration of the coal particles after droplet evaporation as already been observed both with single droplet CWS combustion [5] and CWS spray combustion [6]. The exhaust particle samples collected during actual engine runs were analyzed by scanning transmission electron microscopy. They contained fragments of hollow carbonaceous cenospheres, which are the typical unburned residue of dry coal agglomerate of a CWS droplet described by Monroe et al. [7]. The CWS injection pressure of these runs measured close to the injector tip was only in the vicinity of 52 MPa. Increasing the injection pressure to atomize the CWS spray better should definitely bring improvement.

The coal burnout values shown in Table 1 were calculated for each engine run by the data reduction routine, which uses a heat balance method. A comparison was made for two engine runs by calculating the burnout using the ash balance method with the collected exhaust particulate samples. They are shown in Table 2.

The ash balance method seems to yield slightly higher burnout values. The lower values obtained with heat balance might have resulted from insufficient accounting of heat loss to the cylinder wall during combustion. In any case, for the best run, it is probably prudent to estimate that the coal burnout is close to 95 percent.

The NO_x and CO emissions were measured for several runs. A typical comparison with the standard diesel fuel operation is shown in Table 3.

Both the NO_x and CO emissions are seen to be lower when coal fuel is used. These results are similar to those reported with the slow-speed Sulzer engine burning CWS fuel [9]. The low NO_x emissions probably can be explained by the lower cylinder temperature environment when CWS fuel was used. The in-cylinder temperature histories of the runs listed in Table 1 are compared in Fig. 4. Not only was the peak temperature lower for the CWS fuel, but the entire temperature history of any of the coal fuel runs never exceeded the reference diesel fuel run.

Table 4 Coal nominal lot analysis

	Kentucky Coal	New Zealand Coal
Proximate Analysis		
% Ash	1.01	0.36
% Volatile	39.12	33.67
% Fixed Carbon	59.87	65.97
Ultimate Analysis		
% Carbon	82.59	86.15
% Hydrogen	5.34	5.15
% Nitrogen	2.08	1.26
% Chlorine	0.18	0.11
% Sulfur	1.01	0.36
% Oxygen (diff.)	7.58	6.39
Particle Size		
Mass Mean Dia. (microns)	4.63	2.88
High Heating Value (kJ/kg)	34630	35580

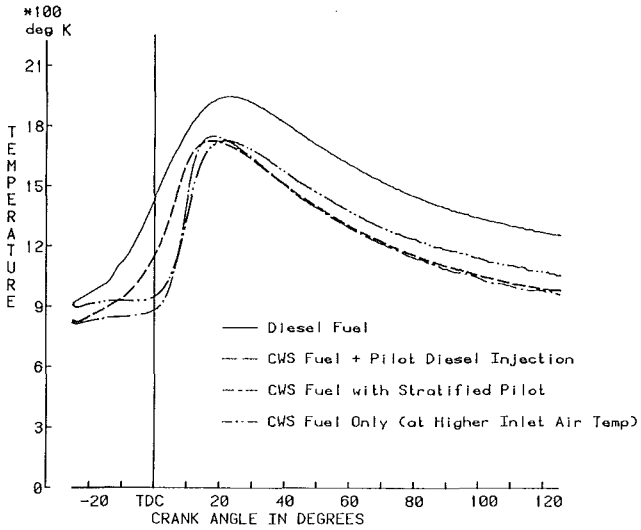


Fig. 4 Heat release and combustion analysis: diesel fuel and coal-water slurry fuel comparison

Fuel Effect

As already mentioned in the introduction, Kentucky Blue Gem coal CWS was used predominantly. At the beginning of this series of tests, Otisca only supplied this kind of CWS with approximately 1 percent ash. As the ash content in coal has always been a major obstacle in burning coal in internal combustion engines, one kind of New Zealand coal that can be cleaned to contain only 0.4 percent ash was purchased for comparison. The nominal coal lot analyses of the two types of coal are listed in Table 4.

Comparison tests were run for the two fuels with and without pilot fuel. The test results are summarized in Table 5 and comparisons of the cylinder pressure traces and calculated heat release curves are shown in Figs. 5 and 6.

It is clearly shown in Table 5 that the fuel efficiencies and the burnouts using Ky coal were much higher than using NZ coal. But the peak cylinder firing pressures of the former were

Downloaded 01 Jun 2010 to 171.66.16.87. Redistribution subject to ASME license or copyright; see http://www.asme.org/terms/Terms_Use.cfm

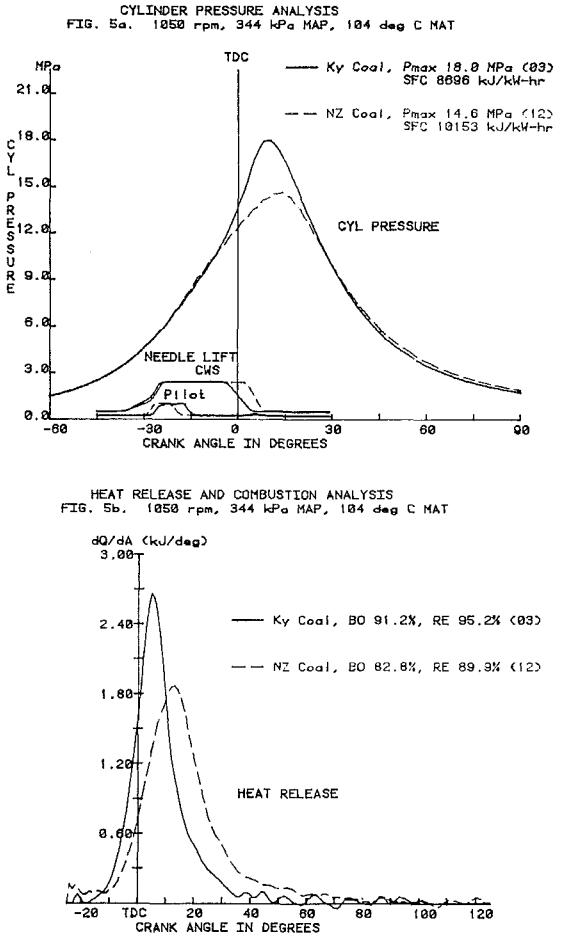


Fig. 5 Ky versus NZ coal CWS (with pilot)

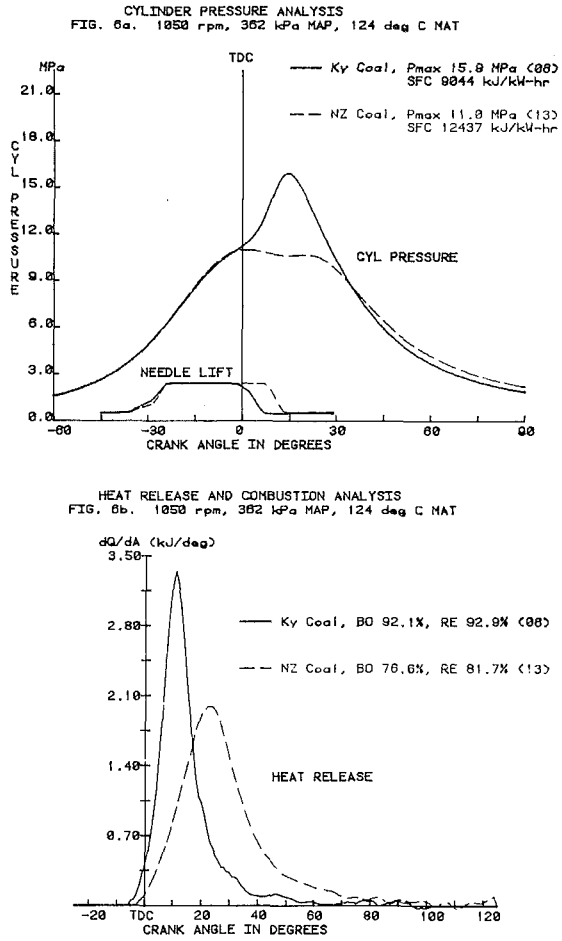


Fig. 6 Ky versus NZ coal CWS (without pilot)

Table 5 Fuel comparison results

Coal Type	Burnout (%)	SFC (kJ/kW-hr)	Pmax (MPa)	Rel. Eff. (%)
3% Pilot Fuel				
Ky Coal	91.2	8696	18.0	95.2
NZ Coal	82.8	10153	14.6	89.9
No Pilot Fuel				
Ky Coal	92.1	9044	15.9	92.9
NZ Coal	76.6	12437	11.0	81.7

Table 6 Two types of CWS

CWS	Coal Particle size (MMD, microns)	Ash (%)	Viscosity at 112/s (cp)	Solids (%)
Old	4.63	1.01	123	50.1
New	3.41	0.79	463	49.2

also very much higher. From the direct comparison of the recorded cylinder pressure traces in Figs. 5(*a*) and 6(*a*), it is not difficult to recognize the slower burning character of the NZ coal.

In Fig. 6(*a*), the NZ coal almost burned in a constant pressure cycle mode. The heat release comparisons shown in Figs. 5(*b*) and 6(*b*) confirmed the difference in combustion. It is interesting to point out that the same two types of fuel were compared in a gas turbine combustor at GE Aircraft Engine Business Group (AEBG) [10]. The NZ coal was found to perform very poorly. Efforts were made at AEBG to increase the volatile content of the NZ coal to the Ky coal level by adding some diesel fuel and other additives. The combustion characteristics were still poor comparing to the Ky coal. The underlying reason for this behavior is not clear.

Even with the same type of coal, the coal particle size, in terms of mass mean diameter (MMD), and the additives used to prepare the CWS fuel have significant effects on the engine performance. The apparent property that has to be dealt with is the viscosity. CWS is a non-Newtonian fluid and exhibits very complex rheology [11]. Depending on the additives used, the viscosity characteristics at low shear rate could be dilatant or pseudoplastic, but at a high shear rate the viscosity generally depends on the coal type, coal loading, and coal particle size [12]. Although the high shear rate viscosity is very important due to the high flow rate at the injector nozzle hole, CWS fuel is transported in the engine fuel system at various flow rates depending on hardware design. Recently some CWS was obtained from Otisca using the same Kentucky Blue Gem coal ground to finer particle size (in order to get a lower ash content) and with additives to prevent coal settling. Here it will be referred to as "New" CWS, whereby the original CWS will be referred as "Old" fuel. The main differences between the two kinds of CWS are summarized in Table 6.

The most significant change in the new fuel is seen to be the increase in viscosity. When the new fuel was put into the engine, fuel starving of the diaphragm pump due to excessive loss in the CWS low-pressure feeding system was immediately detected. The new fuel had to be diluted down to 46.1 percent coal loading, with a viscosity lower than 100 cp at 112/s, before the pump starving problem was overcome. A test run (#30) was made to compare with one of the previous runs (#05) using identical hardware and inlet air conditions. Using the old fuel there was no problem in achieving 178 kW, but only 110 kW could be obtained with the new fuel. The test results are compared in Table 7.

Downloaded 01 Jun 2010 to 171.66.16.87. Redistribution subject to ASME license or copyright; see http://www.asme.org/terms/Terms_Use.cfm

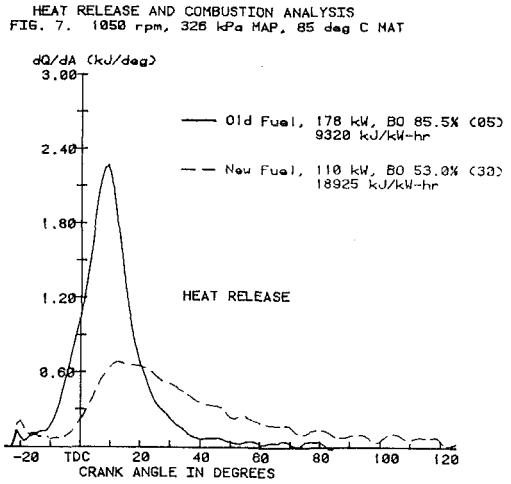


Fig. 7 Old and New fuel comparison

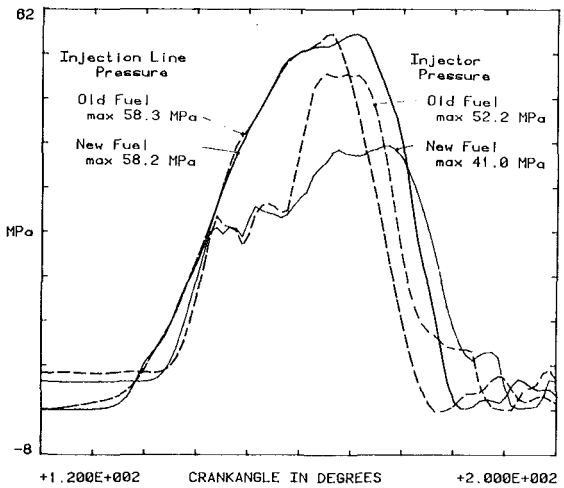


Fig. 8 Two types of fuel: injection pressure comparison

Aside from the much lower load it could carry, the new fuel burnout was much lower and the SFC much higher. The in-cylinder heat releases of the two runs are compared in Fig. 7. It is seen that the maximum heat release rate of the new fuel was much lower and burning prolonged extensively into the expansion stroke of engine cycle. The inferior engine performance of the new fuel evidently was the result of slow, sluggish in-cylinder combustion.

An investigation of fuel injection parameters showed that even though the maximum fuel line injection pressures measured upstream at the drive side of the diaphragm pump (Fig. 2) were about the same (approximately 58 MPa) for both cases, the actual maximum injector pressures measured downstream of CWS fuel close to the injector tip were very different. With the old fuel (run # 05), the maximum was 52.2 MPa, but it was only 41.0 MPa with the new fuel. The recorded upstream fuel line and downstream injector pressure histories for the two fuels are compared in Fig. 8. The much higher pressure loss in the high-pressure fuel line of the new fuel was presumably caused by the higher fuel viscosity.

Although recent studies have not demonstrated conclusively the consistency of atomization quality (using air blast injectors) with CWS fuel viscosity in general [13], the loss in the conduit of pressure atomization due to high viscosity is definitely detrimental. Since finer coal particle size CWS always has higher viscosity and many researchers have pointed out that it is the spray droplet size rather than the coal particle

Table 7 New and old CWS fuel test results

CWS	Run #	Test Load (kW)	Burnout (%)	SFC (kJ/kW-hr)	Pmax (MPa)
Old	05	177.8	85.5	9320	16.4
New	30	109.8	53.0	18925	11.5

size that determines the CWS combustion [13, 14], better combustion results might be obtained with larger particle size CWS. In fact, this is proven by Famayan et al. [14] in a combustion tunnel using boiler grade CWS fuel. With the further development of the coal fuel diesel engine, appropriate fuel specifications will have to be defined.

Inlet Air Effect

In selecting the test ranges of inlet air conditions, the primary concern was to maintain the excess air ratio close to normal diesel fuel operation, which is about 1.9. Taking into account the full load power of 186 kW, the heating value of coal fuel, the estimated energy conversion efficiency, etc., the inlet air density range has to be about 2.88 to 3.37 kg/m^3. The inlet air temperature range was chosen to be 65° to 145°C. High inlet air temperature had to be accompanied with high inlet air pressure in order to maintain the necessary air mass. Excessive inlet air pressure might cause peak firing pressure of the engine to a mechanically unbearable level. Therefore, the inlet air pressure range was limited to 308–377 kPa.

Table 8 lists some of the test results. The table is divided into three sections to show the inlet air effect while maintaining one parameter constant. They are compared in pairs.

Constant Inlet Air Density. In the constant density part, it is seen that higher temperature (therefore higher pressure) improved the burnout, lowered the SFC, promoted timely burning (higher relative cycle efficiency), but increased cylinder firing pressure. Each pair of data was run under about the same injection pressure. Since the charge air densities were the same, then it might be assumed the fuel atomization qualities were very close [15]. Higher temperature was the reason for obtaining better performance indicators. It should be pointed out that the higher pressure that accompanied the higher temperature to maintain the necessary air density accentuated the increases in maximum cylinder firing pressure, which in these cases are much higher than the normal diesel fuel operation level of approximately 15.5 MPa. In Fig. 9 are the comparisons of the recorded cylinder pressure traces and the calculated heat release traces of runs #03 and #05, which were run with pilot fuel. The peak firing pressure difference is easy to see. There are needle lift traces of long and short duration under the pressure traces. The longer duration ones are of CWS fuel and the shorter ones are of pilot fuel. The injection timings of the coal fuel are seen to be the same. On the heat release comparison, the first small peaks reflect the pilot fuel burning. The second high peaks are coal fuel burning, which distinctly show the fast rate of run #03 with higher temperature. It is interesting to note that since these runs are made with pilot fuel, the ignition starting times of CWS, which are reflected by the first valleys on the heat release traces, are the same for the two runs. Lower temperature made the subsequent burning of CWS fuel slower. Figure 10 shows the comparisons of runs #06 and #04, which were made without pilot fuel. The general shapes of the pressure traces are quite different from those with pilot fuel. For the lower temperature run #04, fuel was burned almost in a constant pressure cycle. The lower maximum heat release rate is again seen with the lower inlet air temperature case. It is also seen here that the burning started later with the lower temperature run #04. Since there was no difference in the injection timing, which can be seen with the needle lift traces, the longer ignition delay due to lower temperature is evident.

Downloaded 01 Jun 2010 to 171.66.16.87. Redistribution subject to ASME license or copyright; see http://www.asme.org/terms/Terms_Use.cfm

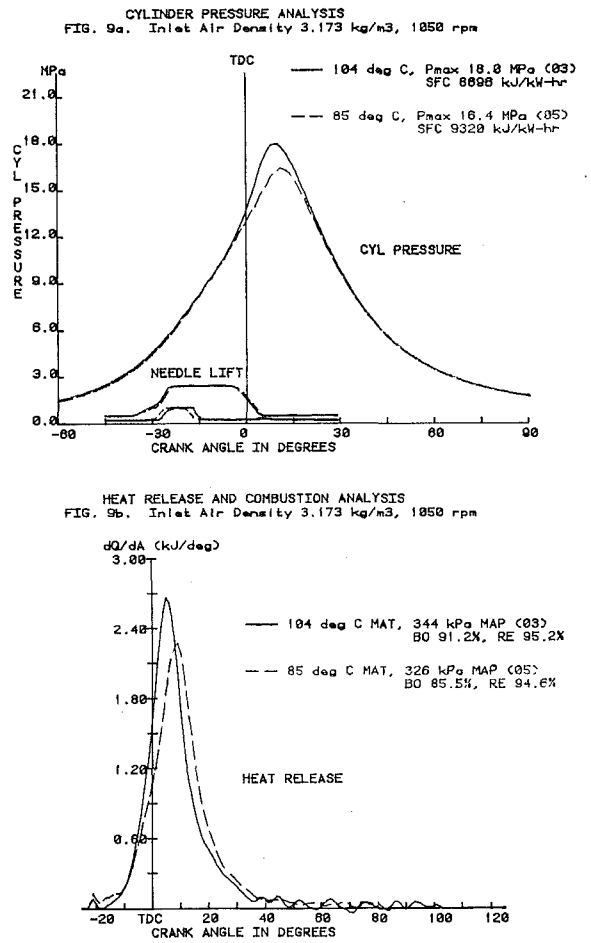


Fig. 9 Constant inlet air density (with pilot)

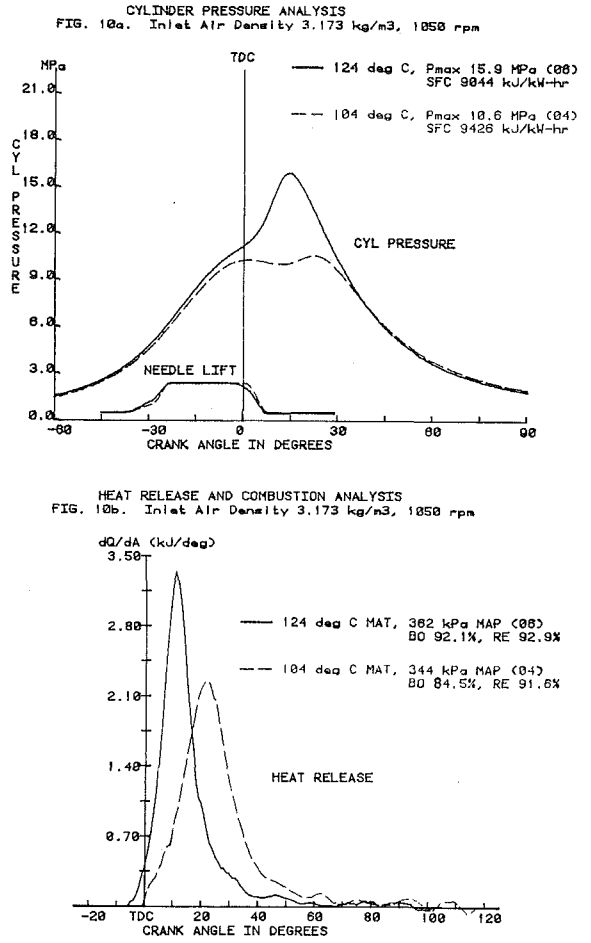


Fig. 10 Constant inlet air density (without pilot)

Constant Inlet Air Temperature. The second section of Table 8 shows the performance effects of inlet air while holding temperature constant. With higher pressure (therefore higher density), the fuel burnout was higher, the fuel consumption was lower, and the peak cylinder firing pressure was higher. But interestingly, there was essentially no change in timely burning (relative cycle efficiency). The higher air density probably improved the CWS atomization, which brought forth the higher burnout and low SFC. A typical comparison of the recorded cylinder pressure traces and the heat release traces are shown in Fig. 11 for runs #03 and #08. The difference in peak cylinder pressure was not as great as the previous constant density case. It is seen in Fig. 11(*b*) that there is almost no difference in the heat release traces except around the peak. The relative cycle efficiency (timely burning) numbers, which are essentially the same, therefore are presented in Table 8. Since timely burning has a predominant effect on maximum cylinder firing pressure, it can be conceived roughly that in this case the relatively small firing pressure discrepancy was caused only by the inlet pressure difference. It should also be pointed out that less fuel was injected into the engine cylinder to get the heat release of the higher inlet air pressure (density) run #03. Therefore the burnout was higher for this case. Within the tested air parameter range, it seems that while holding inlet air temperature constant, timely burning did not change with inlet air pressure (and therefore density).

Constant Inlet Air Pressure. The last section of Table 8 is the effect of inlet air parameters maintaining pressure constant. It is interesting to see that the higher temperature (therefore lower air density) run #08 had the same coal burnout as the lower temperature (higher air density) run #07. The effects of temperature and density on coal burnout seemed to have balanced out. In this test range, the difference in temperature evidently had more effect on SFC than that due to the density change. From the previous discussions, it is not

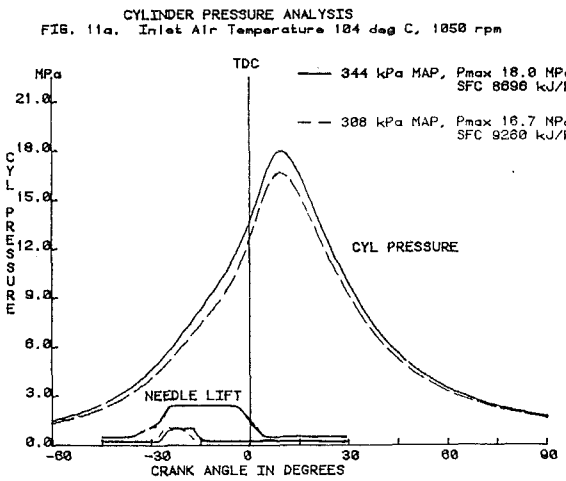
Table 8 Inlet air effect

Run #	Ign. Meth *	Injector **	Inlet Air Density (kg/m3)	Inlet Air Temp (°C)	Inlet Air Press (kPa)	Burnout (%)	SFC (kJ/kW-hr)	Rel. Eff. (%)	Pmax (MPa)
Density Constant									
03	PI	A	3.173	104	344	91.2	8696	95.2	18.0
05	PI	A	3.173	85	326	85.5	9320	94.6	16.4
28	SP	B	3.173	124	362	79.3	11026	88.4	16.2
27	SP	B	3.173	104	344	76.0	11721	85.0	13.0
06	CI	A	3.173	124	362	92.1	9044	92.9	15.9
04	CI	A	3.173	104	344	84.5	9426	91.6	10.6
Temperature Constant									
03	PI	A	3.173	104	344	91.2	8696	95.2	18.0
08	PI	A	2.842	104	308	86.2	9260	95.5	16.7
19	PI	E	3.173	104	344	89.9	8815	94.7	17.0
18	PI	E	3.007	104	326	85.1	9471	94.7	16.4
20	CI	E	3.173	124	362	83.6	10123	89.5	13.1
17	CI	E	3.007	124	344	80.5	10756	88.1	13.0
Pressure Constant									
08	PI	A	2.842	104	308	86.2	9260	95.5	16.7
07	PI	A	3.173	66	308	86.5	10392	82.8	12.1

* PI-Pilot Ignition; SP-Stratified Pilot; CI-Compression Ignition.

** Different hole configuration (see "Test Hardware").

Downloaded 01 Jun 2010 to 171.66.16.87. Redistribution subject to ASME license or copyright; see http://www.asme.org/terms/Terms_Use.cfm



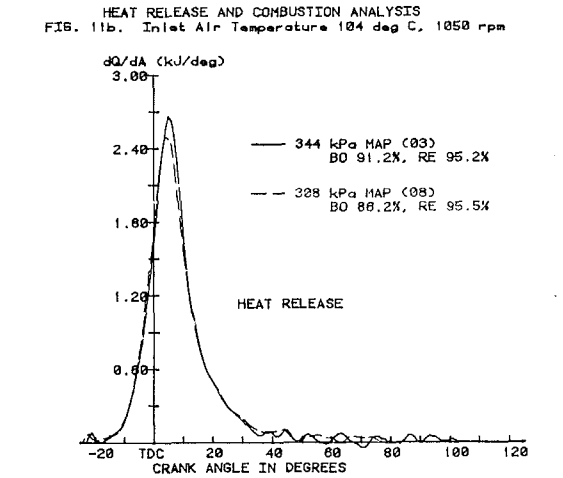
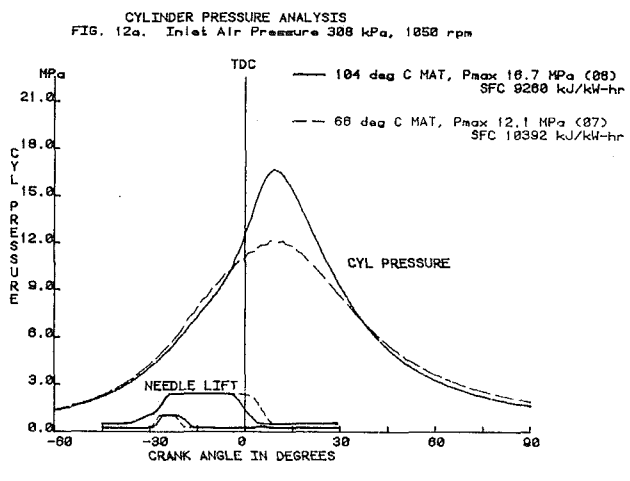


Fig. 11 Constant inlet air temperature



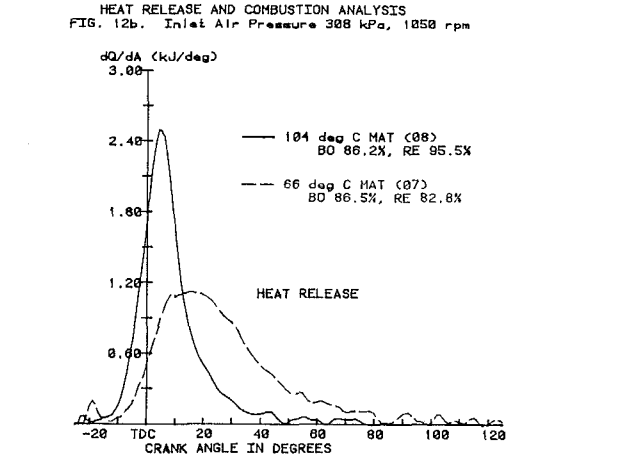


Fig. 12 Constant inlet air pressure

Table 9 Injection pressure effect

Run #	Max. Inj. Pressure (MPa)	Burnout (%)	SFC (kJ/ kW-hr)	Rel. Eff. (%)	Pmax (MPa)
25	52.2	88.8	9114	94.4	17.2
23	46.9	81.1	10432	88.4	14.7

strange to see the higher relative efficiency (better timely burning) of the higher temperature run #08 case. The significant difference in peak firing pressure is again due to the temperature effect being larger than the density effect. Figure 12 shows the comparisons of cylinder pressure and heat release. Due to the low inlet air temperature, although the pilot fuel injection timings were about the same, the start of pilot fuel burning was later for the run #07 case. As is typical with diesel fuel compression ignition, the longer the ignition delay, the more fuel is burned in the kinetic burning phase (larger initial triangle on the heat release trace). The improvement in atomization due to higher air density in this case evidently could not compensate for the lower temperature effect in CWS combustion phase. The heat release of run #07 is seen to be very slow and sluggish.

Summary. Within the test range, the following may be concluded:

- When air density is held constant, the coal burnout, the fuel efficiency, and the timely burning will all improve at higher inlet air temperature (therefore higher pressure or vice versa). The peak cylinder firing pressure will also increase.
- When air temperature is maintained constant, higher air density (therefore higher pressure) will increase coal burnout and fuel efficiency. But due to small change in timely burning (relative cycle efficiency), the peak cylinder firing pressure most probably will not increase very much.
- When inlet air pressure is a constant, the fuel efficiency, relative cycle efficiency, and peak cylinder firing pressure will most probably increase with increase in air temperature (therefore decrease in air density or vise versa). Due to the contradictory effects of air temperature and density, the change in coal burnout is going to be small.

Injection Pressure

In the original matrix, injection pressure was not a separate parameter to be investigated in this phase of the engine test. However, due to the positive displacement characteristics of the system II FIE used, injection pressure changes with the flow rate of the injector tip. As already mentioned, the tips used in this test were of ordinary material. A used tip compared with a new tip would have lower fuel injection pressure and may provide some insights into the effect of injection pressure on engine performance.

The maximum attainable fuel injection pressure at the injector nozzle using one kind of tip (16 holes with 0.5-mm diameter) with the System II FIE was about 52 MPa. Due to the wear of the injector holes, the injector pressure became lower as the test proceeded. It seemed any time the pressure dropped below 47 MPa, engine performance would show marked deterioration. Table 9 lists the comparison results.

It is seen that the lower injector pressure (used injector) run #23 had low burnout, low fuel efficiency (high SFC), and un-

Downloaded 01 Jun 2010 to 171.66.16.87. Redistribution subject to ASME license or copyright; see http://www.asme.org/terms/Terms_Use.cfm

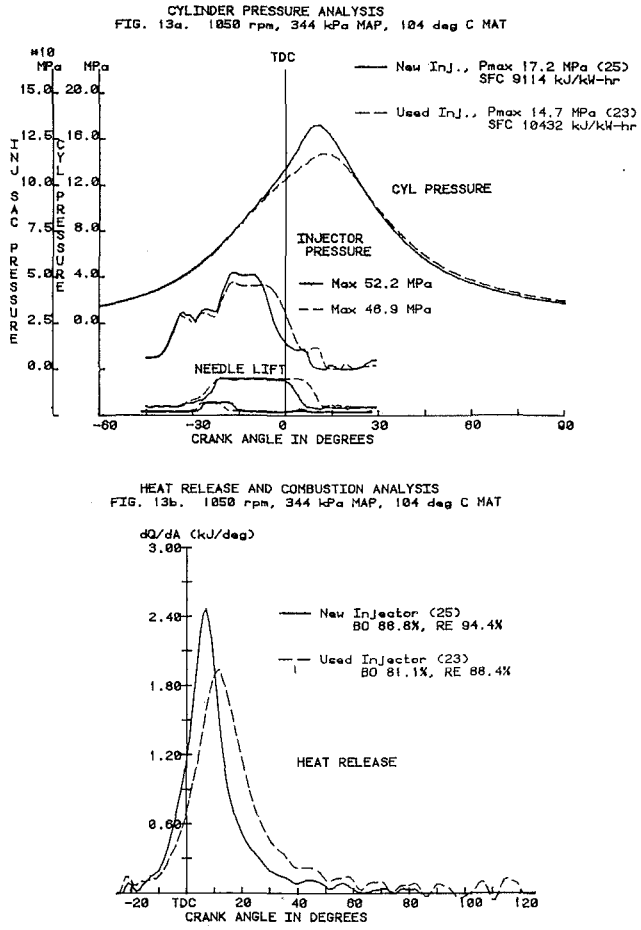


Fig. 13 New and used injector comparison

timely burning (low relative cycle efficiency). The peak cylinder firing pressure was also lower. The cylinder pressure and heat release histories comparisons are shown in Fig. 13. The slower CWS fuel burning phase is evident. This was probably due to the larger droplet sizes of injected fuel in consequence of low injection pressure. This conforms again to the fact that the coal in the CWS burns in the agglomerate particle, which is about the same size as the droplet.

Conclusion

The following conclusions were arrived at with the preliminary results obtained during part of the full load single-cylinder engine test.

1 A full load of 186 kW/cyl at 1050 rpm (1.93 MPa MEP) can be otained on a GE-7FDL engine using CWS fuel. It can be done with or without pilot fuel. The inlet air temperature has to be raised if no pilot fuel is to be used.

2 Using CWS fuel, the engine SFC is comparable to standard diesel fuel operation. The NO_x and CO emissions are about 1/2 of those using diesel fuel.

3 Within the test conditions so far, the maximum heat release rates of the coal fuel runs usually are much higher than the standard diesel operation. The combustion process of the CWS fuel also concentrates in a shorter duration. As a result, the peak firing pressure becomes higher and has to be resolved.

4 Although the burning of coal fuel in the engine cylinder is more concentrated and at a higher maximum rate, part of the fuel is still not burned. The best result obtained at this time is close to 95 percent burnout. Higher fuel injection pressure to provide smaller injected CWS droplet size could be critical in increasing the coal burnout, which is the most important task of further combustion improvement.

5 As more and more tests are done, it becomes necessary to define the CWS specification for coal-fueled diesel engine use. Aside from the basic consideration of ash content, the fuel viscosity is one of the more important characteristics. It affects not only fuel atomization but also fuel transport around the engine. Since coal fuel burns in the agglomerated particles, which are approximately the same size as the injected spray droplets, a smaller original coal particle size in the CWS may even cause combustion to deteriorate if the spray droplets become larger due to an increase in viscosity.

6 The improvement in coal fuel injector materials will greatly facilitate further combustion investigations.

Acknowledgments

The author would like to thank the General Electric Company and the Department of Energy for their permission to publish this work. The many valuable contributions to this project by Mr. J. R. Beal, Mr. E. G. Bricker, Dr. P. L. Flynn, and Mr. D. L. Lecker of GE-TS, Mr. R. J. Johnson, Dr. G. L. Leonard, Dr. S. D. Savkar, and Dr. C. L. Spiro of GE-CRD, and Mr. L. K. Carpenter of DOE-METC are greatly appreciated.

References

1 Hsu, B. D., "Progress on the Investigation of Coal–Water Slurry Fuel Combustion in a Medium Speed Diesel Engine: Part 1—Ignition Studies," ASME JOURNAL OF ENGINEERING FOR GAS TURBINES AND POWER, in press.

2 Leonard, G. L., and Fiske, G. H., "A Comparison of a Positive Displacement Fuel Injection System With an Accumulator Based System for Coal Fueled Diesel Engine Applications," ASME Paper No. 87-ICE-32, 1987.

3 Hsu, B. D., "Heat Release, Cycle Efficiency and Maximum Cylinder Pressure in Diesel Engine: The Use of an Extended Air Cycle Analysis," *S.A.E. Transactions*, 1984, p. 4.766.

4 Siebers, D. L., and Dyer, M. T., "The Autoignition and Combustion of Coal Water Slurry Under Simulated Diesel Engine Conditions," ASME Paper No. 85-DGP-15, 1985.

5 Murdoch, P. L., Pourkashanian, M., and Williams, A., "The Mechanisms of Combustion of Coal Water Slurry," *Twentieth Symposium (International) on Combustion*, The Combustion Institute, Pittsburgh, PA 15236, 1984, p. 1409.

6 Beere, J. M., et al., "The Combustion, Heat Transfer, Pollutant Emission and Ash Deposition Characteristics of the Concentrated Coal Water Slurries," presented at the Fall International Symposium, American Flame Research Committee, International Flame Research Foundation, Akron, OH, Oct. 4–6, 1983.

7 Monroe, L. S., et al., "Slag Deposit Formation in Coal Water Slurry Flames," presented at the DOE First Annual Pittsburgh Coal Conference, Pittsburgh, PA, Sept. 1984.

8 Hsu, B. D., "Combustion of Water in Diesel Emulsion in an Experimental Medium Speed Diesel Engine," S.A.E. Paper No. 860300, 1986.

9 Nydick, S. E., Porchet, F., and Steiger, H. A., "Continued Development of a Coal Water Slurry Fired Slow Speed Diesel Engine: A Review of Recent Test Results," ASME Paper No. 87-ICE-10, 1987.

10 Venkataramani, K. S., "Direct Coal Fueled Combustor Exploratory Development," GE-AEBG Internal Report, Technical Memorandum 86-28, 1986.

11 Heaton, H. L., and McHale, E. T., "Rheology of Coal Water Fuel," *Coal Liquid Mixtures 2*, published by The Institute of Chemical Engineers, England; distributed by Pergamon Press, New York, 1985.

12 Keller, D. V., Personal Communications, 1985.

13 McHale, E. T., "Coal Water Fuel Combustion," presented at the Twenty-First Symposium (International) on Combustion, Munich, Federal Republic of Germany, Aug. 3–8, 1986.

14 Farmayan, W. F., et al., "NO_x and Carbon Emission Control in Coal Water Slurry Combustion," *Proceedings of the Sixth International Symposium on Coal Slurry Combustion and Technology*, Orlando, FL, 1984, p. 165.

15 Reitz, R. D., and Bracco, F. B., "On the Dependence of Spray Angle and Other Spray Parameters on Nozzle Design and Operating Conditions," S.A.E. Paper No. 790494, 1979.

Downloaded 01 Jun 2010 to 171.66.16.87. Redistribution subject to ASME license or copyright; see http://www.asme.org/terms/Terms_Use.cfm

A. K. Rao

C. H. Melcher

Cooper-Bessemer,
Grove City, PA

R. P. Wilson, Jr.

E. N. Balles

Arthur D. Little, Inc.,
Cambridge, MA

F. S. Schaub

Cooper-Bessemer,
Mt. Vernon, OH

J. A. Kimberley

Ambac International, Ltd.,
Springfield, MA

Operating Results of the Cooper-Bessemer JS-1 Engine on Coal-Water Slurry

Successful operation of the Cooper-Bessemer JS-1 engine on coal-water slurry (CWS) fuel has been achieved at full power output, part load, and part speed conditions with varying degrees of diesel pilot fuel including zero pilot (auto-ignition of CWS). Selected results of the effect of pilot fuel quantity, pilot fuel timing, and manifold air temperature on engine performance are presented. Also, the influence of injector nozzle hole size and CWS mean particle size on engine performance is studied. High injection pressures resulted in good atomization of CWS and in combination with heated combustion air resulted in short ignition delays and very acceptable fuel consumption. Low CO/CO_2 ratios in exhaust gas analysis confirmed good combustion efficiency. NO_x emissions are compared for CWS and diesel fuel operation of the engine. Effect of injector nozzle hole size and manifold air temperature on NO_x emissions is studied.

Background

This work is being performed under the sponsorship of the Morgantown Energy Technology Center of the Department of Energy, to establish a foundation of knowledge that will serve as the basis for the development of a coal-fueled diesel engine for stationary power generation applications. Earlier efforts to burn coal fuel in diesel engines have met with qualified success, as summarized in selected papers [1, 2, 9, 10]. Recently, exploratory coal fuel tests have been conducted on the Cooper JS-1 13-in. bore engine, and the present paper describes the operating results that have been achieved during these tests. The coal fuel particle size, air temperature, pilot quantity and timing, and fuel orifice size were varied systematically. Additional JS engine test results are reported in "Analysis of Cylinder Pressure and Combustion Products From an Experimental Coal Fueled Diesel Engine" [4].

Engine and Instrumentation

Cooper-Bessemer is a leading manufacturer of large four-cycle and two-cycle engines that operate on diesel fuel, natural gas, or a combination of the two. The engine chosen for this program is the single-cylinder JS-1 research engine, which has a bore of 13 in. and a stroke of 16 in. and operates in the speed range of 300–450 rpm. This four-stroke cycle engine has many special features. For example, in place of a turbocharger, a separately driven compressor is used to supply combustion air to the engine. This feature, together with the facility to heat or cool the combustion air supplied to the engine, enables the simulation of a wide variety of inlet manifold air conditions. An orifice plate in the exhaust manifold simulates the normal back pressure offered by the turbocharger.

A cross section of the cylinder head is shown in Fig. 1. The main injector is located centrally, and was used to inject CWS. There are two additional openings in the cylinder head, each of which may be fitted with a diesel pilot injector (shown in the right port) or a "Jet Cell" natural gas torch ignitor (shown in the left port). Alternatively, optical diagnostic equipment may be fitted in these ports.

A Hewlett-Packard computer with a high-speed data acquisition unit was used to scan and record all the required pressures, temperatures, engine speed, load, etc., in digital form, for postprocessing. In parallel with the data acquisition unit was an oscilloscope and a 14-channel FM data recorder, which may be used to "play back" any specific engine run. Flywheel timing, combustion, and fuel injection pressures were recorded in analog form as well. The exhaust duct was fitted with a heated sample line; emissions analyzers determined and recorded oxides of nitrogen, total hydrocarbons, carbon monoxide, carbon dioxide, and oxygen. Exhaust particulate samples were collected on filters for gravimetric, morphological, and proximate analyses.

A conventional cam-driven jerk pump was part of the proprietary CWS injection system developed by Ambac International, Ltd. The pilot fuel was delivered by the Cooper-Bessemer (C-B) common rail system. With this system, the injection pressure and timing may be varied while the engine is running, and the stroke of the valve lifter can be adjusted to control the quantity of pilot fuel injected into the cylinder.

Contributed by the Internal Combustion Engine Division and presented at the Eleventh Annual Energy-Sources Technology Conference and Exhibition, New Orleans, Louisiana, January 10–13, 1988. Manuscript received by the Internal Combustion Engine Division November 1987.

Copyright © 1988 by ASME
Downloaded 01 Jun 2010 to 171.66.16.87. Redistribution subject to ASME license or copyright; see http://www.asme.org/terms/Terms_Use.cfm

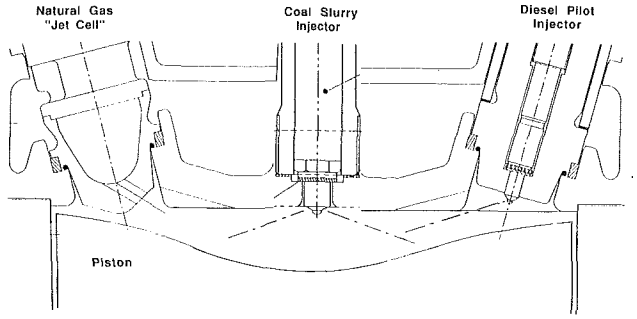


Fig. 1 Configuration of test engine

The stroke of the valve lifter is referred to in the following pages as "pilot lift," which was varied between zero and 0.017 in. in the tests. Higher pilot lift increased the quantity of pilot fuel injected.

Two different low-ash CWS fuels from Amax R & D were used for the engine runs discussed here. These are referred to as "coarse" and "fine". The mass mean particle size was 11 μm for the coarse fuel and 8 μm for the fine fuel. The coal content of the fuel was 53 percent by weight with the additive package contributing another 1 to 2 percent solids. The properties of the fuel are presented in Table 1.

Heat Release Analysis

The cylinder pressure was measured with a strain gage transducer, which was mounted flush with the fire deck of the cylinder head. The pressures were digitized and recorded at 1-deg crank intervals. The pressure data during the compression stroke of each firing cycle, before nay fuel was injected into the cylinder, were compared with the predicted compression pressure to confirm the magnitude and phasing of the measured data. The prediction of the compression pressure was made based on the polytropic compression and expansion process $pV^k = \text{constant}$ with the value of k of 1.38. This predicted pressure was in very good agreement with measured motoring pressure of the JS engine.

Rate of heat release and cumulative heat release were calculated from pressure and volume data using an energy balance and a simple one-zone description of the combustion chamber contents [5]. The heat release model assumes constant average thermodynamic properties of the gas [6, 7]. Heat release rate was calculated according to the following equation:

$$\frac{dQ}{dt} = \frac{\gamma}{\gamma-1} p \frac{dV}{dt} + \frac{1}{\gamma-1} V \frac{dp}{dt}$$

Heat transfer and other losses were not included in the heat release calculations reported here.

Test Variables

During the preliminary runs the engine was operated at part load and part speed, typically at 300 rpm and 100 psi bmep. A large amount of "assist" fuel (usually natural gas) was used to ensure complete combustion of athe CWS. As experience was gained in the use of the fuel injection system and operating the JS engine on CWS, the engine was operated at higher horsepower and the assist fuel was reduced. During these runs, the manifold air temperature was maintained at higher than is normal for diesel operation, again to assist ignition and combustion. Various parameters were changed during this test series and their impact on the engine performance was determined. These were: manifold air temperature, pilot fuel quantity, pilot fuel timing, size of the injector nozzle holes, and the two types of Amax slurries discussed earlier. In all runs, the charge air density was maintained constant by increasing the boost pressure as the manifold air temperature was increased. The engine was always started on diesel fuel and switched over to CWS. For all the runs discussed here, the pilot fuel was diesel fuel and the nominal engine speed and bmep were 400 rpm and 150 psi, respectively. The data presented in this paper came from 24 different runs, which occurred during several days of operation of the engine.

Table 1 Coal-water slurry specifications

CWS Properties	AMAX "Coarse"	AMAX "Fine"
Coal Content (Wt. %)	53	53
Ash Content (Wt. %)	0.20	0.25
Lower Heating Value (Btu/lb)	7280	7280
Viscosity (CP) at 100°F-1000 Sec-1	180	180
Particle Size (Wt. % less Than)	(Microns)	(Microns)
98%	65	45
90%	38	27
50%	11	8
13%	2	1
Coal Properties		
Proximate Analysis (Dry Wt. %)		
Ash	0.4	0.5
Volatiles	41.5	40.9
Fixed Carbon	58.1	58.6
Sulfur	1.1	1.1
Coal Type	High Vol. A Bituminous (Kentucky Splint)	

Results and Discussion

Repeatability. Operating the engine at rated speed and load with higher manifold air temperature and higher CWS injection pressures has given rise to good combustion characteristics, fuel consumption, and a minimum of cycle-to-cycle variation. Also when the same operating conditions were reproduced, the data were closely duplicated with respect to both combustion and emissions. This is demonstrated in Fig. 2 where the combustion pressures from two different runs were plotted on the same graph. The two runs were made using coarse slurry with an intervening straight diesel run, which was conducted while the slurry system was being recharged. The operating parameters common to both the runs were manifold air temperature of 435-440°F, pilot injector lift of 0.017 in., 0.25-mm-dia hole injector, and pilot fuel injection starting at 33 deg before TDC. The measured brake specific fuel consumptions for the two runs were 6790 and 6870 Btu/bhp-h, a difference of about 1 percent, which is within the accuracy limits of our bsfc measurement methods. The peak heat release rate in both runs was 2.5 Btu/deg. The peak CWS in-

Nomenclature and Conversion Factors

CWS = coal-water slurry
MAT = manifold air temperature
SFC = specific fuel consumption
TDC = top dead center
C.A. = crank angle
DF2 = diesel fuel #2
1 psi = 6.895 kPa
1 Btu = 1.055 kJ
1 in. = 25.4 mm
1 deg = 0.01745 rad
tF = 1.8 tK − 459.67

Downloaded 01 Jun 2010 to 171.66.16.87. Redistribution subject to ASME license or copyright; see http://www.asme.org/terms/Terms_Use.cfm

jection pressure was slightly less in the second run, possibly due to nozzle hole wear.

Effect of Air Temperature. Given that the CWS injected into the combustion chamber has to undergo the processes of evaporation of water, devolatilization of coal, combustion of volatile matter, and combustion of char, it is easy to see that the compression temperature, and therefore the temperature of the inlet air to the cylinder, is an important parameter. Two test series, one with coarse slurry and the other with fine slurry, were run, varying the manifold air temperature.

In the first series with coarse slurry, the temperature was varied from 440°F. The results are shown in Figs. 3–5. Other operating parameters were: pilot injector lift of 0.017 in., injector hole size of 0.25 mm diameter, start of pilot injection of 33 deg before TDC, and slurry injection beginning at 18 deg before TDC. The injection pressure was 12,000 psi. As can be seen from Fig. 3, the peak combustion pressure fell from 1350 psia to 1245 psia as the air temperature was reduced. The peak heat release rate rose from 2.5 to 3.0 Btu/deg as shown in Fig. 4. This can be explained by the gradual increase in CWS ignition delay from 4 to 7 deg C.A. as the air temperature is reduced. Presumably this increased ignition delay allowed more fuel to be accumulated in the premixed stage, resulting in a higher heat release rate once slurry combustion had begun. However, the most interesting result is the fuel consumption, which stayed constant at 6870 Btu/bhp-h, as shown in Fig. 5. That is, even though combustion is initiated later for the 290°F case, the ensuing combustion process is apparently more rapid so as to compensate for the delayed start.

The second series of runs with fine slurry followed an identical pattern. The pilot injector lift was maintained at 0.017 in. and 0.25-mm-dia hole injector nozzle was used. The pilot and slurry timings were unaltered. The peak injection pressures were between 14,000 and 15,000 psi. The peak combustion pressure dropped from 1350 psia to 1200 psia as the air temperature was lowered. The peak heat release rate increased from 2.5 to 3.1 Btu/deg. The ignition delay of CWS increased from 3 to 9 degrees C.A. The fuel consumption, however, again stayed constant at 7170 Btu/bhp-h, as shown in Fig. 5.

These observations lead to two important conclusions. First, it does not appear to be necessary to increase the intake air temperature above 290°F in order to improve fuel consumption. Second, all other conditions being equal, operation on "fine" fuel apparently increased the SFC by about 4 percent in the 290–440°F MAT range. It should be noted that this small SFC difference is close to the accuracy and repeatability limits imposed by fuel heating value, fuel flow measurement, and load measurement.

In the absence of pilot fuel, however, MAT has a different effect on combustion and SFC. In order to illustrate this, two runs are compared, one at a MAT of 434°F and the other at 250°F. Both runs used a 0.25-mm nozzle and coarse slurry. At the higher temperature, as seen in Fig. 6, the combustion was good, and peak cylinder pressure was occurring at 6 deg after TDC. Figure 7 shows a heat relaease diagram similar to that of DF2 with a peak heat release rate of 4.1 Btu/deg folllowed by a "diffusion controlled" burning over the first 20 crank deg after TDC. The nominal SFC was 6540 Btu/bhp-h. In contrast, at 250°F MAT, the ignition delay increased from 2.5 ms to 5.4 ms (6 to 13 deg C.A.) with the peak pressure occurring at 18 deg after TDC. The heat release rate curve is triangular in shape with a peak of 6.5 Btu/deg. Interestingly, the SFC increased only by 3 percent to 6730 Btu/bhp-h.

Effect of Pilot Fuel Timing. The differential timing between pilot fuel injection and main slurry injection is another variable of interest. In this test series the main fuel injection timing was fixed, and the start of pilot fuel timing was varied from coincident with the start of main injection to 14 deg in advance of main injection; the results are shown in Figs. 8–10. The manifold air temperature was 260°F, the pilot lift 0.007 in. and the coarse slurry was used with a 0.25-mm hole nozzle tip. The peak injection pressure was 11,000 psi. In all the runs

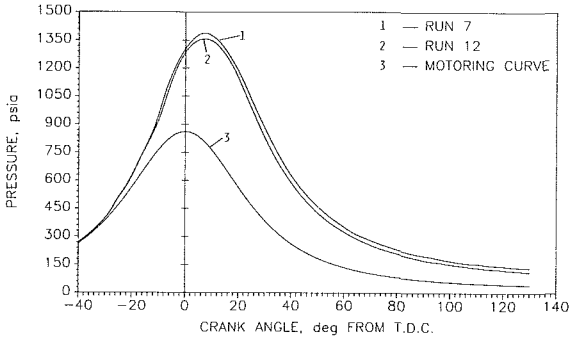


Fig. 2 Repeatability of results; combustion pressure from two runs; MAT 440°F, lift 0.017 in., 0.25-mm-dia nozzle

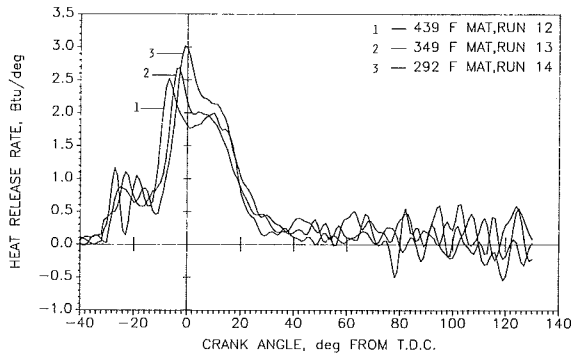


Fig. 4 Effect of MAT on heat release; lift 0.17 in., 0.25-mm-dia nozzle, coarse CWS

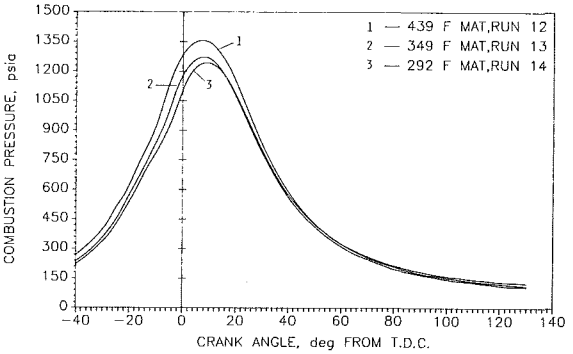


Fig. 3 Effect of MAT on combustion pressure; lift 0.017 in., 0.25-mm-dia nozzle, coarse CWS

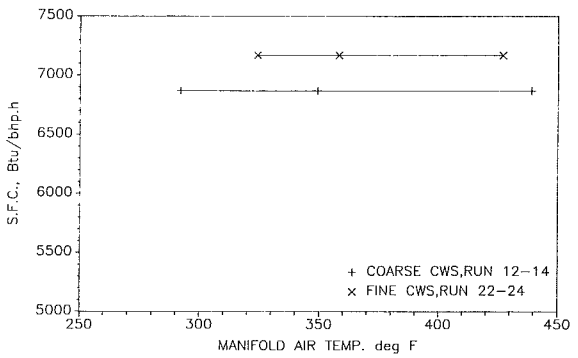


Fig. 5 Effect of MAT on SFC; lift 0.017 in., 0.25-mm-dia nozzle

Downloaded 01 Jun 2010 to 171.66.16.87. Redistribution subject to ASME license or copyright; see http://www.asme.org/terms/Terms_Use.cfm

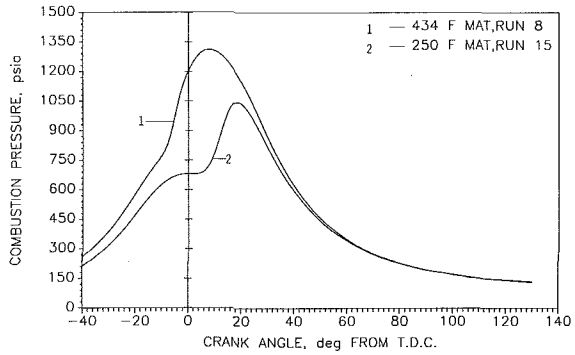


Fig. 6 Effect of MAT on combustion pressure; zero pilot, 0.25-mm-dia nozzle, coarse CWS

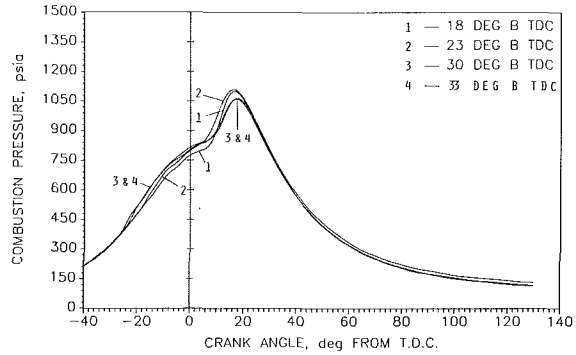


Fig. 8 Effect of pilot timing on combustion pressure; MAT 261°F, lift 0.007 in., 0.25-mm-dia nozzle, coarse CWS

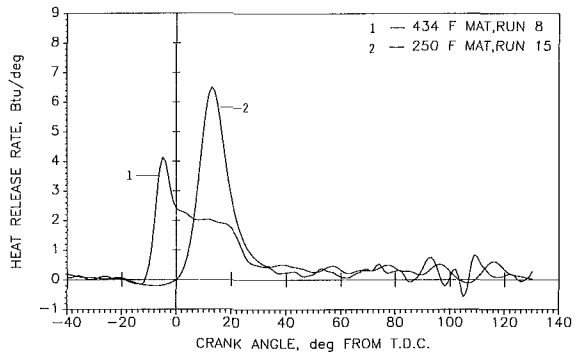


Fig. 7 Effect of MAT on heat release; zero pilot, 0.25-mm-dia, coarse CWS

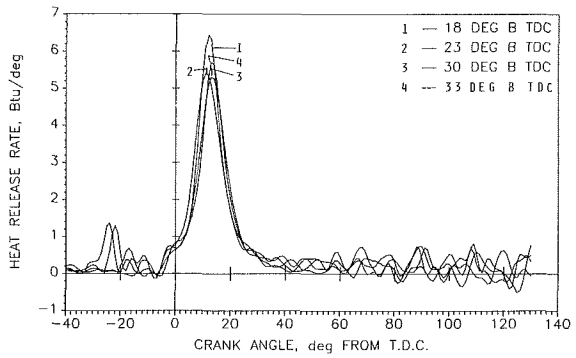


Fig. 9 Effect of pilot timing on heat release; MAT 261°F, lift 0.007 in., 0.25-mm-dia nozzle, coarse CWS

the ignition delay of CWS was nearly constant between 4.5 ms and 5.4 ms (11 and 13 deg C.A.). Peak combustion pressures were occurring between 16 and 18 deg after TDC. As can be seen in Fig. 8, the peak combustion pressure was 1100 psia in the cases where timing differential between injections was zero and 4 deg C.A. The peak pressure fell to about 1065 psia as the pilot injection was advanced. Figure 9 shows that the peak heat release rate was highest at 6.5 Btu/deg when the start of pilot injection coincided with that of the main injection. When the pilot injection was advanced, the maximum heat release rate varied from 5.3 to 5.7 Btu/deg. In all cases the heat release curves have a sharp peak indicating predominantly premixed combustion with very little diffusion-controlled combustion. As shown in Fig. 10, the SFC was best at a pilot injection of 18 deg before TDC, when the starts of the two injections coincided. This can possibly be attributed to the higher heat release rate at this condition. The SFC gradually deteriorated to 7110 Btu/bhp-h as the pilot injection was advanced. One contributing factor for this deterioration may have been that, as shown in Fig. 9, the heat released by the pilot actually occurred during the compression stroke, effectively producing negative work.

While these preliminary tests showed that the SFC was best when start of pilot coincided with start of main injection, further work will be required in order to optimize the start of CWS injection and the injection timing differential.

Pilot Fuel Quantity. Pilot fuel quantity is another important variable that has an impact not only on engine performance, but also on the economics of CWS operation. The pilot fuel is diesel oil, the very fuel being replaced with CWS. Pilot injector lifts of 0.007 in. to 0.017 in. were tested, which corresponded to diesel pilot heat inputs of 7 and 16 percent of the total energy input (about 90 Btu per cycle at this bmep). Also, on selected runs the pilot fuel was completely cut off, resulting in the auto-ignition of CWS.

Two series of tests were performed, the first series with a

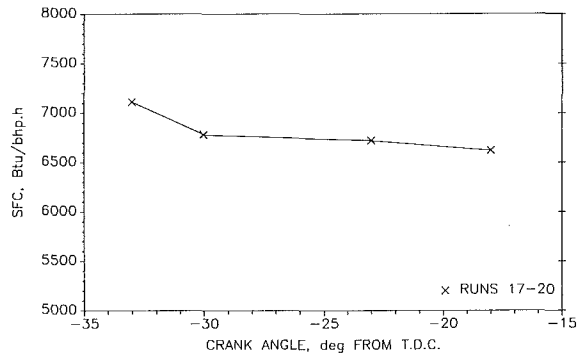


Fig. 10 Effect of pilot fuel timing on SFC; MAT 261°F, lift 0.007 in., 0.25-mm-dia nozzle

0.30-mm hole nozzle tip, coarse slurry, 345–350°F MAT, and injection pressure between 9000 and 10,000 psi. In this series, the peak pressures were around 1200 psia except for the case of zero pilot, for which it was 1050 psia. This lower peak pressure may be attributable to the fact that for zero pilot, the peak pressure occurred somewhat later in the cycle (at 19 deg after TDC). The ignition delay was relatively constant between 5.4 and 6.2 ms (13 and 15 deg C.A.), at this MAT, for all pilot rates. Although the ignition delay remained constant, the peak heat release rate progressively increased from 3.4 to 7.0 Btu/deg as the pilot rate was reduced. On the other hand, as shown in Fig. 11, the SFC increased from 6490 to 6840 Btu/bhp-h as the pilot lift was reduced from 0.017 in. to 0.007 in. However, at zero pilot, the fuel rate improved to 6680 Btu/bhp-h. It should be noted that SFC cannot be measured to better than ±2 percent (±130 Btu/bhp-h).

Identical trends were observed in the second series, when the pilot fuel quantity was varied with a 0.25-mm nozzle, 435°F MAT, and coarse CWS. The higher temperatures lowered the ignition delay and peak heat release rates. The SFC, as before,

Downloaded 01 Jun 2010 to 171.66.16.87. Redistribution subject to ASME license or copyright; see http://www.asme.org/terms/Terms_Use.cfm

increased as the pilot lift (quantity) was reduced from 0.017 in. to 0.007 in., and improved at zero pilot. This also is shown in Fig. 11.

Nozzle Hole Size. In comparing two runs with 0.30 and 0.25-mm hole nozzles with a MAT of 346 ±3°F, pilot lift of 0.017 in., and coarse slurry, it was found that the smaller hole nozzle increased the duration of CWS injection as well as peak injection pressure. The larger hole nozzle resulted in a considerably longer ignition delay of 5.8 ms (14 deg C.A.), as compared to 2.5 ms (6 deg C.A.) with smaller nozzle, presumably due to coarser atomization. However, the SFC with the 0.30-mm nozzle at 6490 Btu/bhp-h was about 6 percent better than with the 0.25-mm nozzle at 6870 Btu/bhp-h. Apparently, much of the fuel energy with the 0.25-mm nozzle was released before TDC, resulting in negative work. Perhaps the SFC with the smaller nozzle could be improved by optimizing CWS injection timing.

Exhaust Gas Analysis

The exhaust gas measurements revealed additional features of coal slurry combustion as follows:

- Very low CO/CO_2 ratios, confirming good combustion efficiency of coal (once ignited). In fact, the CO levels were much lower for CWS than for DF2, despite the higher carbon/hydrogen ratio for CWS, as shown in Table 2.
- NO_x was increased (up to a factor of four) by increased manifold air temperature (by 100–150°F).
- The slurry fuel case had lower NO_x emissions compared to diesel fuel (this was only observed at MAT below 200°F).
- NO_x was affected significantly by the hole size of the injector.

Table 2 gives selected exhaust gas measurements for DF2 and CWS tests; more detailed discussion of these features is given below.

(*a*) *Air Fuel Ratio and Excess Air.* The results (see Table 2) show equivalent exhaust excess air levels for both DF2 and CWS (about 90 to 110 percent). Although excess air is theoretically expected to be slightly lower for coal than for DF2 (given the same air flow and fuel Btu), our measurements were not sufficiently accurate to resolve any difference in air-fuel ratio. In theory, clean coal requires 3–5 percent more air than DF2 to release the same amount of energy in combustion because of its higher carbon–hydrogen ratio.

(*b*) *Carbon Monoxide.* Coal burns by means of a complex mechanism of reaction steps including devolatilization, volatile reactions, char surface reactions, and gas-phase actions near the surface. Carbon monoxide appears in most of these reaction steps, and is a product of combustion when coal burns in fuel-rich atmospheres. Therefore, the CO/CO_2 ratio is often used as a figure of merit in coal flames that are subject to spatially nonuniform and/or limited air availability. For the present CWS tests, as shown in Table 2, the CO/CO_2 ratio was less than 0.5 percent, indicating vigorous carbon burnout (once ignited) and adequate air mixing.

(*c*) *Nitrogen Oxide and the Effect of Air Temperature.* Earlier tests at 100–200°F MAT showed that NO_x levels for CWS runs were substantially reduced compared to DF2 results. Reductions of 32–68 percent were observed. This observed reduction in NO_x has been attributed mainly to the suppression of local peak flame temperatures in the combustion zone by water vapor released by the slurry evaporation.

In the present tests, which were run at elevated air temperatures (330–440°F), the NO_x levels for DF2 and CWS did not differ significantly from each other (see Table 2, runs 1 versus 2, 3 versus 4, and 8 versus 9). However, the elevated air temperature generally increased NO_x levels up to a factor of four. For example, NO_x levels of 380 ± 30 ppm were observed in earlier tests at 203°F air temperature (see [4]), compared to the Table 2 results (up to 1650 ppm). The strong air temperature effect on NO_x can also be seen by comparing runs 5 versus 7. Figure 12 illustrates the effect of air temperature on NO_x, CO, and particulate burnout.

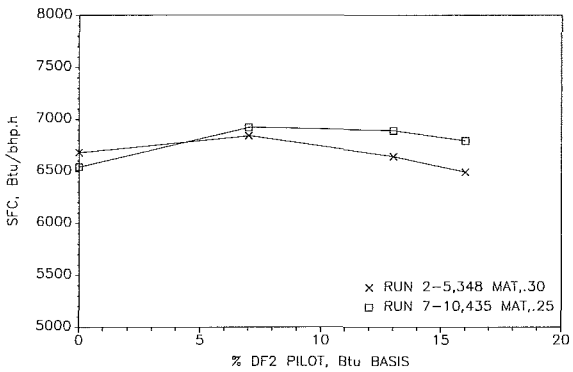


Fig. 11 Effect of pilot fuel quantity on SFC

Table 2 Measured exhaust gas composition

Run	Fuel	Feature	Air Temp. °F	CO_2 %	O_2 %	CO ppm	NO_x, ppm As Meas	NO_x, ppm @ 15%O_2	Excess Air%	CO/CO_2 Ratio
1.	Baseline DF2	Larger Hole	337	9.0	8.75	800	850	403	68	.009
2.	CWS/DF2 pilot	Larger Hole	344	8.7	10.6	360	750	426	100	.004
3.	Baseline DF2	High Air Temp.	440	7.8	10.4	NA	1250	697	92	NA
4.	CWS/DF2 pilot	High Air Temp.	439	8.5	11.2	210	1200	725	108	.002
5.	CWS/DF2 pilot	Repeat Run 4	433	8.4	11.5	95	1650	1029	116	.001
6.	CWS	No Pilot/High Air Temp.	434	8.3	11.6	150	1440	907	120	.002
7.	CWS/DF2 pilot	Moderate Air Temp.	349	8.9	10.8	200	1080	626	100	.002
8.	Baseline DF2	High Air Temp.	425	7.6	10.7	510	1325	764	98	.007
9.	CWS/DF2 pilot	Fine Coal	427	8.8	10.8	108	1200	696	100	.001

All runs at 400 rpm, 150 psi bmep; excess air variations were due to breathing effects (the excess air of trapped cylinder mixture was approximately constant for all runs); DF2 pilot 14% of total fuel energy (when used).

Downloaded 01 Jun 2010 to 171.66.16.87. Redistribution subject to ASME license or copyright; see http://www.asme.org/terms/Terms_Use.cfm

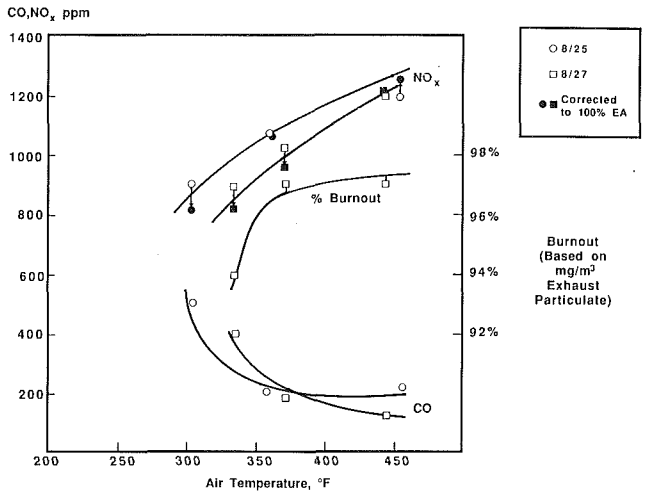


Fig. 12 Increased air temperature affects emissions

(*d*) *Nozzle Hole Size.* The larger fuel nozzle hole size resulted in a 30 percent reduction in NO_x (compare runs 2 and 7 in Table 2). This effect also has been observed for DF2. There are many factors at work here that could affect NO_x, including injection duration, rate of mixing, rate of burning, and slurry atomization (drop size).

(*e*) *Effect of Pilot.* Note that the exhaust gas analysis implies that combustion was not affected during a coal slurry engine run with or without the DF2 pilot. The NO_x, CO, and CO_2 are essentially unchanged between Run 6 and Run 5.

(*f*) *Effect of Fine Coal.* A set of runs was performed with an alternate coal-water slurry, which was prepared using the identical coal but with a slightly smaller particle size distribution (i.e., 20 percent below 2 μm instead of 13 percent below 2 μm; 8 μm versus 11 μm mean size). The exhaust gas analysis revealed no significant difference in CO, NO_x, or CO_2 (compare Run 9 versus 4 in Table 2).

(*g*) *Reproducibility.* Runs 4 and 5 in Table 2 show exhaust gas measurements that were taken one hour apart on two successive tanks of slurry under "identical" engine operating conditions. Excellent agreement was obtained; the difference in NO_x might be attributed to nozzle wear during the first run, which was observed.

Summary and Conclusions

The JS-1 engine was operated at full output rating on CWS with varying degrees of DF2 pilot fuel, including a zero pilot condition, during which the CWS auto-ignited. Satisfactory part-load and part-speed operation was also achieved. The injection system was operated at injection pressures up to 15,000 psi. The resultant fine atomization of the CWS resulted in low and very acceptable ignition delay periods as well as reasonably good fuel consumption rates. Following are some conclusions that can be drawn from the test series.

1 CWS with up to 55 percent solid content was burned successfully. No beneficial effect was found by diluting the slurry. The SFC with CWS was comparable to that with DF2.

2 When the operating conditions were reproduced, the resulting combustion and emissions data were closely duplicated, which established reproducibility.

3 Ignition delays of 5 to 6 ms at the upper end and 2 to 3 ms at the lower end were obtained. These ignition delays are acceptable for a 400 rpm engine.

4 In the 290–440°F temperature range, when DF2 pilot was used, the manifold air temperature had no apparent effect on SFC, with either coarse or fine fuel.

5 With fine fuel, there appears to be a penalty of about 4 percent on SFC (subject to ±2 percent SFC accuracy limit).

6 When no pilot fuel was used (the slurry was auto-ignited), higher MAT improved the ignition process, resulting in better combustion and reduced SFC.

7 With fixed CWS injection timing, as the pilot injection timing was retarded, the SFC improved slightly.

8 A reduction in pilot fuel quantity from 16 to 7 percent of total heat input (from 14 Btu to 5.4 Btu/cycle, respectively) deteriorated the fuel consumption slightly. However, further reduction of pilot fuel to zero improved the SFC. Further tests are needed to optimize pilot timing and quantity.

9 Good combustion efficiency was further verified by low CO/CO_2 ratios in the exhaust gas.

10 High manifold air temperature increased NO_x in the exhaust.

11 At air temperatures below 200°F, CWS generated lower NO_x levels than DF2 did.

12 Hole size of the injector significantly affects NO_x. Larger hole size nozzles generated lower NO_x, both with CWS and DF2 fuels.

13 Fineness or coarseness of slurry, within the range tested, had no significant impact on emissions.

Acknowledgments

We acknowledge the guidance and suggestions offered by Nelson F. Rekos, Jr. and Michael McMillian, the Contract Officer's Technical Representatives of METC during the test series, and that of Larry K. Carpenter, COTR of METC during the earlier stages of the program.

At Cooper-Bessemer's Mount Vernon Research Lab, Terry Baker put the data acquisition system together and made it operational, while Jesse Smith provided valuable assistance in operating the JS engine. Don Blizzard and Mel Helmich of Cooper-Bessemer, Grove City, reviewed the program and offered helpful suggestions. Karen Benedek of Arthur D. Little helped in monitoring the CWS vendor and in collecting the exhaust particulates.

References

1 Soehngen, E. E., "The Development of Coal Burning Diesel Engines in Germany: A State-of-the-Art Review," Report prepared for the United States Energy Research and Development Administration, Report PE/WAPO/3387-1, Aug. 1976.

2 Carpenter, L. K., and Crouse, F. W., Jr., "Coal Fueled Diesels: Progress and Challenges," ASME Paper No. 86-ICE-6, Feb. 1986.

3 Wilson, R. P., "Coal-Fueled Diesel Systems for Stationary Power Applications: Assessment of Merit," Topical Report prepared by Arthur D. Little Inc., under contract to the Department of Energy/Morgantown Energy Technology Center, Sept. 1986.

4 Balles, E. N., Benedek, K. R., Wilson, R. P., and Rao, A. K., "Analysis of Cylinder Pressure and Combustion Products From an Experimental Coal-Fueled Diesel Engine," ASME Technical Conference, *New Technology for Cogeneration*, ICE Vol. 2, Oct. 1987, p. 75.

5 Gatowski, J. A., Balles, E. N., Chun, K. M., Nelson, F. E., Ekchian, J. A., and Heywood, J. B., "Heat Release Analysis of Engine Pressure Data," SAE Paper No. 841359, 1984.

6 Cheng, W. K., Gentry, R. "Effects of Charge Non-uniformity on Diesel Heat Release Analysis," SAE Paper No. 861568, 1986.

7 Chun, K. M., and Heywood, J. B., "Estimating Heat Release and Mass-of-Mixture Burned from Spark-Ignition Pressure Data," submitted for publication in *Combustion Science and Technology*, 1987.

8 Lai, M. C., Zhou, B., Cheng, W. K., Wong, V. W., and Benedek, K. R., "Parametric Studies of Coal-Water Slurry Combustion in a Rapid Compression Machine," ASME Paper No. 87-ICE-9, Feb. 1987.

9 Caton, J. A., and Rosegay, K. H., "A Review and Comparison of Reciprocating Engine Operation Using Solid Fuels," SAE Paper No. 831362, 1983.

10 *Proceedings of the Fourth Annual Heat Exchange Contractors Meeting*, United States Department of Energy, Office of Fossil Energy, Morgantown Energy Technology Center, Apr. 1987.

Downloaded 01 Jun 2010 to 171.66.16.87. Redistribution subject to ASME license or copyright; see http://www.asme.org/terms/Terms_Use.cfm

Coal-Water Slurry Operation in an EMD Diesel Engine

C. M. Urban

H. E. Mecredy

T. W. Ryan, III

M. N. Ingalls

Southwest Research Institute,
San Antonio, TX 78284

B. T. Jett

Electro-Motive Division,
General Motors Corporation,
La Grange, IL

The U.S. Department of Energy, Morgantown Energy Technology Center has assumed a leadership role in the development of coal-burning diesel engines. The motivation for this work is obvious when one considers the magnitude of the domestic reserves of coal and the widespread use of diesel engines. The work reported in this paper represents the preliminary engine experiments leading to the development of a coal-burning, medium-speed diesel engine. The basis of this development effort is a two-stroke, 900 rpm, 216-mm (8.5-in.) bore engine manufactured by Electro-Motive Division of General Motors Corporation. The engine, in a minimally modified form, has been operated for several hours on a slurry of 50 percent (by mass) coal in water. Engine operation was achieved in this configuration using a pilot injection of diesel fuel to ignite the main charge of slurry. A standard unit injector, slightly modified by increasing diametric clearances in the injector pump and nozzle tip, was used to inject the slurry. Under the engine operating conditions evaluated, the combustion efficiency of the coal and the NO_x emissions were lower than, and the particulate emissions were higher than, corresponding diesel fuel results. These initial results, achieved without optimizing the system on the coal slurry, demonstrate the potential for utilizing coal slurry fuels.

Introduction

Coal-based fuels have been the subject of study since the inception of the diesel engine. Ryan et al. [1] included a summary of the prior work in their 1987 ASME paper. Much of the recent work in this area has been sponsored by the Department of Energy (DOE), Morgantown Energy Technology Center (METC). The economic implications of using coal-water slurry (CWS) in a modern freight locomotive were examined by Koch et al. [2]. They found that with a two-year life of the engine power assemblies, along with other assumptions, a coal-fired locomotive would be economically advantageous for the railroads. Similar studies were reported by Hapeman and Savkar [3] and Wilson et al. [4].

The injection of slurries has been the subject of several studies [5–7]. A prevailing concept for liquid fuels is that the atomization characteristics can be improved in pressure-type injectors by increasing the injection pressure. Researchers at General Electric Research Laboratories and at MIT have investigated the application of extremely high injection pressures to coal-water slurries. In the one case [7], there was no experimental evidence to indicate that the increased pressure actually resulted in improved atomization. In another case, the experimental evidence, in the form of high-speed movies, indicated that atomization was actually reduced and the spray tip velocity was increased to the point of significant fuel impingement on the combustion chamber walls. Higher pressures result in the generation of higher shear rates within the injection system. Since the slurries generally exhibit shear thickening at high shear rates, higher injection pressures can actually result in degraded atomization due to the increased viscosities that accompany the higher pressures. Extremely high injection pressures introduce an added complication in that the life expectancy of an injector may be reduced because of the higher material stresses, higher leakage pressures, and higher erosion forces. The problems associated with high injection pressures are severe enough, even when using specification quality diesel fuel, that the injection system manufacturers generally avoid line pressures in excess of about 100 MPa (14,500 psi). Ryan et al. [1] demonstrated good injection of slurries with jerk-pump systems operating in the normal pressure ranges.

Constant volume combustion bomb data reported by Leonard and Fiske [8, 9] indicated that the ignition delay times and the combustion efficiencies approach acceptable values when the precombustion air temperature approaches 1000 K (1340°F). The authors also presented the fraction of coal burned after 12 ms as a function of the initial temperature. The 12-ms limit was imposed because this represents the time available for combustion in a 1000 rpm engine. Beyond 1000 K, the burn rate appears to be essentially unaffected by further increases in the initial temperature. These results suggest that, at least for these fuels examined, 1000 rpm represents the upper limit on speed in a coal-burning diesel engine, even if the compression temperature exceeds 1000 K. Similar results were presented by Siebers and Dyer [10] for a different coal-water slurry. The results of those experiments indicated that the temperature requirement was about 1000 K. The importance

Contributed by the Internal Combustion Engine Division and presented at the Eleventh Annual Energy-Sources Technology Conference and Exhibition, New Orleans, Louisiana, January 10–13, 1988. Manuscript received by the Internal Combustion Engine Division November 1987. Paper No. 88-ICE-28.

Copyright © 1988 by ASME
Downloaded 01 Jun 2010 to 171.66.16.87. Redistribution subject to ASME license or copyright; see http://www.asme.org/terms/Terms_Use.cfm

Table 1 EMD 567B diesel engine

Number of Cylinders	2
Cycle	Two-Stroke
Type	Blower Scavenged
Bore, mm (in.)	216 (8.5)
Stroke, mm (in.)	254 (10.0)
Displacement liters (cu.in.)	9.3 (567)
Compression Ratio	16:1
Rated Speed, rpm	835
Rated Power, kW (hp)	160 (215)
Combustion Chamber Type	Open, Mexican Hat
Type of Injection	Unit Injector

of high combustion chamber temperature was also verified experimentally by Likos et al. [11]. It should be noted that this 1000 to 1100 K temperature range represents both a lower limit for acceptable combustion and an upper limit in terms of effectiveness.

More recently, limited engine test results have been reported. Ryan et al. [1] presented data obtained from a small two-stroke engine in which the combustion behaviors of coal–water and coal–diesel fuel slurries were compared with diesel fuel. Mecredy and Jett [12] continued this work and compared the combustion behavior of three different slurries formulated in diesel fuel, water, and methanol. In all of this work, except for some limited runs with the coal–methanol slurry, a pilot charge of diesel fuel was utilized to ignite the slurries. Similar work on a full-scale medium-speed engine was reported by Hsu [13]. Hsu reported some success with the unaided auto-ignition of CWS but with ignition delays of an order of magnitude longer than normally obtained with diesel fuel.

In the area of engine component durability, limited data have been presented by medium-speed engine researchers. Nydick [14] reported good success in burning CWS in a large, low-speed diesel engine, but he observed power assembly wear rates at least an order of magnitude greater than normally obtained when operating on diesel fuel.

Objective

The overall objectives of this project are to define the limitations of the current technology and to expand the technology base for medium-speed coal-burning engines. The specific objective of the effort reported in this paper was to examine the combustion behavior of coal–water slurry in a minimally modified, medium-speed, Electro-Motive Division diesel engine.

Experimental Apparatus and Procedures

This section of the paper describes the engine, fuel injection systems, instrumentation, and procedures used in this evaluation of coal–water slurry fuel in a medium-speed diesel engine.

EMD Engine. The medium-speed engine used for this investigation was a two-cylinder version of the EMD 567B diesel engine produced by the Electro-Motive Division of General Motors Corporation. This two-cylinder engine, a limited-production version designed specifically for research use, is described in Table 1. For these evaluations, a pilot injector was installed in one of the cylinders, and separate fuel supplies were provided to the main injector in each of the two cylinders. The governor was disconnected for the evaluation conducted, and the fuel flow to each of the three injectors (two main and one pilot) was manually controlled.

Main Fuel Injection System. The main fuel injection system for the experimental cylinder is illustrated in Fig. 1.

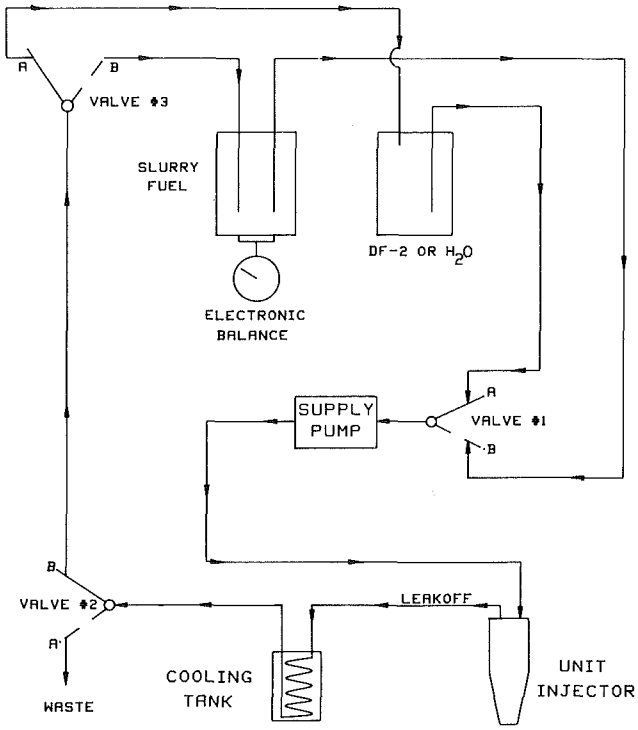


Fig. 1 Fuel system for experimental cylinder of the EMD engine

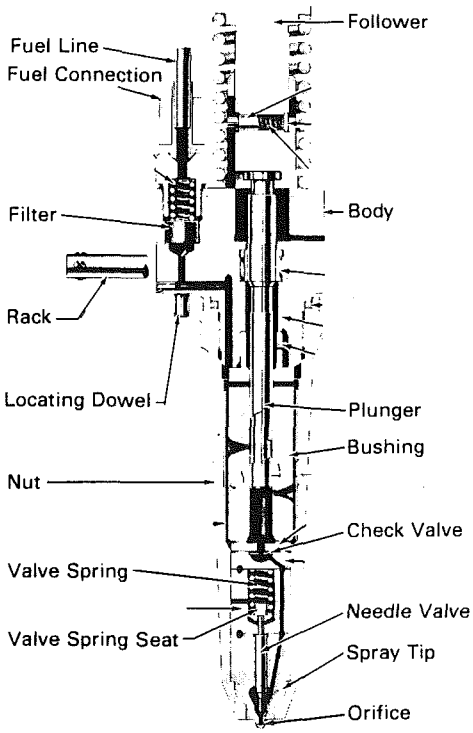


Fig. 2 Main fuel injector

The supply pump was a Moyno Model 6M1 progressive cavity pump capable of supplying diesel fuel, water, or coal–water slurry (CWS) to the unit injector at a flow rate of 2.3 liters/min (0.6 gal/min). System pressures maintained with the CWS were 830 kPa (120 psig) at the outlet of the supply pump and 415 kPa (60 psig) at the outlet of the injector. In the system used, the suction side of the supply pump was equipped with hand-operated valves to enable switching between tanks

Downloaded 01 Jun 2010 to 171.66.16.87. Redistribution subject to ASME license or copyright; see http://www.asme.org/terms/Terms_Use.cfm

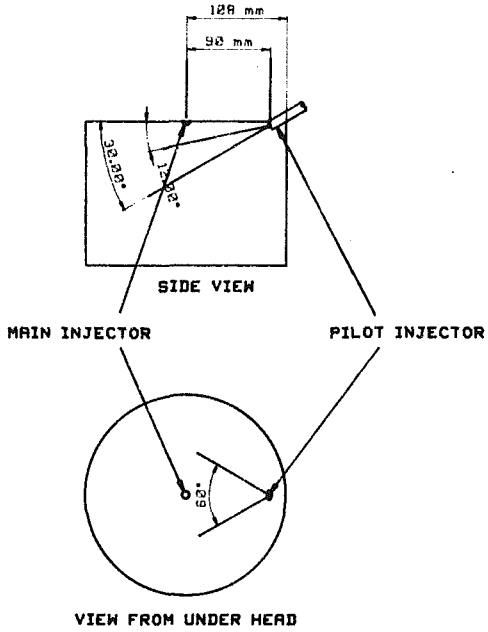


Fig. 3 Pilot fuel injection geometry for experimental cylinder of the EMD engine

containing diesel fuel, water, and CWS. For fuel flow measurements, the tank containing CWS was suspended from a load cell.

The main fuel injector, illustrated in Fig. 2, was an EMD unit injector with a 12.7-mm (0.50-in.) plunger and six-hole, 0.38-mm (0.015-in.) nozzle tip with 160 deg included angle. For this effort, the fuel filter was removed, the diameter of the plunger was reduced by 0.013 mm (0.0005 in.), and the diameter of the needle valve in the spray tip was reduced by 0.038 mm (0.0015 in.). These reductions in diameters were found necessary for operation on CWS.

Experiments with a smaller engine [1] and preliminary efforts with this EMD engine emphasized the importance of providing additional cooling to the fuel injector. On the EMD engine, the approach taken was to circulate water at room temperature through the cavity between the fuel injector and the cylinder head. In addition, the excess fuel returned from the injector was cooled to room temperature before being returned to the supply tank.

Pilot Fuel Injection System. A pilot injection of diesel fuel was required to promote ignition of the coal-water slurry. The pilot fuel charge was injected into the combustion chamber using a jerk pump-line-nozzle system of conventional design. The pilot jerk pump was a Bosch PES, eight-cylinder pump driven from the engine, with the fuel from seven of the cylinders recirculated. A dynamic differential was used between the engine and the pump to allow for adjustment of the pilot injection timing. A Stanadyne pencil nozzle was installed in the cylinder pressure relief port. The quantity of pilot fuel injected per stroke was controlled through the rack on the pilot pump, and the fuel flow rate was measured using a Micro Motion mass flow meter.

The pilot injection geometry consisted of a two-orifice nozzle, with both orifices 0.2 mm (0.008 in.) in diameter. The included angle between the orifices was 60 deg, and the spray was directed at 30 deg below the horizontal plane of the piston crown. A schematic of the pilot spray geometry is shown in Fig. 3.

Fuels Used. The coal-water slurry used in the experimental cylinder for this effort was obtained from a 500-gal batch stored in a special design 500-gal slurry storage system. This

Table 2 Amax coal-water slurry fuel

Composition, wt%	
Coal content	50.0[a]
Preservative (formaldehyde)	0.10
Surfactant (nonionic)	1.50
Stabilizer	0.03
Water	Balance
Heating Value	
Gross, MJ/kg (Btu/lb)	17.4 (7500)
Net, MJ/kg (Btu/lb)	15.5 (6675)
Other Properties	
Coal partical size, microns	15[b]
Ash content, wt%	0.5
Viscosity @ 100 sec-1,[cP]	40

[a]Value as blended.
[b]95% smaller than value shown.

Table 3 Properties of coal used in Amax slurry

Proximate Analysis, %	
Ash	1.01
Volatiles	34.5
Fixed Carbon	64.5
Ultimate Analysis, %	
Carbon	85.4
Hydrogen	3.22
Sulfur	0.86
Nitrogen	1.30
Oxygen	9.20

slurry was obtained from the Amax Corporation and is described in Tables 2 and 3.

The diesel fuel used in the standard cylinder and for pilot injection in the experimental cylinder was a typical DF-2 fuel with a lower heating value of 42.5 MJ/kg (18,300 Btu/lb). Standard tap water, obtained through clean supply lines, was used as the transition fluid between the diesel fuel and the CWS.

Engine Instrumentation. The engine was equipped for two types of data acquisition, one for low-speed data (sampling once every second) and the other for high-speed data (sampling once each half-degree of crankshaft rotation). The low-speed data system was used to monitor engine operating parameters (e.g., speed, power output, pressures, and temperatures) from the lubricating, cooling, intake, and exhaust systems using a Hewlett-Packard 1000E-Series computer system.

The high-speed data system included a BEI shaft encoder, a piezoelectric cylinder pressure transducer mounted in the high-pressure line of the pilot injection system, and a strain gage installed on the injector rocker arm of the test cylinder. Signals from the two pressure transducers, the rocker strain gage, and the encoder were processed through a Preston analog-to-digital converter, and the data were stored in an HP 1000E-Series computer. Combustion information, such as heat-release rate, total heat released, indicated thermal efficiency, and pressure-versus-volume values were calculated from the high-speed data.

Emissions Instrumentation. The gaseous emissions samples for HC, CO, and NO_x were taken from the engine ex-

Downloaded 01 Jun 2010 to 171.66.16.87. Redistribution subject to ASME license or copyright; see http://www.asme.org/terms/Terms_Use.cfm

haust, passed through an ice-bath water condenser, and collected in a Tedlar bag. The emission concentrations in the bag were determined using an FID for HC, a chemiluminescence instrument for NO_x, and NDIR for CO.

A portion of the engine exhaust was diluted using a constant volume sampling system. A sample of this diluted exhaust was collected on Pallflex brand, Teflon-coated, glass fiber filters, and the amount of particulate was determined by gravimetric analysis.

Experimental Procedure. This effort with coal-water slurry (CWS) was directed toward:

- Running the EMD engine using CWS
- Attaining reasonable combustion
- Evaluating combustion characteristics
- Measuring exhaust emissions

The engine operating procedure involved (1) warming up the engine using DF-2 diesel fuel, (2) setting a diesel fuel pilot flow rate that had been found to provide good combustion of the coal-water slurry, (3) setting a predetermined horsepower output, based on the maximum power attainable using CWS, and balancing the exhaust temperatures in the experimental and standard cylinders, (4) flushing the main fuel injector in the experimental cylinder with water and then switching to CWS, and (5) increasing the CWS flow rate to the maximum attainable using the injector described previously. Next, a limited effort was made toward determining the optimum pilot timing and obtaining the minimum pilot fuel flow rate, while maintaining a reasonable combustion efficiency. Engine operating (low-speed data) and engine combustion data (high-speed data) were then taken, and gaseous and particulate exhaust emissions were measured.

Results and Discussion

This section provides a description of the effort involved in achieving engine operation on coal-water slurry (CWS) and the results of the evaluations conducted.

Operating and Performance Observations. The injection characteristics of the EMD 645 unit injector using CWS were initially evaluated using a special EMD injector test rig. This injector test rig uses an electric motor to drive a standard EMD injection cam. The results of the evaluation of the EMD unit injector with coal slurry are summarized as follows:

Diametric clearance, mm

Pump	Nozzle	Result with slurry
Standard	+0.013	Pump plunger seized
+0.013	+0.013	Nozzle needle seized open
+0.013	+0.038	Extended injection

With the diametric clearances increased by 0.013 mm (0.0005 in.) in the injection pump and 0.038 mm (0.00015 in.) in the injector nozzle, an extended period of injection with the CWS was attained. Also, as modified, this system still provided good injection with diesel fuel, whereas previous increases in diametric clearances with a smaller capacity injector resulted in an inability to inject diesel fuel due to the increased leakage.

It was determined that the minimum supply pressure to provide an adequate supply of diesel fuel to the injector was about 60 kPa (10 psig). Equivalent flow rate of the CWS required several times higher pressure drop. It was assumed that a pressure of about 400 kPa (60 psig) should be provided with the CWS to overcome the pressure drop in the system. In addition, because the water in the CWS is considerably more volatile than diesel fuel, a higher pressure was required in the fuel supply system. This was necessary to prevent vaporization from occurring during the filling stroke of the injector plunger.

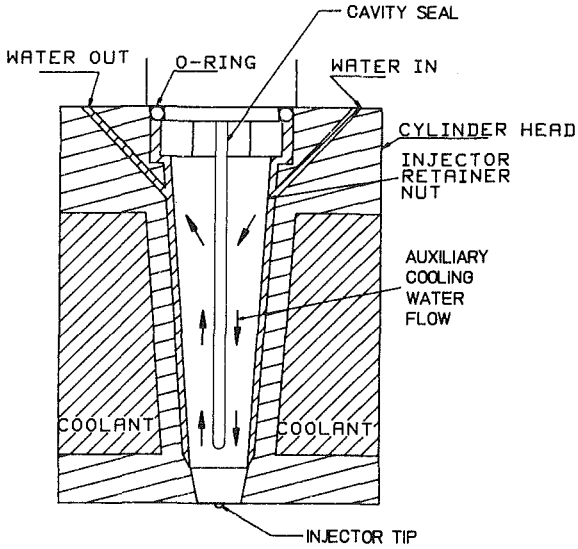


Fig. 4 System for cooling the main fuel injector

In previous work, gear pumps had been used with some degree of success in CWS systems. With the increased pressures specified for this effort, however, the gear pumps were found to be generally unsuccessful. It was determined that a progressive cavity pump could be used successfully for the CWS. A minimum pressure within the injector of about 415 kPa (60 psig) was selected. This pressure was controlled using a hand-operated needle valve in the return line. The resulting supply pressure was about 830 kPa (120 psig) at a flow rate of 2.3 liter/min (0.6 gal/min).

Initially, the assumption was that additional injector cooling would be provided by higher bypass flow through the injector. After reviewing the design of the EMD unit injector, however, it was concluded that higher bypass flow rate had an essentially negligible cooling effect in the areas of concern. The total flow rate to the injector subsequently selected for the experimental cylinder was 2.3 liter/min at the 830 kPa (120 psig) supply pressure.

Cooling the injector was determined to be essential, based on the previous effort with a smaller engine and the initial attempts at running the engine in this effort. Attempts to operate on CWS prior to providing additional cooling resulted in essentially immediate seizure of the injector plunger or needle valve. Cooling was accomplished in the EMD engine by sealing the upper and lower ends and providing a flow directing seal in the cavity between the cylinder head and the injector, as shown in Fig. 4. Holes were then drilled into the cylinder head to provide a flow of cooling water through the cavity. Water at room temperature entered the cavity through the "water in" port, flowed toward the "injector tip," around the "cavity seal" near the injector tip, and exited through the "water out" port. Flow rate of the cooling water was about 3.8 liter/min (1 gal/min), and the outlet temperature of the water at engine operating conditions was about 43°C (110°F).

Plastic containers of 19 liter (5 gal) capacity were used as the supply tank for the CWS. In filling the day tank, the CWS from the special 500-gal storage tank was strained through a 200-mesh sleeve to remove any large particles from the slurry. Only limited optimization of some parameters was conducted, primarily with the pilot injection. Further advance in pilot injection timing, from that selected for these evaluations, did not provide a commensurate advance in the start of combustion. This is a major limiting factor in optimizing for operation on CWS. Obtaining the earlier start and the rate of combustion required to improve combustion efficiency with the CWS will apparently require higher compression temperature.

Downloaded 01 Jun 2010 to 171.66.16.87. Redistribution subject to ASME license or copyright; see http://www.asme.org/terms/Terms_Use.cfm

Table 4 Test cylinder fuel consumption and power output

Run No.	Main Fuel	Fuel Cons. kg/hr Main	Pilot	BP[a] hp	BTE[b] %
17-3	DF-2	11	4.5	72	29
17-5	CWS	36	4.5	69	25
22-1	DF-2	11	4.5	74	30
22-2	CWS	42	4.5	79	25

[a]Brake power output.
[b]Brake thermal efficiency.

Table 5 Comparison of DF-2 and CWS engine data

Main Fuel	DF-2	CWS
Test Number	16	17
Pilot Fuel	DF-2	DF-2
Pilot/Total Energy	28%	23%
Ind. Ther. Eff. (LHV)	35%	30%
Peak Pressure, psi	1130	900
Pilot Start of Inj., BTDC	36°	35°
Main Start of Inj., BTDC	21°	26°
Pilot Duration	18°	16°
Main Duration	16°	25°
Pilot Start of Comb.,BTDC	19°	18°
Main Start of Comb., BTDC	13°	9°
End of Comb., ATDC	23°	26°
Pilot Ign. Delay	17°	17°
Main Ign. Delay	8°	17°

In the experimental cylinder of the engine, the diesel fuel pilot injection flow rate was initially set at 4.5 kg/h (10 lb/hr), and the main injection was set at 11.3 kg/h (25 lb/hr). The switchover from diesel fuel to CWS was made at the 11.3 kg/h (25 lb/hr) flow rate. At that flow rate, the combustion of the coal slurry was not as good as expected. One probable explanation is that the spray characteristics were less than optimum for efficient combustion of the coal. At this flow rate, the injection pressure appeared to have been lower than that required for acceptable injection. Improvement in the combustion of the CWS was apparent with an increase in flow rate.

Following completion of the engine evaluations with CWS, the engine was dissassembled for visual inspection. An estimated 600 g of carbonaceous deposits were present in the engine airbox, 470 g of which were recovered. These deposits were determined to contain about 78 percent carbon and 5 percent ash. On a proximate basis with ash and water removed, the carbon content is about the same as that for the coal used in the slurry. The ash content, however, is about twice that of the coal. The cylinder head surface was generally clean of deposits, but the piston and liner did show signs of wear. There were some carbon buildup on the piston and some lines of abrasion on the cylinder liner.

Combustion Efficiency. Combustion efficiency was determined on a brake power output basis using measured power and fuel flow and on an indicated power basis using high-speed combustion data. Additional combustion parameters were also obtained from the high-speed data. Fuel consumption and power output data for two sets of evaluations are given in Table 4. Data given have been adjusted to represent only the CW3-fired cylinder. Brake thermal efficiency using the CWS as the main fuel was about 85 percent of that observed when using DF-2 as the main fuel.

Cylinder pressure traces, along with associated injection line pressure traces, are shown in Fig. 5. The cylinder pressure data

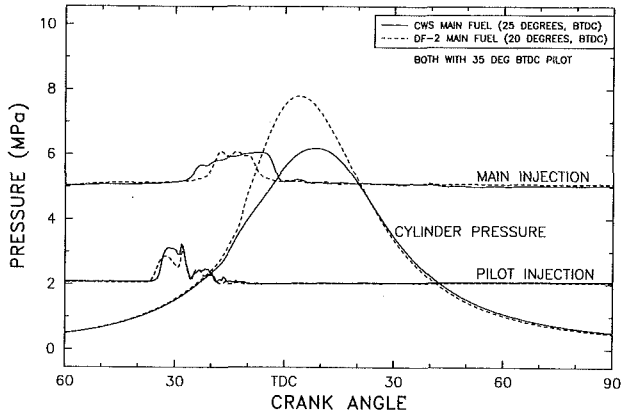


Fig. 5 Cylinder pressure and main and pilot injection timing with CWS and DF-2

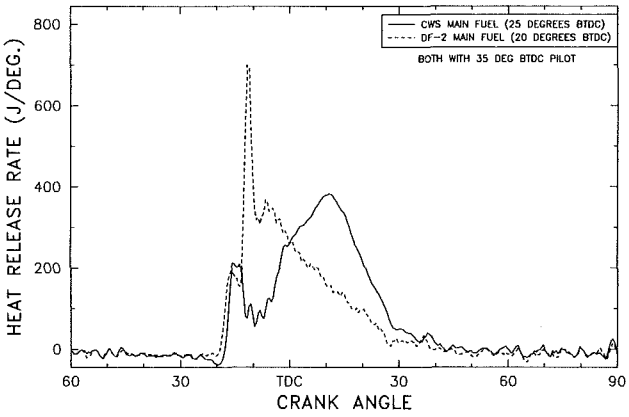


Fig. 6 Rate of heat release with CWS and DF-2

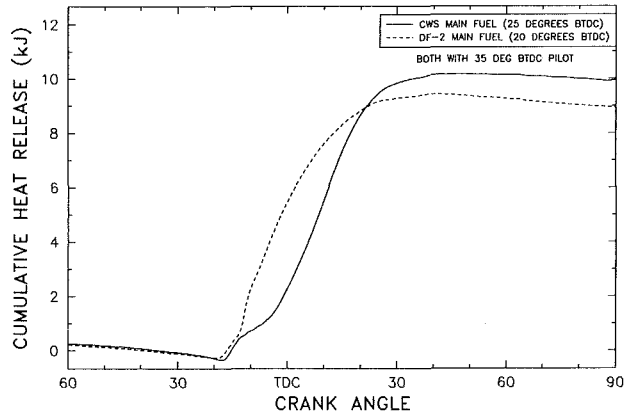


Fig. 7 Total heat release with CWS and DF-2

were used to calculate the rate of heat release, the cumulative heat release, and the indicated combustion efficiency using the methods developed by Callahan et al. [15]. The injection line pressure traces were used to determine start of injection and injection duration. Due to the much larger amounts of CWS injected, the duration was considerably longer with the CWS than with the diesel fuel. The shape of the main injection pressure curves is very interesting. With the CWS, the pressure gradually increased throughout the injection duration and did not reach the same peak attained with DF-2 until near the end of injection. This is indicative that atomization characteristics of the CWS injection might not have been optimum in the early stages of injection.

Heat release rate diagrams, using both the CWS and the

Downloaded 01 Jun 2010 to 171.66.16.87. Redistribution subject to ASME license or copyright; see http://www.asme.org/terms/Terms_Use.cfm

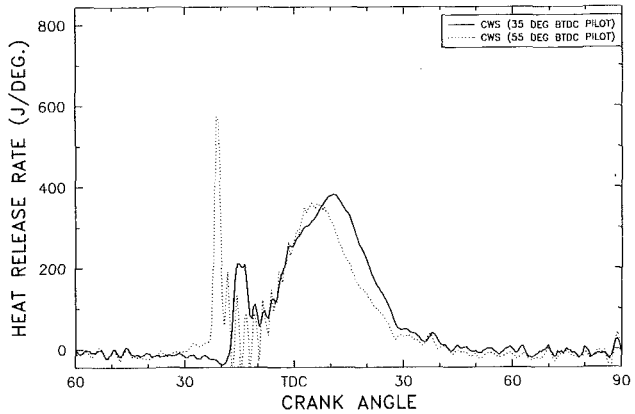


Fig. 8 Rate of heat release with CWS

baseline DF-2 as the main fuel, are presented in Fig. 6. Both experiments were run with the same quantity of pilot fuel injected at 35 deg BTDC. The most apparent result of the use of the CWS is the drastic reduction in the premixed combustion phase for the CWS as indicated by the reduced initial heat release rates. This is also demonstrated in Fig. 7, when the cumulative heat release rates are compared. In these figures, it is apparent that the initial combustion rate of the CWS is very slow. The bulk of the combustion event for the CWS occurs as a diffusion burning process, at least as indicated by the large hump in the heat release rate diagram shown in Fig. 6. This type of heat release rate diagram is typical of slow combustion and is always accompanied by a reduced thermal efficiency. The thermal efficiencies are affected by the fact that slow combustion is not the most effective conversion of thermal energy to mechanical work. The maximum energy conversion is obtained, in a theoretical sense, with a constant volume combustion. Deviations from this ideal theoretical process result in lower than theoretical efficiencies. These effects are sufficient to overcome the fact that the total heat release is higher for the CWS than for the DF-2, as shown in Fig. 7.

Advancing the pilot injection timing by 20 deg, from 35 deg BTDC to 55 deg BTDC, resulted in a 10 deg advance of pilot ignition when firing the CWS. Ignition and combustion of the slurry, however, was advanced by only about 5 deg. These trends are shown in Fig. 8, where the heat release rate diagrams for the 55 deg and 35 deg BTDC pilot timings are compared.

In addition to the advance in the ignition timing with 55 deg BTDC pilot injection, it is obvious that a considerable fraction, if not all, of the pilot charge is burning in a premixed combustion mode. Also, the pilot combustion appears to be completed prior to the ignition of the slurry, as indicated by the fact that the heat release rate goes to zero after combustion of the pilot and prior to ignition of the slurry. The heat release rates for the CWS are very similar for both pilot timings (35 deg and 55 deg BTDC), as can be seen by comparing the CWS heat release rates (apparent diffusion burning phases) for both timings. Also, with pilot injection at 35 deg BTDC, the injection of the CWS apparently had a quenching effect on the pilot combustion, as indicated by the greatly reduced peak rate of combustion of the pilot.

The operating data derived from high-speed data are summarized in Table 5. As with the brake thermal efficiency calculated using fuel consumption and power output data, the indicated thermal efficiency with the CWS as determined from the high-speed pressure data is also about 85 percent of indicated thermal efficiency observed when using DF-2.

The pilot fuel energy required to achieve relatively good combustion of the CWS in these evaluations was about 23 percent of the total energy provided to the cylinder. The percentage of pilot energy can be reduced by increased the amount of CWS injected (i.e., requires a high-capacity CWS injector) or by attaining the cylinder conditions necessary for ignition and effective combustion of the CWS in some manner other than by large amounts of pilot injection (e.g., heating the intake air and/or increasing the compression ratio).

Table 6 Summary of exhaust emissions

Main Fuel	DF-2	CWS	DF-2	CWS
Test No.	17-3	17-5	22-1	22&23
Measured Values for Total Exhaust[a]				
HC,ppm	140	200	190	240
CO,ppm	820	--	990	780
NO_x,ppm	950	680	790	630
Part., mg/SCF	1.6	13	2.9	30
Calculated Values for Test Cylinder				
HC,ppm	140	240	190	310
CO,ppm	820	--	990	860
NO_x,ppm	950	490	790	380
Part., mg/SCF	1.6	24	2.9	59

[a]One of the two engine cylinders operating in standard configuration on DF-2 diesel fuel.

Exhaust Emissions. Limited exhaust emissions measurements were taken at several of the engine operating conditions evaluated. The emissions results for matched sets of engine operation are summarized in Table 6. The calculated emissions values for CWS are adjusted to represent only the CWS-fired cylinder. Comparing the results for the CWS to DF-2, carbon monoxide (CO) was somewhat lower, oxides of nitrogen (NO_x) were about 50 percent lower, total hydrocarbons (HC) were about 50 percent higher, and total particulates were an order of magnitude higher. Visually, the exhaust plume was not significantly different.

Improvements in injection and combustion of the CWS are expected to result in some reduction of HC, major reduction of particulates, and some increase of NO_x. The limit on potential reduction of particulates, without special controls, is the ash content of the CWS fuel. In the evaluations conducted, ash from the CWS is estimated to account for about 1/10 of the total particulates measured.

Summary and Conclusions

An EMD-567B engine was operated on a coal-water slurry (CWS) fuel with relatively good combustion. Except for pilot injection of diesel fuel and some increases in diametric clearances in the fuel injector used for the CWS, the engine was in standard configuration. Thermal efficiency with the CWS was about 85 percent of that obtained with DF-2 fuel under comparable operating conditions. Oxides of nitrogen emissions in the exhaust with CWS were about half that with DF-2, but particulates were about an order of magnitude higher.

These initial results were achieved without optimizing the system for CWS. Review of the system and analyses of the injection and combustion data indicate several areas in which system and parameter optimization could provide major improvements. One area is injection; this includes atomization, orientation, start of injection, and duration of both the main and pilot injection. Another important consideration is the relatively long ignition delay and slow rate of combustion of the CWS. Improvement in this area generally requires higher thermal energy (i.e., temperature) in the combustion chamber

Downloaded 01 Jun 2010 to 171.66.16.87. Redistribution subject to ASME license or copyright; see http://www.asme.org/terms/Terms_Use.cfm

at the start of CWS injection. From data determined in combustion bomb experiments, it appears that precombustion air temperatures of about 1000 K (1340°F) are required to achieve maximum combustion efficiency with CWS in a medium-speed engine. One conventional way to increase the compression temperature is to heat the intake air; another is to increase the compression ratio. A less conventional method is to insulate the combustion chamber. Relative to rate of combustion, in-cylinder air motion can also be an important factor.

Although considerable development remains before a commercially acceptable coal slurry engine can be designed, these initial results demonstrate the potential for utilizing coal slurry fuel. Given adequate development of the slurry and engine, it appears that commercial application of coal–water slurry fuels can be achieved.

Acknowledgments

This work was supported by the U.S. Department of Energy, Morgantown Energy Technology Center, with Messrs. Larry K. Carpenter and Nelson F. Rekos serving as the Contracting Officer's Technical Representatives. Mr. Robert L. Koch, Allison Gas Turbine Division, General Motors Corporation, was the overall program manager.

References

1 Ryan, T. W., III, Callahan, T. J., Mecredy, H. E., III, Baker, Q. A., and Jett, B. T., "Coal Slurry Combustion—Bomb and Small Engine Tests Results," ASME Paper No. 87-ICE-31, 1987.

2 Koch, R. L., Curry, C. E., Mason, D. L., and Slezinger, J. O., III, "Commercialization Considerations for a Coal Fuel Diesel Locomotive," ASME Paper No. 86-ICE-5, 1986.

3 Hapeman, M. J., and Savkar, S. D., "Economic Assessment of Coal-Burning Diesel Locomotives," ASME Paper No. 86-ICE-14, 1986.

4 Wilson, R. P., Benedek, K. R., Ekchian, J. A., Cheng, W., and Rao, A. K., "Assessment of Merits of Coal Fueled Diesel Engines for Stationary Power Applications," presented at the ASME/ETCE Internal Combustion Engine Symposium, New Orleans, LA, Feb. 1986.

5 Ryan, T. W., III, Callahan, T. J., Dodge, L. G., and Moses, C. A., "Injection, Atomization and Combustion of Carbon Slurry Fuels," SAE Paper No. 821199, 1982.

6 Ryan, T. W., III, and Dodge, L. G., "Diesel Engine Injection and Combustion of Slurries of Coal, Charcoal, and Coke in Diesel Fuel," SAE Paper No. 840119, 1984.

7 Cheng, W. K., Lai, M. C., Zhou, B., Wong, V. W., and Benedek, K. R., "Parametric Studies of Coal–Water Slurry Combustion in a Rapid Compression Machine," ASME Paper No. 87-ICE-9, 1987.

8 Leonard, G. L., and Fiske, G. H., "Combustion Characteristics of Coal-Water Mixtures in a Simulated Medium-Speed Diesel Engine Environment," ASME Paper No. 86-ICE-15, 1986.

9 Leonard, G. L., and Fiske, G. H., "A Comparison of a Positive Displacement Fuel Injection System With an Accumulator-Based System for Coal-Fueled Diesel Engine Applications," ASME Paper No. 87-ICE-32, 1987.

10 Siebers, D. L., and Dyer, F. M., "The Autoignition and Combustion of Coal–Water Slurry Under Simulated Diesel Engine Condition," ASME Paper No. 85-KDGP-15, 1985.

11 Likos, W. E., and Ryan, T. W., III, "Combustion Characteristics of Coal Fuels in a High Temperature Diesel Engine," ASME Paper No. 87-ICE-56, 1987.

12 Mecredy, H. E., III, and Jett, B. T., "A Comparison of the Combustion Characteristics of Three Coal Slurry Fuels," presented at the Annual Heat Engines and Gas Stream Cleanup Systems Contractors Review Meeting, Morgantown, WV, Apr. 21–23, 1987.

13 Hsu, B. D., "Coal-Fueled Diesel Systems Research—Full-Scale, Single Cylinder Engine Tests," presented at the Annual Heat Engines and Gas Stream Cleanup Systems Contractors Review Meeting, Morgantown, WV, Apr. 21–23, 1987.

14 Nydick, S. E., "Development of a Coal/Water-Slurry Fueled Engine for Industrial Cogeneration," Topical Report, Task 4.0, Single-Cylinder Engine Test, Apr. 1986.

15 Callahan, T. J., Yost, D. M., and Ryan, T. W., III, "Acquisition and Interpretation of Diesel Engine Heat Release Data," SAE Paper No. 852068, 1985.

Downloaded 01 Jun 2010 to 171.66.16.87. Redistribution subject to ASME license or copyright; see http://www.asme.org/terms/Terms_Use.cfm

Experiments With Coal Fuels in a High-Temperature Diesel Engine

W. E. Likos

T. W. Ryan, III

Southwest Research Institute,
San Antonio, TX 78284

The combustion of 50 wt percent coal slurries, using water, diesel fuel, and methanol as carrier liquids, was investigated in a single-cylinder research engine. High temperatures were achieved in the engine cylinder using low-heat-rejection engine technology, electrically heated glow plugs, and heated inlet air. Comparisons of the fuels and different methods of providing high cylinder temperature were made using cylinder pressure data and heat release calculations. Autoignition of the coal/water slurries was attained using auxiliary heat input. The burning rates of all the autoignited slurries were significantly enhanced by using a pilot injection of diesel fuel. Under some operating conditions the engine thermal efficiency was equal to diesel fuel performance. It was apparent that engines designed for coal slurry should maximize the prechamber volume.

Introduction

Coal, as an energy-containing raw material, represents the largest reserve of fossil energy available within the United States. In its raw form, however, coal is generally not compatible with existing energy utilization devices. This fact should not be a surprise, however, because few raw materials are usable in the unprocessed form, including crude oil. In the case of coal, the incompatibilities are related mainly to the fact that it is solid and that it contains contaminants that are incompatible with most systems.

The direct use of coal in heat engines has been limited mainly to external combustion, e.g., Rankine cycle devices. Direct utilization of coal in internal combustion engines dates back to the initial development of the diesel engine. These efforts, as well as the efforts of German engineers during WW II, were largely unsuccessful and not well documented. Based on the most recent summary of this early work [1], it appears that large-bore diesel engines were run on coal, but the problems of fuel introduction, combustion efficiency, and engine wear remained unsolved at the time the work was halted.

The more recent diesel engine work in the United States was started in 1975 [2] and continued as low level efforts at a number of laboratories [3–7] through the end of the decade. Since 1980 several major activities were initiated by the Office of Fossil Energy (OFE) and the Office of Conservation and Renewable Energy (OCRE) of the US Department of Energy. This work appeared to develop from the ongoing DOE activities in the development of coal/oil and later coal/water slurries for utility boiler applications. The slurry approach is attractive because it potentially eliminates the problems associated with the handling of dry coal powder. The initial results of both of these overall programs have played a major role in the development of this program. The engine work [8] supported by the OCRE demonstrated that coal/water slurries could be used in large-bore, slow-speed diesel engines. The initial engine work [4, 9] sponsored by OFE, in addition to pointing out the difficult problems associated with fuel injection, also demonstrated that the coal slurries could be used in smaller bore engines if adequate injection atomization and a diesel fuel pilot were used. The results of both programs indicated that temperatures higher than typical compression temperatures were required for the ignition of the coal/water slurries. Experimentally, and in practice, these temperatures have been attained through the use of a pilot injection of diesel fuel.

Injection of the slurries has been the subject of several studies [6, 7, 11]. The prevailing wisdom for liquid fuels indicates that the atomization characteristics can be improved in pressure-type injectors by increasing the injection pressure. As a result of this general concept, researchers at General Electric Research Laboratories and at the Massachusetts Institute of Technology have successfully developed an extremely high injection pressure system for coal slurry combustion bomb experiments. However, in one case [10], there was no experimental evidence to indicate that the increased pressure actually resulted in improved atomization. In the other case [11], the experimental evidence, in the form of high-speed movies, tended to indicate that the drop size was actually increased and that the spray tip velocity also increased to the point of significant fuel impingement on the combustion chamber walls. This behavior may be the result of the non-Newtonian nature of the slurries. Higher injection pressures may actually result in poorer atomization since slurries will shear thicken at the extreme shear rates produced during injection. The increased viscosity, in turn, could actually degrade the atomization. Extremely high injection pressures introduce an added complication in that the life expectancy of the injection system is greatly reduced because of the higher material stresses, the higher leakage pressures, and the higher erosion forces. The problems associated with high injection pressures are severe

Contributed by the Internal Combustion Engine Division and presented at the Eleventh Annual Energy-Sources Technology Conference and Exhibition, New Orleans, Louisiana, January 10–13, 1988. Manuscript received by the Internal Combustion Engine Division November 1987. Paper No. 88-ICE-29.

Copyright © 1988 by ASME
Downloaded 01 Jun 2010 to 171.66.16.87. Redistribution subject to ASME license or copyright; see http://www.asme.org/terms/Terms_Use.cfm

enough (even when using specification quality diesel fuel), that the injection system manufacturers generally avoid line pressures in excess of 95 to 100 MPa.

Based on the above discussion, it appears that the ideal design for a coal-burning diesel engine would incorporate features that would result in high air and wall temperatures (approaching 1100 K according to Siebers and Dyer [13]) and that could accommodate as low an injection pressure as possible. A swirl-type indirect-injection engine incorporates design features that can accommodate the above requirements. The high air velocities induced by the intake geometry reduce the atomization requirements placed on the injection system, thus allowing for lower injection pressures and simpler nozzle designs. The indirect-injection configuration also makes it easier to incorporate low-heat-rejection technology because the combustion is initiated in a chamber that can be insulated from the rest of the engine and is isolated from the lubricated piston/cylinder wall interface.

The primary question posed at the start of this work was involved with determining the actual effects of increased operating temperatures on combustion of coal in an actual diesel engine. Addressing this question actually involved several specific problems including:

- development of an engine that would incorporate the desirable features discussed above;
- development of an injection system that would successfully meter and inject the coal fuels;
- development of an engine design that would accommodate both cooled iron and uncooled low-heat-rejection (LHR) components; and
- development of coal slurries that represented state-of-the-art technology in terms of the flow properties, the particle size distribution, and contaminant concentrations.

Objectives

The primary objective of the work was to determine whether the higher temperature environment of an LHR diesel engine offered any new potential for utilization of coal in piston engines. To meet the objective, the project had two specific goals:

1 to determine the ignition and combustion characteristics of three state-of-the-art coal slurries in a LHR diesel engine and compare with those of a baseline diesel fuel;

2 to determine the effects of the LHR engine by comparing the ignition and combustion characteristics of the slurries in the LHR engine to those observed in a similar, but conventional, diesel engine.

Experimental Apparatus

The majority of the engine experimentation involved the use of the uncoated steel head. This engine consisted of a specially designed cylinder head, mounted to a single-cylinder research engine. The engine, manufactured by Laboratory Equipment Co., was originally designed for the evaluation of lubricants, and as such, the cast iron cylinder head was not suitable for high-temperature operation. The specially designed cylinder head, being constructed of steel and devoid of any complex structure, was capable of operation at high temperature without cracking due to thermal expansion.

The cylinder head design, as shown in Fig. 1, utilized a precombustion chamber. It was felt that the precombustion chamber would be easy to insulate and would serve to isolate unburned coal particles from the main chamber, thus reducing abrasive wear of the piston and cylinder.

Table 1 outlines the basic specifications of the engine as it was configured for the initial runs to check out the various instrumentation, as well as the engine itself. The combustion system was considered to be a modified Ricardo swirl chamber design. It differed from a Ricardo system described by Obert [12] in that the precombustion chamber was cylindrical, not spherical; its volume was 67.4 percent of the clearance volume rather than 50 percent; the discharge throat area was 1.6 percent of the piston area or roughly twice the typical area; and the shape of the piston top was slightly concave rather than a double swirl lobe.

The deviations from the standard Ricardo design were made with the intentions of increasing the fraction of burning in the precombustion chamber and providing a larger opening into the main chamber that would be less susceptible to coking. The side plugs of the precombustion chamber were threaded into the prechamber body. The removable side plugs were each fitted with a 200-W electrical heater. Figure 2 shows how each glow plug protruded into the prechamber. They were located such that the spray from both the pilot and the main injector impinged on them.

The fuel injection equipment consisted of an American Bosch single-plunger pump for the pilot fuel and a Mico (manufactured under license from Bosch) single-plunger pump for the main fuel (slurry). The pumps were driven, in series, from a half-speed shaft located on the front of the engine. Injection timing was varied by using the phaser provided on the American Bosch Pump and a specially constructed mount for the Mico pump. The Mico pump was selected for this work due to its simple design, lending ease of disassembly and cleaning.

Following the evaluation of the coal fuels in the uninsulated

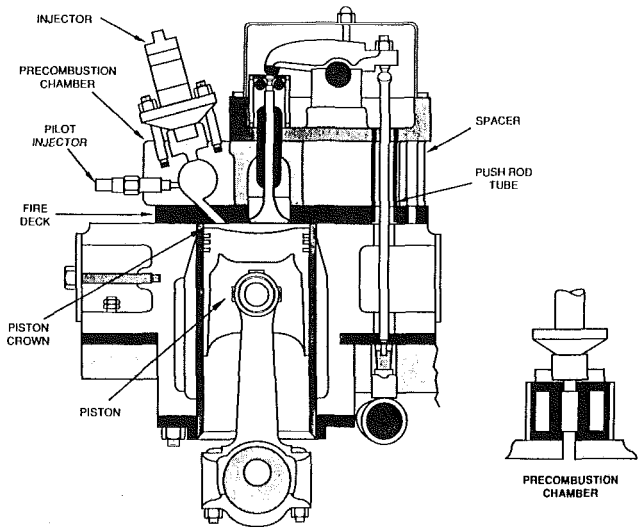


Fig. 1 Basic engine design

Table 1 Initial engine specifications

Type: Modified Ricardo Swirl Chamber
Bore, cm: 9.652
Stroke, cm: 9.525
Compression ratio: 18:1
Intake valve opening, deg BTDC: 12
Intake valve closing, deg BTDC: 136
Exhaust valve opening, deg ATDC: 136
Exhaust valve closing, deg ATDC: 12
Percentage of swirl chamber volume to clearance volume: 67.4 percent
Percentage of swirl chamber throat area to piston area: 1.6 percent
Main injection pump: Bosch (Mico) 8 mm, Part number 3418303005800
Main injector: Bosch DN125012
Pilot injector: Bosch DN125012
Pilot injection pump: Bosch single-plunger 8 mm, Part number 3418303003780921

Downloaded 01 Jun 2010 to 171.66.16.87. Redistribution subject to ASME license or copyright; see http://www.asme.org/terms/Terms_Use.cfm

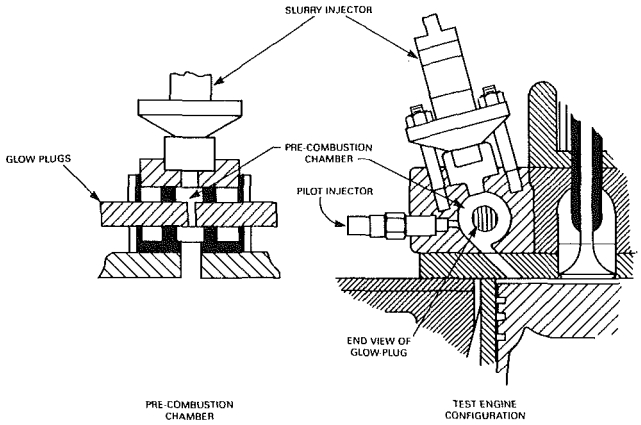


Fig. 2 Glow plug installation in prechamber

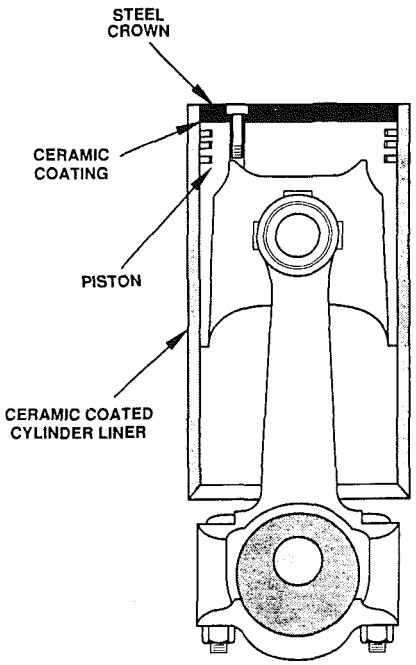


Fig. 3 Ceramic insulated components

engine, the piston and cylinder liner of the basic engine were replaced with ceramic-coated parts, converting the engine to the insulated configuration. A 0.51-cm-thick ceramic coating was applied to a steel piston crown, which was threaded onto the piston as shown in Fig. 3. The ceramic coating was applied by Kaman Sciences, located in Boulder, CO. The thermal barrier was applied to the underside of the steel crown. Having the coating between the crown and piston top served to insulate the piston and protected the coating from the combustion chamber. The thermal conductivity was reported by the manufacturer to be 0.025 W/cm-K.

The cylinder liner was coated with 0.1524 cm of the ceramic material on the outside. There were several advantages to placing the ceramic coating on the outside of the liner. First, the coating provided the same insulating capabilities as if it were on the inside and the problem of obtaining a smooth, low-friction finish on the very hard surface was avoided. Second, the piston/cylinder liner fit remained the same as the standard, avoiding the need to remachine the piston.

High inlet air temperatures were attained using electrically heated inlet air. Volumetric efficiency was held constant by adjusting the inlet pressure to compensate for the density variations.

Table 2 Coal properties

Property	Method	Amount
Proximate Analysis, wt%		
Ash	ASTM D 3174	1.00
Fixed Carbon	ASTM D 3172	61.60
Moisture	ASTM D 3173	0.36
Volatiles	ASTM D 3175	37.04
Ultimate Analysis, wt%		
C	ASTM D 3178	84.26
H	ASTM D 3178	5.44
N	Chemiluminescence	3.75
S	X-Ray Fluorescence	0.6
O	ASTM D 3286	4.95
Ash	ASTM D 3174	1.00
Heating Value, (MJ/kg)		
Gross Heating Value		35.12
Net Heating Value		33.92

Table 3 Coal particle size measurements

Coal Sample	As Received	Ground Once
Log-mean length, microns	7.2	5.1
Top particle size, microns	12.1	8.9
Standard deviation	1.41	1.45
Number of particles measured	1524	1235

Fuel Formulation

The slurries were formulated using coal from Pond Creek Seam, Pike County, KY, which was processed by United Coal Company, Bristol, VA. The coal properties are listed in Table 2.

The coal as received had a log-mean diameter of 7.2 μm. Following one pass through a Sturtevant micronizer mill, the log-mean particle diameter was reduced to 5.1 μm. The particle sizes of the coal powders were measured using a photometric technique.

Samples were dispersed and photographed using a scanning electron microscope. The length and width of each particle in the photographs were measured using a computer-based imaging system. The particle size data are given in Table 3.

The results of the particle measurements indicate the ultrafine character of the coal powder thus obtained. The log-mean length is volume based so that half of the volume of the coal had a size less than the stated value. The top particle size was taken to be the 95 percent cut point, i.e., the stated value. The largest particles were less than 16 μm in size for the as-received coal and 12.7 μm in the ground material.

The slurry fuel formulations were developed experimentally with the goal of obtaining a storage stability of 48 h with a viscosity low enough to allow the use of modified jerk-pump equipment. The formulations that attained these goals are listed in Table 4.

Two methanol slurry formulations are shown. Preliminary engine testing revealed that methanol evaporation was very rapid. The severity of this problem was reduced by using the coal/methanol-water slurry. This formulation was chosen with the intent that the methanol would serve as an antifreeze for the coal/water slurry. Protection from freezing is provided down to $-23°C$. Engine testing was done primarily on the coal/methanol-water slurry after the difficulties of using coal/methanol were encountered. All the engine results presented in this paper are for the coal/methanol-water slurry.

Some experimentation was also done with a coal/methanol slurry with 5 percent castor oil added. The addition of the oil did not reduce the frequency of injector needle seizures as was hoped. No engine data were recorded during these runs.

Downloaded 01 Jun 2010 to 171.66.16.87. Redistribution subject to ASME license or copyright; see http://www.asme.org/terms/Terms_Use.cfm

Table 4 Slurry formulations

Coal/Water(C/W)	
Coal	50.0%
Water	48.4%
SF2068 surfactant	1.25%
Formaldehyde	0.3%
Xanthan stabilizer	0.05%
Coal/Methanol	
Coal	50.0%
Methanol	50.0%
Coal/Methanol-Water (C/M)	
Coal	50.0%
Methanol	15.0%
Water	35.0%
Coal/Diesel (C/DF 2)	
Coal	50.0%
Phillips DF-2 reference fuel	49.0%
Span 80 surfactant	1.0%

Table 5 Fuel heating values (MJ/kg)

Phillips D-2 reference diesel fuel	42.8
Coal/water slurry	16.3
Coal/diesel slurry	38.5
Coal/water/methanol slurry	20.8

The heating values calculated using the net heating value of the coal and the other constituents are listed in Table 5.

Test Matrix

The test matrix consisted of operating the engine at two speeds, 900 rpm and 1500 rpm, at the maximum power that could be attained, and approximately 75 and 50 percent power levels using each slurry fuel. The inlet air was heated to 38°C (100°F) and 204°C (400°F) to study temperature effects on ignition.

Table 6 outlines the engine condition or configuration versus the different fuels tested. The speed and loads described above were attempted at each of the conditions indicated. The most extensive testing was done with the coal/water slurry. In the case of the coal/water slurry, additional heat was provided to the prechamber by using the electrical glow plugs.

The use of a pilot injection system presented a problem in determining the best injection timing for both the pilot injection and the slurry injection. Also, determining the minimum amount of pilot fuel proved to be a tedious task. After some experimentation, the procedure that was followed involved iterating the pilot-fuel injection timing and flow rate at a fixed slurry injection timing.

The slurry was injected at one of three different timing settings, 50, 120, or 180 deg BTDC, and the pilot fuel injection timing was varied until maximum torque was developed. Following the pilot timing adjustment, the operator would increase the slurry flow rate until the combustion became erratic. The pilot timing and flow rate would then again be checked to ensure that peak torque was being maintained. Following this, the slurry injection setting was reset to a new value, i.e., 120 deg BTDC, and the process repeated. After the three slurry timings were run, the engine was returned to the timing that gave the highest torque. In this manner, the injection timing, maximum slurry flow rate, and minimum pilot fuel flow rates that resulted in the best power were obtained.

In those cases in which autoignition of the slurry occurred, the slurry injection timing and flow rate were adjusted to produce maximum torque at the given engine speed.

Table 6 Fuel/engine test matrix

Configuration	Fuel DF2	C/W	C/DF2	C/M
38°C inlet air	X	X	X	X
204°C inlet air	--	X	X	--
38°C inlet air + GP*	--	X	--	--
204°C inlet air + GP	--	X	--	--
38°C inlet & insulated	X	X	X	X
204°C inlet & insulated	--	X	X	--

* Glow Plug

Results

Three energy-related parameters are frequently used while discussing the performance of different fuels. These parameters are: indicated thermal efficiency (ITE), the normalized cumulative heat release (NCHR), and the pilot energy ratio (PER). The indicated thermal efficiency is based upon the power output of the engine as determined from the engine cylinder pressure during the combustion cycle. Thus, the variation of the engine friction does not affect the indicated power. The thermal efficiency is determined by dividing the indicated work output by the rate of energy input into the engine by the fuel.

The NCHR is determined by first integrating the instantaneous heat release, as calculated from cylinder pressure versus crank-angle data, over the portion of the engine cycle in which both valves are closed. The resultant total cumulative energy curve is normalized by the fuel energy that had been injected for that engine cycle. Normal diesel fuel combustion can be considered to be nearly complete, typically 97 percent or greater. The resultant NCHR for diesel fuel may range from 0.45 to 0.60, depending on engine operating conditions. The degree of combustion of the slurry fuels can then be determined by comparison of the slurry NCHR value to that of the base fuel.

The pilot energy ratio (PER) is the fraction of the total energy that was injected into the engine by the diesel fuel pilot injector. The energy inputs were determined using the net heating values of the diesel fuel and the coal/water slurry and their respective flow rates. A value of 1 would indicate that all the energy input to the engine was from the pilot fuel and that no slurry was injected. A value of 0 indicates that pilot fuel injection was not required for ignition of the slurry and that autoignition occurred. Values between the two extremes represent a combination of pilot and slurry energy input. The pilot energy ratio is based solely on the fuel flow rates and fuel heating values and does not provide any indication of how the individual fuels actually burned and contributed to the work output of the engine.

The maximum power output of the engine was considered to be one of the primary dependent variables. The fuel flows and injection timings were varied to obtain the most power possible, following the procedure given earlier. The resultant indicated powers for the different slurries in the standard and ceramic engine are given in Fig. 4 for 38°C inlet air. Data for the coal/methanol-water slurry were not obtained for the standard engine at 900 rpm and for the ceramic engine at 1500 rpm due to frequent jamming of the injector. In general, the power output of the engine was low in comparison to the standard engine. The preliminary engine experiments were aimed at engine and injection system optimization for coal slurry operation and therefore, performance on diesel fuel was not optimum.

Downloaded 01 Jun 2010 to 171.66.16.87. Redistribution subject to ASME license or copyright; see http://www.asme.org/terms/Terms_Use.cfm

The 38°C inlet air temperature represents an expected standard inlet condition. Under these conditions, the performance on diesel fuel was not affected by changing to the ceramic components at either engine speed. For the coal/water slurry, the power dropped at 900 rpm in going to the ceramic components. A similar effect was not observed at 1500 rpm. These trends were reversed for the coal/diesel fuel slurry. The coal/methanol–water slurry produced the same power at both speeds, indicating that the energy conversion to mechanical work was less efficient at the higher speed.

The efficiency and combustion data for the uninsulated engine at 900 rpm are given in Fig. 5. These runs represent the test condition at which the best thermal efficiency was obtained for each fuel in the standard engine using 38°C inlet air. Autoignition occurred in the case of the coal/diesel slurry, as indicated by the zero value of PER. No data were obtained for the coal/methanol slurry due to frequent jamming of the injector.

The thermal efficiency results for the test fuels were found to be essentially equal to the base diesel fuel. The absolute values are low due to the generally low power output of the engine. The NCHR value for the coal/water slurry is less than the base fuel, indicating that the combustion was not as complete as the base diesel fuel. However, the coal/water slurry that did burn was more effective in producing power, counteracting the effect of the lower combustion efficiency. The "counteracting effect" is believed to be due to the water in the slurry serving as an internal coolant. The lower cylinder temperature, due to water evaporation, prolonged the ignition delay period of the pilot diesel fuel. The resultant combustion was faster, approaching the thermodynamic ideal of constant volume combustion. This trend is verified by examining the instantaneous heat release and the cumulative heat release diagrams given in Figs. 6, 7, and 8. These are for the same runs presented in Fig. 5. Both the diesel fuel, Fig. 6, and the coal/water slurry, Fig. 7, show a high initial peak heat release rate. The coal/water slurry indicated a slightly higher burning rate during the premixed portion, as indicated by the height of the initial spike of the rate curve. This higher burning rate occurred even though the coal/water slurry had a slightly advanced ignition timing. A significantly greater portion of the coal/water slurry burned during the premixed portion as compared to the diesel fuel. Also note in comparing the NCHR curves that the coal/water slurry (Fig. 7) stopped burning, as indicated by the plateauing of the curve, near 220 deg. The slight downward trend of the cumulative heat release after reaching the plateau is believed to be due to heat transfer out of the cylinder gases. The base diesel fuel, on the other hand, continued burning up to 270 deg. The coal/diesel slurry, like the diesel fuel alone, continued burning to 270 deg. The trend of the coal/water slurry to stop burning during the diffusion phase of combustion was apparent throughout the data. It suggests that, in order to maximize the coal/water combustion, the majority of the combustion should take place in the hot swirl chamber. Apparently, the partially combusted and burning gases discharge into the main chamber of the engine and quench as the piston descends and the gases cool. In the engine used in this project, approximately 67 percent of the available air charge resides in the swirl-chamber. It appears that the prechamber volume should be increased to as much as 90 percent or more in order to take advantage of the high temperatures and available air in the prechamber.

Comparison of the coal/diesel slurry, Fig. 8, to the base diesel fuel heat release diagrams, Fig. 6, shows that the autoignited slurry had a greatly reduced ignition delay time (advanced ignition timing) relative to the baseline run,

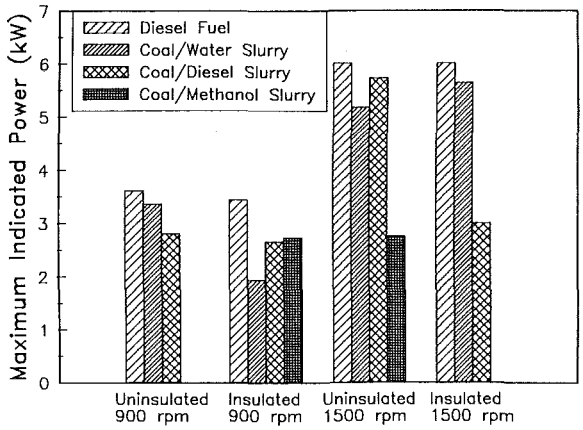


Fig. 4 Maximum indicated power for the different engine configurations

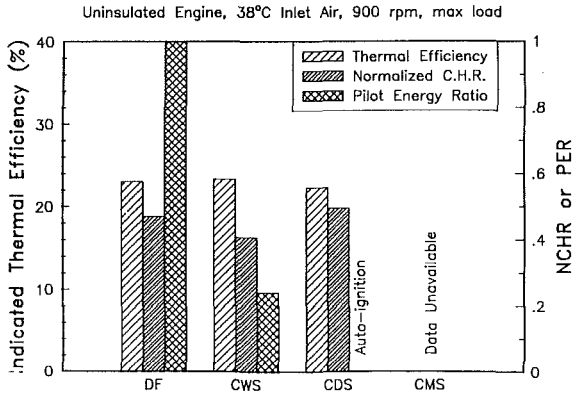


Fig. 5 Indicated thermal efficiency for different fuels at 900 rpm

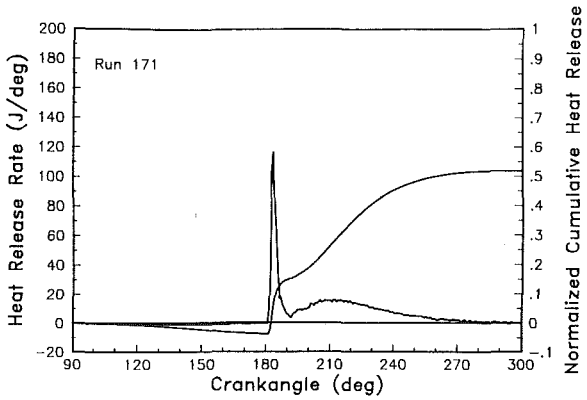


Fig. 6 Heat release diagram for base diesel fuel

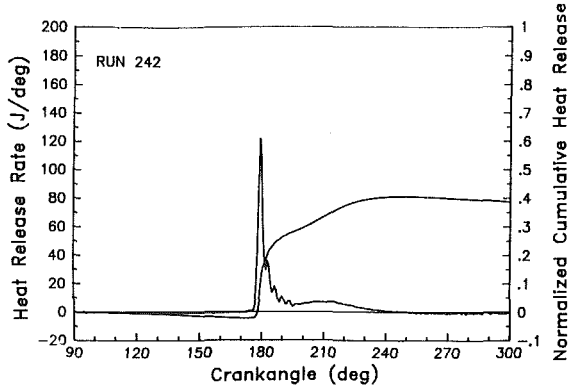


Fig. 7 Heat release diagram for coal/water slurry

Downloaded 01 Jun 2010 to 171.66.16.87. Redistribution subject to ASME license or copyright; see http://www.asme.org/terms/Terms_Use.cfm

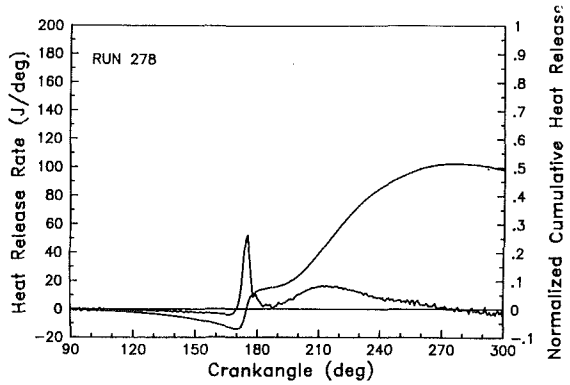


Fig. 8 Heat release diagram for coal/diesel slurry

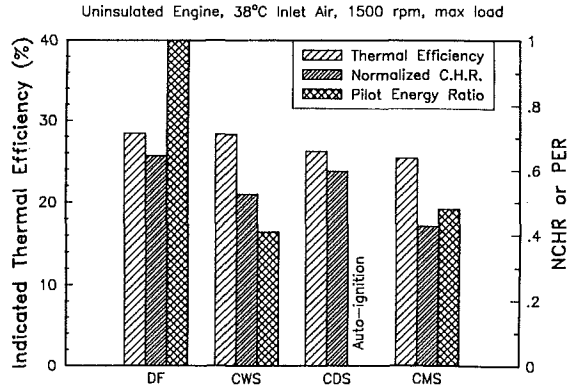


Fig. 9 Indicated thermal efficiency of the test fuels in the uninsulated engine at 1500 rpm

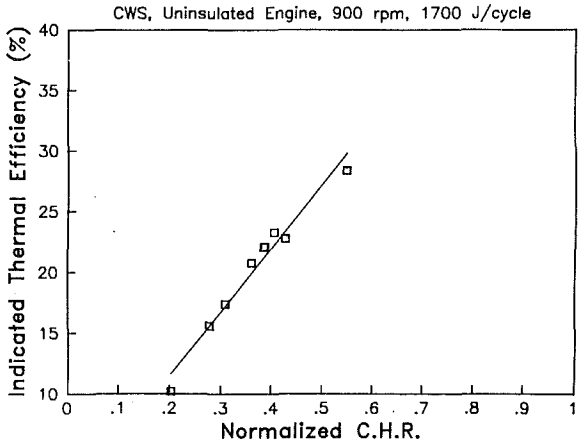


Fig. 10 Indicated thermal efficiency versus the normalized cumulative heat release for selected runs at 900 rpm on the coal/water slurry

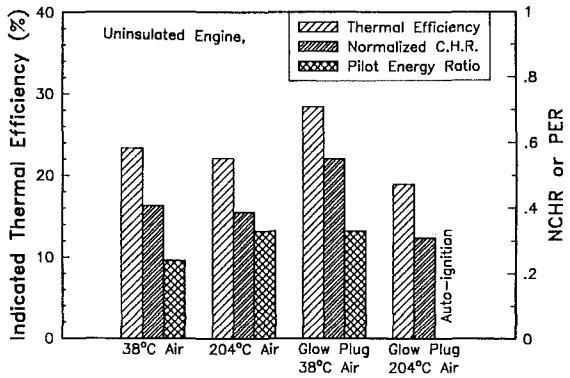


Fig. 11 Indicated thermal efficiency for different engine configurations using coal/water slurry at 900 rpm

resulting in reduced burning rates during the premixed phase of combustion. A significant quantity of slurry did burn during the diffusion flame period but this occurred late in the cycle with a lower conversion of heat to work.

The engine speed appears to have little effect on the performance of the fuels relative to each other. The small effect can be seen in the thermal efficiencies of the different configurations at 1500 rpm, shown in Fig. 9. The thermal efficiencies are higher than at 900 rpm, as are the values of NCHR. Notable differences between 900 and 1500 rpm are that the PER of the coal/water slurry was higher and that data were obtainable for the coal/methanol slurry.

The higher speed results in a higher power output (due to the speed increase) and thus higher thermal efficiencies, assuming that the combustion efficiencies are at least comparable at the two speeds. At the higher speed, the combustion efficiencies are in fact improved over those at the lower speed, as indicated by the higher NCHR values at 1500 rpm. This trend could be due to better fuel/air mixing at the higher speed.

As at the 900-rpm test condition, the coal/diesel fuel slurry autoignited, with an accompanying low heat release rate. The coal/water–methanol slurry has a lower latent heat of vaporization and thus less of an effect on the pilot ignition delay than the water slurry. This resulted in a smaller premixed fraction for the coal/methanol–water slurry and a lower maximum heat release rate than the water slurry.

The variations in indicated thermal efficiency of the engine were found to be related to the NCHR. For example, Fig. 10 is a plot of ITE versus NCHR for coal/water slurry data for runs in which approximately the same amount of energy (1700 joules/stroke) was injected. These data were obtained for all different engine configurations and air temperatures. The best thermal efficiency, 28 percent, was attained at a NCHR of 0.55, using the glow plugs and 38°C inlet air.

Figure 11 is a bar chart showing the thermal efficiency, NCHR, and PER data for the coal/water slurry while using glow plugs and higher air temperatures at 900 rpm. It is apparent that higher inlet air temperature did not improve the performance of the slurry. Slightly greater diesel pilot fuel was required, possibly due to poor combustion of the diesel pilot resulting from a decrease in the ignition delay time and the subsequent decline in the premixed burn fraction. It should be noted that the reported effects cannot be attributed to volumetric efficiency effects because the air mass flowrate was held constant.

The glow plug, however, was effective in improving the performance. Using 38°C inlet air a thermal efficiency of 28 percent was achieved as the NCHR approached 0.6. However, the performance at the 204°C inlet air condition was poor. Autoignition occurred at these conditions. A low NCHR of 0.3 and thermal efficiency of 18 percent resulted from the fact that the ignition process was not enhanced by ignition and combustion of a pilot fuel charge. The lack of the pilot also resulted in lower than desired rates of combustion. The significant finding was that the engine could be operated on coal/water slurry with no pilot.

Figures 12–15 are the instantaneous and cumulative heat release versus the engine crank-angle diagrams for the coal/water slurry cases. Figure 12, which shows the 38°C inlet air condition with no glow plug, shows the highest peak heat release rate, with little burning during the diffusion flame period. Maximum premixed burning was expected since this

Downloaded 01 Jun 2010 to 171.66.16.87. Redistribution subject to ASME license or copyright; see http://www.asme.org/terms/Terms_Use.cfm

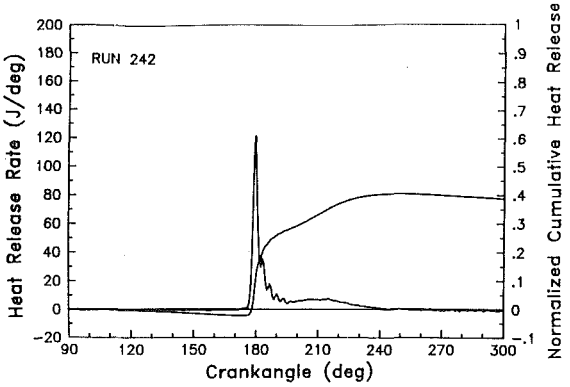


Fig. 12 Heat release diagram for the uninsulated engine using coal/water slurry at 900 rpm and 38°C inlet air

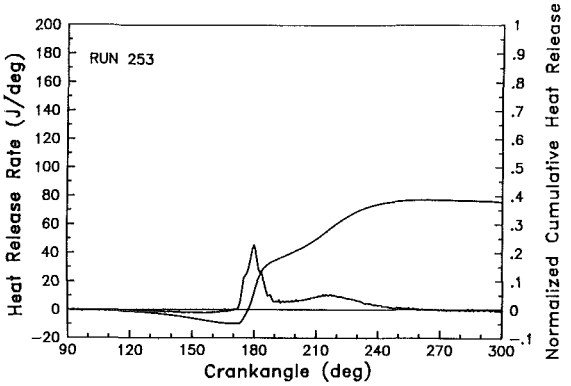


Fig. 13 Heat release diagram for the uninsulated engine using coal/water slurry at 900 rpm and 204°C inlet air

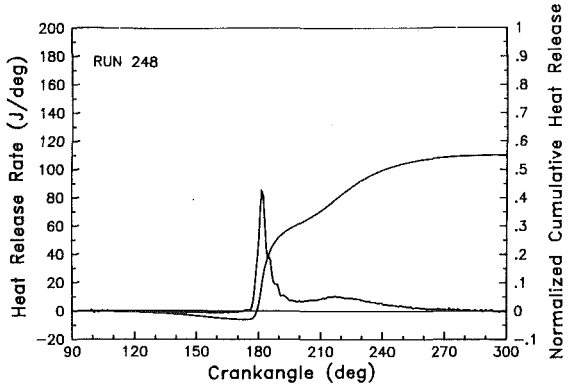


Fig. 14 Heat release diagram for the uninsulated engine using coal/water slurry at 900 rpm, 38°C inlet air and glow plugs

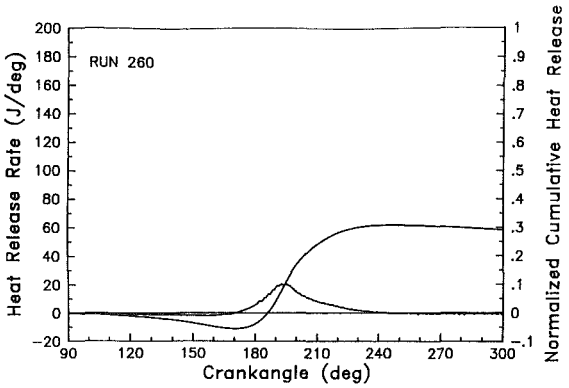


Fig. 15 Heat release diagram for the uninsulated engine using coal/water slurry at 900 rpm, 204°C inlet air and glow plugs

case represents the least added heat input (via hot inlet air or glow plugs).

Figure 13 shows the effect of increasing the inlet air temperature to 204°C. The peak rate of premixed burning has been significantly reduced due to a shorter evaporation time and less vaporization and mixing prior to ignition. However, the duration of premixed phase of combustion increased. Approximately 50 percent of the heat release took place during the diffusion burning phase.

The best performance occurred using the glow plug and 38°C air shown in Fig. 14. The glow plug heat predictably reduced the peak burning rate and increased the duration of the premixed combustion. There was also increased burning during the diffusion phase, which resulted in a high overall NCHR. This condition represents the best slurry performance attained in the engine.

Figure 15 shows the effect of both 204°C inlet air and the glow plug heat. In this case, a pilot charge of diesel fuel was not required for ignition. It was speculated that the high heat input would greatly reduce the premixed burn fraction. In fact, the effect of the heat was so great that there was no longer two distinct phases of combustion. The coal/water slurry was injected at 168 deg BTDC, autoignited, and burned slowly.

Figure 16 is a bar chart of the thermal efficiency data at the maximum load condition for the coal/water slurry in the different configurations at 1500 rpm. Unfortunately, the 38°C glow plug data could not be obtained due to injector jamming. The overall trends are the same as the 900-rpm results except that more pilot energy was required to maintain smooth operation and that autoignition did not occur for the highest heat input case using glow plugs and 204°C inlet air.

The insulated (or ceramic) engine results at 900 rpm are presented in Fig. 17 for 38°C inlet air. The base diesel fuel performance was similar to the standard engine; however, the slurry fuels did not do as well as they did in the steel engine. The higher temperature environment allowed lower PER, but the increased temperatures resulted in lower thermal efficiencies, due to reduced ignition delay times and, consequently, reduced premixed burning of the pilot and slurry charge. This can be seen in Fig. 18, which compares the maximum heat release rates. The maximum heat release rates, in some cases, were less than 50 percent of those obtained in the uninsulated engine.

The instantaneous heat release diagrams for the 900-rpm cases in the insulated engine are shown in Figs. 19–22. In general, the values of peak instantaneous heat release are lower and the duration of this phase of combustion is increased as compared to the steel engine. However, significant burning took place during the diffusion phase as compared to the uninsulated engine. This burning is demonstrated by the large hump in the rate diagrams following the premixed combustion spike.

The coal/water slurry heat release diagram shown in Fig. 20 is interesting in that the premixed burning phase continued into the diffusion phase. There was no sharp distinction between the different phases. This phenomenon was most evident for the coal/diesel slurry shown in Fig. 21. The coal/diesel slurry has the lowest latent heat of evaporation of the fuels. The lack of significant cooling effect from fuel evaporation resulted in essentially no premixed burning. This effect occurred using (38°C) inlet air, producing results similar to those observed in tests with 204°C inlet air in the uninsulated engine.

The heat release diagram for the coal/water–methanol slurry, shown in Fig. 22, demonstrates the improvement in

Downloaded 01 Jun 2010 to 171.66.16.87. Redistribution subject to ASME license or copyright; see http://www.asme.org/terms/Terms_Use.cfm

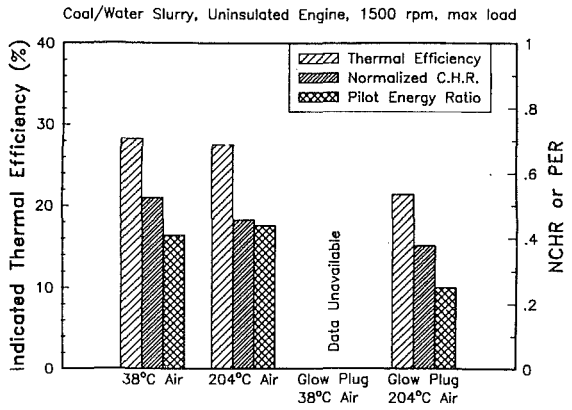


Fig. 16 Indicated thermal efficiency for different engine configurations using coal/water slurry at 1500 rpm

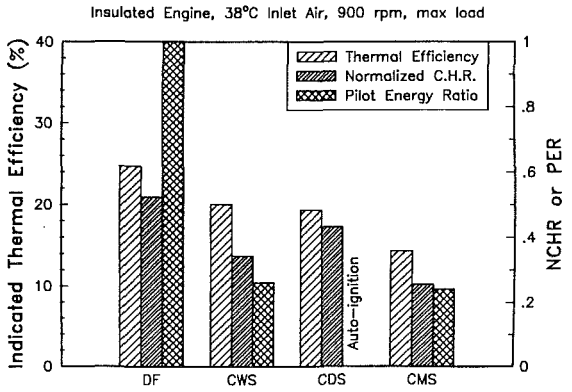


Fig. 17 Indicated thermal efficiency for the test fuels in the insulated engine at 900 rpm

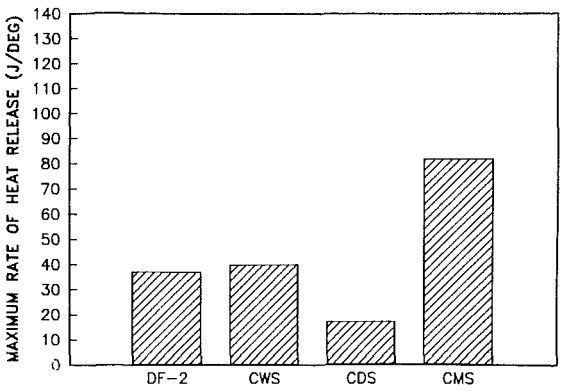


Fig. 18 Maximum rate of heat release for the test fuels in the insulated engine at 900 rpm

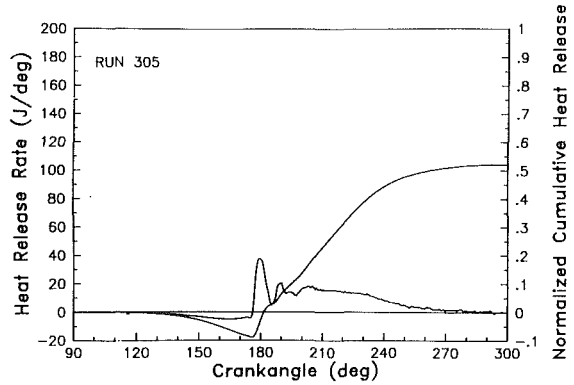


Fig. 19 Heat release diagram for the base diesel fuel in the insulated engine at 900 rpm

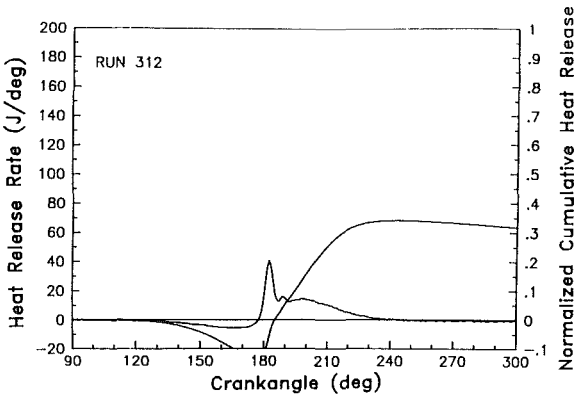


Fig. 20 Heat release diagram for the coal/water slurry in the insulated engine at 900 rpm

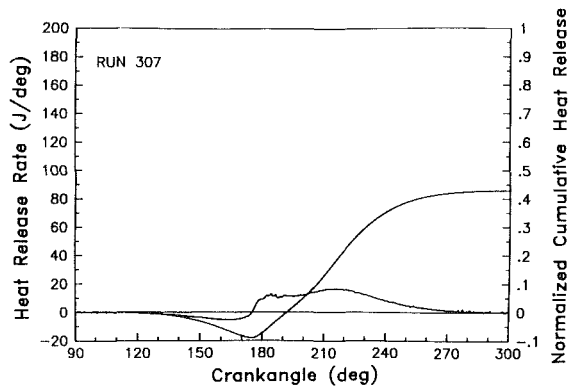


Fig. 21 Heat release diagram for the coal/diesel slurry in the insulated engine at 900 rpm

combustion due to the cooling effects of the water-methanol. The peak heat release rate for this fuel was the highest observed in the insulated engine. The diffusion burning phase was reduced, however, and overall cumulative combustion efficiency was low.

At 1500 rpm the trends, shown in Fig. 23, were similar to those obtained at 900 rpm. The coal/water-methanol slurry data could not be obtained due to injector jamming. Autoignition did occur in the case of the coal/diesel slurry. Autoignition of the coal/diesel did not occur at 900 rpm.

Summary and Conclusions

The majority of effort in this work was directed toward obtaining the best possible performance using a coal/water slurry. Thermal efficiencies and possibly combustion efficiencies equal to the base diesel fuel were obtained. In order to achieve this, coal/water slurries with viscosities compatible with modified jerk pump injection equipment were developed. A specially designed engine was developed that made it possible to explore the effects of increased temperatures on the combustion. Engine temperatures were increased until autoignition of the coal/water slurry occurred.

The following is a listing of the conclusions which have been drawn from the results of these experiments.

- Using hot air and a hot spot (glow plug), autoignition of the coal/water slurry can be achieved.
- The coal/diesel slurries will autoignite; however, the high

Downloaded 01 Jun 2010 to 171.66.16.87. Redistribution subject to ASME license or copyright; see http://www.asme.org/terms/Terms_Use.cfm

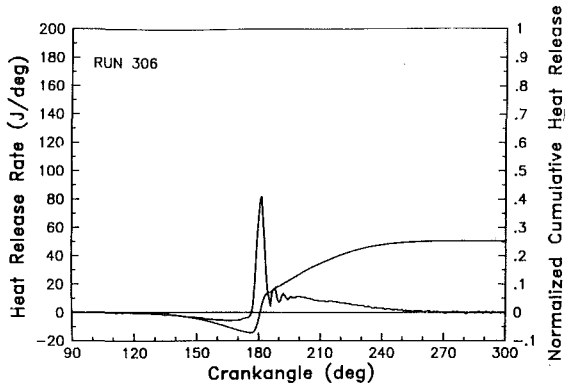


Fig. 22 Heat release diagram for the coal/water-methanol slurry in the insulated engine at 900 rpm

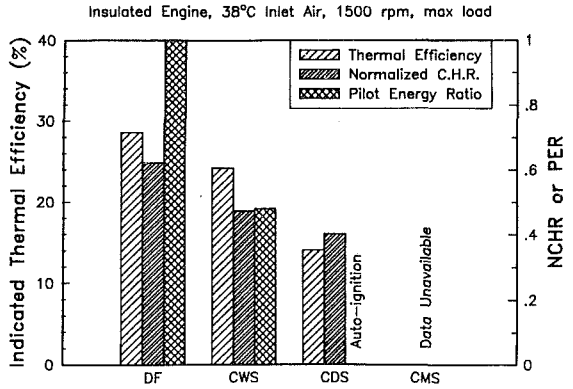


Fig. 23 Indicated thermal efficiency for the test fuels in the insulated engine at 1500 rpm

inlet air temperatures required to burn the coal result in poor combustion of the diesel fuel carrier (elimination of the premixed burning phase).

- Burning rates of the autoignited slurries, both coal/water and coal/diesel, are considerably slower than if a pilot injection of diesel fuel is used.
- Using 38°C inlet air and glow plugs, the coal/water slurry achieved a thermal efficiency equal to the base diesel fuel.
- Additional heat input to the engine via hot inlet air, glow plugs, or LHR technology overcomes the latent heat effects of the coal/water slurry, allowing larger amounts of slurry to be burned.
- Too much supplemental heat results in poor combustion of the normal cetane diesel pilot fuel and subsequent poor ignition and combustion of the slurry.
- The diffusion burning of the slurries is limited. Burning gases exiting from the prechamber are quenched when they encounter the gas in the main chamber, which is rapidly cooling due to expansion. More complete combustion could be attained by maximizing the amount of burning during the premixed phase. This could be done by making the prechamber as large a fraction of the total clearance volume as possible.

Acknowledgments

This work was supported by the U.S. Department of Energy, Morgantown Energy Technology Center, with Mr. Larry Carpenter serving as the technical monitor during the final phases of the project, followed by Mr. Fred Bauer during the final phase of the work. The authors also wish to thank Southwest Research Institute personnel: Stan Moulton, Lee Dodge, Tim Callahan, and Randy Hollon for their assistance.

References

1 Soehngen, E. E., "Development of Coal Burning Diesel Engines in Germany," ERDA Report No. 831747, Nov. 1983.

2 Marshall, H. P., and Walters, D. C., "An Experimental Investigation of a Coal Slurry Fueled Diesel Engine," SAE Paper No.770795, Jan. 1977.

3 Winquist, K., "Injector for Powder Fuels," Final Report for SwRI internal Project No. 11-9240, May 1981.

4 Gurney, M. D., Clingenpeel, J. M., and Eccleston, D. B., "A Program to Examine the Use of Coal Slurry Fuels in Diesel Engines," ASME Paper No. 84-DGP-9, Feb. 1984.

5 Ryan, T. W., III, Callahan, T. J., Dodge, L. G., and Moses, C. A., "The Use of Hybrid Fuel in a Single-Cylinder Diesel Engine," SAE Paper No. 801380, Oct. 1980.

6 Ryan, T. W., III, Callahan, T. J., Dodge, L. G., and Moses, C. A., "Injection, Atomization and Combustion of Carbon Slurry Fuels," SAE Paper No. 821199, Oct. 1982.

7 Ryan, T. W., III, and Dodge, L. G., "Diesel Engine Injection and Combustion of Slurries of Coal, Charcoal, and Coke in Diesel Fuel," SAE Paper No. 840119, Feb. 1984.

8 Nydick, S. E., Porchet, F., and Steiger, H. A., "Continued Development of a Coal/Water Slurry-Fired Slow-Speed Diesel Engine: a Review of Recent Test Results," ASME JOURNAL OF ENGINEERING FOR GAS TURBINES AND POWER, Vol. 109, 1987, pp. 465-476.

9 Clingenpeel, J. M., Gurney, M. D., and Eccleston, D. B., "A Combustion and Wear Analysis for a Compression-Ignition Engine Using Coal Slurry Fuels," ASME Paper No. 84-DGP-8, Feb. 1984.

10 Leonard, G. L., and Fiske, G. H., "A Comparison of a Positive Displacement Fuel Injection System With an Accumulator-Based System for Coal-Fueled Diesel Engine Applications," ASME Paper No. 87-ICE-32, Feb. 1987.

11 Cheng, W. K., Lai, M. C., Zhou, B., Wong, V. W., and Benedek, K. R., "Parametric Studies of Coal-Water Slurry Combustion in a Rapid Compression Machine," ASME Paper No. 87-ICE-9, Feb. 1987.

12 Obert, E. F., "Internal Combustion Engines," 4th ed., Intest Educational Publishers, New York, 1973.

13 Siebers, D. L., and Dyer, F. M., "The Autoignition and Combustion of Coal-Water Slurry Under Simulated Diesel Engine Condition," ASME Paper No. 85-KDGP-15, 1985.

Downloaded 01 Jun 2010 to 171.66.16.87. Redistribution subject to ASME license or copyright; see http://www.asme.org/terms/Terms_Use.cfm

Effects of Fuel Overpenetration and Overmixing During Ignition-Delay Period on Hydrocarbon Emissions From a Small Open-Chamber Diesel Engine

T.-W. Kuo

K.-J. Wu

S. Henningsen

Engine Research Department,
General Motors Research Laboratories,
Warren, MI 48090

A quasi-steady gas-jet model was applied to examine the spray trajectory in swirling flow during the ignition-delay period in an open-chamber diesel engine timed to start combustion at top dead center. Spray penetration, deflection, and the fractions of too-lean-mixed, burnable, and overpenetrated fuel at the start of combustion were calculated by employing the measured ignition delay and mean fuel-injection velocity. The calculated parameters were applied to correlate the measured exhaust hydrocarbon (HC) emissions. The engine parameters examined were bowl geometry, compression ratio, overall air–fuel ratio, and speed. Both the ignition delay and the relative spray-penetration parameter, defined as the ratio of the spray-penetration distances at the moments of start of combustion and wall impingement, gave good correlations for some of the engine parameters examined but could not explain all the measured trends. However, good correlation of the measured exhaust HC emissions was obtained by using the calculated too-lean-mixed and overpenetrated fuel fractions at the start of combustion. Correlation of the overpenetrated fuel with the measured HC indicated that approximately 2 percent of the fuel mass that overpenetrated before start of combustion emitted from the engine as unburned HC. This could account for 0 to 65 percent of the total HC emission from this engine. Additionally, it was found that the too-lean-mixed fuel could contribute 10 to 30 percent of the total HC emission, as found in a previous study on a somewhat similar engine. The remaining HC emission is caused by other sources such as bulk quenching.

Introduction

Hydrocarbon (HC) emissions from open-chamber diesel engines are known to vary substantially with operating conditions, and the prevailing source of HC emissions varies with the mode of engine operation. Among the possible HC-emission sources are: (1) local overmixing of fuel at spray periphery to form a too-lean-mixed mixture that cannot ignite or support combustion [1–3], (2) local undermixing of fuel in the final stage of injection due to poor spray atomization [4, 5], (3) fuel in the sac and hole volumes of the injector [1, 4, 5], (4) lubricating oil [6], (5) wall quenching due to spray overpenetration [5, 7], (6) extinction of flame inside squish region due to heat loss through the wall [5], and (7) bulk quenching due to the rapid diffusion of combustible species or due to a sudden drop in the cylinder gas temperature by piston expansion [2, 5].

In large-bore quiescent-chamber diesel engines, the too-lean-mixed fuel during the ignition-delay period has been identified to be the major source of HC emission [2, 4]. This is supported by the fact that an increase in the ignition delay increases exhaust HC emissions. In passenger-car open-chamber diesel engines, however, the contribution of the too-lean-mixed fuel to HC emissions appears to be secondary because it could explain only a maximum of 20 percent of the HC emission even though HC increases with ignition delay [3]. In view of the smaller piston-bowl diameter used in the small open-chamber diesel engine, the effect of wall quenching due to spray overpenetration cannot be ignored. In fact, as demonstrated previously by Haupais [7], from three to five times as much exhaust HC can result if the spray impinges on the piston-bowl wall before the ignition occurs. Thus, the purposes of this study were: (1) to reassess the contribution of

Contributed by the Internal Combustion Engine Division and presented at the Eleventh Annual Energy-Sources Technology Conference and Exhibition, New Orleans, Louisiana, January 10–13, 1988. Manuscript received by the Internal Combustion Engine Division April 1987.

Copyright © 1988 by ASME
Downloaded 01 Jun 2010 to 171.66.16.87. Redistribution subject to ASME license or copyright; see http://www.asme.org/terms/Terms_Use.cfm

Table 1 Engine specifications

Bore, mm	88.0
Stroke, mm	85.5
Connecting rod length, mm	153.9
Displacement, L	0.52
Intake swirl ratio	2.3
Fuel-injection system	Five 0.22-mm diameter holes 150 deg included angle 33.9 MPa opening pressure 5 mm injector-to-bore offset

Table 2 Piston-bowl geometries

Bowl configuration	R	S1	S2
Bowl volume, mm^3	17.6	19.3	22.4
Compression ratio	21.4	21.4	18.5
Impingement circle diameter, mm	41.3	53.6	53.6
SA,* percent	78.0	45.0	39.0
Bowl depth, mm	16.3	10.2	11.2

*Relative squish area (SA) is defined as 100 times the piston-crown surface area divided by the cylinder-head surface area.

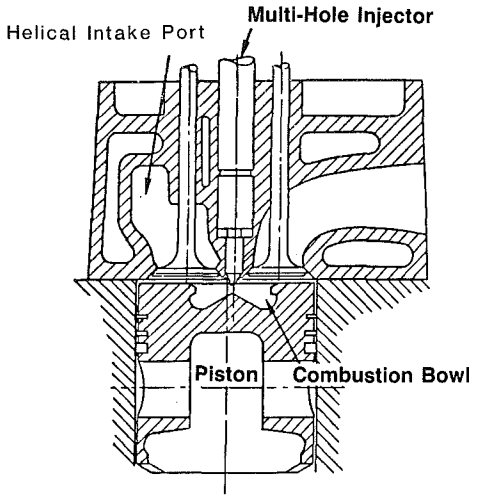


Fig. 1 Schematic of the single-cylinder open-chamber diesel engine

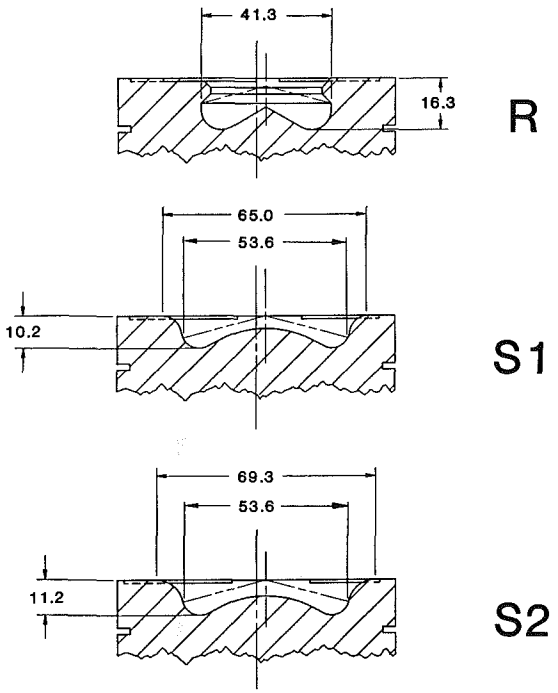
too-lean-mixed fuel on HC emission with an engine similar to that used in [3], and (2) to quantify, if possible, the effect of spray overpenetration on HC emission.

In this study, the spray development in a swirling flow was examined with a semi-empirical quasi-steady gas-jet model in a small open-chamber diesel engine with variations in piston-bowl geometry, compression ratio (CR), speed, and overall air–fuel ratio (A/F). The parameters characterizing the spray at the start of combustion (SOC) were calculated. These include spray penetration and deflection, and fuel fractions in the too-lean-mixed, burnable, and overpenetrated regions. The calculated fuel fractions in the too-lean-mixed and overpenetrated regions were used to correlate the experimentally measured exhaust HC emissions. The calculated burnable fuel at the SOC was compared with the premixed-burned fuel fraction, calculated from heat-release analysis of pressure–time data.

Experimental Aspects

Equipment. The engine used to collect data was a 0.52-L naturally aspirated, single-cylinder open-chamber diesel engine, which was converted from a production four-cylinder engine [8]. The geometry of the engine is shown in Fig. 1, and the engine specifications are listed in Table 1.

Three different piston-bowl geometries were examined (see Fig. 2 and Table 2). The re-entrant bowl, configuration R, had a relatively small bowl diameter and a turbulence rim near the top edge of the bowl. This design was similar to that of [9]. Configuration S1 is of the shallow-bowl design commonly used in medium- and heavy-duty diesel applications. Configuration R has about 10 percent smaller bowl volume than configuration S1, but the compression ratio remains the same at 21.4. This is due to the larger valve pockets associated with the re-entrant bowl. Configuration S2 is similar to configuration S1, but it has a bowl volume about 16 percent larger and a lower compression ratio than configuration S1. The increase in bowl volume for configuration S2 was made by increasing the depth of the bowl slightly. However, the diameter of the impingement circle of fuel sprays was kept essentially the same.



All Dimensions in mm

Fig. 2 Schematic of the bowl geometries

Gaseous HC emissions were measured at all operating conditions with a heated flame ionization detector. The cylinder pressure was measured with a water-cooled piezoelectric

Nomenclature

F = fraction
HC = hydrocarbon
m = mass
S = tip-penetration distance along the spray centerline
t = time
V = velocity
α = relative HC emission parameter
β = relative overpenetration parameter

Subscripts

b = burnable
f = fuel
id = ignition delay
imp = impingement
inj = injection
l = lean limit
op = overpenetrated
p = premixed
r = rich limit
SOC = start of combustion

Downloaded 01 Jun 2010 to 171.66.16.87. Redistribution subject to ASME license or copyright; see http://www.asme.org/terms/Terms_Use.cfm

Table 3 Test conditions

Speed, r/min	1000, 1300, 1500,* 1800, 2400
Overall air-fuel ratio (A/F)	25, 35, 45,* 55, 70

*Indicates baseline condition.

pressure transducer at a resolution of one crank-angle degree for 96 consecutive engine cycles. The cylinder-pressure data were then ensemble averaged and analyzed to determine the premixed-burned fuel fraction from heat-release analysis [8].

Experimental Conditions. Table 3 summarizes the engine test conditions. Tests at various engine speeds were performed at a baseline A/F of 45, and similarly, tests at various A/F were at the baseline speed of 1500 rpm. Both speed and A/F variations were evaluated for each of the bowl geometries (Table 2), giving a total of 27 different test cases (appendix). Variation in A/F was achieved by varying the amount of fuel injected per stroke while keeping the amount of air the same. Start of combustion (SOC) was fixed at top dead center (TDC) in all the cases by adjusting injection timing.

Experimental Data. Appendix A summarizes the measured data, some of which are reported in a previous paper [8]. These data include ignition delay (t_{id}), injection duration (t_{inj}), fuel delivery, mean fuel-injection velocity (V_{inj}), premixed-burned fuel fraction ($F_{f,p}$), and emission index of HC (EIHC). The start-of-injection (SOI) and end-of-injection (EOI) timings were determined from the recorded needle-lift signal. The injection duration and fuel delivery were used to calculate the mean injection velocity of the fuel, which was used as an initial condition for the gas-jet model to characterize the injection event for each case. The measured ignition-delay data were also supplied to the model. The premixed-burned fuel fraction and EIHC data in the appendix were correlated with the spray parameters calculated in this study.

Model Description

The gas-jet model used is similar to that used by Sinnamon et al. to study the spray trajectory under nonfiring conditions in an optical DISC engine [10]. This model can account for the three-dimensional nature of the flow and was derived from an earlier two-dimensional version. However, only the two-dimensional axisymmetric version of the program is used in this study since the in-cylinder flow field is calculated by a two-dimensional axisymmetric flow model as well.

The gas-jet model considers a nonreacting isothermal steady-state gas jet injected into an airflow. The steady-state assumption implies a constant rate of fuel injection in a temporally invariant airflow field. In addition, the model ignores the interaction between the jet and the chamber walls and assumes that the spray has no influence on the air-velocity field. Under these assumptions, the conservation equations for mass and momentum are formulated in integral forms assuming Gaussian similarity profiles for fuel concentration and velocity and using an entrainment expression proposed by Ricou and Spalding [11]. The equations are solved to obtain expressions for jet penetration and width in terms of the spatial coordinates. The jet-width expression and the similarity profiles then provide the spatial distributions of fuel concentration and velocity.

Henningsen [3] modified the three-dimensional version of this model to study the characteristics of fuel sprays in an open-chamber diesel engine during the ignition-delay period. The modifications included incorporation in the program of a computed velocity field in the combustion chamber at a specified time during the injection period. The velocity field was computed using the two-dimensional CONCHAS-Spray computer program [12]. In order to explain the trends in exhaust HC with varying ignition delay, Henningsen [3] used the model to calculate the amount of fuel that mixed with air during the ignition-delay period to become too lean to burn, using a lean flammability limit of 0.6 equivalence ratio. Furthermore, a rich flammability limit of 3.0 was chosen by Henningsen. The validity of this choice was verified by a good correlation between the calculated burnable fuel fraction at the SOC and the premixed-burned fuel fraction estimated from heat-release analysis. Therefore, these limits were adopted in the present study.

In the present study, the CONCHAS-Spray code [12] was modified to generate the airflow tables at every crank angle during the injection period. These airflow tables were read in by the gas-jet model for spray penetration and deflection calculations. For all the cases examined in this study, a solid-body-rotation profile was assumed for the swirl velocity at intake-valve closing.

Because the CONCHAS-Spray computer code was limited to axisymmetric flows, the piston-bowl axis was assumed to be coincident with the cylinder-bore axis. Therefore, the airflow field is symmetric with respect to the cylinder-bore axis. In addition, the multispray injector was assumed to be placed on this axis. Therefore, a symmetric spray pattern evolved from the spray calculation.

Results

In this section, the calculated results on spray penetration, deflection, and too-lean-mixed, burnable and overpenetrated fuel fractions are presented. The results for the baseline reentrant bowl running at 1500 rpm and 45 A/F are presented first. Then the effects of piston-bowl geometry, compression ratio, engine speed, and A/F are shown. As mentioned earlier, the engine geometry and airflow were assumed to be axisymmetric because of the limitation of the in-cylinder flow model. However, in the figures where spray trajectory results are presented, the actual engine geometry tested in the experiment is used instead.

Baseline Condition. Figure 3 shows the typical results of the spray trajectories at the SOC. The solid and dotted curves represent the calculated centerlines and boundaries of the sprays, respectively. Note that large spray deflection was obtained in the swirl direction (Fig. 3*a*), but negligible deflection was obtained in the squish plane (Fig. 3*b*). This is because the air momentums in the radial and axial directions are much smaller than that in the swirl direction. Similar observations were also obtained for other cases. Thus in the following discussions, only spray trajectory in the swirl direction will be shown.

In addition to the spray penetration and deflection, each fuel spray is divided into the rich, burnable, and too-lean-mixed regions based on the equivalence-ratio contours. The fraction of fuel in each region was determined by integrating the fuel mass contained in that region. These parameters quantify the mixing process between fuel and air during the ignition-delay period.

The fuel in the rich region is defined as that with equivalence ratio larger than the rich flammability limit ϕ_r. Similarly, the fuel in the too-lean mixed region is defined as that with equivalence ratio smaller than the lean combustion limit ϕ_l. The remainder of the fuel is burnable. In this study, ϕ_r and ϕ_l were chosen as 3.0 and 0.6, respectively. Note that the spray tips in Fig. 3 have traveled beyond the piston-bowl wall. This is due to the lack of a proper model to account for the spray-wall interference. Realistically, in diesel engines the sprays are deflected after impingement. Some of the liquid fuel is expected to stay on the walls, spread out and subsequently evaporate, while the rest of the liquid fuel is expected

Downloaded 01 Jun 2010 to 171.66.16.87. Redistribution subject to ASME license or copyright; see http://www.asme.org/terms/Terms_Use.cfm

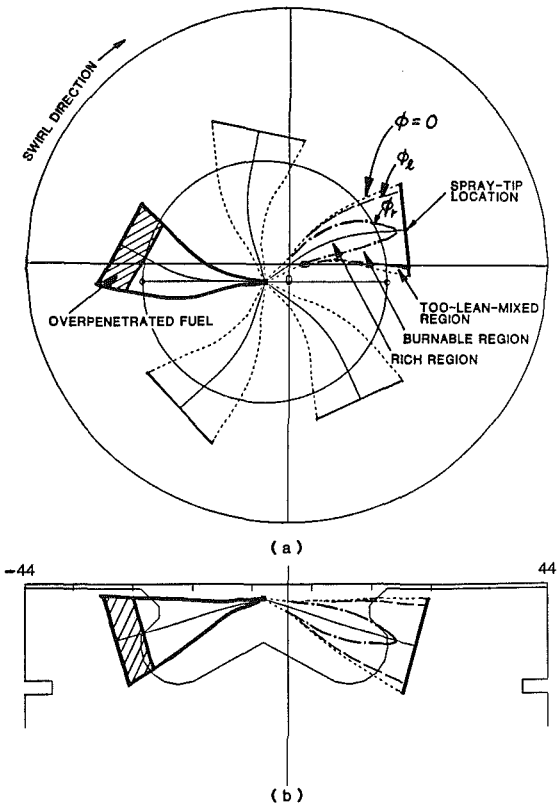


Fig. 3 Projection of spray trajectory (*a*) perpendicular and (*b*) parallel to the cylinder-bore axis at the start of combustion: baseline

to rebound from the walls and mix with the gases. Instead of modeling this complex process, the too-lean-mixed and burnable fuel fractions have been calculated as if the walls were not there, and zero air-swirl velocity has been assumed beyond the piston-bowl wall, as illustrated by the undeflected spray penetration in Fig. 3(*a*).

The overpenetrated fuel includes the fuel vapor deflected by the walls, the liquid fuel rebounded from the walls, and the liquid fuel stuck on the walls. A part of the overpenetrated fuel will be consumed in the combustion process, and the rest, especially that on the walls, could potentially be emitted from the engine as unburned HC. Because of the difficulty of decomposing the overpenetrated fuel into individual components, all of the overpenetrated fuel was used to quantify the extent of wall impingement. For this baseline case, about 1/3 of the total injected fuel was found to have overpenetrated at SOC.

Finally, the tip-penetration distance (S) along the spray centerline, the arrival time (t) of the tip when the spray first impinges (*imp*), and SOC occurred are calculated. These are summarized in Appendix A for all the cases examined. In the discussion, these data are used to correlate the measured emission results.

Effects of Bowl Geometry. Two bowls with different geometries, re-entrant (R) and shallow (S1), but the same CR are considered in this comparison. The relative squish area for each geometry is approximately 78 and 45 percent, respectively (Table 2). Comparisons are made for engine conditions of 1500 rpm speed and 45 A/F (Cases 3 and 8 in the appendix), but the results can be extended to other operating conditions. Figure 4(*a*) shows penetration and deflection for one of the calculated sprays at the SOC for both bowls. It is clear that the re-entrant bowl had larger spray deflection in the swirl direction. This is attributed to the stronger squish-enhanced air swirl in the re-entrant bowl due to its smaller bowl diameter and stronger squish.

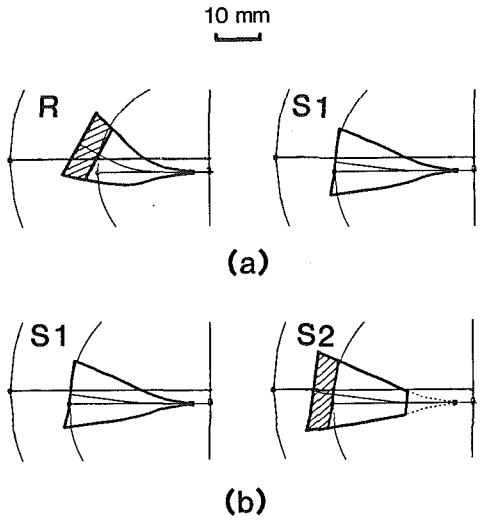


Fig. 4 Calculated spray penetration and deflection at the start of combustion with variations in (*a*) bowl geometry and (*b*) compression ratio at 1500 r/min and 45 A/F

The appendix includes the calculated too-lean-mixed ($F_{f,l}$) and burnable ($F_{f,b}$) fuel fractions for both the re-entrant and shallow bowls. For most of the cases, the re-entrant bowl has larger values for both parameters than the shallow bowl. This is consistent with the larger air-swirl velocity and spray deflection for the re-entrant bowl. The overpenetrated fuel fraction ($F_{f,op}$) is seen to be larger for the re-entrant bowl as well, mainly because of its smaller impingement-circle diameter, although the spray deflection is larger and the ignition delay is slightly shorter (appendix) for the re-entrant bowl. It is interesting to note that the combustion had started in the shallow bowl in most of the cases before the spray tips reached the walls.

Effects of Compression Ratio. The effects of compression ratio on the spray penetration and deflection are examined for two shallow bowls. Figure 4(*b*) shows the calculated spray trajectories for two shallow bowls (S1 and S2) at 1500 rpm speed and 45 A/F (Cases 8 and 13). The spray trajectory is nearly the same for both cases. For the 18.5-CR case (S2), the ignition delay was longer than the injection duration. Therefore, the tail of the spray is evident in the figure.

The calculated too-lean-mixed, burnable, and overpenetrated fuel fractions for the 18.5-CR bowl are all larger than those for the 21.4-CR bowl operating at the corresponding speed and A/F (Table 5). This trend is expected due to the longer ignition delay for the low-CR bowl.

Effects of Engine Speed. Figure 5 illustrates the effects of engine speed on spray penetration and deflection at the SOC for the three piston-bowl configurations. It is clear that the spray deflection in the swirl direction increases substantially with engine speed for the re-entrant bowl (R). This is due to increased intake swirl velocity at increased speed and due to insensitivity of the mean fuel-injection velocity to engine speed (appendix). Similar trends were also observed for the shallow bowls (S1 and S2). However, the deflection of the sprays becomes less significant than for the re-entrant bowl. The calculated fuel fractions for different engine speeds are shown in the appendix for all three piston bowls examined (Cases 1-15).

The calculated fraction of burnable fuel was found to decrease with increasing engine speed for the re-entrant bowl (R). This is the result of two competing mechanisms. First, the airswirl velocity becomes higher at higher speed, which has a tendency to enhance mixing and hence increase the too-lean-

Downloaded 01 Jun 2010 to 171.66.16.87. Redistribution subject to ASME license or copyright; see http://www.asme.org/terms/Terms_Use.cfm

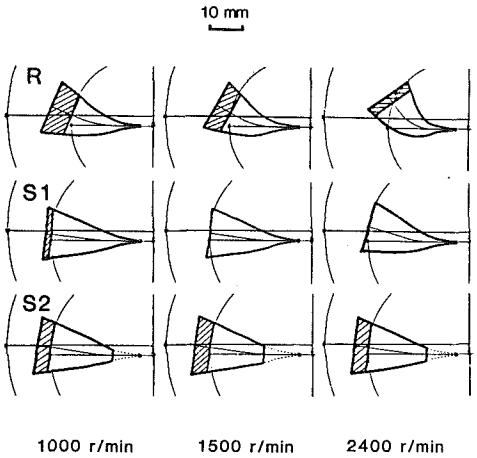


Fig. 5 Calculated spray penetration and deflection at the start of combustion with speed variation at 45 A/F for all three bowls

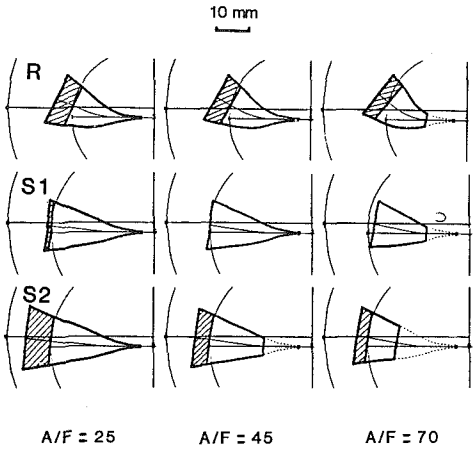


Fig. 6 Calculated spray penetration and deflection at the start of combustion with A/F variation at 1500 r/min for all three bowls

mixed and burnable fuel fractions. Second, the ignition delay in real time decreases with increasing speed, which causes the ratio of the injected fuel at the SOC to the total fuel delivery to decrease for the same injection velocity. Although the too-lean-mixed and burnable fractions of the injected fuel at the SOC may be the same because of the similar structure of the sprays, these fractions tend to decrease with increasing speed. Judging from the calculated results, it is likely that the second mechanism is dominant. The fraction of overpenetrated fuel also decreases substantially with increasing speed. Both mechanisms favor this trend.

The fractions of too-lean-mixed and burnable fuel were nearly unchanged with engine speed for the 21.4-CR shallow bowl (S1). This is because most of the fuel was injected into the combustion chamber before ignition and only a weak swirl was generated in this bowl. The overpenetrated fuel fraction is zero for S1 except at 1000 rpm, at which speed a small amount of fuel overpenetrated.

The too-lean-mixed and burnable fuel fractions for the 18.5-CR shallow bowl (S2) do not show any consistent trends with respect to the engine speed. This is likely to be due to the weak air-swirl velocity in the shallow bowl. Instead, these fuel fractions follow the trends of the mean fuel-injection velocity. An increase in the injection velocity increases the calculated too-lean-mixed and burnable fuel fractions. This observation suggests that, in the absence of strong swirl, the spray development depends strongly on the injection velocity. Except for the case of 2400 rpm, the overpenetrated fuel fraction also increases with the mean fuel-injection velocity.

Effects of Overall Air–Fuel Ratio. The effects of A/F on spray penetration, deflection, and fuel fractions in various spray regions are examined for all three piston bowls running at the constant engine speed of 1500 rpm. In the experiments, variation in A/F was achieved mainly by varying the amount of fuel injected per stroke while keeping the amount of air in the cylinder approximately the same. Thus, the same airflow fields were assumed in calculations for different A/F.

Figure 6 illustrates the effects of A/F on the calculated spray penetration and deflection at SOC for the three bowl geometries. Increasing A/F increases the spray deflection slightly for all the bowls. Since the airswirl momentum is the same for different A/F, the extent of spray deflection depends entirely on the injection momentum of the fuel sprays. The experimentally measured mean fuel-injection velocity (appendix) and injection momentum decrease fairly consistently with increasing A/F. This results in the trend of increasing spray deflection. At large A/F, the injection duration becomes

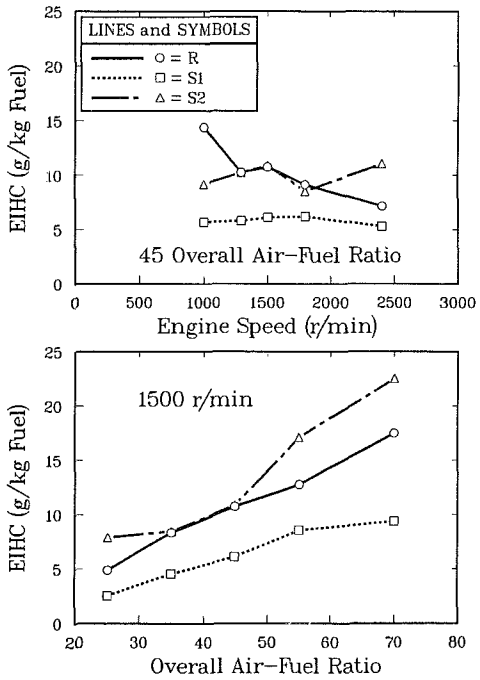


Fig. 7 Variation of EIHC with engine speed and A/F for all three bowls

shorter than the ignition delay. Therefore, the tail of the spray becomes evident.

The results of the too-lean-mixed and burnable fuel fractions showed the same dependence on A/F for all three bowls, as indicated in the appendix (Cases 16–27). The larger the A/F is, in general, the higher the calculated too-lean-mixed and burnable fuel fractions.

As for the overpenetrated fuel fraction at the SOC, no consistent trends could be identified for the three bowls. For the re-entrant bowl (R), the overpenetrated fuel fraction increases as the A/F is increased. For the 21.4-CR shallow bowl (S1), the overpenetrated fuel fraction decreases with increasing A/F and becomes zero when A/F reaches 45. For the 18.5-CR shallow bowl (S2), the overpenetrated fuel fraction seems to correlate with the mean fuel-injection velocity.

Discussion

HC Emissions. The measured variations of EIHC with engine speed and with A/F for all three bowls are shown in

Downloaded 01 Jun 2010 to 171.66.16.87. Redistribution subject to ASME license or copyright; see http://www.asme.org/terms/Terms_Use.cfm

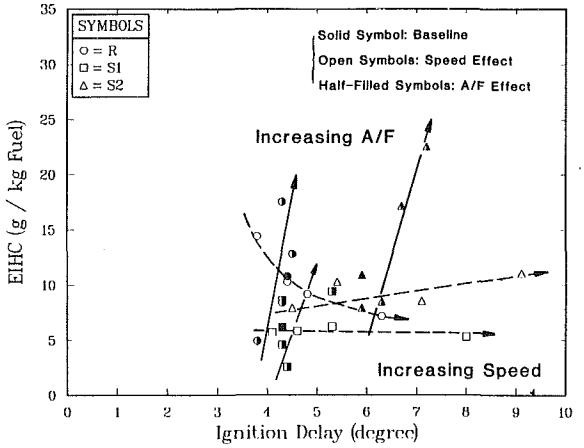


Fig. 8 Correlation of measured EIHC and ignition delay

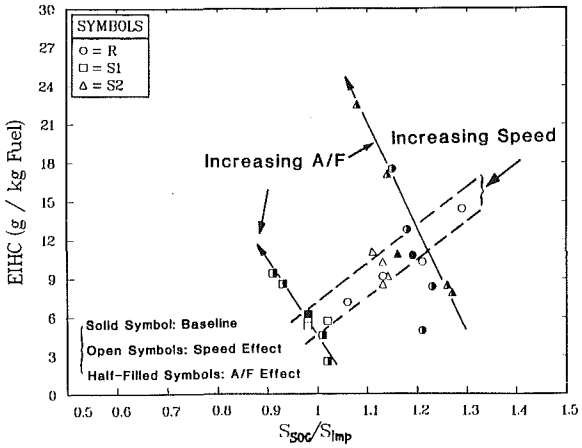


Fig. 10 Correlation of measured EIHC and calculated relative spray penetration

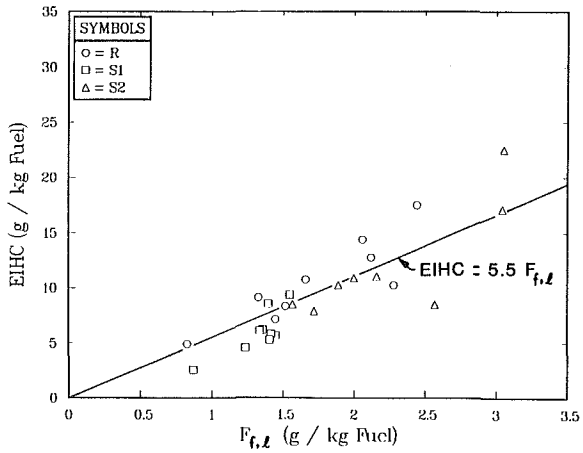


Fig. 9 Correlation of measured EIHC and calculated too-lean-mixed fuel fraction

Fig. 7. Several characteristics can be identified: (1) EIHC for the re-entrant bowl (R) decreased with increasing speed, (2) EIHC for the two shallow bowls (S1 and S2) was insensitive to speed variation, (3) EIHC increased with increasing A/F for all three bowls, and (4) EIHC was higher for both the re-entrant and 18.5-CR shallow (S2) bowls than the 21.4-CR shallow bowl (S1) at the same engine conditions. More specifically, the difference in EIHC between the re-entrant and 21.4-CR shallow bowls at constant A/F reduced from 120 percent at 1000 rpm to 30 percent at 2400 rpm. For various A/F at 1500 rpm, the EIHC was nearly twice as high for bowl R. The subject of this section is to explain these trends. Consider first the effect of too-lean-mixed fuel during the ignition delay on HC emission.

Effect of Too-Lean-Mixed Fuel. Henningsen [3] examined this effect in a previous study on a somewhat similar engine and obtained a linear correlation between EIHC and ignition delay. The data obtained from this study are plotted in Henningsen's coordinates in Fig. 8 but show large scatter. A close examination reveals that the correlation depends on the combustion-bowl geometry, compression ratio, engine speed, and A/F. For instance, EIHC increases with increasing ignition delay when A/F is increased, but may increase or decrease with ignition delay when the engine speed is increased, depending on the bowl geometry. The poor overall correlation in Fig. 8 suggests that the ignition delay alone is insufficient to account for the effect of too-lean-mixed fuel on HC emissions in this engine when a relatively large number of engine parameters are considered.

In Fig. 9, the measured EIHC is plotted versus calculated too-lean-mixed fuel fraction. The quality of correlation is improved substantially, although still with some data scatter. The least-squares fit of the data is shown by the straight line and has a correlation coefficient of 0.73. The results suggest that the too-lean-mixed fuel can possibly contribute to 18 percent of the HC emission measured in the exhaust, which is essentially the same conclusion as obtained by Henningsen [3].

Based on the conclusion obtained from the correlation shown in Fig. 9, it appears that the too-lean-mixed fuel alone cannot explain the observed trends in Fig. 7 completely. In fact, after the calculated too-lean-mixed fuel fraction is subtracted from the corresponding measured EIHC data by assuming that all the too-lean-mixed fuel emits as unburned HC, a difference in HC emission remains.

Effect of Overpenetrated Fuel. In order to identify the major source that caused the observed difference in HC emission for different bowl geometries, the calculated overpenetrated fuel must be considered. As demonstrated by Haupais [7] in a quiescent diesel engine, a steep increase in EIHC resulted if an increasing degree of spray impingement on the piston bowl occurred before SOC. He characterized the effect of overpenetration by comparing the spray penetration at the SOC with the radius of the combustion bowl.

HC data from this study are plotted in Fig. 10 versus a relative spray penetration parameter, S_{SOC}/S_{imp}, which is similar to that of Haupais. The numerator and denominator are the spray-penetration distances at the moments of SOC and wall impingement, respectively. Both parameters are included in the appendix. When the relative spray penetration is less than unity, no wall impingement occurs. On the other hand, when it becomes larger than unity, the fuel sprays reach the walls before ignition. Thus, the extent of wall impingement increases as this parameter becomes larger and larger than unity.

Several features are apparent from Fig. 10. Both the re-entrant and 18.5-CR shallow bowls have high degrees of spray overpenetration at the SOC. This can be seen clearly from the baseline points (solid symbols). The data seem to suggest that the trends of HC emission observed with different bowls are due to spray overpenetration. Indeed, the data collected at variable speeds also support this explanation.

The data representing variable A/F also show good correlation between EIHC and S_{SOC}/S_{imp}, but they deviate substantially from the correlation for the speed effect. In particular, the trend that EIHC increases drastically with decreasing

Downloaded 01 Jun 2010 to 171.66.16.87. Redistribution subject to ASME license or copyright; see http://www.asme.org/terms/Terms_Use.cfm

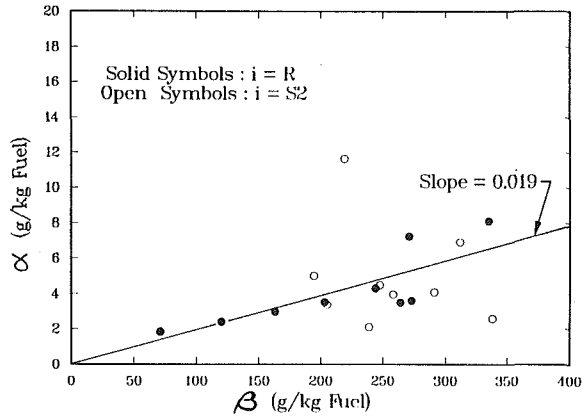


Fig. 11 Correlation between EIHC-$F_{f,l}$ and $F_{f,op}$ for the re-entrant and shallow bowls of 21.4 CR and for the shallow bowls of different CR

overpenetration for both the re-entrant and 18.5-CR shallow bowls is in contradiction to expectation. It appears that when A/F is varied, the gas temperature has a much stronger influence on HC emission than the spray overpenetration, as indicated by the data for the 21.4-CR shallow bowl. However, focusing only on the data points with the same A/F but different bowls, the previous conclusion still holds. The A/F effect will be discussed later in this section.

In order to quantify the effect of overpenetration with all the data, including the A/F variations, the relative differences in EIHC-$F_{f,l}$ and $F_{f,op}$ between different bowls are considered. The reason for examining EIHC-$F_{f,l}$ instead of EIHC is to isolate the effect of too-lean-mixing from the effect of overpenetration. The following parameters are defined for this analysis:

$$\alpha = (\text{EIHC} - F_{f,l})_i - (\text{EIHC} - (F_{f,l})_{\text{S1}} \tag{1}$$

and

$$\beta = (F_{f,op})_i - (F_{f,op})_{\text{S1}} \tag{2}$$

In equations (1) and (2), the subscript i denotes either the re-entrant bowl, R, or the shallow bowl with 18.5 CR, S2. Parameter α assumes that any fuel identified as mixed too lean to burn does not subsequently oxidize during the cycle. This analysis is based on the hypotheses that using the relative parameters can (1) minimize the effects of overmixing and undermixing due to speed variation, and (2) minimize the effect of temperature due to A/F variation.

The second hypothesis was proposed based on analysis that the bulk-gas absolute temperature for the two shallow bowls differed at most by 3 percent throughout the crank-angle degrees of interest. Thus the differences between the bulk-gas temperatures for different CR running at otherwise similar conditions are expected to contribute a rather small portion of the difference in EIHC observed (Fig. 7). To a first approximation, this contribution can be ignored. Then by using the relative parameter α, the effect of bulk quenching can be isolated from the effect of overpenetration and a correlation between α and β for different A/F becomes possible. The results of the correlation are shown in Fig. 11.

The solid symbols, which represent the relative differences between the re-entrant and shallow bowls of the same CR, show a good linear correlation. Also included in Fig. 11 are the results obtained from the same analysis for the shallow bowls of different CR (open symbols). The data for the shallow bowls show much larger scatter. However, the data points follow essentially the same trend, suggesting the validity of the hypotheses and that the HC variations due to differences in overpenetration have been successfully isolated from the other effects. Least-squares fit of the data with a straight line through the origin is also shown in Fig. 11 and has a correlation coefficient of 0.50. The slope of the straight line suggests that about 1.9 percent of the total overpenetrated fuel at the SOC is emitted from the engine as unburned HC either due to local bulk quenching or due to incomplete combustion. The majority of the overpenetrated fuel will eventually be oxidized during the combustion process.

The correlation given in Fig. 11 involves the calculated results for the too-lean-mixed fuel fraction. A sensitivity study on the choice of the lean flammability limit was made to check its effect on the correlation. When a lean flammability limit of 0.3 was used, in contrast to 0.6, essentially the same correla-

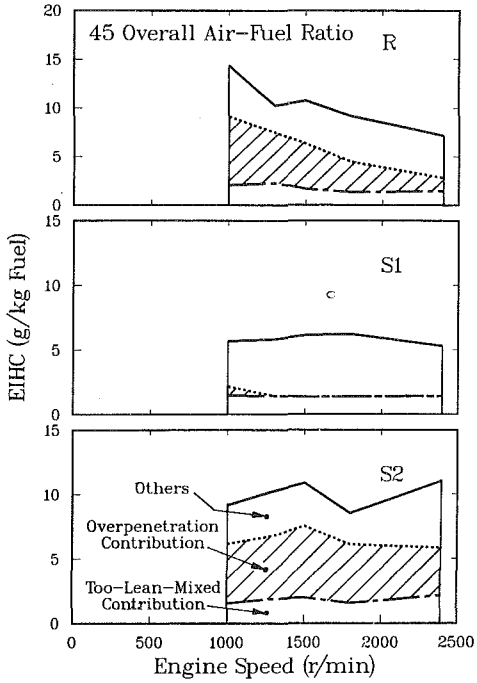


Fig. 12 Sources of HC emission for all three bowls at 45 A/F

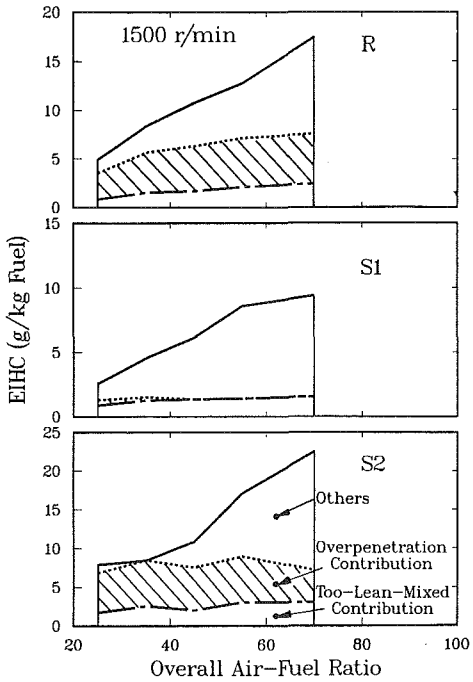


Fig. 13 Sources of HC emission for all three bowls at 1500 rpm

Downloaded 01 Jun 2010 to 171.66.16.87. Redistribution subject to ASME license or copyright; see http://www.asme.org/terms/Terms_Use.cfm

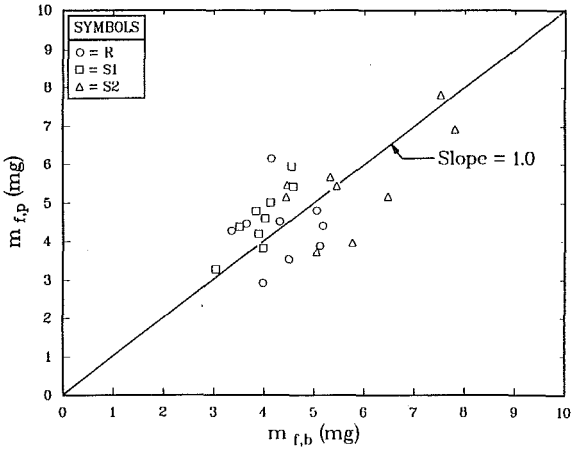


Fig. 14 Correlation between the measured mass of premixed-burned fuel and calculated mass of burnable fuel at the start of combustion for the effects of bowl geometry, compression ratio, speed, and A/F

tion was obtained except for a slight difference in the least-squares-fit slope (0.020 versus 0.019). There are two reasons for the insensitivity of the final correlation to the calculated too-lean-mixed fuel. First, the too-lean-mixed fuel constitutes only a small fraction of the measured EIHC for the engine examined. Second, the influence of the calculated too-lean-mixed fuel on the correlation is further reduced since a relative parameter is employed in the correlation. It is expected that the rich flammability limit has a stronger influence on the correlation. This question is examined in the next section by comparing the calculated burnable fuel mass with the measured premixed-burned fuel mass.

Finally, with the calculated too-lean-mixed fuel and the correlation of overpenetrated fuel with HC emission, the contribution of these two sources to the HC emission can be estimated. The results are shown in Figs. 12 and 13 for the re-entrant (R), 21.4-CR shallow (S1), and 18.5-CR shallow (S2) bowls, respectively. In each figure, the area under the chain-dashed line corresponds to the contribution due to too-lean-mixed fuel. The shaded region is due to the overpenetrated fuel. In the extreme case of heavy load for the 18.5-CR shallow bowl S2, a maximum of 65 percent of the total HC emission could come from spray overpenetration alone, which points to the importance of a proper combustion-system match at all operating conditions. The remaining EIHC can be attributed to the other sources, including the bulk-quenching effect noted earlier.

In summary, this section demonstrates clearly that for a better understanding of the observed HC emissions, consideration of both the spray and its interactions with the in-cylinder airflows is needed. In addition, the importance of bulk quenching is highlighted, particularly at light-load conditions.

Comparison of the Calculated Burnable Fuel With Measured Data. In the spray calculations, the lean and rich flammability limits of 0.6 and 3.0, as suggested by Henningsen [3], were used. An assessment follows to show that these choices were proper. The working hypothesis is that the calculated burnable fuel during the ignition-delay period is fully consumed during the premixed-burning stage. Thus, the calculated burnable fuel mass can be correlated with the premixed-burned fuel mass estimated from heat-release analysis of pressure–time data.

The appendix summarizes the calculated mass of burnable fuel at SOC ($m_{f,b}$) together with the measured mass of premixed-burned fuel ($m_{f,p}$). Figure 14 shows the correlation between the measured premixed-burned fuel mass and calculated burnable fuel mass. A least-squares fit gives a straight line with a slope of 1.0. Since the data scatter is completely random, it can be concluded that the choice of the rich flammability is quite acceptable. It can also be concluded that with this rich flammability limit, a reasonably good estimate of the premixed-burned fuel can be calculated using the gas-jet model.

Summary and Conclusions

A previously developed quasi-steady gas-jet model was applied to examine the spray penetration and deflection in swirling flow in an open-chamber diesel engine. The air-flow fields in the engine during the ignition-delay period computed from a two-dimensional flow code were coupled with the spray calculations. In addition to the spray penetration and deflection, fractions of too-lean-mixed, burnable, and overpenetrated fuel at the start of combustion were calculated. The penetration and deflection parameters, and the fuel fractions, were correlated with measured exhaust HC emissions.

The main findings from this study were:

1 A wide and shallow bowl with 21.4 compression ratio had the smallest amount of overpenetrated fuel at the start of combustion for all engine speeds and overall air–fuel ratios examined. This suggests that this bowl has the potential for low HC emission.

2 At the same intake swirl level, the spray deflection in the re-entrant bowl was much larger than in the shallow bowl because of the difference in air-swirl velocity inside the combustion bowl resulting from the difference in squish area.

3 Increasing engine speed increased the spray deflection in the swirl direction mainly due to an increase in the air-swirl momentum.

4 A linear correlation was observed between the cumulative quantity of fuel that overpenetrated during ignition delay and the exhaust HC emission. The correlation indicated that approximately 2 percent of the overpenetrated fuel at the start of combustion was emitted from the engine as unburned HC. In extreme cases, this could account for up to 65 percent of the total HC emission from this engine.

5 The model calculations indicated that possibly 10 to 30 percent of the toal HC emission is caused by the too-lean-mixed fuel during the ignition-delay period.

6 Using a rich flammability limit of 3.0, good agreement was obtained between the calculated burnable fuel fraction at the start of combustion and the premixed-burned fuel fraction calculated from heat-release analysis of pressure–time data.

7 Neither the ignition delay nor the relative spray-penetration parameter, defined as the ratio of the spray-penetration distances at the moments of start of combustion and wall impingement, could explain all the measured trends. In particular, the measured HC emissions increased with increasing ignition delay when overall air–fuel ratio was increased but either increased or decreased with ignition delay when the speed was increased, depending on the bowl geometry. As for the relative spray-penetration parameter, the data at various speeds indicated that HC emissions increased with increasing relative spray-penetration parameter, but the data at various overall air–fuel ratios showed just the opposite trend.

Acknowledgments

The authors thank Mr. S. R. McEwen and Mr. G. A. Silvas for their help in collecting engine data and Dr. T. Ahmad for many valuable discussions.

References

1 Greeves, G., Khan, I. M., Wang, C. H. T., and Fenne, I., "Origins of Hydrocarbon Emissions From Diesel Engines," *SAE Transactions*, Vol. 86, Section 2, 1977, pp. 1235–1251.

Downloaded 01 Jun 2010 to 171.66.16.87. Redistribution subject to ASME license or copyright; see http://www.asme.org/terms/Terms_Use.cfm

2 Yu, R. C., Wong, V. W., and Shahed, S. M., "Sources of Hydrocarbon Emissions From Direct Injection Diesel Engines," *SAE Transactions*, Vol. 89, Section 1, 1980, pp. 324-335.

3 Henningsen, S., "Hydrocarbon Emissions From the Ignition-Delay Period in a Direct-Injection Diesel Engine," *SAE Transactions*, Vol. 93, Section 6, 1984, pp. 28-40.

4 Yu, R. C., Kuo, T.-W., Shahed, S. M., and Chang, T. W., "The Effect of Mixing Rate, End of Injection, and Sac Volume on Hydrocarbon Emissions From a D.I. Diesel Engine," *SAE Transactions*, Vol. 92, Section 3, 1983, pp. 843-857.

5 Matsui, Y., and Sugihara, K., "Sources of Hydrocarbon Emissions From a Small Direct Injection Diesel Engine," *JSAE Review*, Vol. 7, No. 3, 1986, pp. 4-11.

6 Cartellieri, W., and Tritthart, P., "Particulate Analysis of Light Duty Diesel Engines (IDI & DI) With Particular Reference to the Lube Oil Particulate Fraction," *SAE Transactions*, Vol. 93, Section 3, 1984, pp. 134-149.

7 Haupais, A., "A Phenomenological Approach of Combustion Modeling in DI Diesel Engines," I. Mech. E. Paper C128/82, 1982.

8 Kuo, T.-W., and Wu, K.-J., "Effects of Piston-Bowl Geometry on Combustion Characteristics of a Direct-Injection Diesel Engine," Central States Section of the Combustion Institute, Paper No. 1, Chicago, IL, May 1987.

9 Cichocki, R., and Cartellieri, W., "The Passenger Car Direct Injection Diesel—A Performance and Emissions Update," SAE Paper 810480, 1981.

10 Sinnamon, J. F., Lancaster, D. R., and Steiner, J. C., "An Experimental and Analytical Study of Engine Fuel Spray Trajectories," *SAE Transactions*, Vol. 89, Section 1, 1980, pp. 765-785.

11 Ricou, F. P., and Spalding, D. B., "Measurements of Entrainment by Axisymmetric Turbulent Jets," *Journal of Fluid Mechanics*, Vol. 9, 1961, pp. 21-32.

12 Cloutman, L. D., Dukowicz, J. K., Ramshaw, J. D., and Amsden, A. A., "CONCHAS-Spray: A Computer Code for Reactive Flows With Fuel Sprays," Los Alamos National Laboratory Report No. LA-9294-MS, 1982.

APPENDIX

Summary of Measured and Calculated Parameters

Case	Bowl Geometry*	Compression Ratio (CR)	Speed (r/min)	Nominal Overall Air-Fuel Ratio (A/F)	t_{id} (°CA)	t_{inj} (°CA)	Fuel/ Cycle (mg)	V_{inj} (m/s)	$F_{f,p}$ (g/kg)	EIHC (g/kg Fuel)	t_{imp} (ms)	S_{imp} (mm)	t_{SOC} (ms)	S_{SOC} (mm)	$F_{f,i}$ (g/kg)	$F_{f,b}$ (g/kg)	$F_{f,op}$ (g/kg)	$m_{f,b}$ (mg)	$m_{f,p}$ (mg)
1	R	21.4	1000	45	3.8	4.0	10.7	105	413	14.39	0.394	22.1	0.633	28.4	2.06	484.6	372.0	5.17	4.41
2	R	21.4	1300	45	4.4	4.8	10.7	109	364	10.26	0.395	22.6	0.564	27.4	2.28	479.0	273.0	5.11	3.88
3	R	21.4	1500	45	4.4	5.0	10.7	122	424	10.75	0.354	22.6	0.489	26.9	1.66	403.7	244.0	4.31	4.52
4	R	21.4	1800	45	4.8	6.1	10.7	122	418	9.14	0.354	22.6	0.444	25.5	1.33	342.2	163.0	3.65	4.46
5	R	21.4	2400	45	6.3	9.2	10.7	112	400	7.15	0.393	23.6	0.438	25.1	1.45	314.1	71.0	3.35	4.27
6	S1	21.4	1000	45	4.1	4.1	10.7	100	470	5.68	0.658	28.6	0.683	29.2	1.45	386.5	37.0	4.13	5.01
7	S1	21.4	1300	45	4.6	4.9	10.7	109	431	5.81	0.613	28.6	0.590	28.1	1.42	377.3	0.0	4.02	4.60
8	S1	21.4	1500	45	4.3	4.5	10.7	134	449	6.13	0.495	28.6	0.478	28.1	1.34	359.5	0.0	3.84	4.79
9	S1	21.4	1800	45	5.3	5.7	10.7	131	393	6.21	0.511	28.6	0.491	27.9	1.36	364.5	0.0	3.89	4.19
10	S1	21.4	2400	45	8.0	8.7	10.7	119	357	5.29	0.569	28.6	0.556	28.1	1.41	372.7	0.0	3.98	3.81
11	S2	18.5	1000	45	4.5	4.0	10.7	102	511	9.15	0.589	28.2	0.750	32.1	1.55	417.5	242.0	4.46	5.45
12	S2	18.5	1300	45	5.4	4.4	10.7	119	531	10.24	0.545	29.1	0.692	33.0	1.89	497.0	258.2	5.32	5.67
13	S2	18.5	1500	45	5.9	5.0	10.7	122	510	10.88	0.495	28.1	0.656	32.7	2.00	510.9	291.0	5.45	5.44
14	S2	18.5	1800	45	7.1	6.3	10.7	116	483	8.52	0.518	28.2	0.657	32.0	1.57	416.5	238.7	4.44	5.15
15	S2	18.5	2400	45	9.1	8.0	10.7	123	371	11.05	0.525	29.2	0.632	32.3	2.16	540.4	194.4	5.76	3.96
16	R	21.4	1500	25	3.8	8.0	20.2	147	304	4.90	0.298	22.4	0.422	27.0	0.83	205.4	142.0	4.15	6.15
17	R	21.4	1500	35	4.3**	6.3	14.4	132	333	8.35	0.328	22.6	0.478	27.7	1.52	350.0	217.0	5.05	4.81
18	R	21.4	1500	55	4.5	4.5	9.1	117	387	12.77	0.369	22.6	0.500	26.7	2.12	494.3	264.0	4.50	3.53
19	R	21.4	1500	70	5.0	4.2	7.1	99	410	17.50	0.433	22.5	0.556	25.8	2.44	559.0	271.0	3.98	2.92
20	S1	21.4	1500	25	4.4	8.2	20.2	143	294	2.56	0.469	28.4	0.489	29.0	0.87	225.0	22.0	4.55	5.94
21	S1	21.4	1500	35	4.3	5.9	14.4	142	375	4.56	0.469	28.6	0.478	28.9	1.24	316.5	14.0	4.58	5.42
22	S1	21.4	1500	55	4.3	4.3	9.1	123	481	8.57	0.545	28.6	0.478	26.7	1.40	384.7	0.0	3.51	4.38
23	S1	21.4	1500	70	5.3	4.3	7.1	95	460	9.39	0.712	28.5	0.589	25.8	1.55	427.9	0.0	3.04	3.27
24	S2	18.5	1500	25	5.9	8.1	20.2	145	386	7.90	0.417	28.1	0.656	35.6	1.72	371.6	269.5	7.52	7.80
25	S2	18.5	1500	35	6.3	6.3	14.4	132	479	8.47	0.456	28.1	0.700	35.4	2.57	540.9	352.1	7.81	6.92
26	S2	18.5	1500	55	6.7	4.8	9.1	132	567	17.11	0.582	29.1	0.744	33.2	3.04	710.0	311.7	6.47	5.17
27	S2	18.5	1500	70	7.2	4.4	7.1	94	523	22.52	0.695	29.1	0.800	31.3	3.05	710.4	218.7	5.05	3.72

Start of combustion: TDC

* see Figure 2 and Table 2

** For this particular case, the SOC was 1° CA BTDC according to the measured cylinder-pressure data

Downloaded 01 Jun 2010 to 171.66.16.87. Redistribution subject to ASME license or copyright; see http://www.asme.org/terms/Terms_Use.cfm

The Application of Availability and Energy Balances to a Diesel Engine

A. C. Alkidas
Engine Research Department,
General Motors Research Laboratories,
Warren, MI 48090

The maximum power that can be extracted from an engine operating at a given condition was determined by means of analyses based on the first and second laws of thermodynamics. These analyses were applied to a heavy-duty single-cylinder open-chamber diesel engine operated at constant speed. Over the range of operating conditions investigated, the second-law efficiency (ratio of brake power to maximum extractable power) of the engine, which increased with engine load, was found to vary from 22 to 50 percent. It was concluded that besides heat transfer, the combustion process was the most important source of irreversibility and accounted for 25 to 43 percent of the lost power.

Introduction

The traditional first-law analysis of a system, although it may enable one to determine how the energy is distributed across the boundaries of the system, does not provide the means for evaluating the energy degradation that causes a reduction in work output of the system. The issue of maximum extractable work output (availability) from a system at a given thermodynamic state and in a given environment can be addressed by a second-law analysis.

At present, the concept of availability is well documented in a number of research publications [1–5] and textbooks [6–9], and an ever-increasing amount of work appears in the literature on the application of second-law analysis to practical problems [10–13]. In the field of internal-combustion engines, very recently Flynn and co-workers [14–17] utilized second-law analyses to evaluate various potentially promising concepts such as turbocharging, turbocompounding, charge-air cooling, thermal insulation, and the implementation of bottoming cycles for exhaust-energy utilization.

In this work of Flynn and co-workers [14–17], as well as in an earlier study by Patterson and Van Wylen [18], the availability calculations were coupled to a theoretical simulation model of the engine cycle, which was based on first-law analysis. Thus the availability losses of the various processes during the engine cycle were examined. In contrast, the present study deals with the overall availability balance of an engine, which, as in previous studies of engine energy balance [19–21], relies on experimental measurements and provides an overall characterization of the loss of availability of the engine.

The present study seeks to answer the following questions: First, what is the maximum work that can be extracted from the engine for a given engine test condition and how does it vary with changes in load and speed? Second, for an experimentally determined thermodynamic state of the exhaust gases, what is the maximum work that can be achieved by an exhaust-energy-utilization device?

First- and second-law analyses were applied to a single-cylinder open-chamber diesel engine run at constant speed. Besides comparing the overall availability losses from the engine, an attempt was made to isolate and quantify the various sources of loss of availability.

First- and Second-Law Analysis of an Engine

Figure 1 shows the engine as an open thermodynamic system. Air and fuel enter the combustion chamber of the engine, where they react to produce an output shaft power (brake power) $\dot{W}_s$, and then the products of combustion and

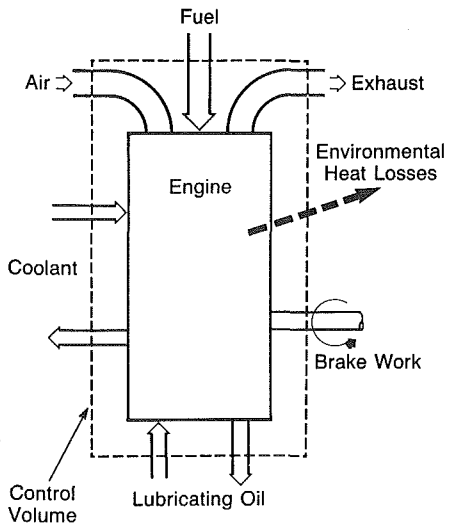


Fig. 1 *The engine as a thermodynamic open system*

Contributed by the Internal Combustion Engine Division and presented at the Eleventh Annual Energy-Sources Technology Conference and Exhibition, New Orleans, Louisiana, January 10–13, 1988. Manuscript received by the Internal Combustion Energy Division April 1987.

Copyright © 1988 by ASME
Downloaded 01 Jun 2010 to 171.66.16.87. Redistribution subject to ASME license or copyright; see http://www.asme.org/terms/Terms_Use.cfm

the excess air leave the system as exhaust in the atmosphere. Cooling water and lubricating oil enter and exit the engine system. For the control volume defined in Fig. 1, the only heat exchange occurs between the engine and the environment, Q_{ENV}. The temperature of the environment T_{ENV} is assumed to be equal to the standard temperature of the environment T_e.

The maximum shaft power that can be extracted from the system is

$$\dot{W}_{s,\max} = \dot{m}_A b_A + \dot{m}_F b_F + \dot{m}_W (b_{W,IN} - b_{W,OUT}) + \dot{m}_O (b_{O,IN} - b_{O,OUT}) - \dot{m}_{EX} b_{EX} \quad (1)$$

The basic equations of the second-law analysis are given in Appendix A and the symbols used throughout this paper are defined in the nomenclature. Details for the evaluation of the thermodynamic properties of the gases are presented in Appendix B.

Considering the water-cooling and lubricating-oil circuits individually as thermodynamic open systems, one can show that

$$\dot{m}_i (b_{i,IN} - b_{i,OUT}) = \dot{Q}_i \left[1 - \frac{T_e}{\bar{T}_i}\right] \quad \text{for } i = W, 0 \quad (2)$$

where

$$\bar{T}_i \simeq (T_{i,IN} + T_{i,OUT})/2 \quad (3)$$

Substituting equation (2) into (1) and redefining terms yields

$$\dot{W}_{s,\max} = \dot{m}_a b_a + \dot{m}_F b_F - (\dot{m}_a + \dot{m}_F) b_{EX} + \dot{Q}_W \left(1 - \frac{T_e}{\bar{T}_W}\right) + \dot{Q}_O \left(1 - \frac{T_e}{\bar{T}_O}\right) \quad (4)$$

Equation (4) can be written for the thermodynamic system represented in Fig. 2. In this system, three heat exchanges occur: one with the cooling circuit at constant temperature $\bar{T}_W$, one with the lubricating-oil circuit at constant temperature $\bar{T}_O$, and the last one with the environment at constant temperature T_e.

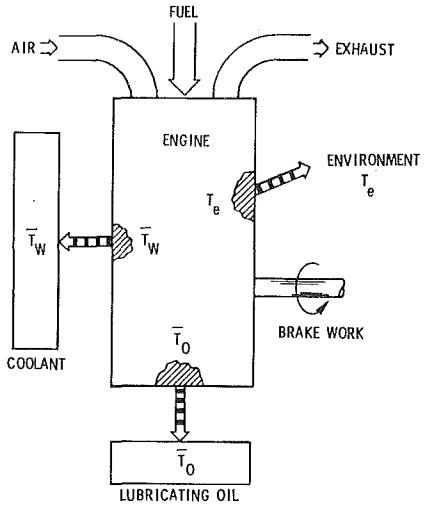


Fig. 2 An equivalent thermodynamic open system for the engine

For the open system of Fig. 2, which is equivalent to the open system of Fig. 1, the equation for $\dot{W}_{s,\max}$ may be written as

$$\dot{W}_{s,\max} = A_{INT} + A_{FUEL} + A_W + A_O - A_{EX} \quad (5)$$

where

$$A_{INT} = \dot{m}_F a_F + \dot{m}_A a_A \quad (6)$$

$$A_{FUEL} = (\dot{m}_F + \dot{m}_A) a_{FUEL} \quad (7)$$

$$A_J = \dot{Q}_J \left(1 - \frac{T_e}{T_J}\right) \quad \text{for } J = W, 0 \quad (8)$$

and

$$A_{EX} = (\dot{m}_F + \dot{m}_A) a_{EX} \quad (9)$$

For the thermodynamic system of Fig. 2, the corresponding energy equation (first-law analysis) is

Nomenclature

a = specific availability (exergy) defined in equation (A5)
A = availability
b = specific availability function defined in equation (A2)
c = specific heat of an incompressible fluid
c_p = specific heat at constant pressure
$\dot{E}_{EX}$ = exhaust power
h = specific enthalpy
h_f^o = specific enthalpy of formation at T_o
I = irreversibility
K = thermal conductivity
$\dot{m}$ = mass flow rate
n_i = number of moles of species i
N = engine speed
p = pressure
$\dot{P}_s$ = rate of entropy production
$\dot{Q}$ = rate of heat transfer
R = universal gas constant
s = specific entropy
T = temperature
$\bar{T}$ = defined in equation (3)
u = specific internal energy
v = specific volume
$\dot{W}_{EX,\max}$ = maximum power that can be extracted from exhaust
$\dot{W}_{lost}$ = lost power defined by equation (A4)
$\dot{W}_s$ = shaft power
$\dot{W}_{s,\max}$ = maximum achievable shaft power
Y_i = mass fraction of species i
$\alpha_{i,j}$ = polynomial coefficients for enthalpy expression
ΔH^o = lower heating value of fuel
η_{EX} = exhaust efficiency defined by equation (15)
η_I = first-law efficiency defined by equation (13)
η_{II} = second-law efficiency defined by equation (11)

Subscripts

A = air
e = standard atmosphere
ENV = environment
EX = exhaust
F = fuel
i = species
IN = in
INT = intake
o = standard conditions
O = oil
OUT = out
p = products
r = reactants
W = water

Downloaded 01 Jun 2010 to 171.66.16.87. Redistribution subject to ASME license or copyright; see http://www.asme.org/terms/Terms_Use.cfm

Table 1 Engine Specifications

Bore (mm)	130
Stroke (mm)	153
Connecting Rod Length (mm)	276
Displacement (L)	2.0
Compression Ratio	16:1
Unit Injector:	
No. of Nozzles	8
Nozzle Diameter (mm)	0.25
Included Angle (deg)	160

Table 2 Energy and availability balances for $N = 1200$ rpm

	1083 kPa		155 kPa	
BMEP	kW	%*	kW	%
ENERGY BALANCE				
Input				
Fuel	57.21	--	14.47	--
Intake	0.00	0.0	0.00	0.0
Oil	2.00	-3.5	2.93	20.2
TOTAL	59.21		17.40	
Output				
Brake	21.99	38.4	3.14	21.7
Exhaust	23.02	40.3	5.76	39.8
Coolant	7.17	12.5	4.09	28.3
Environment	7.03	12.3	4.41	30.5
TOTAL	59.21		17.40	
AVAILABILITY BALANCE				
Input				
Fuel	56.12	--	14.73	--
Intake	1.95	3.5	0.20	1.4
Oil	0.41	0.7	0.59	4.0
TOTAL	58.48		15.52	
Output				
Brake	21.99	39.2	3.14	21.3
Exhaust	10.65	19.0	1.95	13.3
Coolant	1.14	2.0	0.64	4.4
Environment	--	--	--	--
TOTAL	33.78		5.73	
Lost	24.70	44.0	9.79	66.5

*% of fuel energy or availability

$$\dot{W}_s = \dot{m}_F \Delta H^o + \dot{Q}_W + \dot{Q}_O + \dot{Q}_{\text{ENV}} - \dot{E}_{EX} \tag{10}$$

where $\dot{E}_{EX}$, termed the "exhaust power," is equal to the difference in the sensible enthalpies of the exhaust and intake stream per unit time. Equation (10) follows the usual thermodynamics sign convention, which assigns a negative value to heat transfer out of the system. To characterize the departure of the system from the reversible limit $\dot{W}_{s,\max}$, one may define the second-law efficiency as

$$\eta_{\text{II}} = \frac{\dot{W}_s}{\dot{W}_{s,\max}} = 1 - \frac{\dot{W}_{\text{lost}}}{\dot{W}_{s,\max}} \tag{11}$$

where the lost power is defined as

$$\dot{W}_{\text{lost}} = \dot{W}_{s,\max} - \dot{W}_s \tag{12}$$

The thermal efficiency of a heat engine must have values less than 1 because of the second law of thermodynamics, whereas the second-law efficiency could attain a maximum value of 1. To distinguish from the second-law efficiency, the thermal efficiency of the system is termed first-law efficiency and is defined as

$$\eta_{\text{I}} = \frac{\dot{W}_s}{\dot{m}_F(\Delta H^o)} \tag{13}$$

where $\dot{m}_F$ is mass flow rate of the fuel and ΔH^o is its lower heating value, expressed on a mass basis.

Table 3 Energy and availability balances for $N = 1800$ rpm

	1083 kPa		155 kPa	
BMEP	kW	%*	kW	%
ENERGY BALANCE				
Input				
Fuel	86.78	--	25.11	--
Intake	0.00	0.0	0.00	0.0
Oil	1.33	1.5	2.55	10.2
TOTAL	88.11		27.66	
Output				
Brake	32.98	38.0	4.71	18.8
Exhaust	39.47	45.5	11.87	47.3
Coolant	8.55	9.9	4.47	17.8
Environment	7.11	8.2	6.61	26.3
TOTAL	88.11		27.66	
AVAILABILITY BALANCE				
Input				
Fuel	88.61	--	25.48	--
Intake	4.62	5.2	0.39	1.5
Oil	0.28	0.3	0.53	2.1
TOTAL	93.51		26.40	
Output				
Brake	32.98	37.2	4.71	18.5
Exhaust	19.47	22.0	4.61	18.1
Coolant	1.34	1.5	0.71	2.8
Environment	--	--	--	--
TOTAL	53.79		10.03	
Lost	39.72	44.8	16.37	64.2

*% of fuel energy or availability

Experimental Program

The tests were performed in an experimental single-cylinder open-chamber diesel engine. Its specifications are listed in Table 1.

The operating conditions of the engine were chosen to simulate operation of a turbocharged afercooled engine. The tests were run at speeds of 1200 and 1800 rpm, at a fixed static injection timing of 8 deg BTDC, and at various loads. For all operating conditions the intake air, cooling water and lubricating oil were maintained at constant temperatures of about 49, 82, and 94°C respectively, by means of external heat exchangers.

The measurements included heat rejections to the coolant and to the lubricating oil, intake and exhaust temperatures, brake power, intake-air and fuel flow rates, and exhaust emissions.

Results

Energy and corresponding availability balances for the water-cooled engine are listed in Tables 2 and 3 for two load conditions (BMEP = 1083 and 155 kPa) for engine speeds of 1200 and 1800 rpm. Because of the relatively large external surface area of the single-cylinder engine, heat had to be add-

Downloaded 01 Jun 2010 to 171.66.16.87. Redistribution subject to ASME license or copyright; see http://www.asme.org/terms/Terms_Use.cfm

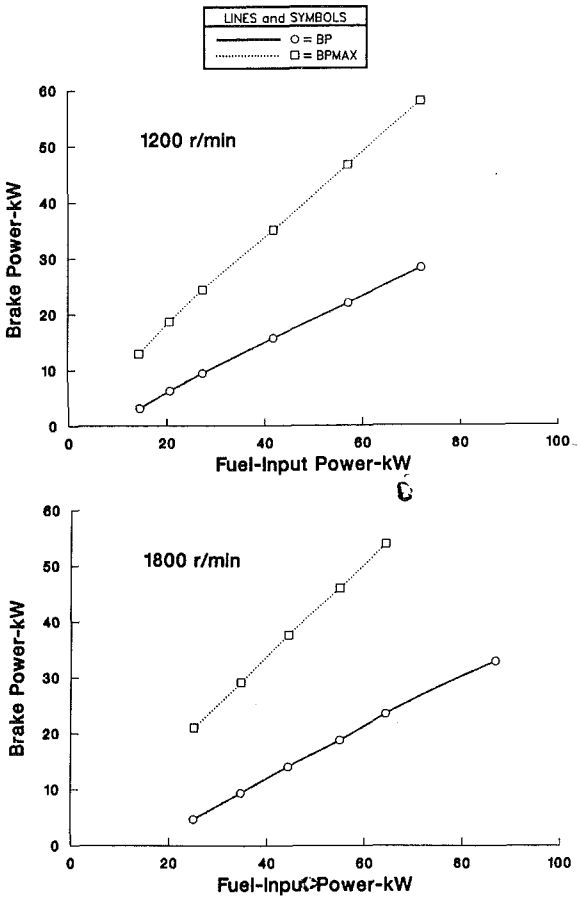


Fig. 3 Variations of maximum brake power and brake power with fuel-input power

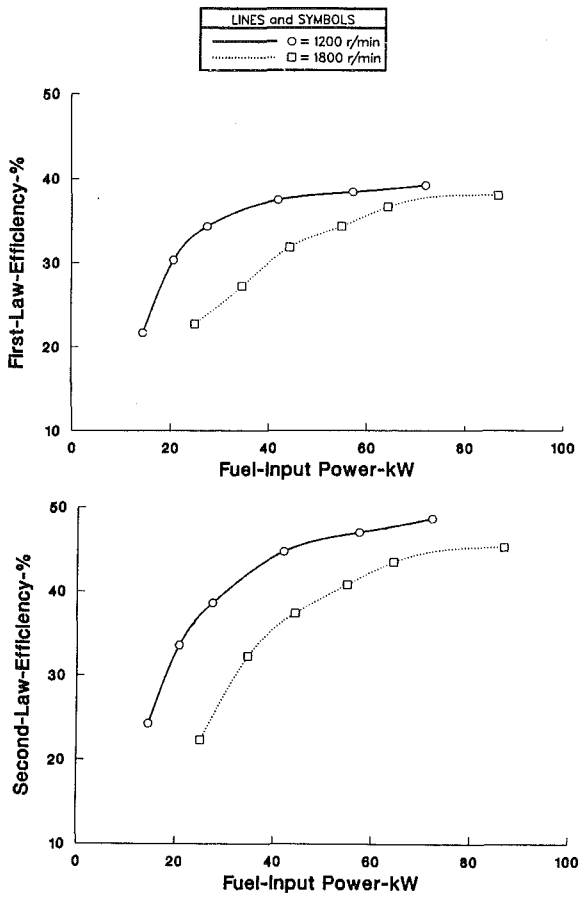


Fig. 4 Variations of the first- and second-law efficiencies with fuel-input power

ed to maintain the prescribed high inlet temperature of the lubricating oil, which was controlled to 94°C with an external heat exchanger.

Several significant observations can be made from these results. First the environmental heat losses represent a significant fraction of the fuel-input energy. This is an artifact of the single-cylinder engine, which has a relatively large surface area per cylinder in comparison to a multicylinder engine.

The second observation that one can make is that the net availability of the three heat-rejection processes (coolant, oil, and environment), expressed as percent of the fuel availability, is small despite the fact that these processes represent a significant fraction of the fuel energy. However, this in not entirely unexpected because the conversion of chemical energy to heat energy is considered an energy-degrading process [7].

Next to the brake-power availability, the exhaust availability is the most important. However, the availability of the exhaust gases in all cases shown in Tables 2 and 3 appears to be less than half of the corresponding energy of the exhaust gases. Consequently, less than half of the energy of the exhaust gases can be used to produce useful work.

Finally, the availability loss, which is a result of the irreversibilities of the system, such as heat transfer, friction, mixing, and combustion, appears to be very significant. This is especially true at the light loads, where it is the predominant term. The absolute value of lost power increases with increasing fuel-input power. This is clearly demonstrated in Fig. 3, which shows the variations of brake power and maximum attainable brake power with fuel-input power for engine speeds of 1200 and 1800 rpm. These results show that, for both engine speeds examined, the brake power and the maximum attainable brake power varied roughly linearly with fuel-input power. In addition, the difference between the above two powers, which was termed lost power, increased with increasing fuel-input power. The consequence of this is that the various irreversibilities of the system, such as friction, heat transfer, mixing, and combustion, which are responsible for the lost power, increased with increasing fuel-input power.

Figure 4 shows the variation of first- and second-law efficiencies of the engine with fuel-input power for engine speeds of 1200 and 1800 rpm. Both efficiencies show similar behaviors with variation in fuel-input power. For the range of values of the fuel-input power examined and for both engine speeds, the first- and second-law efficiencies increased at a decreasing rate with increasing fuel-input power. Furthermore, for a given fuel-input power, both efficiencies were significantly higher at the lower engine speed examined.

Both efficiencies increased with increasing fuel-input power because friction does not increase significantly with engine load and because the relative contribution of heat transfer is reduced with increasing load despite the fact that the absolute value of heat transfer increases with load. For the operating conditions of the engine examined, the first-law efficiency varied from about 22 to 39 percent, whereas the second-law efficiency varied from 22 to 48 percent.

One of the objectives of this study was to evaluate the energy availability of the exhaust stream of the engine. The maximum amount of power that can be obtained from an exhaust stream in a thermodynamic state defined by subscript EX is

$$\dot{W}_{EX,\max} = \dot{m}(b_{EX} - b_e) = \dot{m}a_{EX} \tag{14}$$

Figure 5 shows exhaust power, maximum extractable power, and "actual" turbine power[1] as functions of fuel-

[1] Power produced by the simulated turbine.

Downloaded 01 Jun 2010 to 171.66.16.87. Redistribution subject to ASME license or copyright; see http://www.asme.org/terms/Terms_Use.cfm

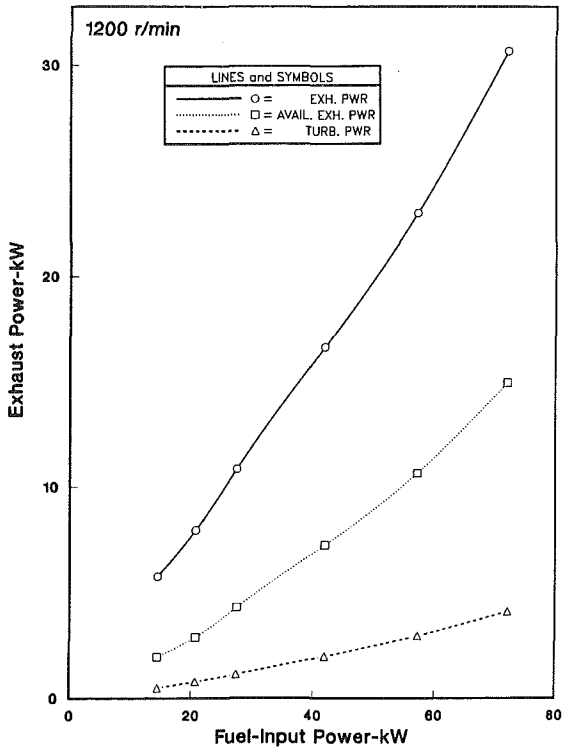


Fig. 5 Exhaut-power-utilization potential of the diesel engine

input power for an engine speed of 1200 rpm. It is apparent that generally the maximum extractable power is less than 50 percent of the exhaust energy and that the "actual" power generated by the turbine is less than 30 percent of the maximum extractable power. This suggests that only a small fraction of the exhaust power may be utilized for useful work. Defining an exhaust efficiency as

$$\eta_{EX} = \frac{\dot{W}_{EX,\max}}{\dot{E}_{EX}} \tag{15}$$

Table 4 shows exhaust-efficiency comparisons for the two engine speeds considered

Sources of Irreversibility

The irreversibility I of the engine system shown in Fig. 2, which is synonymous with the lost power or the rate of destruction of availability of the engine, may be computed from the following equation:

$$I = T_e(\dot{m}_{EX}s_{EX} - \dot{m}_A s_A - \dot{m}_F s_F) - \sum Q_i \frac{T_e}{T_i} \tag{16}$$

The first term accounts for the internal irreversibilities of the system, and the second term accounts for the irreversibilities due to heat transfer processes across the boundary of the system.

Sources of internal irreversibility are viscous dissipation, heat transfer across a finite temperature gradient, turbulence, mixing, and combustion. Of these, combustion is believed to be the most important source of internal irreversibility. Using a grossly simplified mixing model, it was estimated that the irreversibility associated with air–fuel mixing in the combustion chamber of the engine represented less than 3 percent of the total irreversibilities of the cycle.

Heat Transfer. The irreversibility produced by heat transfer across the boundary of the system is given by

$$I = \Sigma Q_j \left(\frac{T_e}{T_j}\right) \tag{17}$$

Table 4 Maximum extractable exhaust power

BMEP kPa	$\dot{m}_F \Delta H^\circ$ kW	$E_{EX,\max}$ kW	η_{EX}
	1200 r/min		
1083	57.21	10.65	46.3
774	41.89	7.24	43.5
464	27..44	4.29	39.5
155	14.47	1.95	33.9
	1800 r/min		
1083	86.78	19.47	49.3
774	64.27	13.56	46.7
464	44.32	8.62	43.3
155	25.11	4.61	38.8

Table 5 Irreversibilities due to heat transfer

Overall A/F	Fuel Power kW	Brake Power kW	Lost Power kW	Irreversibilities kW	Irreversibilities %
25.4	72.1	28.3	27.1	11.30	41.7
33.2	41.9	15.7	18.1	8.99	49.7
65.8	14.5	3.1	9.6	5.52	57.5

Table 6 Irreversibilities due to combustion

				Irreversibility			
				$(A/F)_{st}$		A/F	
Overall A/F	Fuel Power kW	Brake Power kW	Lost Power kW	kW	%*	kW	%*
25.4	72.1	28.3	27.1	11.6	43.0	14.1	52.1
33.2	41.9	15.7	18.1	7.3	40.5	8.9	49.2
65.8	14.5	3.1	9.6	2.4	24.7	3.7	38.2

*Percent of the Lost Power

where $j = W$, O, ENV. One should note that equation (17) accounts also for the heat generated by friction of the piston and crankshaft.

The irreversibilities due to heat transfer, as computed from equation (17), are shown in Table 5 for three different operating conditions of the STD engine. In these tests the engine speed was kept constant at 1200 rpm. The irreversibility due to heat transfer accounted for between 42 and 58 percent of the total irreversibility of the engine.

Combustion. Any system that undergoes a chemical reaction experiences loss of availability due to the irreversibility of the reaction process. In order to evaluate the combustion-generated irreversibilities in an engine, combustion was assumed to occur at constant pressure, and the products of combustion were assumed to be in chemical equilibrium. The reactants were assumed to be at a temperature and pressure that corresponded to those conditions of the in-cylinder air at the time of ignition. Because combustion in the diesel engine is considered to be predominantly diffusion controlled, two cases were considered. In the first case combustion of the fuel was assumed to occur at the stoichiometric composition (i.e., $A/F_{st} = 14.4$), and in the second case combustion of the fuel was assumed to occur at a composition corresponding to the overall air–fuel ratio of the engine.

The results of these computations for the three test conditions of the STD engine examined in Table 5 are summarized in Table 6. This table shows the combustion irreversibilities for the two combustion cases expressed as power loss and as percent of the total power loss. For stoichiometric combustion the combustion irreversibilities represented about 25 to 43 percent of the lost power. For combustion occurring at the overall stoichiometry of the mixture, the generated irreversibilities

Downloaded 01 Jun 2010 to 171.66.16.87. Redistribution subject to ASME license or copyright; see http://www.asme.org/terms/Terms_Use.cfm

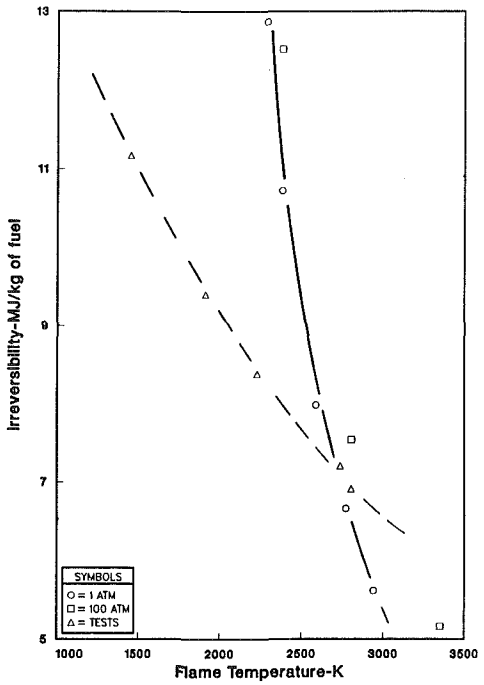


Fig. 6 Combustion-generated irreversibilities as functions of flame temperature

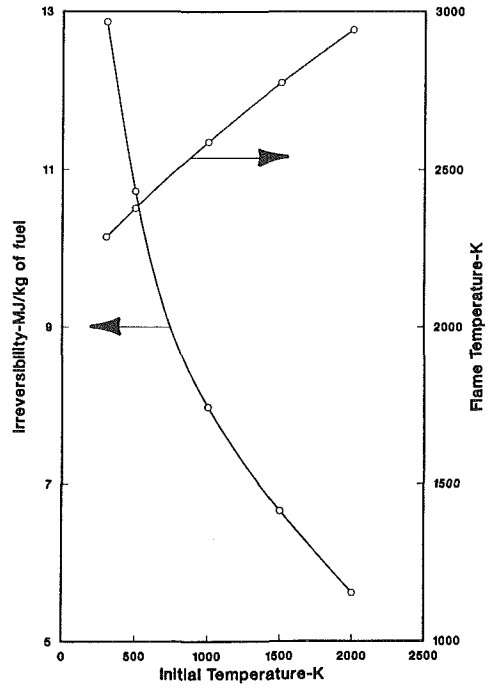


Fig. 7 Combustion-generated irreversibilities and corresponding flame temperature versus initial reactant temperature

represented about 38 to 52 percent of the lost power. The difference in irreversibilities of the two combustion cases is a result of the magnitude of the flame temperature (temperature of the products).

The results of Table 6 are also shown in Fig. 6, which is a plot of combustion-generated irreversibility per cycle per unit mass of fuel versus flame temperature. Also shown are computational results for the stoichiometric, isobaric, and adiabatic combustion of diesel fuel at pressures of 1 atm and 100 atm. The flame temperatures for these cases was altered by varying the initial temperature of the reactants from 298 K to 2000 K. These results indicate that the combustion irreversibility decreased with increasing flame temperature, although, as may be observed by the resulting changes with air-fuel ratio and pressure, irreversibility was not a unique function of flame temperature.

An alternative way of presenting some of the data is shown in Fig. 7, which is a plot of irreversibility and flame temperature as a function of initial temperature of the reactants. The computations shown in Fig. 7 are for stoichiometric combustion at a pressure of one atmosphere. It is apparent that increasing the temperature of the reactants increased the flame temperature, as expected, and decreased the combustion-generated irreversibilities. This is a *significant* result in engine application because it suggests that preheating the intake air or insulating the combustion-chamber walls of the engine, which result in an increase in flame temperature, should significantly decrease combustion-generated irreversibilities and consequently may improve the second-law efficiency of the process.[2] This result has also been arrived at by Rant [22], who investigated the influence of air preheating on the irreversibilities of combustion.

Summary and Conclusions

Based on the results of this study, which was performed on a single-cylinder open-chamber engine of 2-L displacement operating at constant speed, the following conclusions were reached:

1 The environmental heat losses were found to represent a significant fraction of the fuel-input energy. Typical values were 10 percent at high load and 30 percent at light load.

2 The first-law efficiency of the engine, defined as the ratio of brake power to input fuel power, varied from about 22 to 40 percent over the load range evaluated. This efficiency was found to increase with increasing engine load.

3 The second-law efficiency of the test diesel engine, defined as the ratio of brake power to the corresponding maximum extractable power, varied from about 22 to 48 percent over the load range evaluated. This efficiency was found to increase with increasing engine load.

4 Less than half of the energy of the exhaust gases can be utilized for production of useful work.

Several sources responsible for loss of availability of the engine system were examined. From magnitude estimates, it appears that besides friction, combustion is a very important source of irreversibility (loss of availability). The estimated percent of the power loss (maximum power – brake power) attributable to combustion-generated irreversibilities ranged from about 25 to 43 percent of the availability of the fuel for assumed stoichiometric equilibrium combustion. On the other hand, the irreversibilities due to heat transfer ranged from about 42 to 58 percent. The computations also showed that increasing the combustion temperature, as is the case in an uncooled engine, should significantly decrease the combustion-generated irreversibilities.

References

1 Haywood, R. W., "A Critical Review of the Theorems of Thermodynamics Availability With Concise Formulations," *J. Mech. Eng. Sci.*, Vol. 16, 1974, pp. 160–173, 258–267.

2 Clarke, J. M., and Horlock, J. H., "Availability and Propulsion," *J. Mech. Eng. Sci.*, Vol. 17, No. 4, 1975, pp. 223–232.

3 Brzustowski, T. A., "Toward a Second Law Taxonomy of Combustion Processes," *Energy*, Vol. 5, 1980, pp. 753–755.

4 De Nevers, N., and Seader, J. D., "Lost Work: A Measure of Thermodynamic Efficiency," *Energy*, Vol. 5, 1980, pp. 757–769.

[2] Athough preheating the intake air or thermally insulating the combustion chamber of an engine may result in higher combustion temperatures, these two processes are not equivalent and therefore should not be expected to have similar effects on the operation of an engine.

Downloaded 01 Jun 2010 to 171.66.16.87. Redistribution subject to ASME license or copyright; see http://www.asme.org/terms/Terms_Use.cfm

5 Sussman, M. V., "Steady-Flow Availability and the Standard Chemical Availability," *Energy*, Vol. 5, 1980, pp. 793–802.
6 Bruges, E. A., *Available Energy and the Second Law Analysis*, Butterworths Scientific Publications, London, 1959.
7 Moore, D. F., *Thermodynamic Principles of Energy Degrading*, The MacMillan Press, Ltd., London, 1981.
8 Bejan, A., *Entropy Generation Through Heat and Fluid Flow*, Wiley, New York, 1982.
9 Moran, M. J., *Availability Analysis: A Guide To Efficient Energy Use*, Prentice-Hall, Englewood Cliffs, NJ, 1982.
10 Gerkin, E. S., "Second Law Analysis of Fuel Consumption in Furnaces," *Energy*, Vol. 5, 1980, pp. 949–954.
11 Vakil, H. B., "Thermodynamic Analysis of Gas Turbine Cycles with Chemical Reactions," *Efficiency and Costing. Second Law Analysis of Processes*, R. A. Gaggioli, ed., ACS Symposium Series 235, American Chemical Soc. Washington, DC, 1983, pp. 105–117.
12 Horlock, J. H., and Haywood, R. H., "Thermodynamic Availability and Its Application to Combined Heat and Power Plant," *Proc. Inst. Mech. Engrs.*, Vol. 199, No. C1, 1985, pp. 11–17.
13 El-Masri, M. A., "On Thermodynamics of Gas-Turbine Cycles: Part 1—Second Law Analysis of Combined Cycles," ASME JOURNAL OF ENGINEERING FOR GAS TURBINES AND POWER, Vol. 107, 1985, pp. 880–889.
14 Flynn, P. F., Hoag, K. L., Kamel, M. M., and Primus, R. J., "A New Perspective on Diesel Engine Evaluation Based on Second Law Analysis," SAE Paper No. 840032, 1984.
15 Primus, R. J., "A Second Law Approach to Exhaust System Optimization ," SAE Paper No. 840033, 1984.
16 Primus, R. J., Hoag, K. L., Flynn, P. F., and Brands, M. C., "An Appraisal of Advanced Engine Concepts Using Second Law Analysis Techniques," I. Mech E., *International Conference on Fuel Efficient Power Trains and Vehicles*, Paper No. C440/84, 1984, pp. 73–87.
17 Primus, R. J., and Flynn, P. F., "Diagnosing the Real Performance Impact of Diesel Engine Design Parameter Variation (a Primer in the Use of Second Law Analysis)," *International Symposium on Diagnostics and Modeling of Combustion in Reciprocating Engines*, 1985, pp. 529–538.
18 Patterson, D. J., and Van Wylen, G., "A Digital Computer Simulation of Spark-Ignited Engine Cycles," SAE Progress in Technology Series 7, SAE, Inc., NY, 1964, pp. 82–91.
19 McAulay, K. J., Wu, T., Chen, S. K., Borman, G. L., Myers, P. S., and Uyehara, O. A., "Development and Evaluation of the Simulation of the Compression-Ignition Engine," SAE Paper No. 650451, 1965.
20 Ament, F., Patterson, D. J., and Mueller, A., "Heat Balance Provides Insight Into Modern Engine Fuel Utilization," SAE Paper No. 770221, 1977.
21 Cole, R. M., and Alkidas, A. C., "Inventory of Heat Losses for a Divided-Chamber Diesel Engine," *SAE Transactions*, Vol. 91, 1982, pp. 3307–3322.
22 Rant, Z., "The Influence of Air Preheating on the Irreversibilities of Combustion," *Brennst. Warme-Kraft*, Vol. 13, No. 11, 1961, pp. 496–500.
23 Stivender, D. L., "Development of a Fuel-Based Mass Emission Measurement Procedure," SAE Paper No. 710604, 1971.
24 Benson, R. S., and Whitehouse, N. D., *Internal Combustion Engines*, Pergamon Press, Oxford, 1979.

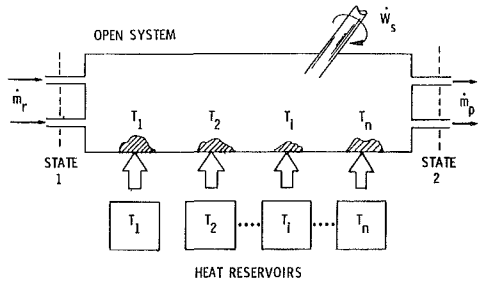


Fig. A1 A general thermodynamic open system

A parameter that is of engineering significance [4, 8, 12] is the lost power. This is defined as

$$\dot{W}_{\text{lost}} = \dot{W}_{s,\max} - \dot{W}_s = T_e \dot{P}_s \tag{A4}$$

The lost power is the power deficit due to the irreversibilities of the system. One may note from equation (A4) that the magnitude of the lost power depends on the choice of the standard temperature of the environment T_e.

An alternative form of equation (A1) may be obtained by defining availability, often called "'exergy," as

$$a_i \equiv b_i - b_{ie} \tag{A5}$$

Substituting equation (A5) into (A1) and collecting terms yields

$$\dot{W}_{s,\max} = \dot{m}(\Sigma(Y_i a_i)_r - \Sigma(Y_i a_i)_p) + \dot{m} a_{\text{FUEL}} + \Sigma \dot{Q}_J \left(1 - \frac{T_e}{T_j}\right) \tag{A6}$$

where the fuel availability a_{FUEL} is defined as

$$a_{\text{FUEL}} = \Sigma(Y_i b_{i,e})_r - \Sigma(Y_i b_{i,e})_p \tag{A7}$$

The fuel availability defined by equation (A7) represents the work done when the products of combustion of the reactants are allowed to expand adiabatically back to the initial temperature of the reactants T_e.

APPENDIX A

Basic Equations

For the open thermodynamic system shown in Fig. A1 the maximum shaft power is given by

$$\dot{W}_{s,\max} = \dot{m}(\Sigma(Y_i b_i)_r - \Sigma(Y_i b_i)_p) + \Sigma \dot{Q}_i \left(1 - \frac{T_e}{T_i}\right) \tag{A-1}$$

where the availability function for steady flow, or stream availability, b_i, is given as

$$b_i = h_i - T_e s_i \tag{A2}$$

and the maximum shaft power $\dot{W}_{s,\max}$ is given by

$$\dot{W}_{s,\max} = \dot{W}_s + T_e \dot{P}_s \tag{A3}$$

where $\dot{P}_s$ is the rate of entropy production due to irreversibilities within the control volume.

Equation (A1) gives the maximum shaft power that may be extracted from a system undergoing a change of state from 1 to 2 while it exchanges specific amounts of heat with the various constant-temperature reservoirs. From equation (A3) the maximum shaft-power output is achieved when the processes within the control volume are reversible. Thus, it represents the reversible limit of power.

APPENDIX B

Evaluation of Thermodynamic Properties

It is seldom appreciated that the most difficult task is the evaluation of the properties of the reactants and products of combustion. In the present study, the intake air was considered to be a mixture of oxygen (O_2) and nitrogen (N_2) in proportions by volume of 21 to 79, the chemical formula of the diesel fuel was assumed to be $C_{14}H_{24.8}$, and the exhaust gases (products of combustion) were assumed to be a mixture of carbon dioxide (CO_2), carbon monoxide (CO), water vapor (H_2O), hydrogen (H_2), oxygen (O_2), and nitrogen (N_2). The mass fractions or corresponding molar fractions of the species in the exhaust stream were calculated from measurements of the exhaust concentrations of CO_2 and CO and the overall air-fuel ratio [23].

Following Benson and Whitehouse [24], the specific absolute molar enthalpies of the gaseous species were represented by empirical relations of the form

$$h_i = R[\alpha_{i,1} T + \alpha_{i,2} T^2 + \alpha_{i,3} T^3 + \alpha_{i,4} T^4] + \alpha_{i0} \tag{B1}$$

The coefficient α_{i0} is equal to the enthalpy of formation of species i evaluated at the temperature of absolute zero.

The values of the coefficients of equation (B1) for the

Downloaded 01 Jun 2010 to 171.66.16.87. Redistribution subject to ASME license or copyright; see http://www.asme.org/terms/Terms_Use.cfm

gaseous species were taken from [24]. For the 2-D diesel fuel, the heat of formation at the standard temperature of 298.15 K was calculated to be -1184 kJ/kg. In addition, because of the scarcity of published information on the thermodynamic properties of diesel fuels, it was assumed that its specific heat was equal to that of octane (C_8H_{18}) for the same temperature.

To evaluate the availability of the intake and exhaust streams, one needs to evaluate the entropy of the mixture. For an ideal gas of species i the entropy is given by

$$s_i = s_{i,o} + \int_{T_o}^{T} \frac{dh_i}{T} - R \ln \frac{p_i}{p_o} \tag{B2}$$

Utilizing equation (B1) yields the following equation for the entropy of species i:

$$s_i = s_{i,o} + R\left[\alpha_{i,1} \ln \frac{T}{T_o} + 2\,\alpha_{i,2}(T - T_o) + \frac{3}{2}\,\alpha_{i,3}(T^2 - T_o^2) + \frac{4}{3}\,\alpha_{i,4}(T^3 - T_o^3)\right] - R \ln \frac{p_i}{p_o} \tag{B3}$$

where T_o is the standard temperature of 298.15 K, and $s_{i,o}$ is the entropy of species i at this temperature.

Downloaded 01 Jun 2010 to 171.66.16.87. Redistribution subject to ASME license or copyright; see http://www.asme.org/terms/Terms_Use.cfm

A Study of Cylinder-to-Cylinder Distribution of Charge in a Six Cylinder Spark Ignition Engine

W. A. Woods
Queen Mary College,
University of London,
London, United Kingdom

O. K. Sag
Faculty of Naval Architecture and
Ocean Engineering,
Istanbul Technical University,
Istanbul, Turkey

An experimental and theoretical study of inlet flow was carried out on a Ford V6 Zephyr four-stroke cycle spark ignition engine. Details of measurements of individual cylinder flows were made on one bank of three cylinders (Nos. 4, 5, and 6) over a range of engine speeds from 1500 to 3500 rpm and throttle positions, full (WOT) down to 1/4 position. The object of the investigation was, first, to determine experimentally the extent of the variation of flow rate from cylinder to cylinder with changes in throttle position and engine speed and, secondly, to determine whether the computer simulation could confirm the trend. The main results of the tests showed that the outer two cylinders, No. 4 and No. 6, had the same flow rate within a variation of about 1/2 percent and that the middle cylinder, No. 5, had about 3 percent more flow at low speeds and 1 percent more at high speeds. In the main these were confirmed by the computer calculations. The volumetric efficiencies were also determined; these produced fairly smooth curves decreasing about 4 to 6 percentage points over the speed range and decreasing progressively as the throttle was reduced. There was evidence of recovery in the magnitude of volumetric efficiency at higher speeds and smaller throttle openings. The computer results also produced these trends.

Introduction

The performance of a multicylinder engine may be optimized for maximum power, best fuel economy, or other prescribed objective. Ideally, this will involve a separate inlet, separate exhaust, and other separate systems for each cylinder so that each one operates in the same optimum manner. If the cylinders operate with different performances then it may be argued that the engine is not running at the overall optimum condition. However, if one or more constraints are imposed on the design, such as the requirement to have a common inlet manifold for a group of cylinders, perhaps for economic reasons, then the optimum overall performance will probably not be achieved by arranging for each cylinder to have equal performance. It is, therefore, useful to have design rules for various systems. These are usually based upon accumulated experience and stored perhaps in diverse technical papers, both published and restricted. It is additionally useful to have the means of evaluating quantitatively various design schemes, proposed by experienced and enlightened designers, and this is the role for a validated computer simulation. References [1, 2] provide the background and details for such a facility.

The object of the present paper is to present some new experimental information on the direct measurement of cylinder-to-cylinder charge distribution, expressed as the flow rate to the cylinders, and to determine whether this information can be predicted by a reasonably detailed computer simulation. The paper reports that on a V6 gasoline engine with the type of inlet manifold used here, the end cylinders have the same mass flow, even though their operation is not symmetric in time. The middle cylinder has a higher mass flow of 3 percent at low engine speed and 1 percent at high engine speed. The paper also presents the results of a theoretical investigation using a computer simulation of the engine gas exchange processes. The findings of this are that the experimental trends are confirmed and that the simulation method can be useful for optimisation design studies. The experimental considerations are discussed first and then a descriptive outline of the computer simulation is given.

The results of the experiments and computations are discussed. Then, finally, the main findings are set out in the conclusions.

Experimental Considerations

A Ford Zephyr V6 engine was used for the experimental investigation; the details of this are given in Table 1. A Heenan and Froude, type G4, hydraulic dynamometer was used to absorb the power. A plenum chamber was used in conjunction with an Alcock viscous flow meter to measure the inlet air flow. The Weber 40 DFA-1 twin-choke carburetor was modified to operate as two independent single carburetors, one serving cylinder numbers 1, 2, and 3 and the second for the test cylinders numbered 4, 5, and 6. The exhaust manifold

Contributed by the Internal Combustion Engine Division and presented at the Eleventh Annual Energy-Sources Technology Conference and Exhibition, New Orleans, Louisiana, January 10-13, 1988. Manuscript received by the Internal Combustion Engine Division April 1987.

Copyright © 1988 by ASME
Downloaded 01 Jun 2010 to 171.66.16.87. Redistribution subject to ASME license or copyright; see http://www.asme.org/terms/Terms_Use.cfm

Table 1 Ford Zephyr V6 engine

Type - six cylinder, O.H.V., 60° V, four stroke cycle	
Bore	.09367 m
Stroke	.07242 m
Inlet valve diameter	.03922 m
Exhaust valve diameter	.03538 m
Connecting rod length	.152 m
Compression ratio	8.9:1
Carburettor	Weber 40 DFA-1
Cubic capacity	3000 cc
Firing Order	1(R),4(L),2(R),5(L),3(R),6(L)
Ignition timing	12° B.T.D.C.
Valve timing	e.v.o. 118° A.T.D.C.
	e.v.c. 374° A.T.D.C.
	i.v.o. 340° A.T.D.C.
	i.v.c. 596° A.T.D.C.

Table 2 Summary of firing tests

Speed (r.p.m.)	Throttle β	Fuel consumption (sec/100 cc)	Brake power kW
1500	Full	25.1	30.8
	3/4	26.7	30.8
	1/2	30.0	28.5
	1/4	40.5	21.5
2000	Full	22.2	41.4
	3/4	23.2	40.7
	1/2	26.9	37.7
	1/4	35.0	27.6
2500	Full	18.2	52.7
	3/4	18.0	51.3
	1/2	23.0	44.3
	1/4	31.5	28.4
3000	Full	14.5	64.9
	3/4	15.0	64.9
	1/2	20.0	50.4
	1/4	31.0	33.6
3500	Full	13.0	74.4
	3/4	13.5	69.2
	1/2	19.0	54.8
	1/4	29.0	37.3

serving the test cylinders was replaced by individual pipes, approximately the same shape and size but connected to large steel tanks, which incorporated orifice plates at the outlet, each one mounted flush with an inside wall of a tank. The pressure difference across each orifice plate was measured with either water or mercury manometers, depending on the engine throttle opening and speed. The temperature of the exhaust gas in each tank was measured with a mercury-in-glass thermometer.

The transient pressures, at various stations in the inlet manifold, were measured with Kistler 7031 pressure transducers, Kistler 566 charge amplifiers, C.E.C. 1.165 DC amplifiers, an SE Laboratories U.V. recorder, and a Tektronix oscilloscope display unit.

The carburetor throttle valve was calibrated by separate steady flow experiments, for use as boundary conditions in the computer simulation. Special steady flow calibration tests were also carried out for the three plenum chambers containing orifice plates. The inlet flow was measured with an Alcock viscous flow meter and recordings of the tank pressure, temperature, and pressure drop across the orifice were made.

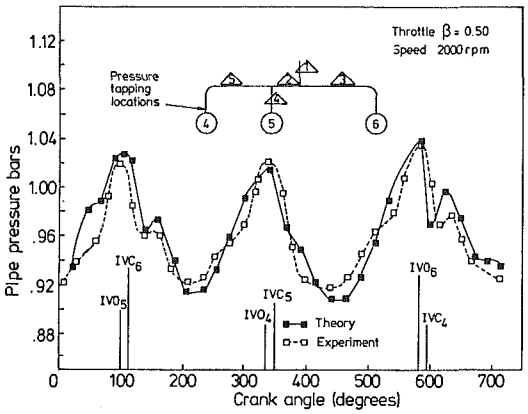


Fig. 1 Pressure in pipe ~ crank angle

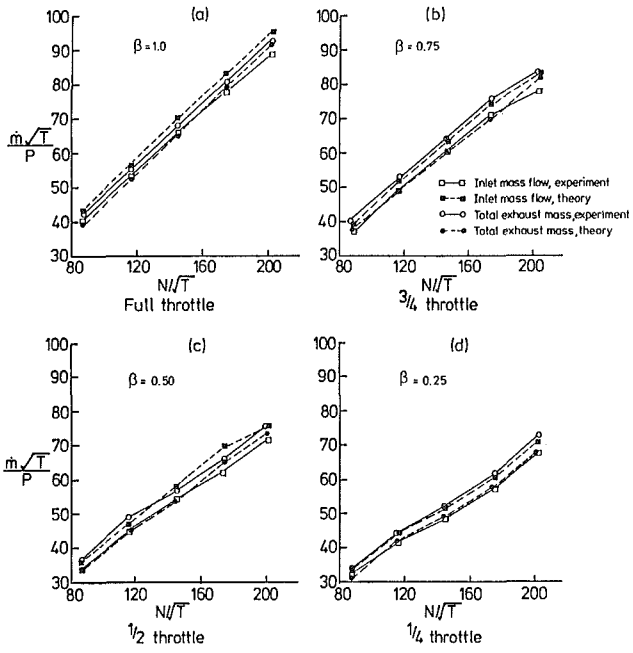


Fig. 2 Inlet and total exhaust parameters

A summary of the firing tests carried out is given in Table 2. A typical pressure-crank angle diagram, taken close to cylinder number 4 in the inlet manifold, is shown in Fig. 1. It is very similar to a computed diagram, also shown in the same figure, which will be discussed later.

The mass flow rate results are presented in three groups. First, the total flows for the three cylinder numbers 4, 5, and 6 are shown in Fig. 2(*a, b, c,* and *d*). Secondly, the exhaust flows for the individual cylinders are shown in Fig. 3(*a, b, c,* and *d*). Thirdly, the relative flow rates are compared in Fig. 4(*a, b, c,* and *d*): here, the flow rates of two cylinders, 5 and 6, are divided by that for cylinder number 4. Discussion on these results is deferred until the theoretical aspects have been presented.

Theoretical Considerations

In order to predict the flow rates to the cylinders, an engine simulation program was used. This program was based upon filling and emptying quasi-steady flow methods for the cylinders, unsteady non-homentropic flow in the pipes using a mesh technique based upon the method of characteristics and empirical boundary conditions. The latter were for (*i*) flow through each poppet valve between a cylinder and a pipe, (*ii*)

Downloaded 01 Jun 2010 to 171.66.16.87. Redistribution subject to ASME license or copyright; see http://www.asme.org/terms/Terms_Use.cfm

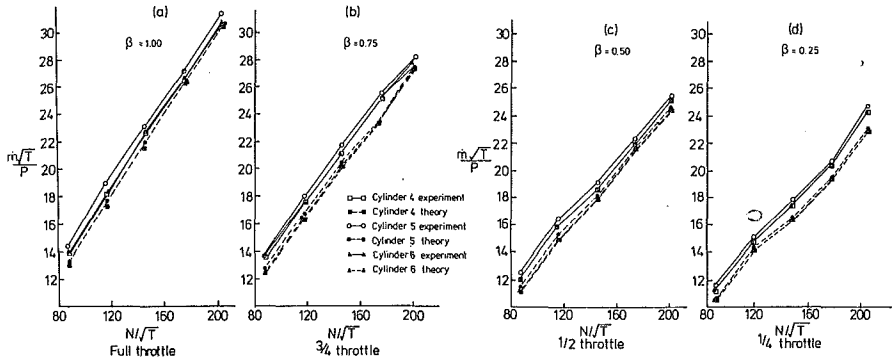


Fig. 3 Individual exhaust parameters

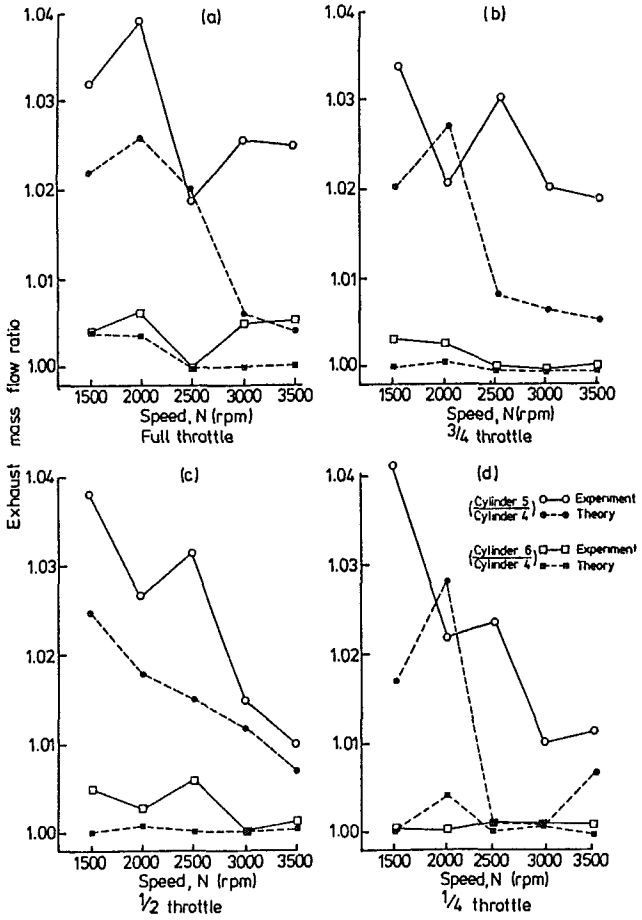
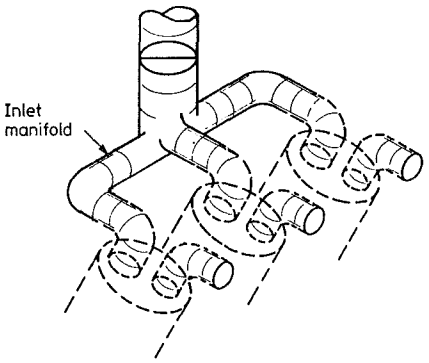


Fig. 4 Mass flow ratio ~ speed



Schematic of actual inlet manifold

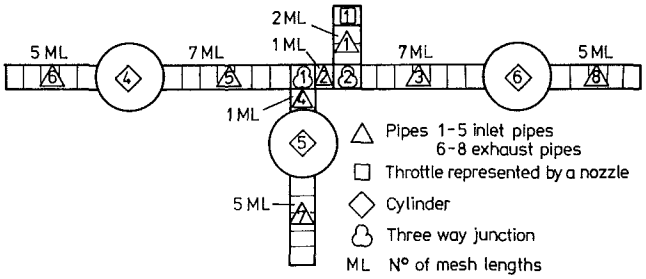


Fig. 5 Computer model of inlet engine system

flow through the carburetor throttle valve into a pipe, and (*iii*) flow through a three-way junction and three pipes.

Most of the work on which the above is based was carried out over many years in the Mechanical Engineering Departments at the University of Liverpool and at the University of Manchester Institute of Science and Technology. This work has recently been well documented in the Benson Memorial Volumes [1, 2]. The papers and theses which have special relevance to the present program are [3–5] for the mesh method using the method of characteristics, [4, 5] for unsteady flow in pipe junctions, [6–8] for flow through poppet valves and [6, 9] for unsteady flow in an engine exhaust system.

The method used for modeling the engine system is discussed next.

Modeling the Inlet, Exhaust, and Engine Cylinders. A diagram illustrating the actual engine system and the theoretical model used is given in Fig. 5. Here the three-dimensional inlet manifold is represented by five straight pipes, each of the same constant cross-sectional area. The extremely complex combined carburetor and four-way junction casting is modeled by two short pipes, numbered 2 and 4, and two three-way junctions. The two longer pipes, numbered 3 and 5, represent the curved ducts running from the carburetor to the outer two cylinders. A short length pipe, numbered 4, represents the duct running to the middle cylinder number 5 from the carburetor. The throttle valve is modeled as a nozzle at the inlet to one short pipe, number 1.

The empirical flow characteristics corresponding to the four throttle positions obtained from steady-flow tests, mentioned in Section 2, were used as boundary conditions at the inlet. Full throttle corresponds to $\beta = 1.0$. The term β is a throttle opening parameter. The combustion process was accounted for by specifying the release pressure in the cylinder just before the exhaust valve opened.

We have outlined the basis of the computer program and il-

Downloaded 01 Jun 2010 to 171.66.16.87. Redistribution subject to ASME license or copyright; see http://www.asme.org/terms/Terms_Use.cfm

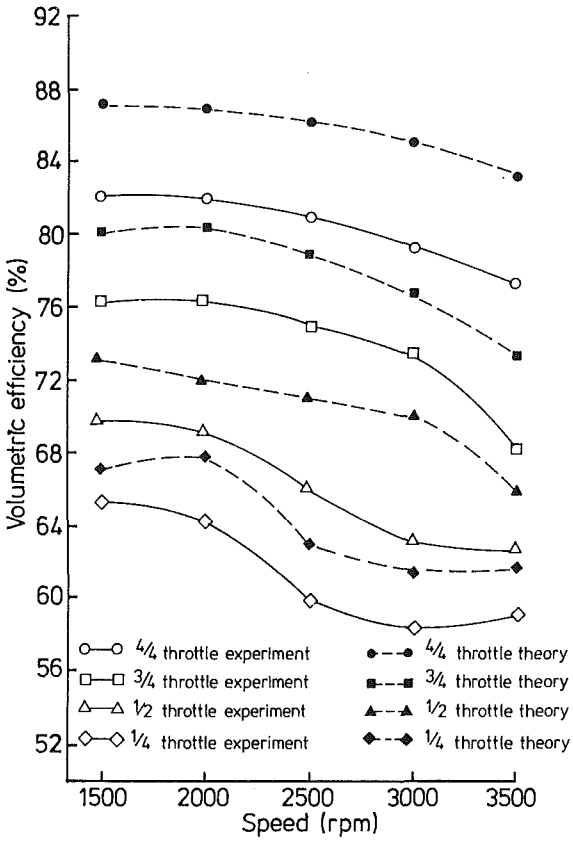


Fig. 6 V6 Zephyr inlet volumetric efficiencies

lustrated the engine modeling procedure; the next section discusses the experimental and computed results.

Discussion of Results

The calculated pressures in the inlet manifold are compared with the corresponding measurements in order to validate the theoretical model. A typical result is presented in Fig. 1 and the level of agreement between the calculated and measured pressures is good.

Total Flow Rate for Cylinder Numbers 4, 5, and 6. The overall mass flow rates were determined from the measurements at the inlet and the three exhaust locations. Mean mass flow rates were also calculated using the computed results. The instantaneous flow rates at the inlet (the mesh point next to the carburetor in pipe number 1) and three exhaust locations (the mesh points next to the exhaust plenum chambers, i.e., the last mesh points in pipes numbers 6, 7, and 8) were integrated over the engine cycle, then the mean flow rates were determined. Then they were expressed as pseudo-nondimensional parameters of mass flow and a corresponding speed parameter was also evaluated. These parameters are the same as those traditionally used in turbomachinery work. It may be shown from a simple analysis of the volumetric efficiency for an engine that

$$\frac{\dot{m}\sqrt{T}}{p} = \text{const}\ \eta_v \frac{N}{\sqrt{T}}$$

where $\dot{m}$ is the air flow rate to the engine, T is the inlet temperature, p is the inlet pressure, N is the speed of the engine, and η_v is the volumetric efficiency of the engine.

Hence, the gradients of the curves for the inlet flows on Fig. 2 are proportional to the volumetric efficiencies; this is discussed later.

All the curves show an almost linear increase in mass flow parameter with speed parameters. On the actual engine, there will be a small amount of air leakage into the engine through the carburetor and the fuel is added; also there may be a small amount of gas leakage past the piston rings in the engine cylinders. The carburetor leakage is probably negligible in the present tests, although this can be significant at idle condition when the throttle is closed and there is a high vacuum in the inlet manifold. Measurements indicate that the mass of fuel added in the present tests is 8 to 9 percent of the inlet air mass flow and the leakage past the piston rings is likely to be small, perhaps about 1 percent of the total mass flow. Thus, the exhaust flow would be expected to exceed the inlet flow and this is so for all speeds and throttle positions shown in Fig. 2(*a, b, c* and *d*). On the figure $\dot{m}$ is used to denote inlet and exhaust mass flow rates, but the symbols on the curves distinguish them.

The average measured exhaust mass flow is just over 4 percent greater than the inlet mass flow. The difference between this figure and the fuel flow contribution may be attributed mainly to cumulative errors in the absolute measurement of exhaust flows. However, the results, which show the variations with speed and throttle setting, are of greatest value.

The calculated results predict very well the changes revealed by the measurements with respect with respect to speed and throttle setting. However, in absolute terms, the theoretical inlet flows appear somewhat high and the theoretical exhaust flows are somewhat low. It should be appreicated that part of this is accounted for by not including the fuel flow in the computer simulation. The remainder can be attributed to the approximate features of the theoretical model and cumulative errors in the numerical method.

There is a highly nonlinear relationship between the throttle position parameter β and the inlet mass flow rate. At 3500 rpm engine speed with a throttle setting of $\beta = 1/4$ there is 76 percent of the flow corresponding to full throttle.

Exhaust Flow Rate For Individual Cylinder Numbers 4, 5, and 6. The exhaust flow rates for the individual cylinders are shown in Fig. 3(*a, b, c* and *d*). They exhibit similar trends to those of the total flows. They vary almost linearly with an increase in speed. The highly nonlinear relationship with the throttle position, found for the total flows, is also seen in the individual cylinder results.

The key result emerging from these experiments is that the middle cylinder (number 5) has a higher flow rate than the other two, numbers 4 and 6. This result is maintained for all speeds and throttle positions covered in the present tests. This point is quantified in the discussion of the results, shown in Fig. 4.

The theoretical results exhibit very similar trends to those of the experimental ones with the exception of the second highest speed (3000 rpm) at $\beta = 0.75$. The absolute values of the theoretical results are consistently lower than the experimental ones and comments made earlier for the total flows are also relevant here.

Perhaps the most important results of the whole investigation are presented in Fig. 4(*a, b, c,* and *d*). Here the exhaust flow results of the middle (number 5) and one outer cylinder (number 6) are expressed relative to the other outer cylinder (number 4).

The flow rates for the outer two cylinders, numbers 4 and 6, are the same to within 1/2 percent. The flow to the middle cylinder (number 5) is shown to vary from about 3 percent higher than that for the other two cylinders, numbers 4 and 6, at an engine speed of 1500 rpm to about 1 percent higher at the highest engine speed, 3500 rpm. Although there is some scatter, this result applies for all throttle positions. Having discussed the individual cylinder results, we return to the discussion on the volumetric efficiency.

Downloaded 01 Jun 2010 to 171.66.16.87. Redistribution subject to ASME license or copyright; see http://www.asme.org/terms/Terms_Use.cfm

Volumetric Efficiency. The volumetric efficiency results are shown collectively in Fig. 6. The experimental results show that the volumetric efficiency decreases about 4 percentage points over the speed range at full throttle and about 6 percentage points at 1/4 throttle.

At full throttle the decrease in volumetric efficiency with speed is progressive but at 1/4 throttle the decrease recovers somewhat at higher speeds.

The computer simulation produces results with almost all the above trends. As mentioned previously, on an absolute basis the computer results appear 5 percent to 6 percent too large. This may be improved by a constant correction factor.

Conclusions

1 An experimental and theoretical investigation of the cylinder to cylinder flow in a V6 Zephyr spark ignition engine has been carried out on the basis of testing one bank of three cylinders and computing the flow in a three-cylinder theoretical model.

2 The flow rates for the engine have been established experimentally over a range of speeds and throttle positions. These trends determined experimentally have also been evaluated using a computer simulation for the engine.

3 The flow rates for the individual cylinders have been investigated by direct measurement of the separate exhaust flows. The outer two cylinders aspirate the same flows and the middle cylinder takes in a higher flow.

4 Over the speed range the mass flow rate to the outer two cylinders is within 1/2 percent. The flow rate to the middle cylinder varies from 3 percent higher than that to each of the outer two cylinders at low engine speeds to 1 percent higher at high engine speeds.

5 At full throttle the volumetric efficiency of the engine decreases about 4 percentage points, with an increase of engine speed from 1500 to 3500 rpm. The maximum value of the volumetric efficiency is 82 percent.

6 The volumetric efficiency decreases as the throttle is closed. The reduction with speed becomes about 6 percentage points at 1/2 and 3/4 throttle. The volumetric efficiency recovers somewhat at higher speeds for the smaller throttle settings.

7 The computer simulation also produces the same trends as shown by the experimental measurements. However, in absolute terms, the computer simulation produces results about 5 percent too large.

Acknowledgments

The work reported was carried out in the Mechanical Engineering Department, University of Liverpool and financial support from the Thorton Research Centre, Shell Research Ltd., is gratefully acknowledged. The authors also wish to mention the helpful discussions they had with Dr. B. D. Caddock.

References

1 Benson, R. S., *The Thermodynamics and Gas Dynamics of Internal Combustion Engines*, Vol. 1, J. H. Horlock and D. E. Winterbone, eds., Clarendon Press, Oxford, 1982, pp. 1–580.

2 Horlock, J. H., and Winterbone, D. E., *The Thermodynamics and Gas Dynamics of Internal Combustion Engines*, Vol. 11, Clarendon Press, Oxford, 1986, pp. 583–1225.

3 Benson, R. S., Garg, R. D., and Woollatt, D., "A Numerical Solution of Unsteady Flow Problems," *Int. Jnl. Mech. Sci.*, Vol. 6, 1964, p. 117.

4 Benson, R. S., Woollant, D., and Woods, W. A., "Unsteady Flow in Simple Branch Systems," *Proc. I. Mech. E.*, Vol. 178, Part (III), 1963-64.

5 Daneshyar, H., "Unsteady Gas Flow Through Branched Exhaust Systems of Multi-Cylinder Engines," Ph.D., Thesis, University of Liverpool, 1966.

6 Woods, W. A., and Khan, S. R., "An Experimental Study of Flow Through Poppet Valves," *Proc. I. Mech. E.*, Vol. 180, Part 3N, 1965-66, pp. 32–41, 105–106.

7 Woods, W. A., and Khan, S. R., "Discharge From A Cylinder Through a Poppet Valve to an Exhaust Pipe," *Proc I. Mech. E.*, Vol. 182, Part 3H, 1967–68, pp. 137–144.

8 Woods, W. A., "Steady Flow Tests on Twin Poppet Valves," *Proc. I. Mech. E.*, Vol. 182, Part 3D, 1967–68, pp. 126–133.

9 Woods, W. A., and Douthwaite, W., "Compressible Flow in a Four-Stroke Supercharged Diesel Engine With Particular Reference to the Effects of Heat Transfer From the Exhaust Gas," *Proc. Thermofluids Conf. Inst. of Eng.*, Melbourne, Australia, 1974, pp. 86–90.

Downloaded 01 Jun 2010 to 171.66.16.87. Redistribution subject to ASME license or copyright; see http://www.asme.org/terms/Terms_Use.cfm

Promises and Challenges of the Low-Heat-Rejection Diesel

C. A. Amann
General Motors Research Laboratories,
Engine Research Department,
Warren, MI 48090-9055

The low-heat-rejection (LHR) diesel promises decreased engine fuel consumption by eliminating the traditional liquid cooling system and converting energy normally lost to the coolant into useful shaft work instead. However, most of the cooling energy thus conserved is transferred into the exhaust stream rather than augmenting crankshaft output directly, so exhaust-energy recovery is necessary to realize the full potential of the LHR engine. The higher combustion temperature of the LHR diesel favors increased emission of NO_x, with published results on hydrocarbon and particulate emissions showing mixed results. The cylinder insulation used to effect low heat rejection influences convective heat loss only, and in a manner still somewhat controversial. The cyclic aspect of convective heat loss, and radiation from incandescent soot particles, also deserve attention. The temperatures resulting from insulating the cylinder of the LHR diesel require advancements in lubrication. The engine designer must learn to deal with the probabilistic nature of failure in brittle ceramics needed for engine construction. Whether ceramic monoliths or coatings are more appropriate for cylinder insulation remains unsettled. These challenges confronting the LHR diesel are reviewed.

Introduction

Only a century ago the diesel engine did not even exist. Today it is the most fuel-efficient known power plant suitable for mobile application. It has assumed a leading role in rail and marine transportation. It dominates the heavy-duty trucking field and is available in light-duty trucks, vans, and passenger cars as well.

In his 1985 Calvin W. Rice Lecture [1], French observed that most of the improvement shown by the diesel engine since its first practical demonstration by MAN in 1893/4 has been the result of steady improvement rather than breakthroughs. He cited only three major developments substantially affecting the diesel engine during those years: introduction of the solid injection system, turbocharging, and currently the application of electronics, as typified by the recent introduction of electronically controlled injection. In a speculative vein, the low-heat-rejection (LHR) diesel, perhaps featuring structural ceramics, may some day be added to that list.

The motivating force behind the LHR diesel has been the prospect of eliminating the traditional liquid cooling system. That system is there to keep engine operating temperatures down to levels tolerated by currently used constructional materials and lubricants. If the energy normally rejected to the coolant could be recovered instead on the crankshaft as useful work, then a substantial improvement in fuel economy would result. At the same time, the cooling water, antifreeze, thermostat, radiator, water pump, cooling fan, and associated hoses and clamps could be eliminated.

Increased thermal efficiency and elimination of the cooling system are the major promises of the LHR diesel. To those might be added the ability to burn lower-grade fuels because of the higher cylinder-gas temperatures attainable without cooling. However, the road to those promises is presently impeded by a series of challenges in the fields of thermodynamics and fuel consumption, combustion and emissions, heat transfer, lubrication, and materials, particularly ceramics. It is the objective of this paper to review the current status of LHR diesel with respect to those impediments.

Thermodynamics and Fuel Consumption

Applying the first law of thermodynamics to the diesel engine, all of the fuel energy injected into the cylinder must appear either as brake output work, as sensible and/or chemical energy in the exhaust stream, or as heat rejected to the coolants, i.e., water, oil and the surrounding air. The distribution of energy among these sinks is illustrated for a passenger-car diesel at road load in the left pie chart of Fig. 1. The first law suggests that if heat rejection to the coolant were eliminated by perfectly insulating the cylinder and deleting the cooling system, the coolant energy could be converted into brake power. In the case illustrated, that transformation would appear to double the brake thermal efficiency of the engine.

Unfortunately, the second law of thermodynamics does not allow that transformation to occur. Although that fact can be demonstrated through a thermodynamic availability analysis, the reason can be recognized qualitatively without resorting to such elegance. Simply put, blocking heat loss from the cylinder gas when the piston is at BDC of the expansion stroke cannot improve cycle efficiency because the piston has already

Contributed by the Internal Combustion Engine Division for publication in the JOURNAL OF ENGINEERING FOR GAS TURBINES AND POWER. Manuscript received at ASME Headquarters March 15, 1988.

Copyright © 1988 by ASME
Downloaded 01 Jun 2010 to 171.66.16.87. Redistribution subject to ASME license or copyright; see http://www.asme.org/terms/Terms_Use.cfm

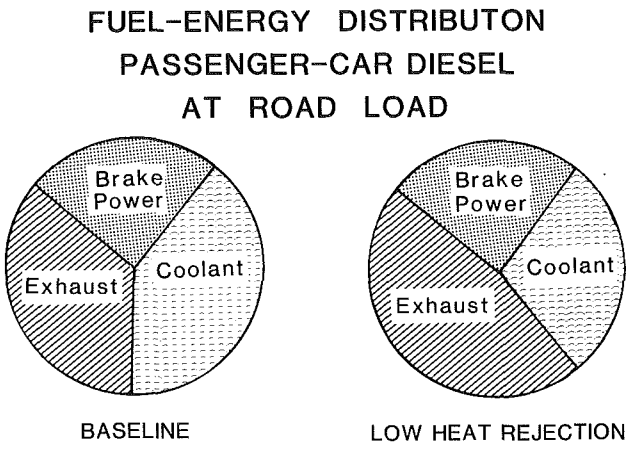


Fig. 1 Typical road-load energy distribution for diesel-powered passenger car, conventionally cooled baseline versus low heat rejection

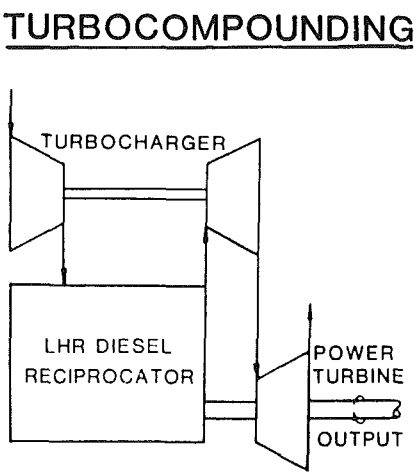


Fig. 2 Schematic of turbocompounded engine

completed its work-extraction process. Clearly, the most can be gained by blocking heat loss at TDC of the expansion stroke, with the gain possible from prevention of cylinder heat loss decreasing as BDC is approached.

If the energy saved by preventing heat loss from the cylinder cannot all be recovered as shaft work, then what is its fate? As shown by the right pie chart of Fig. 1, drawn for an LHR version of the same passenger-car diesel, the result of cylinder insulation is a sizable increase in the fraction of heat exiting with the exhaust gas in the form of increased temperature. This points to the need for adding to the engine some means of recovering energy from the exhaust if significant improvement in thermal efficiency is to be realized from insulating the cylinder.

Another outcome of cylinder insulation that does not appear in Fig. 1 is the effect that the hotter cylinder wall has on the production of net output work by the piston. Those hotter walls heat the incoming air charge, decreasing volumetric efficiency. Expressing cylinder output in the form of indicated mean effective pressure $\tilde{p}_i$

$$\tilde{p}_i = \rho \eta_i \eta_v FH \tag{1}$$

where ρ = reciprocator inlet density; η_i = indicated thermal efficiency; η_v = volumetric efficiency; F = fuel-air ratio; H = fuel heating value.

In a naturally aspirated engine, the reciprocator inlet density is essentially a constant determined by the ambient environment. The heating value is fixed by the fuel. Suppose that the full-load fuel-air ratio is limited by exhaust smoke. Then the lower volumetric efficiency of the insulated cylinder means lower indicated mean effective pressure unless that deficiency is compensated by a corresponding increase in indicated thermal efficiency.

To lose more in volumetric efficiency than is gained in indicated thermal efficiency is not unusual for a naturally aspirated LHR diesel. For that reason, the naturally aspirated LHR diesel is considered unattractive, and some means of boosting the density of the air entering the reciprocator is sought.

Now that two needs have been identified for the LHR diesel—an exhaust-energy recovery system and a means of supercharging the reciprocator cylinder—the attraction of turbocompounding is evident. A turbocompounded engine is diagramed in Fig. 2. It involves the incorporation of a turbocharger, plus a power turbine located downstream of the turbocharger turbine and mechanically connected to the reciprocator crankshaft. The compressor of the turbocharger provides the desired increase in reciprocator inlet density, and the turbocharger turbine extracts energy from the exhaust stream to drive the compressor without mechanically loading the reciprocator. The power turbine is there to extract additional energy from the hotter exhaust gas that results from cylinder insulation.

Although turbocompounding appears to offer all the answers in a simple flow diagram, in practice there are many subtleties that require attention. In particular, high turbomachinery efficiency is desired to avoid imposing unwanted back pressure on the reciprocator, with a consequent increase in reciprocator pumping loss during the gas-exchange strokes. This possibility is of particular concern at light loads, when the gas temperature entering the turbocharger is reduced. If the power turbine is joined to the crankshaft through a fixed-speed-ratio-drive, it may be forced to operate far from its peak efficiency at some engine operating conditions. In fact, at light loads it may actually absorb power, lowering engine efficiency [2].

One might expect that since the LHR concept has been pursued for a decade now, good experimental data would be available that establish its fuel-economy characteristics over the full operating range. Unfortunately, though, such data are surprisingly sparse, so one is forced to turn to analytical estimates.

The first fact that emerges from such studies is that it is impossible to insulate the cylinder completely. That is why applying the term "adiabatic" to the LHR engine is inappropriate. The impossibility of attaining adiabatic conditions, i.e., in which no heat is exchanged between the gas trapped in the cylinder and its surrounding walls, has given rise to the term "adiabaticity." Percent adiabaticity serves as an indicator of how closely the ideal of complete insulation of the cylinder is approached. An adiabaticity of 100 percent corresponds to attainment of that ideal, and an adiabaticity of zero denotes a conventionally cooled engine. It is generally conceded that the highest practically attainable adiabaticity is in the range of 50–60 percent.

From the many analytical studies of the LHR diesel, full-load results from two are chosen here as representative [3, 4]. They are summarized in Fig. 3, where percent reduction in fuel consumption is plotted vertically upward for two types of engines: a conventionally cooled one on the left and an LHR version on the right. All gains are reckoned from the baseline cooled, turbocharged, and intercooled diesel represented at the lower left by the zero-gain axis.

First proceeding up the left-hand stack, both studies agreed that if that cooled baseline engine were turbocompounded, it would experience about a 4 percent decrease in full-load fuel consumption. Adding a Rankine bottoming cycle, i.e., a steam engine running off the heat remaining in the exhaust gas

Downloaded 01 Jun 2010 to 171.66.16.87. Redistribution subject to ASME license or copyright; see http://www.asme.org/terms/Terms_Use.cfm

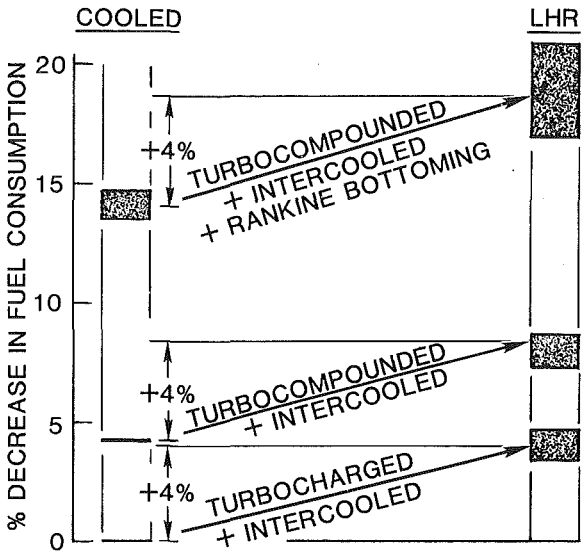


Fig. 3 Effect of insulation on full-load fuel consumption for various versions of conventionally cooled (left) and LHR (right) diesel engines

exiting the power turbine, gives a predicted gain near 15 percent, as indicated by the upper shaded band.

Consecutively executing those same options in the LHR version was projected to offer the gains indicated by the shaded bands on the right. The positively sloped vectors from the cooled stack to the LHR stack were arbitrarily drawn to indicate a 4 percent reduction in fuel consumption for each case. It is seen that for all three engine options illustrated, the 4 percent gain is fairly representative of expectations from cylinder insulation alone. On the other hand, if one compares the LHR engine with turbocompounding and Rankine bottoming (the upper right band) to the baseline cooled, turbocharged, and intercooled engine (the lower left), then the reduction in fuel consumption is close to 20 percent. But most of that gain is available simply by adding that same complexity to the cooled engine (the shaded patch at the top of the left stack).

Most other analysts have estimated reductions in full-load fuel consumption in the range of 2–6 percent for adding enough insulation to turbocharged or turbocompounded engines to achieve adiabaticity in the 40–60 percent range. Published experimental data are generally limited to adiabaticity levels below 40 percent and show gains from insulation alone of from 0–3 percent.

The steam-based Rankine bottoming cycle for which estimates were made in Fig. 3 is just one of several bottoming schemes that have been investigated analytically to recover more of the exhaust energy than can be regained by turbocompounding alone. Other variants considered include the organic-fluid Rankine cycle, the Brayton (gas turbine) cycle, and the Stirling cycle. Despite their virtues as thermal-efficiency improvers, an economic assessment has indicated that as far as the trucking industry is concerned, the time required to recover the additional cost increment of the bottoming engine in fuel savings is too long to make that option attractive [5].

Although most of the attention has been directed toward LHR heavy-duty engines, the passenger-car application has not been overlooked [6]. In comparing both turbocharged and turbocompounded LHR diesels to a water-cooled turbocharged baseline diesel providing comparable acceleration performance when installed in an intermediate size car, attractive fuel savings were projected when optimistic design parameters were used to estimate an upper-limit gain for cylinder insulation. Allowing for this optimism, realistic gains in fuel consumption for the LHR versions are judged to be less than 10 percent. The interesting outcome of this study, however, was that the projected improvement in vehicle fuel consumption was not the direct result of higher indicated thermal efficiency from cylinder insulation, but rather from such factors as reduced engine mass and lower parasitic cooling load. The absence of a more direct benefit from insulation came about because adiabaticity decreased as engine speed was reduced and because exhaust-energy recovery through turbocharging and turbocompounding becomes ineffective at light loads, where passenger cars operate most of the time.

Combustion and Emissions

Irrespective of the reduction in fuel consumption shown by a new engine, in most US applications the engine must be considered an engineering novelty rather than a viable commercial candidate until it has demonstrated the ability to meet applicable emissions standards. The regulated emissions include unburned hydrocarbons (HC), carbon monoxide (CO), oxides of nitrogen (NO_x), and exhaust particulates (or in some cases, smoke). Of these, only CO is not a potential problem for the diesel, because of the overall lean stoichiometry it employs.

One might expect lower HC from a LHR diesel because the shortened ignition delay associated with higher temperatures decreases the opportunity for overmixing of fuel beyond the lean combustion limit and because the generally higher cylinder-gas temperature during the expansion stroke should encourage oxidation of any unburned fuel escaping the primary combustion process. However, a review of the limited published data on measured emissions from the LHR diesel shows that while there are instances where HC did decrease, there are others where it increased.

The most important factors in determining the NO_x produced by the combustion process are stoichiometry and flame temperature. If combustion took place at the overall lean stoichiometry of the engine cylinder, the NO_x problem might be relieved, but it does not. Because of the diffusive mixing of fuel and air occurring along the spray envelope, combustion is dominated by near-stoichiometric burning, where the production of nitric oxide is high.

The flame temperature has a particularly strong effect on the production of nitric oxide, and the higher combustion temperature of the LHR engine would be expected to increase NO_x. In nearly all published experiments, higher NO_x has indeed been measured. Bryzik and Kamo [7] showed, however, that in lowering flame temperature by retarding injection timing, NO_x could be reduced to the level of the conventionally cooled baseline engine. Delaying combustion from the optimum in this manner sacrifices some fuel economy, of course, but at the selected operating point in their engine, there was still a gain in fuel consumption relative to the conventionally cooled baseline. At Hino, experiments were conducted on five different LHR configurations of a heavy-duty diesel, in each case with the injection retarded in this manner to give the same NO_x emission as the cooled baseline engine [8]. Three different operating points were evaluated. In 14 of the resulting 15 cases, HC rose. The Bosch smoke number increased in 8 of the 15 cases.

For US regulatory purposes, exhaust particulates are defined as any solid or liquid, with the exception of water, that collects on a filter sampling a diluted exhaust stream, so long as the dilution is sufficient to maintain the filter temperature at or below 52°C. The collected particulate matter is normally dominated by carbonaceous soot produced but not oxidized during the combustion process, but it may also include unburned HC adsorbed on the surfaces of the soot particles, lubricating-oil constituents, and sulfates from the sulfur in the fuel. Although one might expect the higher cylinder-gas temperatures during the expansion stroke to be effective in ox-

Downloaded 01 Jun 2010 to 171.66.16.87. Redistribution subject to ASME license or copyright; see http://www.asme.org/terms/Terms_Use.cfm

Table 1 Comparative temperature drops through cylinder wall

	Heat-flux reduction	Percentage temperature drop: Inner-wall layer	Wall	Outer-wall layer
Cast iron, water cooled	—	92%	6%	2%
Cast iron, uncooled	30%	64%	3%	33%
Si_3N_4, uncooled	34%	50%	19%	31%
PSZ, uncooled	74%	33%	50%	17%

idizing the soot formed during the diffusion combustion process of the diesel, that higher temperature is also conducive to increased pyrolysis of the fuel prior to combustion, so that there may be more soot to oxidize. A prevailing trend in particulate characteristics for the LHR diesel cannot be deduced from published experiments. At Cummins, a turbocharged LHR diesel with a 30–35 percent adiabaticity showed an 8 percent decrease in total particulate mass when run on the EPA transient heavy-duty test schedule [9]. This was the result of a 24 percent reduction in carbonaceous dry soot, but the extractable balance of the particulate matter actually increased by 50 percent. It is this latter fraction of the exhaust particulate that is of greatest concern with respect to possible health effects.

It is obvious from this brief review that the emissions picture is mixed. Effective use of injection retard and/or exhaust gas recirculation appears necessary to control the inherently higher NO_x of the LHR diesel. Whether this can be accomplished without excessive sacrifice in other areas remains to be established. Evidence suggests that the significance of lubricating oil to HC and/or particulate emissions may be magnified in the LHR engine. If the higher gas temperatures of the LHR diesel could be harnessed to decrease particulate emissions to the point where a particulate trap would become unnecessary, that would be a major plus for the concept. Clearly, additional effort on combustion in the LHR engine is required to clarify the situation.

Heat Transfer

Heat transfer from the cylinder gas is an unsteady process, but much insight can be gained by treating it as a steady process by using average temperatures. Heat is lost by both convection and radiation. The standard approach to cylinder insulation treats convection but is not an effective radiation deterrent.

Steady convective heat loss from the cylinder gas of a conventionally cooled engine through the cast iron cylinder wall to the coolant involves three resistances to heat transfer in series. The first is the gaseous thermal boundary layer on the inner surface of the wall. Second is the conductive resistance offered by the wall itself. Third is the liquid thermal boundary layer on the coolant side of the wall. The temperature drop across each of these elements provides a measure of its resistance to heat transfer. In a typical cooled engine, the percentage drop in temperature from the cylinder gas to the coolant might be divided as shown by the top line of Table 1. Over 90 percent of the temperature drop is seen to occur through the gaseous thermal layer on the inside of the cylinder.

If the liquid coolant is removed from the outside of the wall, allowing the heat transferred through the wall to be rejected to ambient air, the temperature drop from the cylinder gas to ambient is redistributed, as shown by the second line of Table 1. The smaller temperature difference across the thermal layer on the inner surface translates into a 30 percent reduction in heat flux through the wall. It also means that the wall must run hotter. In an operating engine, that higher temperature may exceed the long-term capabilities of cast iron. That is

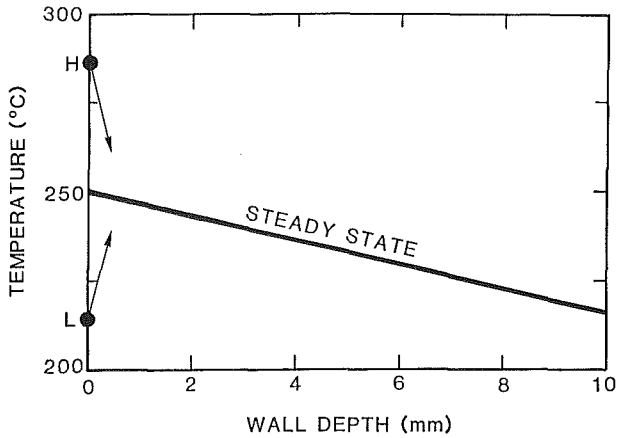


Fig. 4 Steady-state temperature gradient through a cylinder wall and high (H) and low (L) extremes of temperature swing on cylinder inner wall

where ceramics enter the picture, because of their improved high-temperature properties.

The third line of Table 1 shows the changes occurring when the cast iron wall is replaced with one of silicon nitride. Despite the fact that this ceramic is a better insulator than cast iron, having only half its thermal conductivity, the effect on temperature distribution is minimal. The corresponding reduction in heat flux, relative to the original liquid-cooled baseline, is only increased to 34 percent.

The fourth line of Table 1 represents replacement of the uncooled silicon nitride wall with one of partially stabilized zirconia (PSZ). This ceramic has a thermal conductivity an order of magnitude smaller than that of silicon nitride and only 4 percent of that of the original cast iron. This low thermal conductivity signifies a better insulator, as evidenced by the substantially increased temperature drop across the wall itself. This insulative ability is reflected as a 74 percent reduction in heat flux relative to the liquid-cooled baseline. While this insulation effect is admirable, it is unfortunate that today, PSZ lacks the structural integrity to be used as a major structural part like a cylinder liner.

Although the steady-state results of Table 1 provide some sense of the heat transfer situation, they obscure one aspect associated with the unsteady temperature of the cylinder-gas heat source. The heavy line in Fig. 4 represents the steady-state component of temperature drop through the cylinder wall. While the temperature on the outer surface of the wall is indeed essentially steady, the temperature on the inner surface actually rises and falls in response to the rapidly cycling temperature of the cylinder gas. This cyclic temperature penetrates through only a thin skin on the inner surface, but that cycling inner-surface temperature can have a significant effect on the cycle thermodynamics.

Suppose point H on the inner surface of the wall represents the instantaneous peak wall temperature reached during the cycle. It is well above the average surface temperature represented by the left extremity of the steady-state component. The local instantaneous trend in temperature from point H on the surface toward the steady-state, or average, temperature distribution, as indicated by the arrow,

Downloaded 01 Jun 2010 to 171.66.16.87. Redistribution subject to ASME license or copyright; see http://www.asme.org/terms/Terms_Use.cfm

establishes a temporarily steeper temperature gradient at the wall inner surface than the average, steady-state gradient that prevails farther into the wall. Because the temperature gradient is proportional to the rate of heat conduction, it is evident that at this particular time in the cycle, heat is entering the inner surface of the wall faster than it is leaving the outer surface. The difference must be stored in the wall.

Point L on the inner surface of the wall represents the instantaneous minimum temperature reached during the cycle. In this case the instantaneous temperature gradient at the wall is positively sloped, in contrast to the negatively sloped average distribution with which it must merge farther into the wall. This slope reversal indicates a transfer of stored heat from the wall back into the cylinder gas.

The unfortunate consequence of this periodic component of heat transfer is that during combustion, heat is removed from the cylinder gas near TDC, when its thermodynamic availability for doing work is greatest. Then it is returned to the cylinder gas later during the cycle, when it is less useful in producing work and adversely affects volumetric efficiency.

This increment of heat that is removed from the cylinder gas, stored, then later returned during each cycle has been termed "pumped heat." Although pumped heat is unimportant in normal cast iron engines, for highly insulated surfaces it has been estimated to be as large as a third of the net heat flux for a metallic uninsulated surface [10]. This is one of the reasons the LHR engine can never be "adiabatic," despite the frequent use of that misnomer.

The foregoing discussion was concerned with convective heat transfer from the cylinder gas, but radiation must not be overlooked. Radiant heat transfer from the combustion *gas* contributes only a small fraction of the total cylinder heat loss, but radiation from the incandescent soot particles formed during the diffusion-controlled combustion of the diesel engine cannot be ignored. As convection is decreased in the LHR engine through insulation of the walls, the significance of the radiant loss increases. This is partly because as cylinder-gas temperature is increased, and soot temperature along with it, the radiant loss from a soot particle, being sensitive to the fourth power of temperature, rises disproportionately. In one attempt to model heat loss from the cylinder of a turbo charged DI diesel, insulating the cylinder approximately doubled the percentage of the rejected heat that was attributable to radiation at full load—to 43 and 26 percent, respectively, at 1000 and 2100 rpm [11].

In considering heat transfer in the LHR diesel, the recent experiments of Woschni and Spindler must not be overlooked [12]. The convective heat transfer rate is given by

$$q = hA(T_g - T_w) \tag{2}$$

where q = rate of heat transfer; h = convective heat transfer coefficient; A = cross-sectional area; T_g = gas temperature; T_w = wall temperature.

Conventional wisdom says that insulation decreases the temperature difference on the right side of equation (2) and hence the heat flux on the left. That observation is based on experience with nonreacting gas, however. Woschni and Spindler have experimental evidence that with combustion occurring in an operating diesel engine, when the wall temperature is driven upward by insulating the cylinder, the heat transfer coefficient may go up even faster than the temperature difference goes down. Then heat flux actually *increases* as a result of insulation. If that is true, existing fuel-consumption projections for the LHR diesel are likely optimistic because they are based on extrapolations of conventional heat transfer technology. It is expected that experiments to either verify or refute the results reported by Woschni and Spindler will receive high priority in the engine community.

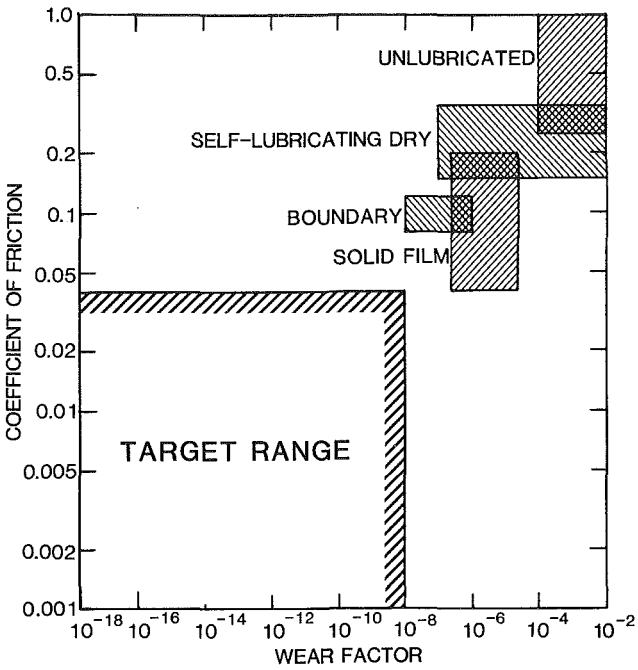


Fig. 5 Coefficient of friction versus wear factor for various lubricant schemes

Tribology

Tribology, which involves lubrication, friction, and wear, is another technology essential to the success of the LHR diesel. The heart of the tribology problem lies in the elevated operating temperature of the LHR engine. For 60 percent adiabaticity, temperatures at the point of top ring reversal in the 550–600°C range are anticipated [2]. This is simply too hot for known liquid lubricants. It is well beyond the capabilities of today's petroleum-based oil. The synthetic lubricant used in aircraft gas turbines is good for another 200°C, but that is still not high enough for reasonable oil-change intervals. Even the more advanced synthetics, which promise another 150°C, appear unable to cope.

There are other concerns with many of these new synthetics. Some are so viscous at wintertime temperatures that they cannot be pumped by traditional means. In addition, current petroleum-based oils contain up to 15 percent additives that include anti-oxidants, anti-wear agents, anti-foam agents, rust inhibitors, detergents, pour-point depressants, etc. Assuming such additives will be necessary in advanced lubricants as well, additives will have to be developed to extend their thermal stability to temperatures not previously experienced. Problems such as these have caused some to focus on nonliquid lubricants.

To appreciate the problem with other lubricant types, it is helpful to refer to Fig. 5, where coefficient of friction is plotted versus a parameter proportional to wear [13]. In today's cooled engine, a hydrodynamic liquid film is normally maintained between the piston and the cylinder wall over most of the piston stroke. Near top and bottom dead center, however, the piston velocity is too slow to support a hydrodynamic and the friction coefficient rises accordingly. Fortunately this happens when the piston velocity is near zero, so the associated power loss is minimal. Averaging the friction over the complete stroke, an equivalent coefficient of friction of 0.04 has been selected as typical for the interface between piston and liner. At the same time, the maximum acceptable wear rate is represented on the abscissa by a factor of 10^{-8}. That defines the target range in the lower left corner.

Downloaded 01 Jun 2010 to 171.66.16.87. Redistribution subject to ASME license or copyright; see http://www.asme.org/terms/Terms_Use.cfm

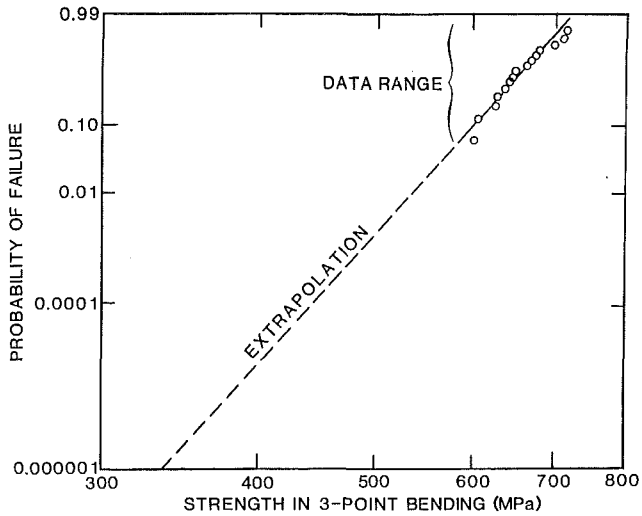


Fig. 6 Probability of failure for 15 ceramic specimens as represented on Weibull coordinates

A number of lubrication options are represented by patches above and to the right. Unlubricated surfaces logically offer the highest friction and the highest wear. The next lowest friction comes from a self-lubricating dry pair, as exemplified by the use of a Teflon surface. Down and to the left is a patch for boundary lubrication. This is encountered when the asperities on the two surfaces pierce the oil film, allowing local contact and leading to excessive friction and wear. The fourth patch is for solid-film lubrication. Molybdenum disulfide and graphite are common solid lubricants. Solid-film lubrication has been suggested as a replacement for liquid lubricants in the LHR engine. Clearly, significant improvements in both friction and wear are necessary for this option, although the lower limit of the patch is getting down to the limiting friction. The importance of attaining competitive friction is emphasized by the fact that estimates of fuel-consumption gains for the LHR engine were on the order of 2–6 percent. It will not suffice to effect those gains through heat conservation and then give them up again because of increased friction.

Having reviewed current limitations for liquid and solid lubricants, gas is left. It has been suggested that the liner and a ringless piston be separated by a thin film of gas leaking from the cylinder. Obviously, a finite clearance must be maintained between them. As engine speed decreases, there is more time for leakage through this clearance to occur, so the fraction of the cylinder charge blowing by the piston must increase. This is bound to decrease compression pressure and temperature, raising questions about the ability to cold-start such an engine by compression ignition. It is also clear that very tight clearance must be maintained between the piston and the cylinder wall lest the leakage penalize the efficiency of the cycle to the point where the anticipated fuel-consumption improvement is lost. When one considers that today's engine is expected to start promptly and to tolerate abrupt shutdowns in ambient-temperature regimes ranging from arctic to desert, the difficulty of simultaneously accommodating differential thermal expansion and tight running clearances becomes a genuine concern. Clearly, what is needed for the LHR diesel is a tribological breakthrough. In the interim, it may prove worthwhile to accept some intermediate level of adiabaticity through partial insulation in order to restrict lubricant requirements to levels attainable with available technology.

Ceramics

The successful LHR diesel needs significant advancements in the materials field, especially with ceramics. A major requirement here is to educate the designer in how to work with brittle materials.

Table 2 Ceramic requirements for coating a metal substrate

	Thermal conductivity	Expansion coefficient
Insulation	Low	——
Thermal stress	High	Low
Adherence	——	High

Dealing with brittle ceramics requires a probabilistic approach. The probability of failure is customarily presented on a Weibull plot, exemplified by Fig. 6. It shows the probability of failure—here for 15 supposedly identical specimens—as a function of bending stress on special coordinates defined by Weibull statistics. When plotting failure probability on Weibull paper, the data points tend to fall along a straight line, as illustrated. Note that no two specimens failed at the same calculated stress. If 15 metal specimens were similarly tested, their ductility would allow for some local yielding around potential failure sites, so their line would be practically vertical. This allows the designer to work with a simple safety factor applied to handbook strength data for metals. With ceramics, on the other hand, the designer has to add a new dimension: the acceptable failure rate. Suppose that a failure rate of one in a million is judged acceptable for a commercial product. Clearly, it is impractical to test anywhere near a million samples, so the designer must rely on Weibull statistics.

In this particular illustrative case, that means the designer must extrapolate the results from the 15 specimens as illustrated in Fig. 6. It takes a lot of faith to trust Weibull statistics over that range. Moreover, it is worrisome to know that the correlation between failures in simple bend-test bars such as used to establish such a Weibull plot and failures in a part of complex shape is often poor. Whether this is caused by anisotropy in the complex part, differences in surface preparation between test bar and part, inability to estimate stress in the part accurately, some other cause, or a combination of such causes is not yet defined.

Experience with structural ceramics to data makes it evident where further work is required before the widespread acceptance of monolithic ceramics in engines becomes an accomplished fact. First, greater uniformity in ceramic parts—as characterized by the Weibull modulus—is needed. Second, recognizing the probabilistic nature of failure inherent in brittle materials, fast and inexpensive inspection techniques for culling out faulty parts need to be developed. Third, finite element stress-estimate methodology must be refined to secure closer agreement between what happens in the computer and what happens in the real world. Fourth, ceramics producers must get their costs down to where the parts produced are competitively attractive.

That list of needs is so difficult that for the time being, many engine practitioners have replaced monolithic structural ceramics for insulating the combustion chamber in their minds with ceramic coatings applied to metal substrates. However, coatings are not without their problems. Consider the conflicting set of requirements presented in Table 2. For good insulation characteristics, a low thermal conductivity is desired, but to minimize the thermal stress in the coating itself, a high thermal conductivity is desired. To minimize thermal stress in the coating itself, a low coefficient of thermal expansion is desired. On the other hand, to encourage adherence of the coating to the metal substrate, a high coefficient of thermal expansion is desired, at least relative to other ceramics.

Despite these difficulties, the ceramic coating has some attractive features that make it worth pursuing. For one, by applying the ceramic to a metal substrate, it is relieved of the job

Downloaded 01 Jun 2010 to 171.66.16.87. Redistribution subject to ASME license or copyright; see http://www.asme.org/terms/Terms_Use.cfm

of carrying structural loads. This allows the use of zirconia, which lacks strength but has extremely low thermal conductivity, as indicated earlier.

Freeing the coating from the load-bearing task also allows it to be applied with increased porosity. This further enhances its insulative capability. The coating has to be thick enough to sustain a temperature drop across it that will prevent overheating of the metal substrate. A typical requirement is a thickness of 5 mm. A consequence of so thick a coating is greater difficulty in getting it to adhere to the substrate. Application of a bond coating between the substrate and the coating itself helps. Varying the composition of the coating in layers through its depth is another option being tried. Time will tell whether the coating technology can beat the monolith into the field.

Summary

The LHR engine may some day be added to the limited list of innovative developments punctuating the history of the diesel engine, but it is not ready today. Among its promises are improved fuel consumption, elimination of the traditional cooling system, and the ability to burn lower-quality fuels. It still offers challenges in a number of disciplines:

1 *Thermodynamics*—How to recover the increased energy in the exhaust stream effectively over the engine operating range needs resolution.

2 *Combustion*—The need to satisfy emission regulations must be addressed.

3 *Heat Transfer*—The question of whether insulation actually increases heat transfer at high temperatures, as held by some, must be settled.

4 *Tribology*—A suitable higher-temperature lubrication system is needed before the LHR engine can reach its full potential.

5 *Ceramics*—Improved uniformity in properties, fast and inexpensive inspection techniques, better failure-prediction methodology, and lower cost are required.

In the process of addressing these challenges, it is likely that many of the lessons learned will facilitate improvements in advanced models of existing engines.

References

1 French, C. C. J., "Internal Combustion Engines for the Nineties and Beyond—Challenges and Opportunities," 1985 Calvin W. Rice Lecture, presented to the ASME, Feb. 1986.

2 Yoshimitsu, T., Toyama, K., Sato, F., and Yamaguchi, H., "Capabilities of Heat Insulated Diesel Engine," SAE Paper No. 820431, 1982.

3 Savliwala, M. N., and Hakim, N. S., "Statistically Optimized Performance Predictions of Low Heat Rejection Engines," *SAE Transactions*, Vol. 95, 1986, pp. 2.384-2.397.

4 Morel, T., Keribar, R., Blumberg, P. N., and Fort, E. F., "Examination of Key Issues in Low Heat Rejection Engines," *SAE Transactions*, Vol. 95, 1986, pp. 2.398-2.414.

5 Bailey, M. M., "Comparative Evaluation of Three Alternative Power Cycles for Waste Heat Recovery From the Exhaust of Adiabatic Diesel Engines," NASA TM-86953, July 1985.

6 Gatowski, J. A., Jones, J. D., and Siegla, D. C., "Evaluation of the Fuel Economy Potential of the Low-Heat-Rejection Diesel Engine for Passenger Car Application," SAE Paper No. 870024, 1987.

7 Bryzik, W., and Kamo, R., "TACOM/Cummins Adiabatic Engine Program," *SAE Transactions*, Vol. 92, 1983, pp. 1.1063-1.1087.

8 Suziki, T., Tsujita, M., Mori, Y., and Suzuki, T., "An Observation of Combustion Phenomenon on Heat Insulated Turbo-charged and Intercooled D. I. Diesel Engines," *SAE Transactions*, Vol. 94, 1986, pp. 4.804-4.819.

9 Sudhakar, V., and Hunter, G., "Transient Emissions From an Uncooled Diesel Engine," SAE Paper No. 860224, 1986.

10 Morel, T., Keribar, R., and Blumberg, P., "Cyclical Thermal Phenomena in Engine Combustion Chamber Surfaces," SAE Paper No. 850360, 1985.

11 Morel, T., and Keribar, R., "Heat Radiation in D.I. Diesel Engines," *SAE Transactions*, Vol. 95, 1986, pp. 2.1141-2.1157.

12 Woschni, G., and Spindler, G., "Heat Transfer With Insulated Combustion Chamber Walls and Its Influence on the Performance of Diesel Engines," *Basic Processes in Internal Combustion Engines*, T. Uzkan and J. M. Bailey, eds., ASME ICE-Vol. 3, 1988, pp. 33-41; ASME JOURNAL OF ENGINEERING FOR GAS TURBINES AND POWER, Vol. 110, 1988, this issue.

13 Peterson, M. B., Wear Sciences Corporation, Personal Communication, 1987.

Downloaded 01 Jun 2010 to 171.66.16.87. Redistribution subject to ASME license or copyright; see http://www.asme.org/terms/Terms_Use.cfm

Heat Transfer With Insulated Combustion Chamber Walls and Its Influence on the Performance of Diesel Engines

G. Woschni

W. Spindler

Technische Universität of Munich,
Munich, Federal Republic of Germany

Recently great expectations were put into the insulation of combustion chamber walls. A considerable reduction in fuel consumption, a marked reduction of the heat flow to the cooling water, and a significant increase of exhaust gas energy were predicted. In the meantime there exists an increasing number of publications reporting on significant increase of fuel consumption with total or partial insulation of the combustion chamber walls. In [1] a physical explanation of this effect is given: Simultaneously with the decrease of the temperature difference between gas and wall as a result of insulation, the heat transfer coefficient between gas and wall increases rapidly due to increasing wall temperature, thus overcompensating for the decrease in temperature difference between gas and wall. Hence a modified equation for calculation of the heat transfer coefficient was presented [1]. In the paper to be presented here, recent experimental results are reported that confirm the effects demonstrated in [1], including the influence of the heat transfer coefficient, which depends on the wall temperature, on the performance of naturally aspirated and turbocharged engines.

Introduction

Today process simulation is not only an important means for the development of an engine but also indispensable for scientific experimental investigations into the problems of internal combustion engines. With simulation it is possible to analyze more precisely the complex process occurring in an internal combustion engine resulting from the interaction of the different physical subprocesses that comprise the different physical events. A remarkable example of this is the experimental evaluation of the heat transfer coefficient between gas and cylinder wall. This heat transfer coefficient differs widely from location to location. For process simulation one therefore needs an area-averaged value. There are several possibilities to evaluate these values experimentally.

The method used most frequently today is the evaluation of measured time-variable surface temperatures, from which one obtains immediately the time-variable heat flux and heat transfer coefficient by applying Fourier's differential equation. The main weakness of this procedure is that one obtains only local values, which differ widely from position to position, and even for spark ignition engines scatter by more than 100 percent [2].

Even if a great number of surface thermocouples is used to obtain area-averaged values, this only yields tendencies, and the dependence on certain parameters such as engine speed, load, boost pressure, and so on, are difficult and uncertain to reproduce. Most disturbing is the influence of the soot layer in diesel engines [3].

A much simpler method is the measurement of the steady-state heat flux with a heat flux probe, as is described for instance in [4, 5]. Of course such a probe gives only local values and usually can be installed only in very few locations in the combustion chamber. Moreover the signal of the heat flux probe is a time-averaged value over the whole cycle.

An area- and time-averaged value of the heat transferred to the walls can be derived from a heat balance, whereby either the heat absorbed by the coolant or the heat given off by the gas can be taken into account. These differ by the friction heat equivalent and a remainder comprising all the uncertainties of the heat balance.

Finally, cylinder pressure analysis for the evaluation of the heat release delivers as a byproduct the heat flow to the wall, which is time averaged and area integrated over the high-pressure phase of the cycle.

With the two previously mentioned methods, equations for the area-averaged heat transfer can be established. They yield systematically reproducible tendencies for these integral heat flows. With a reasonable formulation for an equation of the heat transfer coefficient, these integral heat flows can be calculated making use of a process simulation program. Thus the constants and exponents in the equation for the calculation of the heat transfer coefficient can be determined step by step.

Contributed by the Internal Combustion Engine Division and presented at the Eleventh Annual Energy-Sources Technology Conference and Exhibition, New Orleans, Louisiana, January 10–13, 1988. Manuscript received by the Internal Combustion Engine Division April 1987.

Copyright © 1988 by ASME
Downloaded 01 Jun 2010 to 171.66.16.87. Redistribution subject to ASME license or copyright; see http://www.asme.org/terms/Terms_Use.cfm

In [6] such an equation that was established in the way described was presented. It is

$$h = 130 d^{-0.2} T^{-0.53} p^{0.8} \cdot \left[C_1 c_m + C_2 \frac{V_H T_1}{p_1 V_1} (p - p_0) \right]^{0.8} \quad (1)$$

The formulation of the equation was deduced from the laws of similarity for convective heat transfer. The equation corresponds to the dimensionless relation

$$\mathrm{Nu} = 0.035\ \mathrm{Re}^{0.8}$$

The term

$$C_1 c_m + C_2 \frac{V_H T_1}{p_1 V_1} (p - p_0)$$

is used as an equivalent for the velocity, where

$$C_1 = 6.18 + 0.417 (c_u / c_m)$$

for the scavenging period;

$$C_1 = 2.28 + 0.308 (c_u / c_m)$$

for the compression and expansion strokes;

$$C_2 = 3.24 \times 10^{-3}$$

for nondivided combustion chambers;

$$C_2 = 6.22 \times 10^{-3}$$

for divided combustion chambers.

Here a distinction is made between a gas motion generated by piston displacement, which shows a dependence on intake swirl, and a second term considering the motion and turbulence generated by combustion.

The constant C_2 depends on the kind of combustion system. Of course the combustion term includes the influence of radiation, as well as further influences like heat sources near the wall during combustion.

Excellent results were obtained with this equation during the past two decades. If it is used together with process simulation, one succeeds in reliably calculating the integral heat flow as well as the time-variable curve of the area-averaged heat flux for different size engines, from medium-speed on to high-speed diesel engines and spark ignition engines without the necessity of altering the abovementioned constants, which means matching them to different engines.

Thus knowing the heat release diagram, it is possible to predict with sufficient accuracy the main performance parameters like power, mean effective pressure, fuel consumption, exhaust gas temperature, and heat rejection for both naturally aspirated and turbocharged engines [7].

Engine Performance Prediction With High Surface Temperatures

Very recently it was found that there were considerable differences between cycle simulation prediction and measured values when the combustion chamber was insulated, which means high surface temperatures. In [1] it could be demonstrated by systematic investigations that heat transfer during combustion increases considerably with high surface temperatures.

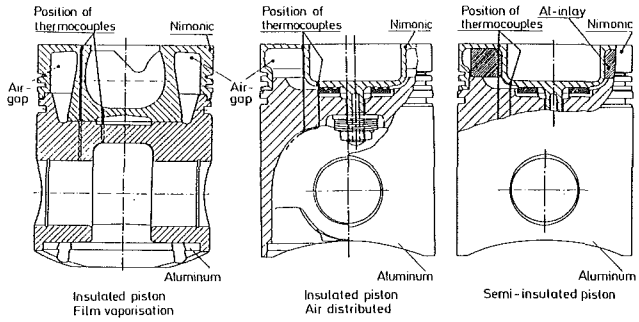


Fig. 1 Low-heat-rejection pistons

Since this knowledge is new and calls into question the effectiveness of insulation, it will be proved in the following by further investigations. Experiments were made with a single-cylinder four-stroke diesel engine with a 125 mm bore, 140 mm stroke, a rated speed of 2200 rpm, and the possibility of supercharging. The engine could be equipped with two different combustion systems, the one with mainly film vaporization, and the other with mainly air distributed fuel.

Heat insulation was provided for the piston only, and not by ceramics but rather by constructing the piston with a Nimonic piston crown, air gaps, and long narrow heat flow paths. All together five pistons were available, including the three insulated pistons shown in Fig. 1. Here the first is for film vaporization, the second one for air-distributed fuel, and the third one also for air distribution, the air gaps however being partially filled by an aluminum inlay to give a lower degree of insulation. Furthermore, standard aluminum pistons were available for reference with both combustion systems.

For natural aspiration, both insulated pistons had a mean piston-top temperature of about 980 K at full load, the semi-insulated piston attained about 600 K, and both standard pistons reached about 480 K, which means that the insulation was very good.

Figure 2 shows the measured specific fuel consumption for both standard pistons in the naturally aspirated engine plotted against engine load. Plotted also in the same figure are the fuel consumptions as calculated by process simulation using the measured heat release diagrams and the heat transfer coefficients obtained from equation (1).

First of all one recognizes that the results of the process simulation coincide very well with the experimentally obtained values for the standard pistons, this again without any matching of the constants in equation (1) to the particular engine. For the insulated pistons the process simulation predicts an improvement in fuel consumption, which is indeed relatively small. The experiments, however, result in a signifi-

Nomenclature

c_m = mean piston speed, m/s
c_u/c_m = swirl factor
d = cylinder diameter, m
h = heat transfer coefficient, W/m²K
k = thermal conductivity, W/mK
Nu = Nusselt number
p = gas pressure, bar abs
p_0 = pressure trace of motored engine, bar abs
p_1 = gas pressure in cylinder—intake valve closes, bar abs
Q_f = fuel input energy, kJ/cycle
Q_{piston} = heat rejection to piston, kJ/cycle
Q_{wall} = heat rejection to cylinder wall, kJ/cycle
T = gas temperature, K
T_1 = gas temperature—intake valve closes, K
V_H = swept volume, m³
V_1 = total cylinder volume—intake valve closes, m³
φ = crank angle

Downloaded 01 Jun 2010 to 171.66.16.87. Redistribution subject to ASME license or copyright; see http://www.asme.org/terms/Terms_Use.cfm

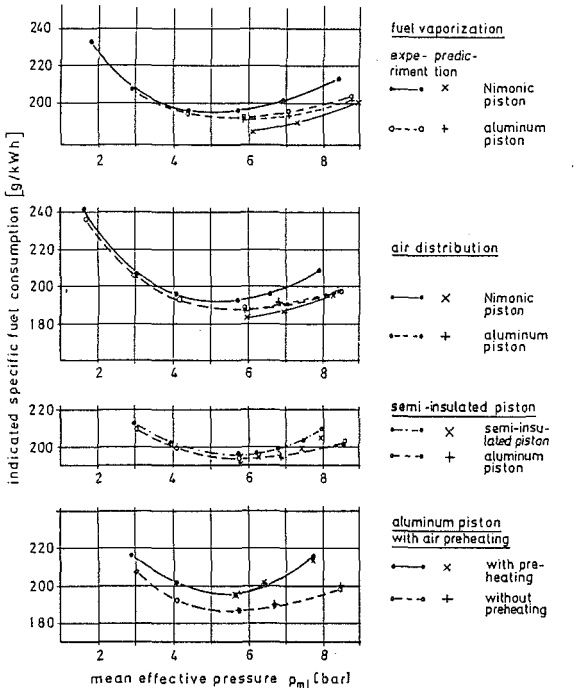


Fig. 2 Indicated specific fuel consumption for different piston configurations

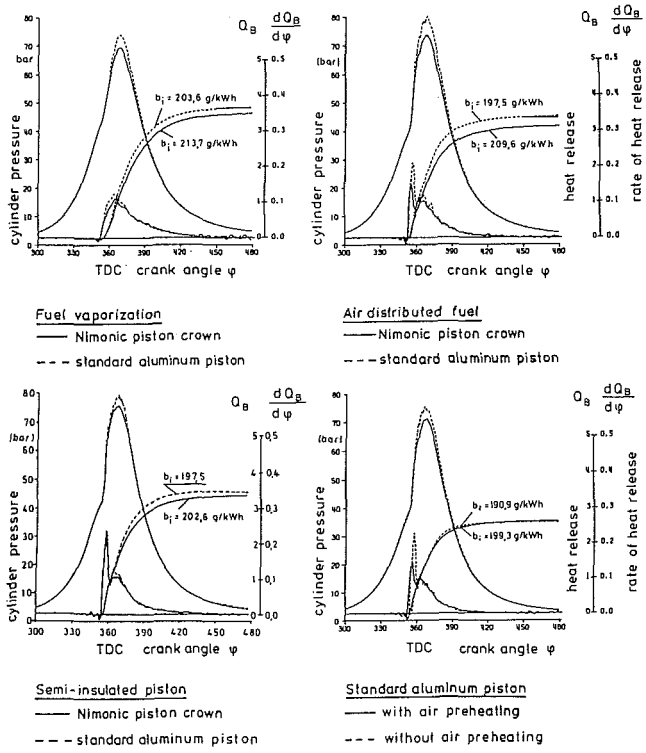


Fig. 3 Combustion process with insulated piston

cant increase in fuel consumption. The difference becomes greater the higher the load and the better the insulation is.

This is a clear indication that the effect is more significant the higher the temperature of the piston crown is. The lowermost curves in Fig. 2 show the results of an experiment where, for the air-distributed fuel combustion system and standard piston, the level of process temperature was increased by external preheating of the intake air to achieve the same exhaust gas temperature as with the insulated piston. Here the coincidence of the results of the process simulation and the experiment is excellent, which again is an indication that the height of the surface temperature is decisive for the difference between measured and predicted results.

In addition these results disprove the thesis discussed among experts [8] that the process temperature level, and consequently the flame radiation, will be increased extremely by high combustion chamber surface temperatures. The results presented here show that equation (1) represents correctly the integral heat transfer, including radiation, as long as the surface temperatures are not excessive.

An increase in fuel consumption with high surface temperature has also been reported in [9–11], so today this result has to be regarded as confirmed. Figure 3 shows the heat release diagrams obtained from measured cylinder pressure diagrams for the three pistons shown in Fig. 1 as well as for the experiment with the standard piston and air preheating for full load in the naturally aspirated engine.

It can be seen that neither for the air-distributed nor for the film-vaporization combustion chamber is there a significant influence on the heat release diagram from the high surface temperature. Because of a shorter ignition delay, the start of combustion advances by about one degree of crank angle. The combustion duration is not altered; only the shapes of the heat release diagrams differ a little bit.

The influence of this modification on the shape of the heat release diagram on fuel consumption can be found easily by the application of process simulation if, for other conditions constant, only the different measured heat release diagrams are used. The influence on the fuel consumption caused by the slight delay of the combustion is on the order of about 1 g/kWh.

However, if one has a look at the integrated heat release diagram, one can see that with the insulated pistons a considerable part of the energy input—on the order of 5 percent of the fuel input—is lost during the first part of the combustion. In the final part of the combustion, from about 390 deg crank angle on, the curves for standard and insulated pistons are practically parallel, while in all experiments with standard pistons, even those with air preheating, the integrated heat release curve at the end of combustion attains the energy level that was calculated from the measured fuel flow.

After having checked that the blow-by of all pistons was of the same magnitude, this result meant that during the combustion phase with heat insulation of the combustion chamber there must be a significant increase in heat transfer due to the high surface temperature of the combustion chamber. Consequently equation (1) loses its validity with very high surface temperatures.

Influence of Surface Temperature on the Heat Transfer Coefficient

The most recent literature gives indications for the reason behind this increase in heat transfer with increasing surface temperatures [12]. For steady-state propane flames it was measured that above a certain surface temperature the heat transfer between a flame and a solid wall suddenly began to rise steeply with further increases in surface temperature.

This phenomenon, in the French language called "convection vive," is explained by the flame burning closer to the wall with high wall surface temperatures. The laminar boundary layer becomes thinner and the temperature gradient immediately at the wall becomes steeper; hence the heat transfer coefficient is increased.

This effect could also occur in internal combustion engines during combustion and could be the reason for the increased heat transfer and fuel consumption with insulated combustion chambers. If the constant C_2 of the combustion term in equa-

Downloaded 01 Jun 2010 to 171.66.16.87. Redistribution subject to ASME license or copyright; see http://www.asme.org/terms/Terms_Use.cfm

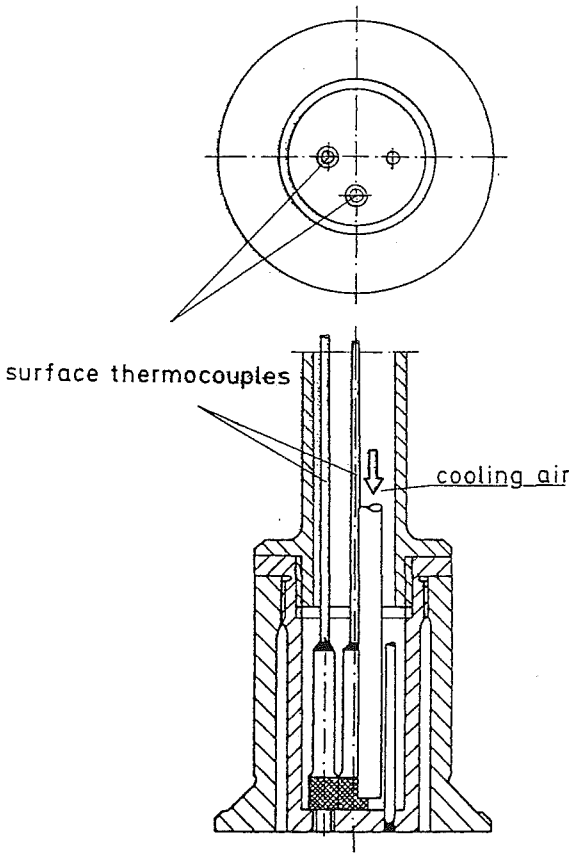


Fig. 4 Surface temperature probe

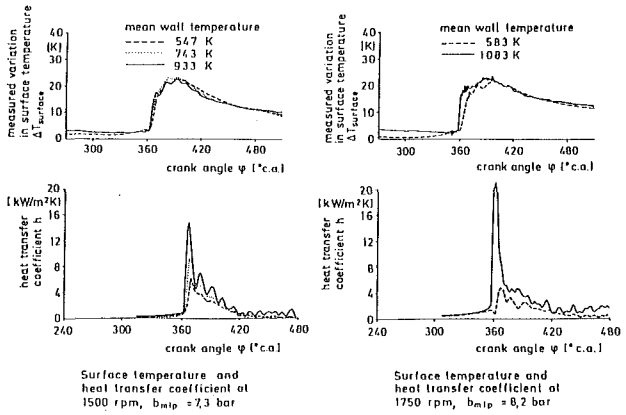


Fig. 5 Surface temperatures and heat transfer coefficients

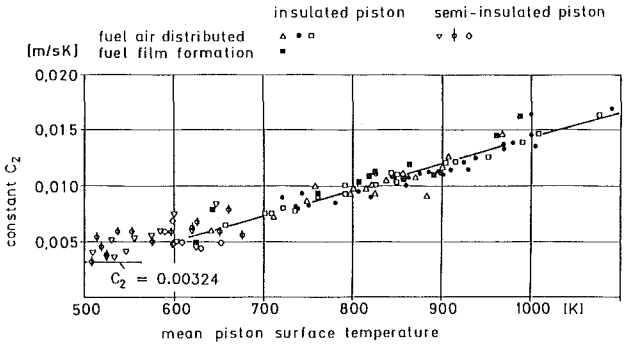


Fig. 6 Constant C_2 in equation (1) as a function of wall temperature

tion (1) were increased to such an extent that the measured and calculated fuel consumptions coincided for engines with insulated combustion chambers, it could be shown that the heat transfer coefficient during the combustion phase ought to be about 2.5 times the previous value to justify the increase in fuel consumption.

This inspired us to prove this phenomenon experimentally by the evaluation of measured surface temperature curves. In a different single-cylinder test engine of similar size having a four-valve cylinder head, one of the two exhaust valves was replaced by an air-cooled probe, shown in Fig. 4, which contained two surface temperature thermocouples of the Medtherm type.

With this probe it was possible to alter its surface temperature level within wide limits between about 650 K and 1100 K at a constant engine operating point by variation of the cooling air quantity without otherwise altering the heat transfer conditions on the gas side.

Since the probe, which attains higher temperatures than the surrounding material, takes just a small area of the whole combustion chamber, the process temperature level and the state of the gas in the cylinder are not influenced. Figure 5 shows the measured surface temperature curves and the evaluated heat transfer coefficients [13].

It can clearly be seen that the heat transfer coefficient during the combustion phase is increased for higher surface temperatures. If the engine operating point is kept constant, the peak value of the heat transfer coefficient is increased from about 4000 W/m^{2}K to about 20,000 W/m^{2}K when the surface temperature is increased from 583 K to 1083 K. These results confirm qualitatively the effect observed.

Of course they represent, as already mentioned, only local values, which cannot be compared with area-averaged values. Nevertheless they are a convincing proof that heat transfer increases strongly with high surface temperatures during the combustion, and that the reason is the effect of "convection vive" and not an excessive flame radiation, since the process temperature level remains almost constant.

In [14, 15] results are presented that confirm the values found here. In [16, 17], however, experiments are reported where such effects were not observed. In these cases the reason may be that the increase in surface temperature was too low. All results presented here show that the effect is more significant, the higher the increase of the surface temperature is.

A further reason may be that in [16, 17] only the heat flux is presented, not the physically more evident heat transfer coefficients, which represent this phenomenon far more clearly. Indeed, as already mentioned initially, results obtained by this method cannot be used to establish a modified equation for the area-averaged heat transfer coefficient.

For this reason the following procedure was selected to extend equation (1) so that it includes the influence of high surface temperatures on heat transfer. One has to proceed from the fact that the increase occurs only during combustion, and furthermore that the effect is caused by the increase in flame-generated local turbulence next to the combustion chamber wall if the flame comes closer to the wall as a result of higher surface temperature. So it is logical to take this effect into account with the constant C_2 for the combustion term.

Therefore for all test results obtained with the three pistons shown in Fig. 1, for a naturally aspirated engine, supercharging, and different engine load and speed, the constant C_2 in equation (1) was adjusted in the process simulation so that for each measured value the calculated and the measured specific fuel consumption coincided.

If the constant C_2 determined this way is plotted against the mean piston-top temperature, it can be seen from Fig. 6 that the experiments with all three pistons of Fig. 1 results in a straight line with relatively little scatter, which can be expressed by the equation

$$C_2 = 2.3 \times 10^{-5}(T_W - 600) + 0.005 \qquad [\text{m/sK}] \qquad (2)$$

Downloaded 01 Jun 2010 to 171.66.16.87. Redistribution subject to ASME license or copyright; see http://www.asme.org/terms/Terms_Use.cfm

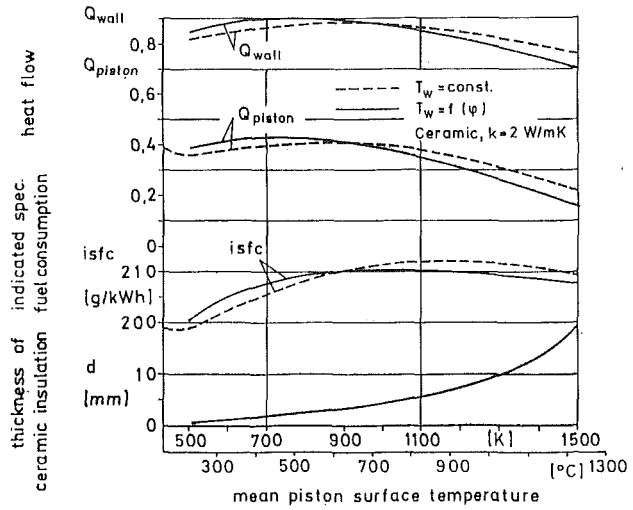


Fig. 7 Heat flow, isfc, and thickness of ceramic insulation versus mean piston crown temperature

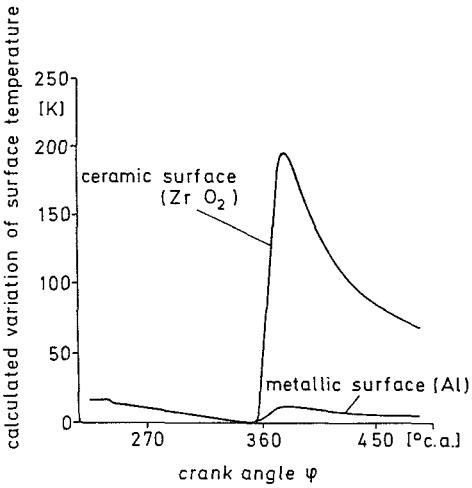


Fig. 8 Surface temperature variation for ceramic and metallic combustion chamber wall, 1500 rpm, full load

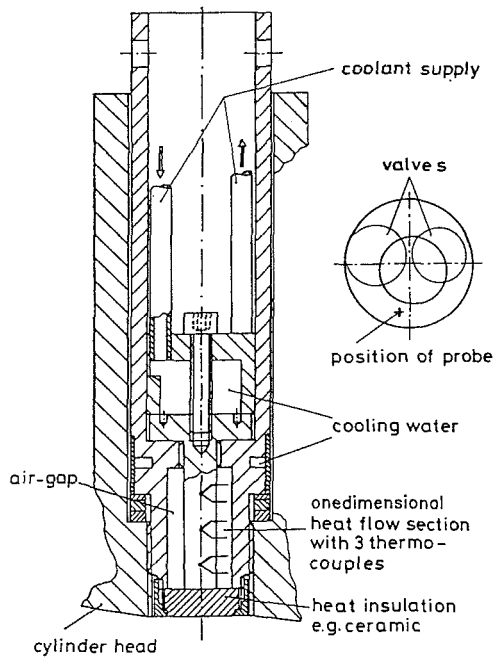


Fig. 9 Heat flux probe

The results from the semi-insulated piston also fit the left end of the curve. If equation (2) is introduced into equation (1), one succeeds in extending the range of validity of equation (1) beyond 600 K.

In the process simulation, of course, at higher surface temperatures the corresponding surface temperature has to be calculated with the aid of a heat flow model for each operating point.

Figure 7 shows results from the process simulation for full load of the naturally aspirated engine with air-distributed fuel for different surface temperatures of the piston top, which means a different degree of insulation. One can distinguish three ranges. Up to a mean surface temperature of the piston top of about 500 K the heat flow to the piston, the heat transferred to the coolant, and the specific fuel consumption decrease with increasing surface temperatures. Surface temperatures below 500 K exist at full load only for both naturally aspirated and turbocharged engines with noninsulated components.

Naturally aspirated, and most of all supercharged engines, may also attain such surface temperatures at part load with some degree of insulation of the components. This explains why there is no significant increase in fuel consumption at part load, as can be seen from Fig. 2.

Occasionally some decrease in fuel consumption at part load [18], or in test cycles which cover mainly part load of the engine [8], has even reported.

A more effective insulation, which means higher mean surface temperatures, results in an increasing fuel consumption and even in an increase of the heat transferred to the coolant (Fig. 7). The necessary thickness of a ceramic layer with a heat conductivity of 2 W/mK to attain the respective temperature is also plotted in Fig. 7.

Only with very high surface temperatures is there a reduction of the heat flow, and with still higher surface temperatures there is even a reduction of the fuel consumption, which never again reaches the low values obtained without insulation, however.

The fuel consumption reacts more sensitively to high surface temperatures than the heat flux. The reason is that the increasing heat transfer coefficient overbalances the positive effect of the decreasing temperature difference between gas and wall, and the marked increase of the heat transfer coefficient occurs only during the main combustion, where the availability of the gas is particularly high.

The dashed lines were calculated under the assumption of a surface temperature that was constant with time as is correct with good approximation for all metallic materials. As can be seen from Fig. 8, where the calculated surface temperature amplitudes for ceramic (ZrO_2) and aluminum are compared, the amplitude for the ceramic material is about ten times higher. If this is taken into account for the process simulation, the full lines in Fig. 7 are obtained.

To verify these results experimentally an attempt was made to measure the heat flux directly with a different degree of insulation. For this purpose the steady-state heat flux probe shown in Fig. 9 was built. The front end of the probe could be covered by metal and ceramic disks of different thickness. By that means it was possible to obtain different degrees of insulation and hence a variation of the surface temperature within wide limits. The probe was installed in the cylinder head in a location shown in the right part of Fig. 9, the only place accessible. Figure 10 shows the results obtained. For comparison, the simulated area-averaged heat flux is also plotted as a dotted line as calculated with the original equation (1) for the heat transfer coefficient, and as a dashed line as

Downloaded 01 Jun 2010 to 171.66.16.87. Redistribution subject to ASME license or copyright; see http://www.asme.org/terms/Terms_Use.cfm

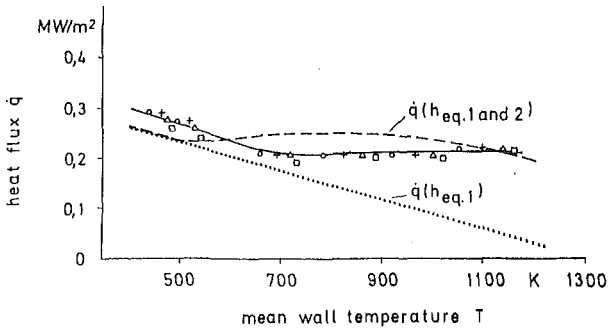


Fig. 10 Heat flux versus wall temperature, 1500 rpm, full load

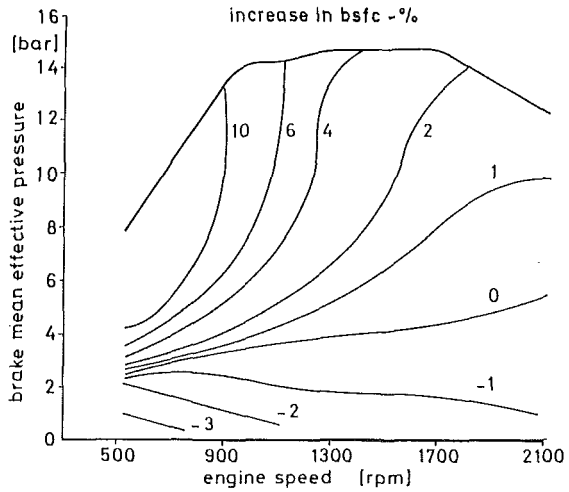


Fig. 11 bsfc of turbocharged diesel engine with heat-insulated piston as related to standard piston

calculated with the modified equation (1) using equation (2) simultaneously.

The reason that experimental results and prediction don't coincide quantitatively is that the calculation gives area-averaged values, while the experiment gives only local values, in this case opposite the piston and outside of the combustion chamber bowl. The qualitative coincidence is very good, however.

Turbocharged and Turbocompound Engines With Heat Insulation

The conditions for turbocharged engines are still more complex. Here the surface temperature is decisively influenced by the air/fuel ratio, which means by the interaction of engine and turbocharger. With the simulation program described in [19] the indicated fuel consumption was calculated for a turbocharged eight-cylinder truck diesel engine with pistons assumed to be insulated by a ZrO_2 layer of 5 mm thickness. Figure 11 shows in a fuel consumption map the difference in specific fuel consumption as related to the basic engine with noninsulated standard piston. There is a decrease in specific fuel consumption at low load. At high load, however, there is a significant increase in specific fuel consumption.

The reason for this effect is the piston surface temperature, which at high load and low engine speed is especially high, as can be seen from Fig. 12, because here the excess air factor of 1.25 is lowest.

To what extent the total heat transferred to the cooling water is influenced by the insulation as related to the basic engine is shown in Fig. 13. It can be seen that the radiator and the fan, which have to be dimensioned for the maximum heat

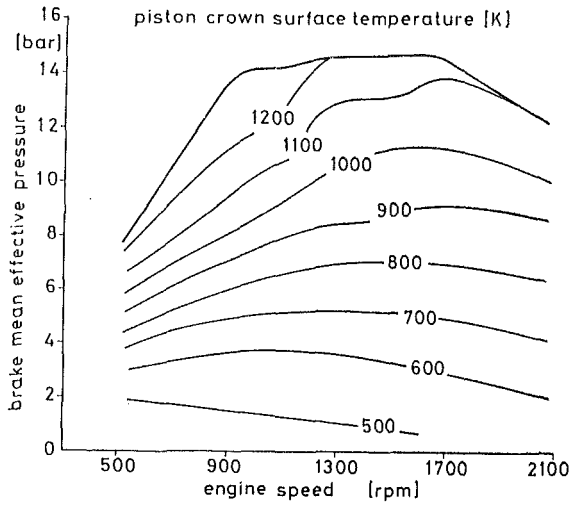


Fig. 12 Calculated piston crown surface temperature, insulated piston

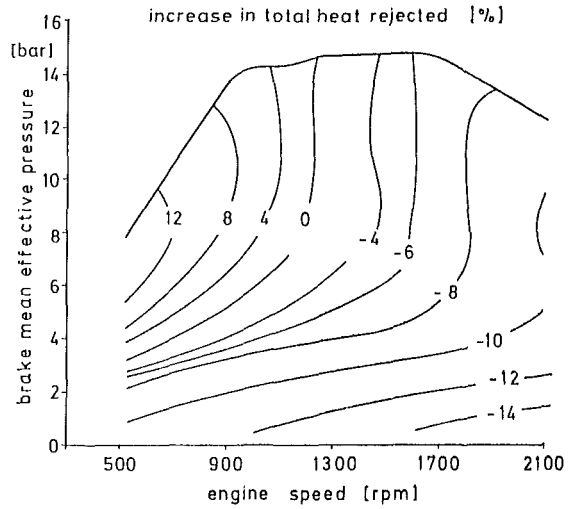


Fig. 13 Effect of piston insulation on total heat rejected

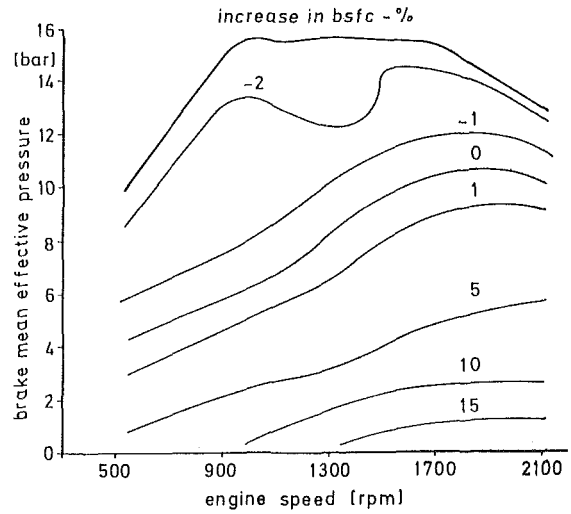


Fig. 14 Effect of turbocompounding on bsfc, standard piston

rejection occurring at maximum speed and full load in the basic engine, could be reduced by 8 percent for the engine with insulated pistons.

Figure 14 finally shows the possible gain in fuel consumption if, for the basic engine without insulated pistons, a power

Downloaded 01 Jun 2010 to 171.66.16.87. Redistribution subject to ASME license or copyright; see http://www.asme.org/terms/Terms_Use.cfm

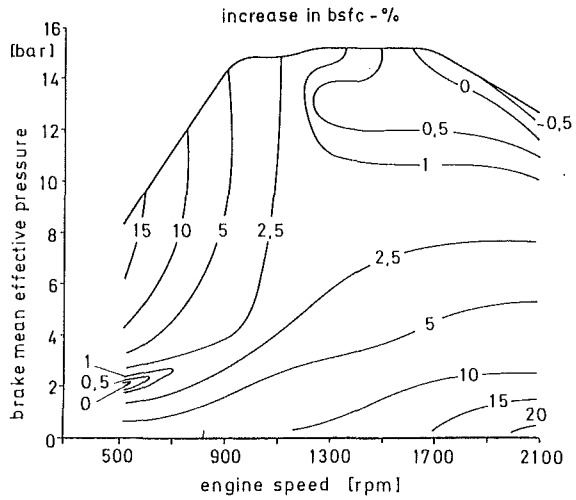


Fig. 15 Turbocompound diesel engine with insulated piston compared with turbocharged engine with standard pistons

turbine is connected downstream of the turbocharger turbine. For this turbocompounded engine a gain in fuel consumption results only in the upper load region.

The turbocompounded engine with insulated pistons would eliminate this gain in consumption, which means that the compounded engine with insulated pistons is inferior to the turbocharged engine with bare aluminum pistons over the whole engine map, as can be seen from Fig. 15.

Conclusion

Further experiments confirmed the fact presented in [1] that insulation of the combustion chamber yields savings in fuel consumption only at low load, if ever. The reason is that only for relatively low surface temperatures of the combustion chamber walls do the heat losses through the combustion chamber walls decrease according to the decreasing temperature difference between gas and surface. With higher surface temperatures the heat transfer coefficient rises rapidly, so the positive effect of the decreasing temperature difference is overcompensated. The possible gain in fuel consumption at part load in any case is paid for dearly with a significant fuel consumption increase at full load. This holds true for the naturally aspirated engine as well as for the turbocharged engine without and with an additional power turbine.

References

1 Woschni, G., Spindler, W., and Kolesa, K., "Heat Insulation of Combustion Chamber Wall—a Measure to Decrease the Fuel Consumption of I.C. Engines?" SAE Paper No. 870339, 1987.

2 Woschni, G., and Fieger, J., "Experimentelle Bestimmung des örtlich gemittelten Wärmeübergangskoeffizienten im Ottomotor," *MTZ*, Vol. 42, 1981, pp. 229-234.

3 Sihling, K., and Woschni, G., "Experimental Investigation of the Instantaneous Heat Transfer in the Cylinder of a High Speed Diesel Engine," SAE SP-449, 1979.

4 Ebersole, G. D., Meyers, P. S., and Uyehara, O. A., "The Radiant and Convective Components of Diesel Engine Heat Transfer," SAE Paper No. 701 C, 1963.

5 Hohenberg, G. F., "Advanced Approaches for Heat Transfer Calculation," SAE Paper No. 790825, 1979.

6 Woschni, G., "An Universally Applicable Equation for the Instantaneous Heat Transfer Coefficient in the Internal Combustion Engine," SAE Paper No. 670931, 1967.

7 Woschni, G., "Engine Cycle Simulation—an Effective Tool for the Development of Medium Speed Diesel Engines," SAE Paper No. 870570, 1987.

8 Van Sudhakar, M., "Development of Uncooled Engines," Congrès International "Moteurs Diesel pour Vèhicules Automobiles et Utilitaires," Lyons, May 1987.

9 Wallace, F., and Kao, T., "Thermally Insulated Diesel Engines," *Proc. IMechE.*, Vol. 198a, No. 5, 1900.

10 Cole, R. M., and Alkidas, A. C., "Evaluation of an Air Gap Insulated Piston in a Divided Chamber Diesel Engine," SAE Paper No 850359, 1985.

11 Alkidas, A. C., "Experiments With an Uncooled Single Cylinder Open-Chamber Diesel," SAE Paper No 870020, 1987.

12 Nguyen, N. N., "Über den Einfluss der Wandtemperatur auf die Reaktionsbedingungen in der Grenz schicht und insbesondere auf den konvek tiven Wärmeübergang einer Propan-Luft-Flamme," *VDI-Fortschrittsberichte*, Vol. 3, No. 89, 1984.

13 Kolesa, K., "Einfuss hoher Wandtemperaturen auf das Betriebsverhalten und insbesondere auf den Wärmeübergang direkt einspritzender Dieselmotoren," Diss., Technische Universität München, Munich, Federal Republic of Germany, 1987.

14 Enomoto, Y., Furuhama, S., and Takai, M., "Heat Transfer to Wall of Ceramic Combustion Chamber of Internal Combustion Engines," SAE Paper No. 865022, 1986.

15 Furuhama, S., and Enomoto, Y., "Heat Transfer Into Ceramic Combustion Wall of Internal Combustion Engine," SAE Paper No. 870153.

16 Hoag, K. L., "Measurement and Analysis of the Effect of Wall Temperature on Instantaneous Heat Flux," SAE Paper No. 860312.

17 Huang, J. C., and Borman, G. L., "Measurement of Instantaneous Heat Flux to Metal and Ceramic Surface in a Diesel Engine," SAE Paper No. 870155, 1987.

18 Wade, W. R., et al., "A Structural Ceramic Diesel Engine—The Critical Elements," SAE Paper No. 870651, 1987.

19 Woschni, G., Beineke, E., and Flenker, H., "Calculation of the Performance of One- and Two-Stage Turbocharged Medium Speed Diesel Engines," *IMechE Paper No. C 53/78, 1978.*

Downloaded 01 Jun 2010 to 171.66.16.87. Redistribution subject to ASME license or copyright; see http://www.asme.org/terms/Terms_Use.cfm

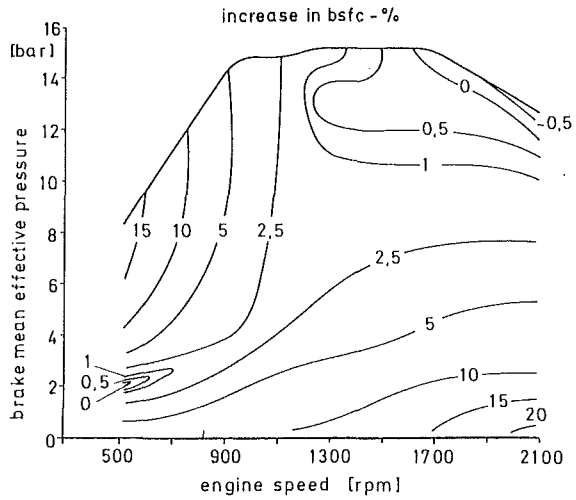


Fig. 15 Turbocompound diesel engine with insulated piston compared with turbocharged engine with standard pistons

turbine is connected downstream of the turbocharger turbine. For this turbocompounded engine a gain in fuel consumption results only in the upper load region.

The turbocompounded engine with insulated pistons would eliminate this gain in consumption, which means that the compounded engine with insulated pistons is inferior to the turbocharged engine with bare aluminum pistons over the whole engine map, as can be seen from Fig. 15.

Conclusion

Further experiments confirmed the fact presented in [1] that insulation of the combustion chamber yields savings in fuel consumption only at low load, if ever. The reason is that only for relatively low surface temperatures of the combustion chamber walls do the heat losses through the combustion chamber walls decrease according to the decreasing temperature difference between gas and surface. With higher surface temperatures the heat transfer coefficient rises rapidly, so the positive effect of the decreasing temperature difference is overcompensated. The possible gain in fuel consumption at part load in any case is paid for dearly with a significant fuel consumption increase at full load. This holds true for the naturally aspirated engine as well as for the turbocharged engine without and with an additional power turbine.

References

1 Woschni, G., Spindler, W., and Kolesa, K., "Heat Insulation of Combustion Chamber Wall—a Measure to Decrease the Fuel Consumption of I.C. Engines?" SAE Paper No. 870339, 1987.

2 Woschni, G., and Fieger, J., "Experimentelle Bestimmung des örtlich gemittelten Wärmeübergangskoeffizienten im Ottomotor," *MTZ*, Vol. 42, 1981, pp. 229-234.

3 Sihling, K., and Woschni, G., "Experimental Investigation of the Instantaneous Heat Transfer in the Cylinder of a High Speed Diesel Engine," SAE SP-449, 1979.

4 Ebersole, G. D., Meyers, P. S., and Uyehara, O. A., "The Radiant and Convective Components of Diesel Engine Heat Transfer," SAE Paper No. 701 C, 1963.

5 Hohenberg, G. F., "Advanced Approaches for Heat Transfer Calculation," SAE Paper No. 790825, 1979.

6 Woschni, G., "An Universally Applicable Equation for the Instantaneous Heat Transfer Coefficient in the Internal Combustion Engine," SAE Paper No. 670931, 1967.

7 Woschni, G., "Engine Cycle Simulation—an Effective Tool for the Development of Medium Speed Diesel Engines," SAE Paper No. 870570, 1987.

8 Van Sudhakar, M., "Development of Uncooled Engines," Congrès International "Moteurs Diesel pour Vèhicules Automobiles et Utilitaires," Lyons, May 1987.

9 Wallace, F., and Kao, T., "Thermally Insulated Diesel Engines," *Proc. IMechE.*, Vol. 198a, No. 5, 1900.

10 Cole, R. M., and Alkidas, A. C., "Evaluation of an Air Gap Insulated Piston in a Divided Chamber Diesel Engine," SAE Paper No 850359, 1985.

11 Alkidas, A. C., "Experiments With an Uncooled Single Cylinder Open-Chamber Diesel," SAE Paper No 870020, 1987.

12 Nguyen, N. N., "Über den Einfluss der Wandtemperatur auf die Reaktionsbedingungen in der Grenz schicht und insbesondere auf den konvek tiven Wärmeübergang einer Propan-Luft-Flamme," *VDI-Fortschrittsberichte*, Vol. 3, No. 89, 1984.

13 Kolesa, K., "Einfuss hoher Wandtemperaturen auf das Betriebsverhalten und insbesondere auf den Wärmeübergang direkt einspritzender Dieselmotoren," Diss., Technische Universität München, Munich, Federal Republic of Germany, 1987.

14 Enomoto, Y., Furuhama, S., and Takai, M., "Heat Transfer to Wall of Ceramic Combustion Chamber of Internal Combustion Engines," SAE Paper No. 865022, 1986.

15 Furuhama, S., and Enomoto, Y., "Heat Transfer Into Ceramic Combustion Wall of Internal Combustion Engine," SAE Paper No. 870153.

16 Hoag, K. L., "Measurement and Analysis of the Effect of Wall Temperature on Instantaneous Heat Flux," SAE Paper No. 860312.

17 Huang, J. C., and Borman, G. L., "Measurement of Instantaneous Heat Flux to Metal and Ceramic Surface in a Diesel Engine," SAE Paper No. 870155, 1987.

18 Wade, W. R., et al., "A Structural Ceramic Diesel Engine—The Critical Elements," SAE Paper No. 870651, 1987.

19 Woschni, G., Beineke, E., and Flenker, H., "Calculation of the Performance of One- and Two-Stage Turbocharged Medium Speed Diesel Engines," *IMechE Paper No. C 53/78, 1978.*

DISCUSSION

G. L. Borman[1]

For some time now considerable effort has been expended to find ways to reduce diesel engine heat rejection so that the increased exhaust energy can be utilized and the coolant system can be either reduced in size or eliminated. The many problems in achieving such goals have been discussed many times and have been excellently reviewed by Amann (Amann, 1988) at this meeting. What has been missing from these previous discussions, however, is experimental evidence of the effects of very high surface temperatures on instantaneous heat flux. Although we now have a number of papers dealing with local flux effects at insulated surfaces, only the Woschni and Spindler paper presents data for very high temperatures that include the integrated effects of a very well-insulated piston. All of the papers indicate some unexpected increase in heat transfer during combustion, but only the present paper, and its companion SAE paper, indicate that these effects can be so large that they will govern the design philosophy. The authors are thus to be congratulated for raising this very important issue.

Although we now have considerable evidence, the issues still seem confounded, especially for the case of ceramic surfaces. Let me explain.

The work of Furuhama and his co-workers shows considerable increases in local flux for ceramic surfaces in both diesel and homogeneous charge engines. Furuhama's data in fact show local flux increases with surface temperature that are slightly larger than those predicted by the authors' equation (2). Of course it is difficult to judge spatial average values from local values.

In the case of data taken in our own laboratory the insulated metal plug on the head surface gave temperatures ranging from 570 to 720 K as the load was changed from 0.3 to 0.5 equivalence ratio. Figures 16–18 show that the increase in surface temperature, due to insulation, increased the peak flux although the time-averaged flux for the cycle decreased. The cause of the decrease is apparent from Fig. 17, which shows that the cooled surface had a higher flux before and after the end of combustion.

Although the local flux measurements of Furuhama et al. [15], Huang [17], and the present authors all show similar trends, they are also all confounded. Furuhama's data were taken with a transducer mounted on metal embedded in the

[1]University of Wisconsin, Madison, WI.

Copyright © 1988 by ASME
Downloaded 01 Jun 2010 to 171.66.16.87. Redistribution subject to ASME license or copyright; see http://www.asme.org/terms/Terms_Use.cfm

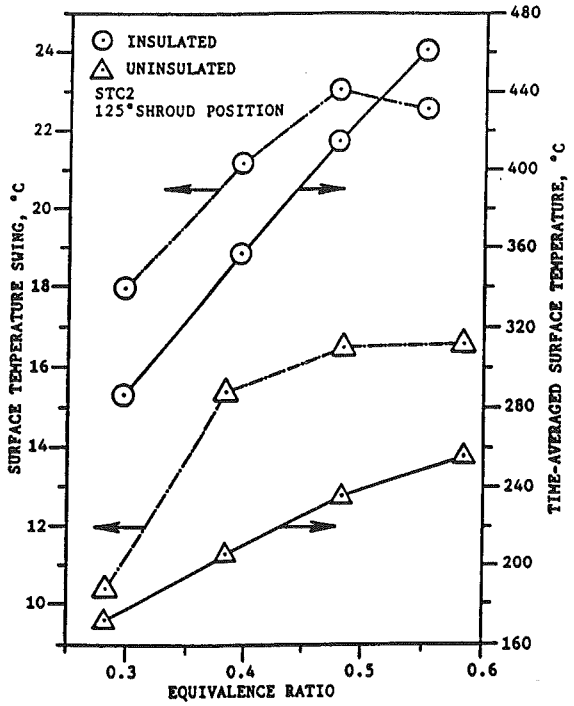


Fig. 16 Time-averaged surface temperature and surface temperature swing versus equivalence ratio for the insulated and uninsulated metal

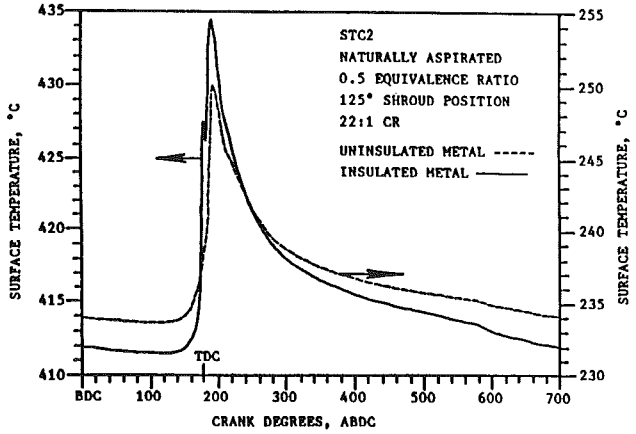


Fig. 17 Cyclic surface temperatures for the insulated and uninsulated metal

ceramic, a technique which certainly leads to many questions. The data of Huang show that for over 700 R the surface of deposit of soot disappears. Thus his comparisons are between cool sooted surfaces and hot, clean surfaces. The instantaneous flux data of the present authors were taken for a small hot surface surrounded by a large cool surface. Gas moving from the cool to the hot surface would experience a high convection coefficient. We must thus view all of these data with some suspicion.

The authors' data based on energy balances, while convincing in their trend, should not be considered conclusive. First, only the piston temperature was changed. Second, the method depends on an energy balance, which can be quite deceptive. For example, the crank angle of crossover from positive to negative flux is not predicted correctly by the sign of the difference between mass-averaged gas and surface temperatures. The resulting phase difference can have a large effect on the "tail" of the heat release. Third, the insulated surface was metal and may thus give different results from some ceramic surfaces. The reason that hot ceramic surfaces could differ from hot metal surface is the possible effects of radiation.

If the ceramic surface is transparent to thermal radiation

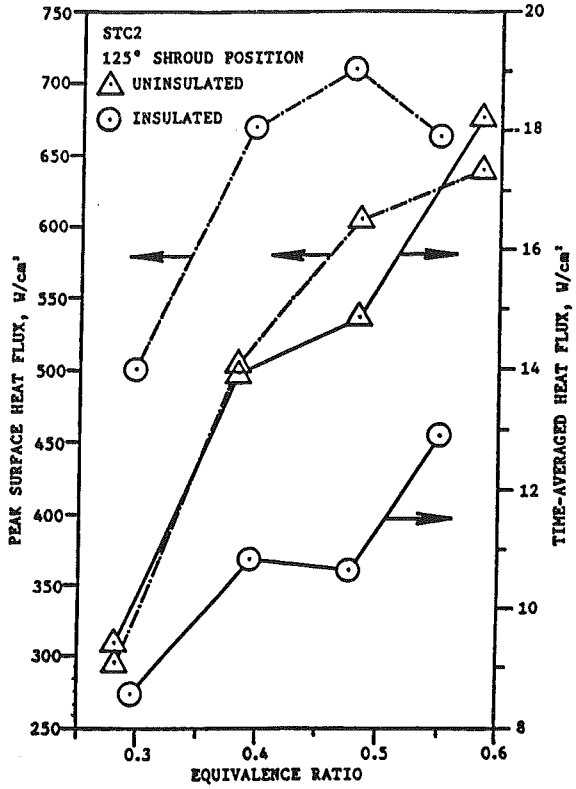


Fig. 18 Peak surface heat flux and time-averaged heat flux versus equivalence ratio for the insulated and uninsulated metal

then the large peak in radiation during combustion will not raise the surface temperature, but will cause "deep heating" of the ceramic. This may cause problems in thermal stress, but will reduce the surface temperature. It must be noted that a metal transducer film on the ceramic surface will block the radiation making the surface opaque. Thus in the measurements of Huang the surface temperature measured with the platinum-rhodium film was probably not the undisturbed (true) temperature of the zirconia plate. If this is true it might explain why the flux observed by Huang for the zirconia plate was lower than expected and much lower than for the hot metal at the same surface temperature. No direct method of solving this problem has been proposed, although an elaborate method of corrections is possible. In order to perform such corrections one would need to know the radiation flux and have a model for the radiation flux interaction with the ceramic. It thus seems that the energy balance approach is better and should be carefully applied to a ceramic insulated engine. It would be interesting to see the data of Woschni and Spindler repeated using their insulated piston covered with a spray coating of zirconia.

In closing, I would like to comment briefly on the whole approach to engine heat transfer. I believe that although empirical formulas are useful and necessary at the moment, they will never provide a totally satisfactory technique for design. What is needed is a method that can be used in conjunction with multidimensional codes. Such methods will also be empirical—they will depend on models for turbulence and reaction—but they will involve the needed fundamental coupling to fluid and combustion phenomena. It is currently a major goal in our Engine Research Center to provide such a methodology.

References

Amann, C. A., 1988, "Promises and Challenges of the Low-Heat-Rejection Diesel Engine," ASME JOURNAL OF ENGINEERING FOR GAS TURBINES AND POWER, this issue.

Downloaded 01 Jun 2010 to 171.66.16.87. Redistribution subject to ASME license or copyright; see http://www.asme.org/terms/Terms_Use.cfm

S. Furuhama[2]

I would like to compliment the very famous authors of this paper. As a whole, this paper perfectly made clear the fact of a larger heat loss during the combustion period of the adiabatic engine than of the conventional one. Almost the same relation of the heat fluxes between the adiabatic high-temperature wall and the conventional wall was obtained in our experiment, as shown in SAE Paper No. 870153.

Also, my concept on this phenomenon is just the same as the authors' concept "convection vive."

By the way, our instantaneous temperature thermocouple was designed by computer analysis based on the theory of heat transfer in the sensor, which had a complicated temperature field.

By this theoretical analysis, we found that the metal-plated film on the gas side of the Medtherm thermocouple is usually *too thin* for uniform temperature distribution is the film around the hot junction, which will cause a large error in heat flux.

Therefore, I would like to ask the authors, did you confirm the accuracy of the Medtherm type thermocouple used in your experiment, and can you give me the details of materials and measurements of your thermocouple?

T. W. Ryan, III[3]

The work performed by Prof. Woschni in 1967 has served as the basis for most of the engine heat transfer models developed and used since the work was originally reported. As in the past, the authors have done an excellent job in reporting their experimental results and in describing the resulting theories relative to the convective heat transfer in insulated engines. The theories are, however, controversial in that the authors are concluding that the addition of insulated surfaces actually increases the heat transfer through those surfaces. This conclusion is based on global engine performance measurements, local heat flux measurements, and the results of computations made using a new film coefficient term adjusted for the higher surface temperatures.

While the evidence and the discussions presented in the paper are convincing, there are several questions that must be answered before it is accepted that an "insulating surface" actually enhances the heat transfer. One of the first questions relates to the drop in the thermal efficiency observed with the heat-insulted engine configurations. It is not clear whether the air mass flow rate to the engine was held constant for all of the experiments. If it was not, the observed drop in thermal efficiency could be due to the decrease in volumetric efficiency accompanying the higher surface temperatures. With the decreased air mass flow rate conditions the overall air–fuel ratio can become too rich, especially at the full load conditions where the authors claim the heat enhanced transfer effects are most evident. Under these conditions, a decrease in thermal efficiency is more likely to be due to poor air utilization than to increased heat transfer.

The authors' description of the performance characteristics of the various engine includes the presentation of a number of heat release rate diagrams. A comparison of the heat release rate for the "film vaporization" and the "air-distributed" configurations reveals that the combustion event is predominantly diffusion controlled in the former case and includes significant premixed burning in the latter case. The authors indicate that differences in the effects of the insulated surfaces on the thermal efficiencies of the two engines are due to differences in the heat transfer resulting from the different applications of insulation. It is more likely that the differences are due to the fact the higher surface temperatures had a significant effect on the initial combustion rates, including a decrease in the premixed burn fraction, and burning later in the cycle. These types of effect are more related to deviations from the ideal constant volume combustion event than to the potential heat transfer effects.

K. L. Hoag[4]

I have chosen to focus my discussion on one aspect of Dr. Woschni's work—the results obtained through the measurement of the impact of wall temperature on instantaneous heat flux. This measurement, made by adjusting the level of cooling air to the back of the probe, in an otherwise unchanged environment, represents a key contribution to a controversial and important topic. In light of the wide disparity of conclusions appearing in the literature, Dr. Woschni's work begins to address the questions upon which future research efforts must focus. His experiment has provided an unambiguous measure of the impact of increasing wall temperature on in-cylinder heat transfer. As Dr. Woschni pointed out, his approach effectively separates questions of the contribution of radiation from the problem. It should further be noted that changes in material properties, which have confounded several previous studies, have not been made, and the use of the same hardware throughout the study has eliminated another source of variability. Although debates on the quantitative results may still remain, it should be clear that qualitatively Dr. Woschni's results cannot be questioned. An increase in heat flux during the combustion process, directly attributable to an increase in wall temperature, has been clearly shown.

Dr. Woschni's experimental results, as described above, agree in principle with recent findings at Cummins. Table 1 summarizes a recent set of multicylinder engine tests under various insulated operating conditions. These experiments were conducted on the Cummins V-903 engine in a turbocharged configuration at rated conditions of 450 kW at 2600 rpm. The results shown here were generated at fixed peak cylinder pressure, and are the results of a statistical analysis of several engine tests. Table 1 summarizes the results as the engine was first insulated with 1.3-mm zirconia coatings on the piston and head, and monolithic zirconia valve seats, and then cooling to the cylinder head minimized with only valve bridge oil drillings. In an attempt to characterize the engine configurations tested further, the distribution of heat rejection was estimated as shown in Table 2. Looking first at the left column, total heat rejection of the baseline configuration was measured, as were the friction and aftercooler terms. The in-cylinder and exhaust port terms were calculated through finite element models carefully matched with measured temperatures. The next column summarizes the predicted impact of insulation. Heat rejection to the ambient and due to friction were assumed constant. Measured heat rejection to the aftercooler was used, and the impact of insulation was calculated using the component finite element models, giving a predicted reduction of in-cylinder heat rejection of 28.6 percent.

This resulted in a calculated specific heat rejection of 0.403 kW/kW. However, referring now to the final column in Table 2, the measured specific heat rejection was 0.448 kW/kW. Assuming the friction and exhaust port conditions not to have changed appreciably, the reduction of in-cylinder heat rejection was only 7.9 percent—less than 1/3 that of the predictions made with detailed finite element models. These and several other experimental results using different engines, and different insulation strategies, yet giving similar results, have led to questions concerning the fundamental assumptions about in-cylinder heat transfer processes.

[2]Musashi Institute of Technology, Japan.

[3]Southwest Research Institute, San Antonio, TX.

[4]Cummins Engine Company, Inc., Columbus, OH.

Downloaded 01 Jun 2010 to 171.66.16.87. Redistribution subject to ASME license or copyright; see http://www.asme.org/terms/Terms_Use.cfm

Table 1 Performance data summary; 450 kW @ 2600 rpm

	BASELINE	INSULATED	LIMITED OIL COOLING
BSFC (gm/kW-hr)	199	201	201
BSHR (kW/kW)	.452	.448	.382
A/F Ratio	29.1	29.0	29.2
Volumetric Efficiency	.90	.87	.87

Table 2 Heat rejection breakdown (kW)

	BASELINE	INSULATED PREDICTED	INSULATED MEASURED
Piston	48.4	30.9	?
Liner	6.4	6.3	
Cylinder Head	43.9	33.1	?
Total In-Cyl.	98.7	70.3	90.9
% Reduction	-	28.6	7.9
Exhaust Port	27.6	27.7	27.7
Ambient	(13.0)	(13.0)	(13.0)
Friction	28.1	28.1	28.1
Aftercooler	60.8	66.4	66.4
Total to Heat Exch.	202.2	179.5	200.1
BSHR (kW/kW)	.452	.403	.448

Dr. Woschni has held up a physical explanation of the measured phenomena, which he refers to as "convection vive." He has then proceeded to incorporate a correction factor into his empirical model of the in-cylinder convection coefficient. This provides an experimentally based correction for "convection vive," and would thus be expected to enhance the ability of his correlation to describe the impact of increased wall temperature. However, I would propose that "convection vive" is but one of several plausible phenomena not currently being addressed by such correlations. Dr. Woschni has provided a strong experimental argument for the need for continued research into the fundamental physical phenomena of in-cylinder heat transfer. Until all such phenomena can be identified and analytically described in cycle analysis, the risk of misleading results must be recognized. Heat transfer correlations remain highly empirical, and whenever a new engine concept goes beyond the physical realm in which the correlation was developed, the risk of inaccuracy must be recognized.

T. Morel[5]

The paper presented by G. Woschni and W. Spindler is interesting and thought provoking. Its main thought is to suggest that raising wall temperatures by insulation will increase the peak heat flux as well as mean heat flux and that as a result insulation cannot improve thermal efficiency of diesel engines or reduce their heat rejection. If true, their conclusion would have far-reaching importance related to large sums being spent on research and development of insulated diesels with the goal of increasing thermal efficiency and/or reducing heat rejection. Another aspect of their conclusions is that they suggest a totally unexpected result, that the heat flux

$$q = h_g A (T_g - T_w) \tag{1}$$

increases as T_w increases (where h_g is gas heat transfer coefficient, A is wall area, T_g is gas temperature, and T_w is wall temperature). As such, their work attracts a lot of attention, as well as scrutiny.

We at ITI have been involved in measurements and modeling of heat transfer in insulated and conventionally cooled diesels for a period of several years. In this work we acquired heat flux data with wall temperatures in the range of 450–940 K, and over this range we have seen the heat flux consistently decrease with increasing temperature (Morel et al., 1986; Morel et al., 1987). Furthermore, we saw that the experimental heat flux follows well the predictions of a flow-based heat transfer model (Morel and Keribar, 1985), indicating that the nature of the heat transfer process was unchanged by the increased wall temperatures.

Several observations can also be made about the results of Woschni and Spindler. Their measurements led them to deduce a new form of the Woschni heat transfer correlation in which the coefficient C_2 is temperature dependent:

$$C_2 = 2.3 \times 10^{-5}(T_W - 600) + 0.005 \qquad T_W > 523 \tag{2}$$

The theoretical foundation of equation (2) is that heat transfer from flames can increase when walls are hot, because the flames can approach the wall closer and the thermal boundary layer becomes thinner. The specific form of the correlation (2) was developed using global pressure data, and calibrating C_2 to satisfy a heat release constraint. This procedure is ambiguous since the temperatures of all surfaces in the combustion chamber are not known. Even more seriously, the procedure goes contrary to the theoretical foundation of the model, as it is being used at all surfaces at all times between start of combustion and EVO. Yet the flame adjoins any given surface only a small fraction of that time and thus the postulated heat transfer augmentation cannot take place.

Woschni and Spindler concluded that due to the effects discussed above, the heat transfer coefficient increased by up to a factor of five due to an increase of wall temperature from 650 K to 1020 K. But that has direct implications for the boundary layer thickness δ. Since the heat transfer coefficient varies with $\delta^{-0.25}$ (Morel and Keribar, 1985), this implies that the thermal boundary layer would have to be thinner by a factor of 625 at all surfaces and at all crank angles. That is clearly not realistic.

Another observation can be made concerning the fast-response thermocouple results presented by Woschni and Spindler. The data presented showed clearly that as the temperature of the wall went up, the engine surface temperature swing magnitude was essentially unchanged. They did not present the heat flux deduced from these temperature records. However, it is a simple matter to digitize these data and calculate the heat flux, and this was done here. The data analyzed were those from Woschni and Spindler, their Fig. 5, and the results produced by our analysis of these data (with $k = 20$ W/mK and $\rho c = 3.0$ MJ/m^{3}K) are shown in Figs. 1 and 2. It can be seen that there is a higher instantaneous heat transfer rate at the measurement point when the wall temperature is high. This is due to the higher slope of surface temperature rise. However, the period of high heat flux is very brief and is immediately followed by a low period. The total heat flux near TDC is about the same, and that is consistent with the fact that the magnitude of the surface temperature was about the same. The data reduction procedure used to produce Figs. 1 and 2 was incomplete in that it did not include the dependence of the product $k\rho c$ on temperature, but used fixed values instead. (This was done because the actual probe materials were not given in the paper.) For example, for iron this product decreases with increasing temperature, and thus the same magnitude swing is associated with a lower heat flux at a high wall temperature than at a low temperature. Thus, if the product $k\rho c$ for their probe material followed the same dependence

[5] Integral Technologies Inc., Westmont, IL.

Downloaded 01 Jun 2010 to 171.66.16.87. Redistribution subject to ASME license or copyright; see http://www.asme.org/terms/Terms_Use.cfm

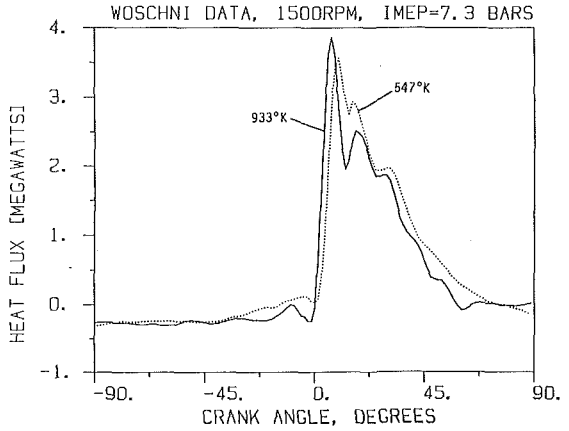


Fig. 19 Heat flux calculated from surface temperature records of Woschni and Spindler obtained at two different mean surface temperatures; IMEP = 7.3 bar

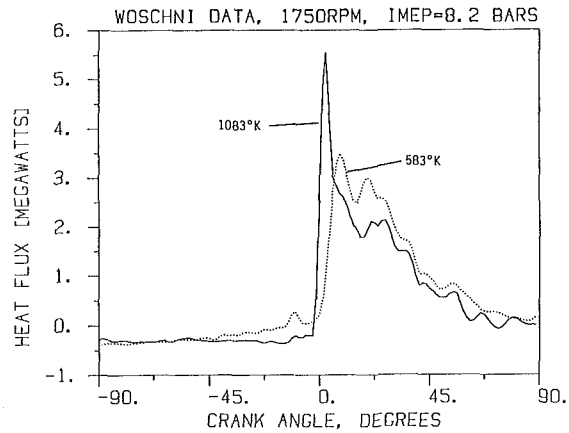


Fig. 20 Heat flux calculated from surface temperature records of Woschni and Spindler obtained at two different mean surface temperatures; IMEP = 8.2 bar

on temperature as for iron, the total flux near TDC measured by Woschni and Spindler could in fact have been lower at higher temperatures than at low temperatures!

References

Morel, T., and Keribar, R., 1985, "A Model for Predicting Spatially and Time Resolved Convective Heat Transfer in Bowl-in-Piston Combustion Chambers," SAE Paper No. 850204, SAE Congress, Detroit.

Morel, T., Wahiduzzaman, S., Tree, D. L., and DeWitt, D. P., 1987, "Effect of Speed Load and Location on Heat Transfer in Diesel Engine—Measurements and Predictions," SAE Paper No. 870154, SAE Congress, Detroit.

Morel, T., Wahiduzzaman, S., and Fort, E. F., 1988, "Heat Transfer Experiments in an Insulated Diesel," submitted for presentation at the 1988 SAE Congress.

W. K. Cheng[6]

In the subject paper, Woschni and Spindler described the results of a series of experiments carried out in a naturally aspirating single-cylinder diesel engine, which had been fitted with a standard aluminum piston, an air-gap insulated nimonic piston, and a nimonic piston without the air-gap insulation. Both the MAN and the normal direct injection combustion systems were tested. Analysis of the pressure data indicated that at high load, the isfc of the insulated engine for both combustion systems was found to be higher than that of the uninsulated one at the same imep. The authors interpreted this difference to be due to the higher heat transfer coefficients at the higher wall temperatures so that the heat flux during combustion actually increases with the insulated engine, even though the gas-to-wall temperature difference has decreased. The increase of heat transfer coefficients was attributed to the effects of flame/wall interaction. The authors reported local heat transfer measurements that supported their hypothesis. An empirical heat transfer correlation was fitted to the engine data to account for the higher heat loss due to the higher wall temperatures. The correlation was incorporated into an engine simulation program. From the computer simulation study of an eight-cylinder diesel truck engine, the authors concluded that the turbocompounded insulated engine would have an inferior specific fuel consumption to a noninsulated engine.

Since the above conclusion has signigicant implication on the low heat rejection (LHR) engine development, the data and analysis that lead to the above conclusion need to be examined critically. The behavior of an insulated engine is quite complex; the volumetric efficiency, the fuel injection properties, the combustion behavior, and the heat transfer characteristics may all change when an engine is switched from a normally cooled to an LHR configuration by simple component replacement. Therefore, the comparison of standard and LHR engine performances under "similar" conditions needs careful consideration.

The discussion will be focused on the following four points:

1 The Effects of Energy Conversion Efficiency

In the LHR configuration, because of the higher wall temperature, there is a decrease of volumetric efficiency. Furthermore, the injection system may behave differently in terms of atomization and air/fuel mixing characteristics, as well as the delivery rate. The injection system for a conventional engine has been optimized for the air charge and the combustion chamber geometry. This optimization is no longer maintained at the higher operating temperature of the LHR configuration, especially at high load. As a result, there is likely to be a loss in the efficiency in converting chemical to thermal energy. In a heat release analysis of pressure trace data, one cannot distinguish between the effects of a loss in energy conversion efficiency and a higher heat transfer. To illustrate this effect, we shall use the authors' data from a report [20] that the paper under discussion was based on.

In Fig. 1, the indicated specific fuel consumption (isfc) is plotted against the imep for the direct injection engine, for both the insulated and noninsulated configurations. The data points are identical to those of the second graph in Fig. 2 of the paper. A sensitive indicator of the combustion process is the emission characteristics. The corresponding emission data are also plotted in Fig. 20. A significant point is that the CO and smoke emission are high in the high imep range with the insulated engine. Therefore, the degradation of isfc at high imep with insulation may be a combustion effect rather than a heat transfer effect.

To illustrate the point further, it is well known that the degradation of isfc in the insulated engine was due to poor volumetric efficiency. Therefore data were obtained with the insulated engine turbocharged. The results are shown in Fig. 22. (The data for the naturally aspirating insulated engine in this figure are different from those of Fig. 21 because, in this case, the cylinder head was run uncooled in addition to the insulated piston.) The isfc, and emission of CO and smoke, decrease with turbocharging compared to the nonturbocharged one. The results suggest that the isfc is mainly influenced by the combustion process rather than the heat transfer. There is, in fact, a good correlation between the smoke number and isfc in the three versions of the engine. This correlation is shown in Fig. 3. An over-simplified interpretation of this correlation is that the insulated and uninsulated engine would have the same isfc if they have the same smoke emission.

[6]Sloan Automotive Lab., MIT, Cambridge, MA.

Downloaded 01 Jun 2010 to 171.66.16.87. Redistribution subject to ASME license or copyright; see http://www.asme.org/terms/Terms_Use.cfm

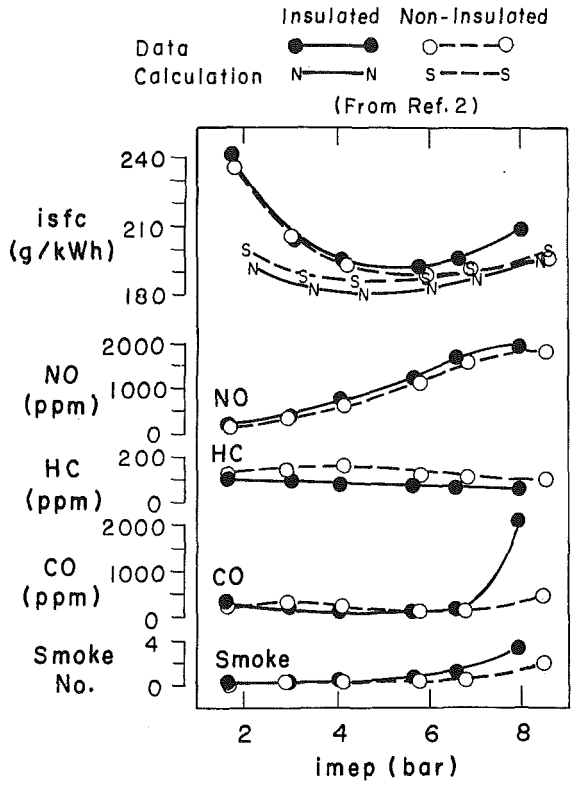


Fig. 21 Specific fuel consumption and emission characteristics of naturally aspirating engines

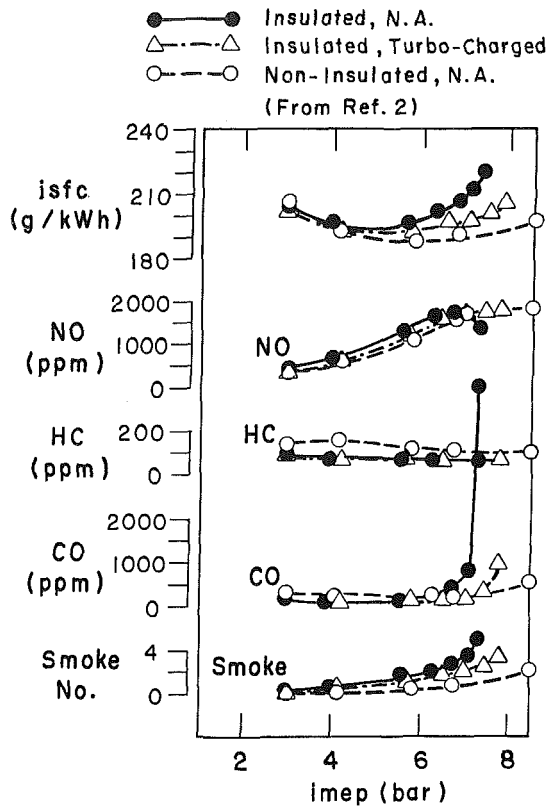


Fig. 22 Specific fuel consumption and emission characteristics of naturally aspirating and turbocharged engines

The above discussion indicates that to attribute the increase of isfc at high load in the insulated engine soley to an increase in heat transfer may be an over-simplification. A major factor in the loss of efficiency of the insulated engine is likely to be a loss of energy conversion efficiency because at the higher chamber temperatures, the injection system and the air charge may no longer be optimally matched. Therefore, direct comparison between a standard optimized engine and one with components replaced by insulating materials may not be meaningful.

2 Validity of the Heat Transfer Model

A strong point made by the paper was that the simulation model had predicted the experimental data for the engine with the standard piston very well. This agreement, however, is only over the high-load range. In Fig. 2 of the paper, the model prediction for imep below 6 bar is not shown. The prediction of the model in the low range is shown in Fig. 21. There is substantial disagreement between the data and the predicted isfc. To account for the discrepancy, the authors may have to adjust the values of C_1 and C_2 in the heat transfer correlation. In light of the previous discussion, the universal validity of the heat transfer coefficient as given by equations (1) and (2) of the paper is questionable.

3 On the Mechanism of the Enhanced Heat Transfer Coefficient

The authors suggested that the mechanism of the enhanced heat transfer coefficient was a result of the flame front moving closer to the wall at the higher wall temperature. This argument, however, may not be applicable to the heat transfer in the piston bowl in their experimental configuration. In their experiment, the major difference in the heat release rate between the insulated and uninsulated engine occurred during the first part of combustion, during which the fuel jet would keep a fuel-rich region at the wall in the piston bowl. This is

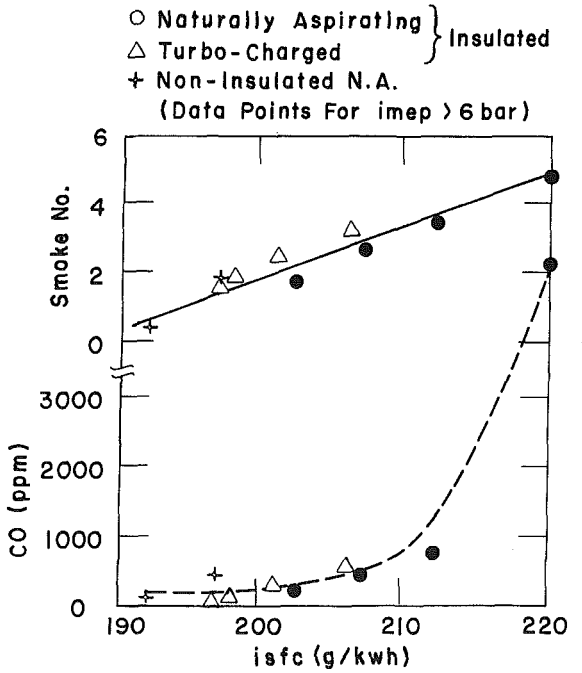


Fig. 23 CO and smoke emission versus specific fuel consumption at imep >6 bar

especially so in the case of the MAN system. Therefore the distance between the flame front and the wall is more likely to be governed by the availability of oxygen rather than by a thermal boundary layer. As a result the flame position would not be sensitive to the wall temperature.

4 On the Instantaneous Heat Flux Measurement Results

The authors reported the measurement of the instantaneous

Downloaded 01 Jun 2010 to 171.66.16.87. Redistribution subject to ASME license or copyright; see http://www.asme.org/terms/Terms_Use.cfm

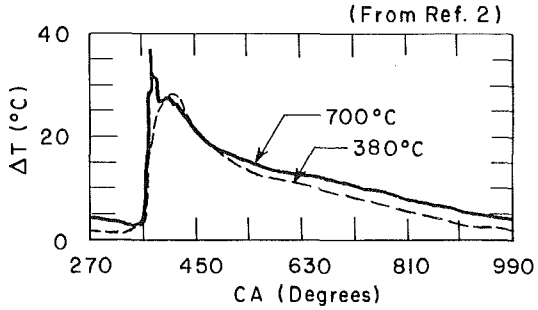


Fig. 24 Surface temperature responses

surface temperatures of a specially instrumented exhaust valve in an engine. From a Fourier analysis of this data, a heat flux and then a heat transfer coefficient may be calculated. This is a difficult measurement and the authors should be congratulated. The data, however, must be interpreted carefully. This is because in the Fourier method, the calculated heat flux is very much dependent on the rise time of the surface temperature. This is particularly evident in the data at imep equal to 8.2 bar in Fig. 5 of the paper. The rise time in this case was very much similar to that of the auto-ignited premixed charge. A plausible explanation is that when the exhaust valve was uncooled to achieve a high surface temperature, the fuel-air mixture prepared during the ignition delay period tends to auto-ignite at the vicinity of the hot valve, thus causing a sharp temperature rise. In some of the data in [20], the instantaneous surface temperature actually shows a spike (Fig. 24). Therefore, the very high apparent heat transfer rate at the high valve temperature may be due to an auto-ignition phenomenon rather than a flame wall interaction phenomenon.

Conclusion

The above discussion indicates that with the present experimental evidence, it is premature to conclude that the instantaneous heat transfer in an insulated engine is higher than that of an uninsulated one. To analyze a particular insulated engine, it is necessary to examine the combustion process in addition to heat transfer. In view of the conflicting results in the literature [20–23], direct comparison between the isfc of an existing engine and the same one with its component substituted by insulating materials may not be a meaningful exercise because the combustion process would no longer be the same. Therefore, a better comparison would be between the "best" insulated engine and an uninsulated one under the same performance requirement.

References

20 FVV, "Examination of the Behavior of a Diesel Engine With Heat-insulated Combustion Chamber," final report, Vol. 376, 1986.

21 Furuhama, S., and Enomoto, Y., "Heat Transfer Into Ceramic Combustion Wall of Internal Combustion Engines," SAE Paper No. 870153, 1987.

22 Wade, W. R., Havstad, P. H., Qunstead, E. J., Trinker, F. H., and Garwin, I. J., "Fuel Economy Opportunities With an Uncooled DI Diesel Engine," SAE Paper No. 841286, 1984.

23 Alkidas, A. C., "Experiments With an Uncooled Single-Cylinder Open-Chamber Diesel," SAE Paper No. 870020, 1987.

A. C. Alkidas[7]

In the present paper and in the earlier companion ones [24, 25] Woschni and co-workers reported that at high loads the thermal efficiency of a single-cylinder water-cooled diesel engine equipped with an air-gap-insulated piston (LHR engine) was significantly less than for the same engine equipped with a standard aluminum piston (STD engine). Furthermore, the comparative thermal efficiency of the LHR engine was found to worsen with increasing load and decreasing engine speed. This result agrees with some experimental studies [26, 27] but disagrees with several analytical studies [28–30] and with other experimental studies [31–33].

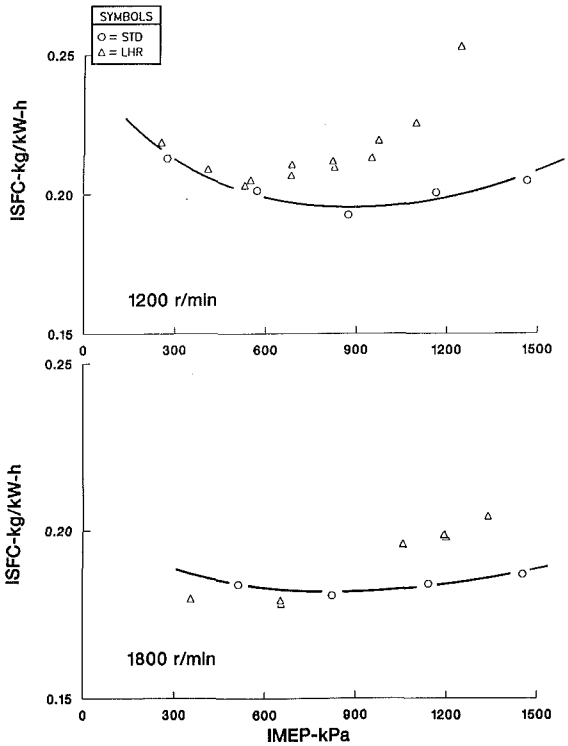


Fig. 25 The ISFC-IMEP characteristics of the STD and LHR engines

For more controversial is the reason given by Woschni and co-workers to explain the efficiency deterioration of the LHR engine at high loads. They argued that the observed deterioration in the LHR engine is brought about by the elevated temperature of its combustion-chamber walls, which causes an augmentation in the convective heat transfer coefficient and consequently an increase in the surface heat transfer. Thus Woschni and co-workers blamed higher heat losses for the poor efficiency of the LHR engine.

Woschni and co-workers suggested that the increase in heat transfer coefficient with increasing wall temperature is due to a phenomenon that is called "convection vive" in French. They went on to explain that increasing the wall temperature allows the flame to come closer to the wall, causing a steeper temperature gradient at the wall and consequently higher surface heat flux. Another explanation given by Woschni and Spindler in their present paper is that the proximity of the flame to the wall augments turbulence near the wall, which in turn causes an increase in the convective heat transfer coefficient and a resultant increase in the surface heat transfer.

In this discussion I would like first to present some data that were obtained very recently at GMR and support the experimental results of Woschni and co-workers [24, 25] on the efficiency of a LHR diesel engine. Then I would like to offer some thoughts on the mechanisms proposed by Woschni and co-workers to explain the efficiency degradation experienced by a LHR engine at high loads.

Figure 25 compares the indicated specific fuel consumption (ISFC) of an uncooled diesel to that of the corresponding water-cooled diesel. The ISFC is based on pressure measurements and is not obtained from motoring tests. These

[7] Engine Research Department, General Motors Research Laboratories, Warren, MI.

Downloaded 01 Jun 2010 to 171.66.16.87. Redistribution subject to ASME license or copyright; see http://www.asme.org/terms/Terms_Use.cfm

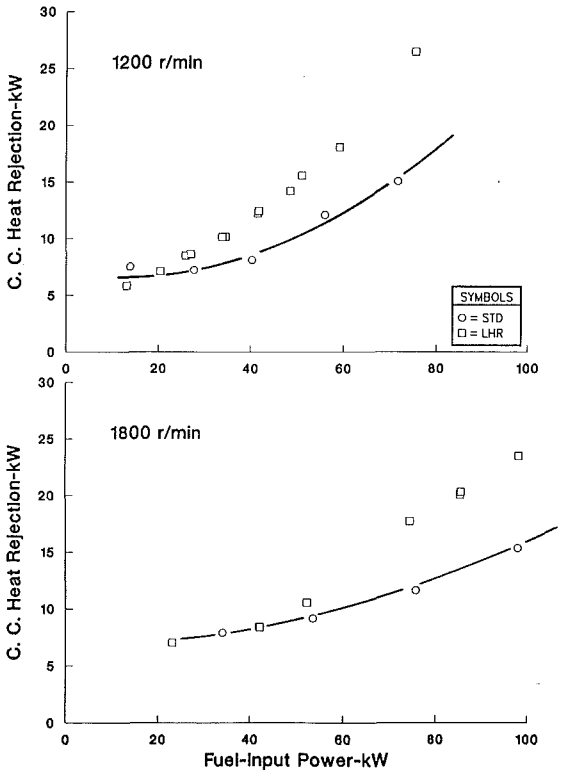


Fig. 26 Comparisons of the closed-cycle heat-rejection rates of the STD and LHR engines

data were measured in our laboratories on a single-cylinder heavy-duty diesel operated as a turbocharged aftercooled engine. The uncooled engine had three air-gap-insulated metallic components: piston, firedeck, and exhaust ports.

The results of Fig. 25 show that with increasing load, the ISFC of the uncooled engine becomes increasingly higher than the ISFC of the water-cooled engine. In addition, the performance of the uncooled engine is the worst at the low speed/high load conditions. These results confirm completely the experimental findings of Woschni and co-workers on the performance of a LHR engine.

One may evaluate the heat losses to the combustion-chamber walls during combustion by performing a heat-release analysis. This analysis, which is an application of the first law of thermodynamics during the valves-closed part of the engine cycle, utilizes the measured pressure history of the gas in the combustion chamber to calcualte the heat-release history of the fuel [12]. The valves-closed heat transfer, which is dominated by the combustion process, was computed as a byproduct of the heat release analysis by means of Woschni's older empirical heat transfer correlation [35]. The Woschni heat transfer coefficient is scaled (constant multiplier) such that the computed final fuel burned fraction is equal to a specified value which is derived from exhaust emissions.

Figure 26 compares the average heat transfer rates during the closed portion of the cycle for the water-cooled and uncooled engines. These results clearly demonstrate that the heat loss to the walls of the combustion chamber during the combustion process was often significantly higher for the uncooled engine than for the water-cooled engine. The difference in the heat loss from the two engines increased with increasing load. It was further found that the increase in the heat loss experienced by the uncooled engine resulted from an increase in the convective heat transfer coefficient, which at the low-speed/high-load conditions was triple the corresponding coefficient for the water-cooled engine.

These results provide strong evidence to support the hypothesis proposed by Woschni and co-workers [24, 25], namely, that for certain engine conditions (most probably low speed/high load) the amount of heat rejected by an uncooled engine during the combustion process can be significantly higher than the amount rejected by a water-cooled engine. This leads to the following question: Could an increase in the surface-temperature level of the combustion chamber of a diesel engine produce an increase in the heat losses during the combustion process?

The main evidence that supports a positive response to that question is provided by two experiments performed in a diesel engine by Woschni and co-workers [24, 25].

1 Transient surface heat flux measurements performed on an instrumented plug with controllable air cooling that replaced one of the exhaust valves of the engine showed that increasing the wall temperature of the plug from 583 to 1083 K increased its peak convective heat transfer coefficient by roughly a factor of three.

2 Steady-state heat flux measurements on the head of the engine using a water-cooled heat-flux probe with variable-thickness ceramic inserts showed that for surface temperatures above 700 K the heat flux remained constant (or slightly increased) with increasing surface temperature.

Additional pieces of evidence exist that support the above measurements. Several studies [36, 37] of surface heat flux from flames impinging on the walls of furnaces have shown that the convective heat transfer coefficient increased with increasing wall temperature. In a recent study, Germerdonk and Nguyen [37] found that the convective heat transfer coefficient increases dramatically for the range of wall temperatures of 925 to 1175 K.

Transient surface heat-flux measurements performed by Enomoto and Furuhama [38, 39] on different pistons of a spark-ignition engine showed that the heat flux during combustion was significantly higher for a silicon nitride (ceramic) piston than for a conventional Loex (aluminum alloy) piston. This occurred despite the fact that the measured cycle-averaged heat flux for the ceramic piston was only half that of the Loex piston because of the lower thermal conductivity of the ceramic material. As a point of information, at 3000 rpm and full load, the cycle-averaged surface temperature of the ceramic and Loex pistons at the location of measurement were 690 K and 490 K, respectively.

Enomoto and Furuhama [38] claimed similar results for a diesel engine.

In contrast to these particular experimental studies, heat flux measurements performed by Hoag [40] and by Huang and Borman [41] in diesel engines showed mixed trends in the behavior of the surface heat flux with surface temperature. Hoag's experiments were done at surface temperatures that were too low to be of much value for LHR studies. He used a normal and a high-temperature coolant in a metallic engine. Huang and Borman [41] found that for an insulated metal surface the peak heat flux during combustion was higher than that for an uninsulated metal surface despite the fact that the steady-state heat flux on the insulated metal surface was significantly lower than that of the uninsulated surface, as expected. On the other hand, they found substantial reductions in both the peak heat flux and steady-state heat flux for a zirconia surface compared to that of the uninsulated surface. Interestingly, the range of the time-averaged surface temperatures of the insulated metal surface was 600 to 740 K, whereas for the ceramic surface it was 550 to 675 K. These surface temperatures are near the lower temperature limit of the phenomenon that Woschni and co-workers proposed as the cause of an augmentation in the surface heat flux with increasing surface temperature.

The results of all of the above measurements may be questioned because of the possible influence of wall deposits on the

Downloaded 01 Jun 2010 to 171.66.16.87. Redistribution subject to ASME license or copyright; see http://www.asme.org/terms/Terms_Use.cfm

transient surface heat flux. These deposits, the thickness of which under normal combustion-chamber conditions is expected to decrease with increasing surface temperature, could greatly suppress the transient heat flux. The wall temperature above which no significant deposits exist is not known precisely. Reported values of the ignition temperature of soot particles [42, 43] ranged from 620 to 870 K, although the ignition temperature could be lowered substantially with additives [42, 44, 45]. Nevertheless these results suggest the possibility that a decrease in the thickness of wall deposits with increasing wall temperature may be the cause of the measured increase in the transient surface heat flux during combustion with increasing wall temperature.

On the other hand, the presence of wall deposits could not explain the results of the steady-state heat-flux measurements performed by Woschni and co-workers, nor could it explain the burner experiments of Germerdonk and Nguyen [37]. In addition, one should recall that Enomoto and Furuhama [38, 39] performed their tests in a spark-ignition engine and found that the transient surface heat flux during combustion was higher for the ceramic piston than for the Loex piston, although the time-averaged surface heat flux was higher for the Loex piston than for the ceramic piston.

In addition to the experimental measurements presented and the results of the heat-release analysis presented in Fig. 26, Alkidas and Jones [46] found in an earlier study that increasing the convective heat transfer coefficient by a factor of two made it possible to obtain good agreement between measurements and analysis for the performance and thermal loading of an uncooled engine. The analytical model was a single-zone simulation model of the gas cycle incorporating a three-dimensional time-varying thermostructural model.

In summary, it appears that there is sufficient evidence to suggest that under certain conditions, increasing the temperature of a surface can augment the heat flux from the combustion gases to the surface.

Despite all the experimental evidence, the mechanism causing the augmentation of the convective heat transfer coefficient is not clear. The suggestion of Woschni and co-workers that increasing the surface temperature causes the flame to come closer to the wall, thus augmenting the surface heat flux due to (*i*) an increase in the temperature gradient at the surface of the wall, and (*ii*) an increase in the turbulence near the wall, is open to question.

According to the thermal theory of extinction [47, 48], the distance of the flame boundary from the wall (standoff distance) is governed by the balance between the heat generated by chemical reaction and the heat loss to the wall. Therefore one expects the standoff distance of the flame to be inversely proportional to the heat loss. The lower the heat loss, the closer the flame approaches the wall. Indeed, computations of premixed combustion in the stagnation-point boundary layer of a wall surface, assuming a single-step kinetic reaction, indicate that increasing the wall temperature results in a decrease in the surface heat transfer and a corresponding reduction in the standoff distance of the flame from the wall [49].

A similar result to that of the above analysis [50] was obtained by Rocard and Veron [51], who termed the influence of combustion on the surface heat transfer as "convection vive." In the case of a boundary-layer flow over a flat plate, they found that combustion significantly augments the convective heat transfer coefficient. However, the heat transfer expression they derived suggests that increasing the surface temperature decreases the surface heat transfer.

The second mechanism proposed by Woschni and co-workers by which closer proximity of the flame to the wall increases the turbulence near the wall, and hence the heat transfer, does not appear plausible because the augmentation by turbulence alone could not explain the observed threefold increase in convective heat transfer coefficient.

A candidate mechanism that might conceivably augment the surface heat flux in engines is the recombination of dissociated products of combustion near the wall. Note, however, that because of the elevated pressures, dissociation of the products of combustion in diesel engines is expected to be suppressed.

Recombination reactions are generally highly exothermic and would therefore result in an increase in the surface heat flux. Some of the dissociation/recombination equilibrium reactions that may be important for the flame conditions prevailing in a diesel engine are [29]:

$$CO_2 \rightleftharpoons CO + \frac{1}{2} O_2$$

$$H_2O \rightleftharpoons H_2 + \frac{1}{2} O_2$$

$$H_2O \rightleftharpoons \frac{1}{2} H_2 + OH$$

Dissociation increases with increasing temperature. Thus as the equilibrium products diffuse through the boundary layer toward the wall, their temperature decreases, which favors their recombination. Recombination would result in a heat release near the wall that augments the surface heat transfer.

However, this mechanism does not explain the increase in convective heat transfer coefficient with increasing temperature because increasing wall temperature tends to decrease the recombination reactions and consequently the amount of heat release near the wall. In fact, this mechanism suggests that lower wall temperatures cause higher surface heat transfer due to recombination of dissociated equilibrium products of combustion.

To this discusser there are two plausible mechanisms that could explain the observed increase in surface heat transfer with increasing wall temperature: ignition and combustion of unburned fuel in the boundary layer of the wall, and radiation.

Increasing the wall temperature facilitates the ignition and subsequent combustion of unburned fuel that has impinged on the chamber walls and thus escapes the main combustion event. The combustion of this unburned fuel in the boundary layer of the wall would result in a release of energy and consequently in an increase in surface heat transfer.

The weakness of this mechanism is that it assumes that unburned fuel exists in the boundary layer of the combustion-chamber surface. Although this is expected to be true for spark-ignition engines and one may expect unburned fuel in the boundary layer of the piston cavity in a diesel engine, it is not generally accepted that significant unburned fuel exists in the boundary layer of the cylinder heat and liner of a diesel engine.

The other plausible mechanism is radiation. In diesel engines, radiation accounts for about 20 to 40 percent of the total surface heat transfer [52]. The main source of this radiation is soot radiation. Gaseous radiation, which is primarily due to emission contribution of the tri-atomic molecules CO_2 and H_2O, has been found to be of the order of 10 percent of the total radiant heat transfer [53].

Insulating the combustion chamber of a diesel engine, or equivalently increasing its surface temperature, may increase soot radiation both by increasing the temperature of the soot particles, which usually are assumed to be near the flame temperature, and by increasing the concentration of soot particles in the chamber.

The amount of soot leaving a diesel engine as exhaust is the net cumulative effect of the two opposing processes: formation and oxidation. Being kinetically controlled, these processes are strongly influenced by temperature. Increasing the temperature increases the rates of both the formation and ox-

Downloaded 01 Jun 2010 to 171.66.16.87. Redistribution subject to ASME license or copyright; see http://www.asme.org/terms/Terms_Use.cfm

idation processes. In general, one expects that formation dominates during the early stages of the diffusion combustion and that oxidation dominates during the last stages of combustion and during the remaining portion of the expansion stroke.

The accurate measurement of radiation heat transfer in a diesel engine is a formidable task. For this reason relatively few experimental studies of radiant heat transfer in engines have been made [48]. Furthermore, none investigated the effects of elevated combustion-chamber temperatures on the radiant heat transfer in a diesel. Thus, for now, one has to rely on the results of analytical studies.

Computations performed by Morel and Keribar [54] indicated that insulating the combustion chamber of a diesel engine increased soot radiation only slightly, although the contribution of radiation itself to the total surface heat transfer was significantly increased. However, the results of this analytical study must be considered with some reservations because of the complexities of the soot-producing processes, which, despite many serious research efforts, have thus far evaded precise characterization.

On the other hand, a number of laboratory studies [55, 56] with steady-state diffustion burners have shown experimentally that increasing the flame temperature substantially increases the soot concentration in the flame. Although these results are not directly applicable to a diesel engine, perhaps they are indicative of what is happening in a diesel engine with insulated combustion chamber.

One of the shortcomings of the radiation mechanism is that is does not explain the measurements of Enomoto and Furuhama [38, 39], which were performed in a spark-ignition engine. In this type of engine the contribution of radiation to the total heat transfer is believed to be unimportant.

It is now expedient to summarize the key points of this discussion.

1 Several experimental studies found that the thermal efficiency of uncooled and/or thermally insulated diesel engines degraded at low-speed/high-load conditions.

2 A number of experimental studies in engines and in steady-state burners have shown that, under certain conditions, insulating the combustion chamber, or equivalently increasing its surface temperature, it increases the surface heat transfer during combustion.

3 Of the proposed mechanisms to explain the augmentation of surface heat transfer with increasing wall temperature, the ignition and subsequent combustion of unburned fuel in the boundary layer of the wall and the augmentation of radiant heat transfer from the flame to the wall are the two most plausible mechanisms.

Woschni and co-workers have suggested that high heat losses during combustion are responsible for the degradation in the thermal efficiency of thermally insulated engines. The above summary supports this hypothesis, although not conclusively. As of yet, there is no conclusive evidence to show that high heat losses are the *cause* rather than the *effect* of the degradation in the thermal efficiency of thermally insulated engines. Some evidence exists [27] that suggests deterioration of the combustion process, caused by the adverse influence of elevated temperatures on the injection process, may be responsible for the loss of thermal efficiency of an uncooled diesel engine. A strong indication that the observed loss in thermal efficiency is a combustion-related problem is given by the fact that the loss in efficiency was usually accompanied by high exhaust smoke. The high exhaust smoke may also signify a substantial increase in radiant heat transfer to the combustion-chamber walls.

Whatever the responsible mechanism, the reported observation of Woschni and co-workers that heat loss increases with surface temperature has enough supporting evidence to raise serious questions about the future of low-heat-rejection engines as highly efficient power plants.

References

24 Woschni, G., Kolesa, K., and Spindler, W., "Heat Insulation of Combustion Chambers—A Worthwhile Topic for Development of I.C. Engines?" *MTZ*, Vol. 47, 1986, pp. 495–500.

25 Woschni, G., Spindler, W., and Kolesa, K., "Heat Insulation of Combustion Chamber Walls—A Measure to Decrease the Fuel Consumption of I.C. Engines?" SAE Paper No. 870339, 1987.

26 Wallace, F. J., Kao, T. K., Tarabad, M., Alexander, W. D., and Cole, A., "Thermally Insulated Diesel Engines," *Proc. IMechE.*, Vol. 198A, 1984, pp. 97–105.

27 Alkidas, A. C., "Experiments With an Uncooled Single-Cylinder Open-Chamber Diesel," SAE Paper No. 870020, 1987.

28 Tovell, J. F., "The Reduction of Heat Losses to the Diesel Engine Cooling System," *SAE Transactions*, Vol. 92, 1983, pp. 1.1088–1.1097.

29 Morel, T., Fort, E. F., and Blumberg, P. N., "Effect of Insulation Strategy and Design Parameters on Diesel Engine Heat Rejection and Performance," *SAE Transactions*, Vol. 94, 1985, pp. 3.753–3.767.

30 Gatowski, J. A., Jones, J. D., and Siegla, D. C., "Evaluation of the Fuel Economy Potential of the Low-Heat-Rejection Diesel Engine for Passenger-Car Application," SAE Paper No. 870024, 1987.

31 Yoshimitsu, T., Toyama, K., and Sato, F., and Yamaguchi, H., "Capabilities of Heat Insulated Diesel Engine," SAE Paper No. 820431, 1982.

32 Bryzik, W., and Kamo, R., "TACOM/Cummins Adiabatic Engine Program," *SAE Transactions*, Vol. 92, 1983, pp. 1.1063–1.1087.

33 Wade, W. R., Havstad, P. H., Ounsted, E. J., Trinker, F. H., and Garwin, I. J., "Fuel Economy Opportunities With an Uncooled DI Diesel Engine," *Fuel Efficient Power Trains and Vehicles*, IMechE., Paper No. C432/84, 1984, pp. 59–72.

34 Alkidas, A. C., "On the Premixed Combustion in a Direct-Injection Diesel Engine," ASME JOURNAL OF ENGINEERING FOR GAS TURBINES AND POWER, Vol. 109, 1987, pp. 187–192.

35 Woschni, G., "A Universally Applicable Equation for the Instantaneous Heat Transfer Coefficient in the Internal Combustion Engine," *SAE Transactions*, Vol. 76, 1967, pp. 3065–3083.

36 Monnot, G., Feugier, A., Le Bouc, F., Mauss, F., Meyer, C., Perthuis, E., and De Soete, G., *Principles of Turbulent Fired Heat*, Gulf Publishing Co., Houston, 1985, pp. 134–159.

37 Germerdonk, R., and Nguyen, N. N., "Increase of the Local Heat Transfer Coefficient by Convection Vive Phenomenon," *Ger. Chem. Eng.*, Vol. 8, 1985, pp. 81–86.

38 Enomoto, Y., and Furuhama, S., "Heat Transfer Into Ceramic Combustion Chamber Wall Of Internal Combustion Engines," SAE Paper No. 861276, 1986.

39 Enomoto, Y., Furuhama, S., and Takai, M., "Heat Transfer to Wall of Ceramic Combustion Chamber of Internal Combustion Engine," *11th FISITA Conference*, Belgrade, 1986, pp. 1.159–1.165.

40 Hoag, K. L., "Measurement and Analysis of the Effect of Wall Temperature on Instantaneous Heat Flux," SAE Paper No. 860312, 1986.

41 Huang, J. C., and Borman, G. L., "Measurements of Instantaneous Heat Flux to Metal and Ceramic Surfaces in a Diesel Engine," SAE Paper No. 870155, 1987.

42 Otto, K., Sieg, M. H., Zinbo, M., and Bartosiewicz, L., "The Oxidation of Soot Deposits From Diesel Engines," *SAE Transactions*, Vol. 89, 1980, pp. 1399–1411.

43 McCabe, R. W., and Sinkevitch, R. M., "A Laboratory Combustion Study of Diesel Particulates Containing Metal Additives," SAE Paper No. 860011, 1986.

44 Oshima, Y., and Fukuda, Y., "Effect of Ash on Combustion Characteristics of Carbons," *Industrial and Engineering Chemistry*, Vol. 27, 1935, pp. 212–217.

45 Peterson, R. C., "The Oxidation Rate of Diesel Particulate Which Contains Lead," SAE Paper No. 870628, 1987.

46 Alkidas, A. C., and Jones, J. D., "An Experimental and Analytical Study of Thermal Loading in an Uncooled Open-Chamber Diesel Engine," *Heat Transfer Engineering*, 1987, in press.

47 Kanury, A. M., *Introduction to Combustion Phenomena*, Gordon and Breach Science Publishers, New York, 1975, pp. 81–141.

48 Potter, A. E., "Flame Quenching," in: *Progress in Combustion Science and Technology*, Vol. 1, J. Ducarme, M. Gerstein, A. H., LeFebvre, eds., Pergamon Press, New York, 1960, pp. 145–181.

49 Alkidas, A., and Durbetaki, P., "Stagnation Point Heat Transfer: The Effect of the First Damkohler Similarity Parameter," ASME *Journal of Heat Transfer*, Vol. 94, 1972, pp. 410–414.

50 Rocard, Y., and Veron, M., "La Convection Vive," Bulletin Technique No. 21, Societe Francaise Des Constructions, Babcock & Wilcox, Dec. 1948.

51 Glassman, I., *Combustion*, Academic Press, New York, 1977, pp. 5–15.

52 Borman, G., and Nishiwaki, K., "Internal-Combustion Engine Heat Transfer," *Prog. Energy Combust Sci.*, Vol. 13, 1987, pp. 1–46.

53 Szekely, G. A., and Alkidas, A. C., "A Two-Stage Heat Release Model for Diesel Engines," *SAE Transactions*, Vol. 95, 1986, pp. 4.1117–4.1133.

Downloaded 01 Jun 2010 to 171.66.16.87. Redistribution subject to ASME license or copyright; see http://www.asme.org/terms/Terms_Use.cfm

54 Morel, T., and Keribar, R., "Heat Radiation in DI Diesel Engines," SAE Paper No. 860445, 1986.
55 Glassman, I., and Yacarrino, P., "The Temperature Effect in Sooting Diffusion Flames," *Eighteenth Symposium (International) on Combustion*, The Combustion Institute, 1981, pp. 1175–1182.
56 Naegeli, D. W., Dodge, L. G., and Moses, C. A., "Effects of Flame Temperature and Fuel Composition on Soot Formation in Gas Turbine Combustors," *Combustion Science and Technology*, Vol. 35, 1983, pp. 117–131.

J. M. Needham[8]

1 Introduction

Considerable attention has been focused on the low heat rejection diesel engine in the recent past due to its theoretical potential for higher thermal efficiency, elimination of the cooling system, improved tolerance to degrade fuel, and potential for lower emissions.

Recently, a more cautious attitude has emerged toward low heat rejection engines and the magnitude of potential improvements over normally cooled engines. Some wide-ranging work by Woschni et al. to determine the potential of the low heat rejection engine [57] has suggested that the heat transfer coefficient describing transfer of heat from combustion gas to chamber wall is a function of wall temperature. Experimental evidence has been reported to suggest an increase in heat transfer from combustion gas to chamber wall, even though the theoretical temperature difference between the two has decreased. The physical explanation for this phenomenon has been described as "convection vive" where the thermal boundary layer between combustion flame and chamber wall reduces with an increase in wall temperature allowing the heat transfer coefficient to rise.

2 Combustion Optimization

One of the arguments often put forward to explain the poor performance of low rejection engines is that the combustion system has not been optimized to operate at higher gas temperatures. Normally cooled engines have been developed over many years to optimize air motion and fuel injection characteristics to reach the levels currently used as the baseline to compare with the low heat rejection engine. Experimental evidence suggests that insulation of the combustion chamber significantly shortens ignition delay such that the initial rate of heat release is much lower than for a conventionally cooled engine. Fuel injected after start of combustion does not mix well with the available air resulting in an extended combustion period and poor fuel economy. It is conceivable that fundamental combustion system optimization is required to realize the potential of the low heat rejection engine. This may involve parameters not considered in work reported to date [58, 59] such as radically altered fuel injection characteristics and combustion chamber geometry. Until work has been carried out to explore these parameters in more detail, the potential of the low heat rejection engine cannot be defined.

3 Convection Vive

The phenomenon of "convection vive," as referenced by Woschni, has not been widely reported. The work of Germerdonk and Nguyen [60] contains reference to other similar work, which is contradictory to their own findings. The results presented by Germerdonk and Nguyen suggests that an exothermic reaction can take place in the boundary layer of a propane/air mixture as it converges on a flat plate. This phenomenon occurs at a wall temperature of above 650°C. Below this temperature the surface heat transfer coefficient is essentially constant.

However, this contradicts the results of Woschni, where the surface heat transfer coefficient increases consistently with wall temperature.

More work is required to investigate the phenomenon of "convection vive" applied to the diesel engine. Combustion in a diesel engine is very different from that of a constant flame. The effects of air/fuel ratio and fuel impingement on the combustion chamber walls must be considered in detail and the effects quantified.

4 Effect of Wall Temperature

The experimental investigation of heat transfer reported by Woschni was carried out with 2 Bendersky [61] type surface thermocouples installed in a dummy valve of a four-valve diesel engine. The important aspect of this experiment was that the only "hot" part of the combustion chamber was that of the dummy valve itself. A critical examination of this experiment therefore excludes that of overall changes in combustion efficiency.

Ricardo has over many years generated a unique data base of thermal measurements from engines. Experimental investigations of thermal gradients within combustion chamber components has shown that cycle-averaged heat flux in engine components is largely independent of combustion chamber wall temperature within the range of normal engine operating conditions. Comparison between identical components manufactured from either aluminum or cast iron with a corresponding surface temperature increase of 150°C has shown no variation in local heat fluxes. This does not agree with either the instantaneous or steady-state heat transfer results presented by Woschni. However, very few data are available at the higher temperatures theoretically required to reduce heat rejection to coolant.

Other work has been published that describes experiments to define instantaneous heat transfer at elevated wall temperatures [62]. However, these have often been limited to small changes in wall temperature well below those considered by Woschni. The effects of "convection vive" are therefore unlikely to be confirmed.

5 Radiation

An argument often put forward to explain the decrease in fuel economy of the low heat rejection engine is that of increased heat loss from combustion due to heat radiation [63]. Poor combustion characteristics may also lead to higher soot formation during the intermediate stages of combustion resulting in even higher radiation losses. The experiment carried out by Woschni to investigate instantaneous heat transfer was in an otherwise conventionally cooled engine. The surface temperature of the dummy valve was not significantly higher than a normally operating exhaust valve. Combustion and therefore gas temperatures should therefore be largely unaffected by the local increase in wall temperature such that no increase in radiation heat transfer would be evident.

6 Instrumentation

The measurement of instantaneous surface temperature is a complex area. It is extremely difficult to measure surface temperature nonintrusively. Analysis of surface temperature fluctuations to determine instantaneous heat transfer is relatively straightforward for a homogeneous material provided accurate material properties can be defined. Most experimental surface temperature investigations have used the Bendersky design of surface thermocouple [61]. However, this design of surface thermocouple is far from homogeneous at the surface and employs materials exhibiting widely differing thermal properties. Work by Ricardo with this type of thermocouple has required substantial dynamic finite element analysis of the surface thermocouple to derive instantaneous

[8]Ricardo Consulting Engineers, West Sussex, United Kingdom.

Downloaded 01 Jun 2010 to 171.66.16.87. Redistribution subject to ASME license or copyright; see http://www.asme.org/terms/Terms_Use.cfm

heat flux from analysis of surface temperature fluctuations. For example, a J-type thermocouple consists of elements of iron and constantan. For the same dynamic heat input the surface temperature fluctuation of constantan is ~50 percent greater than that of iron. The thermal properties of constantan also change significantly with temperature; the variation in mean wall temperature of 270 to 660°C will incur substantial variation in material thermal diffusivity.

The use of steady-state heat flux probes is also an area where substantial errors can be introduced. Again, finite element analysis is often required to investigate the intrusiveness of the probe and to determine the presence of any extraneous heat flow paths. The use of an intrusive probe, where probe tip temperature is significantly higher than the surroundings, may require detailed analysis to determine the relationship between measured probe temperatures and real heat flow input.

7 Conclusions

1 With the current experimental evidence, it is premature to conclude that the fuel economy of the low heat rejection engine is likely to be significantly higher than a normally cooled engine.

2 There are very few experimental data describing the combustion system re-optimization necessary to realize the potential of the low heat rejection engine.

3 The phenomenon of "convection vive" needs further substantial investigation to determine under which conditions it may exist and to define the overall impact on the low heat rejection engine.

References

57 Woschni, G., Spindler, W., and Kolesa, K., "Heat Insulation of Combustion Chamber Walls—a Measure to Decrease the Fuel Consumption of IC Engines?" SAE Paper No. 870339, 1987.

58 Suzuki, T., Tsujita, M., Mori, Y., and Suzuki, T., "An Observation of Combustion Phenomena on Heat Insulated Turbocharged and Inter-cooled DI Diesel Engines," SAE Paper No. 861187, 1986.

59 Yoshimitsu, T., Toyama, K., Sato, F., and Yamaguchi, H., "Capabilities of Heat Insulated Diesel Engine," SAE Paper No. 820431, 1982.

60 Germerdonk, R., and Nguyen, N., "Increase of the Local Heat Transfer Coefficient by 'Convection Vive' Phenomenon," *Ger. Chem. Eng.*, 1985.

61 Bendersky, D., "A Special Thermocouple for Measuring Transient Temperatures," *Mechanical Engineering*, Vol. 75, 1953.

62 Hoag, K., "Measurement and Analysis of the Effect of Wall Temperature on Instantaneous Heat Flux," SAE Paper No. 860312, 1986.

63 Morel, T., and Keribar, R., "Heat Radiation in DI Diesel Engines," SAE Paper No. 860445, 1986.

Authors' Closure

To Mr. Ryan

Of course we also at first supposed that because of the decreasing volumetric efficiency, the combustion efficiency would decrease and that this possibly would be the reason for the existing loss of energy. Therefore we calculated the combustion efficiency from the measured exhaust gas composition. At no operating point that we used for evaluation was lower peak pressure for the insulated pistons than for the standard pistons, and at first we also believed that this was caused by a significant delay of the combustion.

If we have a look at Fig. 3 of our paper, indeed we find a lower peak pressure for the insulated pistons than for the standard pistons, and at first we also believed that this was caused by a significant delay of the combustion.

The heat release diagrams determined from the measured pressure curves, however, show that the combustion delay is very small and results in an increase of the fuel consumption of only about 1 g/kWh. However, we are looking for a difference of 17 g/kWh, which can only be explained by the energy loss. It can be seen clearly that this loss is greater, the higher the surface temperature of the piston.

To Mr. Hoag

The results measured at Cummins as well as results obtained at other engine manufacturers support our theory. As an example, Fig. 11 of the paper shows the results for an eight-cylinder engine, which we investigated by means of cycle simulation. At full load this calculation provides an increase in fuel consumption of about 3 g/kWh, and as can be seen from Fig. 13 of the paper decrease in heat rejection of about 8.5 percent. These results have the same magnitude as the values measured at Cummins. This may be incidental, because the operating conditions as well as the insulation of both engines are different.

Therefore we used the data published by Cummins to calculate the rated power for the same operating conditions and the same degree of insulation (coating of cylinder head and piston with a layer of 1.3 mm ZrO_2). This was done with our cycle simulation program using the modified equation for the heat transfer, and as related to the base line engine we obtained an increase in fuel consumption of 2 g/kWh and a reduction in heat rejection of 7.3 percent against 2 g/kWh and 7.9 percent measured at Cummins.

To Mr. Morel

First I believe I should clarify a misunderstanding. In the course of a process simulation we calculate the heat losses separately for cylinder head, piston, and liner, usually, however, with the same heat transfer coefficient, but different wall temperatures, which for careful investigations such as the present one are known from temperature measurements. Of course here we have C_2 varied only for the insulated piston until the calculation provided the same figure for the fuel consumption as measured. The heat transfer coefficient for the noninsulated areas of cylinder head and liner of course remained unchanged.

The second point is the heat transfer coefficient as a function of crank angle. It must be stated that the experimental investigation of a phenomenon and its mathematical formulation are two entirely different tasks. To succeed in the latter task it is necessary to make compromises. Of course it is an approximation to take the dependence of the heat transfer coefficient from surface temperature by a varied C_2 into account, but in my opinion it is a good approximation. Figure 27 shows the measured curve of the local heat transfer coefficient and for comparison the curve of the area-averaged heat transfer coefficient as obtained from the equation, for low surface temperature on top and high surface temperature on the bottom of the figure.

In view of the fact that of course the local heat transfer coefficient for a short time has a significant peak, the area integration however yields a very smooth curve since the flame does not occur simultaneously at all places; I find it is a very meaningful curve.

The next point mentioned is the heat flux. In the USA obviously it is usual to quote only the heat flux instead of the heat transfer coefficient. In my opinion the heat transfer coefficient allows a much clearer physical statement than the heat flux.

Figure 28 shows the heat flux and the heat transfer coefficient. It can be seen that the heat transfer coefficient shows much more clearly the influence of the surface temperature level than the heat flux.

Downloaded 01 Jun 2010 to 171.66.16.87. Redistribution subject to ASME license or copyright; see http://www.asme.org/terms/Terms_Use.cfm

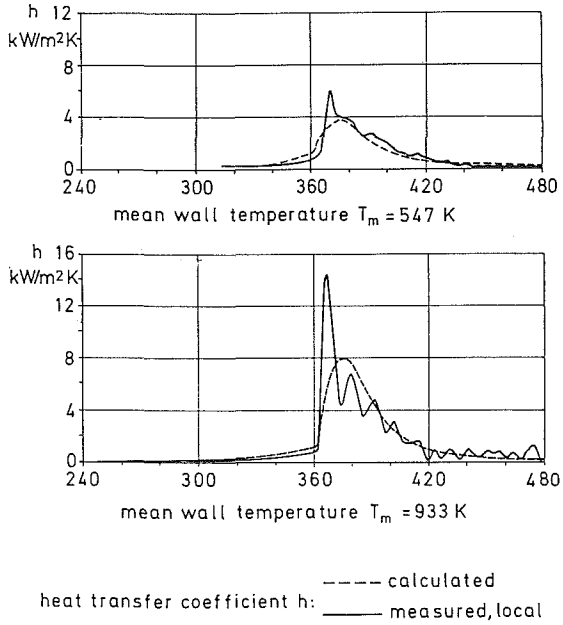


Fig. 27 Measured and calculated heat transfer coefficient at 1500 rpm, imep = 7.3 bar

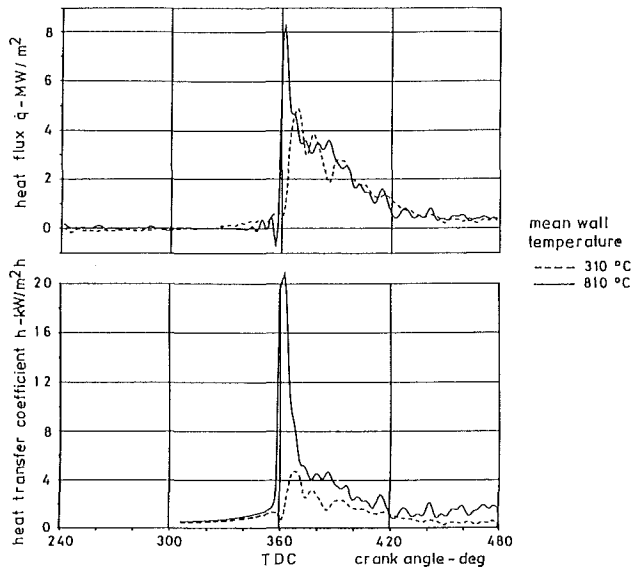


Fig. 28 Local heat transfer fired engine, different wall temperatures, 1750 rpm, imep = 8.2 bar

As has just been demonstrated clearly by the discusser, it is not so easy to find this effect, even from our results, if one considers only the heat flux. So we are not surprised that an influence of the surface temperature level on heat transfer could not be found, although, as has been mentioned, at ITI there have been made a great number of experiments for many years. It is the heat transfer coefficient that has to be considered, and then one will find this effect too.

To Mr. Cheng

This contribution was focused on four points.

Coming to point one, the discusser believes he can conclude from our results that the combustion efficiency is the reason for the observed loss of energy. Of course we checked this first. The combustion efficiency can easily be calculated from the exhaust gas composition shown in Figs. 21 and 22. In all cases, with the exception of one point in Fig. 22, the combustion efficiency was better than 99 percent; for the one point mentioned it was 97 percent.

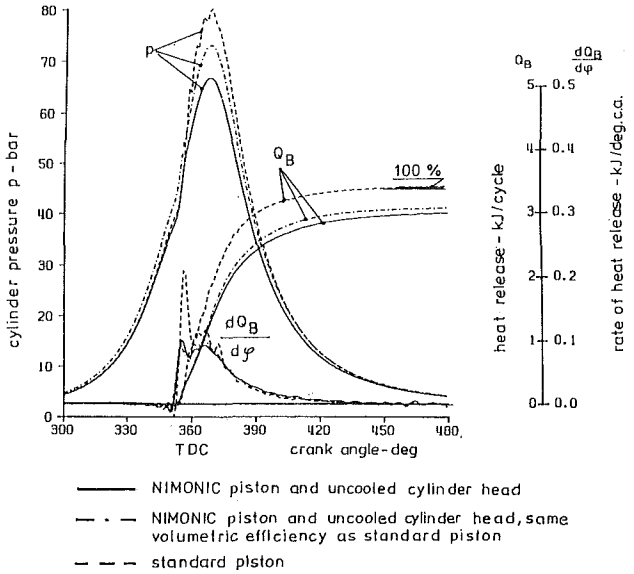


Fig. 29 Heat release with Nimonic piston and uncooled cylinder head, with and without compensation for volumetric efficiency, 1500 rpm, fuel input 77 mg

If we have a closer look at this point we can see from Fig. 29 the result of the evaluation of the heat release. For comparison there again are shown the results of the standard engine (dashed lines) as well as the results of the insulated piston. The latter one is first with the volumetric efficiency as it was (full line) and then with compensation of the volumetric efficiency by supercharging to the amount of the standard engine (dashed-dotted line). The combustion efficiency in this case again was better than 99 percent. The difference between the full line and the dashed-dotted line is caused by the drop in combustion efficiency from 99 to 97 percent. In spite of this there remains the large difference between the dashed-dotted and the dashed lines. This is the energy loss we are talking about and which in our opinion is caused by the increased heat transfer. Therefore we think Fig. 23 is very nice, but not meaningful.

To point two of the discussion it must be said that Fig. 1 is from an internal report, which is confidential and not published. Indeed we have some problems with process simulation at low load with some engines. We are just investigating this problem, but up to now we even are not sure whether the existing differences really can be attributed to heat transfer. However, as this problem is not related to the adiabatic engine we did not publish these low-load values in order to avoid confusion.

To answer point three we again should have a look at Fig. 3 of the paper. Obviously the effect of increased heat transfer exists for both combustion systems. We imagine that in both cases just a part of the combustion chamber surface is covered by a fuel film. Surely the magnitude of the area covered by the fuel film is different for both systems and this may be why the energy loss observed with the fuel vaporization system is a little bit smaller.

Point four: We are not able to agree with the theory of autoignition, because if this phenomenon should occur on the hot valve probe then there ought to occur autoignition on the whole piston surface of an insulated piston, which would result in a significantly different rate of heat release. The first peak in this diagram would increase markedly. Figure 3 of the paper, however, shows a clear decrease of the first peak for the insulated pistons.

Moreover we know from earlier experiments with knocking

Downloaded 01 Jun 2010 to 171.66.16.87. Redistribution subject to ASME license or copyright; see http://www.asme.org/terms/Terms_Use.cfm

gasoline engines that there is indeed an increase of the heat transfer coefficient, but by far not to such an extent as observed with the insulated piston or the heat flux probe.

To Mr. Alkidas

The discusser has made a very elaborate and comprehensive contribution. Starting with the results of his own investigations, which yielded results very similar to ours, there are discussed a number of conceivable reasons for the increase in isfc, which also has been found by his experiments. The discusser critically examined the different reasons and discarded most of them.

We fully agree that fuel consumption increases with insulated combustion chamber walls and that an increased heat transfer coefficient at the very hot insulated surfaces is the physical reason for that. To explain this phenomenon our deliberations were rather similar to those of the discusser.

Decreasing deposits with increasing surface temperature could at most have an influence on the evaluation of the measured transient surface temperature, but not on the steady-state heat flux, measured by the heat flux probe with different degrees of insulation, and also not on the results of the internal heat balance.

Dissociation and recombination can also be excluded for the very reasons mentioned by the discusser. Such an effect should reduce and not increase the heat transfer coefficient with increasing surface temperature level.

Radiation increases with increasing process temperature level and the latter arises with increasing surface temperature. In the case of our transient heat flux probe, as well as of our steady-state heat flux probe, the area where the surface temperature increased was so small that for sure the process temperature level could not be influenced. Nevertheless, the heat transfer coefficient increased. On the other hand, in the case in which we used the standard piston and air preheating, the process temperature level increased; the heat transfer coefficient however remained constant. So we cannot imagine that radiation can be a reason for the increasing heat transfer coefficient. The only explanation we have is that the flame is burning closer to the wall when the wall temperature is higher, thus producing heat sources very close to the wall and simultaneously inducing a higher turbulence near the wall, but we agree that there have to be still more investigations into what really happens in the boundary layer.

To Mr. Borman

We agree that investigations into the heat transfer in an internal combustion engine are extremely difficult. Each method has its specific weaknesses. Therefore we have applied three different methods independent from each other, i.e., the evaluation of an internal heat balance, the evaluation of the measured transient surface temperature of the wall, and the evaluation of the measured steady-state heat flow. All these methods show the same tendency. Moreover all experimental results were combined with cycle simulation and we believe that we can make reliable predictions from the sum of these measured and calculated results.

We also agree that there is still a great number of detailed problems and that multidimensional codes for the calculation of the fluid and combustion phenomena would be an even more effective tool than the thermodynamic cycle simulation of today. Such procedures, however, are not yet available. As engineers we have to solve problems of today by the means available today.

To avoid misunderstandings: We are not against the application of ceramics in internal combustion engines. There may be a great number of reasons for the necessity of applying

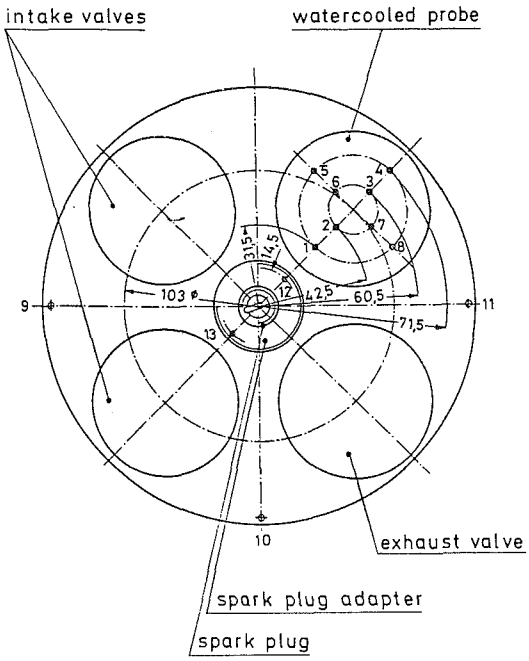


Fig. 30 Position of surface thermocouples, MTU cylinder head

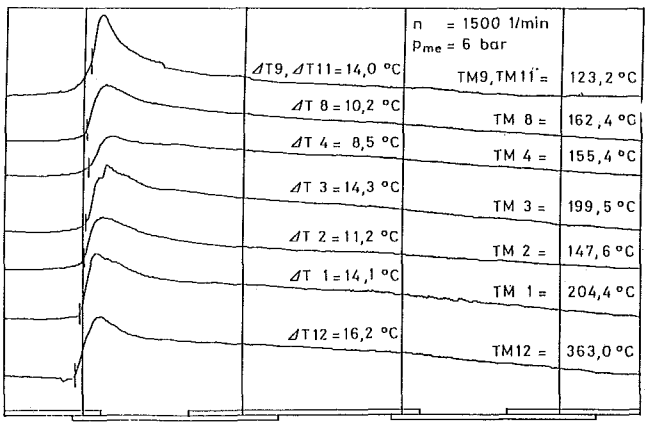


Fig. 31 Measured surface temperatures, MTU engine

ceramics in internal combustion engines, even some we probably do not know today, and frequently in research and development one discovers things initially not being sought.

We believe a further confirmation of the results presented in our paper is necessary, because if they should be confirmed, as indicated by some of recent worldwide publications, they would have the consequences on fuel consumption that were demonstrated in this paper.

To Mr. Furuhama

Professor Furuhama's results, which were found absolutely independently from ours, confirmed and encouraged us in our opinion.

The thermocouples we used were Cromel-Alumel elements of Medtherm. We have already used them for about 20 years without finding a reason to doubt the results. It was not the object of our work to disclose possible weaknesses of such thermocouples, but we are fully aware of the weakness of the whole method.

The main problem is that the method provides only local heat transfer coefficients, which scatter considerably from location to location. Such local values are very difficult to understand and to interpret quantitatively.

Downloaded 01 Jun 2010 to 171.66.16.87. Redistribution subject to ASME license or copyright; see http://www.asme.org/terms/Terms_Use.cfm

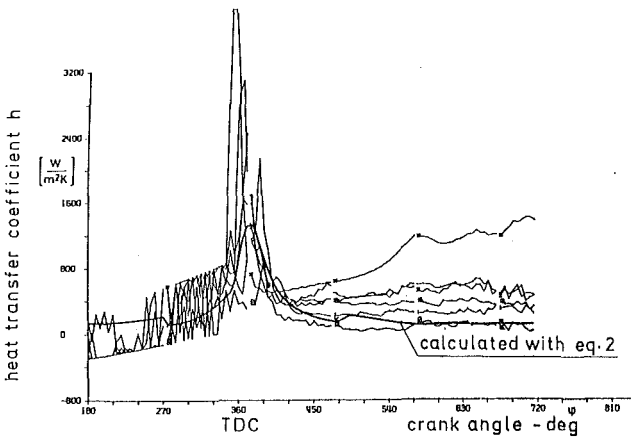


Fig. 32 Local heat transfer coefficients

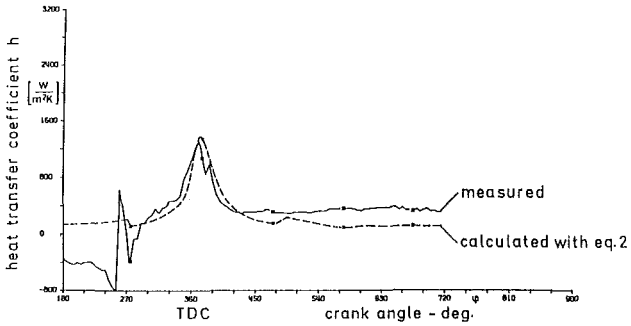


Fig. 33 Area-averaged heat transfer coefficient

To demonstrate this by an example: Fig. 30 shows the installation of surface thermocouples that was used for the cylinder head of a gas engine. In Fig. 31 one can see the temperature signals we obtained for a certain operating point. A significant increase in the temperature rise, marked by vertical strokes, indicates the arrival of the flame at the thermocouple, and hence the flame propagation through the combustion chamber can be seen clearly.

Figure 32 shows the local heat transfer coefficients as determined from the temperature signals and their significant scattering which hardly can be interpreted. Because the engine had a strong air swirl and a centrally located spark plug a rotational symmetry could be assumed, and so from these few measured values an area-averaged heat transfer coefficient could be obtained. As can be seen from Fig. 33 only this area integration yielded a meaningful curve, which agrees fairly well with the results of my equation for the area-averaged heat transfer.

In the investigations presented here we just wanted to demonstrate the influence of increased surface temperatures

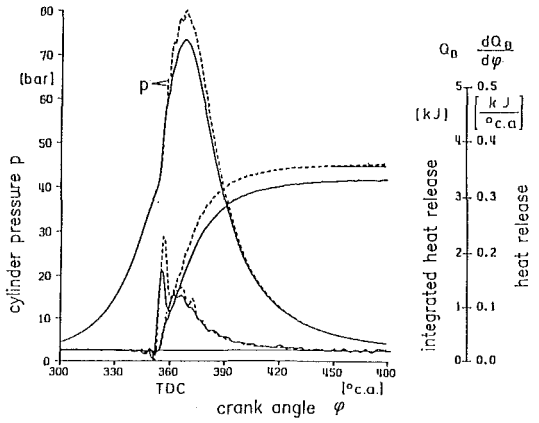


Fig. 34 Rate of heat release of Al-alloy and Nimonic piston, 1500 rpm, full load

on heat transfer. Because we did not change the position of the thermocouples, local values were sufficient.

To Mr. Needham

To begin with topic 3 of the conclusions, I fully agree that further substantial investigation on the phenomenon of "convection vive" is necessary. The results from Germerdonk and Nguyen had just been published, while we stood rather helpless with our results; we could not find an explanation for the increasing fuel consumption with insulated combustion chamber walls. Our results also show, as can be seen clearly from Fig. 10, that the heat transfer coefficient does not increase with increasing surface temperature before a certain surface temperature level is attained. This temperature indeed is lower than the one found for steady-state propane gas flames, but I can see no contradiction to the results of Germerdonk and Nguyen.

To the second topic concerning optimization of combustion for insulated combustion chamber walls, I cannot imagine that here great improvements can be expected. Figure 34 shows the heat release diagrams for the engine with the very hot fully insulated piston and the cold standard aluminum alloy piston for the combustion system with air distributed fuel. The difference is very small. Only a slight delay in the shape can be seen, which causes an increase in fuel consumption of only around 1 g/KWh. Obviously the mixture formation and combustion do not deteriorate so dramatically as is frequently supposed. For this reason in my opinion the potential of improvement can be neglected, and hence it is fair to compare the standard basic engine with the engine with insulated components.

Coming to the first topic of the conclusion, I think insulation of the combustion chamber walls is no successful way to decrease the fuel consumption of diesel engines. If this aim should be attained one has to choose the opposite way. One should not increase the surface temperature level by insulation but decrease the process temperature level by supercharging, high air/fuel ratio, and charge air intercooling.

Downloaded 01 Jun 2010 to 171.66.16.87. Redistribution subject to ASME license or copyright; see http://www.asme.org/terms/Terms_Use.cfm

A Steady-State Air Motion Study in a V-6 Uniflow Scavenged Two-Stroke Diesel Engine

T. D. Doan

E. F. Crawford

S. J. Hinkle

Detroit Diesel Allison Division,
General Motors Corporation,
Detroit, MI 48239

This paper presents new insight into the causes of cylinder-to-cylinder variation in swirl torque and airflow in uniflow scavenged, two-stroke diesel engines. A V-6 model of such an engine was investigated as a flow rig under steady-state conditions. These variations were found to be primarily caused by the effect of the airbox walls on the air motion. The maximum difference in the baseline cylinder-to-cylinder swirl torque and airflow rate was 11 and 3.5 percent, respectively. Two airbox design modifications, resulting from the study, in turn demonstrated increased cylinder airflow rate and reduced cylinder-to-cylinder swirl torque variation on the flow rig.

Introduction

Previous research studies at Detroit Diesel Allison to investigate two-stroke engine performance characteristics have indicated a cylinder-to-cylinder performance variability. This has been observed as cylinder-to-cylinder variation in swirl torque; cylinder-to-cylinder peak firing pressure, exhaust temperature, and exhaust emission differences; and bank-to-bank smoke differences in "vee" block engines. These studies have isolated the contribution of injector-to-injector output differences and results indicate that cylinder-to-cylinder performance variability is linked to nonuniform airflow distribution in the engine.

In general, airflow in a two-stroke cycle cylinder is mainly related to intake side (airbox and cylinder inlet port) and exhaust side (exhaust port and manifold) pressure loss characteristics. Air motion is primarily related to intake side, and scavenging is controlled both by intake and exhaust, but more so by intake parameters due to the effect of air motion on scavenging. To determine the cause of airflow maldistribution in the engine, a study of both intake and exhaust sides is necessary.

This paper presents the results of a first phase study to investigate the airflow distribution in the airbox of a two-stroke uniflow scavenged V-6 diesel engine under steady flow conditions. Two airbox design modifications evolved from the study: One demonstrated increased steady-state cylinder airflow and the other demonstrated equal cylinder-to-cylinder swirl torque under steady flow conditions. The findings leading to these designs are discussed.

Test Setup and Procedure

The study was carried out at the DDA Fluid Dynamics Laboratory at the Romulus Engineering Center. A plenum fixture test was run at the beginning of the study. In the engine block test, an engine block was used. To include the effect of a blower on the air motion in the airbox, a blower was installed on the engine block. A schematic of the test setup is shown in Fig. 1.

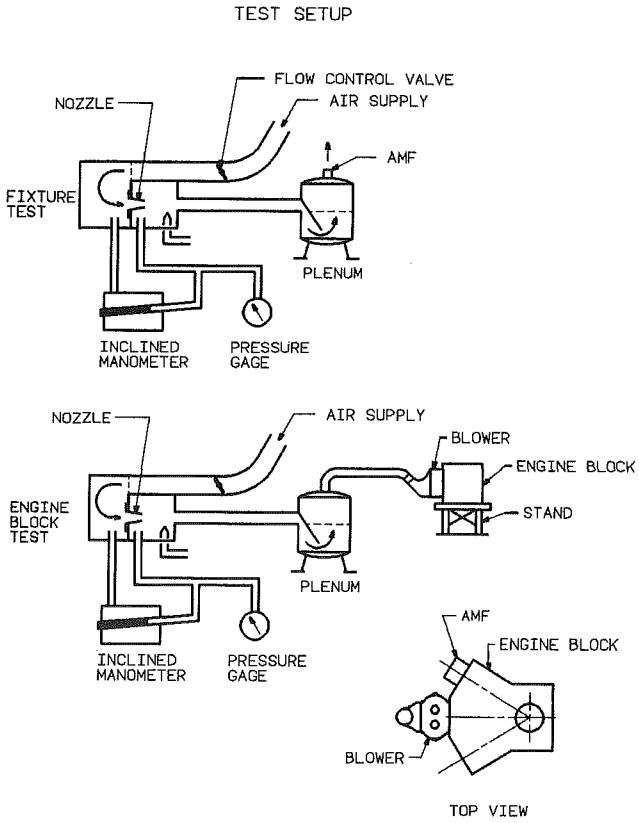


Fig. 1

Contributed by the Internal Combustion Engine Division and presented at the Eleventh Annual Energy-Sources Technology Conference and Exhibition, New Orleans, Louisiana, January 10–13, 1988. Manuscript received by the Internal Combustion Engine Division March 1987.

Copyright © 1988 by ASME
Downloaded 01 Jun 2010 to 171.66.16.87. Redistribution subject to ASME license or copyright; see http://www.asme.org/terms/Terms_Use.cfm

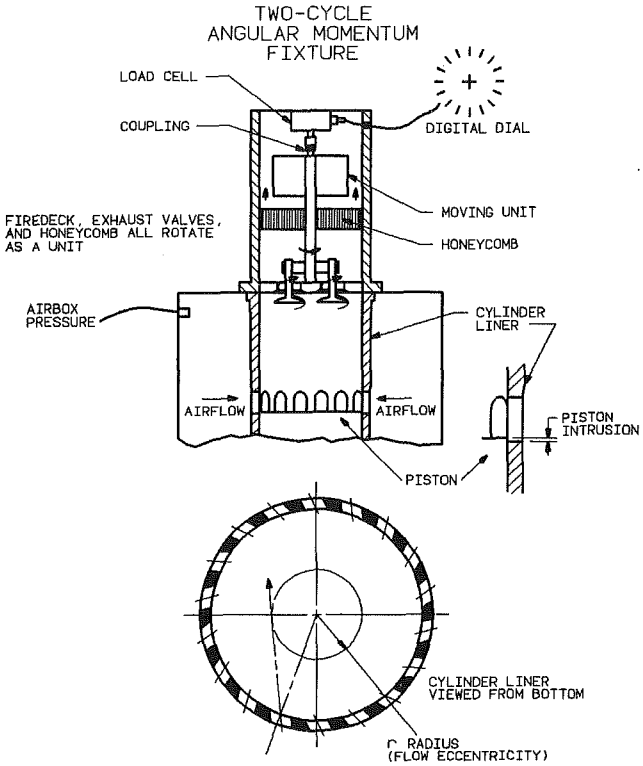


Fig. 2

Swirl torque was measured by an Angular Momentum Fixture (AMF). The operation concept of the AMF is shown in Fig. 2. The swirl is generated when air enters through angled cylinder inlet ports into the cylinder. The firedeck, exhaust valves, and honeycomb assembly were designed to rotate as a unit. With this design feature the swirl torque acting on the honeycomb is equal to the angular momentum flux in the cylinder, where the effect of the downstream restriction of the exhaust valve lift is included.

Relationship of Cylinder Swirl Torque With Respect to Flow Parameter. A linear relationship between the swirl torque and flow condition was derived as follows.

For fluid entering the cylinder the mass flow rate is defined as

$$M = \sum^{N} m \tag{1}$$

The substitution of $m = V \cdot \rho \cdot a$ and $A = \sum^{N} a$ into equation (1) yields

$$V = M/\rho \cdot A \tag{2}$$

The cylinder swirl torque is defined as

$$T = \sum^{N} m \cdot V \cdot r$$

or

$$T = M \cdot V \cdot r \tag{3}$$

The substitution of (2) into (3) yields

$$T = M^2 \cdot r/\rho \cdot A$$

To include the effect of the upstream (airbox environment) and downstream (exhaust valve lift) restrictions, the cylinder swirl torque equation is rewritten as

$$T = K(M^2/\rho)$$

where K is a swirl torque constant that varies with the airbox and cylinder inlet port geometries, and is also dependent on the exhaust valve lift. The squared air mass flow rate and the air density are combined into an airflow parameter.

Relationship of Intake Port Pressure Loss With Respect to Flow Parameter. A linear relationship was also derived for the pressure loss across cylinder inlet ports. A useful concept relative to the effective area is used here (Smith and Morrison, 1970), which is defined as the area of the outlet of an imaginary, frictionless nozzle that would pass the measured flow from a constant pressure reservoir at the measured upstream stagnation pressure into an unrestricted volume at the measured downstream static pressure.

For small pressure drops

$$A = M/\sqrt{2 \cdot \rho_{01}(P_{01} - P_2)} \tag{4}$$

The substitution of

$$\rho_{01} = P_{01}/R \cdot T_{01}$$

into equation (4) yields

$$\sqrt{P_{01}(P_{01} - P_2)} = M\sqrt{R \cdot T_{01}}/A\sqrt{2}$$

or

$$\sqrt{P_{01} \cdot \Delta P} = H(M\sqrt{T_{01}})$$

where $\sqrt{P_{01} \cdot \Delta P}$ = pressure loss parameter, and $M\sqrt{T_{01}}$ = airflow parameter.

Data Discussion

Plenum Fixture Test. A plenum fixture test was carried out at the beginning of the study. The purpose of the test was to investigate the sensitivity of swirl torque and (cylinder inlet port) pressure loss to the hardware setup. This helped improve the quality of measured data and therefore the confidence in the test conclusions.

Effect of Piston Index. The sensitivity of the swirl torque and the pressure loss with respect to the relative position of the piston to the cylinder inlet ports (see Fig. 2) is shown in Fig. 3, where the swirl torque and pressure loss were normalized to the maximum values obtained in this plenum fixture test. A small increase of the piston intrusion caused a significant decrease of the swirl torque; however, it did not affect the pressure loss. Accordingly, great caution in setting the piston index was taken in measuring the swirl torque.

In the plenum fixture test the piston was carefully posi-

Nomenclature

a = inlet port flow area
A = overall inlet port flow area, effective area
H = pressure loss constant
K = cylinder swirl torque constant
m = inlet port mass flow rate
M = overall inlet port mass flow rate
N = number of inlet ports
P = pressure
r = flow eccentricity
R = gas constant
T = cylinder swirl torque, temperature
V = fluid velocity
ρ = density of fluid

Subscripts

0 = stagnation
1 = at airbox
2 = at cylinder

Downloaded 01 Jun 2010 to 171.66.16.87. Redistribution subject to ASME license or copyright; see http://www.asme.org/terms/Terms_Use.cfm

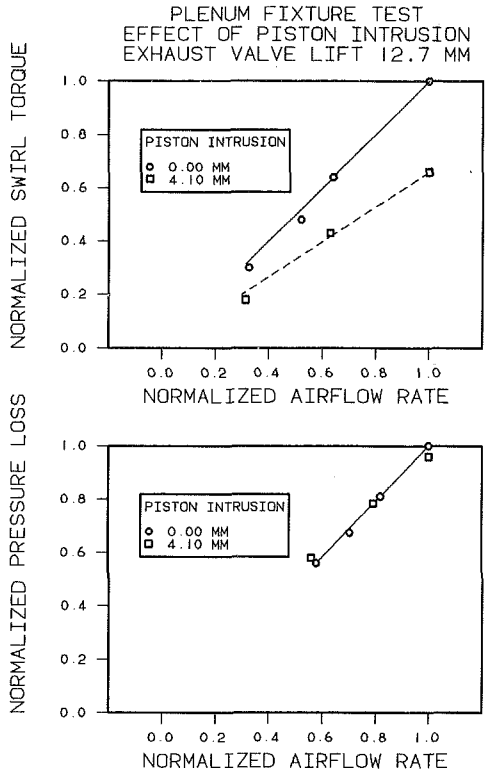


Fig. 3

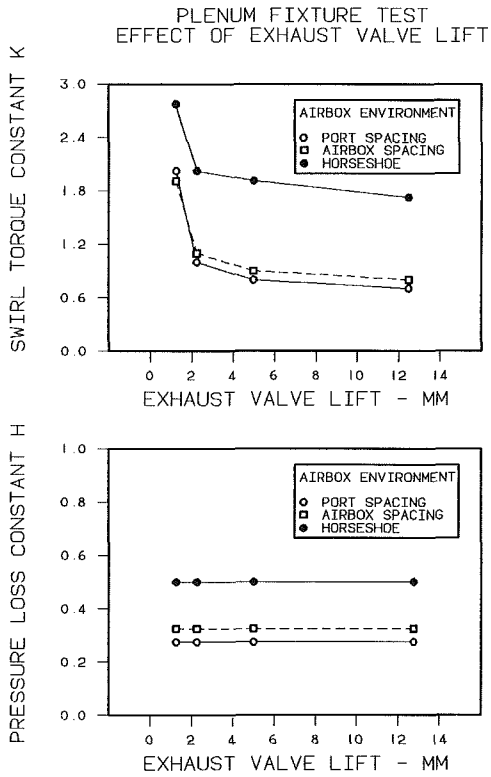


Fig. 4

tioned in the cylinder such that the top of the piston was flush with the bottom of the cylinder inlet ports, i.e., zero piston intrusion; in this way the piston was easily positioned accurately in the cylinder. However, in the engine block test to simulate the true orientation, the piston was positioned at bottom dead center (BDC) with a piston intrusion of 4.1 mm. To help position accurately the piston at BDC, a special gage was designed and used during the test.

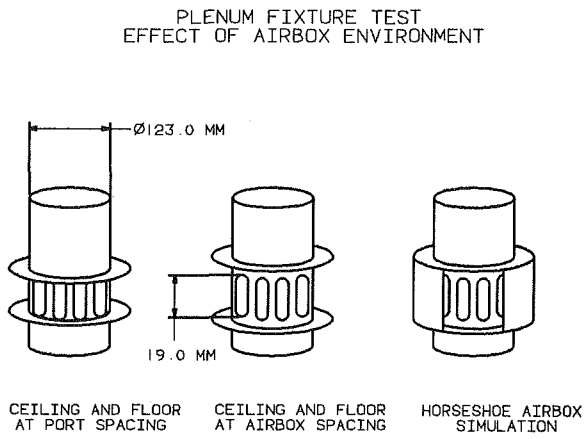


Fig. 5

Effect of Restriction at Exhaust Valves. Figure 4 shows the slope of the swirl torque line or the K constant relative to the exhaust valve lift, obtained from the airbox environment test to be discussed shortly. The K constant was slightly increased when the exhaust valve lift was lowered from 12.7 to 5.1 mm; however, K increased markedly when the exhaust valve lift was less than 5.1 mm. In other words, the swirl of the airflow in a cylinder becomes stronger when severe downstream restriction is imposed by extremely low exhaust valve lift, provided that the airflow rate is maintained constant. The condition of constant airflow rate is not the case in a real engine where the airflow rate goes down as the exhaust valve lift is lowered; consequently, the swirl torque actually is not increased drastically at low exhaust valve lifts in the case of a real engine. In contrast, the exhaust valve lift did not affect the H constant or slope of the pressure loss line; that is, the downstream restriction at the exhaust valves does not affect the pressure loss across the cylinder inlet ports as long as the airflow level is maintained (see Fig. 4).

Effect of Airbox Environment. In the plenum fixture test, since the cylinder was located at the middle of a large box, it can be assumed that a uniform radial airflow enters the cylinder through the inlet ports. The swirl of the airflow in the cylinder therefore must be created by the angled inlet ports only. In a real engine, due to the close proximity of engine block walls, especially airbox walls, to cylinder inlet ports, airbox walls certainly affect the characteristics of the airflow around the outside of cylinders, and therefore, the swirl and the airflow rate in the cylinders. In this part, the effect of the airbox environment on the swirl and the airflow rate in the cylinder is simulated. First, two rings were attached to the outside of the cylinder at the top and bottom of the inlet ports at the port spacing as shown in Fig. 5. Secondly, the spacing was enlarged to normal airbox spacing. Finally, the two rings at the airbox spacing were partly covered (horseshoe airbox simulation). Figure 4 presents the K constant of the swirl torque line and the H constant of the pressure loss line versus the exhaust valve lift for the three configurations.

The horseshoe airbox configuration indicated an extremely strong effect on both the swirl torque and inlet port pressure loss as compared with the other configurations. Figure 6 compares the swirl torque and the pressure loss between the three configurations and the bare cylinder case at the exhaust valve lift of 12.7 mm. The comparison indicates that the rings did not strongly affect the swirl torque and the pressure loss in the cylinder. However, when the rings were partly covered the swirl torque and the pressure loss were quite significantly raised. This confirms a strong and important influence of the

Downloaded 01 Jun 2010 to 171.66.16.87. Redistribution subject to ASME license or copyright; see http://www.asme.org/terms/Terms_Use.cfm

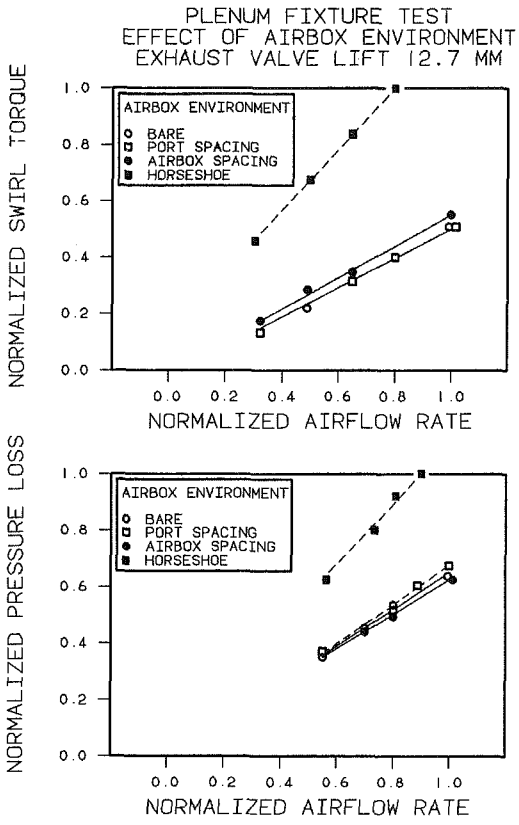


Fig. 6

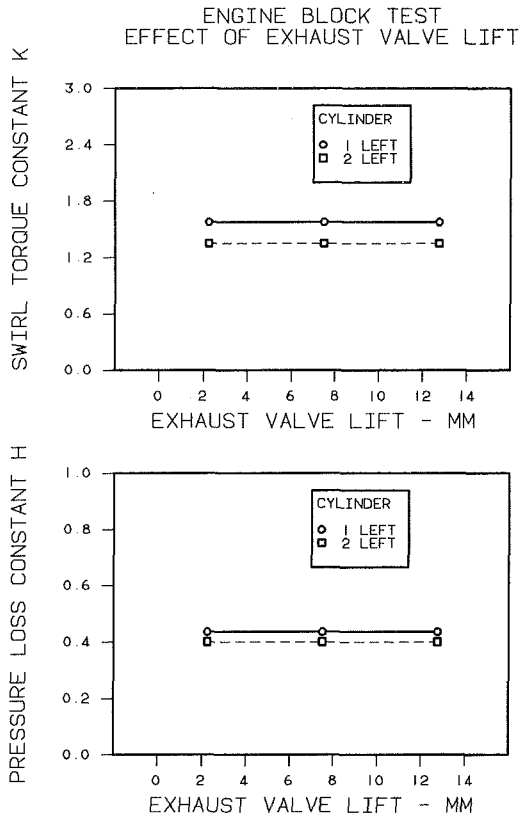


Fig. 8

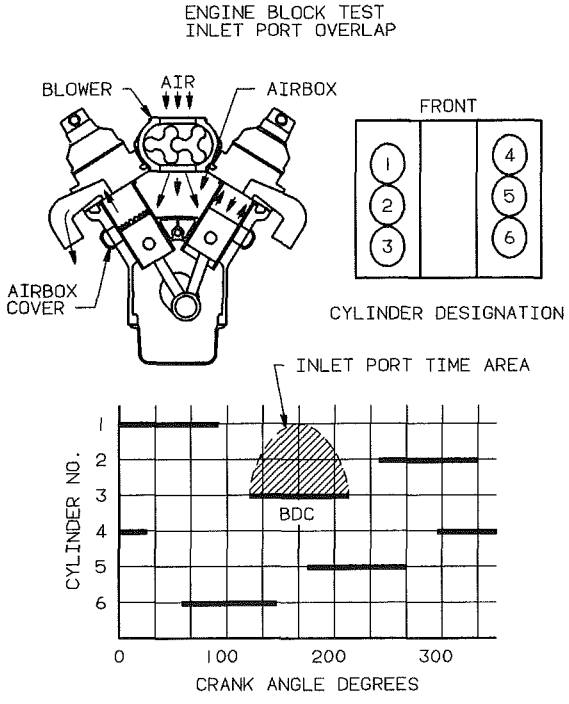


Fig. 7

airbox environment, especially airbox walls, on the swirl and the airflow. The increase of the swirl in the cylinder by the horseshoe configuration was followed by an increased pressure loss, or a reduction of the airflow rate. In other words, at the same upstream condition an increase of the air swirl in a cylinder by airbox walls will reduce the airflow rate due to a resulting increase of the inlet port pressure loss.

Engine Block Test. In this test the swirl torque and the pressure loss were measured for all six cylinders of a test engine block. The cylinder designation is shown in Fig. 7. The inlet port overlap between the cylinders is also shown in Fig. 7. Accordingly, whenever the piston of a cylinder reaches BDC, *the inlet ports of the rest of cylinders are closed completely*; otherwise, at other crank angles there is always an inlet port overlap between two cylinders. The inlet port overlap certainly will complicate the air motion in the airbox; consequently, data obtained under such a condition are hard to interpret. Therefore, throughout the test the piston of a cylinder to be flowed was always set at BDC. As already mentioned, due to the surprisingly high sensitivity of the swirl torque with respect to the piston index, a special gage designed to help set the piston at BDC accurately was employed.

At the beginning of the engine block test the engine block was flowed. In the range of the exhaust valve lift of 2.5 to 12.7 mm no effect of the exhaust valve lift on the swirl torque and pressure loss constants, i.e., K and H, respectively, appeared as shown in Fig. 8, where data were measured at cylinders 1 and 2. Accordingly, only the exhaust valve lift of 12.7 mm was set through the test. As will be discussed later, the swirl level at a specific airflow rate depends on three factors: airbox walls, the angle of inlet ports, and the downstream restriction at the exhaust valves. In the case of the engine block test the first two factors overshadow the third one; therefore, the effect of the exhaust valve lift on the swirl was hardly recognizable. Otherwise, in the bare cylinder case of the plenum fixture test where the effect of the airbox environment was absent, the effect of the exhaust valve lift was recognizable.

Baseline Engine Block. The engine block test was continued with the baseline test where the engine block as supplied was flowed. The cylinder-to-cylinder swirl torque and airflow variations were significant (see Fig. 9), where the swirl torque and airflow rate were normalized to the maximum values ob-

Downloaded 01 Jun 2010 to 171.66.16.87. Redistribution subject to ASME license or copyright; see http://www.asme.org/terms/Terms_Use.cfm

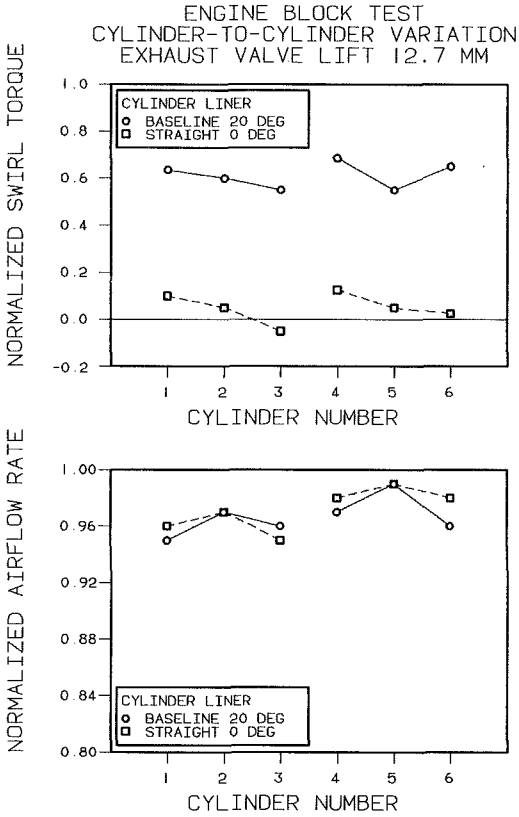


Fig. 9

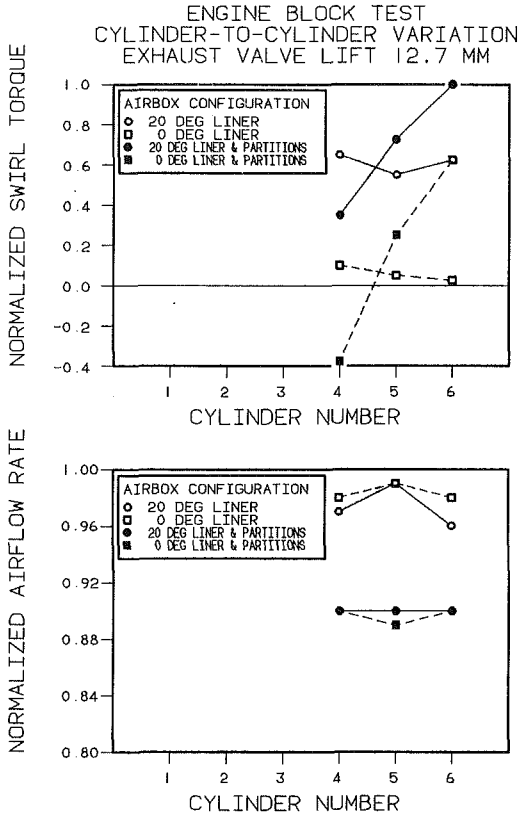


Fig. 11

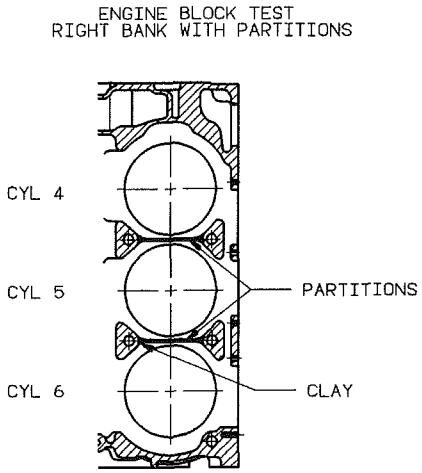


Fig. 10

tained in the engine block test. The maximum difference in the baseline cylinder-to-cylinder swirl torque and airflow rate was 11 and 3.5 percent, respectively. On each bank the corner cylinders had higher swirl torque levels and lower airflow rates than the middle ones, except cylinder 3; an explanation of its lower swirl torque will be presented later. As proved in the plenum fixture test, which was related to the effect of the wall surrounding the cylinder and causing an increase of swirl torque and a decrease of airflow rate, the cylinder-to-cylinder swirl torque and airflow rate variations were due to the effect of the airbox walls on the air motion. The corner cylinders are more closely surrounded by the airbox walls than the middle cylinders; this results in higher swirl torque and lower airflow rate at the corner cylinders.

Cylinder Liner With Straight Inlet Ports. To provide a better understanding relative to the effect of the airbox walls on the cylinder-to-cylinder variations, the engine block test was repeated with a cylinder liner that had straight inlet ports. In this case the contribution by the inlet ports to the swirl torque in the cylinder can be considered negligible. The trends of the cylinder-to-cylinder swirl torque and airflow variations were in general similar to those of the baseline (see Fig. 9). This similarity indicates that the airbox walls were the cause of the airflow maldistribution in the airbox.

The swirl torque was distinguishably strong in cylinder 4, and significantly weak in cylinder 3. The inlet ports of a production cylinder liner are always angled to create a counterclockwise swirl in the cylinder as viewed from the top of the cylinder. On the right bank the effect of the airbox walls resulted in the counterclockwise (positive) swirl in all three cylinders, and the strongest effect was at cylinder 4; this explains the distinguishably strong swirl torque in that cylinder. On the left bank, the effect of the airbox walls caused the counterclockwise swirl in cylinder 1 and 2, and the clockwise (negative) swirl in cylinder 3. Although the corner cylinder 3 in general is more affected by the airbox walls than the middle cylinder 2, the effect creates a clockwise swirl instead of a counterclockwise one, and consequently a low resulting swirl torque in cylinder 3. This was the cause of the significantly weak swirl in cylinder 3.

Right Bank With Partitions. Two partitions were installed in the right bank, as in Fig. 10. The addition of these partitions was expected to amplify the effect of the airbox walls on the swirl and the airflow of the right bank cylinders, and to provide some understanding that would be helpful for the minimization of the cylinder-to-cylinder swirl and airflow variations. The modified right bank was tested with both the production liner and the straight inlet port liner. The same trends of the cylinder-to-cylinder swirl variation of the two liners are shown in Fig. 11. This indicates the clear effect of

Downloaded 01 Jun 2010 to 171.66.16.87. Redistribution subject to ASME license or copyright; see http://www.asme.org/terms/Terms_Use.cfm

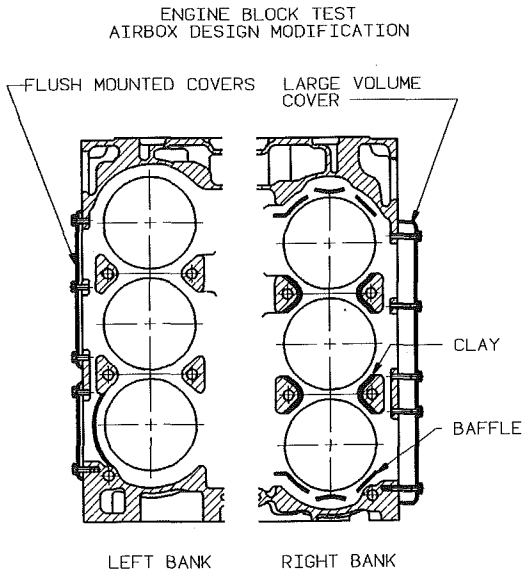


Fig. 12

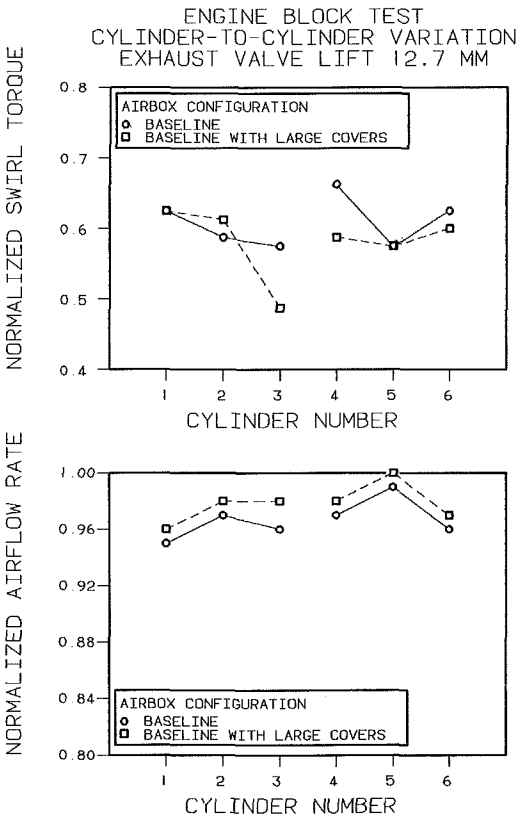


Fig. 13

the partitions on the swirl and the airflow in the three cylinders. The swirl level was increased in cylinders 5 and 6, and reduced in cylinder 4. The airflow was lowered about 8 percent in all three cylinders.

Airbox Design for Increased Cylinder Air Flow. Irrespective of the cylinder swirl, to improve the cylinder airflow rate the effect of the airbox walls was reduced by replacing the two airbox covers on each bank with a large volume airbox cover (see Fig. 12). An improvement in the cylinder airflow over the baseline is shown in Fig. 13.

Airbox Design for Minimized Cylinder-to-Cylinder Swirl Torque Variation. Irrespective of the airflow effects, baffles

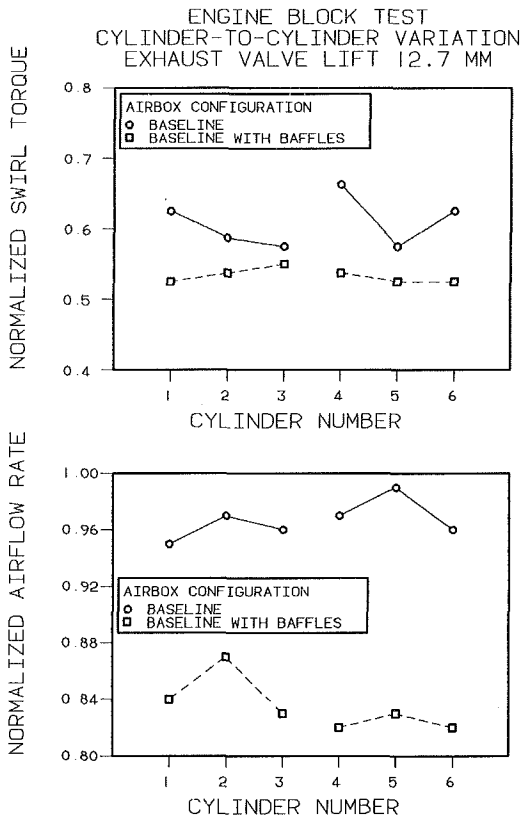


Fig. 14

were used to minimize the swirl torque variation. Based on findings mentioned above, a number of different baffle arrangements were created and tested. A baffle arrangement as shown in Fig. 12, plus the large volume airbox cover on the right bank, eliminated the swirl variation, of course at the expense of the airflow about 14 percent (see Fig. 14). A flow reduction of 14 percent does not mean that a reduction of this magnitude would occur in a running engine. Flow loss through the port area is only one portion of the total engine air system restriction.

Conclusions

The study verified the existence of the cylinder-to-cylinder swirl torque and airflow variations in the airbox of a V-6 uniflow scavenged two-stroke diesel engine block under steady flow conditions. The variations were primarily caused by the effect of the airbox walls on the air motion. The maximum difference in the baseline cylinder-to-cylinder swirl torque and airflow rate was 11 and 3.5 percent, respectively. Linear relationships between the cylinder swirl torque and the airflow parameter, and between the cylinder inlet port pressure loss and the airflow parameter, were obtained. The findings in the study served as design guides and helped arrive at two airbox design modifications: One demonstrated increased cylinder airflow and the other demonstrated equal cylinder-to-cylinder swirl torque under steady flow conditions.

Further work is planned in this area at DDA using simulation models, fixture tests, and running engine tests. It is an important and challenging development area directed toward improved engine performance, high power density, transient response, and emission control.

References

Smith, P., and Morrison, J., 1970, *The Scientific Design of Exhaust and Intake Systems*, 2nd ed.

Downloaded 01 Jun 2010 to 171.66.16.87. Redistribution subject to ASME license or copyright; see http://www.asme.org/terms/Terms_Use.cfm

The Effect of Inlet Velocity Distribution and Magnitude on In-Cylinder Turbulence Intensity and Burn Rate—Model Versus Experiment

G. C. Davis

R. J. Tabaczynski

Ford Motor Company,
Research Staff,
Dearborn, MI 48121

Steady flow measurements of velocity and mass flux distributions around the intake valve were used as input to a General Engine Simulation Model (GESIM) to assess the assumptions of uniform velocity and mass flux distributions and their effects on in-cylinder turbulence intensity and burn rate. In addition, an improved submodel for calculating the instantaneous velocity past the intake valve was developed and its effects on intake generated turbulence and burn rate assessed. Using the improved, inlet velocity submodel, a study was carried out for three different intake port configurations. Burn rate measurements were compared with model results for these configurations, which utilized the same engine head and block assembly. Model predictions, based on the standard port/valve discharge coefficient, indicated that velocity and mass distributions alone had a small effect on the in-cylinder turbulence intensity and burn rate. Significant differences in burn rate and turbulence intensity were predicted when the improved submodel for valve discharge coefficient was used. The new predictions agreed well with experimental measurements of burn rate. This implies that the increased mean velocities (which occur due to the restriction that creates the velocity and mass flow distributions) are the major cause for increased turbulence levels.

Introduction

In the past, thermodynamic, quasi-dimensional engine simulation models have not been able to predict the burn rate and ISFC for different engine combustion chamber/intake port configurations. Measurements of burn rate and average fuel consumption at a minimum of one engine operating condition for each engine configuration were required for model calibration. With this limitation, models of this type may only be used to evaluate combustion chamber geometry effects on burn rate and ISFC while keeping the intake port flow generating characteristics the same [1]. It is well known that intake-generated turbulence and swirl may have a significant effect on burn rate when the combustion chamber geometry remains unchanged and squish effects are small [2, 3].

The approach taken in this work is to use steady flow bench measurements as input to the engine simulation model in order to characterize the turbulence and swirl generation capabilities for a given intake port. One characteristic of an intake port is the unique velocity distributions produced near the valve/head interface as the flow enters the cylinder. The goal of this work is to assess the effects of velocity distribtuion on in-cylinder generated turbulence and burn rate and improve the prediction of the instantaneous inlet velocity past the intake valve during induction.

Engine Description and Measurements

Engine. The engine used for this study was a four-cylinder, 2.3-L engine. The combustion chamber configuration was of the "bathtub" type with the spark located approximately 2.5 cm away from the cylinder axis, as shown in Fig. 1. Table 1 gives additional characteristics of the engine. The induction system (intake manifold, cylinder head, intake port, and valve) was modified from the base configuration by masking the intake valve and inserting flow-restricting/directing tubes upstream of the intake valve inside the intake ports to change the flow processes during induction. Each modification was made for the complete induction system.

The engine was operated at 1500 rpm, 38 BMEP psi, stoichiometric air/fuel ratio, and MBT spark timing. Pressure-time measurements were made for the number one cylinder and burn-rate data obtained.

Steady flow bench measurements were also obtained for all three induction systems. These measurements will be described next.

Contributed by the Internal Combustion Engine Division and presented at the Eleventh Annual Energy-Sources Technology Conference and Exhibition, New Orleans, Louisiana, January 10-13, 1988. Manuscript received by the Internal Combustion Engine Division March 1987.

Copyright © 1988 by ASME
Downloaded 01 Jun 2010 to 171.66.16.87. Redistribution subject to ASME license or copyright; see http://www.asme.org/terms/Terms_Use.cfm

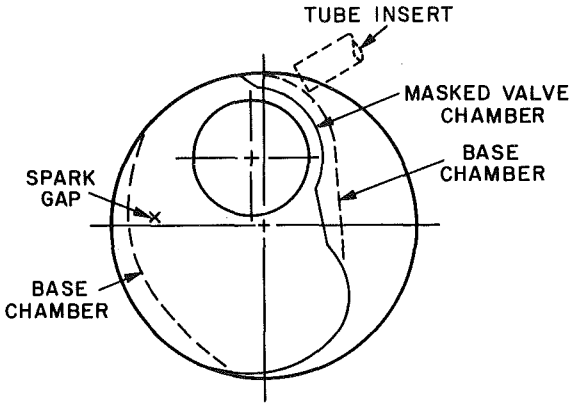


Fig. 1 Combustion chambers; masked valve used with base intake port, tube insert used with base chamber

Table 1 Engine characteristics

Bore	96 mm
Stroke	79.4 mm
Compression ratio	9:1
Piston	Flat
Intake port diameter (inside)	40.6 mm
Maximum lift	10.16 mm

Steady Flow Measurements. Discharge flow coefficients and angular momentum flux measurements were made for the three induction systems using the number one intake port and valve assembly as shown in Figs. 2 and 3.

Using a hot-wire anemometer, measurements of inlet velocity U at 10 deg increments around the intake valve were made. Mass flow rates were obtained corresponding to the velocity locations. Results are shown in Figs. 4 and 5. For more information about these measurements, see [4].

Model Description

The K-ϵ turbulence model currently used in the General Engine Simulation Model (GESIM) has been reported in [1, 3, 5, 6]. However, little has been discussed concerning the assumptions related to the production of turbulence during induction. The equation for the production and dissipation of turbulence kinetic energy can be written as

$$\rho\frac{dK}{dt}=P_{\text{com}}+P_{sq}+P_{\text{gen}}-\rho\epsilon \qquad (1)$$

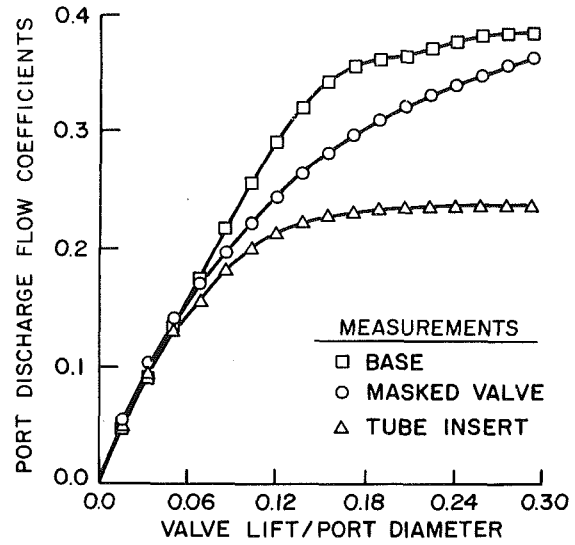


Fig. 2 Port discharge flow coefficients for the number one intake port and valve assembly

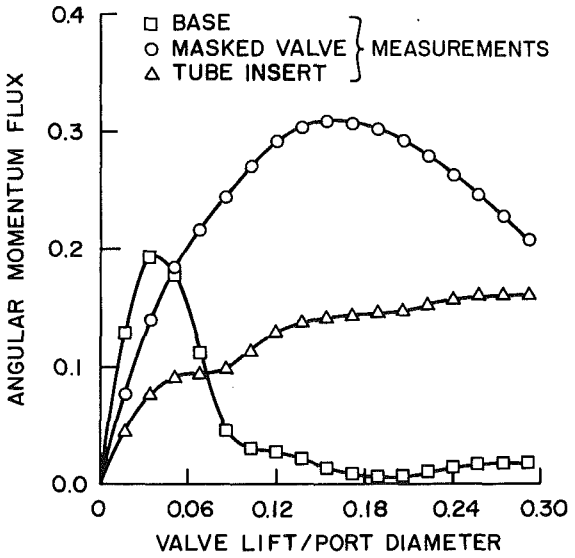


Fig. 3 Angular momentum flux is defined as the actual flux divided by the ideal flux

Nomenclature

A = port area
A_{eff} = effective flow area
A_2 = port area near the valve seat
C_f = overall discharge flow coefficient
C_K = proportionality constant
C_1 = calibration constant of turbulent dissipation
C_{12} = discharge flow coefficient across the port upstream of the valve
C_{23} = discharge flow coefficient across valve
D_i = inside port diameter near the valve seat
IVC = inlet valve closing
K = turbulent kinetic energy
K_{in} = turbulent kinetic energy flux into cylinder
K_o = turbulent kinetic energy at IVC
$\overline{KE}$ = integrated turbulent kinetic energy flux
$\overline{KE_u}$ = uniform turbulent kinetic energy flux
l = valve lift
l_o = integral length scale at IVC
$m(\theta)$ = mass flow rate distribution around valve
m_{in} = mass flow rate into cylinder
P = pressure
P_{com} = production of turbulent kinetic energy due to compression
P_{sq} = production of turbulent kinetic energy due to squish flow
P_{gen} = production of turbulent kinetic energy due to inlet flow
SF = scaling factor
t = time
V = cylinder volume
$V(\theta)$ = inlet velocity distribution around valve
V_{in} = mean inlet velocity
Δ = change in property
ϵ = dissipation of turbulent kinetic energy
ρ = density

Downloaded 01 Jun 2010 to 171.66.16.87. Redistribution subject to ASME license or copyright; see http://www.asme.org/terms/Terms_Use.cfm

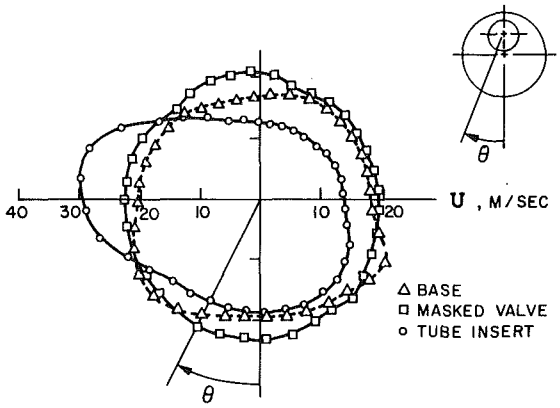


Fig. 4 Distribution of velocity magnitude

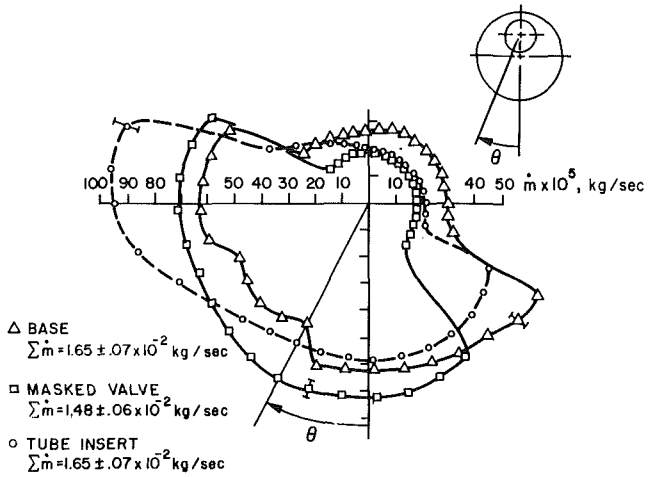


Fig. 5 Distribution of mass flow rate (per 10 deg sector)

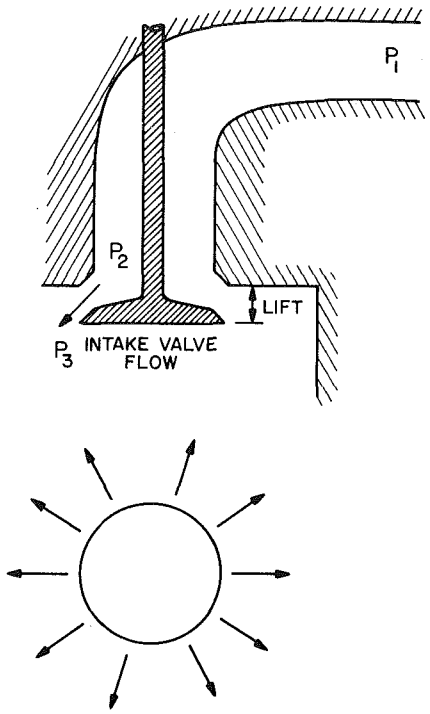


Fig. 6 Sketch of intake port showing pressure locations and uniform flow assumption around the intake valve

where P_{com}, P_{sq}, and P_{gen} are the terms responsible for production due to compression, squish, and intake generated turbulence, respectively, and

$$\epsilon = C_1 K^2 / K_o^{1/2} l_o \tag{2}$$

is the dissipation. In the following discussion, the concentration will be focused on the P_{gen} term.

The generation of turbulence during induction is assumed proportional to the instantaneous mass flow rate and mean kinetic energy flux. In equation form this is represented by

$$P_{gen} = \dot{m}_{in} (K_{in} - K)/V \tag{3}$$

where

$$K_{in} = (C_k V_{in})^2 \tag{4}$$

and V_{in} is the instantaneous velocity past the intake valve. The proportionality constant (C_k) is normally taken as 0.15, which is similar to that of a turbulent jet and is a reasonable fraction of total flow that is converted to turbulence. The instantaneous inlet velocity (V_{in}) in equation (4) is calculated by knowing the instantaneous inducted mass flow rate ($\dot{m}_{in}$) and inlet valve effective area (A_{eff}) as shown in equation (5)

$$V_{in} = \dot{m}_{in} / A_{eff}\, \rho \tag{5}$$

The effective area is calculated as a function of valve lift knowing the measured overall discharge flow coefficient (see Fig. 2) for the port of a function of lift

$$A_{eff} = C_f(l)\, \pi D_i^2 / 4 \tag{6}$$

where D_i = inside port diameter at the valve seat and C_f = overall discharge flow coefficient.

The above expressions assume that the velocity distribution around the perimeter of the intake valve is uniform as shown in Fig. 6. This assumption may lead to an underestimation of the kinetic energy flux term, K_{in}, and thereby affect the resulting in-cylinder turbulence intensity level and burn rate. Equations (2) and (4) also assume that the instantaneous mass flux distribution past the intake valve is uniform, which may cause further differences to occur in the inducted kinetic energy flux calculation.

The measurements given in Figs. 4 and 5 show that the inlet velocities and mass flow rates may vary significantly in distribution about the valve. This suggests that the assumption of a uniform flux may cause differences in the kinetic energy flux calculation for P_{gen}. In order to assess the effect of a nonuniform distribution, the experimentally observed distribution was used as input to the model to calculate P_{gen} during intake. The assumption is made that changes in the inlet velocity and mass flow rate distributions around the intake valve are small with changes in intake valve lift. It is expected that these assumptions may introduce small differences in P_{gen}, but should represent a good approximation for calculating turbulence generated by nonuniform velocity effects past the intake valve.

The differences in C_f shown in Fig. 2 indicate the change in effective flow area and mass flow rate for three configurations. Since C_f is used to calculate A_{eff} and M_{in} in equations (5) and (6), an additional effect on the inlet velocity magnitude is expected, further causing the in-cylinder turbulence levels to be different for the three ports considered. Since the model uses these coefficients normally, the effect of a different C_f is present irrespective of distribution effects.

The in-cylinder swirl levels are calculated by using the angular momentum flux measurements given in Fig. 3 as input to the GESIM swirl model. For a detailed description of the swirl model see [5].

Development of Distribution Factor. In order to use the measurements shown in Figs. 4 and 5 as input to the model, a scaling factor representing the velocity and mass distribution effects on the kinetic energy entering the cylinder during intake must be obtained. This development is carried out next.

Downloaded 01 Jun 2010 to 171.66.16.87. Redistribution subject to ASME license or copyright; see http://www.asme.org/terms/Terms_Use.cfm

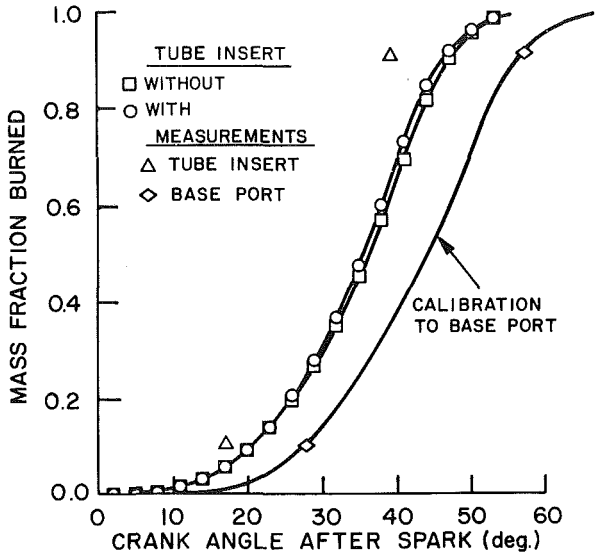


Fig. 7 Effect of velocity distribution on mass fraction burned versus crank angle

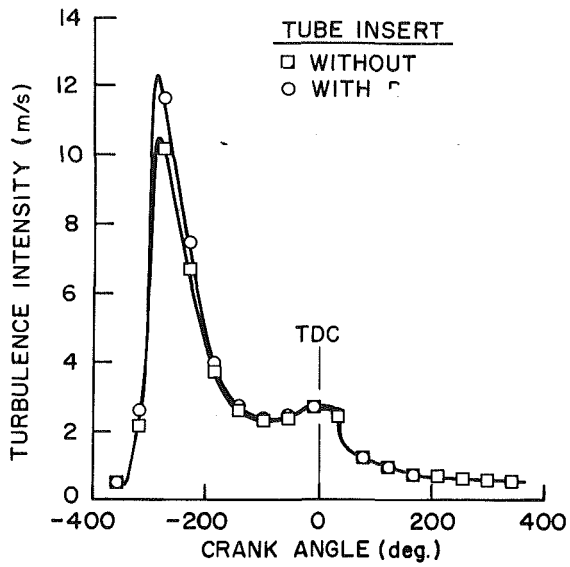


Fig. 8 Effect of velocity distribution on turbulence intensity versus crank angle

From the measured data, the averaged kinetic energy about the valve seat can be expressed as

$$KE = 1/2\dot{m}(\theta) \cdot V^2(\theta) \tag{7}$$

KE around the valve can be expressed by the integral

$$\overline{KE} = \frac{1}{2\pi}\int_0^{2\pi} KE d\theta \tag{8}$$

The kinetic energy, assuming distribution effects are small (uniform), is given as

$$\overline{KE_u} = 1/2\overline{\dot{m}(\theta)} \cdot \overline{V(\theta)}^2 \tag{9}$$

The scaling factor may then be written as the ratio of equations (8) and (9) giving a measure of the distribution effect on the kinetic energy entering the cylinder during intake

$$SF = \overline{KE}\,/\overline{KE_u} \tag{10}$$

Further expressing equation (10) in terms of the production term K_{in}, given by equation (4) previously, we obtain the expression

$$K_{in} = (C_K V_{in})^2 \left[\frac{\overline{\dot{m}(\theta) \cdot V^2(\theta)}}{\overline{\dot{m}(\theta)} \cdot \overline{V(\theta)}^2}\right] \tag{11}$$

where the bracketed term is extracted from the experimental data.

Thus, the average kinetic energy is scaled by the distribution factor multiplied by the original flux term given by equation (4).

The model described above the steady flow measured input data were used to assess the distribution effects on turbulence and burn rate. Results of this study will be presented in a later section of this paper.

Development of Valve Discharge Flow Coefficient. C_f in equation (6) is normally measured from the overall pressure drop $(P_3 - P_1)$ across the intake port/valve configuration as described in Fig. 6.

While this definition of C_f is reasonable for the mass flow rate calculation, it may not adequately represent the inlet velocity past the valve. Thus, a more detailed analysis of the discharge flow coefficient, which allows the velocity determination at the intake valve/head interface, was undertaken. The approach is to consider two pressure drops across the port, one representing the drop across the intake valve $(P_2 - P_3)$ and one upstream of the valve representing the drop across the intake port $(P_1 - P_2)$. This should allow a better approximation of the local discharge flow coefficient near the valve/head interface (see Fig. 6). Thus the following equation may be written over the intake port/valve assembly:

$$\Delta P_{1,3} = \Delta P_{1,2} + \Delta P_{2,3} \tag{12}$$

The overall discharge flow coefficient for the intake port is defined as

$$C_f = C_{13} = \dot{m}_{\text{actual}}/\dot{m}_{\text{ideal}} \tag{13}$$

where $\dot{m}_{\text{actual}}$ is a steady-flow measurement of mass flow rate through the port as a function of valve lift [5]. $\dot{m}_{\text{ideal}}$ is calculated from the steady-flow relation for incompressible flow as

$$\dot{m}_{\text{ideal}} = A\sqrt{2\rho\Delta P} \tag{14}$$

Thus, the overall discharge flow coefficient may be written as

$$C_{13} = \dot{m}/A_2\sqrt{2\rho\Delta P_{13}} \tag{15}$$

Similar expressions for C_{12} and C_{23} may also be written

$$C_{12} = \dot{m}/A_2\sqrt{2\rho\Delta P_{12}} \tag{16}$$

and

$$C_{23} = \dot{m}/A_2\sqrt{2\rho\left(\Delta P_{23} + \rho\frac{V_{in}^2}{2}\right)} \tag{17}$$

Solving for ΔP in equations (15), (16), and (17) and substituting into equation (12), an expression for the valve discharge flow coefficient is given as

$$C_{23} = \frac{C_{12} \cdot C_{13}}{\sqrt{C_{13}^2 \cdot C_{12}^2 - C_{13}^2 + C_{12}^2}} \tag{18}$$

Thus, C_{23} replaces C_f in equation (6), causing A_{eff} and V_{in} to change accordingly. C_{12} is defined as the port flow coefficient when all restrictions are removed from the port.

Results and Discussion

Effect of Velocity Distribution. In order to assess the effect of velocity and mass flow rate distribution around the intake valve on in-cylinder turbulence and burn rate, the following study was undertaken.

The model was calibrated to the base configuration as described in [6]. Model predictions were made with and without the distribution effects included. Results were compared to assess these distribution effects on turbulence intensi-

Downloaded 01 Jun 2010 to 171.66.16.87. Redistribution subject to ASME license or copyright; see http://www.asme.org/terms/Terms_Use.cfm

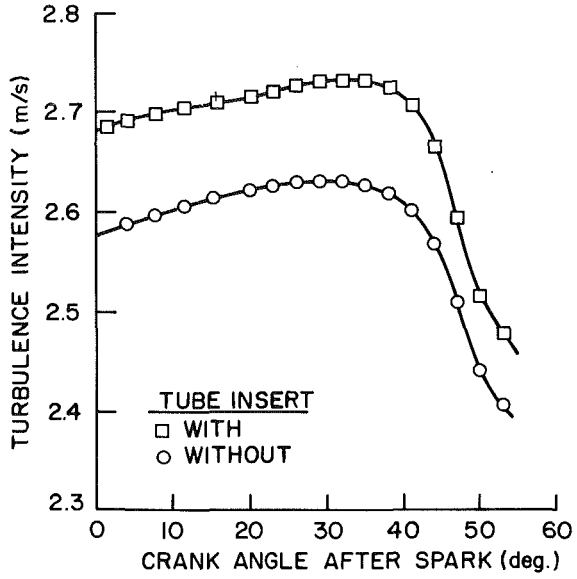


Fig. 9 Effect of velocity distribution on turbulence during combustion

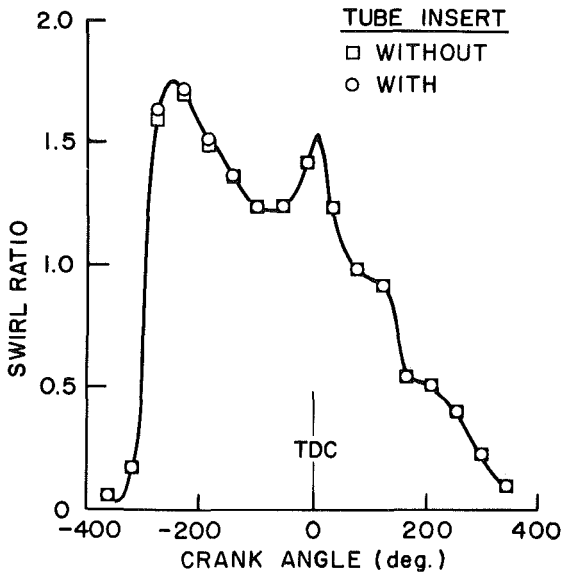


Fig. 10 Effect of velocity distribution on swirl ratio versus crank angle

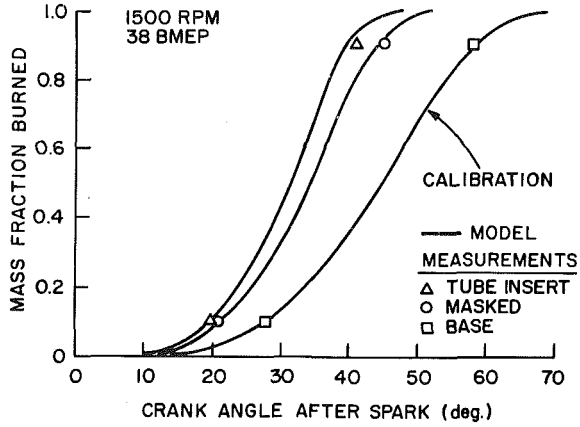


Fig. 11 Effect of intake port configuration on mass fraction burned

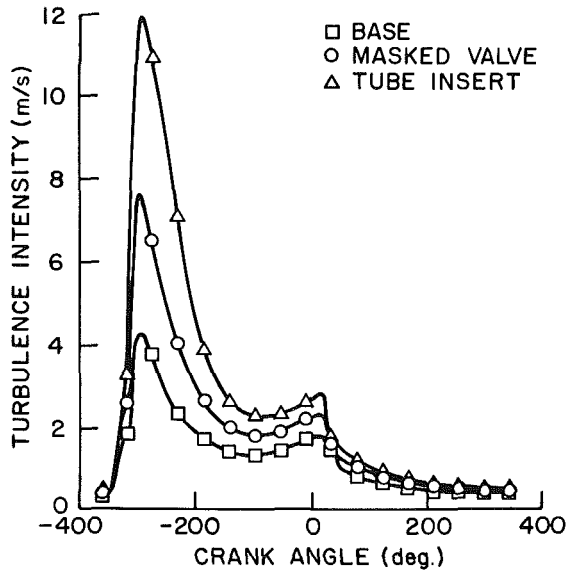


Fig. 12 Effect of intake port configuration on turbulence intensity

ty and burn rate. The intake port (tube insert) giving the largest change in distribution (see Figs. 4 and 5) was used for this comparison.

Figure 7 shows the comparison of mass fraction burned with and without distribution effects. Results show a small difference in burn time caused by small changes in the in-cylinder turbulence levels as shown in Fig. 8. Even though a 20 percent increase in peak turbulence occurred during induction (over the uniform flow case), dissipation effects caused the difference to diminish to approximately 5 percent by the time combustion was initiated, as shown in Fig. 9. The corresponding swirl levels were identical, as shown in Fig. 10. The kinetic energy flux scale factor for the nonuniform flow case (equation (11) above) increased about 44 percent over the uniform flow case. However, the effect of this increase in kinetic energy flux is significantly reduced when expressed as turbulence intensity, which is reflected in Figs. 8 and 9. Thus, model results indicate that a large change in flow distribution is necessary to cause a significant change in turbulence intensity and burn rate.

Effect of Intake Port Configuration on Inlet Velocity, Turbulence, and Burn Rate. The above model predictions indicate small overall effects of velocity and mass flow rate distribution on burn rate. However, experimental results reported by Lancaster [2] showed that mean inlet velocity differences caused significant changes in the turbulence generated during induction as discussed above. The improved estimation of the valve discharge flow coefficient is now used in the model to assess its effect on inlet velocity, turbulence, and burn rate for the three intake ports discussed above.

Model results were obtained for the masked valve and tube insert intake port configurations. Figure 11 shows a comparison of model predictions and measurements of mass fraction burned versus crank angle for the masked valve and tube insert configurations. Model results show good agreement with data for both configurations. The corresponding predicted turbulence intensity levels are shown in Fig. 12.

Significant differences in the predicted intake generated turbulence are seen to exist and persist up to the time of spark and during combustion (see Fig. 13). These differences are caused by the large differences in inlet velocity past the valve, as shown in Fig. 14, for the three configurations considered.

The large differences in inlet velocity are also reflected by the large differences in the valve discharge flow coefficients calculated by equation (18). Figure 15 shows C_{23} versus dimensionless valve lift for the three intake ports considered.

Downloaded 01 Jun 2010 to 171.66.16.87. Redistribution subject to ASME license or copyright; see http://www.asme.org/terms/Terms_Use.cfm

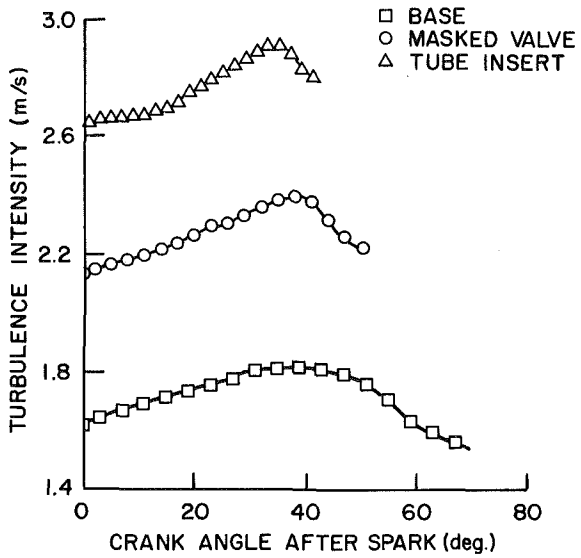


Fig. 13 Effect of intake port configuration on turbulence during combustion

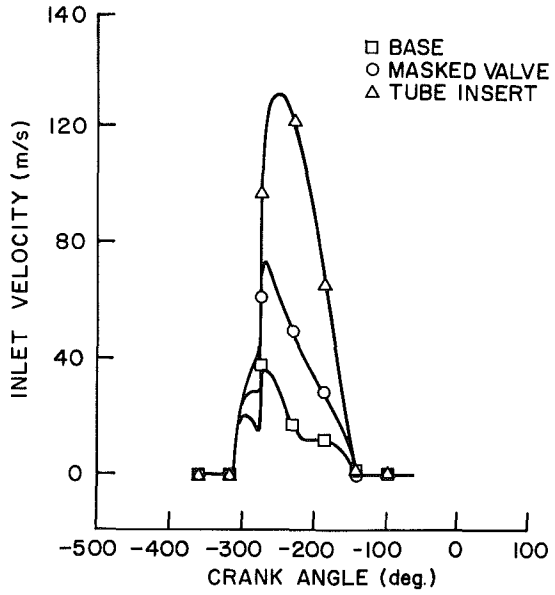


Fig. 14 Effect of intake port configuration on inlet velocity

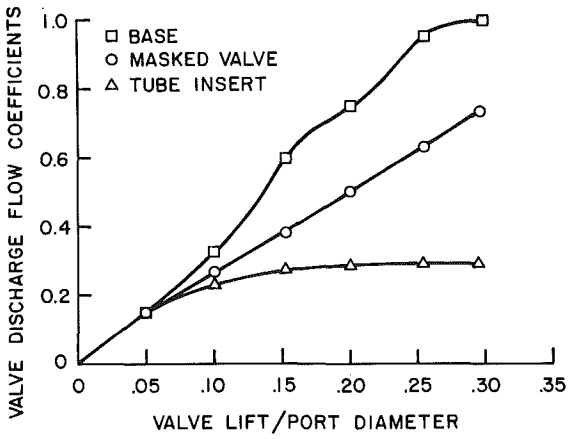


Fig. 15 Effect of intake port configuration on valve discharge flow coefficient

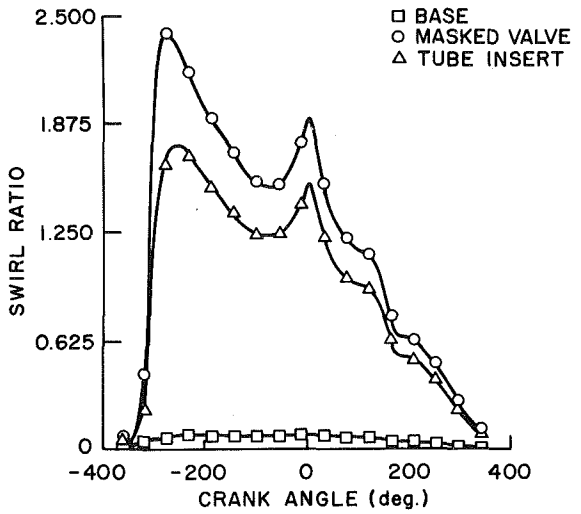


Fig. 16 Effect of intake port configuration on swirl ratio

A significant difference in C_{23} near maximum valve lift is observed, which will reflect large differences in A_{eff} and V_{in}. In this case the port flow coefficient (in contrast to the valve coefficient) $C_{d,p}$ (equal to C_{12}), is the same for the three points since the base port is the same in all cases.

Part of the differences in burn rate observed in Fig. 11 between the base and the masked valve port may be a result of a change in swirl level (see Figs. 6 and 16). The effect of swirl could be to enhance the turbulence during induction and compression, thus causing the increases in turbulence near the time of spark for the perspective cases. Separating the effects of swirl and turbulence on burn rate is a very complex problem and is a subject for further research.

Conclusions

Using steady-state measurements of velocity and mass flux distributions for flow past the intake valve as input to the GESIM model, the following conclusions were reached:

The effects of velocity and mass distribution on in-cylinder turbulence and burn rate were predicted to be small.

The new model predicted significant changes in discharge flow coefficients for the port/valve geometries considered. The effect on discharge flow coefficient caused significantly higher levels of turbulence intensity and rates of burn when compared to the base configuration.

The above two conclusions indicate that in order to create the observed velocity and mass flux distributions the discharge flow coefficient of the valve must be reduced. This decrease in $C_{d,v}$ is then reflected in higher shear velocities and turbulence levels resulting in the observed faster rates of burn.

References

1 Belaire, R. C., Davis, G. C., Kent, J. C., and Tabaczynski, R. J., "Combustion Chamber Effects on Burn Rates in a High Swirl Spark Ignition Engine," SAE Paper No. 830335, 1983.

2 Lancaster, D. R., "Effects of Engine Variables on Turbulence in a Spark Ignition Engine," SAE Paper No. 760159, 1976.

3 Borgnakke, C., Davis, G. C., and Tabaczynski, R. J., "Predictions of In-Cylinder Swirl Velocity and Turbulence Intensity for an Open Chamber Cup in Piston Engine," SAE Paper No. 810224, 1981.

4 Haghgooie, M., Kent, J. C., and Tabaczynski, R. J., "Intake Valve Cylinder Boundary Flow Characteristics in an Internal Combustion Engine," *Combustion, Science and Technology*, Vol. 38, 1984, pp. 49–57.

5 Davis, G. C., and Borgnakke, C., "The Effect of In-Cylinder Flow Processor (Swirl, Squish and Turbulence Intensity) on Engine Efficiency-Model Predictions," SAE Paper No. 820045, 1982.

6 Davis, G. C., Tabaczynski, R. J., and Belaire, R. C., "The Effect of Intake Valve Lift on Turbulence Intensity and Burnrate in S. I. Engines—Model Versus Experiment," SAE Paper No. 840030, 1984.

Downloaded 01 Jun 2010 to 171.66.16.87. Redistribution subject to ASME license or copyright; see http://www.asme.org/terms/Terms_Use.cfm

Study of the Steady-State Flow Pattern in a Multipulse Converter by LDA

P. Flamang

R. Sierens

Laboratory for Machines and Construction of Machines,
University of Gent,
Gent, Belgium

This paper describes pressure and velocity measurements on a multipulse converter under steady-state conditions. Pressure loss coefficients were measured on this four-entry pulse converter system for a large number of flow configurations. Three-dimensional velocity measurements were done (with Laser-Doppler anemometry) for several flow configurations and at different cross sections in the converter. The normal flow situation (incoming flow at the four entries) and back flow situations were examined. For each cross section the axial velocity profiles, the secondary flow patterns, and the turbulent velocities are presented. From the pressure measurements mixing losses are derived. These are compared with the results of a one-dimensional calculation, which is based on the impulse law for incompressible flow. Taking into account the velocity measurements, this simplified model gives a remarkable agreement with the measured mixing losses.

Introduction

In a previous paper [1], pressure and velocity measurements on two theoretical compact manifold-type junctions (compact pulse converters) under steady-state conditions were described.

This paper gives the same measurements carried out on a scale model of a multipulse converter of an eight-cylinder supercharged diesel engine (type ABC). Again, as for the compact manifold junction, it is the first time that such detailed experiments are carried out on a multipulse converter system. The measurements give a detailed and quantitative picture of the flow pattern in the converter for different flow configurations and different mass flow ratios.

The measured pressure loss coefficients can be used as input data for a numerical simulation model of the gas exchange process of the engine (calculated by the method of characteristics).

The velocity measurements give an insight into the flow pattern inside the multipulse converter and can be used for comparison with a numerical algorithm for simulating the three-dimensional turbulent quasi-steady flow in the converter (together with the pressure measurements).

From the enormous possibilities for flow configurations in the multipulse converter, only those are examined that are most likely to happen (e.g., mass flow ratios in the entry pipes of 0.5/0.2/0.1/0.2).

At the moment, the measurements are extended to nonstationary flow conditions. For this, a special test rig is built, which simulates the nonsteady but cyclic flow of the real engine.

Contributed by the Internal Combustion Engine Division and presented at the Eleventh Annual Energy-Sources Technology Conference and Exhibition, New Orleans, Louisiana, January 10–13, 1988. Manuscript received by the Internal Combustion Engine Division March 1987.

Theoretical Considerations

Pressure Loss Coefficients. To study the nonsteady flow in the inlet and exhaust pipes of IC engines, the method of characteristics has been extensively used. The inlet and exhaust system is divided into a number of ducts. At the beginning and end of each duct, the flow in the duct interacts with boundaries. The interaction between the flow and these boundaries is described in so-called boundary conditions. The method of characteristics and the different boundary conditions (valve, carburetor, turbine, compressor, junctions, . . .) have been described extensively in the literature [2–5].

The multipulse converter, in the same way as the compact converter [1] or a carburetor [5], can be considered as a junction of ducts with an adiabatic pressure loss at the junction for each of the possible flow directions. The loss coefficients are obtained under stationary flow conditions. For the carburetor two branches are considered (junction at the position of the throttle valve), for the compact converter there are three branches, and for the multipulse converter five branches are connected to the boundary. This increases the possible flow configurations enormously.

For the multipulse converter the pressure loss coefficient L_i is defined as (Fig. 1)

$$L_i = \frac{p_i - p_5}{p_5} \qquad i = 1\text{–}4$$

The pressures p_i, p_5 are static (mean) pressure readings in sections at equal distance (five times the diameter of the duct) from the junction.

The pressure loss coefficients L_i are a function of

$$L_i = f(\dot{m}_1/\dot{m}_5,\ \dot{m}_2/\dot{m}_5,\ \dot{m}_3/\dot{m}_5,\ \mathrm{M}_5)$$

where $\mathrm{M}_5 = u/a$ is the Mach number in pipe 5.

Pipe 5 is the connection pipe from the converter to the turbine. For the examined eight-cylinder engine one can assume

Copyright © 1988 by ASME
Downloaded 01 Jun 2010 to 171.66.16.87. Redistribution subject to ASME license or copyright; see http://www.asme.org/terms/Terms_Use.cfm

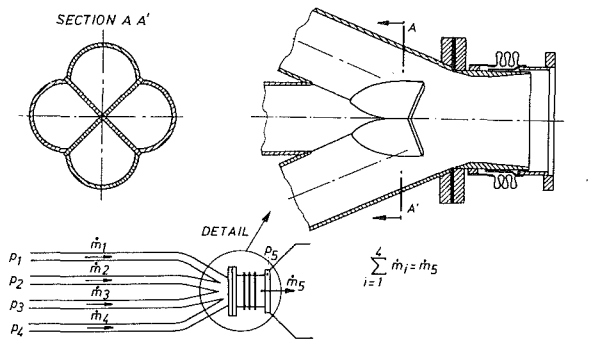


Fig. 1 Pipe arrangement of the multipulse converter

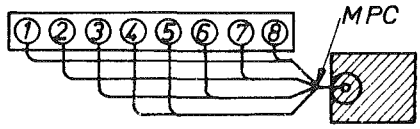


Fig. 2 Exhaust pipe system eight-cylinder engine

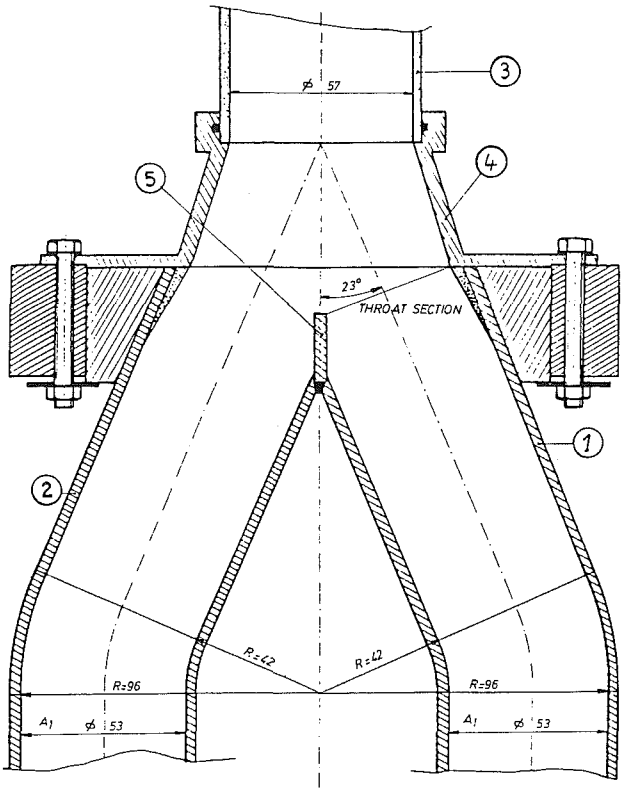


Fig. 3 Longitudinal section of the converter model

that the flow in this connection pipe is always from the converter to the turbine, and therefore that $\dot{m}_5$ is always positive. Configurations with a negative $\dot{m}_5$ flow are not taken into account.

The mass flow rates $\dot{m}_1$, $\dot{m}_2$, $\dot{m}_3$, and $\dot{m}_4$ are taken positive in the direction toward the junction, and $\dot{m}_5$ positive away from the junction. Back flow situations in the pipes 1 to 4 are possible ($\dot{m}_1, \ldots, \dot{m}_4$ negative). Defining the mass flow ratio $m_i = \dot{m}_i/\dot{m}_5$, it follows from the law of conservation of mass for steady flow

$$\sum_{i=1}^{4} m_i = 1$$

or $m_4 = 1 - (m_1 + m_2 + m_3)$.

Dynamic Similarity of the Model. The measurements are carried out on a scale model of the real multipulse converter. For the gas flow, air is sucked through the model instead of the high-temperature exhaust gases of the engine. Therefore a number of conditions must be fulfilled in order to get useful results from the model study. More specifically there must be similarity between the model and the real converter. For a geometrically similar model the flow has to be dynamically similar. This means that the Mach and Reynolds numbers should be the same for the model and the real converter.

The pressure loss coefficients are given as a function of the Mach number, so immediately the Mach number of the flow in the engine geometry is set equal to the Mach number of the flow in the model. Equality of the Mach numbers, for calculations where the pressure losses are used, is always fulfilled.

For both the flow through the model (Re_1) and for the nominal engine condition (Re_2) (1000 rpm, full load), the Reynolds numbers are calculated: $Re_2/Re_1 = 1.8$ with $Re_1 = 720{,}000$. This means a high turbulent flow, in which the influence of the Reynolds number is an order smaller than the influence of the Mach number. The influence of the Reynolds number can therefore be neglected.

Experimental Setup

Test Bed Description. The examined multipulse converter is a scale model (scale 0.5) of the converter for the 8DZC-1000-166 engine of the Anglo Belgian Corporation. A schematic view of the exhaust system of this eight-cylinder

Nomenclature

a = velocity of sound $= \sqrt{\kappa RT}$
a_i = parabolic pressure loss coefficient
A = pipe area
A_{unif} = inlet area cone
D = diameter of pipe
K', K'' = wall friction coefficients
L = pressure loss coefficient
M = Mach number $= u/a$
$\dot{m}$ = mass flow rate
m_i = mass flow ratio $= \dot{m}_i/\dot{m}_5$
p = pressure
pf_0 = punching factor
R = universal gas constant
Re = Reynolds number $= uD\rho/\mu$
T = temperature
TR = throat ratio
u = mean velocity (general flow)
v = velocity
v' = turbulent fluctuation
w_R = flow losses
w_{R1} = wall friction losses
w_{R2} = mixing losses
α = inclination of inlet pipes
κ = ratio of specific heats
μ = dynamic viscosity
ρ = density

Subscripts

1, 2, 3, 4, i = number of pipe
5 = connection pipe (converter to turbine)
a = axial
r = radial
t = tangential

Downloaded 01 Jun 2010 to 171.66.16.87. Redistribution subject to ASME license or copyright; see http://www.asme.org/terms/Terms_Use.cfm

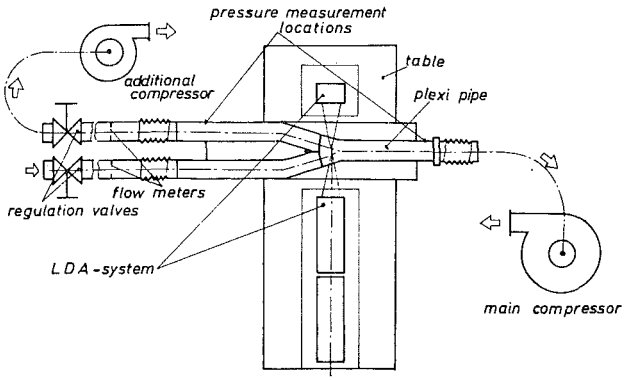


Fig. 4 Test rig for stationary flow

engine is shown in Fig. 2. The most important characteristics of this engine, used as a generator, are:

power output: 1768 kW
engine speed: 1000 rpm
supercharged: 166 percent

The multipulse converter consists of four entries and one connection pipe to the turbine (see Fig. 1). The construction of the real converter is quite rudimentary; the four pipes are welded to each other with an angle of 23 deg to the axis of the converter.

Partitions are brought in (welded) at the end of the entry pipes to create the convergent part of the converter. The pulse converter has a throat ratio of 0.54 (Throat Ratio TR = throat section area/A_1). The area ratio between connection pipe and the entry pipes is 1.16.

A longitudinal section of the model converter is shown in Fig. 3. In this figure (1) and (2) are two of the four entry pipes, (3) is the connection pipe made out of plexi, (4) a cone with windows, and (5) the partition at the end of two entry pipes.

A test rig is developed so that pressure and velocity measurements can be carried out under steady flow conditions. A schematic view of the test rig is shown in Fig. 4.

The air is sucked through the converter by the main compressor. To examine back flow in one (or more) entry pipes an additional compressor is used. The total mass flow rate is dependent on the main compressor speed. Valves regulate the mass flow ratios for the different pipes. Diaphragm type flow meters are installed in each entry pipe and at the exit pipe of the main compressor.

LDA System. The LDA setup is a dual beam system operating in forward-scatter mode. The characteristics of the LDA system are given in Table 1.

The counter is connected to a data acquisition system for subsequent data processing. Seeding of the flow is obtained by atomization of oil at the entrance of the pipes.

The setup of the LDA is shown in Fig. 5. The model, which can rotate around its axis, is mounted on a table that allows translations in three perpendicular directions. Together with the transparent walls of the connection pipe and the windows in the cone, this allows three-dimensional velocity measurements within the model.

The photomultiplier and receiving optics can be adjusted to obtain a correct alignment. The relative position of the converter model to the LDA is corrected for refraction by the plexi walls.

Data Acquisition System. To reconstruct the velocity profiles the mean value and the standard deviation are calculated from the first and second-order moments of a probability distribution. The probability-density distribution contains all statistical information of n individual samples (each time a particle crosses the beam-intersection area). This procedure is exactly the same as described in [1]. More extended description of the used LDA system and a detailed error analyses of the system are given in [7–9].

Table 1 LDA system characteristics

He-Ne laser	power 12 mW
beam splitter	beam separation 50 mm
Bragg cell	frequency shift 40 MHz
focusing lens	beam intersection angle 11°
photomultiplier	pinhole 0.2 mm
	quantum efficiency 13 %
signal processor	counter type
	maximum frequency 100 MHz
	resolution 2 ns
measuring volume	1.7 x 0.17 x 0.17 mm^3

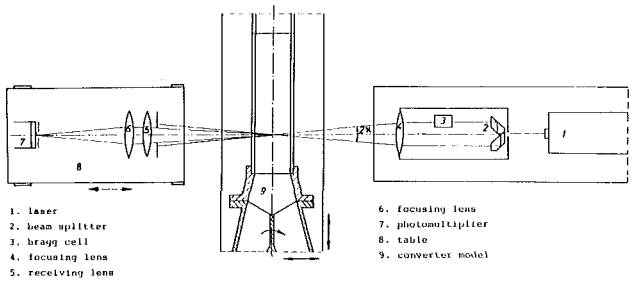


Fig. 5 LDA system

Experimental Results

Pressure Loss Coefficients

Flow Configurations. A significant reduction in the number of possible flow configurations follows from the axisymmetric construction of the converter. Moreover, it was found that in most flow cases the pressure loss coefficients were hardly influenced by any permutation of the mass flow ratios over the inlet pipes of the converter. For this reason, only combinations of different mass flow ratios must be considered.

Presentation of the Pressure Loss Coefficients. The pressure loss coefficient L_1 (or general L_i) for pipe 1 (pipe i) is plotted as a function of the Mach number M_5 of connection pipe 5.

The mass flow ratio for pipe 1 (i) is mentioned on the figure (first number on top of the plot; 0.25 for Fig. 6). The second mass flow ratio m_2 is also fixed, and is mentioned (second number on top of the plot; 0.25). The two other mass flow ratios are arbitrarily chosen. The different possibilities of the mass flow ratios m_3 and m_4 are then presented as separate curves, with the indication, e.g., 0.250/0.250 and so on, at the end of the curve.

This way each figure shows the pressure loss coefficients L_1 for fixed m_1 and m_2, and variable but corresponding m_3 and m_4 values. A total of 74 figures are presented this way, which are all given in [6].

In all these figures the measured pressure losses are indicated with discrete points. A curve fit on these points shows the parabolic relation

$$L_i = f_i(m_1,\ m_2,\ m_3,\ M_5) = a_i(m_1,\ m_2,\ m_3)M_5^2$$

The coefficients a_i are calculated from the static pressure readings, the mass flow rates, and the atmospheric conditions, and these curves are plotted on the figures.

Discussion of the Results. A full discussion of the pressure loss coefficients is beyond the scope of this paper. Only mentioned here is that within any given figure (e.g., Fig. 6), the

Downloaded 01 Jun 2010 to 171.66.16.87. Redistribution subject to ASME license or copyright; see http://www.asme.org/terms/Terms_Use.cfm

position of a curve is lower as the mass flow ratio of one of the other pipes becomes higher. This shows the ejector effect of the multipulse converter.

Presentation of the Flow Pattern

Measuring Grid. The velocity measurements are grouped in planes perpendicular to the axis of the connection pipe. Each plane is divided into a number of points P, specified by the coordinates r and θ. The dimensions of the grid are $\Delta r = 6$ mm, $\Delta\theta = 30$ deg (49 points).

This way five planes are considered, three in the connection pipe and two in the cone (Fig. 7).

Presentation of the Velocity Measurements. The velocity at a point P of the grid is defined in magnitude and direction if three orthogonal components are known (an axial, tangential, and radial component). For each of the components, the mean velocity v and the turbulent fluctuation v' were measured.

Each flow pattern is presented by three figures (Fig. 8). The first (top) figure gives the mean axial velocity distribution (lines of equal axial velocity). A flow away from the entry pipes is chosen as a positive flow (full lines), and a flow back to the entry pipes is a negative flow (dotted lines).

The second (middle) figure presents the two-dimensional flow pattern in the measured plane. The point of measurement is indicated by a dot; the length of the line is proportional to the velocity value.

The third (bottom) figure presents the turbulent velocity v' (lines of equal turbulent velocity). The turbulent velocity is defined as the rms value of the turbulent fluctuation on each of the velocity components

$$v' = \sqrt{v_a'^2 + v_t'^2 + v_r'^2}$$

On each figure the division of the four entry pipes is indicated. The figures are identified by the Mach number M_5 in the connecting pipe, the mass flow ratios $m_1/m_2/m_3/m_4$, and the position of the measuring plane (also indicated on the small figure). The reference for this position is the intersection of the connecting pipe with the cone. A positive position number stands for a plane in the connection pipe and a negative number for a plane in the cone.

Velocity Measurements. The velocity measurements are carried out for different mass flow ratios and different mass flow rates.

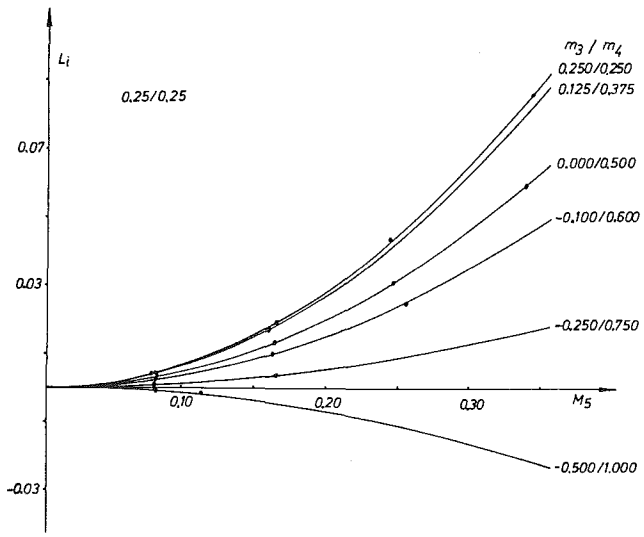


Fig. 6 Pressure loss coefficients L_i as a function of Mach number M_5 of the connection pipe

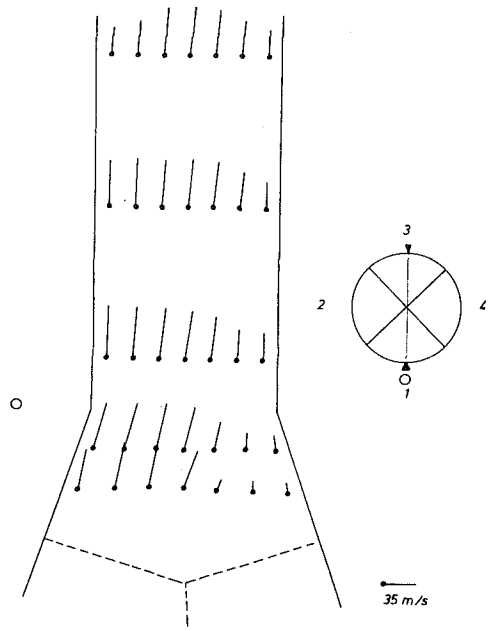


Fig. 7 LDA results; flow configuration 0.5/0.2/0.1/0.2, $M_5 = 0.1214$

All these results are given in detail in [6, 11, 12]. As an example the results for the configuration with mass flow ratios 0.5/0.2/0.1/0.2 and $M_5 = 0.1214$ are shown in Figs. 7 and 8. Figures 8(*a*,*b*,*c*,*d*) show the flow development in the planes −25, −12, 17, and 110 mm. Figure 7 gives a total flow pattern of the same flow configuration.

The corresponding pressure readings at the pipe ends (1 to 5) for the configuration of the Figs. 7 and 8 are given in Table 2.

Figure 9 shows the evolution of the axial flow for the flow configuration 0.5/0.5/0.5/−0.5 at the planes −25, −12, and 17 mm. Back flow velocities occur only in the plane at −25 mm (dotted lines).

Discussion of the Velocity Measurements. The flow patterns for fixed mass flow ratios but different total mass flow rates (different M_5 values) are nearly similar.

Figure 10 shows the axial velocity distribution for the 17 mm plane and the configuration 0.5/0.2/0.1/0.2 with $M_5 = 0.2$. To compare Fig. 10 with the axial velocities of Fig. 8(*c*), the axial velocities in Fig. 10 are first multiplied by the ratio of the Mach numbers = 0.1214/0.2. The agreement between the two figures (8*c* and 10) is remarkably good. This shows that for the lower Mach numbers, for which the flow can be considered as incompressible, the flow patterns at different Mach numbers are similar.

This explains the good agreement between the pressure measurements and the parabolic curves, as can be seen on Fig. 6.

The flow from the pipe with the highest mass flow ratio has a sudden expansion at the junction of the pipes. On the other hand, mixing of the flows of the different entry pipes occurs in a convergent section, so that the total flow will be accelerated. The measurements (Figs. 8*a*,*b*,*c*) show that this last effect is predominant on the sudden expansion; this has also been seen for the cases 0.6/0.1/0.2/0.1 and 1./0./0./0.

From Fig. 8, a secondary flow field is detected perpendicular to the axial direction of the flow. This exists not only for the mass flow ratios 0.5/0.2/0.1/0.2, but also for similar ratios, e.g., 0.6/0.1/0.2/0.1. A more general flow pattern shows this phenomenon in Fig. 11, which is calculated from the velocity measurements at the configuration 0.5/0.2/0.1/0.2. It shows the streamline pattern of the

Downloaded 01 Jun 2010 to 171.66.16.87. Redistribution subject to ASME license or copyright; see http://www.asme.org/terms/Terms_Use.cfm

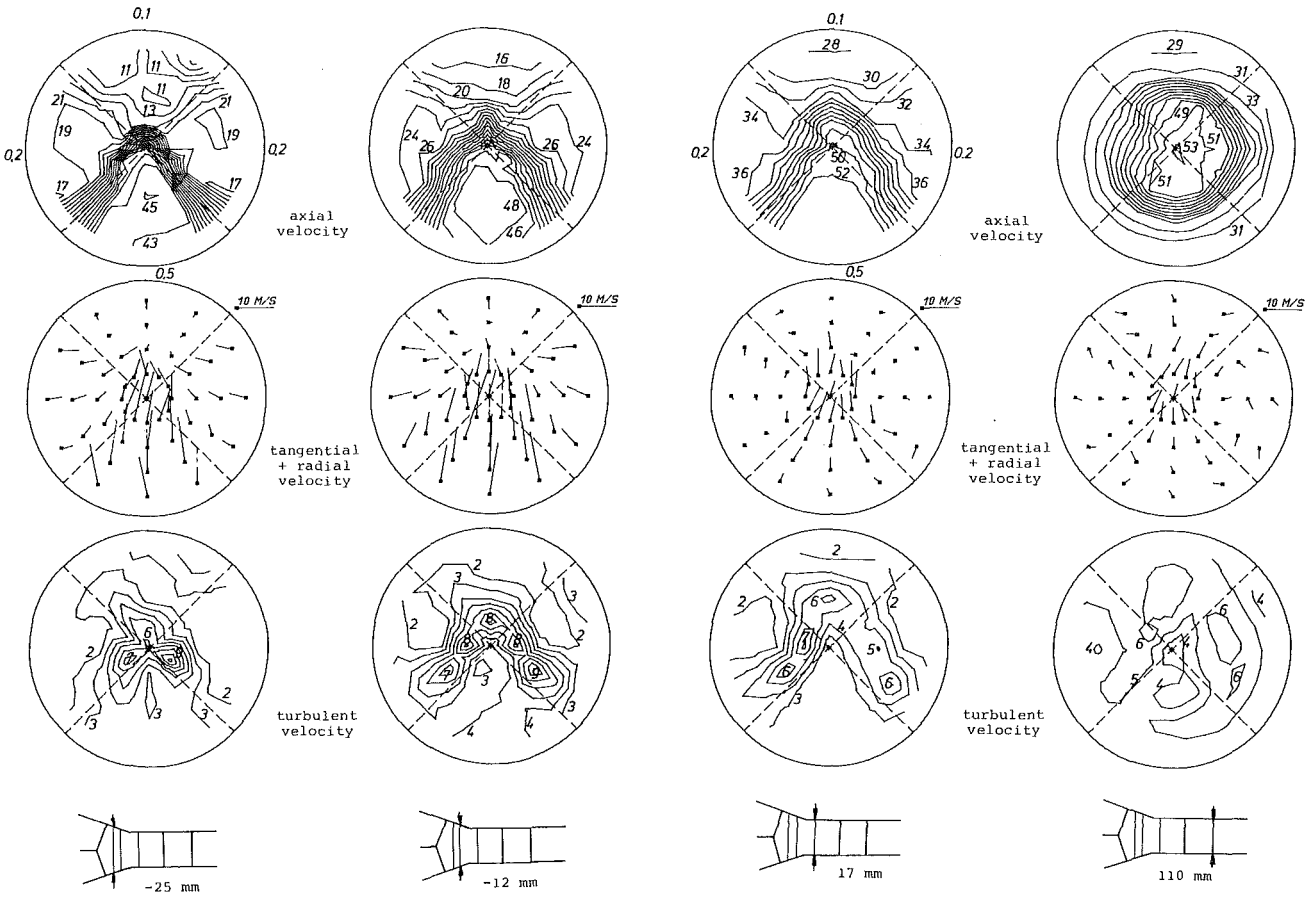


Fig. 8(a) Fig. 8(b) Fig. 8(c) Fig. 8(d)

Fig. 8 LDA results, flow configuration 0.5/0.2/0.1/0.2, $M_5 = 0.1214$

Table 2

	p_1 $m_1 = 0.5$	p_2 $m_2 = 0.2$	p_3 $m_3 = 0.1$	p_4 $m_4 = 0.2$	p_5 [Pa]
$M_5 = 0.1214$	96760.5	96072.2	95913.4	96072.2	95292.8

secondary flow in the plexi cylinder (at reference 20 mm), perpendicular to the main flow, which has an inclination of 3 deg to the axis of the cylinder.

Since the secondary flow is one order of magnitude smaller than the main flow, it is very sensitive to a small disadjustment of the mass flow ratios.

In those cases where there is no back flow, the streamlines can be considered as mostly axial. This leads to the assumption of uniform pressure as explained further on.

In Fig. 9 only small negative velocities were measured in the flow configuration $0.5/0.5/0.5/-0.5$. This was also found for the configuration $1.5/0./-0.5/0$. This means that backflow occurs in a small region behind the throat section.

Calculation of the Flow Losses

Applying the first law of thermodynamics on the control volume of Fig. 12, and assuming incompressible flow, it follows that

$$|w_R| = \sum_{i=1}^{4} m_i \left(\frac{p_i}{\rho} + \frac{u_i^2}{2}\right) - \frac{p_5}{\rho} - \frac{u_5^2}{2}$$

where $|w_R|$ are the flow losses per unit of mass. With

$$u_i = \frac{A_5}{A_i} u_5 m_i$$

$$u_5 = \sqrt{\kappa R T_5}\, M_5$$

$$L_i = \frac{p_i - p_5}{p_5} = a_i M_5^2$$

the dimensionless flow losses may be derived

$$|w_R| \frac{1}{\frac{p_5}{\rho} M_5^2} = \sum_{i=1}^{4} m_i a_i + \frac{\kappa}{2} \left(\sum_{i=1}^{4} m_i^3 \left(\frac{A_5}{A_1}\right)^2 - 1 \right)$$

The flow losses $|w_R|$ can be divided in two parts:

$$|w_R| = |w_{R1}| + |w_{R2}|$$

where $|w_{R1}|$ = the wall friction losses in the converter; $|w_{R2}|$ = the mixing losses. The wall friction losses are given by

Downloaded 01 Jun 2010 to 171.66.16.87. Redistribution subject to ASME license or copyright; see http://www.asme.org/terms/Terms_Use.cfm

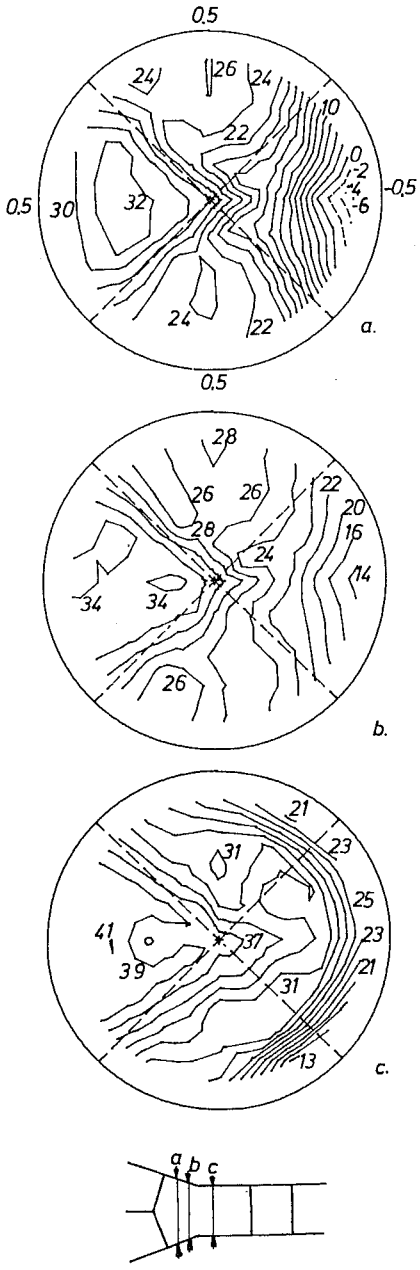


Fig. 9 Axial velocity profiles: $M_5 = 0.0996$, flow configuration 0.5/0.5/0.5/—0.5

$$|w_{R1}| = \sum_{i=1}^{4} m_i \frac{u_i^2}{2} K' + \frac{u_5^2}{2} K''$$

The wall friction coefficients K' and K'' are found in the literature [10].

The dimensionless mixing losses

$$|w_{R2}| \frac{1}{\frac{p_5}{\rho} M_5^2} = |w_R| \frac{1}{\frac{p_5}{\rho} M_5^2} - |w_{R1}| \frac{1}{\frac{p_5}{\rho} M_5^2}$$

are then a function of the measured pressure loss coefficients and the mass flow ratios.

These values have been presented in tables for all the measured flow configurations [11].

For symmetric inlet flow conditions (e.g., 0.25/0.25/0.25/0.25) the mixing losses are very small. For very asymmetric flow configurations (e.g., 1.5/−0.5/0/0) the highest mixing losses are detected. Therefore, the mixing losses are presented as a function of

$$\frac{1}{2} \sum_{i \neq j} (m_i - m_j)^2$$

in Fig. 13 (measured mixing losses).

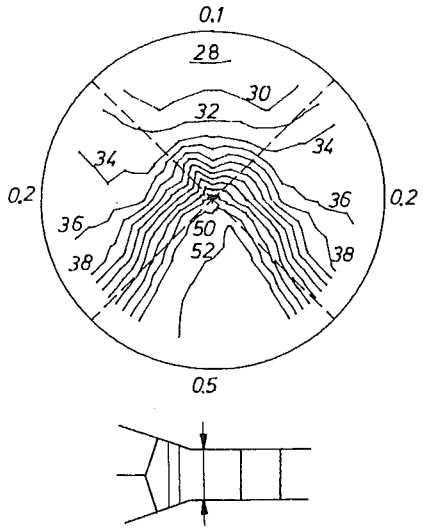


Fig. 10 Axial velocities (multiplied by 0.1214/0.2); flow configuration 0.5/0.2/0.1/0.2, $M_5 = 0.2$

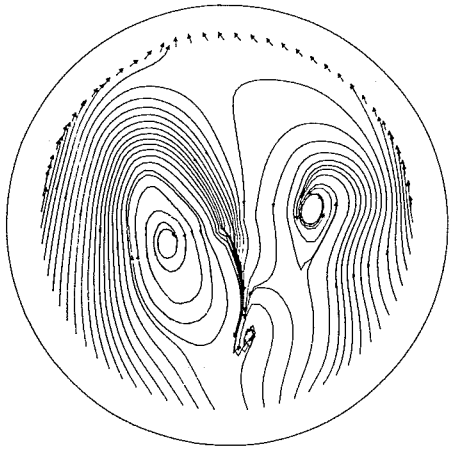


Fig. 11 Secondary flow streamline pattern; flow configuration 0.5/0.2/0.1/0.2, $M_5 = 0.1214$

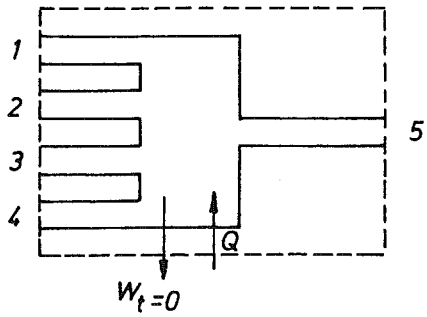


Fig. 12 Control volume

Downloaded 01 Jun 2010 to 171.66.16.87. Redistribution subject to ASME license or copyright; see http://www.asme.org/terms/Terms_Use.cfm

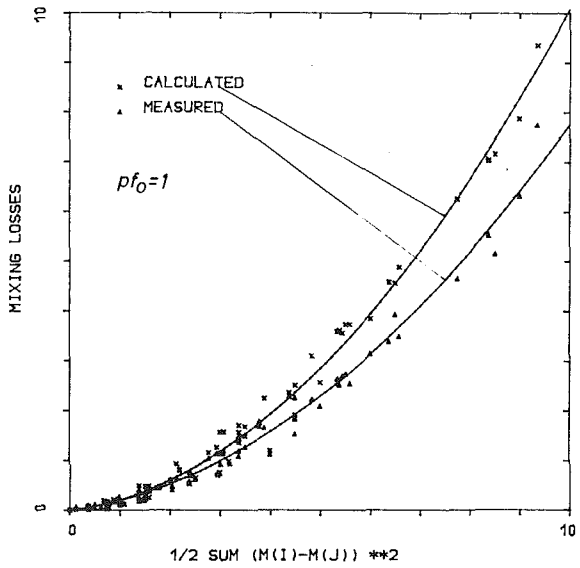


Fig. 13 Measured and calculated mixing losses

Calculation of the Pressure Loss Coefficients

By means of a simplified model, a good estimation of the pressure loss coefficients can be made based on the equation of Bernoulli and on the law of conservation of impulse.

The following simplifying assumptions are taken into account (see Fig. 14):

- one-dimensional and incompressible flow
- $\dot{m}_5$ is always positive
- no wall friction in the cone (mixing volume between throat section and connecting pipe)
- uniform velocity distribution at the pressure reading locations of the converter
- uniform pressure from the throat section on for inlet pipes with positive flow

The calculation can then be divided into three parts. The first part consists of the entry pipes between the pressure reading locations and the throat section.

When there is a positive flow for the inlet pipes i, Bernoulli's equation is used, taking into account the total pressure losses, which can be found in the literature [10].

When there is a negative (back) flow for the inlet pipes j, an infinite small control volume is considered at the throat section. For this control volume, it is assumed that the impulse of the incoming mass flow is perpendicular to the main axial flow direction. Furthermore, it is assumed that there is no pressure recovery inward on the pipes j.

The impulse law is applied on the control volume of the cone between the throat section and the connecting pipe. At the end of the cone, a punching factor pf_o is defined as the ratio of the real impulse of the flow to the impulse of a uniform flow with the average velocity

$$pf_o = \frac{\int_{A_5} u^2 dA}{1/A_5 \left(\int_{A_5} u dA\right)^2}$$

The punching factor value can be obtained from detailed velocity measurements (LDA measurements) at the end of the cone (see Figs. 8 and 9). Thus, for a uniform flow $pf_o = 1$.

Finally, the impulse law is used again on the connecting pipe. Due to lack of space, it is impossible to write down and solve all equations here. This is fully given in [12].

Table 3 Measured and calculated a_i coefficients

m_i	a_i meas.	a_i calc.	m_i	a_i meas.	a_i calc. pf_O = 1	a_i calc. pf_O=1.3
0.25	0.76	0.77	0.5	1.05	1.08	1.07
0.25	0.76	0.77	0.2	0.56	0.54	0.52
0.25	0.76	0.77	0.1	0.44	0.46	0.45
0.25	0.76	0.77	0.2	0.56	0.54	0.52

m_i	a_i meas.	a_i calc. pf_O = 1	a_i calc. pf_O=1.12	m_i	a_i meas.	a_i calc. pf_O = 1	a_i calc. pf_O=1.9
0.6	1.10	1.21	1.16	1	1.27	1.75	1.37
0.1	0.23	0.31	0.25	0	-1.41	-0.84	-1.22
0.2	0.31	0.38	0.33	0	-1.41	-0.84	-1.22
0.1	0.23	0.31	0.25	0	-1.41	-0.84	-1.22

After rearranging, it is found that:

for a pipe with incoming flow:

$$a_i = L_i \frac{1}{M_5^2} = \frac{\kappa}{2}\left(m_i^2\left(\frac{A_5}{A_1}\right)^2\left(\left(\frac{1}{TR}\right)^2 - (1-K')\right) + K''\right.$$

$$+ 2(1-pf_o) + \frac{4A_5}{A_5 + A_{\text{unif}}}\left(pf_o - \cos\alpha \frac{A_5}{A_1 TR}\sum_{i=1}^{4} m_i^2\right.$$

$$\left.\left. + \frac{A_{\text{unif}} + A_5}{8A_5}\left(\frac{A_5}{A_1 TR}\right)^2 \sum_{\text{neg}} m_i^2\right)\right)$$

for a pipe with back flow:

$$a_i = L_i \frac{1}{M_5^2} = \frac{\kappa}{2}\left(-2m_i^2\left(\frac{A_5}{A_1 TR}\right)^2 + K'' + 2(1-pf_o)\right.$$

$$+ \frac{4A_5}{A_5 + A_{\text{unif}}}\left(pf_o - \cos\alpha \frac{A_5}{A_1 TR}\sum_{i=1}^{4} m_i^2\right.$$

$$\left.\left. + \frac{A_{\text{unif}} + A_5}{8A_5}\left(\frac{A_5}{A_1 TR}\right)^2 \sum_{\text{neg}} m_i^2\right)\right)$$

When there is no velocity information, a uniform flow field at the outlet of the cone is assumed: $pf_o = 1$.

The calculated pressure loss coefficients can be presented in tables and compared with the measured pressure loss coefficients.

For a better survey, the calculated a_i coefficients are brought into the equation for $|w_{R2}|$. These values for $|w_{R2}|$ are called the calculated mixing losses. A comparison between calculated and measured mixing losses is made on Fig. 13 ($pf_o = 1$).

Table 3 shows a few examples of measured and calculated a_i coefficients. Without any experimental input, the values with $pf_o = 1$ are obtained (assuming a uniform flow field at the end section of the cone).

Bringing in the velocity information by calculating pf_o from the LDA measurements, an important improvement of the coefficients is obtained. An extrapolation of the punching factor to all the measured flow configurations gives the improved calculated mixing losses as shown in Fig. 15.

Conclusions

This paper describes the results of pressure and velocity measurements on a scale model of a real multipulse converter system.

The measurements are done for different mass flow ratios in the entry pipes of the converter and different total mass flow

Downloaded 01 Jun 2010 to 171.66.16.87. Redistribution subject to ASME license or copyright; see http://www.asme.org/terms/Terms_Use.cfm

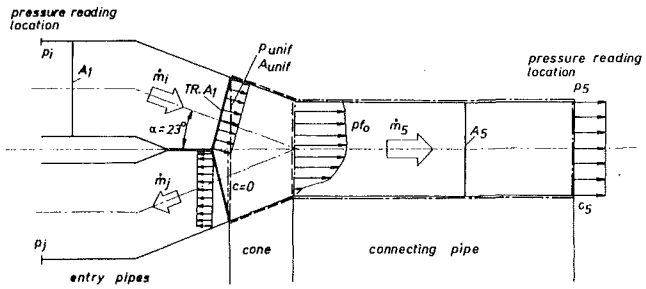


Fig. 14 Pressure loss calculation model

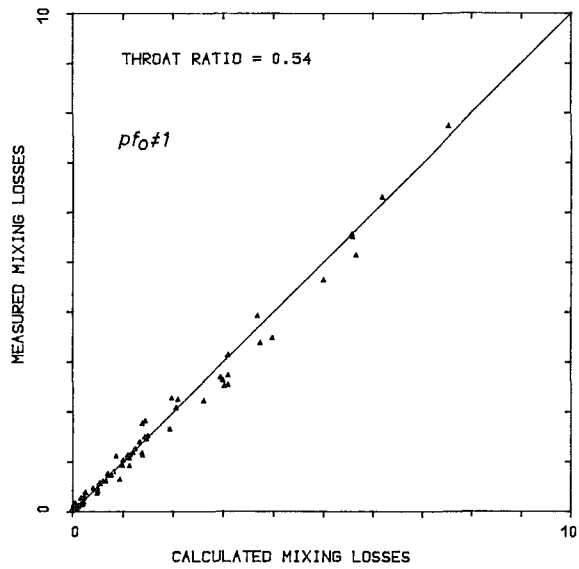


Fig. 15 Comparison between measured and calculated mixing losses

rates (different Mach numbers in the common branch). Once the mass flow ratios are chosen, the succession of these flow ratios (m_1, m_2, m_3, m_4, or m_1, m_3, m_2, m_4, or any other) can be neglected.

Pressure loss coefficients are defined and presented. Some 300 flow combinations are examined [6]. The pressure losses are related to the Mach number in the connecting pipe by a parabolic equation.

Three-dimensional velocity measurements with an LDA system are carried out in the connecting pipe and the cone of the converter. The flow pattern in the converter is little dependent on the total mass flow rate (for chosen mass flow ratios). A secondary flow movement perpendicular to the main direction of the flow is observed.

These measurements can be used for updating numerical algorithms for simulating the turbulent quasi-steady flow in the converter (or in multibranch junctions).

A simplified model for the converter has been established, based on Bernoulli's equation and on the impulse law. Comparison with the measured loss coefficients shows that the model gives good agreement with the measurements, particularly for flow configurations with relatively low mixing losses. These results can be used in a simulation of the exhaust system of a diesel engine with multipulse converter to derive the best dimensions of the converter. However, updating the model by means of velocity information obtained by LDA measurements gives remarkable agreement with the pressure measurements.

At the moment, a special test rig is developed, to simulate the nonsteady cyclic flow of the real engine. A simulation program for this test rig exists and will be used to compare the nonsteady pressure and velocity measurements with the calculated values for different geometries of the multipulse converter.

Acknowledgments

The research reported in this paper was supported by the Belgian Institute for the Encouragement of Scientific Research in Industry and Agriculture (IWONL-IRSIA).

References

1 Sierens, R., and Snauwaert, P., "Study of the Flow Pattern in Compact Manifold Type Junctions by LDA," ASME JOURNAL OF ENGINEERING FOR GAS TURBINES AND POWER, Vol. 109, 1987, pp. 452-458.

2 Benson, R. S., *The Thermodynamics and Gas Dynamics of Internal Combustion Engines*, Vol. 1, Clarendon Press, New York, 1982.

3 Benson, R. S., Garg, R. D., and Woolatt, D. A., "A Numerical Solution Unsteady Flow Problems," *Int. J. Mech. Sci.*, Vol. 6, 1964, pp. 117-144.

4 Baruah, P. C., "A Generalized Computer Program for Internal Combustion Engines Including Gas Exchange Systems," Ph.D. Thesis, University of Manchester, United Kingdom, 1973.

5 Benson, R. S., Baruah, P. C., and Sierens, R., "Steady and Non-steady Flow in a Simple Carburetor," *Proc. Inst. Mech. Eng.*, Vol. 188, pp. 53-74.

6 De Foer, P., and Van Aken, P., "Studie van de stroming in een multipulse converter," *eindejaarswerk RUG*, 1986.

7 Snauwaert, P., "Studie van be swirlbeweging bij direkte injektie dieselmotoren door middel van Laser Doppler Anemometrie," Ph.D. Thesis, Rijksuniversiteit Gent, 1984.

8 Snauwaert, P., and Sierens, R., "Experimental Study of the Swirl Motion in Direct Injection Diesel Engines Under Steady State Flow Conditions (by LDA)," SAE Paper No. 860026, 1986.

9 Snauwaert, P., and Sierens, R., "A Study of the Swirl Motion in Direct Injection Diesel Engines by Laser Doppler Anemometry," Fisita Paper No. 865007, 1986.

10 Miller, D. S., "Internal Flow Aspects and Circuit Design of Heating and Ventilation Systems," von Karman Institute for Fluid Dynamics, Lecture series 68, May 1974.

11 Flamang, P., "Studie van de stroming in multi-pulse convertor systemen van opgeladen dieselmotoren, I," IWONL report, 1986.

12 Flamang, P., "Studie van de stroming in multi-pulse convertor systemen van opgeladen dieselmotoren, II," IWONL report, 1987.

Downloaded 01 Jun 2010 to 171.66.16.87. Redistribution subject to ASME license or copyright; see http://www.asme.org/terms/Terms_Use.cfm

The Effects of Engine Speed on the Scavenging Characteristics of a Two-Cycle Engine

T. Uzkan
General Motors Corporation,
Electro-Motive Division,
La Grange, IL 60525

The effects of engine speed on the fresh air breathing characteristics of a uniflow, two-cycle engine were studied by using a multidimensional computational code for in-cylinder flows. Computed results are presented describing both global and detailed features of the flow field during the air breathing and compression stroke, at four different engine speeds, namely, 400, 700, 900, and 1000 rpm. Global features are presented including the variations of cylinder pressure, mass, angular momentum, turbulence kinetic energy, and the exhaust mass as a function of crank angle. Detailed features of the flow field are presented in terms of the velocity vector plots, fresh air concentration contour plots, and swirl velocity contour plots at certain crank angles. The volumetric scavenging, and charging efficiency decreases, but the trapping efficiency increases with increasing engine speed. A simple scavenging model (correlating the fraction of fresh air in exhaust to the fraction of fresh air in cylinder) suitable for use in engine performance algorithms is presented. Predictions indicate that the effect of engine speed on such a model is not negligible. The use of similar models would be questionable and limited in range, if they are insensitive to engine speed. The residual gas concentration at TDC is shown to be relatively uniform at low engine speeds, but at high speeds, the residual gases are more concentrated at the squish region and the fresh air is more concentrated near the bowl center.

Introduction

Studies of engine breathing processes are not new. Several very valuable papers and reviews are available, even in the classical I.C. engine textbooks [1, 2]. All these studies consider the engine breathing process from an idealized viewpoint and as a mixing process. The fresh air replenishment characteristics of two-stroke engines are different from four-stroke engines. In four-stroke cycle engines, there is a separate stroke to exhaust the combustion gases and replenish them with new fresh air. In two-stroke cycle engines these air exchange processes are limited to about 1/3 of the cycle and considerably more residual gases remain in the cylinder, even when more fresh air is utilized just to sweep away residual gases. Reducing the amount of residual gases remaining in the cylinder is very important, and is a difficult design problem for two-cycle engines. A high scavenging efficiency (the ratio of fresh air mass to the total gas mass trapped in the cylinder) and high trapping efficiency (the ratio of fresh air mass trapped in cylinder to the total fresh air supplied to the cylinder) are desirable design goals. Residual gases remaining in the cylinder would also act as an internal EGR and reduce the engine power and/or efficiency, while low trapping efficiency would result in lower turbine inlet temperatures and ineffective use of high-pressure fresh air for combustion.

Although the replacement of the residual gases with fresh air is very important, it is rather difficult to measure the scavenging and trapping efficiency. Therefore, the available data are rather limited and not reliable. On the other hand, there are some scavenging models of engine breathing processes, as described in several sources (e.g., [2]). Recent developments in multidimensional modeling techniques have enabled researchers to study the details of in-cylinder processes. Very recently the application of these methods was extended to complex processes such as the fluid motion in rather unusual piston bowls [3–6], fuel spray developments [7–10], ignition [11], and even engine combustion [12]. Therefore, it was a very logical expectation to use these tools for predicting the engine breathing process details. Previously, Adachi [13] used such scavenging efficiency prediction and compared with experimental data with success. Diwakar [14, 15] has applied two-dimensional and three-dimensional calculations to a uniflow two-cycle engine and compared the capabilities of two-dimensional and three-dimensional calculations. Uzkan [16–18] has applied the methodology to study the effects of several parameters on the scavenging and trapping efficiency calculations. In these studies [16–18], the operation of the engine at a selected speed was considered. This work is an extension of previous studies, and covers the effects of engine

Contributed by the Internal Combustion Engine Division and presented at the Eleventh Annual Energy-Sources Technology Conference and Exhibition, New Orleans, Louisiana, January 10–13, 1988. Manuscript received by the Internal Combustion Engine Division March 1987.

Copyright © 1988 by ASME
Downloaded 01 Jun 2010 to 171.66.16.87. Redistribution subject to ASME license or copyright; see http://www.asme.org/terms/Terms_Use.cfm

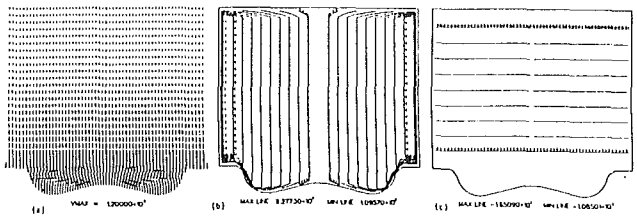


Fig. 1 Initial conditions at EVO: (*a*) velocity vectors; (*b*) swirl velocity contours; (*c*) vertical velocity contours

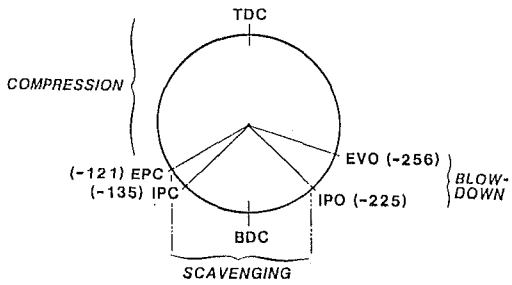


Fig. 2 Engine timing used in the computations

speed on the scavenging and trapping characteristics of the same engine.

Methodology

There are two different ways of studying the effects of engine speed on the scavenging characteristics of an engine, using a multidimensional model. In the first, the operation of the engine at a specified condition is taken as reference, and the computer program is used to calculate the air exchange characteristics of the engine at this operating condition. Then only the engine speed is modified while all other parameters are kept constant and the analysis is repeated. This exercise is somewhat unrealistic, because the new calculation points do not represent the actual operation of the engine. However, it is easier to interpret the effects on a relative basis, and identify the results directly attributable to the engine speed. In the second way, the operating conditions of the engine at different engine speeds are simulated by changing all other relevant parameters at the same time, such as airbox and exhaust manifold pressures and temperatures, fuel amounts, etc. This would more realistically represent the operation of the engine, but the results would be influenced not only by the speed directly, but also by the changes in other parameters that themselves may be a function of engine speed. In this study, the first method is utilized for the purpose of learning more about the effects directly attributable to the engine speed, rather than simulating the operation of an engine at different speeds.

Model Assumptions

The objective of this work is to study the effects of engine rpm on the air breathing characteristics of the engine. The initial thermodynamic states of the working fluid at the beginning of the exhaust valve opening, in the airbox, exhaust manifold, and in the cylinder are inputs to the computer program. They are calculated through a two-zone, engine system simulation model [16–18], and held constant throughout this study. They are given below:

Intake manifold pressure	261.04 kPa
Exhaust manifold pressure	239.04 kPa
Intake manifold temperature	379.0 K
Initial cylinder pressure	898.4 kPa
Initial cylinder temperature	1198.9 K

Major features of the engine and the operating conditions considered are as follows:

Bore	0.2302 m
Stroke	0.2794 m
Con. rod L	0.5842 m
Engine speed	900 rpm

The analysis is performed by using the CONCHAS-SPRAY code as modified by El-Tahry [19] for k–ϵ turbulence model and previously used by Diwakar [14], Uzkan [16–18], Plee [20], and others. The modeling of the flows at the inlet port and exhaust valves was done by Diwakar [14] and described in [16] in detail. In review, the valves are treated as an annular slot on the head. Valve opening processes are simulated through variation of the flow coefficients of this slot in a manner to account for the changes in the valve flow area and also its flow coefficient. Inlet ports are simulated as a circular opening on the liner with effective area controlled by the piston motion. Compressible flow equations with constant flow coefficients are used to calculate the flow rates to and from the cylinder. Backflow is not permitted at the exhaust valves. The details of the turbulence modeling and the boundary conditions are essentially the same as described in [16–19]. The details of the initial velocity field are shown in Fig. 1, and are assumed as follows:

(*a*) Radial velocities: zero; (*b*) axial velocities: axially downward, from the engine head toward the piston. Zero on the head, equal to the piston velocity on the piston and changing linearly in between; (*c*) swirl velocity: zero at the center and on the liner. Triangular velocity profile in between (solid body rotation).

To simulate the mixing process in the cylinder, the residual gas is assumed to have the composition of air. The fresh charge composition is assumed to be NO at the above-mentioned thermodynamic states [17]. The intake port angle is held constant at 20 deg. The engine valve and port timing diagram used is shown on Fig. 2. Computations were started at the exhaust valve opening (EVO,256 deg BTDC) and continued through the inlet port opening (IPO,225 CA BTDC) up to TDC. The available VAX-11 computer system together with the FPS-164 vector processor were utilized. The computational mesh size used is (31×32) in the half-plane. Each run took about 6 h CPU time with FPS-164.

In [17], the effects of the inlet port angle on the flow field within the cylinder were reported for several inlet port angles and for 900 rpm. The case for 20 deg inlet port angle was also studied further during the blowdown period with results presented in [18]. The details for the 900 rpm case can be found in these references and are not repeated here.

Results and Discussion

(A) Global Features of the Flow Field. The global features of the flow field are given in Figs. 3–10 in terms of: (*a*) total gas mass, (*b*) fresh air mass, (*c*) residual gas mass, (*d*) cumulative inflow at ports, (*e*) cumulative outflow at exhaust valves, (*f*) turbulence kinetic energy, in the combustion chamber, on a relative basis, as a function of crank angle covering a span from −256 to TDC and for four different engine speeds (namely 400, 700, 900, and 1000 rpm) as parameters.

In Fig. 3 the total cylinder mass is shown as a function of the crank angle. The cylinder mass decreases during the blowdown period, up to about −225 deg CA (for the 400 rpm case) and then increases until the inlet port closure (IPC). After that point the cylinder mass decreases until exhaust valve closure (EVC), at about −121 deg CA. During the compression period the cylinder mass stays constant. Figure 3 shows that: (1) The cylinder mass at TDC decreases with

Downloaded 01 Jun 2010 to 171.66.16.87. Redistribution subject to ASME license or copyright; see http://www.asme.org/terms/Terms_Use.cfm

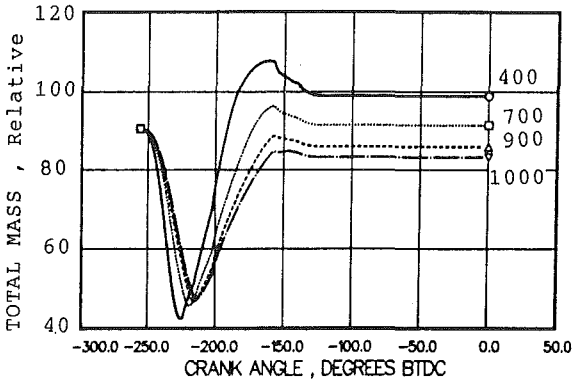


Fig. 3 Total gas mass in cylinder

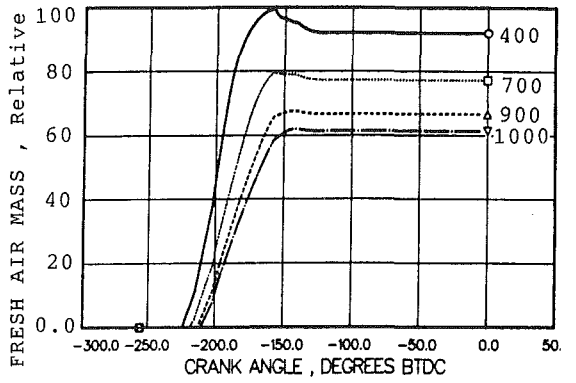


Fig. 4 Fresh air mass in cylinder

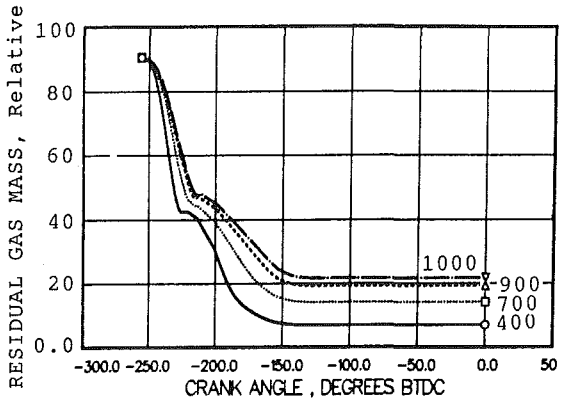


Fig. 5 Residual gas mass in cylinder

engine speed; (2) the location of minimum total mass in the cylinder changes with engine speed. This will be discussed further in section B. Although the initial gas mass in the cylinder is assumed to be the same, the final masses are different for different engine speeds. As the initial mass should include the fuel mass injected into the cylinder, the final mass should be less than the initial mass, by the amount of fuel injected. This mass conservation criterion is not met in the solutions presented here. This implies that further iterative solutions are needed to obtain a more realistic solution, satisfying this mass conservation criterion. Further iteration on the solutions to achieve a better mass balance between the initial and final chamber total mass was not attempted. The present calculations can be used to indicate trends but numerical values may not be accurate.

In Fig. 4 the fresh air mass in the cylinder is shown as a function of crank angle for the four speeds considered. This figure shows that: (1) Initially, there is a CA period when

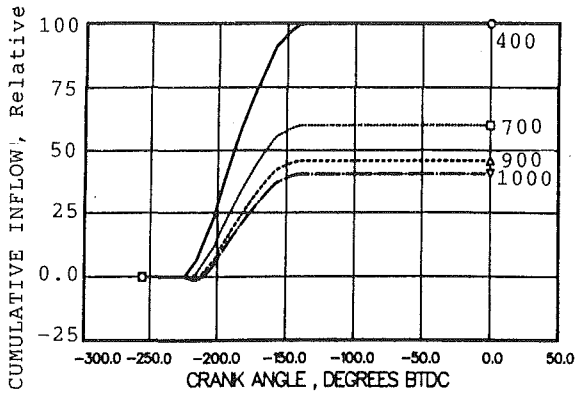


Fig. 6 Cumulative inflow mass at inlet ports

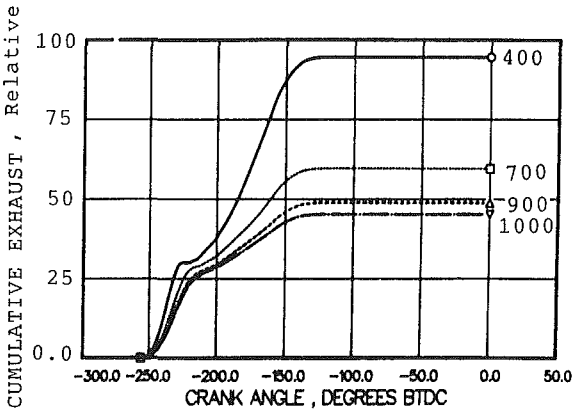


Fig. 7 Cumulative outflow at exhaust valves

there is no fresh air in the cylinder. This is the blowdown period from EVO to IPO. The formulation of the problem requires zero fresh air in the cylinder during this time. The calculations show that the duration for zero fresh air in the cylinder is changing with engine speed. This means that with increasing engine speed, the duration for backflow from cylinder to the airbox is increasing. This is also observable on Fig. 6. (2) The cylinder fresh air mass increases (almost linearly at the beginning) up to a peak near IPC. At low engine speeds, the cylinder fresh air decreases a little during the period from IPC to EVC, indicating some loss of fresh air at the exhaust valve. The decrease in this fresh air becomes smaller with increasing engine speed, such that at 1000 rpm it is almost negligible. This is an indication that if the CA duration between inlet port and exhaust valve closing is selected for negligible fresh air at high speed, then it may cause a large fresh air loss at lower engine speeds. Hence, in the choice of this duration, the operation of the engine at lower speeds also should be considered. This also implies that the duration from port closing to valves closing should be different for different engine speed ideally. In addition, this implies that changing the valve timing with engine speed may improve the cylinder air breathing process and so the engine performance.

Figure 5 shows the residual gas mass calculations corresponding to the previous cases given on Figs. 3 and 4. This figure shows that: (1) There is a certain similarity in the shape of these curves; (2) the blowdown period (the period of the initial rapid decrease in the residual gas mass) increases with increasing engine speed; (3) the residual gases trapped in the cylinder increase with engine speed.

The cumulative inflow mass at the ports and the outflow mass at the valves are shown on Figs. 6 and 7. These figures show that both the inflow and outflow masses decrease with an increase in the engine speed. These figures also suggest the

Downloaded 01 Jun 2010 to 171.66.16.87. Redistribution subject to ASME license or copyright; see http://www.asme.org/terms/Terms_Use.cfm

presence of similarity transformation to bring them into one curve. In Fig. 8 the total angular momenta of the cylinder contents are shown as a function of crank angle, for the four engine speeds. There are several interesting characteristics in this plot. First, the initial angular momenta of these cases are different. The initial angular momentum is larger for higher engine speeds due to the assumption that the initial swirl ratio was constant. During the blowdown period the total momenta decrease to a minimum, then increase due to new swirl generated by incoming new fresh air. During the compression stroke the instantaneous total momentum is different for different engine speeds. At TDC the difference in the total angular momentum is not so large. This indicates that the initial angular momentum is not so important for the total angular momentum at TDC, as previously observed by several authors. However, as the total cylinder masses are varied for these cases (Fig. 1), the average angular momentum per unit mass increases with engine speed.

Figure 9 shows the total turbulence kinetic energy with the characteristic initial peaks during the blowdown process as well as the turbulence peaks generated by the air induction and exhaust processes. The initial peak is larger at higher engine speeds. Engine speed has an influence on the turbulence during compression and at TDC, although the difference at TDC is less pronounced.

(B) Global Features During Blowdown Period. The global features of the chamber gases during the blow down period are shown in Fig. 10 for the same engine speeds on an enlarged scale. An important observation in Fig. 3 was that the duration for the chamber mass to drop to minimum was not constant with engine speed. Therefore, the period from EVO to −200 CA is covered in these plots, showing: (*a*) cylinder pressure, (*b*) total cylinder mass, (*c*) total angular momentum, (*d*) fresh air mass in cylinder, (*e*) residue gas mass in cylinder, and (*f*) turbulence kinetic energy.

Important points to note in these figures are: (1) With a decrease in the engine speed the cylinder pressure decreases rapidly. As an example, the cylinder pressure decreases from the same initial value to the final value in 45 CA for 900 rpm but in 30 CA for 400 rpm, suggesting about a 15 CA later opening of the exhaust valve for the 400 rpm case for an approximately comparable blowdown process. On the other hand, at slower engine speeds the actual time for the blowdown period is longer than at higher speeds. For the above example, the actual time for the pressure to drop to the minimum is about 1.5 times longer for the 400 rpm case than for the 900 rpm case. (2) The turbulence energy generated by the blowdown process increases with increasing engine speed (Fig. 10*f*), but the peak for the ratio of turbulence to mean flow kinetic energy is higher for slower engine speeds. (3) At high engine speeds there is backflow into the airbox. With decreasing speed, this backflow decreases and is completely eliminated at 400 rpm (not shown).

(C) Effects of Engine Speed on Global Properties at TDC. The effects of the engine speed on the engine breathing characteristics are shown in Figs. 11–13 as a function of engine speed. These plots are obtained through cubic best-fit curves fitted to the solutions obtained at 400, 700, 900, and 1000 engine rpm. They are normalized with corresponding values for the 900 rpm case. These curves show the following trends

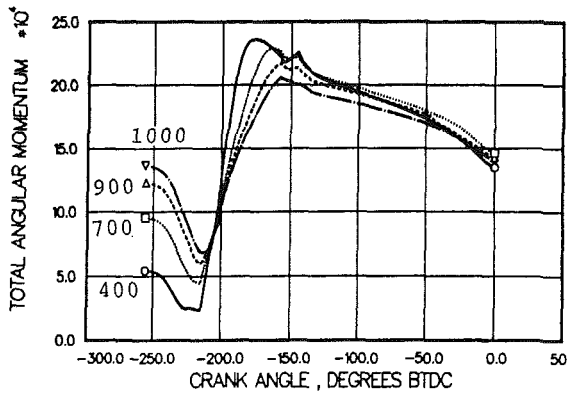


Fig. 8 Total angular momentum of gases

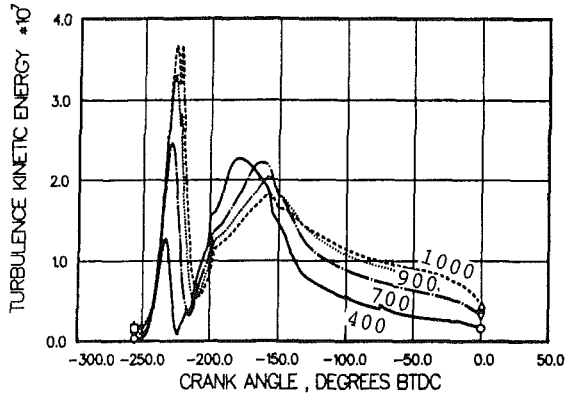


Fig. 9 Turbulence kinetic energy of gases

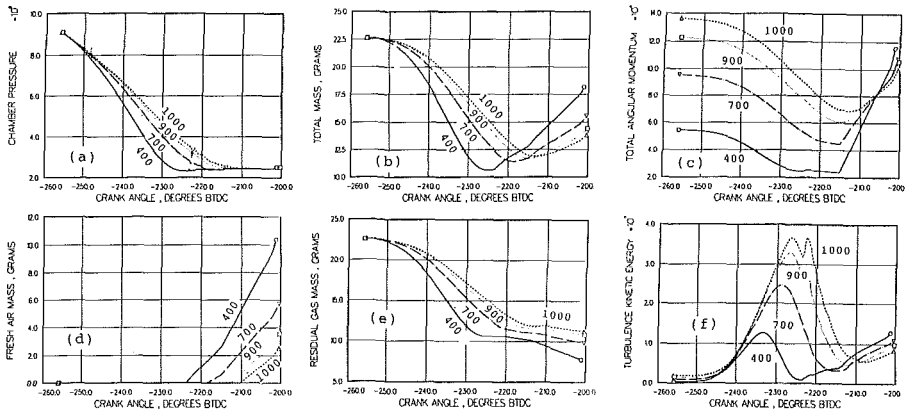


Fig. 10 Variation of global properties during blowdown: (*a*) cylinder pressure; (*b*) total mass; (*c*) total angular momentum; (*d*) fresh air mass; (*e*) residual gas mass; (*f*) turbulence kinetic energy

Downloaded 01 Jun 2010 to 171.66.16.87. Redistribution subject to ASME license or copyright; see http://www.asme.org/terms/Terms_Use.cfm

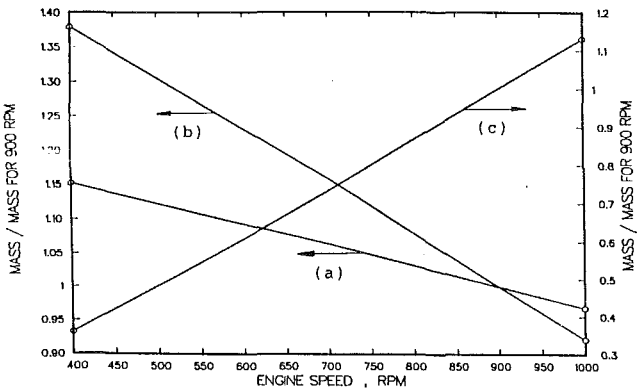


Fig. 11 Cylinder gas mass versus engine speed: (*a*) total gas; (*b*) fresh air; (*c*) residual gas (normalized with values at 900 rpm)

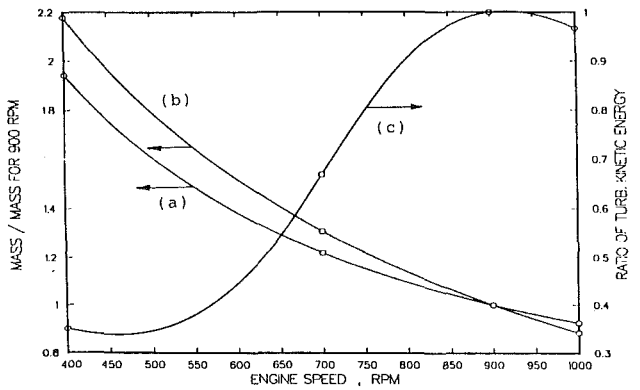


Fig. 12 Total flows at exhaust and inlet and turbulence kinetic energy at TDC: (*a*) total exhaust flow; (*b*) total inlet flow; (*c*) turbulence kinetic energy at TDC

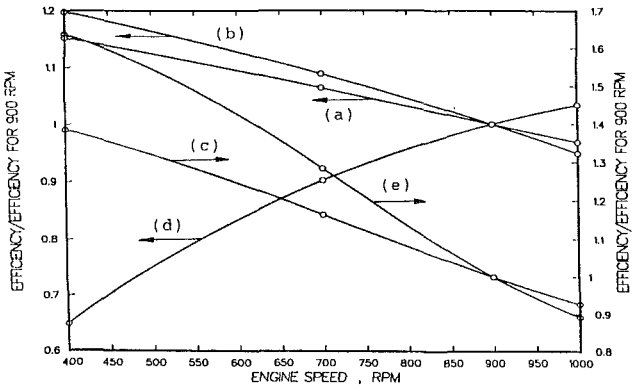


Fig. 13 Variation of scavenging, trapping, volumetric and charging efficiencies and scavenge ratio versus engine speed: (*a*) volumetric efficiency; (*b*) scavenging efficiency; (*c*) charging efficiency; (*d*) trapping efficiency; (*e*) scavenge ratio

at TDC: (1) The total gas mass in the cylinder decreases linearly with engine speed at about 0.0065 Gr/rpm (Fig. 11*a*); (2) the fresh air mass decreases and the residual gas mass increases (both linearly) with increasing engine speed (Figs. 11*b* and *c*); (3) both the exhaust and inflow masses decrease with increasing engine speed, not linearly but with decreasing slope (Figs. 12*a*, *b*).

Other important trends not shown in the figures are: (1) Backflow mass to the airbox increases with engine speed; (2) the effective swirl velocity (defined as the ratio of total angular momentum over the total gas moment of inertia) at TDC increases with engine speed, linearly at high speeds but not

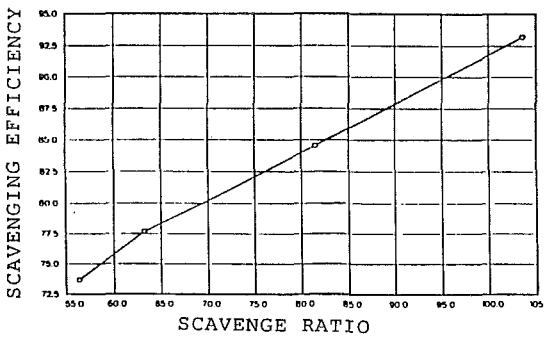


Fig. 14 Scavenging efficiency versus scavenge ratio

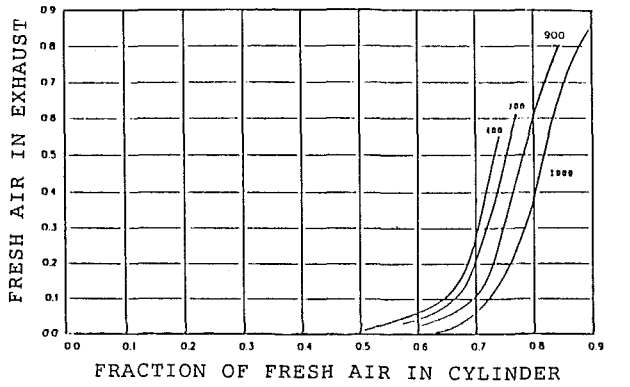


Fig. 15 Fraction of fresh air in exhaust versus fraction of fresh air in cylinder

linearly at low speeds. This is somewhat surprising as the engine swirl at TDC is usually assumed to be a linear function of engine speed; (3) The average turbulence time scale decreases with engine speed and is approximately constant over the 900 rpm range; (4) the total turbulence kinetic energy increases with engine speed, but becomes constant at about 900–100 rpm.

(D) Effect of Engine Speed on Engine Breathing. The air breathing characteristics of two-cycle engines are generally described in terms of the volumetric, scavenging, charging, trapping, efficiencies, and the scavenge ratio of the engine. These characteristics are presented in Figs. 13(*a*–*e*), respectively, showing that with an increase in engine speed from 400 to 1000 rpm: (1) The volumetric efficiency is decreasing with engine speed (defined as the ratio of total cylinder mass over the maximum air trappable at airbox density); (2) the scavenging efficiency is decreasing from 93 to 73 percent, almost linearly, with a slope of about 0.0331 percent per engine rpm; (3) the charging efficiency (defined as the ratio of fresh air trapped to the maximum air trappable at airbox density) is decreasing linearly with engine speed from about 78 percent to about 52 percent, with an average slope of 0.043 percent per engine rpm; (4) the trapping efficiency increases with engine speed from 57 percent to about 92 percent, not linearly but somewhat parabolically. An average rate of change is about 0.0572 percent per engine rpm; (5) the engine scavenging ratio (defined as the total inflow at ports over the maximum air trappable at airbox density) is almost linearly decreasing with engine speed from about 104 percent to about 56 percent, with an average slope of 0.0767 percent per engine rpm.

These trends are considered to be correct but the numbers should be used only as a trend indicator until more reliable values are obtained. They could be inaccurate due to the cylinder mass balance considerations discussed previously.

Downloaded 01 Jun 2010 to 171.66.16.87. Redistribution subject to ASME license or copyright; see http://www.asme.org/terms/Terms_Use.cfm

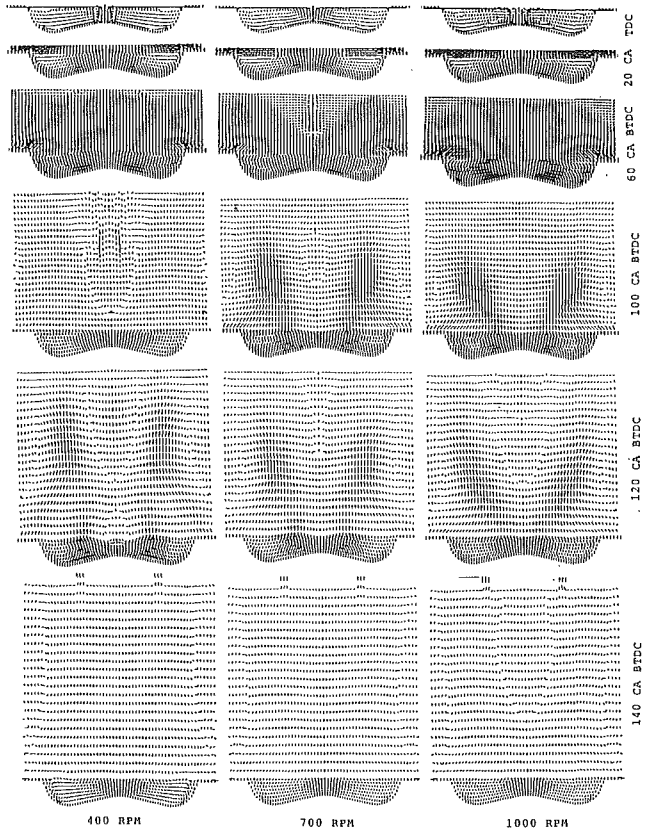


Fig. 16 Velocity vector plots at selected crank angles for engine speeds 400, 700, and 1000 rpm at crank angles 140, 120, 100, 60, 20, and TDC

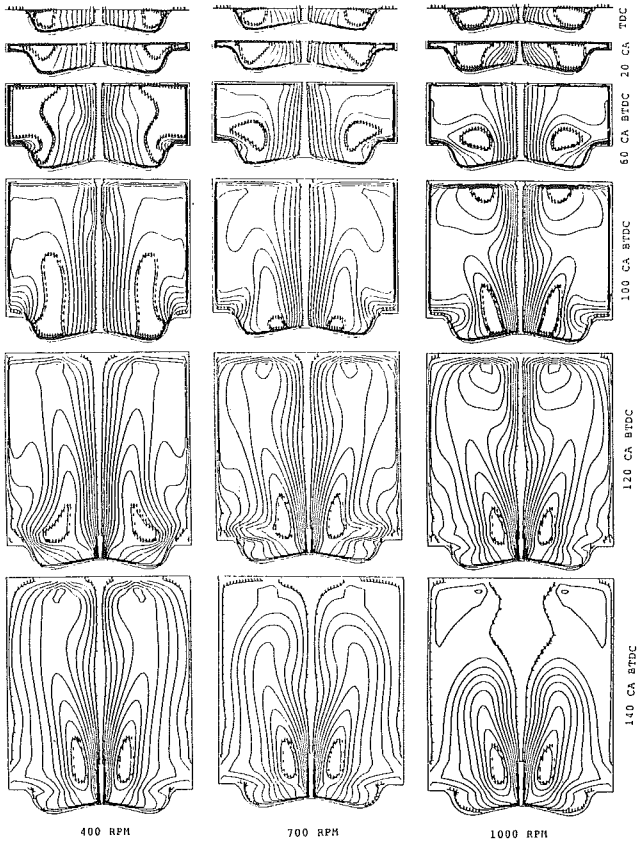


Fig. 18 Constant swirl velocity contours for engine speeds 400, 700, and 1000 rpm

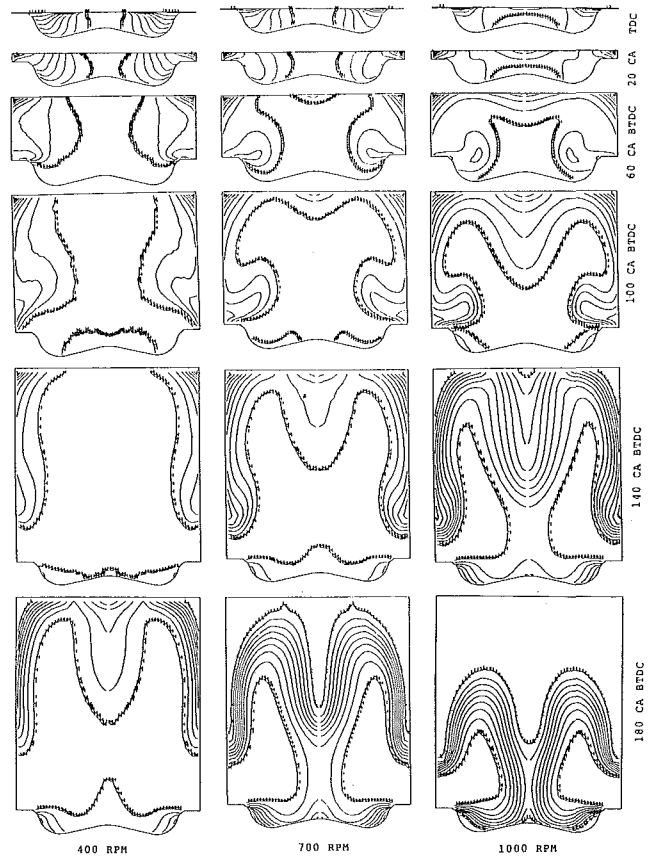


Fig. 17 Constant fresh air contour plots for engine speeds 400, 700, and 1000 rpm

(E) Physical Model for Scavenging. One important need is to develop a physical model representing the air breathing process of the two-cylinder engine suitable for use in engine performance calculation algorithms. Benson [2] reviews the so-called scavenging efficiency calculation methods available in the literature. They are all based on the correlation between the scavenging efficiency and the scavenge ratio. Such a plot calculated from the results presented is given in Fig. 14, which shows an increase in the scavenging efficiency with an increase in the scavenging ratio, with a slope of about 0.41.

Another method of defining the scavenging process in engine performance models is to represent the correlation between the fraction of fresh air at the exhaust and the fraction of fresh air in the cylinder (21). In Fig. 15 such a plot is shown for the four different engine speeds considered. This plot shows that: (1) There will not be any fresh air in the exhaust until the fresh air fraction in the cylinder reaches at least about 50 percent; (2) the correlation between the fresh air fraction in the exhaust and the mass fraction of fresh air in cylinder is different for different engine speeds. Moreover, the shapes of the curves look similar, suggesting the presence of a similarity transformation to bring these curves together and to represent the engine speed effects with one correlation. Preliminary regression analysis on these curves indicates that both the multipliers and exponents of the functions fitted to these curves are functions of engine speed. Hence, the use of such correlations, which are insensitive to engine speed, is questionable. Further work is needed on this subject.

(F) Detailed Features of the Flowfield. The results of the flowfield calculations are presented in Figs. 16, 17, and 18 in terms of velocity vector plots, fresh air concentration contours, and swirl velocity contours, at selected crank angles and for the engine speeds 400, 700, and 1000 rpm. Similar plots for

Downloaded 01 Jun 2010 to 171.66.16.87. Redistribution subject to ASME license or copyright; see http://www.asme.org/terms/Terms_Use.cfm

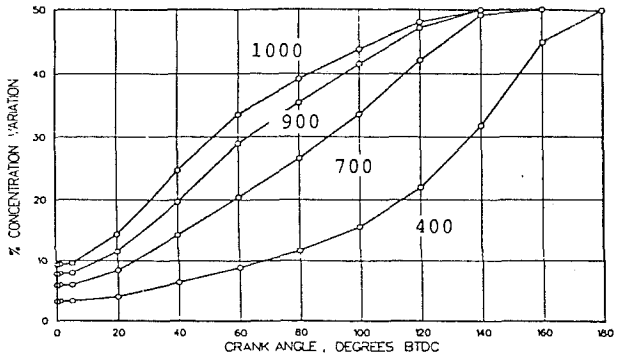


Fig. 19 Percent concentration variation versus engine rpm

the 900 rpm case are available in [17, 18] and due to space limitations they are not repeated here.

Some interesting observations on these plots are as follows: (1) The velocity vector plots during blowdown (not shown) indicate that the propagation of the zero vertical velocity contour (see [18] for conceptual details), toward the piston becomes slower as the engine speed increases. This is consistent with Figs. 3, 12, and 15, which also show some delay in the blowdown process with increasing engine speed; (2) at low engine speed (400 rpm) the wall vortex develops at about the same CA as in higher speeds, but the backflow vortex (in the center) develops at later CA (120 CA plot) and survives to CAs after EVC. This is observable at 100 CA plot, where the 1000 rpm case does not show any central backflow vortex, but the 400 rpm case does. Apparently, during the crank angle period from 220 to 140 (BTDC), the central backflow region restricts the short circuiting at the fresh air to the exhaust valve at high speeds, but is not effective in blocking the short circuiting at low engine speeds. This would cause a large amount of fresh air to short circuit directly to the exhaust. At the same crank angle, the instantaneous fresh air flow at the exhaust valve also shows a rather large increase from 700 to 400 rpm. The backflow vortex is known to be generated by the swirl and vertical flow interaction [17]. Apparently, at low engine speeds, the effective swirl rate is rather low, and does not generate the backflow vortex during the open period of valves and ports. However, the backflow vortex appears later, after the valves are closed. The reason for the late appearance of this backflow vortex needs further study; (3) the fresh air concentration contours are shown in Fig. 17 at selected crank angles, during the open-valve and compression period. This figure also shows that the fresh air short circuits at an earlier crank angle as the engine speed is reduced. Fresh air reaches the exhaust valve region at about 160 CA for 400 rpm, while it could not reach the exhaust valve at 100 CA BTDC for the 700 rpm case well after the valves are closed. At low speeds there is so much fresh air lost to exhaust that the trapping efficiency is reduced considerably (Fig. 13*d*); (4) a study on the effects of the engine swirl level on the residue gas stratification was presented in [17]. It was shown that with increasing swirl levels, more residual gases would be pushed toward the piston rim area and more fresh air would be in the center of the piston bowl at TDC. Here in Fig. 17, at TDC, the residual gases are also more concentrated at the piston squish region. There seems to be a similarity about the effects of the engine rpm and the engine swirl level as far as the residual gas stratification at TDC is concerned. An increase in both the swirl level and engine rpm seem to cause more fresh air near the center of the bowl. This similarity should be studied further; (5) the development of the swirl velocity distribution within the combustion chamber can be studied from Fig. 18 where the swirl velocity contours are given for the 400, 700, and 1000 rpm cases at selected crank angles.

Table 1 Fresh air concentration distributions at *TDC*

rpm	MAX	MIN	Mean	Percent difference
400	95.44	90.33	92.885	2.555
700	87.87	78.44	83.115	4.715
900	81.07	68.52	74.795	6.275
1000	77.10	62.14	69.620	7.480

The distribution of the fresh air concentration within the combustion chamber is also affected by the engine speed. In Fig. 19 the "Concentration Variation" (CV) is plotted as a function of crank angle (BTDC). Here the concentration variation is defined as the mean of the maximum and minimum fresh air concentrations in the flow field $((Q_{max} - Q_{min})/2.0$ where Q is local instantaneous fresh air concentration). When this function is 0.5, there is at least one point with 100 percent fresh air and another point with 0.0 percent fresh air in the flow field. Considering that the inlet ports and exhaust valves close at about 135 and 121 CA BTDC, Fig. 19 shows that at the port closing, the fresh air concentration variation is about 29 percent for the 400 rpm case, while it is about 50 percent for all other cases. At EVC, concentration variations are increasing with engine speed, and are about 23, 43, 47, and 48 percent for the 400, 700, 900, and 1000 rpm cases, respectively.

In Table 1 some selected statistical data on the fresh air distribution within the cylinder are given at 1 CA BTDC for different engine speeds. On this table MAX and MIN, respectively, indicate the 90 and 10 percent values of the difference between highest and lowest values of the fresh air concentrations in the field. This table shows that max is about 95.44 percent for the 400 rpm case while it is only about 77.10 percent for 1000 rpm case. At low engine speeds the fresh air mixed relatively well with the residual gases while at higher speeds the mixing was not as good as the percent difference increases with engine speed. Figure 17 shows that at TDC, the fresh air is mainly concentrated in the middle of the bowl and the residual gases are concentrated at the clearance volume at high speed. With a decrease in the speed, more residual gases are observable near the middle. Residual gas stratification is stronger and more observable at high engine speeds.

Conclusions

Effects of engine speed on the air breathing characteristics of a uniflow, two-cycle engine were studied by using a multidimensional computer code. Solutions were obtained by changing only the engine speed, while keeping all other parameters constant around a reference point simulating engine operation at full load. Under this calculation methodology, the important conclusions are as follows:

1 With an increase in engine speed: (*a*) The blowdown period increases in terms of crank angle, but decreases in terms of actual time; (*b*) both the total mass in the cylinder and the cumulative flows at the ports and valves during the air breathing period decrease; (*c*) the backflow to the airbox just after the IPO increases, (*d*) the TDC swirl velocity increases linearly with engine speed over the high engine speeds but does not increase linearly at low engine speed range; (*e*) the TDC turbulence kinetic energy increases with engine speed, but becomes constant at about the 900–1000 rpm range.

2 The scavenging efficiency decreases about 3.3 percent and the trapping efficiency increases about 5.7 percent per 100 rpm increase in engine speed.

3 With a proportionality constant of about 0.41, the scavenging efficiency is proportional to the scavenge ratio.

4 The mass fraction of fresh air in the exhaust is negligible until the mass fraction in the cylinder becomes at least about

Downloaded 01 Jun 2010 to 171.66.16.87. Redistribution subject to ASME license or copyright; see http://www.asme.org/terms/Terms_Use.cfm

50 percent. The correlation between the mass fraction of fresh air in the exhaust and in the cylinder is different for different engine speeds for the conditions analyzed. Therefore, a constant correlation between these parameters may not be valid for a large range of engine speeds.

5 At low engine speeds, the residual gases mix relatively well with fresh air, but with increasing engine speed they do not mix as well. At TDC, the maximum difference in the residual gas concentrations between any two points in the combustion chamber increases with engine speed. At low engine speeds, the residual gas concentration is uniform, but at high speeds, residual gases are more concentrated at the squish region and the fresh air is more concentrated near the bowl center.

References

1 Taylor, C. F., *The Internal Combustion Engine in Theory and Practice*, 2nd ed., MIT Press, Cambridge, MA, 1965.

2 Benson, R. S., and Whitehouse, N. D., *Internal Combustion Engines*, Pergamon Press, New York, 1979.

3 Masatoshi, S., Masashi, S., and Shongo, T., "Effects of Combustion Chamber Configuration on In Cylinder Air Motion of DI Diesel Engine," *Proc. Int. Symp. on Diagnostics and Modelling Combustion in Reciprocating Engines*, Tokyo, Sept. 1985, p. 353.

4 Wakisaka, T., Shimamoto, Y., and Isshiki, Y., "Three Dimensional Numerical Analysis of In-Cylinder Flows in Reciprocating Engines," SAE Paper No. 860464, 1986.

5 Schapertons, H., and Thiele, F., "Three Dimensional Computations for Flowfields in DI Piston Bowls," SAE Paper No. 860463, 1986.

6 Watkins, A. P., Dessipris, S., and Khalegli, H., "The Combined Effects on Fluid Flow During Compression of Piston Bowl Shape and Offset and Swirl Ratio," SAE Paper No. 870595, 1987.

7 Bracco, F. V., "Modelling of Engine Sprays," SAE Paper No. 850394, 1985.

8 Watkins, A. P., Gosman, A. D., and Tabrizi, B. S., "Calculation of Three Dimensional Spray Motion in Engines," SAE Paper No. 860468, 1986.

9 Reitz, R. D., and Diwakar, R., "Structure of High Pressure Fuel Sprays," SAE Paper No. 870598, 1987.

10 Khalegli, H., and Watkins, A. P., "Calculation of Three Dimensional Diesel Spray Into Curvilinear Piston Bowls and Comparison With Experiment," ASME Paper No. 87-FE-1.

11 Theobald, M., and Cheng, W., "Study of Diesel Ignition Processes Using Kiva Computer Program," ASME Paper No. 87-FE-2.

12 Bracco, F. V., "Modelling and Diagnostics of Combustion in Spark Ignition Engines," *Proc. Int. Symp. on Diagnositcs and Modelling Combustion in Reciprocating Engines*, Tokyo, Japan, Sept. 1985, p. 1.

13 Adachi, T., Kato, S., and Tsujima, H., "Numerical Analysis of Scavenging Flow in Two-Cycle Internal Combustion Engines," ASME *Symp. on Flows in IC Engines*, Nov. 1982, pp. 29–39.

14 Diwakar, R., "Multidimensional Modelling of the Gas Exchange Process in a Uniflow-Scavenged Two-Stroke Diesel Engine," *Int. Symp. on Flows in IC Engines—3*, ASME FED-Vol. 28, pp. 107–115.

15 Diwakar, R., "Three Dimensional Modelling of the In-Cylinder Gas Exchange Processes in a Uniflow-Scavenged, Two Stroke Engine," SAE Paper No. 870596, 1987.

16 Uzkan, T., Savage, T. J., and Hazelton, J. R., "The Effects of Piston Bowl Shape Modifications on the In-Cylinder Flow Characteristics of the EMD-710 Engine," ASME Paper No. 85-DGP-23, 1985.

17 Uzkan, T., and Hazelton, J. R., "The Influence of Swirl on the Fresh Charge Stratification in an IC Engine Combustion Chamber," SAE Paper No. 860466, 1986.

18 Uzkan, T., "An Analysis of the Engine Blowdown Process Using Multidimensional Computations," ASME JOURNAL OF ENGINEERING FOR GAS TURBINES AND POWER, Vol. 109, 1987, pp. 459–464.

19 El-Tahry, S. H., "A Numerical Study on the Effects of Fluid Motion at Inlet Valve Closure on Subsequent Fluid Motion in a Motored Engine," SAE Paper No. 820035, 1982.

20 Plee, S. L., "A Computational Study of the Effects of Swirl Ratio, Squish Height and Bowl Geometry on the In-Cylinder Flow Field in DI Diesel Engine," *Int. Symp. on Flows in IC Engines*, ASME FED-Vol. 28, p. 107.

21 Hayashi, Y., and Meyer, W., "An Analytic Method for Optimizing the Scavenging Process of Uniflow Two-Cycle Diesel Engines," SAE Paper No. 650447, 1965.

Downloaded 01 Jun 2010 to 171.66.16.87. Redistribution subject to ASME license or copyright; see http://www.asme.org/terms/Terms_Use.cfm

A Three-Zone Scavenging Model for Two-Stroke Uniflow Engines

N. P. Kyrtatos

I. Koumbarelis

Department of Naval Architecture and Marine Engineering, National Technical University, Athens, Greece

A three-zone scavenging model for two-stroke uniflow engines was developed and used in conjunction with a control-volume-type engine simulation code for performance prediction of long stroke uniflow-type marine engines. In this model it is attempted to simulate the three different regions perceived to exist inside the cylinder during scavenging, namely the air, mixing, and combustion products regions, by modeling each region as a separate control volume. Two time-varying coefficients are used to specify the rates of entrainment of the air and the burned gases into the mixing region. Results of the use of the model for predicting the performance of a large marine two-stroke engine are presented.

Introduction

In the study of marine propulsion systems by simulation, it is important to have an accurate model of the main engine, which, apart from basic engine design and matching calculations, can also be used to provide input for component retrofit and energy recovery tradeoff studies.

Slow-speed uniflow-type engines account for a large percentage of installed marine propulsion powerplants. In order to model this type of engine, a general purpose "control-volume" type engine simulation code was suitably revised, with models of the various subprocesses transformed accordingly. Control-volume-type engine models treat a multicylinder engine as a series of thermodynamic control volumes, interconnected via ports or valves, assuming spatial uniformity and quasi-steady rates of change within every control volume, with work, heat, and mass transfer taking place through the control volume boundaries [1].

The paper describes the development of a model for the scavenging process, and its use in conjunction with an engine modeling code [2], for slow-speed marine engine simulation.

Scavenging Models

The use of the control volume concept implies that instant and perfect mixing takes place between the instantaneous incoming flows and the contents of the control volume. Using this concept to describe the scavenging process of an engine cylinder will be reasonable for four-stroke engines, possibly erring on the safe side. For two-stroke engines, the above assumption may be acceptable in certain cases of cross flow or loop flow engines where the charge air may mix extensively with the burned gases, but it cannot be adopted for uniflow engines, where displacement scavenging can be quite pronounced.

A better approximation to the scavenging process would be a two-part (two-zone) model, consisting of a combination of pure displacement and complete mixing, as in Benson's model [3], and the two-part model of Metz et al. [4], and further accounting for the possibility of charge air short circuiting to the exhaust [5] and also the existence of "dead" gas zones [3].

Attempts to model the changing scavenge conditions with time have also been made [6, 7]. Sher [8] has developed a correlation for the instantaneous exhaust gas composition. This correlation is based on results from a two-dimensional finite difference solution of the flow equations inside the cylinder of a small-bore two-stroke Schnürle-type scavenged engine and some experimental results obtained from a flow visualization rig [9]. This two-dimensional scavenging model uses three zones of computational mesh. At any time, in general, two zones remain fixed in volume and the third changes volume while, at certain times, there might be either one or two zero volume zones.

Such correlations as Sher's, known as S-type correlations, could be used for engine performance predictions with proper calibration. However they will not be sensitive to adverse conditions (e.g., backflow induced by blowdown of adjacent cylinders) and cannot give accurate input for a detailed cylinder heat transfer model within a performance prediction code. These shortcomings are to a certain extent alleviated by using a multizone model.

A dynamic model for a step-by-step description of the scavenging process was put forward by Benson [10], partly based on experimental data by Dedeoglu [11]. This model includes the effect of phenomena such as the turbulent jet mixing and diffusion in the air–gas mixing process inside the cylinder, in addition to accounting for the heat transfer of the working fluid with the surrounding walls. The cylinder was divided into three zones: an air zone, a gas zone, and a mixing zone, and the scavenging process was considered to be in three phases: a displacement phase, a short-circuiting phase, and a mixing phase. The assumption of at least three distinct periods of operation involves numerous discontinuities such as these for the exhaust temperatures and for the gradient of the curve of charging efficiency versus delivery ratio [3]. There are numerical instabilities at the commencement of the calculation and the timing of the phases is not sufficiently validated, while

Contributed by the Integral Combustion Engine Division and presented at the Eleventh Annual Energy-Sources Technology Conference and Exhibition, New Orleans, Louisiana, January 10–13, 1988. Manuscript received by the Internal Combustion Engine Division April 1987.

Copyright © 1988 by ASME
Downloaded 01 Jun 2010 to 171.66.16.87. Redistribution subject to ASME license or copyright; see http://www.asme.org/terms/Terms_Use.cfm

the overall heat transfer from the cylinder is based on a weighted mean gas temperature and the proportion from each zone based on the ratio of the zone volume to the cylinder volume.

In a different class altogether, spatial (multidimensional) models have been used to determine the flow field inside the cylinder during the scavenging process. Additionally they can provide useful insight for improving one-dimensional control-volume-type models, which are used within engine performance prediction programs. However the existing three-dimensional codes for modeling the in-cylinder air motion make very heavy demands on computer storage and time [12–16] and therefore are not practical for inclusion within an engine simulation code to predict the overall engine performance.

In the present model, scavenging is considered as a continuous process giving satisfactory numerical stability. At the same time it depicts with sufficient detail the in-cylinder composition, allowing for accurate input to the cylinder heat transfer model, and gives good response to adverse flow and pressure conditions. Hence the model is practical for inclusion within performance prediction codes.

Scavenging Model

Mass Exchange. The scavenging model developed can be considered to be of the control-volume type. The engine cylinder is subdivided into three zones, namely, a zone of pure air, a zone of burned gas, and a zone comprised of a mixture of air and exhaust gas. The three zones are designated (Fig. 1):

Zone I : air
Zone II : mixing zone (air and gas)
Zone III : burned gas

The content of each zone is assumed homogeneous and in thermodynamic equilibrium with ideal gas behavior; hence the equation of state can be used.

Within any zone the temperature is assumed to be uniform but is different in each zone. The pressure throughout the cylinder is uniform at any instant or computational step.

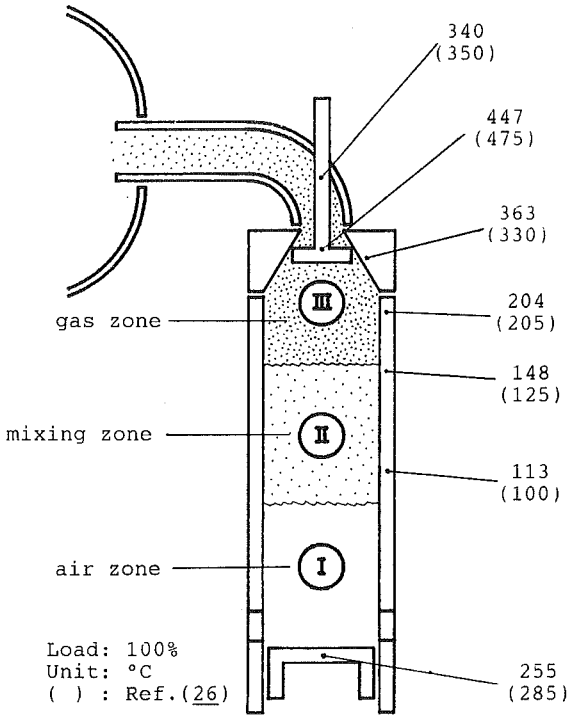


Fig. 1 Combustion chamber model

Nomenclature

A = effective area, m^2
C = 0.00234
C_m = piston velocity, m/s
C_1, C_2 = constants of Woschni correlation
c_f = local skin coefficient
D = engine bore, m
F = equivalence ratio
G = 1.56×10^{-4}
H = heat transfer coefficient, kW/(K•m²)
h = specific enthalpy, kJ/kg
I = moment of inertia, m²•kg
k = constant of mixing coefficient
M = mass, kg
m = mass, kg
p = pressure, kNt/m²
Q = heat flow, kJ
R = gas constant, kJ/(kg•K)
S = engine stroke, m
$S(\vartheta)$ = instantaneous distance from TDC, m
T = temperature, K
u = specific energy, kJ/kg
V = volume, m²
ϑ = crank angle
λ = constant of mixing coefficient
μ = mixing coefficient
ξ = constant of mixing coefficient
ρ = density, kg/m³
σ = dynamic viscosity, kg/(m•s)
$\tau = \dfrac{\vartheta - \vartheta_{EBF}}{\vartheta_{IPC} - \vartheta_{EBF}}$ = normalized scavenging time
τ_1 = first mixing phase normalized duration
$\tau_2 = \dfrac{\vartheta - \vartheta_{EFP}}{\vartheta_{IPC} - \vartheta_{EFP}}$ = normalized scavenging time for second mixing phase
φ, ψ = angles of air velocitiy vector at inlet port, rad
ω = angular velocity, rad/s

Subscripts

a = air
c = cylinder head
cyl = cylinder
e = exhaust gas
EBF = end of backflow
EFP = end of first mixing phase
g = burned gas
in = inlet port
IPC = inlet port close
o = motored cycle
p = piston crown
r = reference state
sw = swept volume
tot = total

Superscripts

$\bar{}$ = mean value
$'$ = mixing value
$\dot{}$ = rate of change with respect to time

Downloaded 01 Jun 2010 to 171.66.16.87. Redistribution subject to ASME license or copyright; see http://www.asme.org/terms/Terms_Use.cfm

Every zone is treated as an open system where the first law of thermodynamics may be applied

$$-p\cdot\dot{V}+\sum_i \dot{Q}_i+\sum_j h_j\dot{M}_j=\frac{d}{dt}(Mu) \tag{1}$$

In the temperature range encountered during the scavenging period the dissociation effects can be neglected. Therefore, the internal energy and the gas constant can be expressed as

$$u=f(T,F),\quad R=f(F) \tag{2}$$

Since the cylinder control volume is subdivided into three zones, the conservation of the total cylinder mass is expressed as follows:

$$\dot{M}_a-\dot{M}_e=\dot{M}_{\rm I}+\dot{M}_{\rm II}+\dot{M}_{\rm III} \tag{3}$$

where $\dot{M}_a$ is the mass flow rate from the inlet manifold, assumed positive when entering the cylinder, and $\dot{M}_e$ the mass flow rate to the exhaust manifold, assumed positive when leaving the cylinder.

The mass exchange between the zones is assumed to take place only in two ways: scavenge air enters the mixing zone ($\dot{M}'_{\rm I}$); burned gas enters the mixing zone ($\dot{M}'_{\rm III}$). Hence, the rate of change of the mass for each zone control volume is

$$\dot{M}_{\rm I}=\dot{M}_a-\dot{M}'_{\rm I} \tag{4a}$$

$$\dot{M}_{\rm II}=\dot{M}'_{\rm I}+\dot{M}'_{\rm III} \tag{4b}$$

$$\dot{M}_{\rm III}=-\dot{M}'_{\rm III}-\dot{M}_e \tag{4c}$$

The most important assumptions for the scavenging simulation are those concerning the determination of the mixing rate values $\dot{M}'_{\rm I}$ and $\dot{M}'_{\rm III}$.

These rates control the growth of the air zone and mixing zone and contribute to the reduction of the exhaust gas zone, so that effectively they influence the engine breathing conditions and the heat transfer during the scavenging period.

In the uniflow scavenge process two phases of mixing may be distinguished. In the first stages of the scavenging period immediately after any backflow, air together with a portion of backflow gases enters into the cylinder in the form of jets issuing from the inlet ports. It can be assumed that jet mixing mechanisms are dominant during this phase and data for multiple confined jets can be used [17-21].

As more air enters into the cylinder, displacing the exhaust gases, which flow out to the exhaust manifold, the influence of jet mixing mechanisms in the penetration of air into the mixing zone deteriorates since the boundary between air and mixing zone will be displaced upward, away from the inlet ports. Therefore the mixing zone and the gas zone become oblivious to the air jets now flowing only into the air zone. In this second phase, mixing between the zones continues due to turbulent diffusion, and is influenced by port geometry induced swirl, diminishing as the zone interfaces move away from the ports. Within the time taken for the scavenging process, diffusion induced by thermal gradients may be neglected.

When the intake port closes, no further mixing is assumed to take place until the exhaust valve closes, when the whole cylinder is again considered as a single control volume.

It is convenient to express the mixing rates as percentages of the instantaneous airflow into the cylinder. Thus the air penetration coefficient

$$\mu_a=\frac{\dot{M}'_{\rm I}}{\dot{M}_a} \tag{5}$$

and the gas penetration coefficient

$$\mu_g=\frac{\dot{M}'_{\rm III}}{\dot{M}_a} \tag{6}$$

Variations of the two coefficients with time during the scavenging process can be postulated, based on the above description of the phenomenon. The assumed variation of μ_a is shown in Fig. 2 and can be explained as follows. The initial scavenge air flow is rapidly mixed with exhaust gases, hence initially $\mu_a = 1$, and all air is assumed to go into the mixing zone. As the exhaust gases in the lower part of the cylinder are rapidly diluted and displaced, and an air zone is formed, the value of the coefficient falls, approaching that for mixing as predicted by considering angular velocity differences between zones (Appendix B).

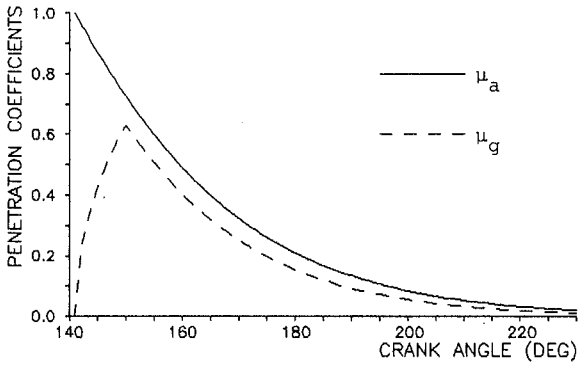


Fig. 2 Variation of coefficients μ_a, μ_g

An equation of exponential decrease can be used

$$\mu_a=e^{-k\tau}(\lambda\tau+1)\qquad 0<\tau<1 \tag{7}$$

The postulated variation of μ_g is shown in Fig. 2. During the first phase of mixing, the variation of μ_g resembles that of entrainment of ambient fluid into jets, and increases parabolically

$$\mu_{g_1}=2\tau^{0.5}\qquad 0<\tau<\tau_1 \tag{8}$$

The initial phase of increasing entrainment of exhaust gas by jet expansion will be terminated due to jet interaction and confinement, and the displacement of the exhaust gas zone. These depend on parameters such as engine port geometry, engine speed, and pressure ratio across the cylinder.

The duration of first mixing phase τ_1 was estimated as follows: The mean air jet velocity at the ports was calculated based on the time-averaged flow through the ports, which depends on the pressure ratio across the cylinder and the port effective area.

A hyperbolic jet velocity decay in accordance with single jet data [17] was assumed up to the point where strong interaction between the jet under consideration and the air jets flowing through adjacent ports occurs. This point was assumed to be at a jet trajectory distance $l = 0.6 \times D$.

The above assumptions for the trajectory distance and the jet velocity distribution across it led to the calculation of the first mixing phase time period. This time period was normalized with the total scavenging time to give τ_1.

Since the gas penetration coefficient is zero at the start of scavenging, while the air penetration coefficient has the value of one, the mixing zone will be initially fed only by the air zone, the contents of which will initially include diluted backflow gases.

In the second phase the coefficient should drop rapidly approaching the value predicted by considering turbulent diffusion due to variations in swirl between zones (Appendix B).

An equation of the following form can be used:

$$\mu_{g_2}=e^{-k\tau_2}(\xi\tau_2+\mu_{g_1}(\tau_1)),\qquad 0<\tau_2<1 \tag{9}$$

where $\mu_{g_1}(\tau_1)$ is the value of μ_{g_1} at $\tau = \tau_1$.

The above assumptions for the mass exchange processes are used for the computation of the rate of change of mass for each zone, which are subsequently used in the computation of the rates of change of temperature and pressure (Appendix A).

It must be noted that at this stage of model development the

Downloaded 01 Jun 2010 to 171.66.16.87. Redistribution subject to ASME license or copyright; see http://www.asme.org/terms/Terms_Use.cfm

gas inside the cylinder at inlet port opening is assumed to have no swirl, ignoring any swirl imparted from the fuel jets during injection.

Heat Exchange. Heat transfer takes place between each zone and its adjacent walls by convection. "Walls" are considered to be all the inner surfaces of the cylinder in contact with the cylinder contents: liner, piston crown, head, exhaust valve.

Each zone has the shape of a cylindrical body with diameter equal to the bore diameter. The air zone is placed near the inlet ports, at the lower part of the cylinder, the gas zone near the exhaust valve, at the upper part, and the mixing zone is placed between the other two zones.

Radiation between zones is assumed negligible, since any high-temperature soot particles still in the cylinder at the early stages of scavenging are soon exhausted or cooled down.

The temperature distribution along the cylinder axis is based on the mean temperature of each zone for each time step.

Heat Transfer and Combustion Submodels

The heat transfer process between the working fluid and the surroundings consists of three parts: heat transfer from gas to wall, conduction through the wall, and conduction from wall to coolant.

For the first part a correlation is needed giving the instantaneous heat transfer coefficient between gas and cylinder wall. According to Bulaty [22] the Woschni heat transfer correlation [23] may be applied for long-stroke engines, after taking into account the dependence of Prandtl number on Nusselt number. The Prandtl number cannot be considered constant in uniflow scavenged engines, since significant temperature differences exist in the engine cylinder at least during the early stages of scavenging.

The correlation of the heat transfer coefficient used within the present engine simulation code is

$$H = C \cdot \left[C_1 \cdot \bar{C}_m + C_2 \cdot \frac{V_{sw} \cdot T_r}{p_r \cdot V_r} (p - p_o) \right]^{0.8} \cdot D^{-0.2} \cdot p^{0.8} \cdot$$

$$T^{-0.5876} \cdot (1 - G \cdot T)^{-0.45} \cdot \left(1 + \left(\frac{D}{S} \right)^{2/3} \right) \qquad (10)$$

where [Pr] is being evaluated according to Woschni [24] and [Nu] is expressed using Hausen's equation [22] for turbulent flow.

The heat transfer coefficient used for the heat transfer at the exhaust port is based on the correlations suggested by Zapf [25], where a variable Prandtl number is considered.

The coefficient for the heat transfer at the exhaust valve seat is based on Hausen's equation with appropriate characteristic lengths [22].

For the wall conduction part, a one-dimensional heat flux model was used. The geometry of the combustion chamber is shown in Fig. 1. The liner is subdivided into three parts axially, to improve the definition of the temperature distribution. There is also a temperature distribution across the piston surface and the cylinder head. The temperature of each surface is updated every engine cycle by integration of the instantaneous heat flows and is assumed uniform over the area of the boundary wall and constant over an engine cycle.

Combustion is modeled as a heat release process. The cumulative heat release diagrams (Fig. 3) at full and part load were kept unchanged for all the runs at the corresponding load condition in order to minimize the influence of the combustion process in the scavenging-related prediction results.

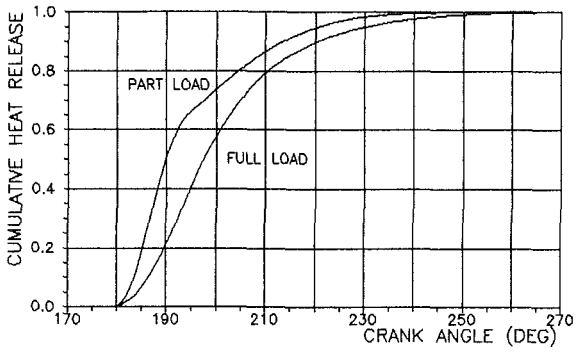


Fig. 3 Cumulative heat release diagram

Table 1 Engine specifications and operating conditions

Number of cylinders	6
Bore	0.35 m
Stroke	1.05 m
Connecting rod length	1.26 m
Compression ratio	17.0
Engine speed	200.0 rpm
Inlet manifold pressure	3.10 bar
Brake power	500 kW/cyl
Inlet ports opening	130° ATDC
" " closing	230° ATDC
Exhaust valve opening	105° ATDC
" " closing	265° ATDC

Table 2 Performance data comparisons

	Three-Zone Model		Perfect Mixing Model		Pure Displacement Model		Measured Data Ref. (26)	
Load	100%	60%	100%	60%	100%	60%	100%	60%
B.Power (kW)	2958	1747	2779	1643	2996	1746	3000	1800
p_{max} (bar)	120.0	106.5	114.0	100.5	121.0	106.5	125.0	108.0
imep (bar)	15.84	11.17	14.94	10.54	16.03	11.16	16.0	-
bmep (bar)	14.65	10.11	13.75	9.50	14.83	10.11	14.8	10.6
p_{inl} (bar)	3.14	2.09	3.14	2.08	3.12	2.08	3.10	2.05
T_{exh} (°C)	399.2	312.5	395.7	308.0	400.8	313.0	420.0	385.0
Air flow (kg/s)	7.01	4.67	6.96	4.65	6.99	4.67	7.02	4.40
Component Temp.(°C) Liner (upper)	204	175	226	191	201	178	205	No Measured Data Available
Liner (middle)	148	127	163	137	148	130	125	
Liner (lower)	113	104	122	111	114	105	100	
Piston crown	255	222	302	258	247	225	285	
Exh. valve	447	395	515	457	427	397	475	
Exh. valve stem	340	307	389	350	330	308	350	
Cylinder head	363	349	412	394	350	347	330	
scavenging eff.	0.930	0.969	0.815	0.835	1.000	1.000	-	
trapping eff.	0.793	0.763	0.574	0.532	0.905	0.775	-	

Downloaded 01 Jun 2010 to 171.66.16.87. Redistribution subject to ASME license or copyright; see http://www.asme.org/terms/Terms_Use.cfm

Prediction Results

The engine simulation code including the scavenging model was used to predict the performance of a two-stroke engine, the specifications of which are shown in Table 1. Engine performance prediction runs were conducted at full load and 60 percent load along the propeller curve. These two points were chosen because published performance data were available for comparison.

Engine performance data predicted by the model are presented in Table 2. These are compared with measured data of a similar engine [26] and performance data predicted by the simulation code using a single-zone (perfect mixing) model and a two-zone (pure displacement) model. For the runs with the three-zone model concept the values $k = 5$, $\lambda = 1$, $\xi = 1$ were used for the mixing coefficient constants. The two-zone model was obtained by setting the mixing coefficients values to $\mu_a = 0$ and $\mu_{g_1} = \mu_{g_2} = 0$ in the three-zone model.

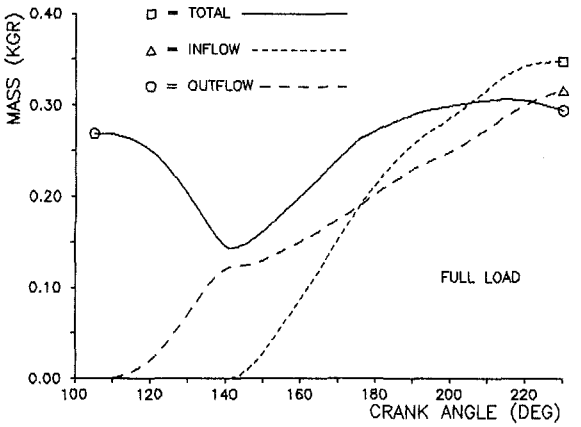


Fig. 4 Mass variation with crank angle

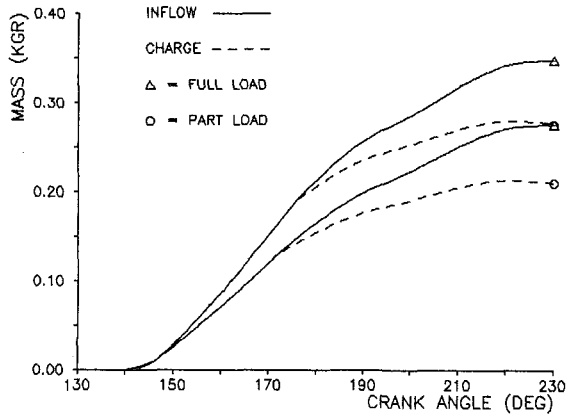


Fig. 5 Variation of air charge retained and air inflow with crank angle

It can be observed that the engine performance predictions using the three-zone model compared with measured data are definitely improved over the predictions using the single zone complete mixing model.

On the other hand the differences between the two-zone and three-zone model are generally small. However, the two-zone model implies the unrealistic value of one for the scavenging efficiency. In addition the three-zone model gives improved detailing in the cylinder charge composition and the temperature distribution.

Shown in Fig. 1 are temperatures of the various components inside the combustion chamber. In brackets appear measured results from a similar engine [26].

The mass variation of the cylinder contents, the inflow, and the outflow with crank angle are shown in Fig. 4.

The variation of the fresh air charge retained in the cylinder and the air inflow with crank angle are shown in Fig. 5. At approximately 180 deg ATDC it can be noted that the fresh charge starts passing through to the exhaust manifold. At this point the model predicts the gas zone elimination.

The variation of the scavenging efficiency with delivery

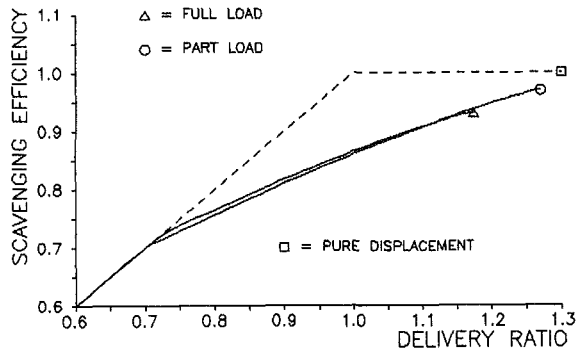


Fig. 6 Variation of scavenging efficiency with delivery ratio

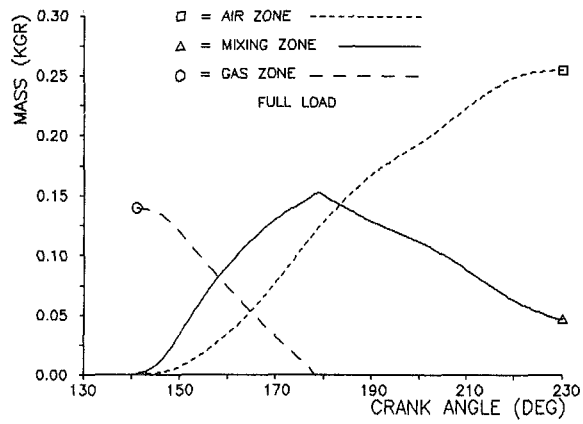


Fig. 7 Zone mass variation with crank angle

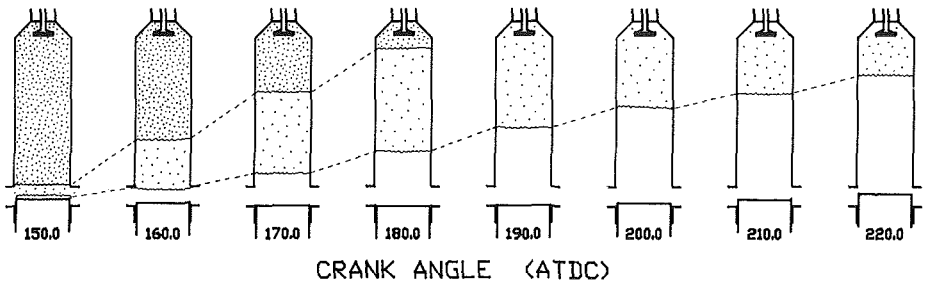


Fig. 8 Evolution of scavenging process

Downloaded 01 Jun 2010 to 171.66.16.87. Redistribution subject to ASME license or copyright; see http://www.asme.org/terms/Terms_Use.cfm

ratio (as defined in [7]) is shown in Fig. 6. The deviation from perfect scavenging, i.e., perfect displacement, can be noted.

The mass variation of the three zones with crank angle is shown in Fig. 7. The mass of the mixing zone decreases after the gas zone is exhausted; hence at the last stages of scavenging, the air zone occupies almost the whole of the cylinder volume.

The various phases of the scavenging process, as predicted by the model, are shown in Fig. 8.

Conclusions

A three-zone scavenging model for two-stroke uniflow engines was developed. Each of the three zones (air, gases, and mixing) is considered as a control volume and two time-varying coefficients are specified to describe the mixing of air and combustion gases to form the mixing zone. The influence of the flow mixing mechanisms, as obtained by experiments and multidimensional flow calculations, was implicitly included in the coefficients, by considering the scavenging process to be comprised of an initial phase with mixing dominated by jet growth mechanisms, followed by a second phase of swirl-driven turbulent diffusion.

When used in conjunction with an engine performance prediction code the model was found to offer improved definition of the combustion chamber component temperatures and improved prediction of engine performance, compared with a complete mixing model.

References

1 Watson, N., and Janota, M., *Turbocharging the Internal Combustion Engine*, Macmillan Publishers Ltd., London, 1984.

2 Kyrtatos, N., "Engine Simulation and Performance Prediction," Seminar: Applications of High Technology to Shipping, Paper No. 4, RINA + IMARE/NTUA, Athens, Sept. 1986.

3 Baudequin, F., and Rochelle, P., "Some Scavenging Models for Two-Stroke Engines," *Proc. Instn. Mech. Engr.*, Vol. 194, 1980, pp. 203–210.

4 Metz, J. R., Urben, A., and Steiger, A., "Contribution to Investigation of the Diesel Cycle With the Aid of Digital Computer," *Proc. Instn. Mech. Engrs.*, Vol. 182, Pt. 3L, 1967–1968.

5 Oka, T., and Ishihara, S., "Relation Between Scavenging Flow and Its Efficiency of Two-Stroke Engine," *J. Soc. Mech. Engrs.*, No. 69, 1971.

6 Mayashi, Y., and Meyer, W. E., "An Analytical Method for Optimising the Scavenging Process of Uniflow Two-Cycle Diesel Engines," SAE Paper No. 650447, 1965.

7 Streit, E. E., and Borman, G. L., "Mathematical Simulation of a Large Turbocharged Two-Stroke Diesel Engine," SAE Paper No. 710176, 1971.

8 Sher, E., "A New Practical Model for the Scavenging Process in a Two-Stroke Cycle Engine," SAE Paper No. 850085, 1985.

9 Sher, E., "Prediction of the Gas Exchange Performance in a Two-Stroke Cycle Engine," SAE Paper No. 850086, 1985.

10 Benson, R. S., "A New Gas Dynamic Model for the Gas Exchange Process in Two-Stroke Loop and Cross Scavenged Engines," *Int. J. Mech. Sci.*, Vol. 19, 1977, pp. 693–711.

11 Dedeoglu, N., "Scavenging Model Solves Problem in Gas Burning Engine," SAE Paper No. 710579, 1971.

12 Tsuneya, R., "Development of Mitsubishi VEC-L Type Engine With MET-SC Turbocharger," III HIMT Symposium, Athens, Mar. 1985.

13 Wiss, D., Metzen, G., and Borth, J., "Numerische Simulation von Strömungen and ihre Verifikation," *Sulzer Technische Rundschau*, No. 3, 1986.

14 Johns, R. J. R., "Multidimensional Modelling of Engine Processes: Progress and Prospects," *Proc. 15th CIMAC Congr.*, 1983.

15 Arcoumanis, C., and Whitelaw, J. H., "Fluid Mechanics of Internal Combustion Engines: A Review," *Intl. Symp. on Flow in I.C. Engines*, ASME FED-Vol. 28, 1985.

16 Diwakar, R., "Multidimensional Modelling of the Gas-Exchange Processes in a Uniflow-Scavenged Two-Stroke Diesel Engine," *Int. Symp. on Flow in I.C. Engines*, ASME FED-Vol. 28, 1985.

17 Rajaratnam, N., ed., *Turbulent Jets*, Elsevier Scientific Publishing Co., Amsterdam, 1976, Ch. 9, pp. 184–210.

18 Keffer, J. F., and Baines, W. D., "The Round Turbulent Jet in a Cross Wind," *J. Fluid Mech.*, Vol. 15, No. 4, 1963, pp. 481–496.

19 Ruggeri, R. S., Callaghan, E. E., and Bowden, D. T., "Penetration of Air Jets Issuing From Circular Square and Elliptical Orifices Directed Perpendicular to an Air Stream," NASA-TN-2019, Feb. 1950.

20 Kamotani, Y., and Greber, I., "Experiments on Confined Turbulent Jets in Cross Flow," NASA CR-2392, Mar. 1974.

21 Le Grives, E., "Mixing Process Induced by the Vorticity Associated With the Penetration of a Jet Into a Cross Flow," ASME JOURNAL OF ENGINEERING FOR POWER, Vol. 100, July 1978, pp. 465–475.

22 Bulaty, T., "Beitrag zur Berechnung des Wärmeüberganges insbesondere in langsgespülten, langhubigen Dieselmotoren," *MTZ Motortechnische Zeitschrift*, Vol. 46, No. 2, 1985, pp. 67–70.

23 Woschni, G., "A Universally Applicable Equation for the Instantaneous Heat Transfer Coefficient in Internal Combustion Engines," SAE Paper No. 790823, 1979.

24 Woschni, G., "Beitrag zum Problem des Wärmeüberganges im Verbrennungsmotor," *MTZ Motortechnische Zeitschrift*, Vol. 26, No. 4, 1965, pp. 128–133.

25 Zapf, H., "Untersuchung des Wärmeüberganges in einem Viertakt-Dieselmotor während der Ansug- und Ausschubperiode," *MAN Forschungsheft*, Vol. 14, 1968–1969, pp. 5–35.

26 "The L35MC Two-stroke Crosshead Diesel Engine," MAN-B & W Diesel, Report P.8308-081, Copenhagen, 1983.

27 Dent, J. C., and Derham, J. A., "Air Motion in a Four-Stroke Direct Injection Diesel Engine," *Proc. Inst. Mech. Engrs.*, Vol. 188, No. 21, 1974, pp. 269–280.

28 Tanabe, S., Hamamoto, Y., and Ohigashi, S., "Swirl in a Four-Stroke Cycle Engine Cylinder," *Bulletin of the JSME*, Vol. 21, 1978, pp. 287–294.

APPENDIX A

Equations of the Rate of Change of Temperature and Pressure

After applying the chain rule of calculus to equation (2), the following expressions are obtained for the rate of change of internal energy and gas constant with respect to time:

$$\dot{u} = \dot{T} \cdot \left(\frac{\partial u}{\partial T}\right)_F + \dot{F} \cdot \left(\frac{\partial u}{\partial F}\right)_T \tag{A1}$$

$$\dot{R} = \dot{F} \cdot \frac{\partial R}{\partial F} \tag{A2}$$

The energy equation for the i zone of the engine cylinder ($i = 1, \ldots, n$, $n = 2, 3$) can be written, according to equation (1) and equation (A1)

$$\sum_k \dot{Q}_k + \sum_j \dot{M}_j h_j - \dot{M}_i u_i - M_i \dot{F}_i \left(\frac{\partial u}{\partial F}\right)_{T_i}$$

$$= M_i \dot{T}_i \left(\frac{\partial u}{\partial T}\right)_{F_i} + p\dot{V}_i = C_i$$

where

$$C_i = M_i \dot{T}_i \left(\frac{\partial u}{\partial T}\right)_{F_i} + p\dot{V}_i = B_i \frac{\dot{T}_i}{T_i} + p\dot{V}_i \tag{A3}$$

$$B_i = T_i M_i \left(\frac{\partial u}{\partial T}\right)_{F_i} \tag{A4}$$

The differential form of the state equation is applied to each of the subvolumes of the cylinder control volume. Subtracting the equation for the j subvolume from the one for the i subvolume ($i \neq j$) we get, combining with equation (A2)

$$\frac{\dot{V}_i}{V_i} - \frac{\dot{V}_j}{V_j} = \frac{\dot{T}_i}{T_i} - \frac{\dot{T}_j}{T_j} + A_{ij}$$

where

$$A_{ij} = \frac{\dot{M}_i}{M_i} - \frac{\dot{M}_j}{M_j} + \frac{\dot{F}_i}{R_i}\left(\frac{\partial R}{\partial F}\right)_i - \frac{\dot{F}_j}{R_j}\left(\frac{\partial R}{\partial F}\right)_j$$

and substituting for $\dot{T}_j/T_j$ from equation (A3), we obtain after some manipulation

$$\dot{V}_j\left(\frac{1}{V_j} + \frac{p}{B_j}\right) = \frac{C_j}{B_j} + \frac{\dot{V}_i}{V_i} - A_{ij} - \frac{\dot{T}_i}{T_i} \tag{A5}$$

From equation (A3) the rate of change of volume is

Downloaded 01 Jun 2010 to 171.66.16.87. Redistribution subject to ASME license or copyright; see http://www.asme.org/terms/Terms_Use.cfm

$$\dot{V}_i = \frac{C_i}{p} - \frac{B_i}{p} \cdot \frac{\dot{T}_i}{T_i} \tag{A6}$$

The rate of change of the whole cylinder volume $\dot{V}_{tot}$ is equal to the summation of the rates of change of the n subvolumes of which the cylinder control volume consists

$$\dot{V}_{tot} = \sum_{k=1}^{n} \dot{V}_k = \dot{V}_i + \sum_{j} \dot{V}_j \qquad i, j = 1, \ldots, n, \quad j \neq i \tag{A7}$$

Substituting for $\dot{V}_i$ from equation (A6) and for $\dot{V}_j$ from equation (A5) we obtain an equation for the rate of change of temperature of any of the n subvolumes (zones) of which the cylinder consists.

This temperature rate of change does not depend explicitly on the pressure rate of change of the control volume under consideration

$$\dot{T}_i \left[\sum_{j}^{n} \frac{1}{\frac{1}{V_j} + \frac{p}{B_j}} \left(1 + \frac{B_i}{V_i p}\right) + \frac{B_i}{p} \right]$$

$$= T_i \left[\sum_{j}^{n} \frac{\frac{C_j}{B_j} + \frac{C_i}{V_i p} - A_{ij}}{\frac{1}{V_j} + \frac{p}{B_j}} - \dot{V}_{tot} + \frac{C_i}{p} \right] \tag{A8}$$

where $i, j = 1, \ldots, n, j \neq i$, and $n = 2, 3$.

Solving the differential form of the state equation for $\dot{p}$ we obtain

$$\dot{p} = p\left(\frac{\dot{R}_i}{R_i} + \frac{\dot{M}_i}{M_i} + \frac{\dot{T}_i}{T_i} - \frac{\dot{V}_i}{V_i}\right), \qquad i = 1, \ldots, n, \quad n = 2,3 \tag{A9}$$

The summation of equation (A9) applied to each of the n subvolumes that occupy the total cylinder volume, combined with equation (A2) and equation (A3), gives the rate of change of the spatially uniform cylinder pressure with respect to time

$$\dot{p} = \frac{p}{n} \sum_{i=1}^{n} \left[\frac{\dot{M}_i}{M_i} + \frac{\dot{F}_i}{R_i} \left(\frac{\vartheta R}{\vartheta F}\right)_i + \frac{\dot{T}_i}{T_i} \left(1 + \frac{B_i}{p V_i}\right) - \frac{C_i}{p V_i} \right] \tag{A10}$$

where $n = 2, 3$.

APPENDIX B

Swirl-Induced Mixing

The port induced swirl was calculated according to Dent and Derham [27] and Tanabe et al. [28], in which the rate of change of angular momentum of the cylinder contents during the induction period is

$$\frac{d}{dt}[I\omega] = \frac{m_{in}^2 \cdot \cos\varphi \cdot \cos\psi}{\rho \cdot A_{in}} \cdot \frac{D}{2} - \frac{\pi}{16} \cdot \rho^{0.8} \cdot \sigma^{0.2} \cdot D^{3.6} \cdot \omega^{1.8} \cdot [0.0761 S(\vartheta) + 2 \cdot 0.00895 D] \tag{B1}$$

The first term of the right-hand side of equation (B1) denotes the moment of momentum of the air entering the inlet ports [27], while the second denotes the torque due to the fluid–solid interface.

The piston crown and cylinder head are assumed to be flat disks, where the restraining torque acts at a mean radius

$$\bar{r} = \left(\frac{2}{5}\right)^{1/3} \cdot \frac{D}{2} \tag{B2}$$

at which the geometric mean shear stress $\bar{\tau}$ is obtained [28].

The friction coefficients $c_{f_{cyl}}$ and $c_{f_p} - c_{f_c}$ are evaluated similarly to the case of a flat plate, while the velocity terms are $\omega \cdot D/2$ and $2/3\ \omega \cdot D/2$, respectively [28], and the length terms are $D/2$ and $2/3\ D/2$, respectively.

The shear mixing rate between zones is estimated using the value of the boundary layer thickness computed according to Prandtl's (1-D) mixing length theory.

The free-stream velocity used corresponds to the difference in mean swirl velocity between the zones, which was calculated using equation (B1) in an appropriate form for each zone.

This mixing rate was found at least one order of magnitude smaller than that due to jet mixing; hence an equation of exponential decrease may be used for coefficients m_a and m_{g_2}.

Acknowledgments

The research work reported in this paper is partly supported by the Ministry of Industry/R + D Secretariat Contract No. 5955/EPE/479 monitored by Dr. E. Karabateas.

Engine simulation code development is also funded by Lloyd's Register of Shipping, London, and the "A. S. Onassis" Foundation, Liechtenstein, as part of the research project "Diesel Engine Design and Operation on Variable Quality Fuels."

Downloaded 01 Jun 2010 to 171.66.16.87. Redistribution subject to ASME license or copyright; see http://www.asme.org/terms/Terms_Use.cfm

Mathematical Modeling of the Scavenging Process in a Two-Stroke Diesel Engine

A. Carapanayotis
Advanced Industrial Mechanical Systems,
Ottawa, Ontario, Canada

M. Salcudean
Department of Mechanical Engineering,
University of British Columbia,
Vancouver, British Columbia, Canada

A multidimensional investigation of the scavenging process in the GM6V53T General Motors diesel engine has been carried out. This six-cylinder two-stroke engine features uniflow scavenging with four exhaust valves per cylinder, direct fuel injection, and turbocharging. The conservative equations of mass, energy, concentration, turbulence kinetic energy, and energy dissipation rate have been written in finite difference form and solved explicitly in time. The scavenging process has been studied by using a configuration of two exhaust valves as compared with the actual configuration, which has four exhaust valves. The computed flow characteristics and scavenging efficiency are very similar if the exhaust areas of the two different configurations are equivalent.

1 Introduction

The scavenging process in two-stroke uniflow scavenged engines takes place when the exhaust valves and inlet ports are open and the incoming fresh air replaces the combustion products. The process is very important because the available oxygen for combustion is strongly dependent on the scavenging efficiency, which is defined as the mass of air trapped in the cylinder divided by the mass of air required to fill the cylinder volume at air-box pressure and temperature. The scavenging efficiency is a function of the scavenging ratio, which is the mass of air supplied to the cylinder divided by the mass of air required to fill the cylinder volume at air-box pressure and temperature. The amount of air retained in the cylinder during scavenging is very difficult to calculate because it depends on the cylinder geometry (inlet ports, piston bowl, cylinder head shape, and exhaust valves), inlet port and exhaust valve timing, pressure and temperature in the cylinder, the exhaust manifold, and the air-box. Recently, a number of studies have been reported based on the multidimensional analysis of the scavenging process in two-stroke engines [1–3]. Diwakar [4] investigated the scavenging process in a two-stroke uniflow-scavenged engine by using the "CONCHAS SPRAY" two-dimensional axisymmetric code. The work concentrated on the effect of the swirl angle on the scavenging efficiency assuming the flow entered the cylinder horizontally. Carapanayotis and Salcudean [5] studied the scavenging process with a two-dimensional code and derived a scavenging efficiency–scavenging ratio equation, which was used in a thermodynamic model for engine performance predictions. Later, Salcudean and Carapanayotis [6, 7] studied the scavenging process using a three-dimensional model and compared the results with those of a two-dimensional model. They concluded that the two-dimensional model overestimated the recirculation zones in the cylinder close to the axis but the overall efficiency at the end of the scavenging process was similar. Diwakar [8] reached a similar conclusion, after investigating the scavenging process using the KIVA three-dimensional code [9, 10] in comparison with his earlier two-dimensional results. The three-dimensional effects were found to be significant mainly close to the valves. Based on this observation Carapanayotis and Salcudean [11] carried out an investigation of the effects of inflow parameters on the scavenging efficiency using the more economical two-dimensional code. They determined that the optimum swirl angle of the flow entering the cylinder was between 20 and 30 deg and the scavenging efficiency increased with the flow inclination.

The General Motors GM6V53T is a two-stroke uniflow scavenged engine with four overhead exhaust valves. In the present work the scavenging characteristics are studied assuming that the engine has two exhaust valves with the same exhaust valve area. The inlet ports are assumed to be the same as those in the stock engine. One should mention that the two-valve engine used in this analysis is not an existing one but rather a possible alternative design.

Physical Problem

The engine specifications and operating conditions are given in Table 1. The GM6V53T engine has 18 inlet ports, which are inclined at 22 deg to the radius and are located in the cylinder sleeve close to the Bottom Dead Center (BDC). Figure 1 shows the top view of the cylinder heads with four and two exhaust openings, respectively, which are considered in this study. In the model the following assumptions are made:

1 The available exhaust area in two configurations is the same. This was obtained assuming different valve lifts. The

Contributed by the Internal Combustion Engine Division and presented at the Eleventh Annual Energy-Sources Technology Conference and Exhibition, New Orleans, Louisiana, January 10–13, 1988. Manuscript received by the Internal Combustion Engine Division April 1987.

Copyright © 1988 by ASME
Downloaded 01 Jun 2010 to 171.66.16.87. Redistribution subject to ASME license or copyright; see http://www.asme.org/terms/Terms_Use.cfm

Table 1 Engine specifications

Manufacturer	Detroit Diesel Allison
Model	6V53T, Turbocharged
Compression ratio	17.5:1
Number of cylinders	6
Bore	98.4 mm
Stroke	114.3 mm
Piston displacement	5.22 ℓ
Number of valves per cylinder	4
Valve face radius	13.89 mm
Valve to cylinder center dist.	33.65 mm
Number of ports	18
Height of ports	21.33 mm
Width of ports	12.7 mm

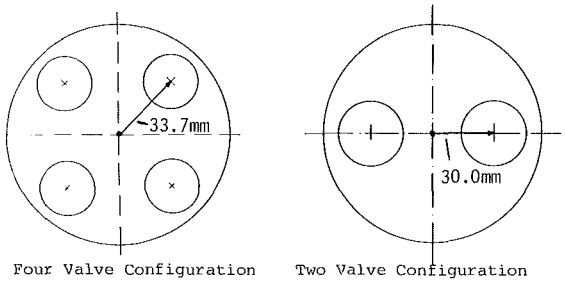


Fig. 1 Cylinder piston geometry

discharge coefficients for the two cases are assumed equal, which implies that the same quantity of air flows through the engine.

2 The piston is assumed to be stationary at the BDC and the flow area through the ports is assumed to change with time. This is carried out by utilizing a fine grid at the inlet ports and assuming that some cells behave as wall or port openings depending on the crank angle. The assumption that the piston is stationary is probably acceptable for engines with small piston displacement during scavenging.

3 In the multidimensional model in cylindrical grid is used; therefore, the piston bowl can not be modeled. Instead a cup-shaped piston is used with the volumes of the actual piston cavity and the one used in the model being equal. The effect of the piston shape on the scavenging efficiency is expected to be very small because the residual gases in the lower part of the cylinder are replaced by fresh air in an early stage of the scavenging process.

4 The valve is assumed to be a flat surface and is located at some distance from the cylinder head (valve lift). The valve shape is not circular because the model uses cylindrical coordinates (see Fig. 2). It is expected that this assumption will have a small effect of the scavenging characteristics; however this can be a source of loss of accuracy in the predictions. The outlet area is defined by the valve periphery and the cylinder head. This area changes with time by moving the valve location upward or downward. This motion is performed in finite steps using the grid nodal points. This explains the fine grid used close to the cylinder head. This modeling of the valve assures that: (*a*) The outlet area is very close to the actual engine exhaust area; therefore, the mass flow rate and the gas velocity through the exhaust valves are realistic; (*b*) the exhaust valve obstructs the cylinder gases from exiting the

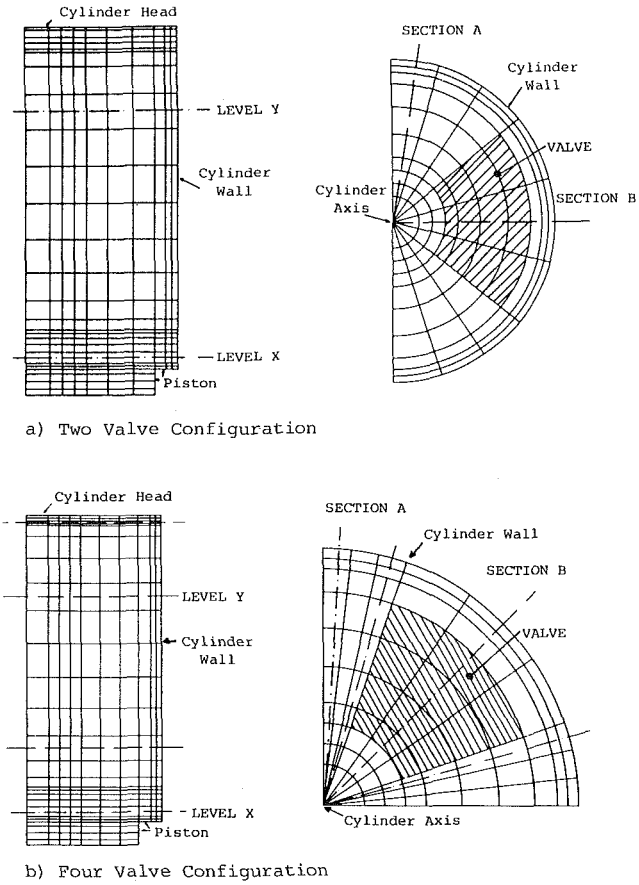


Fig. 2 Grid used in the computations

cylinder providing realistic outlet gas velocity. The modeling of the valves used here is quite different from the ones used by Diwakar [8]. He assumes the exhaust valve as an annular sector in the cylinder head with the sector area changing with time. He imposes the actual mass flow rate in the outlet openings using the compressible flow equations through an orifice, and he assumes the cylinder gases flow out of the cylinder axially.

5 The inlet and outlet flow conditions are established from a thermodynamic model developed by the authors [5]. In the thermodynamic model constant pressures are assumed in the air-box and in the exhaust manifold. The mass flow through the inlet ports and exhaust valves was calculated using the quasi-steady approach for isentropic compressible flow through an orifice. Back flow through the inlet ports and exhaust valves is allowed in the model. Diwakar [4, 8] also assumes constant air-box and exhaust manifold pressures and computes the mass flow rate in the multi-dimensional model using equations for compressible flow through an orifice. The latter approach needs an initial estimation of the cylinder gas pressure and temperature.

6 Initially a zero gas velocity field is assumed in the cylinder. The assumption of zero initial velocity will affect on-

Nomenclature

C = concentration
K = turbulence kinetic energy
P = pressure
Pr = Prandtl number
r = radial coordinate
Sc = Schmidt number
t = time
T = temperature
u = radial velocity
v = axial velocity
w = circumferential velocity
y = axial coordinate
ϵ = energy dissipation rate
μ = effective viscosity
η_l = fluid dynamic viscosity
ρ = density

Downloaded 01 Jun 2010 to 171.66.16.87. Redistribution subject to ASME license or copyright; see http://www.asme.org/terms/Terms_Use.cfm

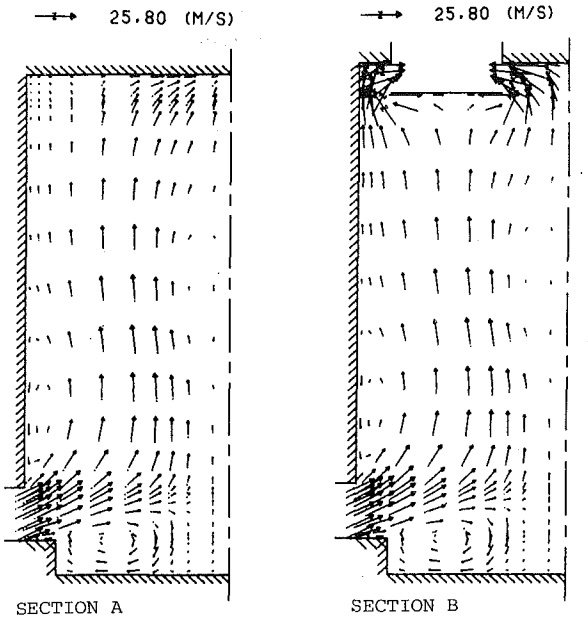


Fig. 3 Velocity patterns during scavenging at different cylinder sections at 178 deg ATDC

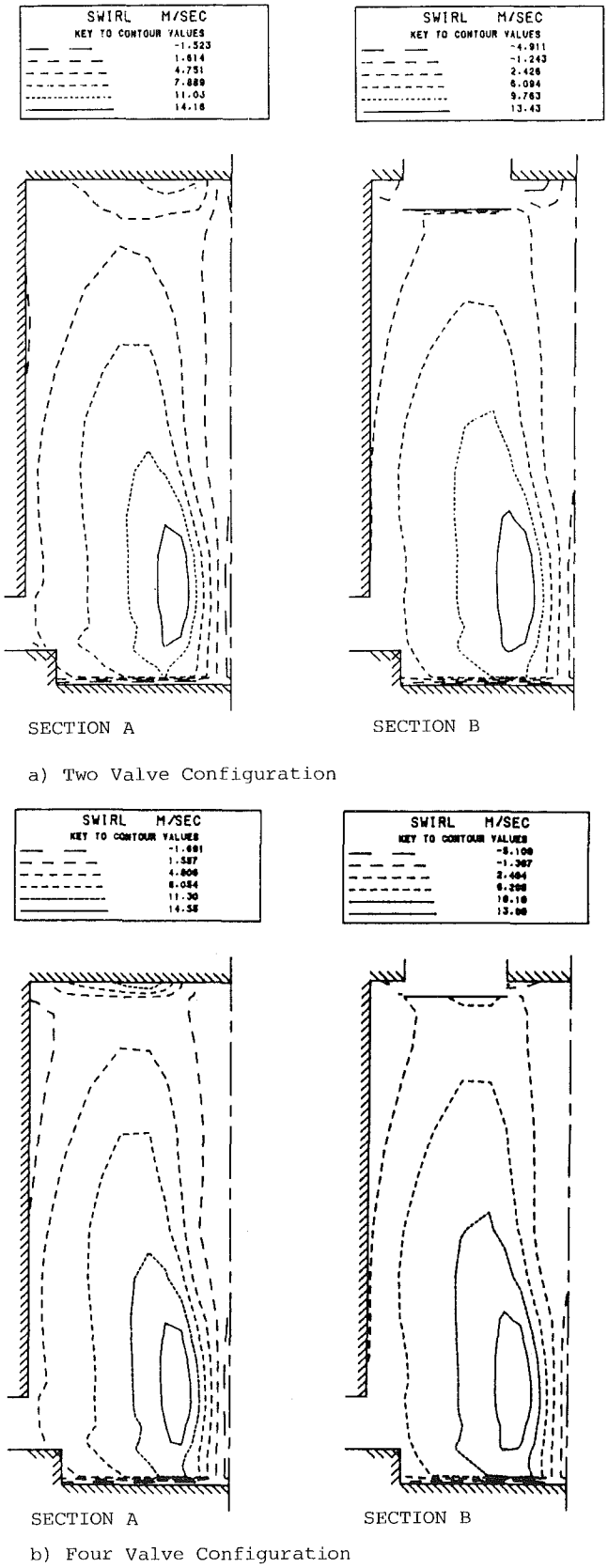


Fig. 4 Swirl velocity contours during scavenging at different cylinder sections at 178 deg ATDC

ly a short period at the beginning of the scavenging process. After that, the strong inflow will be dominant, eliminating the effect of the initial zero velocity. The cylinder residual gases are assumed to be at a temperature of 700.0 K, the air-box at 320.0 K, and the pressure to be 115.1 kPa [5]. The flow is assumed to enter the inlet ports with a 15 deg swirl angle to the radius and 20 deg to the horizontal as discussed in [5].

Mathematical Formulation

A transient three-dimensional code-developed by the authors [6, 7] is used in this study. The code is based on the Implicit Continuous-fluid Eulerian (ICE) numerical technique [12] for solving the continuity and momentum equations. The K-ϵ turbulence model is used for computing the effective viscosity [13]. The energy and mass species conservation equations are solved explicitly in time. In the conservation equations, the convective and diffusive terms are written in finite

Downloaded 01 Jun 2010 to 171.66.16.87. Redistribution subject to ASME license or copyright; see http://www.asme.org/terms/Terms_Use.cfm

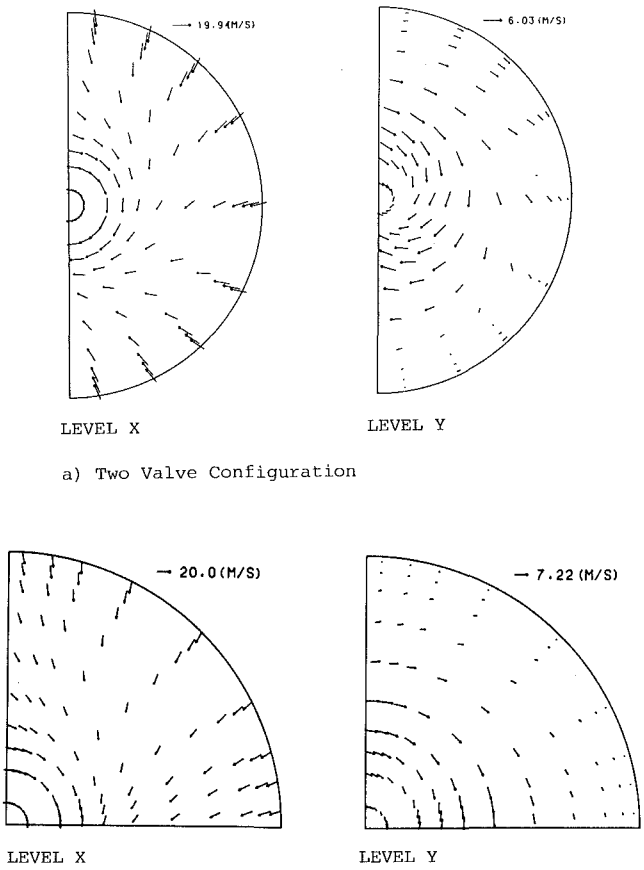
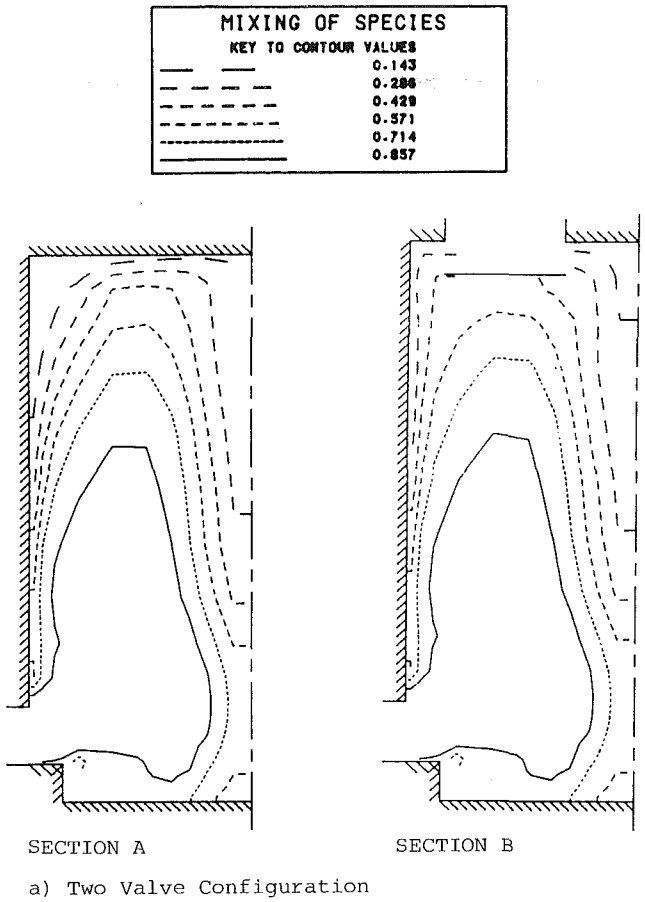


Fig. 5 Velocity patterns during scavenging at different cylinder levels at 178 deg ATDC



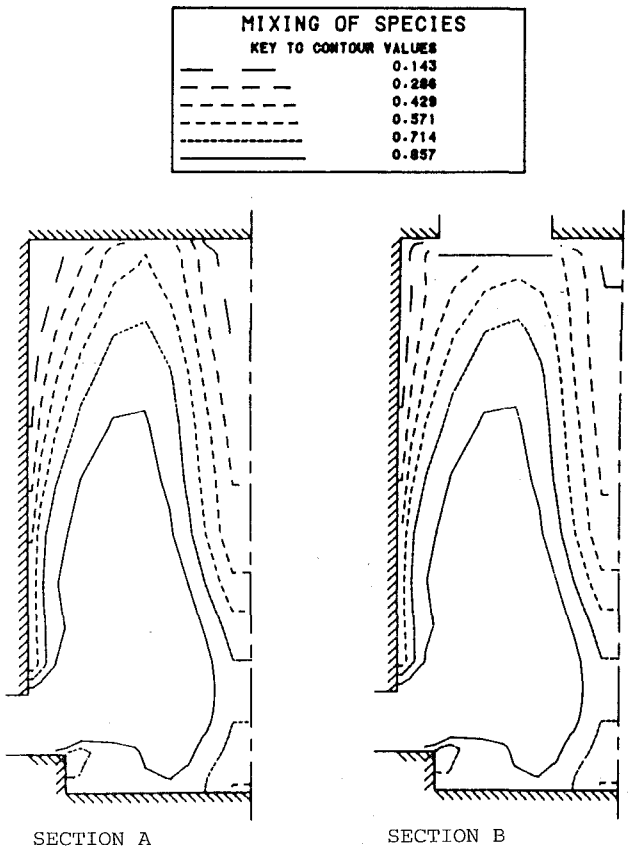


Fig. 6 Concentration contours during scavenging at different cylinder sections at 178 deg ATDC

difference form using the hybrid differencing scheme [14]. Some details of the model are presented in the appendix. The boundary treatments for the types of the boundaries encountered in the present problem are outline below.

Axis. At the axis of the cylinder, no transport occurs and the scalar and velocity gradients are set equal to zero.

Inlet. The flow velocity components, temperature, and concentration are specified. It is assumed that only fresh air is present at the inlet ports. The inlet area is modeled as described earlier.

Outlet. The outlet area is between the valve surface and the cylinder head. The area changes because of the valve motion during scavenging. This motion is performed in finite steps and this explains the fine grid used close to the cylinder head.

Wall. The cylinder wall is treated as impermeable. The tangential velocity at the wall is set equal to zero. The "wall function" method based on one-dimensional Couette flow yielding the universal logarithmic law is used to model the near-wall conditions. Expressons for the corresponding shear stresses have been implemented in the finite difference form of the momentum equations. Appropriate modifications based on the near-wall conditions are made to the turbulence kinetic energy equation and the turbulence generation term. The energy dissipation rate close to the wall is obtained from the assumption that the turbulence production rate is equal to the dissipation rate. The treatment of the energy equation is similar to the momentum equations.

Downloaded 01 Jun 2010 to 171.66.16.87. Redistribution subject to ASME license or copyright; see http://www.asme.org/terms/Terms_Use.cfm

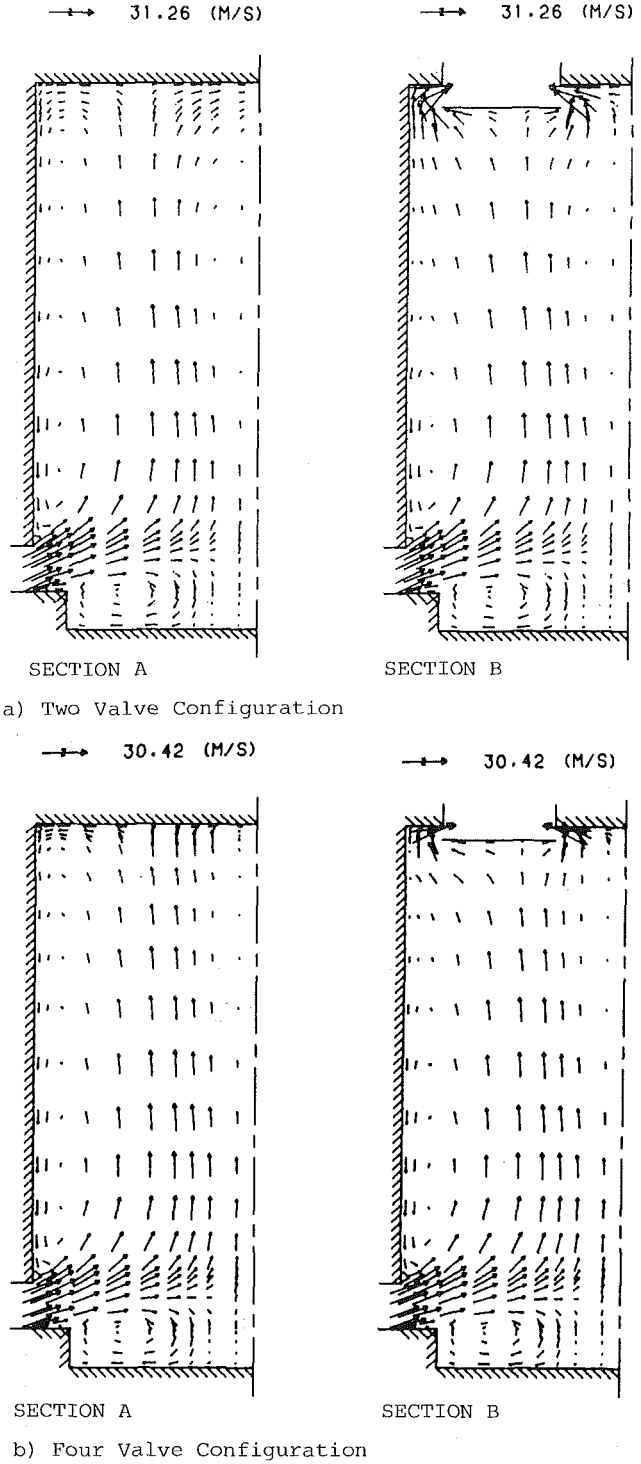


Fig. 7 Velocity patterns during scavenging at different cylinder sections at 205 deg ATDC

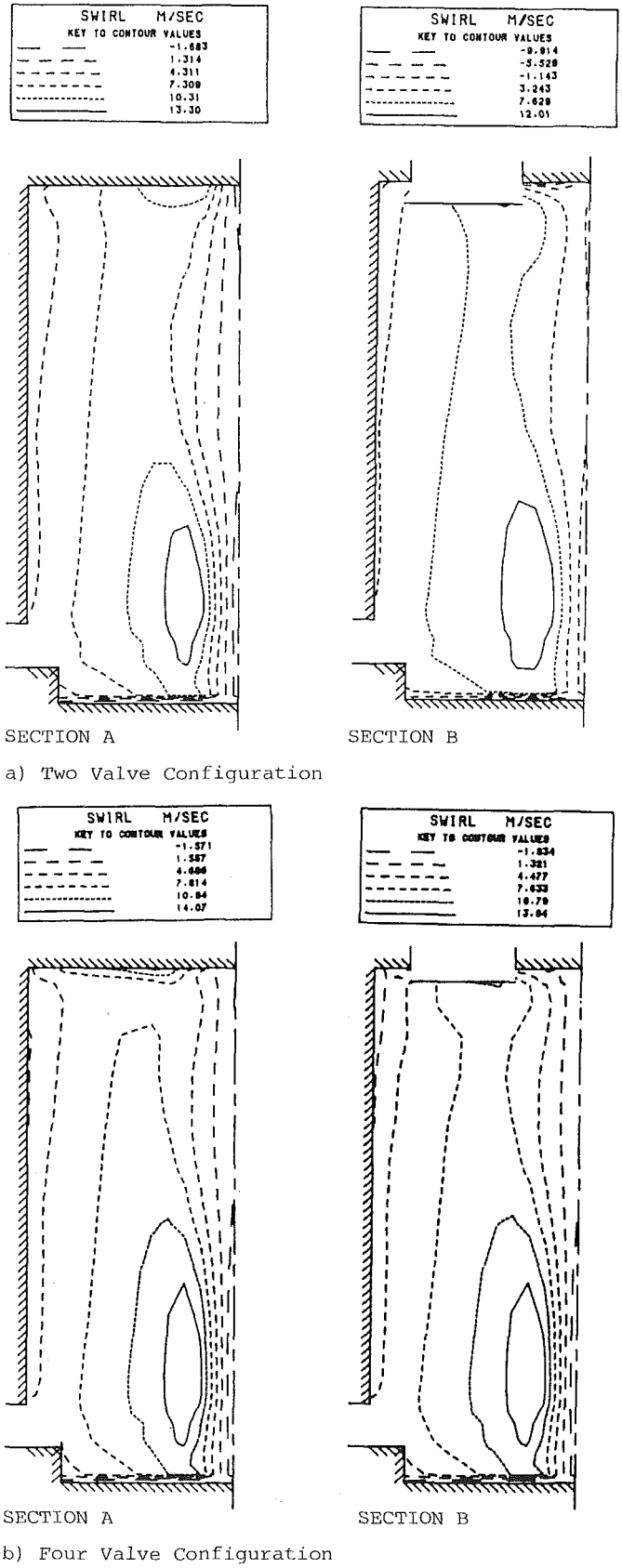
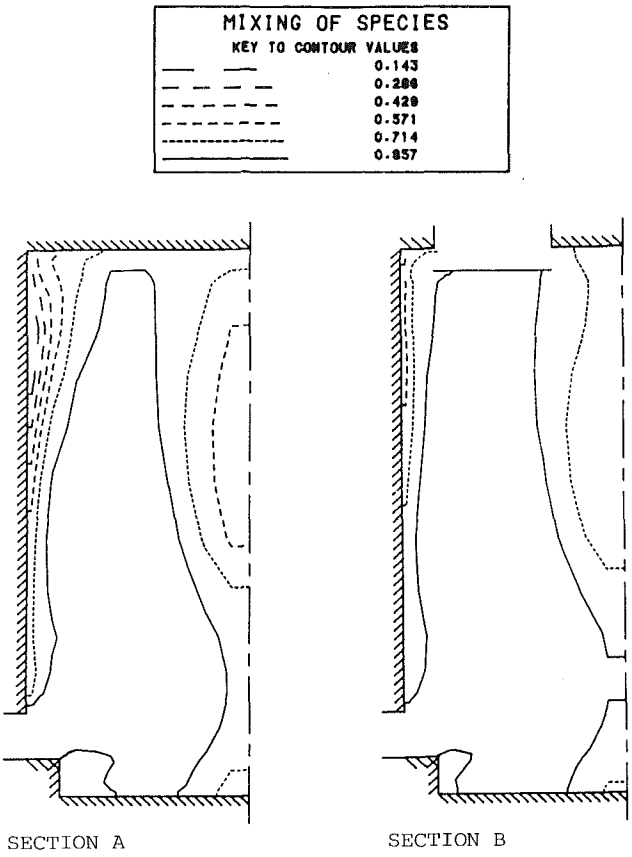


Fig. 8 Swirl velocity contours during scavenging at different cylinder sections at 205 deg ATDC

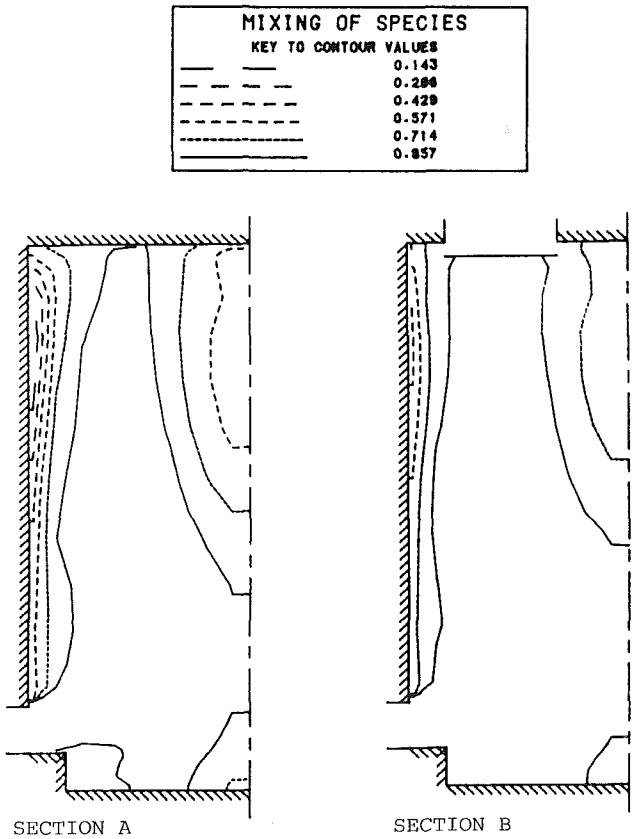
Discussion

The scavenging characteristics (velocity patterns, concentration, temperature, etc.) were found very similar during the whole scavenging process for both geometries. The velocity patterns at cylinder sections A and B at 178 deg. After Top Dead Center (ATDC) for the two cases are shown in Fig. 3. In both cases the flow fields appear to be similar. There are three recirculation zones in the cylinder. The first one is in the piston bowl (bowl vortex), the second close to the cylinder wall (wall vortex), and third close to the cylinder axis due to the swirl (back flow vortex). The flow is also quite similar in section B passing through the valve. The swirl velocity contours for sections A and B are shown in Fig. 4. In the upper part of

Downloaded 01 Jun 2010 to 171.66.16.87. Redistribution subject to ASME license or copyright; see http://www.asme.org/terms/Terms_Use.cfm



a) Two Valve Configuration



b) Four Valve Configuration

Fig. 9 Concentration contours during scavenging at different cylinder sections at 205 deg ATDC

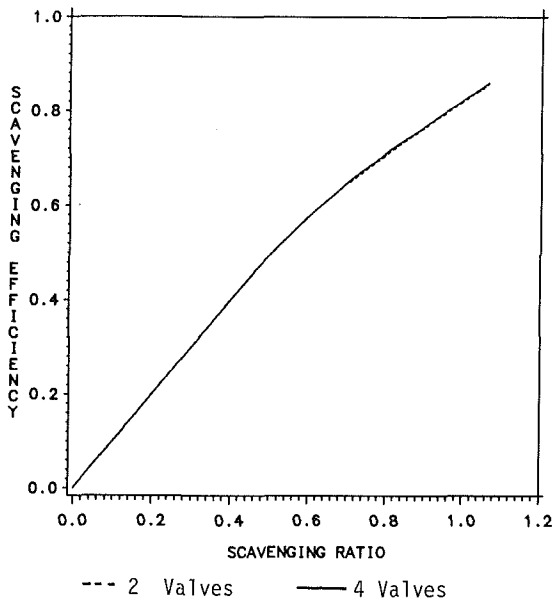


Fig. 10 Comparison of the scavenging efficiency computed using the two and four-valve configurations

the cylinder in section A the swirl velocities are quite different. In the four-valve configuration high swirl velocities are observed that are not present in the two valve configuration. The circumferential velocities in the two configurations can be seen in Fig. 5 for levels X and Y.

A better understanding can be gained from the air concentration contours. The concentration of the pure air is assumed to be equal to one and the concentration of the "pure" residual gases equal to zero. Therefore, low concentration contours indicate the presence of residual gases. The concentration contours for crank angle 178 ATDC for sections A and B are shown in Fig. 6. It can be seen that in section B the concentration contours are almost identical in both cases. In section A, in the two-valve geometry, the air has been advanced to the cylinder head slower as compared to the case with the four exhaust valves. This is because in the two-valve configuration section A is located farther away from the center of the valve than section A in the four-valve configuration. It should be mentioned that this difference is very small and does not affect the overall scavenging performance.

The situation is quite similar at 205 deg ATDC. Figure 7 shows the velocity patterns for sections A and B for the two configurations. The flow patterns are very similar with a slightly larger recirculation zone close to the cylinder axis in the case of the two exhaust valve cylinder head. The swirl velocities at cylinder sections A and B are shown in Fig. 8. The swirl velocity patterns are similar with some differences in the upper part of the cylinder section A. Figure 9 shows the concentration contours for the two sections, A and B. In the cylinder with four valves at the upper part, a slightly larger volume of the cylinder has been replaced by air. These small differences in the concentration contours do not affect the scavenging efficiency in the two configurations, which was found to be the same (see Fig. 10).

Diwakar did a sensitivity analysis of the exhaust outlet location on the scavenging efficiency [4]. The model he used was two-dimensional axisymmetric, and the exhaust outlet was modeled as an annulus split in the cylinder head. He changed the location of the annulus split keeping the valve area constant. He found that the scavenging efficiency was increasing as the annulus slit was moving close to the cylinder wall. This, we believe, is caused by the reduction of the wall vortex in size and in consequence the decrease of the amount of residual gas-

Downloaded 01 Jun 2010 to 171.66.16.87. Redistribution subject to ASME license or copyright; see http://www.asme.org/terms/Terms_Use.cfm

es trapped. However he concluded that the scavenging efficiency increase was small and the slit location influence was not significant.

Conclusion

The scavenging characteristics were studied for the General Motors GM6V53T engine with four versus two exhaust valves cylinder head. While some differences in flow, swirl, and concentration patterns were observed, the scavenging efficiencies were found to be practically the same for the two geometries.

Acknowledgments

The authors wish to acknowledge the financial support of the Department of National Defense of Canada and particularly Dr. C. L. Gardner (DRDA) for his continuing support.

References

1 Sher, E., "An Improved Gas Dynamics Model Simulating the Scavenging Process in a Two Stroke Cycle Engine," SAE Paper No. 800037, 1980.

2 Sung, N. W., and Patterson, D. J., "Air Motion in a Two Stroke Engine Cylinder—The Effects of the Exhaust Geometry," SAE Paper No. 820751, 1982.

3 O'Rourke, P., and Amsden, A., "Three Dimensional Numerical Simulation of the UPS-292 Stratified Charge Engine," SAE Paper No. 870597, 1987.

4 Diwakar, R., "Multidimensional Modeling of the Gas Exchange Processes in a Uniflow-Scavenged Two-Stroke Diesel Engine," presented at the Winter Annual Meeting of the ASME, Nov. 17-22, 1985.

5 Carapanayotis, A., and Salcudean, M., "Thermodynamic Simulation of a Two-Stroke Direct Injection Turbocharged Diesel Engine and Comparison With Experimental Measurements," ASME-JSME Thermal Engineering Joint Conference, Mar. 1987, pp. 209-217.

6 Carapanayotis, A., "Modeling of Fluid Flow and Heat Transfer Processes in an Engine," Ph.D. Thesis, University of Ottawa, Canada, 1986.

7 Salcudean, M., and Carapanayotis, A., "Multi-dimensional Study of the Scavenging Process in a Uniflow Scavenged Engine," *International Journal of Engineering Fluid Mechanics*, 1987, in press.

8 Diwakar, R., "Three-Dimensional Modeling of the In-Cylinder Gas Exchange Processes in a Uniflow-Scavenged Two-Stroke Engine," SAE Paper No. 870596, 1987.

9 Amsden, A. A., Ramshaw, J. D., O'Rourke, P. J., and Dukowicz, J. L., "KIVA: A Computer Program for Two- and Three-Dimensional Fluid Flows With Chemical Reactions and Fuel Sprays," Los Alamos National Laboratory Report LA-10245-MS, 1985.

10 Amsden, A. A., Ramshaw, J. D., Cloutman, L. D., and O'Rourke, P. J., "Improvements and Extensions to the KIVA Computer Program," Los Alamos National Laboratory Report LA-10534-MS, 1985.

11 Carapanayotis, A., and Salcudean, M., "The Effects of Inlet Velocity Orientation on the Scavenging Efficiency in a Uniflow Scavenged Engine," *Numerical Problems in Thermal Problems*, Proceedings of Fifth International Conference, Montreal, Canada, June 29-July 3, 1987, pp. 1622-1633.

12 Harlow, F. H., and Amsden, A. A., "A Numerical Fluid Dynamics Method for All Flow Speeds," *Journal of Computational Physics*, Vol. 8, 1971, pp. 197-213.

13 Launder, B. E., and Spalding, D. B., "The Numerical Computation of Turbulent Flows," *Comp. Meth. in Applied Mech. and Eng.*, Vol. 3, 1972, pp. 269-289.

14 Spalding, D. B., "A Novel Finite Difference Formulation for the Differential Expressions Involving Both First and Second Derivatives," *International Journal for Numerical Methods in Engineering*, Vol. 4, 1972, pp. 551-559.

15 Serag-Eldin, M. A., and Spalding, D. B., "A Computational Procedure for Three-Dimensional Recirculating Flows Inside Can Combustors," *Numerical Methods in Heat Transfer*, Wiley, New York, 1981.

APPENDIX

The governing differential equations for nonreacting flows are those for the conservation of mass, momentum, energy, and species. For three-dimensional flows these equations are written as follows:

Mass Conservation Equation

$$\frac{\partial \rho}{\partial t}+\frac{1}{r}\frac{\partial}{\partial r}(\rho r u)+\frac{\partial}{\partial y}(\rho v)+\frac{1}{r}\frac{\partial}{\partial \theta}(\rho w)=0 \tag{1}$$

Momentum Conservation Equations

r component

$$\begin{aligned}\frac{\partial}{\partial t}(\rho u)+\frac{1}{r}\frac{\partial}{\partial r}(\rho r u u)+\frac{\partial}{\partial y}(\rho v u)+\frac{1}{r}\frac{\partial}{\partial \theta}(\rho w u=\\ -\frac{\partial P}{\partial r}+\frac{1}{r}\frac{\partial}{\partial \theta}\left(\mu\frac{1}{r}\frac{\partial u}{\partial \theta}\right)+\frac{\partial}{\partial y}\left(\frac{\partial u}{\partial y}\right)\\ +\frac{2}{r}\frac{\partial}{\partial r}\left(\mu r\frac{\partial u}{\partial r}\right)+\frac{\partial}{\partial y}\left(\mu\frac{\partial v}{\partial r}\right)\\ +\frac{1}{r}\frac{\partial}{\partial \theta}\left(r\mu\frac{\partial}{\partial}\frac{w}{r}\right)+\frac{2\mu}{r^2}\frac{\partial w}{\partial \theta}-\frac{2\mu u}{r^2}+\frac{\rho w w}{r}\end{aligned} \tag{2}$$

y component

$$\begin{aligned}\frac{\partial}{\partial t}(\rho v)+\frac{1}{r}\frac{\partial}{\partial r}(\rho r u v)+\frac{\partial}{\partial y}(\rho v v)+\frac{1}{r}\frac{\partial}{\partial \theta}(\rho w v)=\\ -\frac{\partial P}{\partial y}+\frac{1}{r}\frac{\partial}{\partial \theta}\left(\mu\frac{1}{r}\frac{\partial v}{\partial \theta}\right)\\ +2\frac{\partial}{\partial y}\left(\frac{\partial v}{\partial y}\right)+\frac{1}{r}\frac{\partial}{\partial r}\left(\mu r\frac{\partial v}{\partial r}\right)\\ +\frac{1}{r}\frac{\partial}{\partial r}\left(\mu r\frac{\partial u}{\partial y}\right)+\frac{1}{r}\frac{\partial}{\partial \theta}\left(\mu\frac{\partial w}{\partial y}\right)\end{aligned} \tag{3}$$

θ component

$$\begin{aligned}\frac{\partial}{\partial t}(\rho w)+\frac{1}{r}\frac{\partial}{\partial r}(\rho r u w)+\frac{\partial}{\partial y}(\rho v w)+\frac{1}{r}\frac{\partial}{\partial \theta}(\rho w w)=\\ -\frac{1}{r}\frac{\partial P}{\partial \theta}+\frac{1}{r}\frac{\partial}{\partial r}\left(\mu r\frac{\partial w}{\partial r}\right)+\frac{\partial}{\partial y}\left(\mu\frac{\partial w}{\partial y}\right)\\ +\frac{2}{r}\frac{\partial}{\partial \theta}\left(\mu\frac{1}{r}\frac{\partial w}{\partial \theta}\right)\\ -\frac{\rho u w}{r}+\frac{\mu}{r}\frac{\partial w}{\partial r}+\frac{1}{r^2}\frac{\partial}{\partial r}\left(\mu r\frac{\partial u}{\partial \theta}\right)-\frac{1}{r^2}\frac{\partial}{\partial r}(\mu r w)\\ +\frac{2}{r}\frac{\partial}{\partial \theta}\left(\mu\frac{u}{r}\right)+\frac{\partial}{\partial y}\left(\mu\frac{1}{r}\frac{\partial v}{\partial \theta}\right)\end{aligned} \tag{4}$$

Energy Conservation Equation

$$\begin{aligned}\frac{\partial}{\partial t}(\rho T)+\frac{1}{r}\frac{\partial}{\partial r}(\rho r u T)+\frac{\partial}{\partial y}(\rho v T)+\frac{1}{r}\frac{\partial}{\partial \theta}(\rho w T)\\ =\frac{1}{r}\frac{\partial}{\partial r}\left(r\frac{\mu}{\mathrm{Pr}}\frac{\partial T}{\partial r}\right)\frac{\partial}{\partial y}\left(\frac{\mu}{Pr}\frac{\partial T}{\partial y}\right)\\ +\frac{1}{r}\frac{\partial}{\partial \theta}\left(\frac{\mu}{Pr}\frac{1}{r}\frac{\partial T}{\partial \theta}\right)\end{aligned} \tag{5}$$

Downloaded 01 Jun 2010 to 171.66.16.87. Redistribution subject to ASME license or copyright; see http://www.asme.org/terms/Terms_Use.cfm

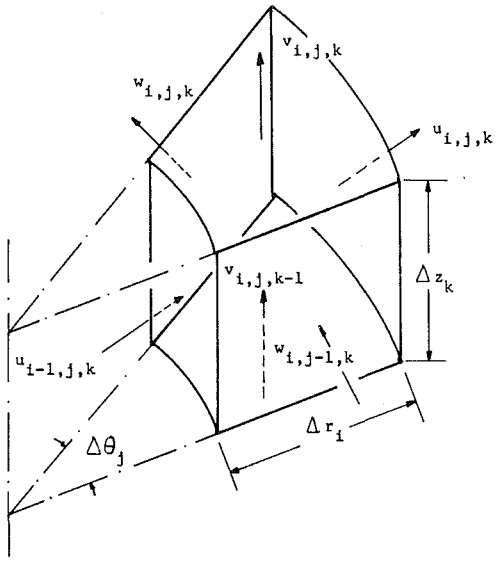


Fig. 11 Typical cell used in the computations

Species Conservation Equation

$$\frac{\partial}{\partial t}(\rho C)+\frac{1}{r}\frac{\partial}{\partial r}(\rho ruC)+\frac{\partial}{\partial y}(\rho vC)+\frac{1}{r}\frac{\partial}{\partial\theta}(\rho wC)$$
$$=\frac{1}{r}\frac{\partial}{\partial r}\left(r\frac{\mu}{\mathrm{Sc}}\frac{\partial C}{\partial r}\right)\frac{\partial}{\partial y}\left(\frac{\mu}{\mathrm{Sc}}\frac{\partial C}{\partial y}\right)$$
$$+\frac{1}{r}\frac{\partial}{\partial\theta}\left(\frac{\mu}{\mathrm{Sc}}\frac{1}{r}\frac{\partial C}{\partial\theta}\right) \tag{6}$$

The turbulence effects are modeled using the K-ϵ model. The conservation equation of the turbulent kinetic energy and turbulence dissipation rate are written as follows:

Turbulent Kinetic Energy Equation

$$\frac{\partial}{\partial t}(\rho K)+\frac{1}{r}\frac{\partial}{\partial r}(\rho ruK)+\frac{\partial}{\partial y}(\rho vK)+\frac{1}{r}\frac{\partial}{\partial\theta}(\rho wK)$$
$$=\frac{1}{r}\frac{\partial}{\partial r}\left(\frac{\mu}{S_k}r\frac{\partial K}{\partial r}\right)\frac{1}{r}\frac{\partial}{\partial\theta}\left(\frac{\mu}{S_k}\frac{1}{r}\frac{\partial K}{\partial\theta}\right)$$
$$+\frac{\partial}{\partial y}\left(\frac{\mu}{S_k}\frac{\partial K}{\partial y}\right)+\rho\epsilon C_d+G \tag{7}$$

G is the turbulence generation and is written as:

$$G=\mu\left[2\left(\left(\frac{\partial v}{\partial y}\right)^2+\left(\frac{\partial u}{\partial r}\right)^2+\left(\frac{1}{r}\left(\frac{\partial w}{\partial\theta}+\frac{u}{r}\right)^2\right)\right.\right.$$
$$+\left(\frac{\partial v}{\partial r}+\frac{\partial u}{\partial y}\right)^2$$
$$\left.\left.+\left(\frac{1}{r}\frac{\partial u}{\partial\theta}+r\frac{\partial}{\partial r}\left(\frac{w}{r}\right)\right)^2+\left(\frac{\partial w}{\partial y}+\frac{1}{r}\frac{\partial v}{\partial\theta}\right)^2\right]\right.$$
$$-\frac{2}{3}\nabla\cdot\mathbf{u}(\mu\nabla\cdot\mathbf{u}+\rho K) \tag{8}$$

where

$$\nabla\cdot\mathbf{u}=\frac{1}{r}\frac{\partial}{\partial r}(ru)+\frac{\partial v}{\partial y}+\frac{1}{r}\frac{\partial w}{\partial\theta}$$

Energy Dissipation Rate Equation

$$\frac{\partial}{\partial t}(\rho\epsilon)+\frac{1}{r}\frac{\partial}{\partial y}(\rho ru\epsilon)+\frac{2}{\partial y}(\rho v\epsilon)+\frac{1}{r}\frac{\partial}{\partial\theta}(\rho w\epsilon)$$
$$=\frac{1}{r}\frac{\partial}{\partial r}\left(\frac{\mu}{S_e}r\frac{\partial\epsilon}{\partial r}\right)\frac{1}{r}\frac{\partial}{\partial\theta}\left(\frac{\mu}{S_e}\frac{1}{r}\frac{\partial\epsilon}{\partial\theta}\right)$$
$$+\frac{\partial}{\partial y}\left(\frac{\mu}{S_e}\frac{\partial\epsilon}{\partial y}\right)+\epsilon(C_1G-C_2\rho\epsilon)/K \tag{9}$$

The effective viscosity is calculated from the turbulent kinetic energy and dissipation rate as follows:

$$\mu=\mu_l+C_\mu\rho K^2/\epsilon \tag{10}$$

where S_k, S_e, C_d, C_1, and C_2 are constants given in Table 2.

A numerical method based on the Implicit Continuous-fluid Eulerian (ICE) [12] technique is used for solving the momentum and continuity equations (equations (1)-(4)). Equations for energy, turbulence kinetic energy, domain is divided into a finite grid. The governing differential equations are discretized by finite differences and the resultant algebraic equations are solved for every grid point of the domain. This solution procedure is repeated in time. Figure 11 shows a typical cell in the cylindrical coordinate system used in the computations. The velocities are defined at the cell faces while the scalar quantities are defined at the cell center. The computations feature a nonuniform grid spacing, therefore a weighted average procedure is used to compute quanities in locations different from those where they are defined. The hybrid differencing scheme is used for writing the convective and diffusive terms in finite difference form. For example, the convective and diffusive terms in the momentum equation in the radial direction

$$CUX=\frac{1}{r}\frac{\partial}{\partial r}(\rho ruu)-\frac{1}{r}\frac{\partial}{\partial r}\left(\mu r\frac{\partial u}{\partial r}\right)$$

are written in finite differnce form as follows:

$$CUX=\frac{r_{i+1}COEFE-r_iCOEFW}{r_{i+\frac{1}{2}}(\Delta r_i+\Delta r_{i+1})}$$

where

$$COEFE=\rho_{i+1,j,k}U_R[u_{i,j,k}+u_{i+1,j,k}$$
$$+SIGN(\mathrm{Pe})(u_{i,j,k}-u_{i+,j,k})]\text{ for }|\mathrm{Pe}|\geq 2$$

or

$$COEFE=2\rho_{i+1,j,k}U_RU_R-2\mu_{i+1,j,k}(u_{i+1,j,k}-u_{i,j,k})/\Delta r_{i+1}\text{ for }|\mathrm{Pe}|\leq 2$$

with

$\mathrm{Pe}=$ Peclet number $=\rho_{i+1,j,k}U_R\Delta r_{i+1}/\mu_{i+1,j,k}$

$UR=0.5(u_{i,j,k}+u_{i+1,j,k})$

$SIGN(\mathrm{Pe})$ is the algebraic sign of Pe

$$COEFW=\rho_{i,jk}U_C[u_{i,j,k}+u_{i-,j,k}+SIGN(P_w)(u_{i-1,j,k}-u_{i,j,k})]$$

for $|P_w|\geq 2$

or

$$COEFW=2\rho_{i,j,k}U_CU_C-2\mu_{i,j,k}(u_{i,j,k}-u_{i,j,k})/\Delta r_i\text{ for }|P_w|\leq 2$$

with

$P_w=\rho_{i,j,k}U_c\Delta r_i/\mu_{i,j,k}$

$U_C=0.5(u_{i,j,k}+u_{i-1,j,k})$

$SIGN(P_w)$ is the algebraic sign of P_w

Due to symmetry considerations only one quarter of the cylinder domain is studied for the case with four exhaust valves. In the case of the two valves, half of the cylinder domain is studied.

Downloaded 01 Jun 2010 to 171.66.16.87. Redistribution subject to ASME license or copyright; see http://www.asme.org/terms/Terms_Use.cfm

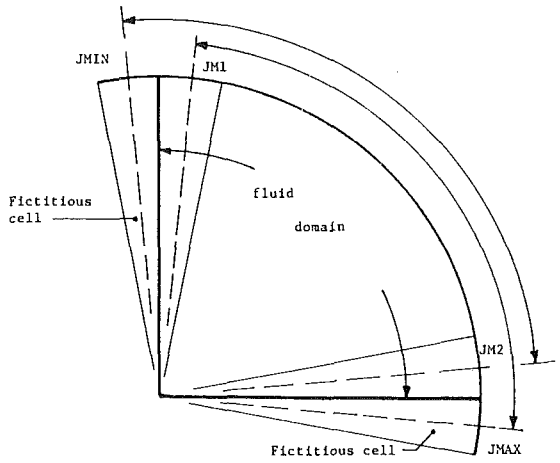


Fig. 12 Symmetry boundary conditions for the four valve geometry

The symmetry for the case with two exhaust valves is imposed as follows [15] (see Fig. 12):

Scalar (P, T, C, K, ϵ, and ρ)

$$S_{i,JMAX,k} = S_{i,JM1,k}$$
$$S_{i,JMIN,k} = S_{i,JM2,k}$$

Velocities

$$w_{i,JMAX,k} = w_{i,JM1,k}$$
$$w_{i,JMIN,k} = w_{i,JM2,k}$$
$$v_{i,JMAX,k} = v_{i,JM1,k}$$
$$v_{i,JMIN,k} = v_{i,JM2,k}$$
$$u_{i,JMAX,k} = u_{i,JM1,k}$$
$$u_{i,JMIN,k} = u_{i,JM2,k}$$

The grid used has twelve nodal points in the radial direction, eleven nodal points in the circumferential direction, and 28 nodal points in the axial direction. The calculation domain and the grid used for the computations are shown in Fig. 2.

Downloaded 01 Jun 2010 to 171.66.16.87. Redistribution subject to ASME license or copyright; see http://www.asme.org/terms/Terms_Use.cfm

The Matching of Diesel Engine to Exhaust Turbocharger—Improved Calculation Model at T-Junction

T. Morimune

N. Hirayama

Department of Mechanical Engineering,
Faculty of Technology,
Tokyo Metropolitan University,
Tokyo, Japan

The suitability of the analysis of the unsteady flow through the exhaust junction plays an important role in developing a computer program for matching a diesel engine to an exhaust turbocharger. This paper describes an improvement of the calculation procedure for computing the behavior of the unsteady gas flow at the exhaust junction. Measured values of pressure, temperature, and mass flow rate are compared with computer predictions using four different pipe junction computations: constant pressure model, momentum model, simplified model, and the improved exact model developed in this study. This comparison shows that the new technique gives the best agreement with the measured values, while the computer time required is twice as long. Under unsteady flow conditions the exhaust junction gives six types of flow configuration, and calculations indicate that only some of these types of flow dominate; the rest occur for only short intervals.

1 Introduction

Matching of a diesel engine and turbocharger usually depends on empirical techniques, and therefore requires a great deal of labor. To save on these expenses and time, it would be desirable to accomplish a practical and precise analysis for the evaluation of the performance of an engine–turbocharger system with consideration of unsteady gas flow phenomena.

The suitability of the analysis for the flow through a three-pipe junction plays an important role in developing the computer program for obtaining the maximum available power in the exhaust gases. Therefore, it is necessary to develop the program to be able to calculate how the presence of the junction affects the flow variables in each pipe at the point of the junction. These engine simulation computer programs can be readily adapted to assist in the design of exhaust systems for internal combustion engines.

The simplest approach, which is called "constant pressure model at the junction," described by Benson (1982a), Azuma et al. (1980), and Shimamoto et al. (1977), is to assume that at each time increment of calculation, the pressures in the ends of all the pipes next to the junction are equal. This procedure neglects the pressure changes across the junction.

Another "momentum model" proposed by Benson (1982a) is based on an empirical form of the momentum equation using the empirical coefficients obtained from steady flow tests. This model is, however, limited to applications involving an exceptional configuration. Recently, Bingham and Blair (1985) have proposed an improved momentum model for the three-pipe junction of a multicylinder engine.

We have already proposed two models (Morimune et al., 1982a, b) for the junction calculation; firstly, the exact model and, secondly, the simplified model for the junction. The results obtained from the former model are precise and agree well with the measurements. The exact model, however, has the disadvantageous point that the computer time taken for convergence of the solution is enormous in the low-velocity region that includes reverse flow at the junction.

The latter has a weak point of neglecting the small reflected waves from the engine during the exhaust valve overlap. Three-way exhaust pipe junctions are considered to be either bend or straight at each time increment of computation in the simplified model.

In the present paper, "the improved exact model" has been proposed in order to correct these defects. In the improved calculation procedure, the momentum model is adopted when it is difficult converge the solutions by using the exact model. This new procedure considerably reduces the computer time compared to that of the exact model. The results of calculation using four calculation models are compared with measured diagrams of pressure, temperature, and mass flow in a practical four-stroke diesel engine. The results of the improved exact model have shown the best correlation between measured and predicted pressures, temperatures, and mass flow.

2 Engine and Engine Test Bed

2.1 Engine. The engine used in the investigation is a turbocharged six-cylinder four-stroke diesel engine (bore × stroke = 250 × 320 mm). A turbocharger receives the exhaust gas from two groups of cylinders, 1 to 3 and 4 to 6, in two entries as shown in Fig. 1. The exhaust gas flow from cylinders E1, E2, and E3 (firing order E1–E3–E2) was mainly studied.

2.2 Transient Pressure and Temperature Measurement. Transient pressure ($P1$ to $P8$) and cylinder pressure

Contributed by the Internal Combustion Engine Division and presented at the Eleventh Annual Energy-Sources Technology Conference and Exhibition, New Orleans, Louisiana, January 10–13, 1988. Manuscript received by the Internal Combustion Engine Division April 1987.

Copyright © 1988 by ASME
Downloaded 01 Jun 2010 to 171.66.16.87. Redistribution subject to ASME license or copyright; see http://www.asme.org/terms/Terms_Use.cfm

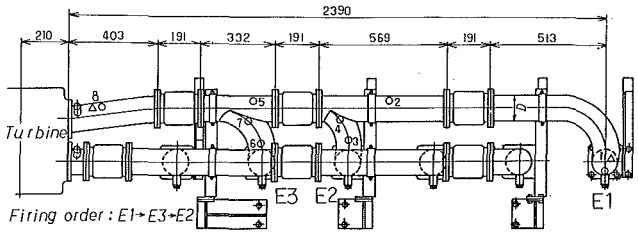


Fig. 1 Exhaust pipe configurations of tested engine

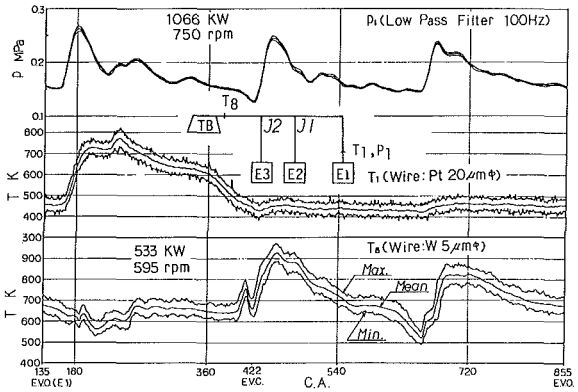


Fig. 2 The amount of scatter in measured values of some 100 cycles

P_{cyl} (E1) were measured by using water-cooled strain gage pressure transducers. Transient temperatures ($T1$, $T8$) were measured by means of fine-wire resistance thermometers (Morimune et al., 1982a) with tungsten wire ($\phi 5\mu$m) and platinum wire ($\phi 5$-μm, $\phi 20$-μm). All the pressure and temperature records were taken simultaneously. A twelve channel data recorder was used for this purpose. The physical locations of these transducers are illustrated in Fig. 1.

Since the exhaust gas pressures and temperatures vary from cycle to cycle due to differences in combustion a representative cycle would be the mean of some 50 or 100 cycles. Figure 2 indicates the amount of scatter in measured values of some 100 cycles. The differences between mean and extreme values are about ± 5 percent.

2.3 Test Program. Six series of tests were carried out at 441 ~ 1066 kW with engine speed 595 ~ 750 rpm.

3 Theory of Exhaust Gas Flow and Boundary Condition

The basic theory contribution to the development of the program has been previously described (Morimune et al., 1982a). The present paper gives the outlines of the theory and boundary conditions.

3.1 Basic Equations of Exhaust Gas Flow

$$\frac{\partial \rho A}{\partial t}+\frac{\partial \rho u A}{\partial l}=0 \tag{1}$$

$$\frac{\partial u}{\partial t}+u\frac{\partial u}{\partial l}=-\frac{1}{\rho}\frac{\partial p}{\partial l}+f \tag{2}$$

$$\frac{\partial s}{\partial t}+u\frac{\partial s}{\partial l}=-\frac{(qw+uf)}{T} \tag{3}$$

Equations (1)-(3) are transformed into nondimensional forms and can be solved by the computer mesh method (Benson et al., 1964) based on the method of characteristics.

3.2 Boundary Conditions Within Pipe Systems

3.2.1 Friction and Heat Transfer in Exhaust Pipe

$$f=-\frac{\lambda}{2}\frac{1}{D}u^2\frac{u}{|u|} \tag{4}$$

$$q_w=\frac{\alpha\pi Dl(T-T_w)}{(\pi/4)D^2 l\rho}=\frac{\lambda}{2D}C_p u(T-T_w) \tag{5}$$

where λ, α indicate the friction loss coefficient and coefficient of heat transfer, respectively.

3.2.2 Bend and Sudden Enlargement in Exhaust Pipe. Empirical formulas of losses for compressible flow through these pipe fittings have been proposed by Morimune et al. (1980a, b), and the entropy change Δs is formulated as a function of Mach number M

$$\Delta s=f(\mathrm{M}) \tag{6}$$

3.2.3 Combustion Chamber

$$\frac{dT}{T}+(\gamma-1)\left(\frac{dV}{V}-\frac{dG}{G}\right)-\frac{\gamma-1}{RT}dq_E=0 \tag{7}$$

where G, V, and R are, respectively, fluid mass, volume, and gas constant in the combustion chamber.

3.2.4 Inlet and Exhaust Valves. Mass flow rate through valves is written

$$G=CiA\sqrt{\Delta P} \tag{8}$$

where Ci is the flow coefficient of the inlet or exhaust valve and has been obtained from steady flow tests (Morimune et al., 1982c, 1983) using the real cylinder head of the diesel engine. Both the equation of continuity and the energy equation are adopted elsewhere for computing the flow through valves.

3.2.5 Exhaust Turbine. Correlated mass flow rate through the turbine is written

$$G\sqrt{T}/P=f(x) \tag{9}$$

where x denotes the turbine expansion pressure ratio.

Nomenclature

A = area, m^2
C_p = specific heat at constant pressure, J/kg K
D = exhaust pipe diameter, m
EE = exhaust energy, J
f = friction loss work, J/kg m
l = distance coordinate, m
P, p = pressure, N/m^2
q = rate of heat transfer, J/kg s, J/kg
S, s = entropy, J/kg K
T = temperature, K
t = time, s
u = velocity, m/s
γ = ratio of specific heats
ρ = density, kg/m^3

Subscripts

A, B, C = location of the ends of each pipe
st = reference condition
w = wall surface

Downloaded 01 Jun 2010 to 171.66.16.87. Redistribution subject to ASME license or copyright; see http://www.asme.org/terms/Terms_Use.cfm

Table 1 Junction models and results of computation

Model No.	Junction model	Flow type	Equation or calculation procedure at junction	Calculated results 1*	2*	3*
1	Costant pressure model	① B, C, A	$P_A = P_B = P_C$	121	-1.8	6.7
		⑤ B, C, A	$P_A = P_B = P_C$			
2	Momentum model	① B, C, A	① $P_A - P_B = C_1(\rho_B u_B^2 - \rho_A u_A^2)$, $P_B - P_C = C_2(\rho_C u_C^2)$	136	2.2	8.8
		⑤ B, C, A	⑤ $P_A - P_B = C_3(\rho_B u_B^2 - \rho_A u_A^2)$, $P_A - P_C = 0$			
3	Simplified model	① B, C, A	A computer program for a multi-cylinder engine consists of superimposition of a single-cylinder program.	117	8.6	14.8
		⑤ B, C, A	TB, E3, E2, E1 — Firing order E1 → E3 → E2			
4	Improved exact model	① B, C, A	$S_B = S_A + K_{AB}\frac{u_A^2}{2T_A}$, $S_C = S_A + K_{AC}\frac{u_A^2}{2T_A}$ K : Loss coefficient for dividing flow (Ito and Imai ,1973)	297	0 EEst	6.3
		⑤ B, C, A	$S_B = \frac{G_A}{G_B}(S_A + K_{AB}\frac{u_A^2}{2T_A} + C_p \mathrm{Ln}\frac{T_B}{T_A}) + \frac{G_C}{G_B}(S_C + K_{CB}\frac{u_C^2}{2T_C} + C_p \mathrm{Ln}\frac{T_B}{T_C})$, $P_A = P_C$ K :Loss coefficient for joining flow (Morimune et al., 1981, 1987)			

1* Computer time for each revolution (seconds)
2* Exhaust energy (EEst - EE) / EEst %
3* Mass flow rate (Gex - G) / Gex % , Gex=measured mass flow rate

Exhaust gas energy EE is defined as

$$EE = \int_{1\text{cycle}} G(h_0 - h_1)dt \tag{10}$$

where h_0 and h_1 are the enthalpy of the flow at the turbine inlet and outlet, respectively.

4 Improved Calculations Procedure for Junction

Four different calculation models for junction are shown in Table 1. Calculation procedure No. 1 in Table 1 is the simplest approach, called the constant pressure model, and assumes that at each time step of calculation the pressures in the ends of pipes next to the junction are equal, $P_A = P_B = P_C$. Procedure No. 2 is the momentum model proposed by Benson (1982a), based on an empirical form of the momentum equation using empirical coefficients $C1$, $C2$, $C3$; for example, $P_A - P_B = C1\ (\rho_B u_B{}^2 - \rho_A u_A^2)$, $P_B - P_C = C2(\rho_C u_C^2)$. The simplest model No. 3 proposed by authors (1982a) is to assume that a computer program for a multicylinder engine consists of the superposition of a single-cylinder program. This procedure neglects the effects of other cylinders (shown by broken line in the figure in Table 1). The speical feature of the exact method proposed by the authors (1982a) is that the evaluation of the entropy change caused by the friction loss and by the temperature difference between two pipes in which the flow is toward the junction becomes possible for joining flow.

There are six possible flow configurations at the three-pipe junction including the dividing and the joining flow as shown in the upper part of Fig. 3. In Table 1, typical flow type is illustrated. Both the equation of continuity and the energy equation are employed in order to obtain the flow variables at the junction, besides the equation in this Table. Calculation procedure No. 4 is a new model proposed in the present study for calculating the unsteady gas flow at exhaust junction.

Firstly, the flow equations based on the exact model (Morimune et al., 1982b) at the **T**-junction are solved by the numerical techniques at each time step, and if the solutions of the continuity and energy equations are not convergent mathematically, then the flow properties at the junction are computed by using the momentum model, and in the next step, the exact model is again used for the computation of flow variables.

As an example for flow type 1 (dividing flow) the energy and continuity equations are written

$$\frac{\gamma}{\gamma-1}\frac{p}{\rho} + \frac{u^2}{2} = E, \quad E_A = E_B = E_C \tag{11}$$

$$\rho_A u_A = \rho_B u_B + \rho_C u_C \tag{12}$$

The values of the judgment in convergence are defined as follows:

$$\Delta E_1 = |E_A - E_C|/E_A, \quad \Delta E_2 = |E_B - E_C|/E_A \tag{13}$$

$$\Delta G = |\rho_A u_A - \rho_B u_B - \rho_C u_C|/\rho_A u_A \tag{14}$$

The momentum model is employed if the values $\Delta E_{1,2}$ and ΔG do not converge to the standard value of judgment δs (taken as 0.5 percent in this study) in each time step using Newton-Raphson method. The momentum model is often adopted when the flow velocities in each pipe near the junction approximate zero, particularly at the time when the flow type changes. The disadvantages of the exact model can be avoided by using this improvement of the calculation. Joining flow loss coefficients under the unsteady flow and compressible flow have been obtained by authors (Morimune et al., 1981, 1987) and are applied to the improved exact model.

5 Comparison of Calculated and Experimental Results (800 kW, 681 rpm)

Figures 3 and 4 show the comparison between measurements and calculations for four different models of the **T**-junction, while the same initial conditions of computation are employed for four models. The flow type-time histories at exhaust junctions J1, J2 are illustrated in Fig. 3. Computing time, exhaust energy EE defined by equation (10), and mass flow are indicated in Table 1.

For the calculations described in this study the FACOM M 180 II computer time for each revolution was about 2 to 5 min, as shown in Table 1. In Figs. 3 and 4 each calculation corresponds to the fourth revolution.

The main results are summarized as follows:

Downloaded 01 Jun 2010 to 171.66.16.87. Redistribution subject to ASME license or copyright; see http://www.asme.org/terms/Terms_Use.cfm

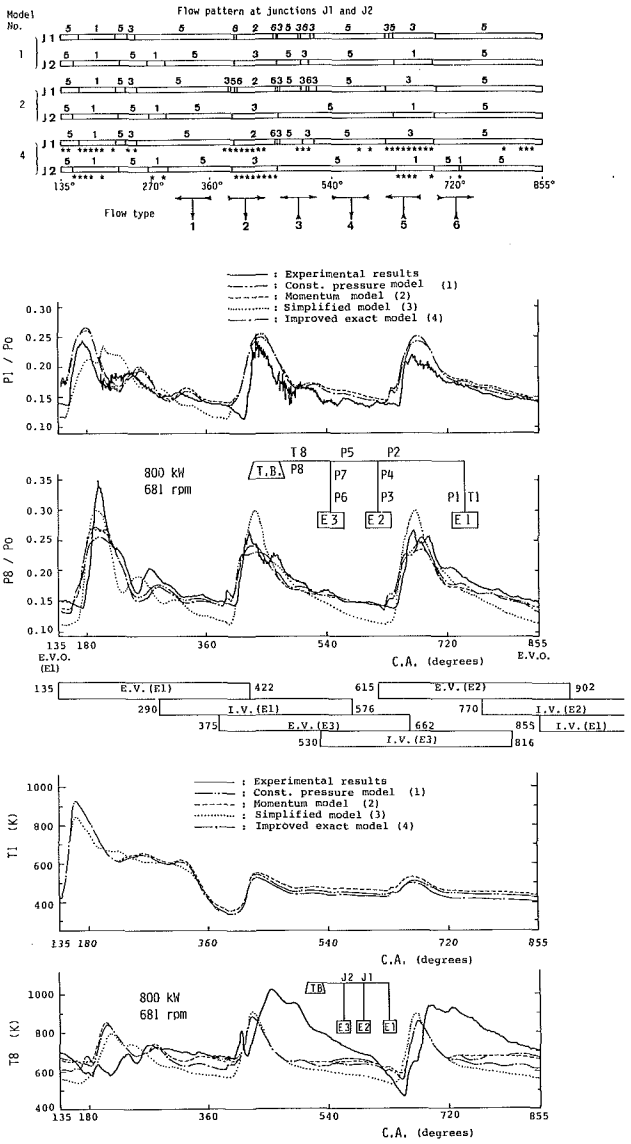


Fig. 3 Exhaust-pipe pressure and temperature (P_1, P_8, T_1, T_8)

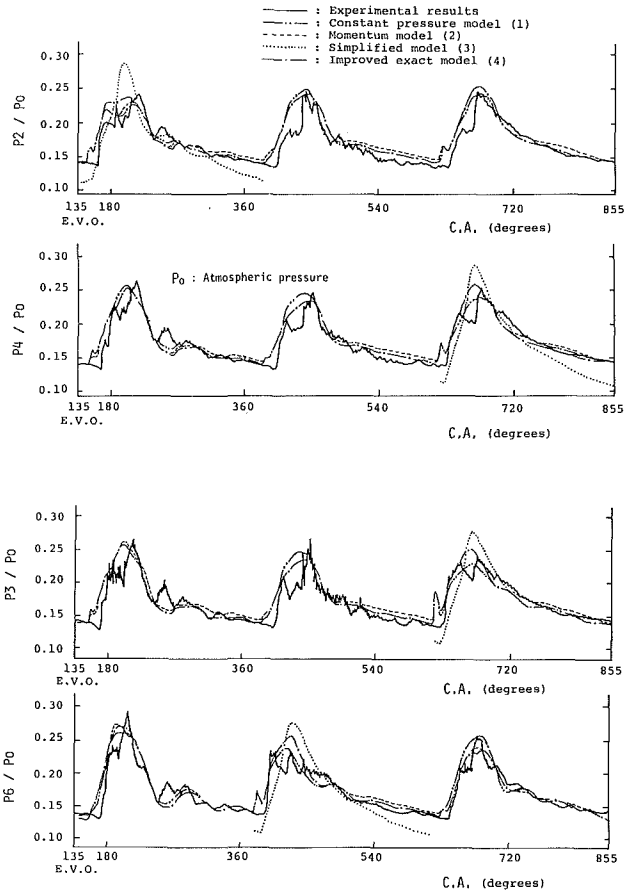


Fig. 4 Exhaust-pipe pressure (P_2, P_3, P_4, P_6)

(*a*) Examination of the results in Figs. 3 and 4 shows that the theoretical diagrams give good agreement with the measured ones except for the results by using the simplified model.

(*b*) The differences between experimental and calculated diagrams by the constant pressure model in the peak pressure region are due to the problematical assumption that the pressure is considered to be equal at the junction in the case of dividing flow. Becasue the flow types at the junction are almost dividing flow types during the peak pressure part as shown in Fig. 3, the constant pressure assumption is not a good one in dividing flow.

(*c*) There are some discrepancies between measurements and computed results by the momentum model in the low-pressure region of the diagrams. These are caused by the unreasonable assumption in which the change in entropy is ignored, which occurs as the flows with different temperatures are joined. The flow type in the low pressure region is mostly a joining flow (type 5).

(*d*) There is poor agreement between experiments and calculations predicted by the simplified model for the junction. The differences in the peak pressure levels are especially remarkable. Moreover, the small reflected waves in the neighborhood of the junctions are not found in diagrams of the simplified model, and the exhaust energy is smaller than that of other models.

(*e*) As for the improved exact model, i.e., the exact model linked up with the momentum model, the results of this computation are similar to those of the momentum model. The best agreement exists between experiments and calculations by the proposed model, particularly for the low-pressure periods as shown in Figs. 3 and 4. This model, however, requires the longest computing time among models for the junction, and the computing mass flow is in good agreement with the measured result (0.1449 kg, one cycle, three cylinders).

The frequency in use of the momentum model is about 30 percent of the total number of time steps when $\delta s = 0.5$ percent. The time steps computed by the momentum model are marked with an asterisk in the upper side of Fig. 3. It is rather difficult to converge the solution, particularly for the dividing flow case, and the momentum model is mainly employed in these cases.

(*f*) As shown in Fig. 3, flow type 5, i.e., fully joining flow, persists over 2/3 of the revolution for the diagrams at the junction. Flow types 1 and 3 occur for about 15 and 12 percent of the revolution, respectively, and flow types 2 and 6 occur for only shorter intervals, while type 4, i.e., the reversely joining flow in the direction of the engine, does not appear in the revolution.

6 Conclusions

1 The improved exact model, i.e., the exact model linked up with the momentum model, has been developed for calculating the behavior of unsteady flow at T-junctions in a turbocharged four-stroke diesel engine exhaust system. This model gives good predictions of pressure, temperature, and mass flow rate as compared to those computed from other

Downloaded 01 Jun 2010 to 171.66.16.87. Redistribution subject to ASME license or copyright; see http://www.asme.org/terms/Terms_Use.cfm

models, while the computer time required by the improved exact model is doubled.

2 Although the simplified model does not calculate the small reflected waves of the engines during the exhaust valve overlap angle, this model should be highly recommended for its simplicity and economy if the optimum initial conditions are introduced in these computations.

3 The momentum model is also an excellent one judging from its short computing time and good agreement with measured values. Moreover, the constant pressure model is the simpler one and is probably sufficiently accurate for practical purposes.

Acknowledgments

The authors wish to acknowledge Niigata Engineering Co., Ltd. for their supply of a diesel engine for some of the experimental work.

References

Azuma, T., Tokunaga, Y., and Yura, T., 1980, "Characteristics of Exhaust Gas Pulsation of Constant Pressure Turbo-Charged Diesel Engines," ASME JOURNAL OF ENGINEERING FOR POWER, Vol. 102, pp. 827–835.

Benson, R. S., et al., 1964, "A Numerical Solution of Unsteady Flow Problems," *Int. J. Mech. Sci.*, Vol. 6, pp. 117–144.

Benson, R. S., 1982a, *The Thermodynamics and Gas Dynamics of Internal Combustion Engine*, Clarendon Press, Oxford, Vol. 1, pp. 424–442.

Bingham, J. F., and Blair, G. P., 1985, "An Improved Branched Pipe Model for Multi-cylinder Automotive Engine Calculation," *Proc. IMechE*, Vol. 199, pp. 65–77.

Ito, H., and Imai, K., 1973, "Energy Losses at 90° Pipe Junctions," *ASCE J. Hyd. Div.*,, Vol. 99, pp. 1353–1368.

Morimune, T., et al., 1980a, "Study of Compressible High Speed Gas Flow in Piping System, 1st Report, Bends and Elbows," Bulletin of the JSME, Vol. 23, pp. 1997–2004.

Morimune, T., et al, 1980b, "Study of Compressible High Speed Gas Flow in Piping System, 2nd Report, Sudden Enlargement," *Bulletin of the JSME*, Vol. 23, pp. 2005–2012.

Morimune, T., et al., 1981, "Study of Compressible High Speed Gas Flow in Piping System, 3rd Report, Junctions," *Bulletin of the JSME*, Vol. 24, pp. 2082–2089.

Morimune, T., et al., 1982a, "Study of Gas Flow in Exhaust System of Actual Turbocharged 4-Cycle Diesel Engine," *Bulletin of the JSME*, Vol. 25, pp. 812–820.

Morimune, T., et al., 1982b, "Study of Gas Flow in Exhaust System of Actual Turbocharged 4-Cycle Diesel Engine, 2nd Part," *Preprints Lect. JSME*, No. 820-3, pp. 73–75.

Morimune, T., et al., 1982c, 1983, "Flow Characteristics Through Poppet Valves of Diesel Engines, Exhaust Valves, Intake Valves," *Preprints Lect. JSME*, No. 820-14, pp. 117–119; No. 830-12, pp. 288–290.

Morimune, T., and Hirayama, N., 1987, "Unsteady Flow at Pipe Junctions," *Trans. JSME*, Vol. 53, Part B, pp. 1925–1930.

Shimamoto, Y., et al., 1977, "Research on Inertia Charging Effects of Multicylinder Engines," *Trans. JSME*, Vol. 43, pp. 2726–2737.

Downloaded 01 Jun 2010 to 171.66.16.87. Redistribution subject to ASME license or copyright; see http://www.asme.org/terms/Terms_Use.cfm

E. C. Miller
Graduate Research Assistant.

M. R. L'Ecuyer
Professor.

Thermal Sciences and Propulsion Center,
School of Mechanical Engineering,
Purdue University,
West Lafayette, IN 47907

E. F. Benisek
Senior Staff Engineer.
Schwitzer Division,
Household International Corporation,
Indianapolis, IN 46206

Flow Field Surveys at the Rotor Inlet of a Radial Inflow Turbine

Experiments were performed using a five-port cobra probe to survey the flow field at the rotor inlet of a 110-mm-dia turbocharger radial inflow turbine wheel. The turbine housing was modified to accommodate a probe insert to position the probe tip 4.1 mm above the rotor tip while preserving the internal contour of the production turbine housing. The cobra probe was traversed axially and circumferentially to determine the rotor inlet flow properties while the turbine was operated at design flow conditions with a reduced turbine inlet temperature. Measurements were made with the probe tip in the near-nulled position to determine the local values of total pressure, static pressure, velocity, and flow angle as functions of Z and θ. Results are presented showing the distribution of the housing total pressure loss coefficient, the rotor inlet mass flux, and the rotor inlet tangential velocity. In addition, values for rotor inlet mass average properties are given.

Introduction

The highly competitive nature of the turbocharger industry has emphasized the need for improving the performance of the radial inflow turbine. One limitation in improving the design of the turbine is the incomplete understanding of the complex flow field inside the turbine housing volute that delivers the angular momentum to drive the turbine wheel. An item of particular interest is the influence of the turbine housing design on the overall turbine stage performance.

The present study was initiated to obtain detailed surveys of the flow field at the inlet of a radial inflow turbine rotor. The experiments were performed using a five-port cobra probe to survey the flow field at the inlet of a 110-mm (4.35 in.) diameter turbine wheel operating at design conditions in a symmetric, open flow turbine housing of 25.8 mm (1.015 in.) A/R. This paper presents the results defining the axial and circumferential distributions of the total pressure, static presure, velocity, flow angle, and mass flux at the rotor inlet and the integrated mass-averaged properties for the rotor inlet flow.

Experimental Apparatus

Turbocharger Gas Stand. The present investigation was conducted with the turbocharger operating on a steady flow gas stand. Air flow to the turbine, supplied by a high-pressure air facility, passed through a pneumatically actuated flow control valve, a combustor, and a mixing/transition section connected to the turbine housing flange. Methanol was burned in the combustor to obtain the desired turbine inlet total temperature and to deliver clean products of combustion required to minimize probe fouling. The turbine discharged into a round exhaust duct that was equipped with a translating conical plug used to maintain a constant turbine exit static pressure throughout the experiments. The turbine housing and exhaust duct were thoroughly insulated to reduce heat loss.

Turbine Housing Instrumentation. The turbine was equipped with conventional instrumentation to measure the turbine inlet and exit flow conditions and rotational speed. The turbine inlet total temperature (T_{01ref}) and total pressure (P_{01ref}) were measured using a combination Kiel total pressure/total temperature probe positioned at the center of the turbine inlet flange (Station 1). The turbine exit static pressure (P_4) was measured by four equally spaced wall static pressure taps installed in the exhaust duct three diameters downstream from the rotor exducer trailing edge. The turbine exit total temperature (T_{04}) was measured by three total temperature probes positioned in the exhaust duct. The turbine gas flow rate was determined from the air and fuel flow rates that were measured using calibrated flat plate orifices. The turbocharger rotational speed was measured using a magnetic pickup and a magnetized washer on the compressor end of the shaft.

A production turbine housing was modified, as shown in Fig. 1, to incorporate the instrumentation used in surveying the flow field at the rotor inlet. The exducer portion of the housing was bored out and a cylindrical sleeve (with a circular flange welded to one end) was welded to the housing. The probe insert (with a large circular flange) was installed with a slip fit so that it rotated freely within the cylindrical sleeve. The probe insert was machined to match the shroud contour of the original production housing. A five-port cobra probe was installed in the probe insert and positioned above the tip of the turbine wheel. The large circular flange on the probe insert supported a probe traversing mechanism that was used to vary the axial position of the probe during the flow survey. The circumferential position of the probe within the turbine housing was varied by rotating the probe insert in 30 deg increments.

The rotor inlet flow field was measured with a five-port

Contributed by the Internal Combustion Engine Division for publication in the JOURNAL OF ENGINEERING FOR GAS TURBINES AND POWER. Manuscript received at ASME Headquarters March 15, 1988.

Copyright © 1988 by ASME
Downloaded 01 Jun 2010 to 171.66.16.87. Redistribution subject to ASME license or copyright; see http://www.asme.org/terms/Terms_Use.cfm

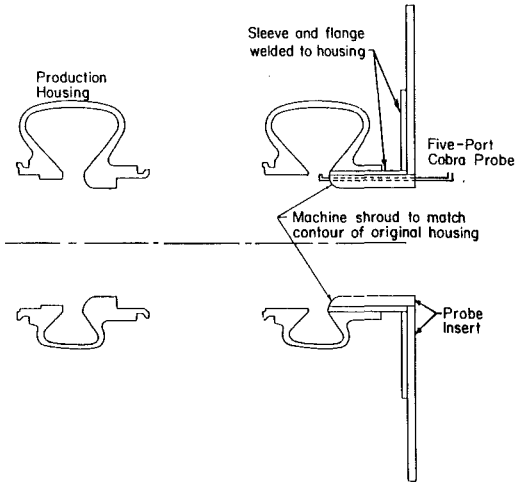


Fig. 1 Turbine housing modification for rotor inlet instrumentation

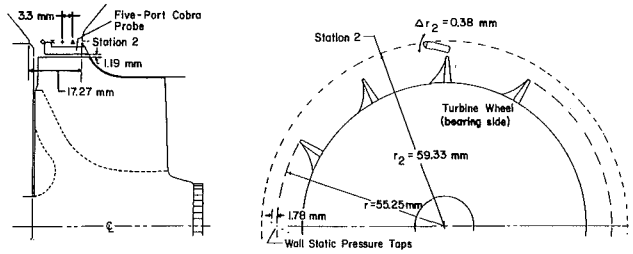


Fig. 2 Cobra probe location for rotor inlet flow survey

cobra probe (United Sensor, DC-093) as illustrated in Fig. 2. The cobra probe had a stem and tip diameter of 2.362 mm (0.093 in.) and a tip length of 8.128 mm (0.320 in.) that resulted in a rotor inlet survey plane (Station 2) at $r_2 = 59.334$ mm (2.336 in.), a distance of 4.1 mm (0.161 in.) above the rotor tip. The five-port cobra probe was calibrated in a free jet (for a Mach number range of 0.35 to 0.80) so that the total pressure, static pressure, pitch angle, and yaw angle of an unknown flow were determined from the five pressure measurements.

The probe insert also was instrumented with four wall static pressure taps (see Fig. 2) to measure the radial variation of the shroud wall static pressure in the vicinity of the rotor tip.

Figure 3 illustrates the turbine stations (1, 2, 3) defined for

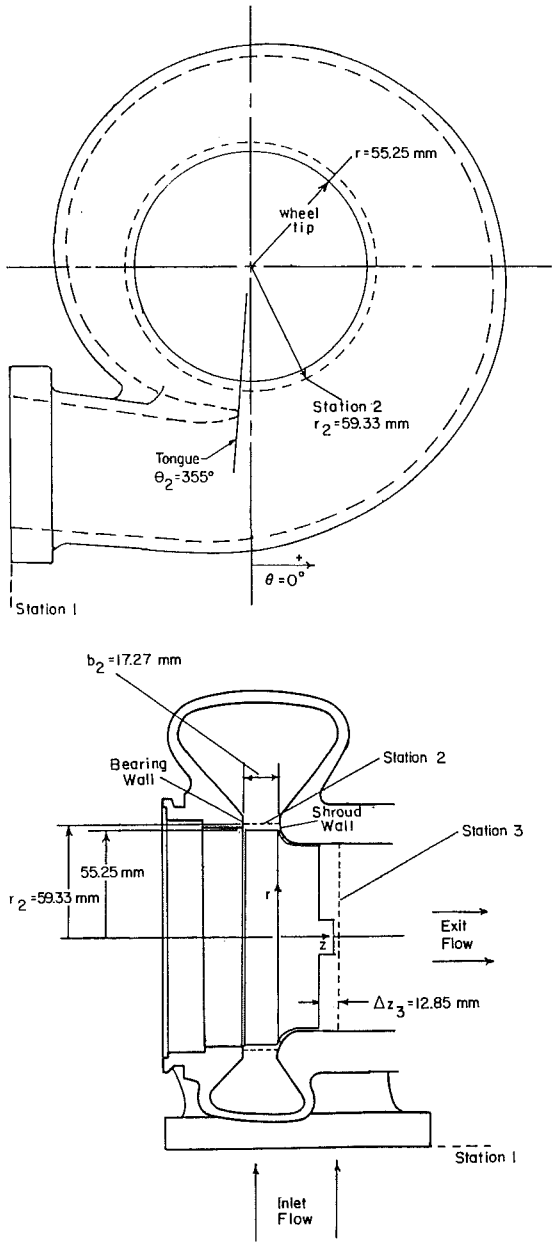


Fig. 3 Coordinate system

Nomenclature

A = turbine housing volute cross-sectional area
DMF = differential mass flow parameter
K_θ = scroll coefficient
$\dot{m}$ = mass flow rate
N = rotational speed
P_0 = stagnation or total pressure
P = static pressure
R = centroid radius of turbine housing volute cross sectional area
r = radial coordinate
T_0 = stagnation or total temperature
U = rotor velocity
V_m = meridional velocity
V_θ = tangential component of absolute velocity
V_r = radial component of absolute velocity
V_z = axial component of absolute velocity
W = relative velocity
Z = axial coordinate
$Z_{2\max}$ = axial width at rotor inlet survey station = 17.27 mm (0.680 in.)
α = absolute flow angle, referenced to radial direction
β = relative flow angle, referenced to radial direction
δ = meridional flow angle
θ = circumferential coordinate
ρ = density
ψ_{Nref} = housing total pressure loss coefficient = $(P_{01\text{ref}} - P_{02})/(P_{02} - P_2)$
$\bar{(\ )}$ = mass average value

Subscripts

$(\ )_1$ = turbine inlet flange
$(\ )_{1\text{ref}}$ = turbine inlet flange centerline
$(\ )_2$ = rotor inlet survey station
$(\ )_3$ = rotor exit station
$(\ )_4$ = turbine exit station
$(\ )_{\text{th}}$ = turbine housing volute throat cross section

Downloaded 01 Jun 2010 to 171.66.16.87. Redistribution subject to ASME license or copyright; see http://www.asme.org/terms/Terms_Use.cfm

Table 1 Volute cross-sectional area

Θ_2	A/A_{th}	Θ_2	A/A_{th}
355°	1.0	180	0.515
30°	0.919	210	0.435
60	0.839	240	0.354
90	0.758	270	0.273
120	0.677	300	0.192
150	0.596	330	0.112

the flow field surveys and the right-hand cylindrical coordinate system used to describe the rotor inlet flow field. The tongue was located at $\theta_2 = 355$ deg, where the measured volute throat cross-sectional area was $A_{th} = 24.6$ cm^2 (3.81 in.^{2}) and the centroid radius of the throat area was $R = 95.3$ mm (3.753 in.) defining the turbine housing A_{th}/R as 25.8 mm (1.015 in.). Table 1 presents the circumferential variation of the volute cross-sectional area.

Experimental Procedure. The experiments were performed with the turbine operating at the following conditions:

T_{01ref} = 499.6 K (899 R), $\bar{T}_{01}$ = 497 K (895 R)
P_{01ref} = 207.4 kPa (61.25 in. Hg abs)
N = 50,000 rpm
P_4 = 108.4 kPa (32.00 in. Hg abs)

The reduced turbine inlet total temperature and the thermal insulation were used to minimize heat loss from the turbine housing allowing the rotor inlet total temperature (T_{02}) to be assumed equal to the mass-averaged turbine inlet total temperature ($\bar{T}_{01}$). The reduced temperature also minimized instrumentation problems and permitted operation at a moderate turbine rotor speed while simulating a rotor speed-to-isentropic jet speed ratio of 0.7.

The rotor inlet flow survey was performed by traversing the cobra probe to four different axial positions (see Fig. 2(*a*)) at each of twelve circumferential locations. The axial positions were spaced at equal intervals of 3.30 mm (0.130 in.) starting at 3.30 mm (0.130 in.) from the shroud wall. At each axial location the probe was rotated about the stem (see Fig. 2(*b*)) until the yaw ports were in the near-nulled position. Near nulled was defined by a yaw port pressure difference less than ±1.49 kPa (±6 in. H_20), which corresponded to a probe tip angle that was within 1 deg of the flow angle in the yaw direction. Nulling of the yaw pressure ports at each measurement point resulted in a radial variation of 0.38 mm (0.015 in.) of the location of Station 2. When the probe tip was set in the near-nulled position, the probe angle was read from a protractor attached to the probe stem and the pressure data were recorded using differential pressure transducers and a datalogger. Preliminary experiments were performed to compare the rotor inlet total pressure measured with the five-port cobra probe to the total pressure measured with a miniature Kiel probe. The results were in good agreement when the five-port probe was set in the near-nulled position. The experimental apparatus and procedure are described in greater detail by Miller and L'Ecuyer (1985).

Experimental Results

Static Pressure. Static pressure measurements at the rotor

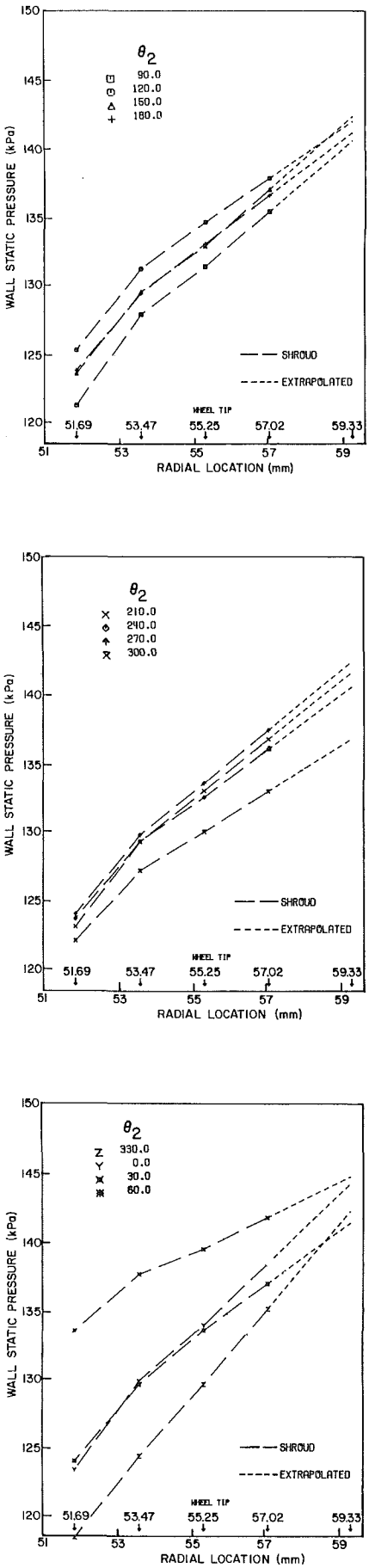


Fig. 4 Radial distribution of shroud wall static pressure

Downloaded 01 Jun 2010 to 171.66.16.87. Redistribution subject to ASME license or copyright; see http://www.asme.org/terms/Terms_Use.cfm

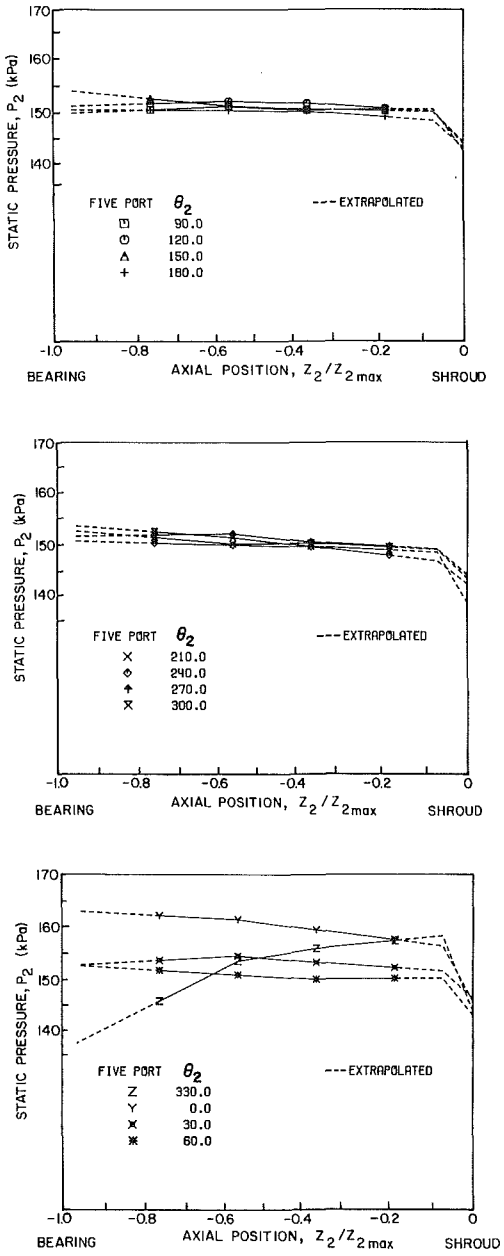


Fig. 5 Axial distribution of rotor inlet static pressure

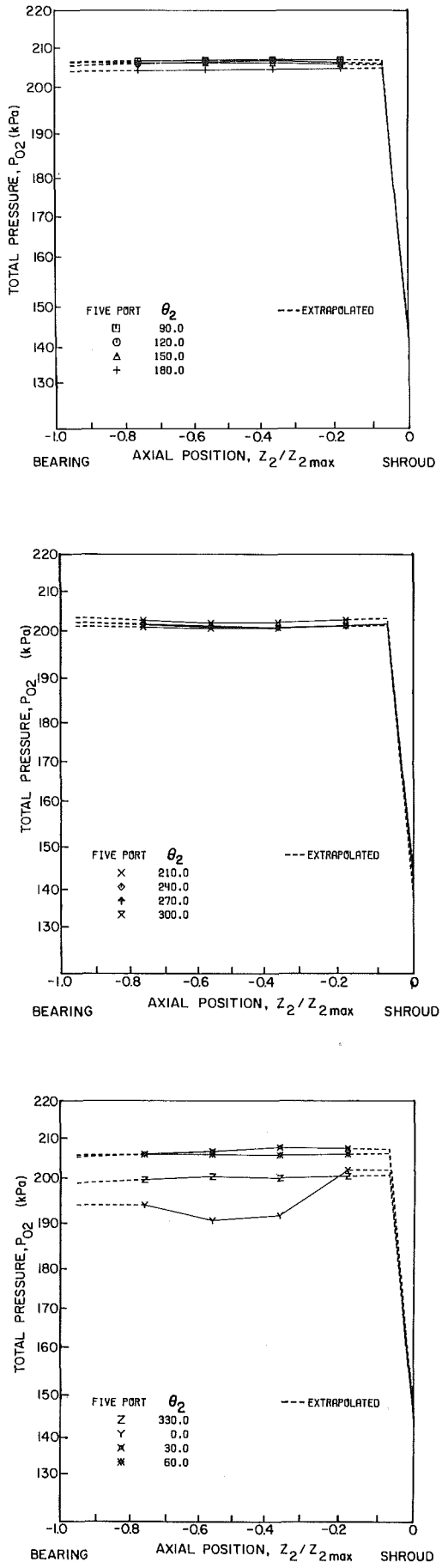


Fig. 6 Axial distribution of rotor inlet total pressure

inlet were made with both the calibrated cobra probe and wall static taps on the shroud wall. Figures 4(*a*) through 4(*c*) present the results from the shroud wall static pressure measurements. The data show that the wall static pressure increased approximately linearly with radius. Space limitations within the turbine and the probe insert precluded the location of wall static taps at r_2, the probe measurement location. Consequently, it was necessary to extrapolate the data measured by the four shroud wall static pressure taps (see Figs. 4(*a*)–4(*c*)) to estimate the wall static pressure at Station 2.

Figures 5(*a*) through 5(*c*) show the axial distribution of the core static pressure at Station 2 as measured by the cobra probe for select circumferential locations (θ_2). For the range $\theta_2 = 60$ to 300 deg, the core static pressure was approximately constant with respect to θ_2 and Z_2. In the tongue region, $\theta_2 = 330$ to 30 deg, the data show a significant change in the level of the core static pressure and a stronger variation with respect to Z_2.

To approximate the static pressure distribution across the

Downloaded 01 Jun 2010 to 171.66.16.87. Redistribution subject to ASME license or copyright; see http://www.asme.org/terms/Terms_Use.cfm

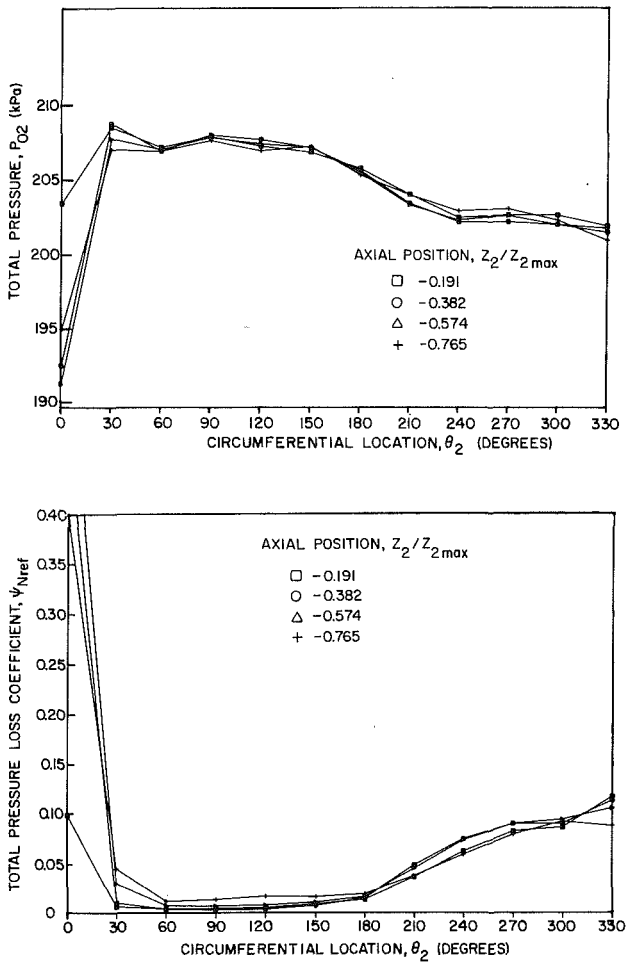


Fig. 7 Circumferential distribution of rotor inlet total pressure and total pressure loss coefficient

entire wheel tip, values of the shroud wall static pressure (estimated by the extrapolation in Figs. 4(*a*)-4(*c*)) are presented in Figs. 5(*a*) through 5(*c*) at $Z_2/Z_{2max} = 0$. The core values of static pressure measured by the cobra probe were linearly extrapolated toward the walls to *edge values* at $Z_2/Z_{2max} = -0.074$ and -0.964 (see dashed lines in Figs. 5(*a*)-5(*c*)). The data show extrapolated shroud wall static pressure values that are consistently 6.8 to 10.5 kPa (2 to 3 in. Hg) lower than the core static pressure edge values. This variation of the static pressure near the shroud wall was attributed to streamline curvature effects and flow area change in the extrapolation region of Figs. 4(*a*)-4(*c*). A calculation of the axial pressure gradient near the shroud wall (radius of curvature = 12.7 mm) showed a static pressure increase due to streamline curvature of 4.1 kPa (1.2 in. Hg) over the distance $Z_2/Z_{2max} = 0$ to -0.191 (Miller and L'Ecuyer, 1985).

Total Pressure. Figures 6(*a*) through 6(*c*) present the rotor inlet total pressure distribution as measured by the cobra probe. The data show that the axial variation of P_{02}, across the wheel tip, did not exceed ± 1.69 kPa (± 0.50 in. Hg) for all circumferential locations except $\theta_2 = 0$ deg. In that region (downstream from the tongue), the rotor inlet total pressure was substantially lower and exhibited more axial variation.

To approximate the total pressure distribution across the entire wheel tip, the total pressure at the shroud wall in Figs. 6(*a*), 6(*b*), and 6(*c*) was set equal to the shroud wall static pressure from Figs. 5(*a*), 5(*b*), and 5(*c*). The core values of total pressure measured by the cobra probe were linearly ex-

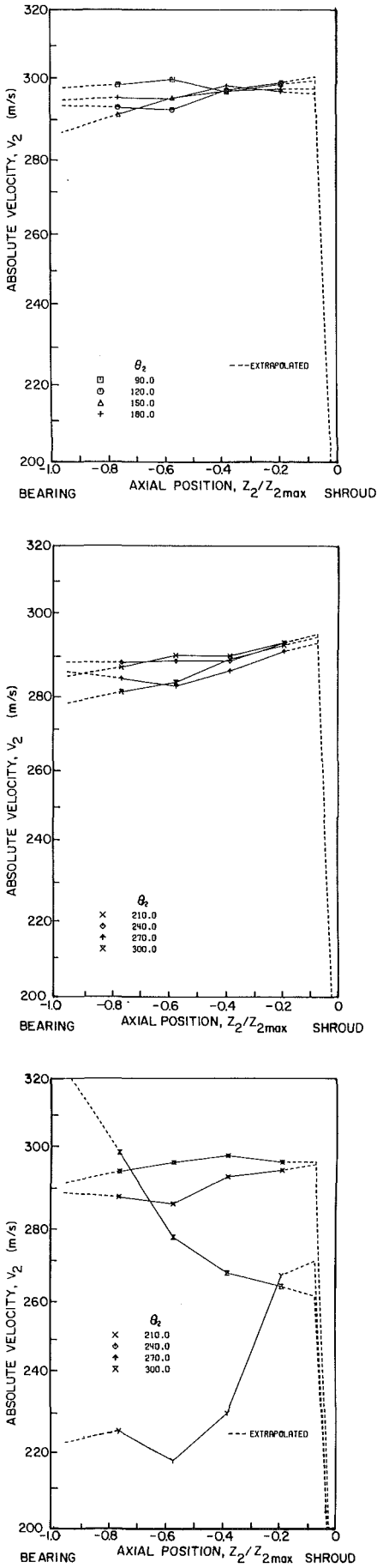


Fig. 8 Axial distribution of rotor inlet absolute velocity

Downloaded 01 Jun 2010 to 171.66.16.87. Redistribution subject to ASME license or copyright; see http://www.asme.org/terms/Terms_Use.cfm

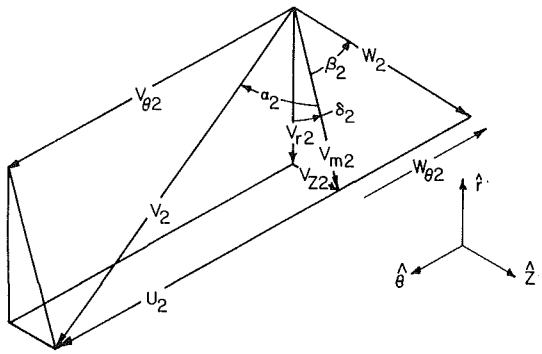
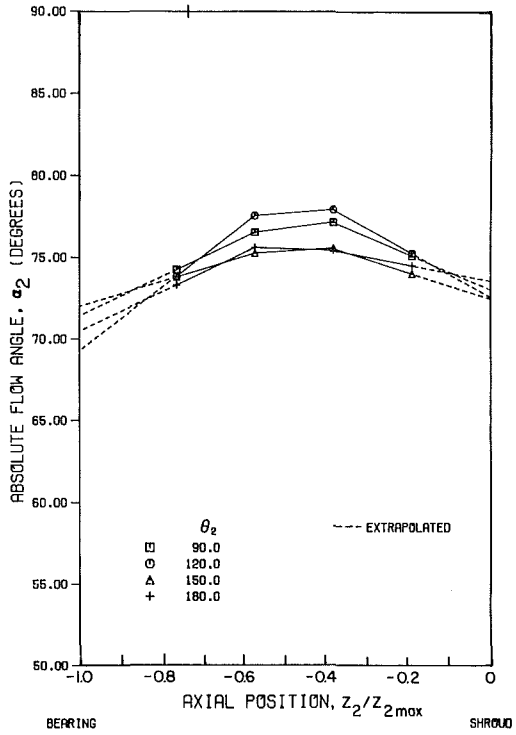
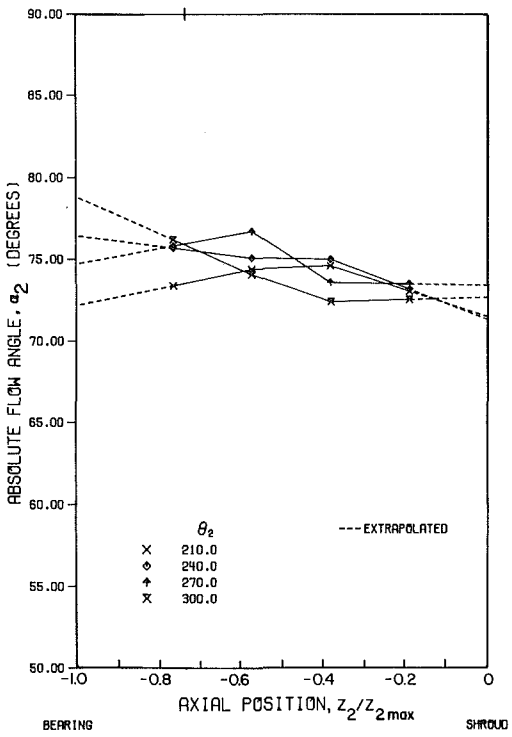


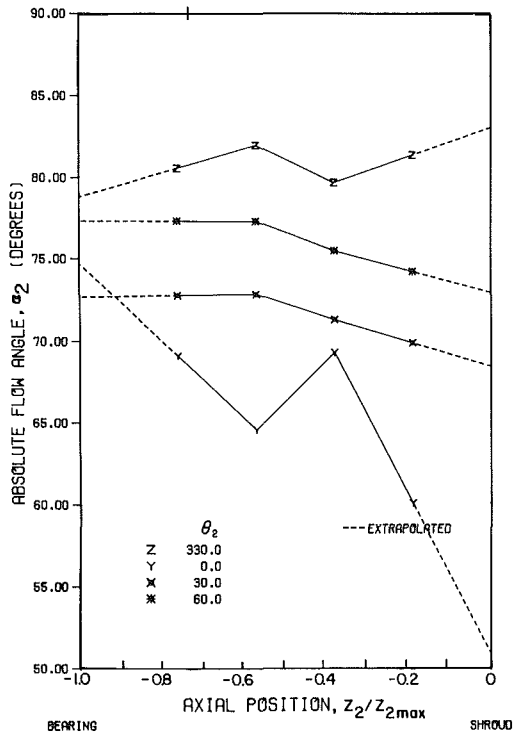
Fig. 9 Rotor inlet velocity and flow angle definition



(a)



(b)



(c)

Fig. 10 Axial distribution of rotor inlet absolute flow angle

trapolated toward the walls to *edge values* at $Z_2/Z_{2max} = -0.074$ and -0.964.[1]

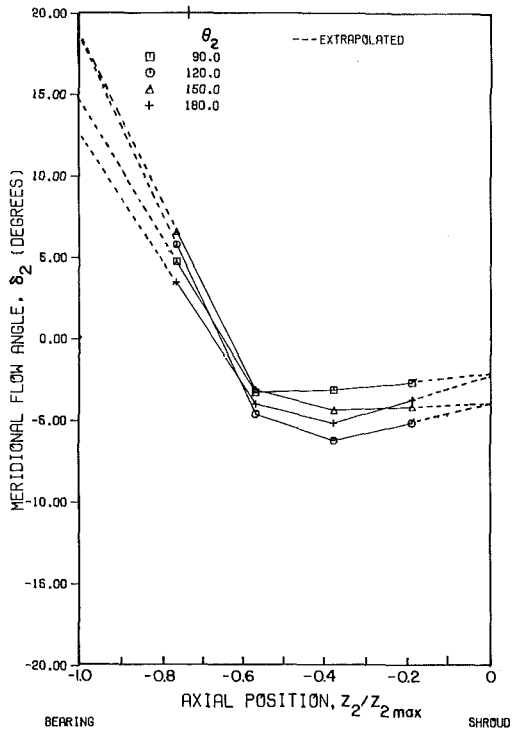
Figure 7(*a*) shows the circumferential distribution of the core total pressure at the rotor inlet. A gradual decrease in total pressure from 207.4 to 201.5 kPa (61.25 to 59.5 in. Hg) can be seen in the region from $\theta_2 = 30$ to 330 deg. The low total pressure in the tongue region ($\theta_2 = 330$ to 30 deg) is evident. Figure 7(*b*) gives the circumferential distribution of the total pressure loss coefficient, with $(P_{01ref} - P_{02})$ normalized by the rotor inlet dynamic head, $P_{02} - P_2$. The total pressure loss coefficient increased slightly (from 0.01 to 0.02) from $\theta_2 = 60$ to 180 deg, and then increased more rapidly from $\theta_2 = 180$ to 330 deg, to a level of 0.11. At $\theta_2 = 0$ deg, the loss coefficient varied from 0.10 near the shroud wall to 0.56 at $Z_2/Z_{2max} = -0.574$.

Absolute Velocity. Figures 8(*a*) through 8(*c*) show the core values of absolute velocity (V_2) calculated from the cobra probe total and static pressure measurements. The edge values of V_2 were calculated from the extrapolated values of total and static pressure presented above. The core values of velocity were nearly uniform axially and circumferentially (280 to 297 m/s) (920 to 975 ft/sec) except in the tongue region where significant circumferential and axial velocity variations were observed.

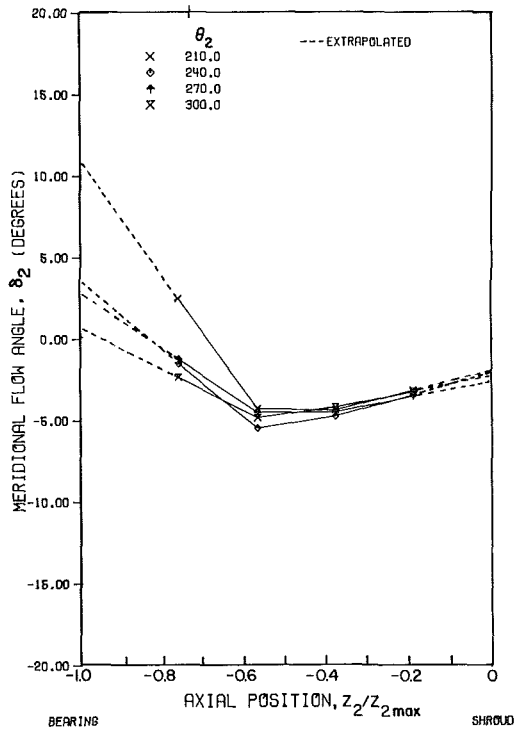
Flow Angles. The cobra probe was set in the near-nulled position and the pitch port and yaw port pressure differences were used (in conjunction with the probe calibration) to deter-

[1] The edge coordinates, $Z_2/Z_{2max} = -0.074$ and -0.964, were determined from preliminary measurements of P_{02} with a miniature impact tube (0.80 mm dia) to define the extent of the core flow.

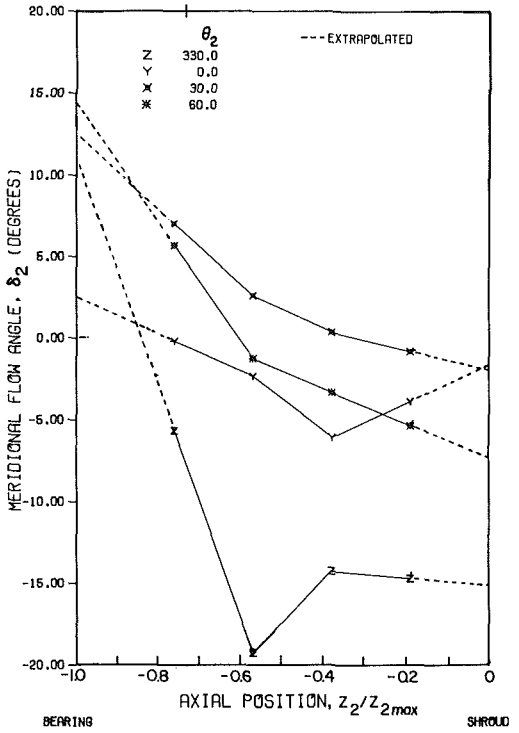
Downloaded 01 Jun 2010 to 171.66.16.87. Redistribution subject to ASME license or copyright; see http://www.asme.org/terms/Terms_Use.cfm



(a)



(b)



(c)

Fig. 11 Axial distribution of rotor inlet meridional flow angle

mine the pitch and yaw angles of the flow with respect to the probe tip. The probe setting angle and the pitch and yaw angles were then used to determine the rotor inlet absolute flow angle (α_2), meridional flow angle (δ_2), and relative flow angle (β_2), with the angles shown in Fig. 9 defined as positive. Figures 10(*a*) through 10(*c*) present the distribution of the rotor inlet absolute flow angle, showing that α_2 was relatively constant near 75 deg for $\theta_2 = 90$ to 300 deg. Just downstream of the tongue, the data at $\theta_2 = 0$ deg show values of α_2 from 60 to 70 deg indicating that the flow was more radial in that region.

Figures 11(*a*) through 11(*c*) present the meridional flow angle distribution, illustrating that δ_2 varied in the range of ± 5 deg except at $\theta_2 = 330$ deg, where an extreme value of -20 deg was observed.

Figures 12(*a*) through 12(*c*) show the relative flow angle distribution (β_2), which also corresponds to the *rotor incidence angle* since, in the present study, the rotor vanes were radial. The values of β_2 varied in the range of 0 to 5 deg for $\theta_2 = 90$ to 180 deg, and 3 to 13 deg for $\theta_2 = 210$ to 300 deg. In the tongue region ($\theta_2 = 330$ to 30 deg), β_2 varied from 10 to 45 deg.

Rotor Inlet Mass Flow. The distributions of flow properties at the rotor inlet, presented above, were used to determine the rotor inlet mass flow distribution given by

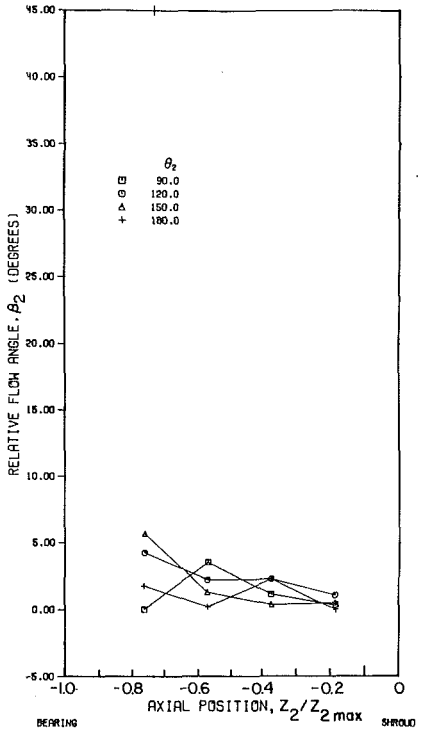
$$d\dot{m}_2 = \rho_2 V_2 \cos \alpha_2 \cos \delta_2 \, r_2 \, dZ \, d\theta$$

The flow properties determined from the flow survey were used to calculate a differential mass flow parameter (DMF_2) defined as

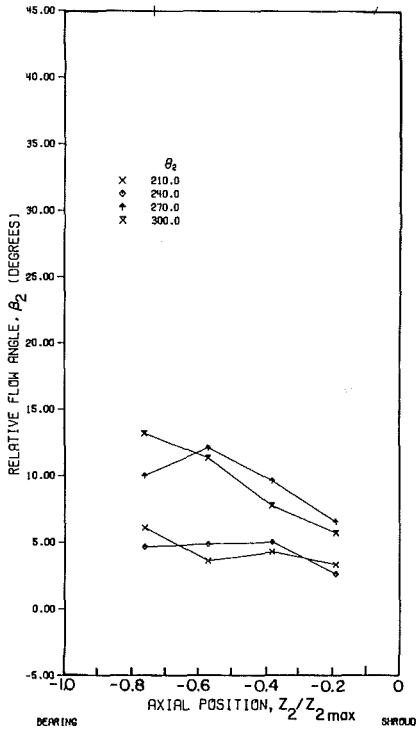
$$DMF_2 = \rho_2 \, V_2 \cos \alpha_2 \cos \delta_2 \, r_2$$

Figure 13 shows the distribution of the differential mass flow parameter calculated from the flow properties measured for the core flow and the edge values obtained by linear extrapolation of the data. The results illustrate that DMF_2 was relatively constant from $\theta_2 = 60$ to 300 deg. In the region upstream from the tongue ($\theta_2 = 330$ deg), the value of DMF_2 was noticeably lower, while downstream from the tongue ($\theta_2 = 0$ deg) the value of DMF_2 was substantially higher near the shroud wall. These trends are illustrated further in Fig. 14, which presents a three-dimensional carpet plot of the radial velocity component (V_{r2}). Larger values of radial velocity component are observed near the shroud wall in the vicinity of the tongue. This is largely due to a 10 to 15 deg reduction in the absolute flow angle in the shroud wall/tongue region, which results in an increase of V_{r2} of approximately 80 percent.

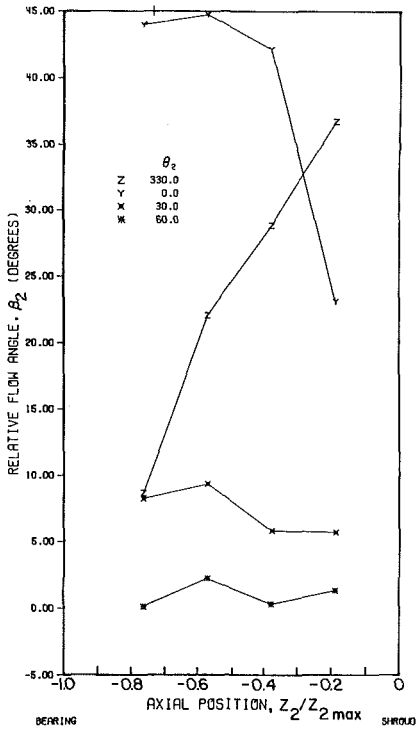
Downloaded 01 Jun 2010 to 171.66.16.87. Redistribution subject to ASME license or copyright; see http://www.asme.org/terms/Terms_Use.cfm



(a)



(b)



(c)

Fig. 12 Axial distribution of rotor inlet relative flow angle

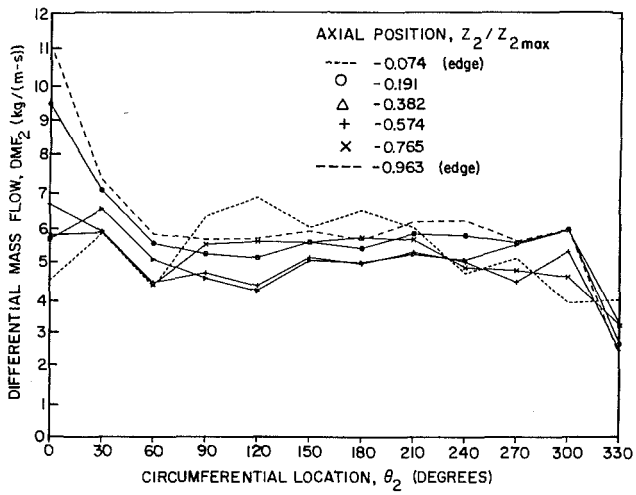


Fig. 13 Circumferential distribution of rotor inlet differential mass flow parameter

The differential mass flow parameter was integrated over the rotor inlet survey plane to calculate the rotor inlet mass flow rate

$$\dot{m} = \int_{\theta=0}^{2\pi} \int_{Z=0}^{-17.27\ \text{mm}} \text{DMF}_2 DZ\, d\theta$$

The results of the mass flow integration yielded $\dot{m}_{\text{integ}} = 0.54$ kg/s (1.19 lbm/sec), which was 3 percent lower than the measured turbine inlet mass flow rate, $\dot{m}_{\text{meas}} = 0.56$ kg/s (1.23 lbm/sec). The agreement between the calculated and the measured turbine mass flow rates is one indication of the validity of the extrapolation of flow properties to edge coordinates near the walls.

Scroll Coefficient. The distributions of the rotor inlet absolute velocity and flow angle were used to calculate the rotor inlet tangential velocity component ($V_{\theta 2}$). The tangential velocity component then was used to characterize the rotor inlet angular momentum by defining a scroll coefficient

$$K_\theta = (r_2 V_{\theta 2})/(R\ V_{th})$$

The turbine housing throat velocity, $V_{th} = 179.0$ m/s (587.3 ft/sec), was calculated from the measured turbine inlet flow conditions and the measured throat area, $A_{th} = 24.6$ cm^2 (3.81 in.^{2}), assuming a 10 percent area reduction due to blockage.

Figure 15 presents the circumferential distribution of the core flow scroll coefficient, showing K_θ decreasing from 1.0 to

Downloaded 01 Jun 2010 to 171.66.16.87. Redistribution subject to ASME license or copyright; see http://www.asme.org/terms/Terms_Use.cfm

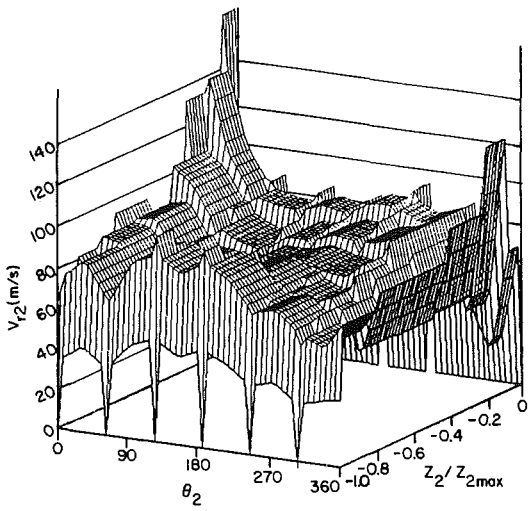


Fig. 14 Rotor inlet radial velocity distribution

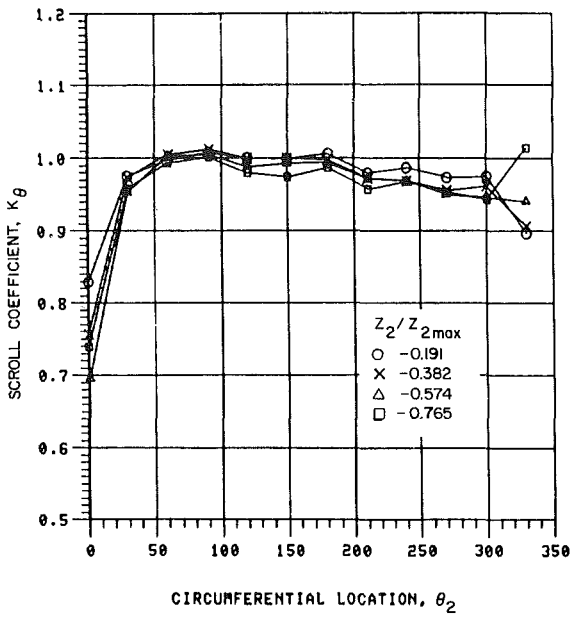


Fig. 15 Rotor inlet scroll coefficient

0.96 for the region $\theta_2 = 60$ to 300 deg. The values of K_θ near the shroud wall were 0.01 to 0.03 higher than the values near the bearing wall. In the tongue region, K_θ varied more strongly with θ_2 and Z_2, indicating values as low as 0.7 at $\theta_2 = 0$ deg.

Mass-Averaged Properties. The distribution of the rotor inlet mass flow parameter DMF_2 was used to calculate the mass-averaged value $\bar{X}_2$ of a given property X_2.

$$\bar{X}_2 = \iint X_2 \mathrm{DMF}_2 dZ\, d\theta / \iint \mathrm{DMF}_2\, dZ\, d\theta$$

For illustration, the mass-averaged value $\bar{X}_2$ was calculated: (*a*) using the entire rotor inlet profile of X_2 and DMF_2 (with extrapolation to edge and wall values), and (*b*) using only the core flow values of the select property and DMF_2. The results of the mass-average calculations are presented in Table 2. Generally, the mass-averaged properties based on the core flow values were in reasonable agreement with the properties derived from the entire rotor inlet profile. However, the total pressure loss and total pressure loss coefficient were 26 percent lower when based on core flow values only.

Table 2 Rotor inlet mass-averaged properties

Property	Entire Profile	Core Only
P_{02} (kPa abs)	203.0	204.1
P_2 (kPa abs)	151.1	151.6
V_2 (m/s)	280.6	285.4
V_{r2} (m/s)	78.7	77.6
$V_{\Theta 2}$ (m/s)	268.4	274.0
W_2 (m/s)	88.8	81.5
α_2 (degrees)	73.4	74.0
β_2 (degrees)	8.9	9.0
K_Θ	0.934	0.953
$P_{01ref} - P_{02}$ (kPa)	4.44	3.28
Ψ_{Nref}	0.085	0.063

Discussion

The rotor inlet flow measurements in this study were performed using a 2.362-mm-dia five-port probe in a turbine housing having a 17.27 mm axial width at the rotor inlet survey station. The probe was calibrated in a free jet and the rotor inlet flow properties were determined using the free jet calibration. It is expected that use of this probe in such a narrow flow channel may introduce calibration errors due to probe blockage and wall-proximity effects. To minimize these errors, the probe measurements were obtained with: (*a*) the probe in the near-nulled position (within 1 deg) and (*b*) the probe tip no closer than 1.4 diameters from the walls. The validity of determining rotor inlet flow properties, without quantitative corrections to the free jet probe calibration, was checked by preliminary experiments with a miniature Kiel probe, a miniature impact tube, and the five-port probe. The results showed good agreement of the rotor inlet total pressure measured by the three probes. Use of the five-port probe in the near-nulled position is expected to yield accurate measurements of the absolute flow angle (α_2). However, the static pressure (P_2) and the meridional flow angle (δ_2) are expected to be the most influenced by probe calibration errors, and it is expected that probe blockage and wall-proximity effects may be partially responsible for the stronger variation of P_2 and δ_2 indicated in the tongue region ($\theta_2 = 0$ and 330 deg). One indication of the validity of the rotor inlet flow properties reported is the good agreement obtained between the measured turbine mass flow rate and the flow rate calculated by integrating the rotor inlet flow properties.

An approximation of the distribution of the rotor inlet properties across the entire wheel tip was obtained by shroud wall static pressure measurements and extrapolation of the measured core flow values. While these extrapolated profiles were necessary to obtain good agreement between the measured and calculated turbine mass flow rates, they had no effect on any of the flow properties reported for the core flow.

Similar measurements of rotor inlet flow properties have been reported by Scrimshaw and Williams (1984) for a 101.6-mm-dia turbine rotor with a nonsymmetric turbine volute. Figure 16 illustrates a comparison of data for the rotor inlet total pressure loss at $Z_2/Z_{2max} = 0.5$ in terms of the loss coefficient, $(P_{01ref} - P_{02})/(P_{01ref} - P_4)$, as defined by Scrim-

Downloaded 01 Jun 2010 to 171.66.16.87. Redistribution subject to ASME license or copyright; see http://www.asme.org/terms/Terms_Use.cfm

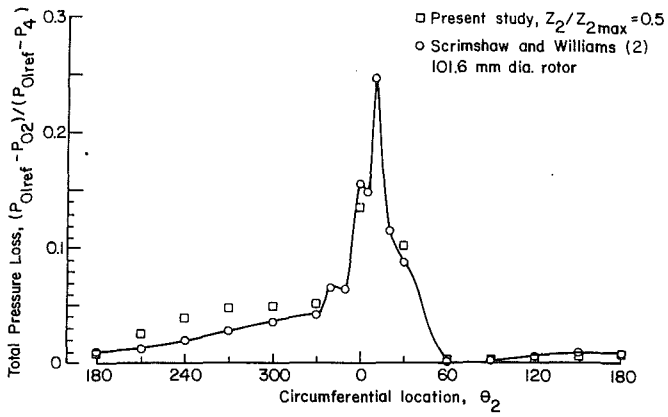


Fig. 16 Comparison of rotor inlet total pressure loss data

Table 3 Comparison of rotor inlet total pressure loss data

	$(P_{01ref}-P_{02})/P_{01ref}$		$(P_{01ref}-P_{02})/(P_{01ref}-P_4)$	
Θ_2	Present Study ($Z_2/Zmax=0.5$)	Hussain et al. (1982) (Figure 7)	Present Study	Hussain et al. (1982)
0	0.0654	0.006	0.1372	0.018
30	0.0049		0.0103	
60	0.0016	0.006	0.0034	0.018
90	0.0016		0.0034	
120	0.0020		0.0041	
150	0.0029	0.007	0.0062	0.021
180	0.0041		0.0086	
210	0.0123		0.0257	
240	0.0188	0.008	0.0394	0.024
270	0.0226		0.0473	
300	0.0232		0.0487	
330	0.0245	0.009	0.0514	0.027

shaw and Williams. Data from the present study show rotor inlet total pressure loss values that are noticeably higher for $\theta_2 = 210$ to 300 deg. However, the agreement between the two sets of data is generally good considering the difference in the volute cross-sectional shape and turbine expansion ratio. Unfortunately, data were not obtained at $\theta_2 = 15$ deg to corroborate the maximum total pressure loss observed by Scrimshaw and Williams.

Table 3 illustrates a comparison of the rotor inlet total pressure loss from the present study with the data of Hussain et al. (1982). Evaluation of the data in terms of the loss parameter defined by Hussain et al., $(P_{01ref} - P_{02})/P_{01ref}$, shows values in the low loss region ($\theta_2 = 60$ to 180 deg) that are approximately one-half to one-third of the magnitudes reported by Hussain et al. However, the peak levels of loss observed in the present study are approximately two to three times larger than reported by Hussain et al. When the rotor inlet total pressure loss is expressed in terms of the loss parameter defined by Scrimshaw and Williams (1984), using the expansion ratio ($P_{01ref}/P_4 = 1.5$) for the Hussain data, the comparison shown in Table 3 is somewhat improved. However, the loss data reported by Hussain et al. (1982) are substantially higher in the range $\theta_2 = 60$ to 150 deg and substantially lower in the range $\theta_2 = 240$ to 360 deg.

An examination of the data for rotor inlet absolute flow angle reported by Scrimshaw and Williams (1984) (Fig. 6(*ii*)) shows values of α_2 that are approximately constant at 85–86 deg for $\theta_2 = 60$ to 360 deg. In the present study ($Z_2/Z_{2max} = 0.5$), α_2 was observed to decrease approximately linearly from 77 deg (at $\theta_2 = 90$ deg) to 73 (at $\theta_2 = 300$ deg). The difference in the magnitudes of α_2 is attributed to a difference in the A/R for the two turbine housings.

Conclusions

This survey of the flow field at the rotor inlet of a radial inflow turbine showed that the core flow properties measured with a five-port cobra probe (static pressure, total pressure, velocity, flow angle, mass flux, tangential velocity) were generally uniform in the axial direction and around the turbine housing for $\theta_2 = 60$ to 300 deg. In that region the rotor incidence angle increased from 0 to 13 deg. In the tongue region, $\theta_2 = 330$ to 30 deg, significant variations in velocity and absolute flow angle resulted in an increase in the mass flux into the rotor. The axial variation of the flow properties near the shroud wall was inferred from wall static pressure measurements and extrapolation of core flow values. The rotor inlet mass flow rate determined by integrating the mass flux distribution agreed with the orifice measured mass flow rate within 3 percent. The rotor inlet mass flux distribution was used to calculate mass-averaged rotor inlet properties for the turbine housing showing a 26 percent decrease in the housing integrated total pressure loss coefficient when the wall regions are ignored.

Acknowledgments

This work was sponsored by Schwitzer Division, Household International Corporation, Indianapolis, IN. The authors are indebted to Mr. W. A. Spraker, Jr., Manager, Turbomachinery Aerodynamics, Schwitzer, for his many contributions throughout the investigation.

References

Hussain, M., Ilyas, M., and Bhinder, F. S., 1982, "A Contribution to Designing a Nozzle-less Volute Casing for the Inward Flow Radial Gas Turbine," *Turbocharging and Turbochargers*, IMechE Conference, Paper No. C35/82.

Miller, E. C., and L'Ecuyer, M. R., 1985, "Flow Field Surveys at the Inlet and Exit of a Radial Inflow Turbine Rotor," Technical Report No. ME-TSPC-TR-85-12, Thermal Sciences and Propulsion Center, Purdue University, West Lafayette, IN.

Scrimshaw, K. H., and Williams, T. J., 1984, "Size Effects in Small Radial Turbines," ASME Paper No. 84-GT-215.

Downloaded 01 Jun 2010 to 171.66.16.87. Redistribution subject to ASME license or copyright; see http://www.asme.org/terms/Terms_Use.cfm

ERRATA

Errata for "The Design and Development of an Advanced Heavy-Duty Gas Turbine" by D. E. Brandt, published in the April 1988 issue of the ASME JOURNAL OF ENGINEERING FOR GAS TURBINES AND POWER, Vol. 110, pp. 243–250:

The photographs below were omitted from the first printing of the issue. They were included in subsequent printings.

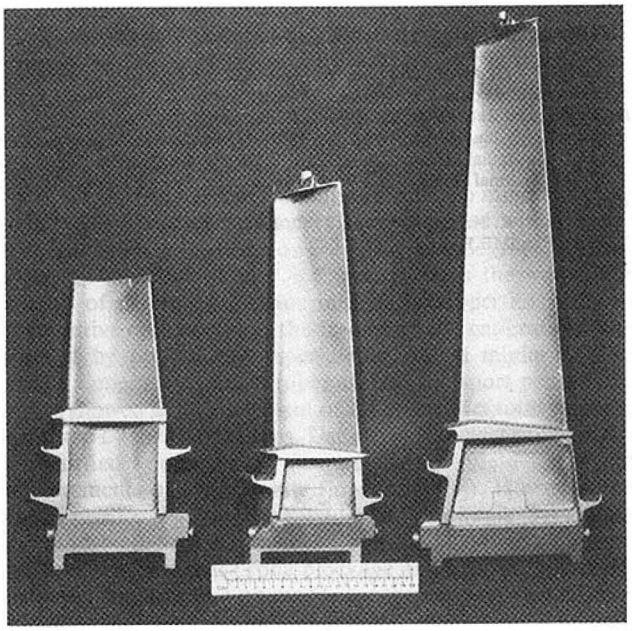


Fig. 6 Buckets

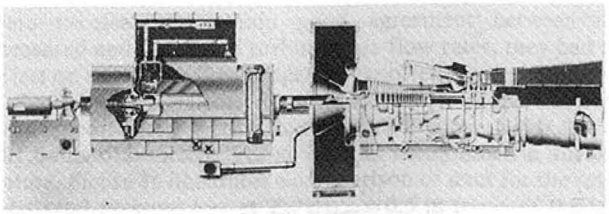


Fig. 16 MS7001F arrangement

Copyright © 1988 by ASME
Downloaded 01 Jun 2010 to 171.66.16.87. Redistribution subject to ASME license or copyright; see http://www.asme.org/terms/Terms_Use.cfm